

**Dual and targeted photodynamic therapy ablation of
bacterial and cancer cells using phthalocyanines and
porphyrins in the presence of carbon-based nanomaterials**

By

Yolande Ikala Openda

A thesis submitted in fulfillment of the requirements for the degree of

DOCTOR OF PHILOSOPHY

At

Rhodes University



RHODES UNIVERSITY

Where leaders learn

June 2022

Declaration

I declare that the thesis: “**Dual and targeted photodynamic therapy ablation of bacterial and cancer cells using phthalocyanines and porphyrins in the presence of carbon-based nanomaterials**” is my original work and has not been submitted elsewhere for examination. Where other people’s work has been cited, this has properly been acknowledged and referenced following Rhodes University’s requirements.

Signature:



Date:22/06/2022.....

Yolande IKALA OPENDA

(Student number: G19O8266)

Dedication

In Memory of My Mother

Léa MUIBU KABANGA

1972-2018

This is the most awaited fruit of your lifetime; hope I will always make you proud Mama.

This Thesis is dedicated to:

My late grand-mothers

Marie-Louise Openda and Jacqueline Lukusa Mesu

My daughter

My beautiful “first life success” Nahsael NGOY LISENGE, here is the fruit of our sacrifices.

My Family

my father IKALA Medard, my siblings DJEMA IKALA Murielle, MUIBU Guelord, MESU IKALA Romelie, TEWO IKALA Melissa, and IKALA Prunel; IKALA family, MUIBU family, EYALA family, KAMALENGE family, NEMO family, for total support and reassurance, may Yahweh redeem you all.

Acknowledgments

The research work presented in this thesis was fully carried out at the Institute for Nanotechnology and Innovation (INI) at Rhodes University. This work was supported by the Department of Science and Technology (DST) Innovation and National Research Foundation (NRF), South Africa through the DST/NRF South African Research Chairs Initiative for Professor of Medicinal Chemistry and Nanotechnology (UID 62620), Rhodes University, the Organization for Women in Science for the Developing World (OWSD) and Swedish International Development Cooperation Agency (Sida), from February 2019 until January 2022.



**ORGANIZATION
FOR WOMEN IN
SCIENCE FOR THE
DEVELOPING WORLD**



RHODES UNIVERSITY
Where leaders learn



**Institute for
Nanotechnology
Innovation (INI)**

Acknowledgments Contd...

A truly great and unforgettable coach, there are no words that can describe the appreciation and respect that I have towards you my supervisor **Distinguished Professor Tebello Nyokong**. Thank you for your exceptional support, guidance, and patience that kept me up on my feet. Not only you are a true model of empowerment and motivation for young scientists, especially women, but your depth of knowledge in chemistry and nanotechnology will continuously inspire me.

I wish to thank my fellow postgraduate students in the S22 research group, especially Drs. Sen Pinar, Managa Muthumuni, Refilwe Matshitse, Prof. Pitchou Ngoy Bokolombe, and Mr. Sithi Mgidlana for their unconditional teamwork and support.

I would like to express my appreciation to Ms. Gail Cobus, Dr. Jonathan Britton, and Mr. Francis Chindeka, for their facilitation and assistance during this study.

Exceptional appreciation to my closest friends Sixolile Centane, Gabriel Darong, and Aviwe Magadla for their everyday wholehearted support, prayer, and guidance.

My sincere gratitude to Safari Bazibuhe, Bafokeng Sekaleli, and Urbain Ndagano for their supportive friendship.

In closing, I want to thank my family for their tireless support from thousands of miles away.

“Grace !!! Yes, nothing but a product of your grace Jehovah, thank you for proving yourself faithful till now Jireh ”

Abstract

Phthalocyanines (Pcs) and porphyrins bearing substituents that possess antibacterial/anticancer properties are used as photosensitizers (PS) for the first time in the work. For targeting specificity and improved photoactivity, the PSs were afterward functionalized with carbon nanomaterials such as graphene quantum dots (GQDs) and detonation nanodiamonds (DNDs) *via* covalent conjugation (amide or ester bonds) or by non-covalent conjugation (π - π stacking and electrostatic interactions).

Furthermore, the PSs-DNDs nanoconjugates were conjugated to either chitosan-capped silver nanoparticles (CSAg) *via* amide bonds or to the bare silver nanoparticles (Ag NPs) using the silver-nitrogen affinity. The as-synthesized nanoconjugates were also fully characterized by spectroscopic and microscopic methods together with thermal analysis.

The potential photocytotoxicity of the complexes alone and their nanoconjugates against *S. aureus* and/or *E. coli* planktonic and biofilm cultures has been evaluated *in vitro*. Compared to the non-quaternized PSs, the cationic analogs exhibited a higher photodynamic inactivation against the planktonic cells with \log_{10} reduction values above 9 in the viable count using a concentration of ca. 1.25 μ M following 30 min exposure to light (Light dose: 943 J/cm² for Pcs and 250 mW/cm² for porphyrins). Whereas, at a concentration of ca. 100 μ M the cationic PSs showed complete eradication of biofilms upon 30 min exposure to light.

As a result of conjugation to carbon-based nanomaterials and silver nanoparticles, the compounds proved to be more effective as they exhibited stronger antibacterial and anti-biofilm activities on the multi-drug resistant bacteria strains due to synergetic effect, compared to PSs alone. This suggests that the newly prepared nanohybrids (PS concentration ca. 100 μ M) could be used as potential antimicrobial agents in the treatment of biofilm-related infections. The target nanoconjugates showed all the advantages of two different groups existing on a single entity.

In light of the potential advantages of combined chemotherapy and photodynamic antimicrobial chemotherapy (PACT), this work reports for the first time the use of PACT-ciprofloxacin (CIP) dual therapy using selected indium quaternized PSs which showed higher photoactivity with complete eradication of both Gram-positive and Gram-negative bacteria biofilms at concentrations of 8 μ M of PS versus 2 μ g/mL of the antibiotic following 15 min irradiation time (light dose: 471 J/cm² for Pcs and fluence: 250 mW/cm² for porphyrins) on *S. aureus*. Whereas the total killing of *E. coli* was obtained when combining 8 or 16 μ M of PS combined with 4 μ g/mL of CIP. The

combined treatment resulted in the complete eradication of the matured biofilms with the highest \log_{10} reduction values of 7.05 and 7.20 on *S. aureus* and *E. coli*, respectively.

Used as a model, positively charged dimethylamino-chalcone Pcs also exhibited interesting photodynamic therapy (PDT) activity against MCF-7 cancer cells giving IC_{50} values of 17.9 and 7.4 μ M, respectively following 15 min irradiation.

Additionally, the TD-B3LYP/LanL2DZ calculations were run on the dimethylaminophenyl-porphyrins to compare the singlet excitation energies of quaternized and non-quaternized porphyrins *in vacuo*. the study shows excellent agreement between time-dependent density-functional theory (TD-DFT) exciting energies and the experimental $S_1 \rightarrow S_0$ excitation energies. The small deviation observed between the calculated and experimental spectra arises from the solvent effect. The excitation energies observed in these UV-Vis spectra mostly originated from electron promotion between the highest occupied molecular orbital (HOMO) for the less intense band and the HOMO-1 for the most intense band of the ground states to the lower unoccupied molecular orbital (LUMO) of the excited states.

Table of Contents

Declaration.....	i
Dedication.....	ii
Acknowledgments.....	iii
Abstract.....	v
Table of Contents.....	vii
List of Abbreviations.....	xiv
List of Symbols.....	xvii
PART I.....	1
General Introduction.....	1
Problem Statement and Significance of the Work.....	2
Chapter One: Introduction and Overview.....	3
1.1. “Living in a Microbial and Cancer World”.....	4
1.1.1. Bacteria.....	4
1.1.1.1. Background.....	4
1.1.1.2. Bacterial Biofilms.....	5
1.1.1.3. Biofilms Formation and Resistance to Treatment.....	6
1.1.2. Breast Cancer.....	7
1.1.3. Summary of the Section.....	7
1.2. Photodynamic Mechanisms: Antimicrobial (PACT) and Anticancer (PDT).....	8
1.2.1. An Outline History of PACT/PDT.....	8
1.2.2. Photodynamic Mechanism of Action.....	8
1.2.3. Oxygenation and Light Delivery in Photodynamic Process.....	10
1.2.4. Photosensitizers.....	10
1.3. Phthalocyanines and Porphyrins-based Photosensitizers.....	12
1.3.1. Structure and Applications.....	12
1.3.1.1. Phthalocyanines (Pcs).....	12
1.3.1.2. Porphyrins.....	13
1.3.2. Synthesis.....	14
1.3.2.1. Phthalocyanines.....	14
1.3.2.2. Porphyrins.....	15
1.3.3. UV-Vis Absorption Spectra of Phthalocyanines and Porphyrins.....	17
1.3.4. Improving Water Solubility and Reducing Aggregation.....	19

1.4.	Carbon Nanomaterials	20
1.4.1.	Structure and Applications.....	20
1.4.2.	Synthesis	20
1.4.3.	Loading Mechanisms of PSs on Carbon Nanomaterials.....	21
1.4.4.	Electronic Absorption Properties	22
1.5.	Phthalocyanines and Porphyrins-loaded GQDs/DNDs Nanohybrids and their Various Applications	23
1.5.1.	Previous Works Reported in the Literature.....	23
1.5.2.	Phthalocyanines/Porphyrins and their Nanohybrids used in the Present Work	26
1.5.3.	The Logical Basis used in the Present Work	31
1.6.	Aims of the Study	33
1.6.1.	Main Objective.....	33
1.6.2.	Specific Objectives	33
PART II.....		35
Methodology and Experimental.....		35
Chapter Two: General Techniques, Instruments, and Methods.....		36
2.1.	Chemical Reagents and Equipment	37
2.1.1.	Chemicals for the Synthesis of Phthalonitriles	37
2.1.2.	Chemicals for the Synthesis of Phthalocyanines and Porphyrins	37
2.1.3.	Chemicals for the Synthesis of Nanomaterials and Nanoconjugates.....	37
2.1.4.	Chemicals for the Determination of Photophysicochemical Parameters	37
2.1.5.	Chemicals used in PACT/PDT	38
2.1.6.	Solvents.....	38
2.1.7.	Equipment.....	38
2.2.	Synthetic Methods	44
2.2.1.	Synthesis of the Phthalonitriles, Scheme 3.1A	44
2.2.2.	Synthesis of the Neutral Phthalocyanines.....	48
2.2.2.1.	Free-base Pc (1-H ₂), Scheme 3.2.....	48
2.2.2.2.	Synthesis of Zinc (II) Pc Complexes.....	48
2.2.2.2.1.	Symmetrical Zinc Pc Complexes, Schemes 3.2-3.5.....	48
2.2.2.2.2.	Asymmetrical Zinc Pc Complexes, Scheme 3.6	49
2.2.3.	Synthesis of Neutral Asymmetrical and Symmetrical Porphyrins.....	55
2.2.3.1.	Asymmetrical Free-base Porphyrin Complexes, Schemes 3.7, 3.8.....	55
2.2.3.2.	Synthesis of Zn (II) Porphyrin Complex, Schemes 3.7.....	55
2.2.3.3.	Synthesis of Ga (III) Porphyrin Complexes, Schemes 3.7, 3.8.....	56
2.2.3.4.	Synthesis of In (III) Porphyrin Complexes, Schemes 3.7, 3.8	57

2.2.4.	Quaternization of Selected Pcs and Porphyrins to form Complexes Schemes 3.4, 3.5, and 3.8	58
2.2.5.	Synthesis of the Nanoparticles	60
2.2.5.1.	Synthesis of the GQDs, Scheme 3.9A	61
2.2.5.2.	Synthesis of the GSH@GQDs, Scheme 3.11	61
2.2.5.3.	Synthesis of CSAg NPs, Scheme 3.10A	61
2.2.5.4.	Synthesis of the Bare Ag NPs	61
2.2.6.	Conjugation of PSs to Nanomaterials	62
2.2.6.1.	The π - π Stacking Conjugation, Schemes 3.9B	62
2.2.6.2.	Covalent Conjugation (amide bond), Scheme 3.10B, 3.11	62
2.2.6.3.	Covalent Conjugation and Chemisorption through Ag-N Affinity, Scheme 3.12	63
2.3.	Photophysical and Photochemical Methods	64
2.3.1.	Fluorescence Quantum Yield (Φ_F) and Fluorescence Lifetime (τ_F)	64
2.3.2.	Förster Resonance Energy Transfer (FRET)	64
2.3.3.	Triplet Quantum Yield (Φ_T) and Triplet Lifetime (τ_T)	65
2.3.4.	Singlet Oxygen Quantum Yield (Φ_Δ)	65
2.4.	Theoretical Calculations	66
2.5.	Photodynamic Antimicrobial Chemotherapy (PACT)	67
2.5.1.	Bacteria Culture and Biofilms Formation	67
2.5.2.	Antimicrobial Assays	67
2.5.2.1.	Photoinactivation of Bacteria Planktonic Cultures	67
2.5.2.2.	Photoinactivation of Bacterial Biofilms	68
2.5.3.	Statistical Analysis	68
2.6.	PACT-Ciprofloxacin Combined Therapy	69
2.6.1.	Susceptibility of Matured Biofilms to PACT and Ciprofloxacin as Monotherapies	69
2.6.1.1.	Minimum Biofilm Eradication Concentration (MBEC ₅₀) Assay	69
2.6.1.2.	Minimum Biofilm Inhibitory Concentration (MBIC ₅₀) Assay	69
2.6.2.	Susceptibility of Matured Biofilms to PACT and Ciprofloxacin in Combination	70
2.7.	Photodynamic Therapy (PDT)	71
2.7.1.	Cell Culture Preparation	71
2.7.2.	Cellular Uptake	71
2.7.3.	Dark Toxicity and PDT Activities	71
2.7.4.	Lipophilicity Studies	72
PART III.		73
Results and Discussion		73

Chapter Three: Synthesis and Characterization	74
Publications.....	75
3.0. General	78
3.1. Phthalonitriles	79
3.1.1. Synthesis	79
3.1.2. ¹ H NMR and ¹³ C NMR Spectra	82
3.1.3. FT-IR Spectroscopy	82
3.2. Phthalocyanines	83
3.2.1. Symmetrical Pcs.....	83
3.2.1.1. Synthesis of Group 1: 1-H ₂ , 1-Zn, and 1-In	83
3.2.1.2. Synthesis of Group 2: 2-Zn and 2-In.....	84
3.2.1.3. Synthesis of Group 3: 3-Zn, 3-In, 3-ZnQ, and 3-InQ.....	85
3.2.1.4. Synthesis of Group 4: 4-Zn, 4-In, 4-ZnQ and 4-InQ.....	86
3.2.2. Synthesis of Symmetrical and Asymmetrical A ₃ B-type Pcs of Groups 5 and 6: 5-Zn and 6-Zn	88
3.2.3. FT-IR Spectra of the Studied Pcs.....	89
3.2.4. Electronic Absorption and Emission Spectra of the studied Pcs	91
3.3. Porphyrins.....	97
3.3.1. Symmetrical and Asymmetrical Porphyrins	97
3.3.1.1. Synthesis of Group 7: 7- H ₂ , 7- Zn, 7-In, and 7-Ga	97
3.3.1.2. Synthesis of Group 8: 8-In, 8-Ga, 8-InQ, and 8-GaQ	98
3.3.2. FT-IR Spectra of the Studied Porphyrins.....	100
3.3.3. Electronic Absorption and Emission Spectra of the Studied Porphyrins.....	101
3.4. Synthesis and Characterization of the PSS-nanoconjugates	105
3.4.1. Effect of Different Nanomaterials: Conjugation of 1-H ₂ , 1-Zn, and 1-In to QDs and DNDs	107
3.4.1.1. Synthesis.....	107
3.4.1.2. FT-IR Spectra	109
3.4.1.3. UV-Vis Absorption and Emission Spectra.....	110
3.4.1.4. Raman Spectra.....	112
3.4.1.5. TEM Micrographs and DLS Analysis.....	114
3.4.1.6. TGA and DSC Analysis	116
3.4.2. Effect of Double Conjugation on Pcs: Conjugation of 2-Zn and 2-In to DNDs then to CSAg	118
3.4.2.1. Synthesis.....	118
3.4.2.2. FT-IR Spectra.....	119
3.4.2.3. UV-Vis Absorption and Emission Spectra.....	120

3.4.2.4.	Raman Spectra.....	121
3.4.2.5.	TEM Micrograph Analysis.....	122
3.4.3.	Effect of Quaternization: Conjugation of 3-Zn, 3-In, 3-ZnQ, and 3-InQ to DNDs 124	
3.4.3.1.	Synthesis.....	124
3.4.3.2.	UV-Vis Absorption and Emission Spectra.....	124
3.4.3.3.	Raman Spectra.....	126
3.4.3.4.	TEM Micrographs	126
3.4.4.	Effect of Symmetry: Conjugation of 5-Zn and 6-Zn to GSH@GQDs	126
3.4.4.1.	Synthesis.....	126
3.4.4.2.	FT-IR Spectra	128
3.4.4.3.	UV-Vis Absorption and Emission Spectra.....	128
3.4.4.4.	DLS Analysis	130
3.4.4.5.	TGA and DSC Analysis	130
3.4.5.	Effect of Double Conjugation on Porphyrins: Conjugation of 7-H ₂ , 7-Zn, 7-In, and 7-Ga to DNDs then to Ag NPs.....	131
3.4.5.1.	Synthesis.....	131
3.4.5.2.	FT-IR Spectra.....	133
3.4.5.3.	UV-Vis Absorption and Emission Spectra.....	134
3.4.5.4.	TEM Analysis.....	135
3.4.5.5.	TGA Analysis.....	136
3.5.	Summary of the Chapter.....	137
Chapter Four: Photophysical and Photochemical Parameters		138
4.1.	Fluorescence Quantum Yields (Φ_F) and Lifetimes (τ_F).....	139
4.1.1.	Phthalocyanine Complexes and Nanoconjugates.....	141
4.1.1.1.	Effect of Central Metal.....	141
4.1.1.2.	Effect of Substituents	142
4.1.1.3.	Effect of Positive Charges	142
4.1.1.4.	Effect of Symmetry	142
4.1.1.5.	Effect of Nanomaterials.....	142
4.1.1.6.	FRET	143
4.1.2.	Porphyrin Complexes and Nanoconjugates	146
4.2.	Triplet Quantum Yield (Φ_T) and Lifetime (τ_T).....	147
4.2.1.	Phthalocyanine and Nanoconjugates	147
4.2.1.1.	Effect of Central Metal.....	149
4.2.1.2.	Effect of Substituents	149

4.2.1.3.	Effect of Symmetry	149
4.2.1.4.	Effect of Nanomaterials.....	149
4.2.2.	Porphyrins and their Nanoconjugates	150
4.3.	Singlet Oxygen Quantum Yield (Φ_{Δ})	152
4.3.1.	Phthalocyanine and Nanoconjugates	152
4.3.1.1.	Effect of Central Metal.....	155
4.3.1.2.	Effect of Substituents	155
4.3.1.3.	Effect Positive Charge.....	155
4.3.1.4.	Effect of Symmetry	156
4.3.1.5.	Effect Nanomaterials.....	156
4.3.2.	Porphyrin and Nanoconjugates	156
4.3.2.1.	Effect of Central Metal.....	156
4.3.2.2.	Effect of Positive Charges	158
4.3.2.3.	Effect of Nanomaterials.....	158
4.4.	Summary of the Photophysical Properties of the Studied Photosensitizers....	159
Chapter Five: Theoretical Calculations.....		160
5.1.	TD-DFT Analysis	161
5.2.	Summary of the Chapter.....	164
PART IV.....		165
Singlet Oxygen Biological Applications.....		165
Chapter Six: Photodynamic Antimicrobial Chemotherapy (PACT).....		166
6.1.	Introduction	167
6.2.	Lipophilicity Studies.....	169
6.3.	Biological Assays on Planktonic Cells	170
6.3.1.	Statistical Analysis	170
6.3.2.	Control Groups.....	170
6.3.3.	Bacteria Optimization	171
6.3.4.	Photosensitizer-Concentration Optimization	171
6.3.5.	Dark Toxicity Studies	172
6.3.6.	Photoinactivation Studies.....	175
6.3.6.1.	Effect of Central metal and Singlet Oxygen.....	178
6.3.6.2.	Effect of Substituents	178
6.3.6.3.	Effect of Symmetry	179
6.3.6.4.	Effect of Positive Charges	179
6.3.6.5.	Effect of Cell Wall	182
6.3.6.6.	Effect of Conjugation to Nanomaterials.....	183

6.4.	Biological Assays on Bacteria Biofilm Cells	186
6.4.1.	Photosensitiser-Concentration Optimization	186
6.4.2.	Dark Toxicity Studies	186
6.4.3.	Photoinactivation Studies.....	187
6.4.3.2.	Effect of Positive Charges	188
6.4.3.3.	Effect of Cell Wall	193
6.5.	Summary of the Chapter.....	195
Chapter Seven: PACT-Antibiotic Dual Therapy		196
7.1.	General.....	197
7.2.	Antibacterial Effect of PACT alone on Biofilm Cultures	198
7.3.	Antibacterial Effect of Ciprofloxacin alone on Biofilm Cultures.....	201
7.3.1.	MBEC ₅₀ and MBIC ₅₀ Determination	201
7.4.	Dual PACT-Ciprofloxacin Biofilm Activities.....	203
7.5.	Summary of the Chapter.....	208
Chapter Eight: Photodynamic Therapy (PDT).....		209
8.1.	Photodynamic Activity (PDT).....	210
8.1.1.	Cellular uptake	210
8.1.2.	Photocytotoxicity studies	211
8.1.3.	Lipophilicity.....	214
Chapter Nine: Conclusions and Recommendations.....		215
9.1.	General Conclusions.....	215
9.2.	Perspectives and Recommendations.....	217
References.....		218
Appendices.....		241

List of Abbreviations

Abs: Absorbance/Absorption

ADMA: Anthracene-9,10-diyl-bis-methylmalonate

AlPcSmix: Aluminium sulfonated phthalocyanine, a mixture of sulfonated derivatives

ATCC: American type culture collection

CDCl₃: Deuterated chloroform

CFU: Colony forming units

CIP: Ciprofloxacin

d: Doublet

DBU: 1,8-diazabicyclo[5.4.0]undec-7-ene

DCC: N, N'-dicyclohexylcarbodiimide

DCM: Dichloromethane

dd: Doublet of doublets

DLS: Dynamic light scattering

DMA: 9,10 Dimethylantracene

DMAE: Dimethylaminoethanol

DMEM: Dulbecco's modified eagle's medium

DMF: Dimethylformamide

DMSO: Dimethylsulfoxide

DMSO-d₆: Deuterated dimethyl sulfoxide

DNDs: Detonation nanodiamonds

DPBF: Diphenylisobenzofuran

DPBS: Dulbecco's modified phosphate buffer saline

DSC: Differential scanning calorimetry

EDTA: Ethylenediaminetetraacetic acid

EDX: Energy-dispersive X-ray spectroscopy

Eff: FRET efficiency

Em: Emission

EPS: Exopolymeric substance

EtOH: Ethanol

FDA: Food and drug administration

FRET: Förster resonance energy transfer

FT-IR: Fourier-transform infrared spectroscopy

GO: Graphene oxide

GQDs: Graphene quantum dots

GSH: Glutathione

HOMO: Highest occupied molecular orbitals

IRF: Instrument response function

ISC: Intersystem crossing

LASER: Light amplification by the stimulated emission of radiation

LED: Light-emitting diode

LUMO: Lowest unoccupied molecular orbitals

m: Multiplet

MALDI-TOF MS: Matrix-Assisted Laser Desorption/Ionisation Time-of-Flight Mass Spectrometry

MCF-7: Michigan cancer foundation-7

MeOH: Methanol

NaOAc: Sodium acetate

Nd-YAG: Neodymium-doped Yttrium Aluminium Garnet

NHS : *N*-hydroxysuccinimide

NMR: Nuclear Magnetic Resonance

NPs: Nanoparticles

PACT: Photodynamic antimicrobial chemotherapy

PBS: Phosphate-buffered saline

Pc: Phthalocyanine

PDT: Photodynamic therapy

PET: Photo-induced electron transfer

PS: Photosensitizer

RB: Rose Bengal

ROS: Reactive oxygen species

rt: Room temperature

s: Singlet

SPR: Surface plasma resonance

Std: Standard

t: Triplet

TCSPC: Time-correlated single photon

TEM: Transmission electron microscope

TGA: Thermal gravimetric analysis

THF: Tetrahydrofuran

TLC: Thin layer chromatography

TMS: Tetramethyl silane

TPP: Tetraphenyl-porphyrin

UV-Vis: Ultraviolet-visible spectroscopy

List of Symbols

α : Non-peripheral position

β : Peripheral position

δ : Chemical shift

J : Coupling constant

λ_{\max} : Wavelength at maximum absorption

λ_{em} : Wavelength at maximum emission

λ_{exc} : Wavelength at maximum excitation

m/z : Mass to charge ratio

ν : Frequency

Φ_{Δ} : Singlet oxygen quantum yield

Φ_{F} : Fluorescence quantum yield

Φ_{T} : Triplet quantum yield

τ_{F} : Fluorescence lifetime

τ_{T} : Triplet lifetime

PART I.

General Introduction

Problem Statement and Significance of the Work

“The real voyage of discovery consists not in seeking new landscapes but in having new eyes”

- Marcel Proust

(1871-1922, French novelist)

Despite the significant advancements in the treatment of chronic infections and breast cancer over the past years, the rapidly increasing multidrug resistance toward common drugs has become a global health peril [1–4]. The World Health Organization (WHO) has estimated that antibiotic-resistant bacteria will cause 10 million human deaths annually by 2050 [2,5]. To control this burden, new and more effective treatment alternatives are needed.

Recently, photodynamic antimicrobial chemotherapy (PACT) and photodynamic therapy (PDT) have been approved as alternatives to the conventional treatments since they are both refined for selectively killing bacteria or cancerous cells [5]. PACT and PDT are minimally invasive procedures that use photosensitizer (PS) drugs that are structurally different and react *via* the photosensitized production of reactive oxygen species (ROS) [5–8]. To date, no mechanism of resistance has been reported towards the use of PACT and PDT while using Pcs or porphyrins [9–12].

Nanoparticles (NPs) have been extensively proven to improve the therapeutic efficacy of PACT/PDT [13–15]. Yet far less attention has been given to the development of nanohybrids of carbon nanomaterials mainly the graphene quantum dots (GQDs) and the detonation nanodiamonds (DNDs) combined with PSs as antibacterial drug derivatives. Meantime, antimicrobial research continues to only focus on bacterial planktonic cells instead of treating the biofilms which form the greatest threat despite the availability of antibiotics [16–18]. Thus, this study tackles this deficiency by applying PACT and the potential of combining PACT with an antibiotic for the fast removal of stubborn bacterial biofilms. Theoretical studies of a few model PSs will also be addressed.

Chapter One: Introduction and Overview

This chapter provides a general background overview as well as the aims of the subject of this thesis. The history and the scientific basis of the microbial world, breast cancer, photodynamic mechanisms, and carbon-based nanomaterials, are also reviewed and presented.

1.1. “Living in a Microbial and Cancer World”

“Bacteria have been around for billions of years. Will stealing some antibacterial drugs from fungi do us good for long?”

**- Stephen Jay Gould
(1941-2002; Evolutionary biologist)**

1.1.1. *Bacteria*

1.1.1.1. *Background*

Bacteria are the tiniest (0.5-10 μm in length) and most numerous living creatures on Earth. Some can tolerate harsh environments, from icy Arctic water to boiling underwater volcanoes [19,20]. The domain of bacteria is split into two groups: Gram-positive and Gram-negative bacteria. Both groups differ in the biochemical composition of their cell wall which reflects the differences in their response to antimicrobial agents [21].

Gram-positive bacteria (i.e., *S. aureus*) have thick peptidoglycan layers of 20-80 nm, which are traversed by negatively charged lipoteichoic and teichuronic acids. This cell wall acts as a protective layer where neutral or charged compounds with molecular weight up to 60,000 Da can easily diffuse through. In contrast, Gram-negative bacteria (i.e., *E. coli*) have much fewer peptidoglycan layers, but they possess an extra 10-15 nm dense layer composed of lipoproteins and lipopolysaccharides as an outer membrane [22,23] as shown in **Figure 1.1**.

These constituents for Gram-negative bacteria provide a polyanionic external surface to the outer membrane and thus interfere with the cellular uptake of neutral or anionic substances or drugs with a molecular weight larger than 600-700 Da. The transport proteins (called Porins) found on the outer membrane are water-filled channels that allow the free diffusion of cationic and hydrophilic compounds such as sugars and amino acids [24,25]. In addition, some other bacteria may have an extra gelatinous layer, the capsule, surrounding the cell wall or may also contain external structures such as flagella and pili [23,26].

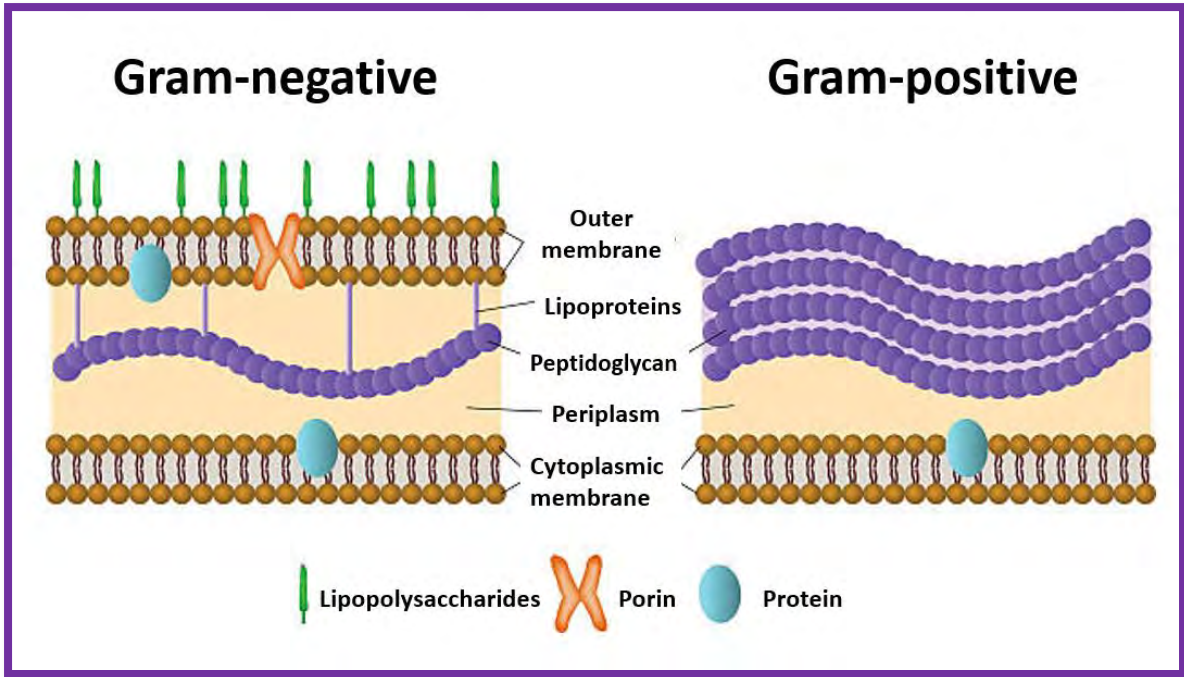


Figure 1.1 Images of Gram-negative (**Left**) and Gram-positive (**Right**) bacteria structure. Retrieved from Shutterstock [27].

Bacteria reproduce mainly by binary fission or sometimes by budding division. In both scenarios, bacteria can grow either in suspension or attached to surfaces. The free-floating specimens are called bacterial planktonic cells and those who attach to surfaces tend to develop into bacterial biofilm which is the most common growth form of bacteria in nature [28].

1.1.1.2. *Bacterial Biofilms*

A biofilm is a well-organized community of phototrophic and/or chemotrophic bacteria embedded in an exopolymeric substance (EPS) that is attached to a biotic or abiotic surface [29–31]. The EPS is made of polysaccharides, proteins, microbial nucleic acids, and other substances. It plays a key role in the development, maintenance as well as protection of biofilms against dehydration and the effects of antimicrobials [32,33].

Compared to planktonic cells, biofilm cells exhibit different physiological and metabolic states. Bacterial biofilms affect many aspects of our lives, including human health. They account for up to 80% of all bacterial chronic infections in humans and the formation of bacterial biofilms is one of the major causes of bacterial resistance [34–36].

1.1.1.3. Biofilms Formation and Resistance to Treatment

As pictured in **Figure 1.2**, a biofilm develops in four stages starting with the stage (1) the reversible attachment of planktonic cells to a surface *via* motility, physical interactions, or molecular docking mechanisms. This is followed by stage (2) where the EPS formation occurs and eventually there is also irreversible attachment and further growth of cells. In stage (3) the formation of an impenetrable mature biofilm takes place. In this stage, cells undergo phenotypic changes by intercommunicating through the release and uptake of small diffusible molecules. This process is known as quorum sensing [29,37,38]. Stage (4): due to the lack of nutrients and enough oxygen inside the matured biofilm (where the pH becomes acidic), cells detach themselves to re-enter the planktonic state and may reattach to new areas to restart a new process of biofilm formation and hence causing reinfection [29,39].

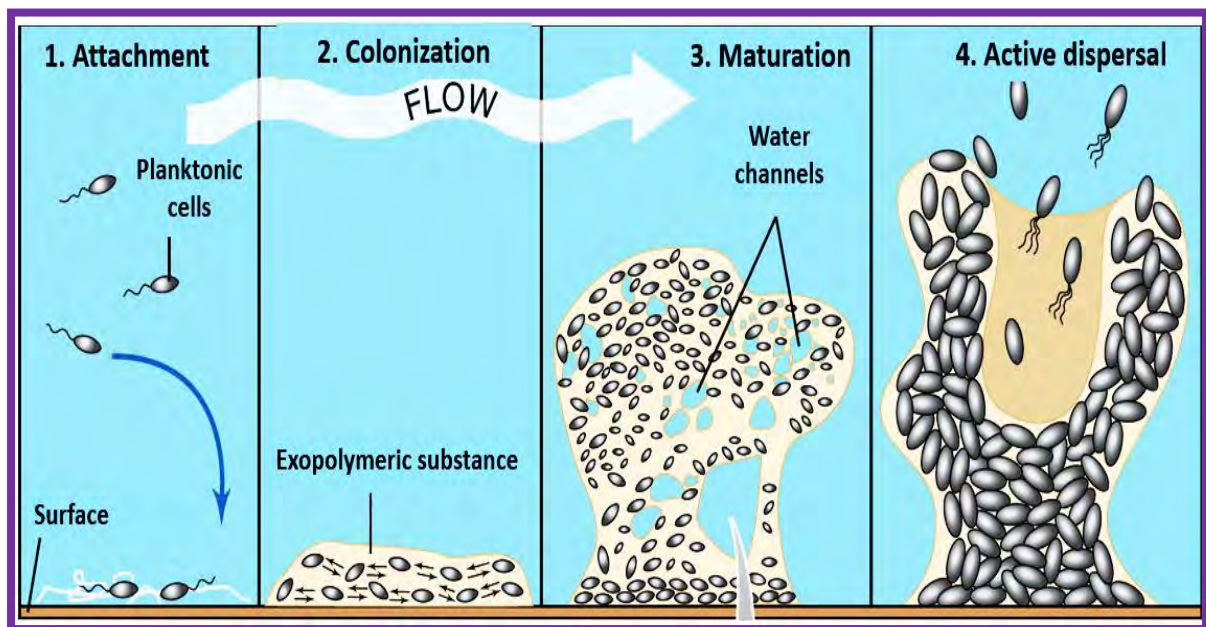


Figure 1.2 Diagrammatic representation of biofilm formation. Image from [28].

Because of factors such as the protective EPS, the heterogeneity of population, gene hypermutation, and gene transfer, biofilm cells exhibit increased resistance to usual concentrations of antibiotics [40–42]. Reports have also demonstrated the complete failure of the destruction of matured biofilms using different techniques such as physical, chemical, or biological methods [37,43]. For these reasons, biofilms remain the leading agents in the pathogenesis of difficult-to-eradicate infections [44] leading to increased microbial resistance to many antibiotics and biocides [45]. New anti-biofilm approaches are needed to manage biofilm-associated chronic infections [46].

Photodynamic antimicrobial chemotherapy (PACT) has been recently suggested as an efficient alternative approach to fight relevant biofilms such as dental biofilms and chronic wound infections. PACT uses non-toxic drugs, the photosensitizers (PSs), which produce cytotoxic effects on bacteria cells following irradiation by harmless visible light at a specific wavelength [47]. Hence, in the present study, the *in vitro* killing effect of PACT alone against clinically relevant bacterial biofilms was analyzed and the antibiofilm effect using a dual therapy whereby two modes of action are involved, i.e., PACT combined with low doses of antibiotics were investigated as well. This is done to lower the toxic effects of antimicrobial chemotherapy on normal host tissues.

1.1.2. Breast Cancer

Breast cancer ranks as the most common malignancy diagnosed in females and is a leading cause of cancer deaths in women. It ranks second most common cancer globally accounting for 14% of cancer deaths [48]. Breast cancer develops because of increased transcriptional activity due to over-expressed oestrogen receptors. Research shows that breast cancer does not represent a single disease but a compilation of molecularly distinct tumors growing from the epithelial cells of the breast [49,50]. They can grow on any area of the breast.

Consequently, this results in a challenging public health burden that requires deep research at the molecular level to define a specific treatment. Michigan Cancer Foundation-7 (MCF-7) cells lines are particularly used worldwide as suitable *in vitro* models in cancer research [51]. Considerable research has gone into finding new promising anticancer drugs or treatments, but most have failed in animal models or clinical trials [51–53]. One of the most notable clinical problems in breast cancer treatment is the development of therapeutic resistance. Data suggest that, if used properly, photodynamic therapy (PDT) is an effective substitute treatment in tumors including their application in breast cancer patients because the breast area is easily accessible with the PDT method.

1.1.3. Summary of the Section

Concerned about the statistics around the number of deaths caused by the occurrence of biofilms-related chronic infections and breast cancer in the world, this research project intends to enlighten the usefulness of basic research on PACT, PDT, and PACT-antibiotics (used to treat bacterial infections in chemotherapy) for their dual therapy effects by using more promising moieties and strategies.

1.2. Photodynamic Mechanisms: Antimicrobial (PACT) and Anticancer (PDT)

“I don't understand it, Dr. von Tappeiner, the paramecia were all wiggling just fine a minute ago, but now those by the window seem to be dead”.

- Oscar Raab
(1900; German Physician)

1.2.1. An Outline History of PACT/PDT

The modern era of photodynamic therapy is known to have begun in the early 19th century with the discovery by one of Hermann von Tappeiner's students, Oscar Raab, who was investigating the toxicity of acridine dye against *Paramecium caudatum* culture. Raab realized that the toxic effects of the as-used dye on the culture were dependent on the amount of light absorbed. He noticed that the solutions he kept near a bright window had a lethal effect on the microorganism compared to those kept away from light. He concluded that this photosensitization is a result of the energy transfer process from the light to the dye as it similarly occurs with the chlorophyll in plants [54–56]. But unfortunately, his antimicrobial concept was rapidly suppressed at that time due to the description of the new antibiotic, Penicillin, by Alexander Fleming. Hence, the fatal potential of PDT was only fixated on cancer therapy [57]. It is only of late that the antimicrobial aspect of PDT, i.e., to control multidrug resistance, has regained the attention of the scientific world [58,59] as it is now seen as the appropriate alternative to common antibiotic treatments [60]. The current study refers to this antimicrobial PDT approach as PACT.

1.2.2. Photodynamic Mechanism of Action

The photodynamic process is a photochemistry-based mechanism that relies on three main components: (1) a photosensitizer (PS), a molecule with low to zero dark toxicity which should accumulate selectively in the target tissue/cells; (2) light of a specific wavelength to excite the photosensitizer to a higher energy level and (3) the presence of molecular oxygen in the environment [55,61]. This mechanism is a two-steps process where the PS is firstly administered, followed by its activation by harmless visible light irradiation.

Jablonski diagram (please see **Figure 1.3**) depicts the photodynamic process as follows: a PS on its singlet ground state absorbs a photon, thus promoting it to the singlet excited state. From the singlet excited state, two different photo-processes can take place: either the PS will degenerate

back to its ground state, through fluorescence or the PS can undergo intersystem crossing (ISC) that leads to the promotion of the PS to the triplet excited state [57,62,63]. The spin conversion of the more external electron of the PS that happens in the triplet state renders it more stable than the singlet state. This means that the PS on the triplet excited state has enough time to interact and this is what leads to the toxic photosensitization effect [64].

In the triplet state, the PS can react with biomolecules/oxygen present in the environment in two different photo-processes called type I and II reactions. In type I reaction, an electron or hydrogen transfer takes place from the PS to the biomolecules. This process generates free radicals which can interact with molecular oxygen to produce reactive oxygen species (ROS) such as superoxides, hydrogen peroxide, and hydroxyl radicals which are harmful to cell membrane integrity, causing irreparable biological damage [65]. While in type II reaction, the PS directly reacts with the molecular oxygen to generate a very reactive excited singlet oxygen (1O_2) [57,66,67].

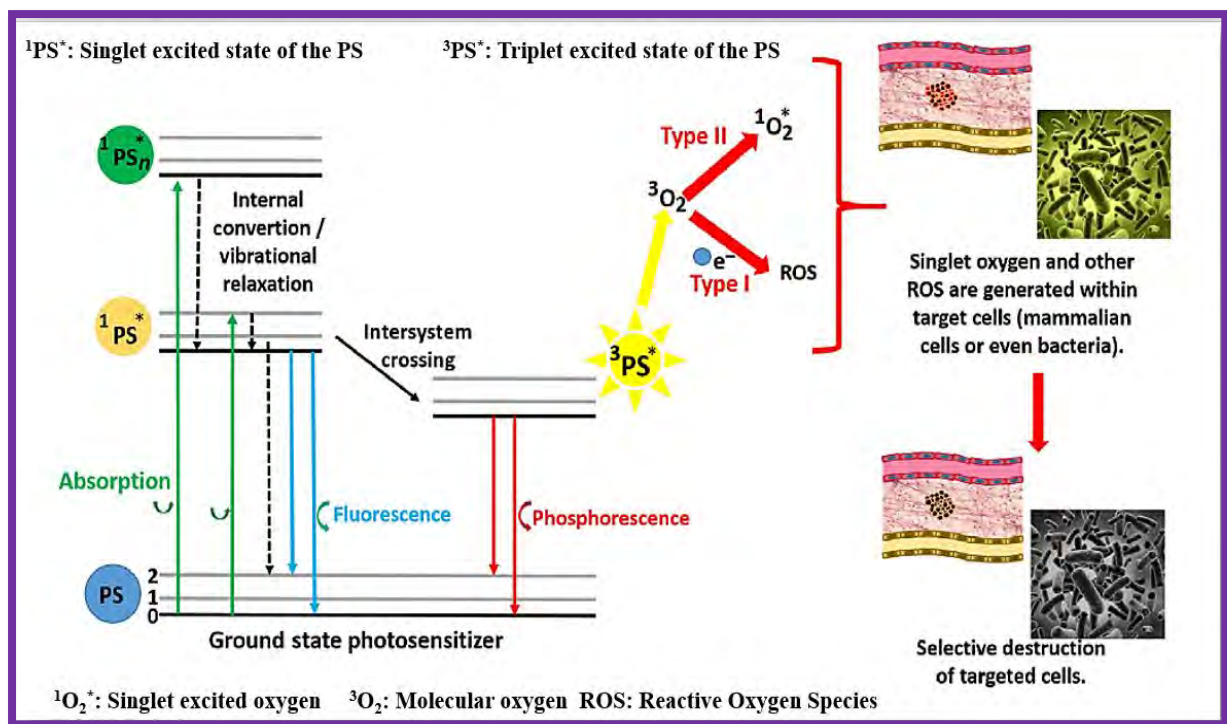


Figure 1.3 Jablonski diagram showing the processes involved in the photodynamic mechanism. Image from [68].

1O_2 is known as the main mediator in the photodynamic mechanisms. Its high reactivity can be useful for many therapies, such as preventing the progression of tumors and also by eradicating pathogenic bacteria that cause infections. This occurs through oxidative stress of the membrane or cell wall that leads to cell death [69–71]. 1O_2 has a short radius of action ($0.02 \mu\text{m}$) and lifetime

(2.80 sec at 23 C° and 1 atm). It reacts within a limited space, leading to a localized response without affecting distant cells [65].

Both type I and II mechanisms occur simultaneously but type II reaction is recognized as the major pathway for PACT and PDT treatments [5,66,67].

1.2.3. Oxygenation and Light Delivery in Photodynamic Process

As stated above photodynamic mechanism is oxygen-dependent. Molecular oxygen is required because PACT/PDT displays a low efficacy in hypoxic conditions which can lead to resistance. When the oxygen concentration in the environment is not enough, the phototoxicity effect will be minimal or completely absent [72]. This dependence is believed to increase the production of $^1\text{O}_2$ which is responsible for most photodynamic processes in biological systems [73].

On the other hand, light dose (fluence in J/m^2 and a fluence rate in W/m^2), light source, and irradiation wavelength are critical to achieving optimal efficiency in PACT and PDT. The chosen light wavelength should resonate with the PS maximal absorption peak [57]. Light sources with irradiation wavelengths of 400-500 nm should be used with an optic fiber to limit cell necrosis while those with wavelengths greater than 900 nm can be absorbed by water. Thus, most used PSs are activated by red light (between 600 and 900 nm often called the “therapeutic window” where maximal light penetration is 0.5-1.5 cm) [57,74]. Due to their monochromaticity, LASERs (light amplification by stimulated emission of radiation, postulated by Albert Einstein in 1917) are the most efficient and most utilized light sources. The light-emitting diode (LED) which is monochromatic, cheaper, and economical has also been included. Researchers have also studied other lamps such as Xenon red filtered lamps [75]. In the current case, appropriate LASER and LED lamps (described in Chapter two) were employed.

1.2.4. Photosensitizers

Commonly used PSs in PACT and PDT contain a tetrapyrrole backbone, a structure comparable to the protoporphyrin prosthetic group found in hemoglobin. PSs with maxima absorption in the 600-900 nm (the deep-red spectral region) are preferred since these absorptions allow deeper light penetration into tissues [76]. These PSs include chlorins, bacteriochlorins, and phthalocyanines which tend to be much more effective PSs even though many other factors should be looked at.

Since the discovery of Photofrin®; the first clinically approved PS and other first-generation PSs faced problems, several conditions have been proposed for what an ideal PS should have: chemical purity and stability, low or absence of dark cytotoxicity, selectivity at target cells, able to generate

$^1\text{O}_2$ and other ROS, high coefficient of absorption in the therapeutic window, rapid clearance from the body, soluble in biological fluids, a broad spectrum of action to act efficiently in polymicrobial infections and should allow for scalable formulation and be inexpensive [57,77,78]. Moreover, a PS must also have appropriate photophysicochemical properties: e.g., high singlet quantum yield, high triplet quantum yield, and long triplet state lifetime [79].

In the search for PSs possessing the above-mentioned criteria, new classes of PSs have been born: the so-called 2nd and 3rd generation PSs. Amongst them are phthalocyanines (Pcs) and modified porphyrins along with their respective polycationic derivatives, which all exhibit different photophysicochemical properties [80]. In this study, Pcs, porphyrins, and their quaternized derivatives constitute the main focus for the investigation of antibacterial (planktonic and biofilm cells) and anticancer effects based on PACT/PDT.

1.3. Phthalocyanines and Porphyrins-based Photosensitizers

“I think you might dispense with half your doctors if you would only consult Dr. Sun more”

- Henry Ward Beecher

(19th Century; American minister)

1.3.1. Structure and Applications

1.3.1.1. Phthalocyanines (Pcs)

Pcs were accidentally discovered as stable blue pigments in 1928 by Dandridge and co-workers in Scottish Dyes Limited [81]. Patrick Reginald Linstead and co-workers proposed for the first time the structure and synthetic methods of Pcs at Imperial College from 1929 to 1939 [82]. Pcs are synthetic porphyrins derivatives systematically known as tetraazatetrabenzporphyrins. Pcs are 18 π electron aromatic and planar macrocycles due to the extended π -system of the four fused isoindole rings as illustrated in **Figure 1.4**.

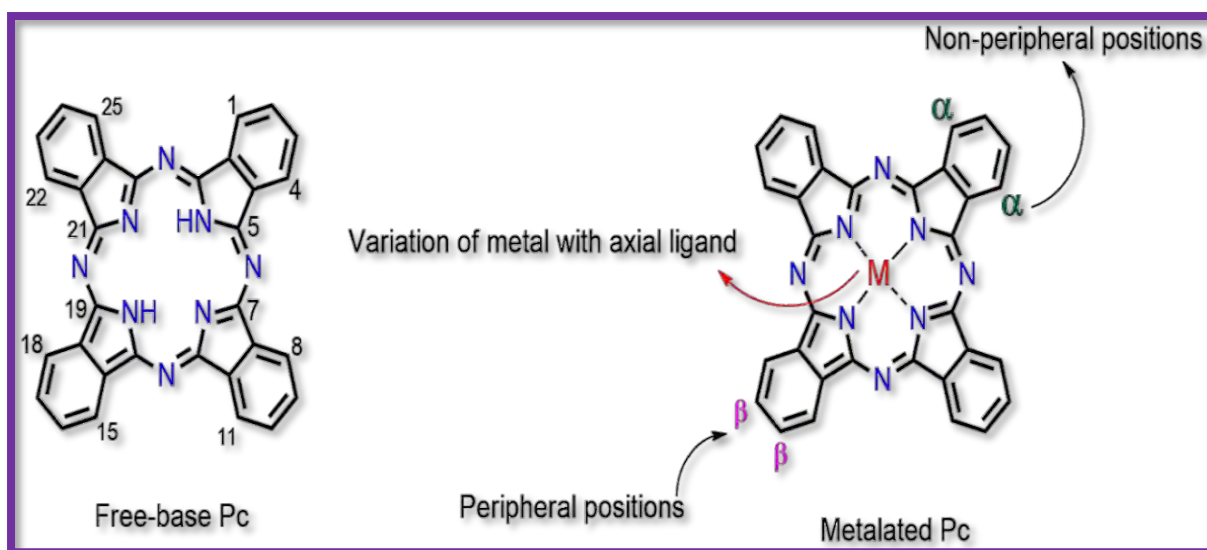


Figure 1.4 General molecular structure of unmetalated phthalocyanine (left) and metalated phthalocyanine (right), showing isoindoline unit, ring numbering, and α , β substituent positions on the macrocycle.

The chemical and photophysical properties of Pcs can be tuned thanks to their dianionic form which allows for the insertion of different central metals or semimetals. Adding diamagnetic metals such as zinc (II), gallium (III), and indium (III) augments photoactivity due to the increased triplet state

population. Another way to modify Pcs is to add substituents on the macrocycle. Axial ligation and peripheral substitution improve solubility and interactions with biological systems [83–86].

Pcs possess several distinctive properties such as excellent thermal and chemical stability in solid state [86], high extinction coefficients, non-toxicity, and high phototoxicity following irradiation with light, which adds to their effectiveness in different research areas. In recent decades, Pcs have proved to be versatile in a variety of fields ranging from technological and industrial to biomedical applications. These include nonlinear optics [87,88], optical data storage [89], solar cells [90], charge-generating materials in xerography [91], water splitting for fuel cells [92], photocatalysis [93], PDT of tumours [94–96], PACT [58,97,98].

1.3.1.2. Porphyrins

Chemically, porphyrins are naturally occurring tetrapyrrolic aromatic macrocycles with an 18 π -conjugated electronic system linked by four methylene bridges [99,100]. A porphyrin structure has two main positions: β and *meso* positions where functionalization can be performed (Figure 1.5). Substitution at the β -positions exerts much higher steric and electronic effects on the porphyrin ring than at the *meso*-positions [101,102]. The β -substitution gives a non-planar conformation to the porphyrin ring, this modifies their biological properties. The free base porphyrins can accommodate a variety of metal cations in their cavity (e.g., Ga, Zn, In, and Co) [102,103]. Thanks to their unique structure, moderate singlet oxygen production, and interesting photophysical properties, porphyrins have been widely used in industrial and clinical applications [104].

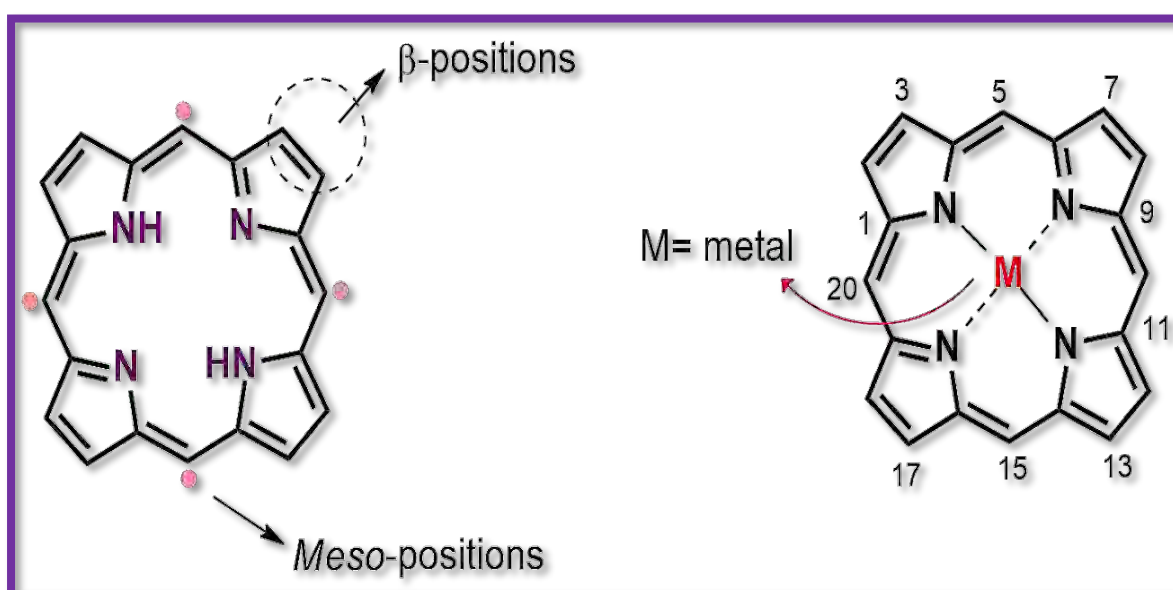


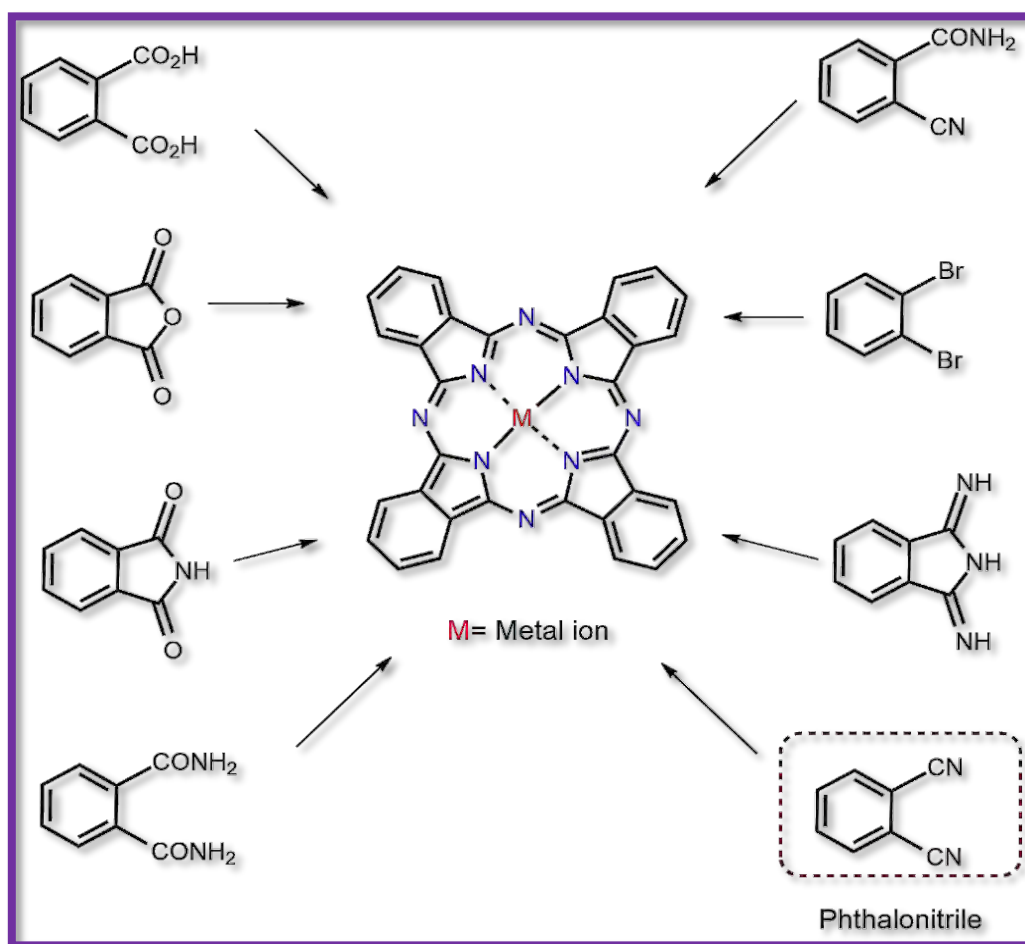
Figure 1.5 Typical structures, i.e., (left) free-base porphyrin, and (right) metallated porphyrin, showing the ring numbering, the β , and *meso*-positions.

1.3.2. Synthesis

1.3.2.1. Phthalocyanines

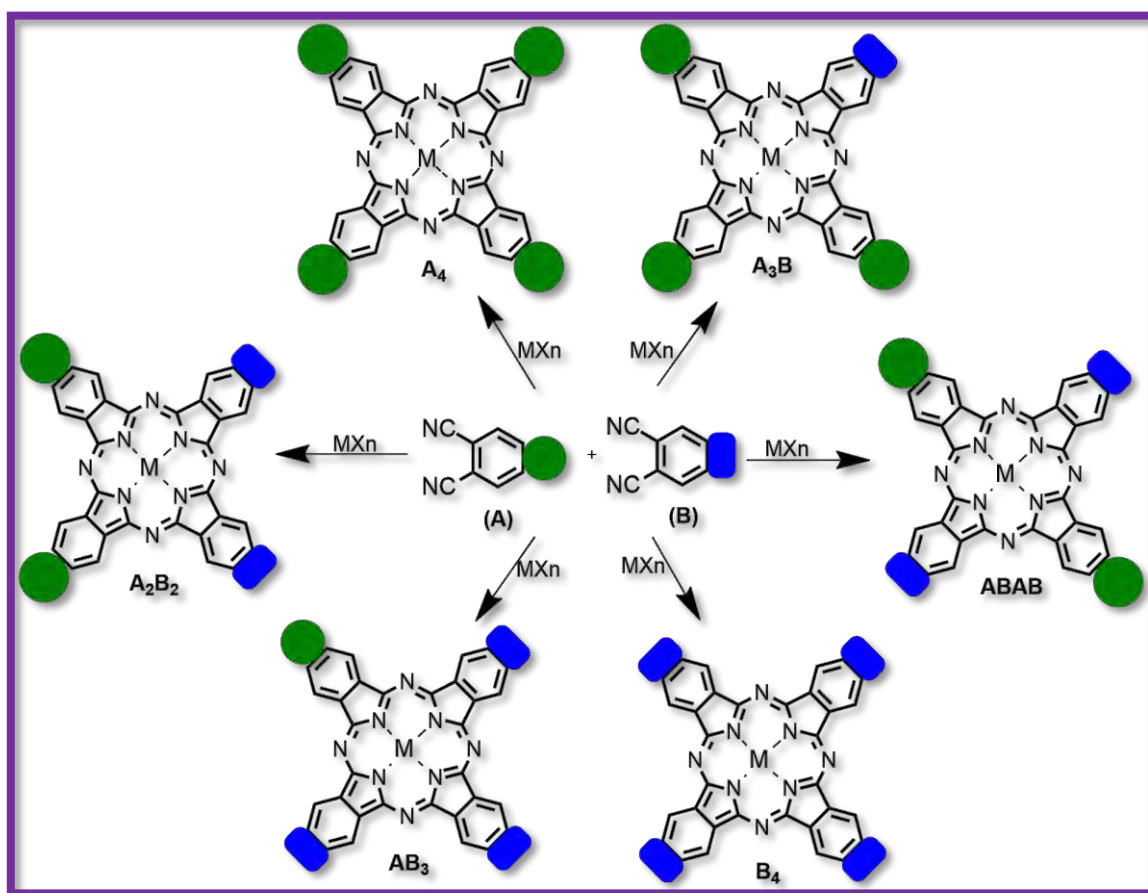
Numerous synthetic routes exist for both free-base and metalized symmetrical Pcs. As illustrated in **Scheme 1.1**, Pcs can be synthesized using different precursors such as phthalic acid, phthalic anhydride, phthalimide, phthalamide, *O*-cyanobenzamide, *O*-dibromobenzene, diiminoisoindoline, and phthalonitrile [105–107]. However, in this study the phthalonitrile precursor was used, whereby various tetrasubstituted Pcs were synthesized by modifying the 4-nitrophthalonitrile precursor to obtain the β -tetrasubstituted Pcs.

The synthesis of symmetrical Pcs in this work involves a refluxing cyclotetramerization reaction under an inert atmosphere of the substituted phthalonitrile derivative in a high boiling point solvent in the presence of a metal salt and a basic catalyst. Other procedures such as microwave synthesis and solvent-free reactions have also been reported elsewhere [108].



Scheme 1.1 Commonly used phthalocyanine precursors as enumerated above.

If one targets to achieve a selective surface functionalization, for example, they will need to design an asymmetric Pc that contains a single anchor group. To achieve this, two key factors are considered: the stoichiometry and reactivity of the precursors being used. In the present work, the most popular and non-selective statistical cross-condensation method was used to form the A_3B asymmetric Pc type whereby two phthalonitrile precursors A and B are used (**Scheme 1.2**) [109,110]. If A and B have similar reactivities, then the reaction of A and B in 3:1 ratio will result in the formation of the symmetrical A_4 -type Pc (33%), the target asymmetrical A_3B Pc (44%), and the remaining minor products A_2B_2 , AB_3 , and B_4 Pcs (23%) [109] as shown in **Scheme 1.2** which might be eliminated by column chromatography using silica or alumina.



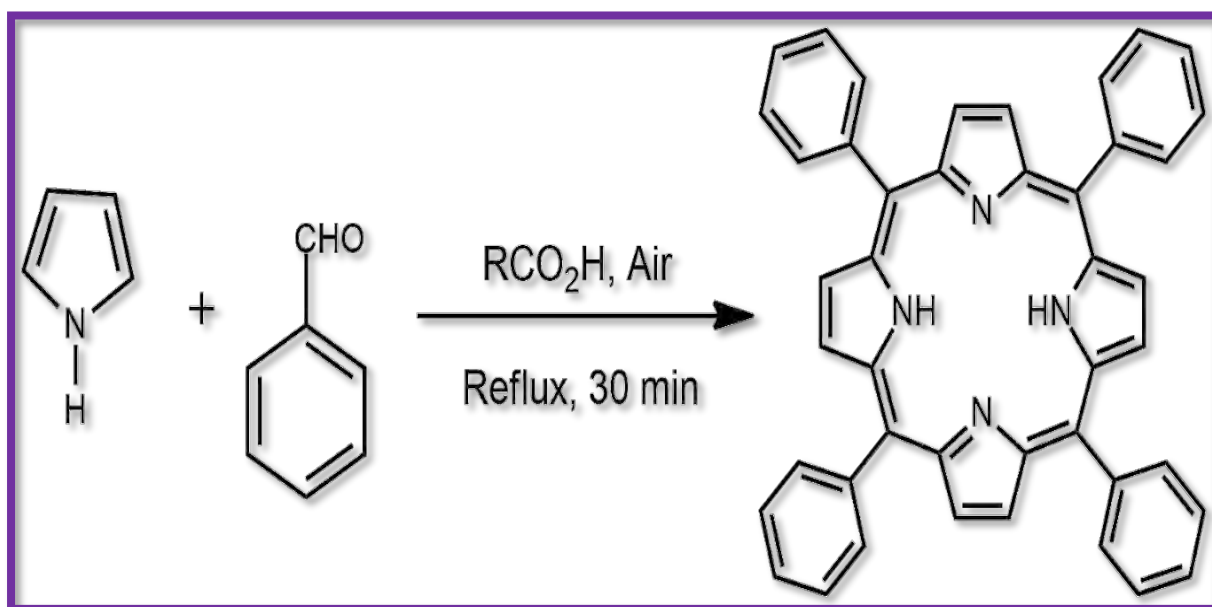
Scheme 1.2 General types of asymmetric phthalocyanines and their symmetric derivatives resulting from a reaction mixture prepared by a statistical condensation approach.

1.3.2.2. Porphyrins

In general, there are two types of porphyrins: synthetic and biological porphyrins. Synthetic porphyrin complexes such as *meso*-tetraphenyl porphyrins have shown interesting photophysical, chemical, and biological properties for medicinal and industrial applications. In this work, the

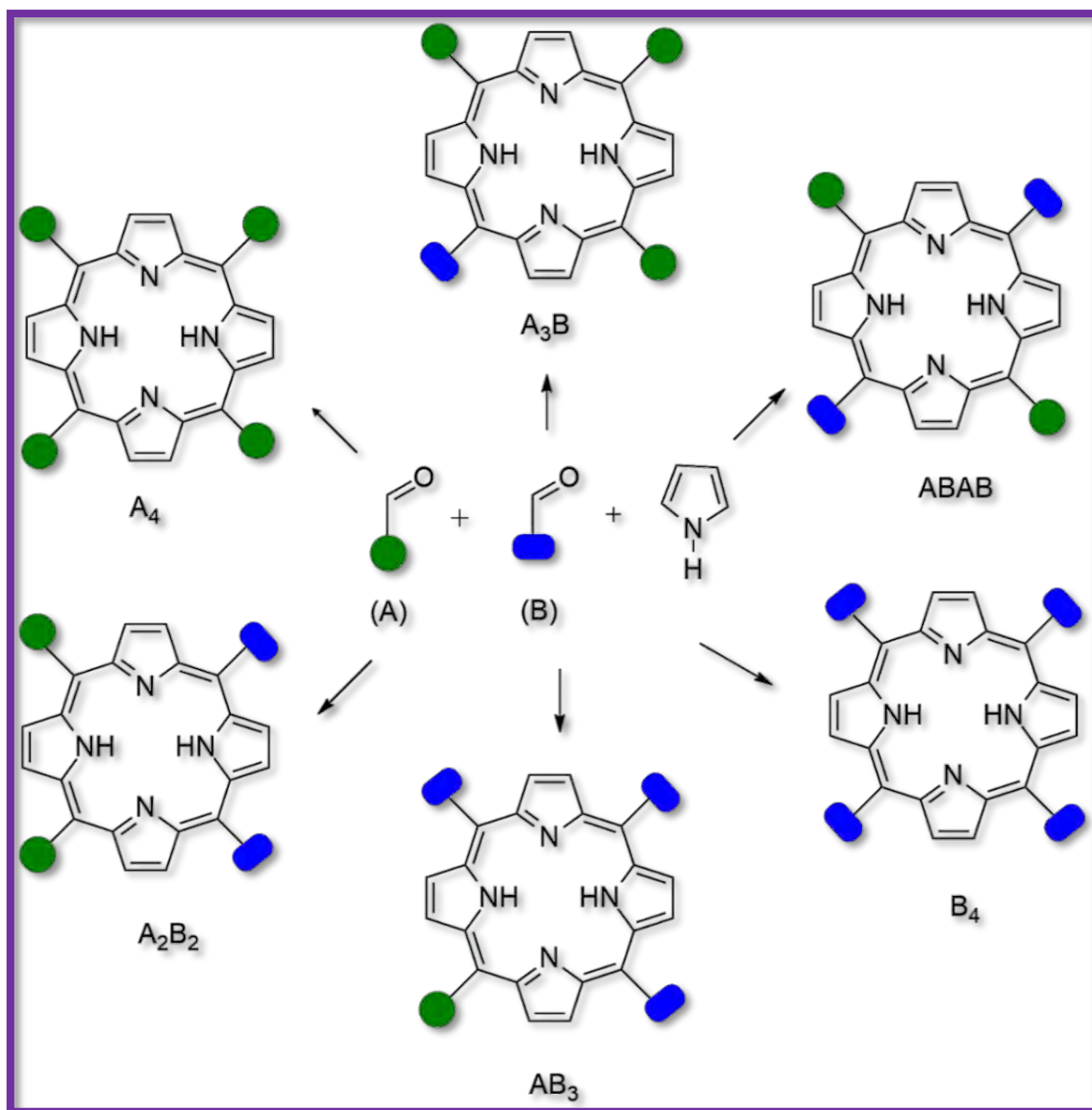
symmetrical (A_4 -type), asymmetrical (A_3B -type), and cationic *meso*-substituted tetraphenyl porphyrins were synthesized following Adler and Longo method. This method was implemented to improve the low yield problem encountered in the previously used procedure described by Rothmund and Menotti [111,112]. In the Adler and Longo method, an aldehyde and pyrrole are reacted in refluxing propionic acid to afford ~20% yields (Scheme 1.3). Other methods such as the Lindsey method are used in the case of aldehyde precursors bearing acid-sensitive functional groups (hydroxyl, thiol, and amino groups) and the microwave-assisted methods have also proven to yield enough amount of porphyrins in a short reaction time [111].

The above synthetic procedure for the synthesis of A_4 type *meso*-substituted porphyrins used in this work is simple and includes a one-step or two-step one-flask condensation reaction of pyrrole with the one desired aldehyde (please see Scheme 1.3) [112,113].



Scheme 1.3 Alder-Longo procedure for the synthesis of *meso*-substituted porphyrins.

The A_3B type can also be prepared following the same procedure used for the symmetrical A_4 porphyrins except that two different aldehydes A and B are used at the same time in a 1:3 molar ratio to reduce the formation of respective A_4 and B_4 porphyrins type [114,115]. This reaction results in the formation of other by-products depicted in Scheme 1.4. They may be removed from the reaction product by column chromatography.



Scheme 1.4 General illustration of asymmetrical porphyrins and their symmetrical analogs resulting from the reaction mixture.

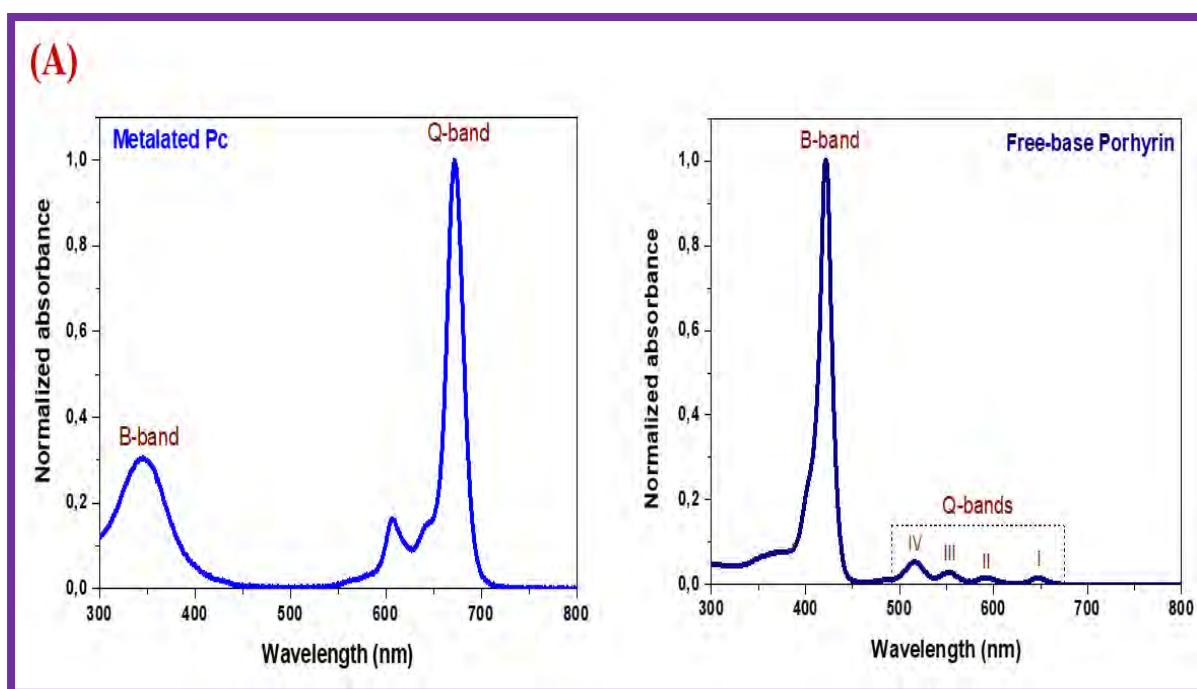
1.3.3. UV-Vis Absorption Spectra of Phthalocyanines and Porphyrins

For Pcs, the intense blue-green color is due to the electronic delocalization of the 18 π electrons in the Pc core. The ground state electronic absorption spectra of a typical metallated Pc with D_{4h} symmetry has an unsplit lowest energy band (Q band) and a less-intense Soret band (B band) [84] (Figure 1.6A left). For the free-base Pcs, the Q band splits into two bands as a result of lower symmetry. As per Gouterman's four orbital model, the Q-band is associated with the π - π^* transition between the ground state highest occupied molecular orbital (HOMO) a_{1u} to the lowest unoccupied molecular orbital (LUMO) degenerate e_g , while the B-band is due to the overlap of B_1 and B_2 bands

arising from the a_{2u} and b_{2u} of the HOMO to the e_g of the LUMO (**Figure 1.6B**), hence explaining its broadness [116,117].

On the other hand, the porphyrins absorption profile (**Figure 1.6A right**) indicates an intense absorption in the region around 400 nm (the Soret band) and several weaker absorptions (Q bands) at around 450 to 700 nm. The insertion or change of metal ions into the cavity of a porphyrin usually strongly changes the visible absorption spectrum, resulting in shifts of absorption bands to longer or shorter wavelengths [118]. Following Gouterman's four orbitals model, four Q-bands are observed for free-base porphyrins as a result of the N-H protons that splits the symmetry, **Figure 1.6A**, and only two Q-bands are observed for the metalated porphyrins [111,119]. The absorption bands in porphyrins arise from transitions between a_{1u} and a_{2u} orbitals to e_g orbitals, **Figure 1.6B**.

The absorption spectra of Pcs are different from those of porphyrins regardless of their similar structures. The Q-bands are more intensified in the Pcs spectra because meso-carbons are substituted with nitrogen atoms and the fused benzene rings to the core of a Pc. Consequently, these modifications enhance the energy imbalance between the HOMOs a_{1u} and a_{2u} . For instance, for Pcs, a_{1u} and a_{2u} orbitals are widely separated whereas for porphyrins they are close enough (please see **Figure 1.6B**). This leads to an extensive configuration interaction of their transitions to e_g which results in a difference in the intensity of the B-bands of Pcs compared to porphyrins [86,117,120].



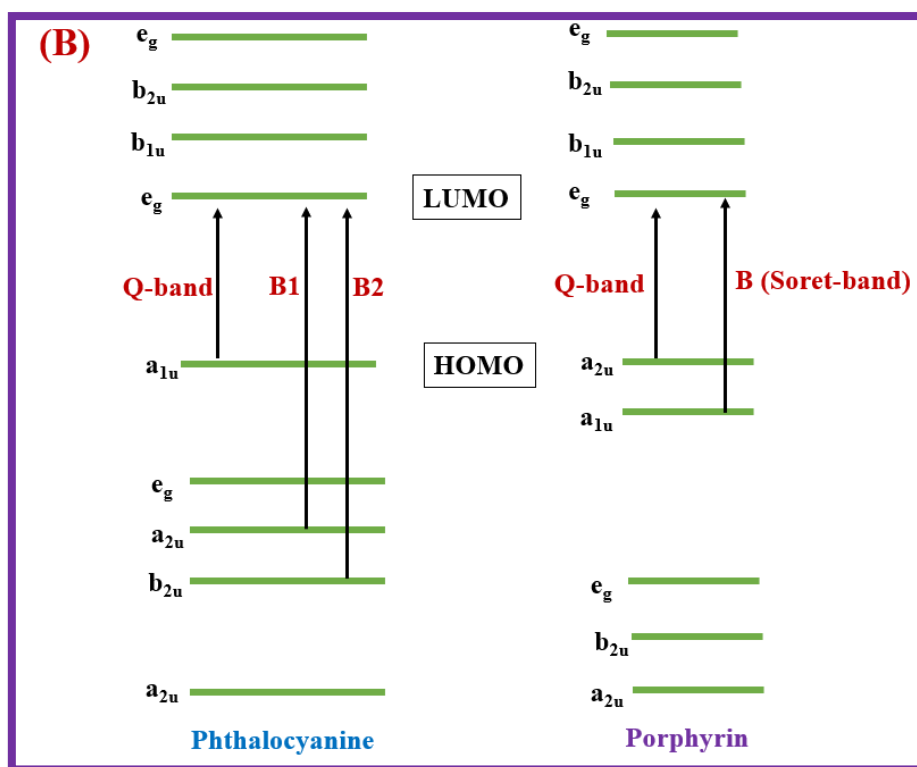


Figure 1.6 (A) Typical UV-Vis ground state electronic absorption spectra of a metallated Pc on the left and a free-base porphyrin on the right. **(B)** shows the electronic energy levels of the set of eg orbitals showing the origin of Q and B bands.

1.3.4. Improving Water Solubility and Reducing Aggregation

Pcs and porphyrins tend to aggregate. Aggregation affects their optical properties, and physicochemical properties (decrease of the singlet oxygen quantum yield by dissipating energy through internal conversions), hence lesser photoactivity [121–123]. This problem can be overcome by incorporating central metals with axial ligands, bulky peripheral substituents, quaternization of the PSs, and functionalization of PSs with nanomaterials. Additionally, incorporating PSs in nanoparticles also plays an influential role. Nanoparticles improve the targeting of specific cells, increase the bioavailability of the PSs, and improve photoactivity [124,125]. All these potential strategies were applied to the PSs synthesized in the present work in order to increase their water-solubility, targeting specificity as well as photophysical properties. In particular, this thesis reports for the first time on the conjugation of Pcs and porphyrins to carbon nanomaterials such as graphene quantum dots (GQDs) and detonation nanodiamonds (DNDs) for application in PACT and PACT-antibiotics dual therapy. These nanomaterials have a high affinity for pathogenic bacteria and tumor cells thanks to the functional groups on their surfaces which improve the solubility of the nanoconjugates.

1.4. Carbon Nanomaterials

“Graphene is dead, long live graphene. What is important about graphene is the new physics it has delivered.”

- Andre Geim
(2010; Nobel Prize in Physics)

1.4.1. Structure and Applications

Carbon nanomaterials are characterized by unique structural dimensions, chemical versatility, attractive mechanical, electrical, thermal, and optical properties [126]. They include fullerenes, carbon nanotubes, graphene, and its derivatives; graphene oxide, GQDs, and DNDs [127]. Carbon nanomaterials have emerged as promising platforms for theragnostics due to their unique structural dimensions, the large surface area that favours high loading efficiency of drugs, ease of functionalization using a panoply of reactions, and their biocompatibility [125,128].

The additional properties such as stable photoluminescence, low toxicity, chemical stability, antibacterial properties, and their great ability to form π - π interaction with other π electron-rich molecules such as Pcs and porphyrins [129–132] were the main points in investigating the effect of the **GQDs**, glutathione (GSH) capped GQDs (labeled as **GSH@GQDs**), and DNDs functionalized with chitosan-capped silver nanoparticles (**DNDs-CSAg**) and DNDs capped with Ag NPs (**DNDs@Ag**) on the PACT/PDT activity. The choice made upon GSH, CSAg, and Ag NPs as capping agents is to improve the photophysicochemistry and photoactivity of the nanomaterials.

1.4.2. Synthesis

There are two general methods for the synthesis of GQDs/DNDs nanomaterials: the top-down and bottom-up approaches.

The “top-down” approach (defined as the breaking down of the bulk carbon-based materials into nanosized particles) includes electrochemical methods [133], chemical exfoliation [134], chemical oxidation cutting graphene sheets derived from graphene oxide, [134,135], and hydrothermal [136] to cite but a few. The top-down approach is used in this work for the synthesis of GQDs. Whereas the “bottom-up” approach (or the synthesis of the nanomaterials from small particles) includes chemical synthesis [137].

The DNDs used in this work were purchased from suppliers. DNDs contain extra functional groups such as -NH_2 , NO_2 , and -C(O)NH_2 on their surface, and not just -OH and -COOH as is the case for GQDs [138]. The functional groups predetermine the hydrophilicity and ability for conjugation to drugs *via* chemical bonding. On top of that, the presence of sp^2 hybridization on DNDs and the GQDs allows for π - π stacking and electrostatic interactions with other π -containing molecules or positively charged compounds, respectively. Both cases were considered and applied in the current work as well.

1.4.3. Loading Mechanisms of PSs on Carbon Nanomaterials

As mentioned above, the conjugation of the GQDs and DNDs to other molecules can be achieved by either physical adsorption through noncovalent interactions or by covalent linkage through the surface functional groups for stable and site-specific bonding. The two different loading mechanisms of PSs on nanomaterials are represented in **Figure 1.7**.

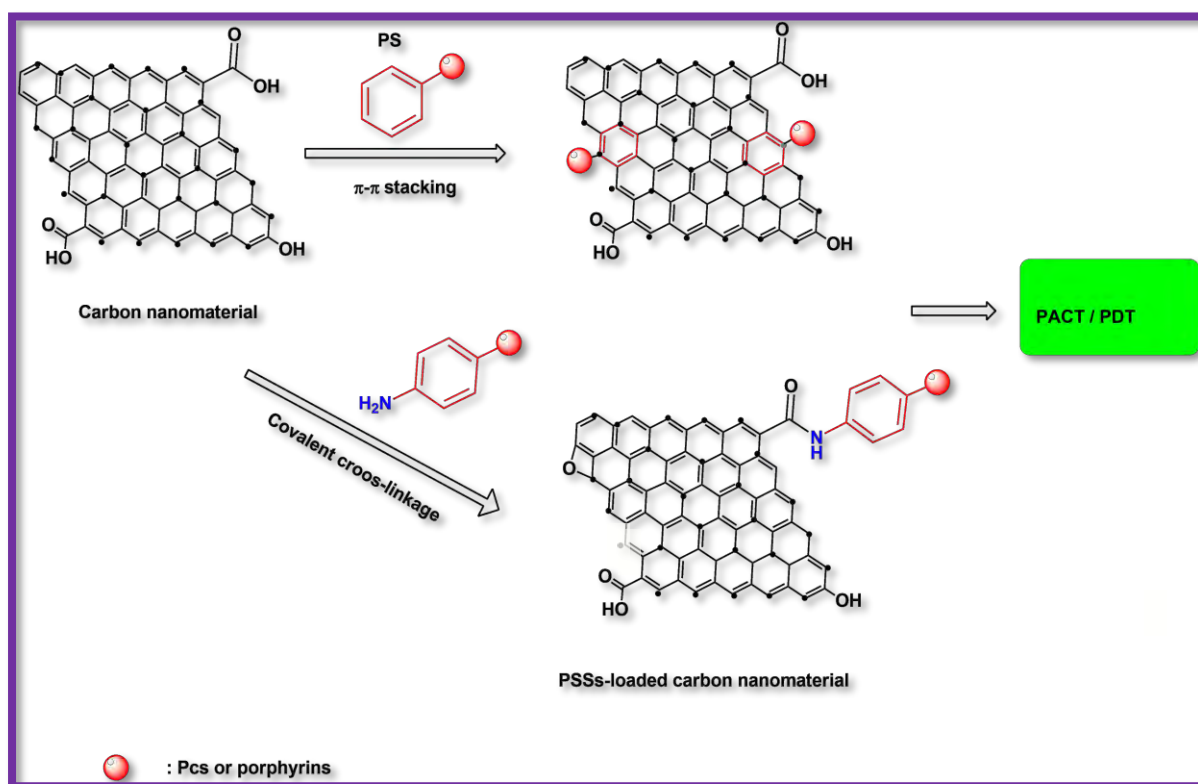


Figure 1.7 Schematic illustration of loading mechanisms of PSs on carbon nanomaterials.

Non-covalent bonding process includes the hydrophobic and electrostatic interactions, Van der Waal's forces, and the π - π stacking interaction which was used in this work. Both the GQDs or

DNDs and Pcs or porphyrins have aromatic ring carbon structures, so they can stack on each other's surface by π -bonds [125]. The advantage of this noncovalent bonding is that there is no damage to the structure and properties of both the drugs and nanomaterials.

The covalent linkage is like introducing a defect in the open ends of the nanomaterial [139]. In this work, the COOH group on GQDs/DNDs and the NH₂ group on PSs will be coupled to form an amide bond using activating agents.

1.4.4. Electronic Absorption Properties

Typical ground-state absorption spectra of the GQDs and DNDs exhibit a broad absorption peak around 300-350 nm which is associated with the n - π^* and π - π^* transitions of the carboxylic C=O group and aromatic sp^2 hybridization on the surface of the nanomaterials respectively, as shown in **Figure 1.8** [140–142]. Please also note that the sizes [140,143] and functional groups [144,145] on the nanoparticles can alter the bandgap and result in red or blue spectral shifts.

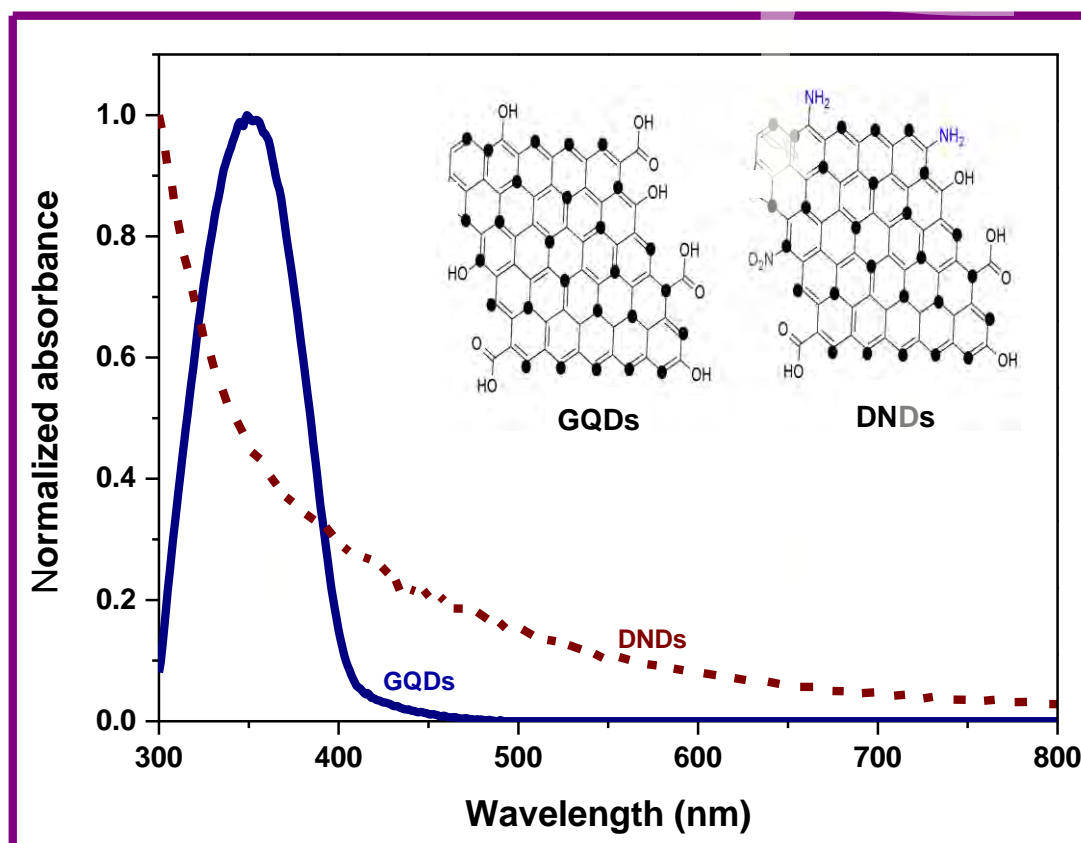


Figure 1.8 Typical absorption spectra of GQDs and DNDs in DMSO.

1.5. Phthalocyanines and Porphyrins-loaded GQDs/DNDs Nanohybrids and their Various Applications

“The real voyage of discovery consists not in seeking new landscapes but in having new eyes.”

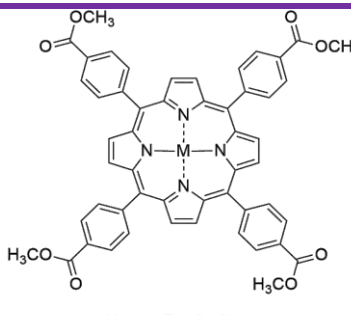
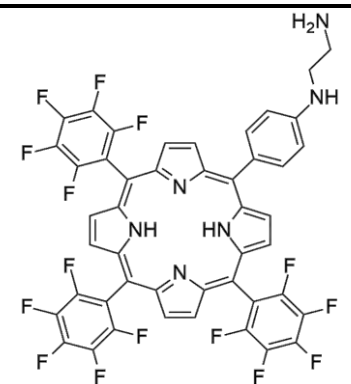
- Marcel Proust

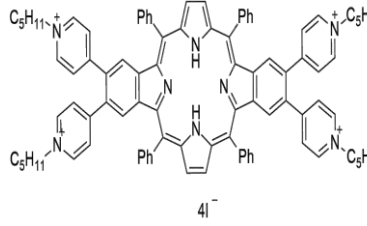
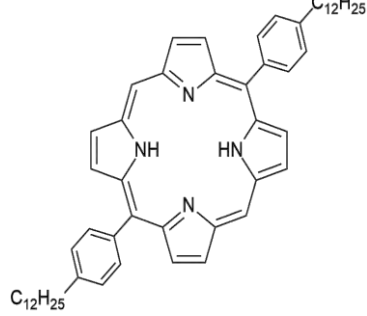
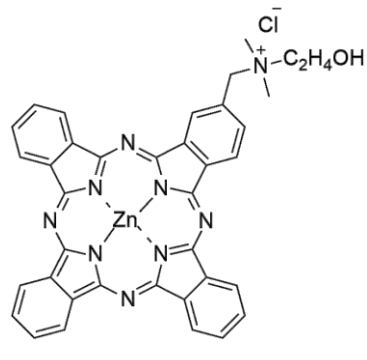
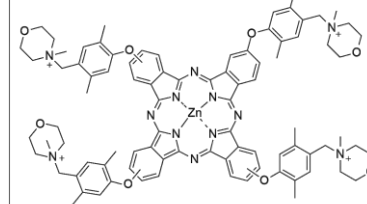
(1922; French Novelist)

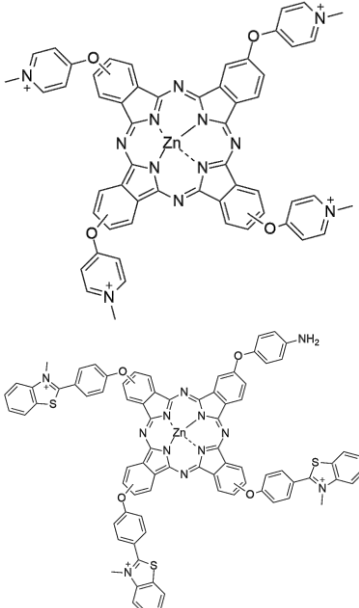
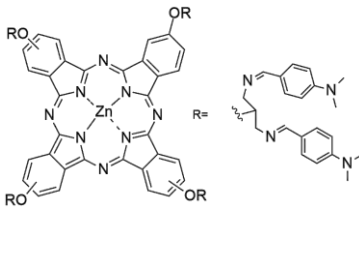
1.5.1. Previous Works Reported in the Literature

Table 1.1 shows previously reported works on PSs-loaded carbon nanomaterials hybrids (Pcs/porphyrins and GQDs/DNDs for the present study) and their PACT/PDT applications [146-154].

Table 1.1 Examples of Pcs/porphyrins and their carbon nanomaterials hybrids used in PDT and PACT.

Photosensitisers	Carbon-based nanomaterials	Types of bonding	Phototherapy/ applications	Refs.
(A) Porphyrins				
 <p>M= H₂, Zn, GaCl</p>	GQDs	Noncovalent (π - π stacking)	PDT/ Breast cancer MCF-7	[146]
	GQDs	Covalent (Amide cross-linking)	PDT/T-47D breast cancer	[147]

 <p style="text-align: center;">4⁻</p>	GQDs	Noncovalent	PDT/ T24 Human Bladder Cancer Cells	[148]
	Polyethylene glycol-GQDs	Noncovalent (π - π stacking)	PDT/A549 cells and MCF-7 cells	[149]
(B) Phthalocyanines				
	DNDs	Non-covalent cross-linkage (Adsorption)	PACT/ <i>E. coli</i> planktonic cells	[150]
	GQDs-Biotin	Noncovalent (π - π stacking)	PDT/MCF-7 cancer cells	[151]

	<p>Bodipy-DNDs</p> <p>and</p> <p>DNDs B@DNDs S@DNDs N@DNDs S, N@DNDs P@DNDs</p>	<p>Noncovalent (π-π stacking)</p> <p>Covalent (Amide cross-linking)</p>	<p>PDT/ MCF-7 Breast cancer</p>	<p>[152]</p> <p>[153]</p>
	<p>N, S doped GQDs</p>	<p>Noncovalent (π-π stacking)</p>	<p>PACT/ <i>S. aureus</i> planktonic cells</p>	<p>[154]</p>

Bodipy: boron-dipyrromethene

From the data presented in **Table 1.1**, one can notice the following: (1) no work has reported the dual antimicrobial activity of porphyrins and DNDs nanoconjugates. (2) DNDs have been combined with a few phthalocyanines for PDT but there is only one report about PACT on planktonic cells of *E. coli* (a Gram-negative bacteria). (3) All PACT works focus on methods utilizing planktonic bacteria but not on the more difficult to treat bacterial biofilms [150].

As illustrated in **Table 1.2** below, herein this thesis reports for the first time, on the use of these types of hybrids (PSs-DNDs: covalent and non-covalent hybrids) for applications in PACT against both planktonic and most difficult-treated biofilms cells of *S. aureus*, a Gram-positive bacteria as well as *E. coli*, a Gram-negative bacteria that cause chronic diseases in humans. The current work also presents the first study of antimicrobial activity using Pcs and porphyrins conjugated to either GQDs, DNDs, DNDs@Ag, DNDs-CSAg, or GSH@GQDs.

No report has demonstrated so far, the potential impact of PACT-antibiotic dual therapy using Pcs, porphyrins, and their various nanoplateforms in sequential administration of these agents with

ciprofloxacin (quinolone type of antibiotic). This work describes and addresses this for the very first time.

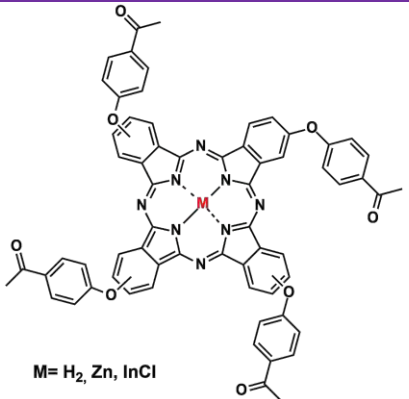
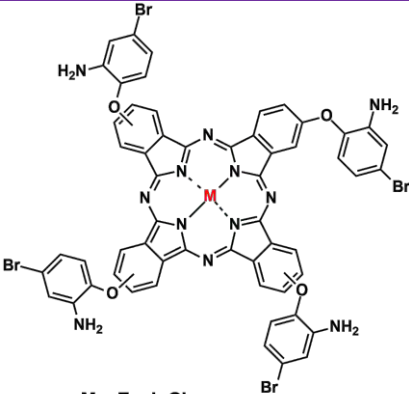
1.5.2. Phthalocyanines/Porphyrins and their Nanohybrids used in the Present Work

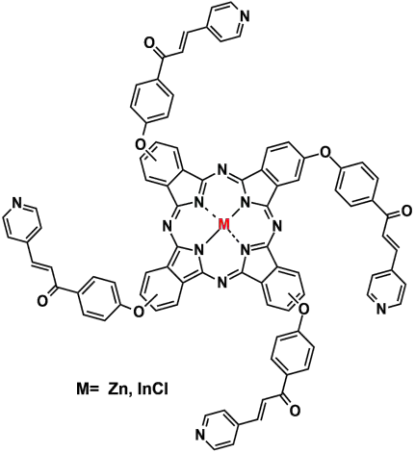
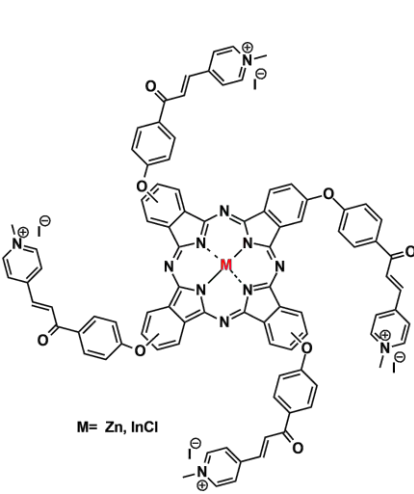
This work describes the synthesis of novel metal-free and metallated symmetrical and asymmetrical substituted Pcs and porphyrins containing bulky substituents. The central metals of interest in this study are the diamagnetic metal ions: zinc (II), gallium (III), and indium (III). They were specially chosen for their closed-shell structure and heavy atom effect which are known to promote the intersystem crossing (ISC) process which populates the triplet state [155].

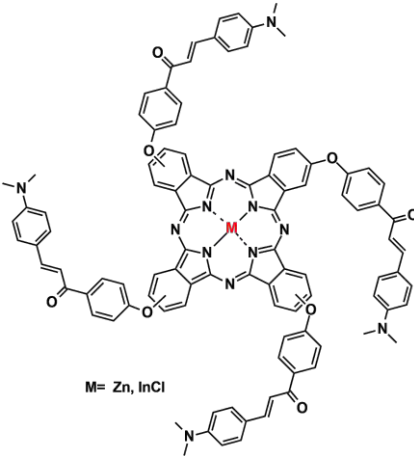
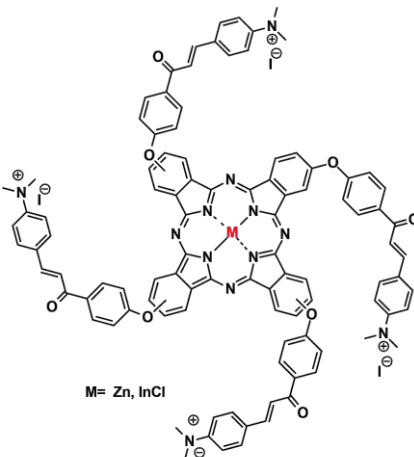
The aim for quaternization of some of the complexes used in this work was to improve complexes' solubility and specificity to target cells, thus subsequently improving photophysical properties of the complexes and PACT/PDT efficiencies.

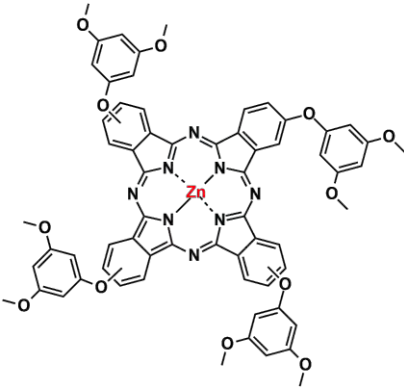
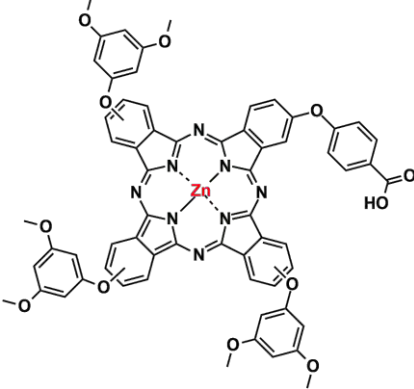
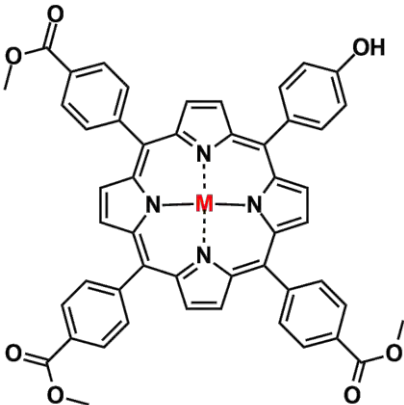
All groups of complexes (**1** to **8**) used in this study are novel and listed in **Table 1.2**. Please note that **Table 1.2** includes the carbon-based nanomaterials employed as well as the applications applied in this work.

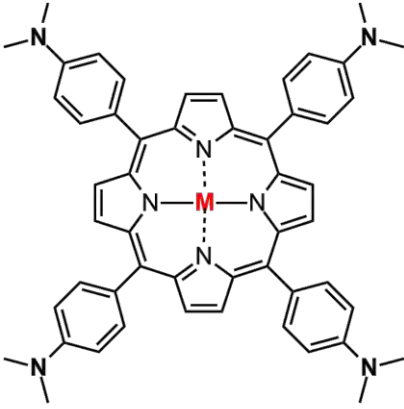
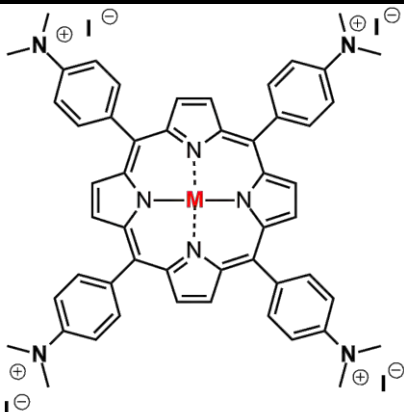
Table 1.2 Phthalocyanines/porphyrins groups and their carbon-based nanohybrids synthesized in the current work.

Photosensitisers	PSs name and Group label	Types of bonding	Studies and Applications
(A) Phthalocyanines			
 <p>M= H₂, Zn, InCl</p> <p>(All NEW)</p>	<p><i>Tetrakis</i>-[4-(acetophenoxy) Phthalocyaninato]</p> <p>Group: (1)</p> <p>M: H₂ = 1-H₂ Zn = 1-Zn InCl = 1-In</p>	<p>GQDs / DNDs</p> <p>Noncovalent (π-π stacking)</p>	<p>Physicochemical</p> <p><u>PACT</u> <i>S. aureus</i> Planktonic cells</p>
 <p>M= Zn, InCl</p> <p>(All NEW)</p>	<p><i>Tetrakis</i>[4-(2-amino-4-bromophenoxy) Phthalocyaninato]</p> <p>Group: (2)</p> <p>M: Zn = 2-Zn InCl = 2-In</p>	<p>DNDs</p> <p>Noncovalent (π-π stacking)</p> <p>DNDs-CSAg</p> <p>Covalent (Amide cross-linking)</p>	<p>Physicochemical</p> <p><u>PACT</u> <i>S. aureus</i> Planktonic and Biofilm cells</p>

 <p>M= Zn, InCl</p> <p>(All NEW)</p>	<p><i>Tetrakis[(E)-4-(4-(3-(pyridin-4-yl)acryloyl)phenoxy)phthalocyaninato]</i></p> <p>Group: (3)</p> <p>M: Zn = 3-Zn InCl = 3-In</p>	<p>DNDs</p> <p>Noncovalent (π-π stacking)</p>	<p>Physicochemical</p> <p><u>PACT</u> <i>S. aureus/ E. coli</i> Planktonic and Biofilm cells</p>
 <p>M= Zn, InCl</p> <p>(All NEW)</p>	<p><i>Tetrakis[(E)-4-(4-(3-(pyridin-4-yl)acryloyl)phenoxy)phthalocyaninato] tetraiodide</i></p> <p>Group: (3)</p> <p>M: Zn = 3-ZnQ InCl = 3-InQ</p>	<p>DNDs</p> <p>Noncovalent (π-π and electrostatic interactions)</p>	<p>Physicochemical</p> <p><u>PACT</u> <i>S. aureus/ E. coli</i> Planktonic and Biofilm cells</p>

 <p>M= Zn, InCl</p> <p>(All NEW)</p>	<p><i>Tetrakis</i>[(<i>E</i>)-4-(4-(3-(dimethylamino)-4-yl)acryloyl)phenoxy]phthalocyaninato]tetraiodide</p> <p>Group: (4)</p> <p>M: Zn = 4-Zn InCl = 4-In</p>	<p>-</p>	<p>Physicochemical</p> <p><u>PDT</u> Breast cancer MCF-7</p> <p><u>PACT</u> <i>S. aureus/ E. coli</i> Planktonic and Biofilm cells</p>
 <p>M= Zn, InCl</p> <p>(All NEW)</p>	<p><i>Tetrakis</i>[(<i>E</i>)-4-(4-(3-(dimethylamino)-4-yl)acryloyl)phenoxy]phthalocyaninato]tetraiodide</p> <p>Group: (4)</p> <p>M: Zn = 4-ZnQ InCl = 4-InQ</p>	<p>-</p> <p>Ciprofloxacin (Dual chemo-PACT)</p>	<p>Physicochemical</p> <p><u>PDT</u> Breast cancer MCF-7</p> <p><u>PACT</u> <i>S. aureus/ E. coli</i> Planktonic and Biofilm cells</p>

 <p>(NEW)</p>	<p><i>Tetrakis</i>[(3, 5-dimethoxyphenoxy)phthalocyanato] zinc (II)</p> <p>Group: (5)</p> <p>5-Zn</p>	<p>GSH@GQDs</p> <p>Noncovalent (π-π stacking)</p>	<p>Physicochemical</p> <p><u>PACT</u> <i>S. aureus</i> Planktonic cells</p>
 <p>(NEW)</p>	<p><i>mono</i>-[(4-carboxylic acid phenoxy)-tris-(3, 5-dimethoxyphenoxy)phthalocyanato] zinc (II)</p> <p>Group: (6)</p> <p>6-Zn</p>	<p>GSH@GQDs</p> <p>Covalent (Amide cross-linking)</p>	<p>Physicochemical</p> <p><u>PACT</u> <i>S. aureus</i> Planktonic cells</p>
<p>(B) Porphyrins</p>			
 <p>M= H₂, Zn, InCl, GaCl</p> <p>(All NEW)</p>	<p>5-(4-Hydroxyphenyl)-tris-10, 15, 20-(4-acetylphenyl)-porphyrin</p> <p>Group: (7)</p> <p>M: H₂ = 7-H₂ Zn = 7-Zn InCl = 7-In GaCl = 7-Ga</p>	<p>DNDs@Ag</p> <p>Covalent (Ester cross-linking)</p>	<p>Physicochemical</p> <p><u>PACT</u> <i>S. aureus</i> Planktonic and Biofilm cells</p>

 <p style="text-align: center;">M= InCl, GaCl</p> <p style="text-align: center;">(All NEW except 8-H₂)</p>	<p style="text-align: center;">5,10,15,20-tetrakis(4-dimethylaminophenyl)-porphyrins</p> <p style="text-align: center;"><u>Group: (8)</u></p> <p>M: H₂ = 8-H₂ InCl = 8-In GaCl = 8-Ga</p>	-	<p style="text-align: center;">Physicochemical</p> <p style="text-align: center;"><u>PACT</u> <i>S. aureus/ E. coli</i> Planktonic and Biofilm cells</p>
 <p style="text-align: center;">M= InCl, GaCl</p> <p style="text-align: center;">(All NEW except 8-H₂Q)</p>	<p style="text-align: center;">5,10,15,20-tetrakis[(4-dimethylaminophenyl)-porphyrins] tetraiodide</p> <p style="text-align: center;"><u>Group: (8)</u></p> <p>M: H₂ = 8-H₂Q InCl = 8-InQ GaCl = 8-GaQ</p>	-	<p style="text-align: center;">Physicochemical</p> <p style="text-align: center;"><u>PACT</u> <i>S. aureus/ E. coli</i> Planktonic and Biofilm cells</p> <p style="text-align: center;">Ciprofloxacin (Dual chemo-PACT)</p>

1.5.3. The Logical Basis used in the Present Work

- ✓ Complexes within the same group (**1** to **8**) will be studied to compare the effect of central metal on the photophysicochemical properties and PACT or PDT activity.
- ✓ Phthalocyanines containing the same central metals: (i) **1-Zn, 2-Zn, 3-Zn, 4-Zn, 5-Zn**, and (ii) **1-In, 2-In, 3-In, 4-In** will be compared for the effect of different substituents on the photophysicochemical properties and PACT activity.
- ✓ Porphyrins containing the same central metals: (i) **7-Ga, 8-Ga**, and (ii) **7-In, 8-In** will also be compared for the effect of different substituents on the photophysicochemical properties and PACT activity.
- ✓ Complexes: (i) **3-Zn, 3-In** will be compared to **3-ZnQ, 3-InQ**; (ii) **4-Zn, 4-In** will be compared to **4-ZnQ, 4-InQ** and (iii) **8-Ga, 8-In** will be compared to **8-GaQ, 8-InQ** to

study the effect brought by quaternization on the photophysicochemical properties and PACT or PDT activity.

- ✓ **5-Zn** will be compared to **6-Zn** to evaluate the effect of symmetry then both will be compared to their nanoconjugates to study the effect of GSH@GQDs.
- ✓ Complexes from **Group 1** will be used to compare the effect brought by the presence of different carbon nanomaterials (GQDs vs DNDs) on the photophysicochemical properties and PACT activity.
- ✓ Complexes from **Groups 2 and 7** and their nanoconjugates will be studied to compare the effect brought by functionalizing DNDs with CSAg and Ag NPs, respectively on the photophysicochemical properties and PACT activity.
- ✓ Susceptibility of planktonic cells in comparison to biofilms cells for both *S. aureus* and *E. coli* strains towards PACT activity of quaternized complexes will be investigated.
- ✓ Complexes of **Group 4** will be used to study both PDT and PACT activity.
- ✓ **4-InQ** and **8-InQ** complexes will be used as models to further study PACT-Ciprofloxacin dual therapy.

1.6. Aims of the Study

“Science is the only light in the dark paths of the unknown.” ... “Let there be light.”

-Genesis 1:3

(Holy Bible)

1.6.1. Main Objective

It is imperative to explore new photosensitizers since they play a crucial role in the phototherapeutic outcomes of PACT and PDT. The overall goal of this study was to design and synthesize novel Pcs-based and porphyrins-based photosensitizers along with their GQDs and DNDs nanoplateforms to improve efficiency in PACT and their specificity to target bacterial planktonic and biofilm cells that invade surfaces such as diabetic wounds and medical devices.

Hence, this study gained insight into the following queries: (1) can Pcs bearing antibacterial molecules like acetophenoxy groups or naturally occurring substituents such as chalcones, be effective for PACT? (2) can Pcs or porphyrins-loaded in GQDs or DNDs also eradicate multidrug-resistant surface-bacterial biofilms without inducing the development of undesired resistance? (3) can the dual photobactericidal effect of PACT combined with ciprofloxacin be a feasible strategy to overcome multidrug resistance? And the anticancer photodynamic therapy of the new carbon nano hybrids was also investigated.

1.6.2. Specific Objectives

The present study aims at the following specific objectives:

1. Design and synthesize of new series of Pcs and porphyrins (neutral, cationic, symmetrical, and asymmetrical molecules),
2. Synthesize the nanoparticles of interest, in this case; **GQDs** alone, GQDs capped with GSH (**GSH@GQDs**), DNDs functionalized with **Ag NPs** and **DNDs** functionalized with chitosan-mediated silver nanoparticles (**CSAg**),
3. Design and construct different Pcs/porphyrins-loaded carbon nanomaterials hybrids with an overall goal of enhancing their photophysicochemical properties,
4. Characterize all the synthesized molecules and their nano hybrids,
5. Investigate the photochemical and photophysical properties of the as-prepared photosensitizers and nanoconjugates,

6. Provide the theoretical studies of selected PSs,
7. Evaluate the possible photo-antimicrobial activity enhancements of the molecules and nanohybrids on *S. aureus* and *E. coli* planktonic and biofilms cells by assessing:
 - The potential of quaternized PSs against multidrug-resistant planktonic and biofilms microbial cells *in vitro*,
 - The effect of central metal: Zn (II), Ga (III), and In (III), a significant factor for PACT efficiency,
 - The effect of symmetry by comparing complexes inhibition efficiencies on PACT,
 - If the loading of PSs into different GQDs and DNDs influences the photophysicochemical parameters and PACT activities,
8. Evaluate the PACT-Ciprofloxacin dual therapy of some model PSs against *S. aureus* and *E. coli* and their biofilms counterparts, and
9. Investigate the ability of some model PSs on MCF-7 breast cancer cells lines. The chalcone-derived Pcs were chosen due to their anticancer properties of chalcones.

PART II.

Methodology and Experimental

Chapter Two: General Techniques, Instruments, and Methods

This chapter outlines the specific materials, equipment, and methods used in the experimental processes involved in this work.

2.1. Chemical Reagents and Equipment

Unless otherwise indicated, all commercially available starting materials and solvents were of analytical grade purity and used without any further purification. Reactions were carried out under anhydrous conditions in dried solvents under an argon or nitrogen atmosphere. The reaction completion was monitored by thin-layer chromatography (TLC) using silica gel plates with a UV activator.

2.1.1. Chemicals for the Synthesis of Phthalonitriles

4-Nitrophthalonitrile, 4-hydroxyacetophenone, 2-amino-4-bromophenol, and potassium carbonate, 4-pyridinecarboxaldehyde, 4-(dimethylamino)benzaldehyde were acquired from Sigma Aldrich. 4-(3,5-Dimethoxyphenoxy)phthalonitrile (**5**) [156] and 4-(4-carboxyphenoxy)phthalonitrile (**6**) [157] have been reported elsewhere.

2.1.2. Chemicals for the Synthesis of Phthalocyanines and Porphyrins

Zinc acetate anhydrous (ZnOAc), indium (III) chloride, gallium (III) chloride, lithium (I) chloride anhydrous, 1,8-diazabicyclo [5.4.0]undec-7-ene (DBU), silica gel 60 (0.04-0.063 mm), iodomethane, 4-hydroxybenzaldehyde, methyl 4-formylbenzoate, pyrrole, sodium acetate (NaOAc), glacial acetic acid, propionic acid, and iodomethane were acquired from Sigma Aldrich.

2.1.3. Chemicals for the Synthesis of Nanomaterials and Nanoconjugates

Detonation nanodiamonds (DNDs), were obtained from Nanocarbon Research Institute Ltd. Graphene oxide (GO), *N, N'*-dicyclohexylcarbodiimide (DCC), *N*-hydroxysuccinimide (NHS), silver nitrate, sodium borohydride, sulfuric acid, nitric acid, sodium hydroxide, trisodium citrate, citric acid, glutathione (GSH), and chitosan were acquired from Sigma Aldrich. The synthesis of the GQDs [158,159], the glutathione capped GQDs (GSH@GQDs) [160], chitosan-capped silver nanoparticles (CSAg) [161], and the bare Ag NPs [162] were achieved following procedures previously described in the literature with slight modifications.

2.1.4. Chemicals for the Determination of Photophysicochemical Parameters

Diphenylisobenzofuran (DPBF), anthracene-9,10-bis-methylmalonate (ADMA), Ludox solution, unsubstituted zinc phthalocyanine (ZnPc) standard, zinc tetraphenyl-porphyrin (ZnTPP),

tetraphenyl-porphyrin (TPP), and 9,10-dimethylanthracene (DMA) were purchased from Sigma Aldrich. Rose Bengal (RB) was purchased from Fluka. Aluminum sulfonated phthalocyanine, a mixture of sulfonated derivatives (ALPcSmix) was synthesized according to literature methods [163].

2.1.5. Chemicals used in PACT/PDT

Tryptic soy broth (TSB), Triton X100, and crystal violet (CV) were acquired from Sigma Aldrich. Phosphate-buffer saline (PBS, pH 7.4) was prepared using appropriate amounts of Na₂HPO₄ and KH₂PO₄ in ultra-pure Type II water supplied by ELGA, Veolia water PURELAB, flex system (Marlow, UK) and was employed for aqueous solutions. Nutrient agar, nutrient broth, and agar bacteriological BBL Mueller Hinton broth were purchased from Merck and prepared as specified by the suppliers. *Staphylococcus aureus* (ATCC 25923) and *Escherichia coli* (ATCC 25922) were obtained from Davies Diagnostics. Ciprofloxacin hydrochloride was obtained from Aspen Pharmacare (Durban, South Africa).

Michigan Cancer Foundation-7 (MCF-7) breast cancer cell lines were obtained from Cellonex. Trypsin ethylenediaminetetraacetic acid (EDTA), trypan blue, neutral red cell proliferation reagent (WST-1), Dulbecco's phosphate-buffered saline (DPBS), and Dulbecco's modified Eagle's medium (DMEM) were obtained from Lonza, 10% (v/v) heat-inactivated fetal calf serum (FCS) and 100 mg per mL-penicillin-100 unit per mL-streptomycin-amphotericin B mixture were obtained from Biowest®.

2.1.6. Solvents

Some solvents such as dimethyl sulfoxide (DMSO), tetrahydrofuran (THF), *N,N*-dimethylformamide (DMF), methanol (MeOH), ethanol (EtOH), hexane, ethyl acetate, and chloroform were purchased from Merck. Deuterated dimethyl sulfoxide (DMSO-d₆), deuterated chloroform (CDCl₃), quinoline, toluene, dimethylaminoethanol (DMAE), 1-pentanol, and 1-hexanol were acquired from Sigma Aldrich. hydrochloric acid was purchased from SAARChem. Glacial acetic acid (AA) was purchased from Minema chemicals.

2.1.7. Equipment

1. Mass spectra were collected on a Bruker AutoFLEX III Smart-beam MALDI TOF/TOF mass spectrometer using α -cyano-4-hydrocinnamic acid as the matrix in the positive ion mode.

2. Proton and Carbon-13 Nuclear magnetic resonance (^1H and ^{13}C NMR) measurements were recorded in deuterated solvents (DMSO- d_6 or CDCl_3) at room temperature with Bruker[®] AVANCE 600 and 400 MHz NMR spectrometers. Chemical shifts were expressed in parts per million (ppm) relative to the tetramethylsilane (TMS) signal as an internal reference.
3. Elemental analyses data were collected from a Vario-Elementar[®] Microcube ELIII CHNS instrument analyzer.
4. A Shimadzu UV-2250 spectrophotometer was used to record all the ground-state absorption spectra in solution using a 1 cm path length cuvette and wavelength ranging between 300 and 800 nm.
5. Varian Eclipse spectrofluorimeter equipped with 360-1100 nm filter was used to conduct the fluorescence excitation and emission measurements in solution using a 1 cm path length quartz cuvette.
6. Fourier transform-infrared spectroscopy was performed using a Bruker Alpha IR (100 FT-IR) spectrophotometer with universal attenuated total reflectance (ATR).
7. Raman spectroscopy data were collected on a Bruker Vertex 70-Ram II Raman spectrometer equipped with a 1064 nm Nd: YAG laser and liquid nitrogen cooled germanium detector.
8. Dynamic light scattering (DLS) Malvern Zetasizer Nanoseries, Nano-ZS90 particle distribution samples were investigated using dynamic light scattering (DLS) to provide information about the average size distribution in solution.
9. Transmission electron microscopy (TEM) micrographs were obtained from a Zeiss Libra 120 TEM operating at 80 kV and an INCA PENTA FET coupled to the VAGA TESCAME using 20 kV accelerating voltage.
10. Thermogravimetric analysis (TGA) was carried out using a Perkin Elmer TGA 800 thermogravimetric analyzer and the data were analyzed with Pyris Version 13.1.1 software.
11. Differential scanning calorimetry (DSC) analysis was done using a DSC 2500 TA instrument.
12. Time correlation single photon counting (TCSPC) setup (FluoTime 300, Picoquant GmbH) equipped with a Picoquant GmbH containing an LDH-P-670 diode laser with a 44 ps pulse width and 20 MHz rate repetition was used (**Figure 2.1**) to determine fluorescence lifetimes for all Pcs and their nanoconjugates, and a diode laser LDH-P-485 with 10 MHz repetition rate, 88 ps pulse width for GQDs. For porphyrins, a diode laser with excitation source: LDH-P-420 with 10 MHz repetition rate, 88 ps pulse width, Picoquant GmbH was used.

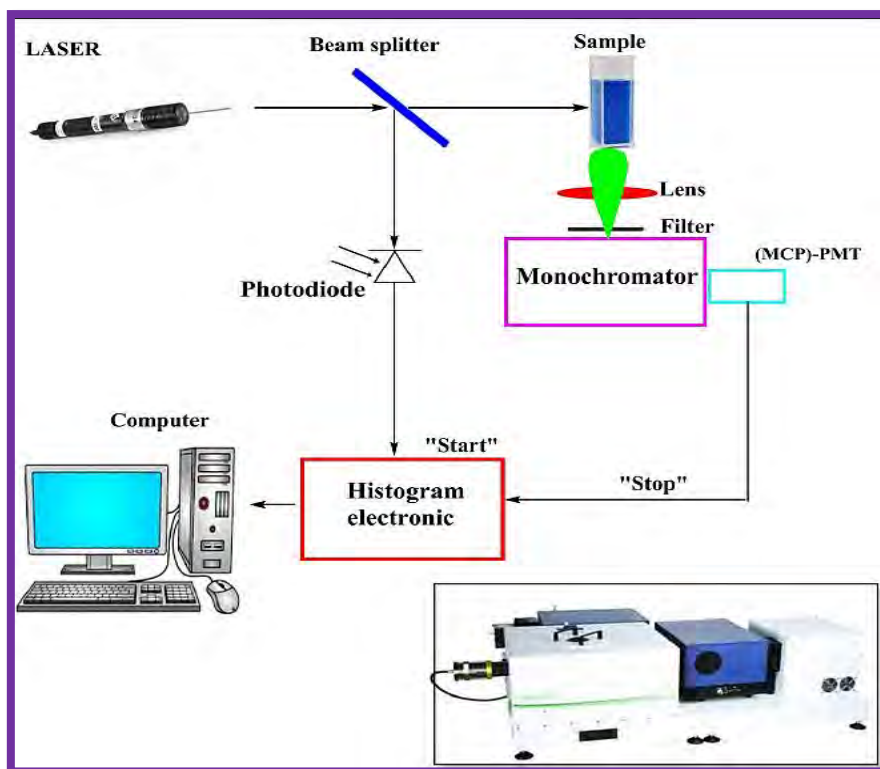


Figure 2.1 Representative diagram of a TCSPC setup.

(MCP)-PMT= (Multichannel plate detector)-Photomultiplier tube. Insert shows the actual TCSPC setup that was used.

Fluorescence was detected using a thermoelectrically cooled photomultiplier tube Peltier cooled photomultiplier tube (PMT) (PMA-C 192N-M, Picoquant), and integrated electronics (PicoHarp 300E, Picoquant GmbH). A monochromator with a spectral width of 4 or 8 nm was used to select the specific emission wavelength band. Ludox solution (DuPont) standard with full width at half-maximum (FWHM) of about 300 ps was utilized for the calibration and indication of the response function of the system. All fluorescence decay curves were measured at the λ_{em} maxima. The data were examined with the FluoFit software (Picoquant[®]) and the statistical significance was kept below 0.05.

13. Triplet state quantum yields were determined using a laser flash photolysis system consisting of an LP980 spectrometer with a PMT-LP detector and an ICCD camera (Andor DH320T-25F03). The signal from a PMT detector was recorded on a Tektronix TDS3012C digital storage oscilloscope. The excitation pulses were produced by a tunable laser system consisting of an Nd:YAG laser (355 nm, 135 mJ/4-6 ns), pumping an optical parametric oscillator (OPO, 30 mJ/3-5 ns) with a 420 to 2300 nm (NT-342B, Ekspla) wavelength range. The schematic representation of the setup is shown in **Figure 2.2**.

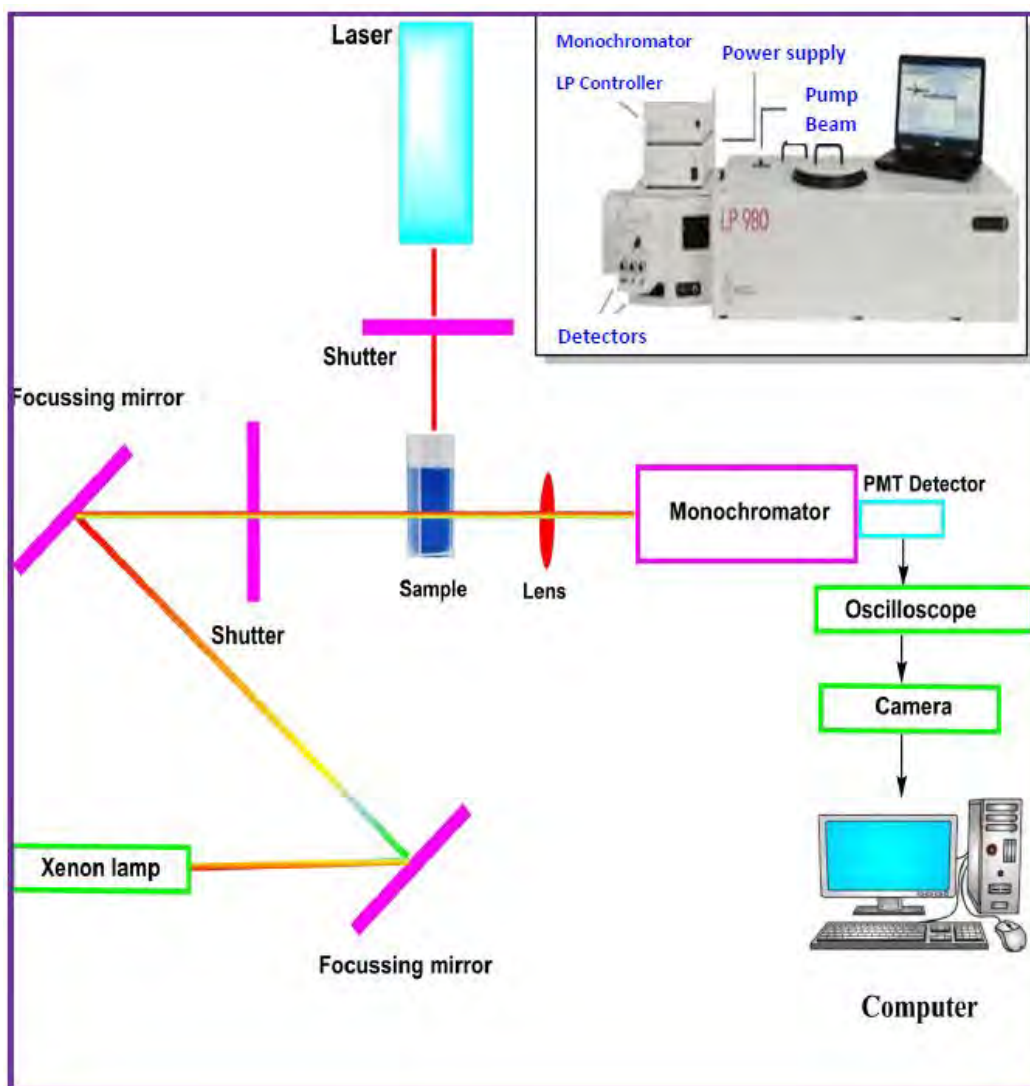


Figure 2.2 Schematic diagram of an LP980 laser flash photolysis setup.

PMT = Photomultiplier tube.

Triplet lifetimes were determined by the exponential fitting of the kinetic curves using Origin Pro 8 software.

14. Singlet oxygen determination on Pcs was done using a General Electric quartz line projector lamp combined with a 600 nm cut-off filter along with a water filter. An additional interference filter (Intor, 670 nm having a bandwidth of 40 nm) was aligned before the sample (the setup is given in **Figure 2.3** [164]). Light intensities were measured with a POWER MAX5100 (Molelectron detector incorporated) power meter. Light intensity was determined to be 2.87×10^{15} photons $\text{s}^{-1} \text{cm}^{-2}$.

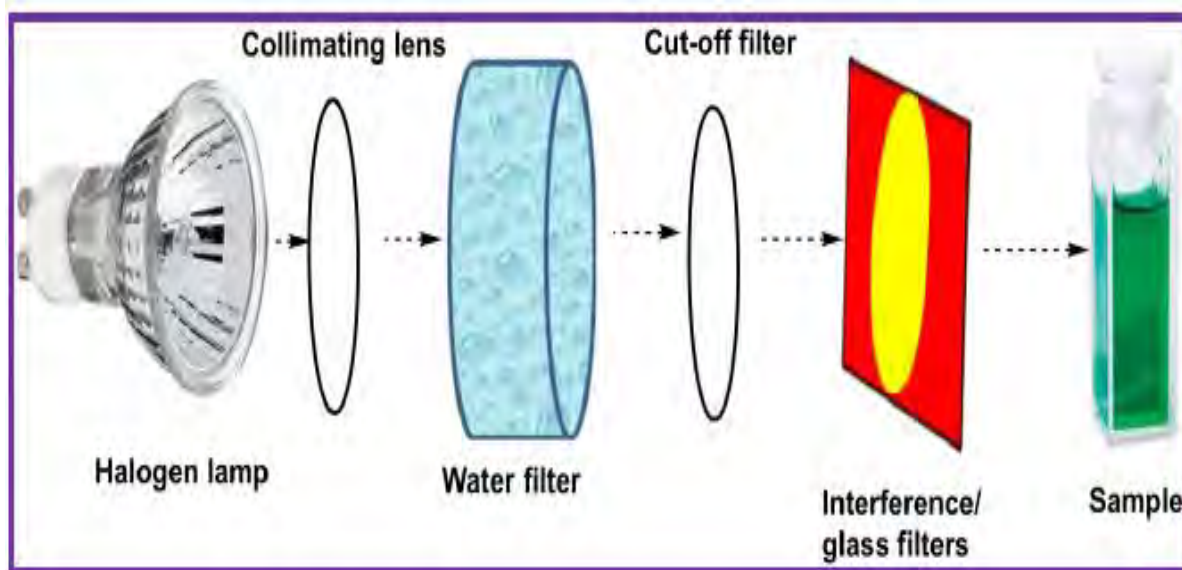


Figure 2.3 Schematic representation of the set-up of indirect detection of singlet oxygen.

15. Singlet oxygen determination for porphyrins, a Spectra-Physics^R primoScan OPO series, driven by Spectra-physics Quanta Ray INDI lab with maximum pump energy of 750 mJ and output energy of 27 mJ coupled to Shimadzu UV-2550 spectrophotometer was employed.

16. A Metrohm Swiss 827 pH meter was used for pH measurements.

17. HERMLE Z233M-2 centrifuge was used for the harvesting of the bacteria cells.

18. PRO VSM-3 Labplus Vortex mixer was used for the homogenization of the bacteria suspension.

19. A thermostatic oven was used for incubation processes. The optical density of the bacteria was determined using the LEDETECT 96.

20. Scan[®] 500 automatic color colony counter was used to evaluate the colony forming units CFU/mL of the bacteria.

21. Autoclave RAU-530D was used for the sterilization and autoclaving of nutrient broth, nutrient agar, phosphate buffer, and other various apparatus used during PACT experiments.

22. Irradiation studies on Pcs were conducted using Modulight laser system ML7710-680-RHO (at 670 nm, 524 mV/cm² and dose: 943 J/cm² for 30 min irradiation for PACT and a dose of 471 J/cm² for 15 min irradiation for PDT), **Figure 2.4**.

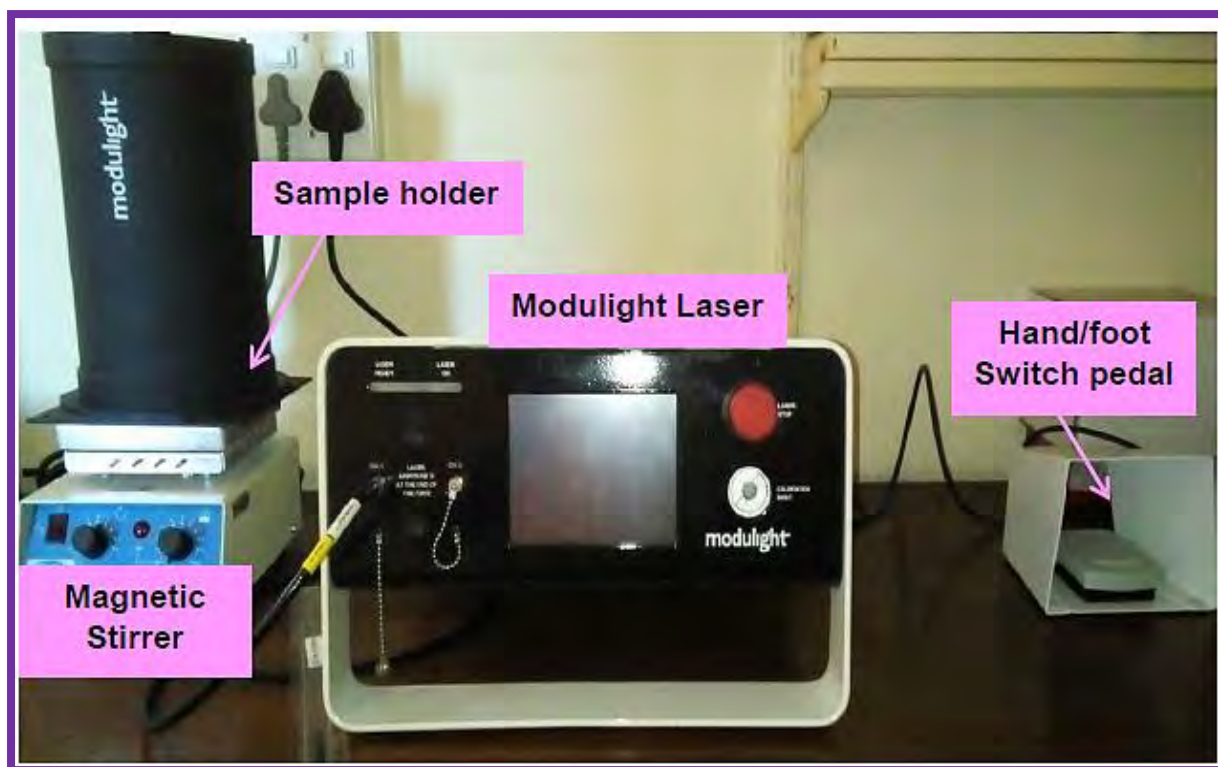


Figure 2.4 Irradiation setup used for PACT studies of Pcs.

23. Irradiations for porphyrins were conducted using a light-emitting diode (LED) Thorlabs M415L4 at 415 nm with an irradiance of 250 mW cm^{-2} mounted into the housing of a Modulight 7710 medical laser system.

24. A Zeiss® AxioVert. A1 Fluorescence LED (FL-LED) inverted microscope was used for routine microscopic examination for PDT studies.

25. Theoretical calculations were performed using Gaussian 09 program [165].

2.2. Synthetic Methods

This work presents the synthesis of novel phthalonitriles and complexes along with their nanoconjugates. Five phthalonitrile derivatives, **1**, **2**, **3**, **4**, **5**, and **6**, named according to group number listed in **Table 1.2**, were synthesized, of which compounds **5** [156] and **6** [157] had been reported before, hence will not be reported here.

A total of 15 new Pcs and 8 new (2 known) porphyrins were also synthesized, these include the neutral symmetrical and asymmetrical complexes along with the positively charged derivatives.

2.2.1. Synthesis of the Phthalonitriles, *Scheme 3.1A*

The phthalonitriles **1** and **2** were prepared following a one-pot procedure based on a base-catalyzed aromatic nucleophilic substitution reaction [166]. Briefly, 4-nitrophthalonitrile (1 eq) was mixed with each phenolic substituents (1 or 1.2 eq) separately and stirred in dry DMF (20 mL) under an argon atmosphere for 15 min. Afterwards, K₂CO₃ (1.5 eq) was added in batches for ~1.5 h while continuously stirring the reaction mixture at 60°C (**Scheme 3.1A.**). TLC was used to monitor the completion of the reactions. Thereafter, the reaction mixtures were poured into iced-water (200 mL) and the precipitate was filtered off under *vacuum* and recrystallized in MeOH or EtOH. In case the reaction product partially dissolve in ice water, the mixture was adjusted to pH 2-3 using 1M HCl, followed by extraction with ethyl acetate and drying over anhydrous sodium sulphate. The dry organic residue was then purified by recrystallization from MeOH or EtOH. **Table 2.1** illustrates the amounts of reagents used for the synthesis of new phthalonitriles **1-4**.

4-(4-Acetylphenoxy)phthalonitrile (1), Schemes 3.1A

Compound **1** was obtained as whitish powder in 80 % yield. FT-IR (UATR-TWO™) ν max/cm⁻¹: 3045 (Alph. C-H), 3035-2917 (Ar. C-H), 2231 (-C≡N), 1666 (C=O), 1577 (C=C), 1490-1416 (C-C), 1258-1168 (Asym., Ar-O-Ar), 1103 (Sym., Ar-O-Ar), 835. ¹H NMR (600 MHz, CDCl₃): δ 8.09 (1H, *d*, *J*= 8.5 Hz, for Ar-H); 7.80 (2H, *d*, *J*= 12.1 Hz, for Ar-H acetophenoxy ring); 7.37 (1H, *s*, for Ar-H); 7.33 (1H, *d*, *J*= 8.7 Hz, for Ar-H); 7.17 (2H, *d*, *J*= 12.3 Hz, for Ar-H acetophenoxy ring); and 2.65 (3H, *s*, for -CH₃) ppm. ¹³C NMR (600 MHz, CDCl₃): δ = 196.6, 159.7, 158.07, 136.4, 134.4, 134.0, 133.8, 131.0, 123.8, 123.4, 119.6, 116.9, 115.8, 115.3, 109.3, and 26.7 ppm.

4-(2-Amino-4-bromophenoxy)phthalonitrile (2), Schemes 3.1A

Compound **2** was obtained as a whitish powder in 75% yield. FT-IR (UATR-TWO™) ν max/cm⁻¹: 3456-3362 (-NH₂), 3074 (Alph. C-H), 2921-2856 (Ar. C-H), 2229 (-C≡N), 1724-1592 (C=C), 1483-1415 (C-C), 1276-1238 (Asym., Ar-O-Ar), 1186 (Sym., Ar-O-Ar), 1086, 1046, 798. ¹H NMR (600 MHz, DMSO-d₆): δ 8.05 (1H, *d*, *J*= 9.4 Hz, for Ar-H); 7.67 (1H, *d*, *J*= 3.0 Hz, for Ar-H); 7.24 (1H, *dd*, *J*= 3.1, 9.0 Hz, for Ar-H); 7.01 (1H, *d*, *J*= 2.0 Hz, for Ar-H amino ring); 6.91 (1H, *d*, *J*= 9.1 Hz, for Ar-H amino ring); 6.72 (1H, *dd*, *J*= 2.0, 9.1 Hz, for Ar-H amino ring); and 3.93 (2H, broad *s*, for NH₂) ppm. ¹³C NMR (600 MHz, DMSO-d₆): δ = 160.9, 142.5, 138.0, 136.0, 123.5, 122.0, 120.7, 119.1, 118.6, 118.2, 116.2, 115.9, and 107.5 ppm.

(E)-4-(4-(3-(pyridin-4-yl)acryloyl)phenoxy)phthalonitrile (3), Schemes 3.1B

At first, the chalcone precursor, (*E*)-1-(4-hydroxyphenyl)-3-(pyridin-4-yl)prop-2-en-1-one (**i**), was synthesized (**Scheme 3.1B**) as previously reported [**167**]. Briefly, a solution of 4-hydroxyacetophenone (1 g, 7.3 mmol) and 4-pyridinecarboxaldehyde (0.7867 g, 7.3 mmol) in ethanol (20 mL) was added drop-wise to a stirred solution of 30% KOH cooled at 0 °C in an ice bath under argon atmosphere. The reaction mixture was kept at room temperature for 24 h and the completion of the reaction was monitored by thin layer chromatography (TLC) with hexane: ethyl acetate (2:1 v/v). At the completion, the reaction mixture was poured into iced water and adjusted to neutral pH with 1M HCl then the precipitate was filtered out. The desired product was obtained by recrystallization from ethanol.

Chalcone (**i**) resulted as yellow powder in 65 % yield. FT-IR (UATR-TWO™) ν max/cm⁻¹: 3140 (OH), 3050 (Ar. C-H and intermolecular H bonds), 2917 (Alph. C-H), 1658 (C=O), 1586 (C=C), 1570 (C=N), 1509-1419 (C-C). ¹H NMR (600 MHz, DMSO-d₆): δ (ppm): 10.57 (1H, *bs*, for -OH), 8.65 (2H, *d*, *J*= 6.4 Hz, for Ar-H pyridyl ring), 8.12 (1H, *d*, *J*= 16.1 Hz, for *trans*-H), 8.09 (2H, *d*, *J*= 9.2 Hz, for Ar-H), 7.81 (2H, *d*, *J*= 6.5 Hz, for Ar-H), 7.61 (1H, *d*, *J*= 16.0 Hz, for *trans*-H), 6.93 (2H, *d*, *J*= 6.1 Hz, for Ar-H pyridyl ring). ¹³C NMR (600 MHz, DMSO-d₆): δ (ppm): 187.3, 162.9, 150.6, 142.3, 140.1, 131.7, 128.9, 126.8, 122.7 and 115.8.

In step two, 4-nitrophthalonitrile (0.369 g, 2.1 mmol) and chalcone **i** (0.400 g, 1.8 mmol) were dissolved in 15 mL of DMF in a round-bottom flask and stirred under argon atmosphere. K₂CO₃ (0.368 g, 2.7 mmol) was added then the stirring was continued for 24 h at 60 °C. The reaction mixture was afterward poured into 50 mL iced water. The obtained product was filtered out and recrystallized in ethanol to obtain **3**.

Compound **3** resulted as orange powder in 83 % yield. FT-IR (UATR-TWO™) ν max/cm⁻¹: 3068 (Ar. C-H), 2937 (Aliph. C-H), 1667 (C=O), 1583 (C=C), 1538 (C=N), 2231 (C≡N), 1486-1360 (C-C), 1287-1166 (*Asym.*, Ar-O-Ar), 1098 (*Sym.*, Ar-O-Ar), 802. ¹H NMR (600 MHz, DMSO-d₆): δ (ppm): 8.93 (2H, *d*, *J* = 8.4 Hz, for Ar-H pyridyl ring); 8.88 (2H, *d*, *J* = 9.3 Hz, for Ar-H); 8.34 (1H, *d*, *J* = 8.0 Hz, for Ar-H); 8.03 (1H, *d*, *J* = 16.0 Hz, for *trans*-H); 7.95 (1H, *s*, for Ar-H); 7.92 (1H, *d*, *J* = 15.6 Hz, for *trans*-H); 7.44 (2H, *d*, *J* = 8.3 Hz, for Ar-H); 7.37 (1H, *d*, *J* = 8.1 Hz, for Ar-H); and 7.26 (2H, *d*, *J* = 9.3 Hz, for Ar-H pyridyl ring). ¹³C NMR (600 MHz, DMSO-d₆): δ (ppm): 186.7, 162.8, 154.2, 151.8, 143.6, 131.6, 130.8, 130.7, 130.5, 129.2, 124.5, 1223, 116.3, 115.5, 115.4, 111.8, and 111.1.

(E)-4-(4-(3-(4-(dimethylamino)phenyl)acryloyl)phenoxy)phthalonitrile (4), Schemes 3.1C

Firstly, the chalcone precursor (*E*)-3-(4-(dimethylamino)phenyl)-1-(4-hydroxyphenyl)prop-2-en-1-one (**ii**), **Scheme 3.1C** was prepared according to the Claisen-Schmidt condensation procedure with slight modifications [167]. Then a mixture of 4-nitrophthalonitrile (0.971 g, 5.6 mmol) and chalcone **ii** (1 g, 3.7 mmol) and K₂CO₃ (0.775 g, 5.6 mmol) was dissolved in 20 mL of dry DMF and stirred under argon atmosphere for 24 h at 60 °C. The reaction was monitored using thin-layer chromatography (TLC). At the reaction completion, the product was precipitated out in ice water, then filtered while washing with water. The resulting solid was filtered out and recrystallized in ethanol to obtain **4**.

Chalcone (**ii**) resulted as yellow powder in 72 % yield. FT-IR (UATR-TWO™) ν max/cm⁻¹: 3094 (OH), 2805 (Ar. C-H and intermolecular H bonds), 2710 (Aliph. C-H), 1663 (C=O), 1591 (C=C), 1536 (C=N), 1437-1356 (C-C). ¹H NMR (600 MHz, DMSO-d₆): δ (ppm): 9.66 (1H, *bs*, for -OH), 8.01 (2H, *d*, *J* = 8.4 Hz, for Ar-H ring), 7.67 (1H, *d*, *J* = 16.1 Hz, for *trans*-H), 7.64 (2H, *d*, *J* = 8.1 Hz, for Ar-H dimethylamino ring), 6.86 (2H, *d*, *J* = 8.1 Hz, for Ar-H), 6.78 (1H, *d*, *J* = 15.9 Hz, for *trans*-H), 6.73 (2H, *d*, *J* = 8.2 Hz, for Ar-H dimethylamino ring), and 2.99 (6H, *s*, for N-(CH₃)₂). ¹³C NMR (600 MHz, DMSO-d₆): δ (ppm): 190.5, 158.7, 136.9, 125.2, 125.2, 124.9, 121.3, 117.6, 116.2, 115.8, 111.5, 111.1 and 40.5.

Compound **4** resulted as a yellowish powder. Yield: 85%. FT-IR (UATR-TWO™) ν max/cm⁻¹: 2911 (Ar. C-H), 2806 (Aliph. C-H), 1667 (C=O), 1588 (C=C), 1536 (C=N), 2225 (C≡N), 1477-1387 (C-C), 1299-1160 (*Asym.*, Ar-O-Ar), 1075 (*Sym.*, Ar-O-Ar), 812. ¹H NMR (600 MHz, DMSO-d₆): δ (ppm): 7.87 (2H, *d*, *J* = 8.0 Hz, for Ar-H); 7.75 (2H, *d*, *J* = 8.0 Hz, for Ar-H dimethylamino ring); 7.73 (1H, *s*, for Ar-H); 7.64 (1H, *d*, *J* = 16.0 Hz, for *trans*-H), 7.57 (1H, *d*, *J* = 8.3 Hz, for Ar-H); 7.47 (1H, *d*, *J* = 16.1 Hz, for *trans*-H); 7.21 (2H, *d*, *J* = 8.3 Hz, for Ar-H); 7.17 (1H, *d*, *J* = 8.1 Hz, for Ar-H); 6.71 (2H, *d*, *J* = 8.0 Hz, for Ar-H dimethylamino ring); and 3.07 (6H,

s, for N-(CH₃)₂). ¹³C NMR (600 MHz, DMSO-d₆): δ (ppm): 187.2, 163.3, 152.2, 144.2, 131.3, 130.9, 122.8, 116.8, 115.9, 112.3, 111.5, and 40.2.

Table 2.1 Amounts of reagents used in the syntheses of phthalonitriles **1-4**.

Phthalonitrile	Precursors	K ₂ CO ₃	Reaction conditions	Purification methods
1	4-nitrophthalonitrile (1.270 g, 7.3 mmol) and 4-hydroxyacetophenone (1 g, 7.3 mmol)	1.520 g, 11.0 mmol	Stirring at 60°C for 16-24h in dry DMF (20 mL) under argon/nitrogen atmosphere	Precipitate in iced water (200 mL) and recrystallize the filtrate in methanol
2	4-nitrophthalonitrile (0.552 g, 3.2 mmol) and 2-amino-4-bromophenol (0.500 g, 2.7 mmol)	0.549 g, 4.1 mmol		Precipitate in ice water (pH 2-3 with 1 M HCl) and recrystallize the filtrate in methanol
3	4-nitrophthalonitrile (0.369 g, 2.1 mmol) and (<i>E</i>)-1-(4-hydroxyphenyl)-3-(pyridin-4-yl)prop-2-en-1-one (i) (0.400 g, 1.8 mmol)	0.368 g, 2.7 mmol		The reactions for 3 and 4 were done in two steps starting with the formation of the chalcone precursors i and ii .
4	4-nitrophthalonitrile (0.971 g, 4.5 mmol) and (<i>E</i>)-3-(4-(dimethylamino)phenyl)-1-(4-hydroxyphenyl)prop-2-en-1-one (ii) (1 g, 3.7 mmol)	0.775 g, 5.6 mmol		Precipitate in ice water (200 mL) and recrystallize the filtrate in ethanol

DMF: Dimethylformamide 1M HCl: 1 Molar of hydrochloric acid

2.2.2. Synthesis of the Neutral Phthalocyanines

2.2.2.1. Free-base Pc (1-H₂), Scheme 3.2

Phthalonitrile **1** (0.5 g, 2.0 mmol) was mixed with anhydrous lithium chloride (0.081 g, 2.0 mmol) in 2 mL of dry DMAE where a few drops of DBU were added under argon atmosphere while constantly stirring at reflux temperature for 16 h. At completion, the mixture was cooled to room temperature, then poured in water-acetic acid (1:1 v/v) mixture and left to stir overnight to remove lithium metal in the Pc core. The free-base Pc **1-H₂** was obtained as a green solid after multiple centrifugations using a water-ethanol (1:1 v/v) mixture to remove the unreacted starting materials.

Tetrakis-[4-(acetophenoxy)phthalocyaninato], 1-H₂, Yield: 48 %. FT-IR (KBr, ν , cm⁻¹): 3372 (NH-inner core), 3035 (Ar. C-H), 2920-2853 (Alph. C-H), 1714 (C=O), 1667-1586 (C=N, C=C), 1465-1314 (C-C), 1223 (Asym., Ar-O-Ar), 1159 (C-N), 1095 (Sym., Ar-O-Ar), 1008, 938. ¹H NMR (600 MHz, DMSO-d₆): δ 8.09 (4H, *d*, *J*= 8Hz, for ArH-Pc core); 7.48 (8H, *d*, *J*= 8.6 Hz, for Ar-H); 7.36 (4H, *d*, *J*= 2.1 Hz, for ArH-Pc core); 7.33 (4H, *dd*, *J*= 2.0, 8.9 Hz, for ArH-Pc core); 7.15 (8H, *d*, *J*= 8.1 Hz, for Ar-H); 5.64 (2H, *s*, for NH-core); and 2.58 (12H, *s*, for -CH₃) ppm. Elemental analysis: expected for C₆₄H₄₂N₈O₈ (%): C= 73.13, H= 4.03, N= 10.66, found (%): C= 73.10, H= 3.99, N= 10.62. MALDI-TOF-MS simulated *m/z* : 1051.09. Found [M+H]⁺: 1052.44 .

2.2.2.2. Synthesis of Zinc (II) Pc Complexes

2.2.2.2.1. Symmetrical Zinc Pc Complexes, Schemes 3.2-3.5

Table 2.2 portrays the amounts of the chemicals used during the synthesis of zinc Pcs.

All the A₄-type zinc metallated Pcs (**1-Zn**, **2-Zn**, **3-Zn**, and **4-Zn**) were synthesized using a similar procedure described in the literature [168,169] with slight modifications as follows: under argon atmosphere, phthalonitriles **1** to **4** (2 eq) were individually mixed with anhydrous zinc acetate (1 eq) and a catalytic amount of DBU (1-3 drops) in either dry DMAE or 1-pentanol or 1-hexanol. Each mixture was then refluxed in a sealed glass tube for 16-24 h. After cooling to room temperature, ethanol was added to the reaction mixture which was left to further stir for about 1h then centrifuged. The collected solid was repeatedly dissolved in DMSO and poured in a water-ethanol mix then centrifuged. The precipitated pure complexes were obtained as green solids and dried under *vacuum*. On some occasions, the precipitates were furthermore purified by column chromatography on silica gel using THF as the eluent to afford pure products.

2.2.2.2.2. Asymmetrical Zinc Pc Complexes, *Scheme 3.6*

The asymmetrical (A₃B-type) Pc **6-Zn** and its symmetrical analog **5-Zn** were obtained as follows [170]: Phthalonitriles **5** (0.796, 2.84 mmol) and **6** (0.250 g, 0.95 mmol), an excess of anhydrous zinc acetate (1.373 g, 7.48 mmol) and DBU (0.5 mL) were mixed in 1-hexanol (5 mL) and refluxed for 18 h under argon atmosphere for 16 h. Afterward, the reaction mixture was cooled, and the crude product was then precipitated out with ethanol followed by purification on column chromatography packed with silica gel. The first fraction which is the complex **5-Zn** (the A₄ Pc type) was collected using THF as eluent. Then, upon increasing the polarity of the eluent system to (THF: methanol 5:1 v/v), the A₃B target product **6-Zn**.

Table 2.2 Amounts of reagents used in the syntheses of zinc (II) Pc complexes.

Complex	Precursor	Zn(OAc)	Reaction conditions	Purification methods
1-Zn	1 (0.2 g, 0.7 mmol)	(0.07 g, 0.4 mmol)	Solvent: DMAE (2-3 mL)	Precipitate with water-ethanol, centrifuge, dissolve in DMSO (repeat)
2-Zn	2 (0.2 g, 0.6 mmol)	(0.06 g, 0.3 mmol)	1-3 drops of DBU	Column chromatography on silica gel using THF as the eluent
3-Zn	3 (0.25g, 0.72 mmol)	(0.065 g, 0.4 mmol)	Stirring at 160°C for 16-24h under argon atmosphere	Column chromatography on silica gel with CHCl ₃ : EtOH (9:1) as an eluting solvent
4-Zn	4 (0.52g, 1.31 mmol)	(0.121 g, 0.66 mmol)	3 mL 1-pentanol 3 drops DBU Stirring at 160°C for 24 h under argon atmosphere	Centrifugation with EtOH, Precipitate in ice water (200 mL)

5-Zn (A ₄ -Pc)	5 (0.796, 2.84 mmol)		1-hexanol	Column chromatography on silica gel using THF as the eluent for 5-Zn then THF : MeOH (5:1 v/v) for 6-Zn
and	and	(1.373 g, 7.48 mmol)	0.5 mL DBU	
6-Zn (A ₃ B-Pc)	6 (0.25g, 0.95 mmol)		18 h stirring at 160 °C under an argon atmosphere	

Tetrakis-[4-(acetophenoxy)phthalocyaninato] zinc (II), 1-Zn; Yield: 38 %. FT-IR (KBr, ν , cm^{-1}): 3056 (Ar. C-H), 2918-2853 (Alph. C-H), 1715 (C=O), 1666-1587 (C=N, C=C), 1471-1318 (C-C), 1225 (Asym., Ar-O-Ar), 1158 (C-N), 1089 (Sym., Ar-O-Ar), 1041, 944. ¹H NMR (600 MHz, DMSO-*d*₆): δ (ppm): 8.51 (4H, *d*, *J*= 8.0 Hz, for ArH-Pc core); 8.26 (8H, *d*, *J*= 8.4 Hz, for Ar-H); 7.87 (4H, *d*, *J*=1.02, for ArH-Pc core); 7.72 (4H, *dd*, *J*= 1.02, 8.3 Hz, for ArH-Pc core); 7.42 (8H, *d*, *J*= 8.1 Hz, for Ar-H); and 2.85 (12H, *s*, for -CH₃) ppm. Elemental analysis: expected for C₆₄H₄₀N₈O₈Zn (%): C= 68.97, H= 3.62, N= 10.05, found (%): C= 68.93, H= 3.61, N= 10.01. MALDI-TOF-MS simulated *m/z*: 1114.45. Found [M+H₂O]⁺= 1132.57 and [M+H]⁺= 1115.58.

Tetrakis[4-(2-amino-4-bromophenoxy)phthalocyaninato] zinc (II), 2-Zn; yield: 21%. FT-IR (UATR-TWO™) ν max/ cm^{-1} : 3335 (-NH₂), 2949 (Alph. C-H), 2917-2853 (Ar. C-H), 1707-1607 (C=C, C=N), 1459-1385 (C-C), 1330-1209 (Asym., Ar-O-Ar), 1184 (Sym., Ar-O-Ar), 1083, 948, 801. ¹H NMR (600 MHz, DMSO-*d*₆): δ 8.09 (4H, *d*, *J*= 9.0 Hz, for ArH-Pc core); 7.67 (4H, *d*, *J*= 3.1 Hz, for ArH-Pc core); 7.47 (4H, *d*, *J*= 9.1 Hz, for ArH-Pc core); 7.03 (4H, *d*, *J*= 2.0 Hz, for Ar-H); 6.86 (4H, *d*, *J*= 9.0 Hz, for Ar-H); 6.62 (4H, *d*, *J*= 9.0 Hz, for Ar-H); and 4.00 (8H, broad *s*, for -NH₂) ppm. Elemental analysis: expected for C₅₆H₃₂N₁₂O₄Br₄Zn (%): C= 50.88, H= 2.44, N= 12.71, found (%): C= 50.93, H= 2.40, N= 12.74. MALDI-TOF-MS simulated *m/z*: 1321.93. Found [M+H]⁺: 1322.53.

Tetrakis[(E)-4-(4-(3-(pyridin-4-yl)acryloyl)phenoxy)phthalocyaninato] zinc (II), 3-Zn; Yield: 36 %. FT-IR (UATR-TWO™) ν max/ cm^{-1} : 3055 (Ar. C-H), 2923-2855 (Aliph. C-H), 1721 (C=O), 1583-1490 (C=C, C=N), 1413-1362 (C-C), 1228-1164 (Asym., Ar-O-Ar), 1086 (Sym., Ar-O-Ar), 832. ¹H NMR (600 MHz, DMSO-*d*₆): δ (ppm): 8.97-8.95 (8H, *m*, for ArH-pyridyl ring); 8.90 (8H, *d*, *J*= 9.0 Hz, for Ar-H); 8.25 (2H, *d*, *J*= 8.2 Hz, for ArH-Pc core); 8.20 (2H, *d*, *J*= 8.2 Hz, for ArH-Pc core); 8.03 (4H, *d*, *J*= 16.0 Hz, for *trans*-H); 7.96-7.92 (8H, *m*, for ArH-Pc core and the *trans*-H); 7.46-7.44 (8H, *dd*, *J*= 3.01, 8.0 Hz, Ar-H pyridyl ring), 7.39 (4H, *d*, *J*= 2.1 Hz, for ArH-Pc

core); and 7.28 (8H, *d*, *J* = 8.3 Hz, for Ar-H). Elemental analysis: expected for C₈₈H₅₂N₁₂O₈Zn (%): C = 71.86, H = 3.56, N = 11.43, found (%): C = 71.81, H = 3.59, N = 11.49. MALDI-TOF MS simulated *m/z*: 1470.81. Found: [M+H]⁺ = 1471.88.

Tetrakis[(E)-4-(4-(3-(dimethylamino-4-yl)acryloyl)phenoxy)phthalocyaninato] zinc (II), 4-Zn; Yield: 42%. FT-IR (UATR-TWO™) ν max/cm⁻¹: 2920 (Ar. C-H), 2903-2855 (Aliph. C-H), 1716 (C=O), 1582-1462 (C=C, C=N), 1350 (C-C), 1220-1164 (Asym., Ar-O-Ar), 1027 (Sym., Ar-O-Ar), 816. ¹H NMR (600 MHz, DMSO-d₆): δ (ppm): 8.29 (8H, *d*, *J* = 8.6 Hz, for Ar-H); 8.21 (2H, *d*, *J* = 8.5 Hz, for Ar-H Pc core); 8.11 (4H, *d*, *J* = 15.4 Hz, for *trans*-H); 7.98 (2H, *d*, *J* = 9.1 Hz, for Ar-H Pc core); 7.77 (2H, *d*, *J* = 9.0 Hz, for Ar-H Pc core); 7.75 (8H, *d*, *J* = 8.5 Hz, dimethylamino ring); 7.72 (4H, *s*, for Ar-H Pc core); 7.47 (4H, *d*, *J* = 15.4 Hz, *trans*-H); 7.37 (8H, *d*, *J* = 8.7 Hz, for Ar-H); 7.27 (2H, *d*, *J* = 9.1 Hz, for Ar-H Pc core); 6.83 (8H, *d*, *J* = 8.5 Hz, for Ar-H dimethylamino ring); and 3.09 (24H, *s*, for N-(CH₃)₂). Elemental analysis: expected for C₁₀₀H₇₆N₁₂O₈Zn (%): C = 73.09, H = 4.67, N = 10.25, found (%): C = 73.13, H = 4.45, N = 9.59. MALDI TOF MS simulated *m/z*: 1639.13. Found: [M+H]⁺ = 1640.08.

Tetrakis[4-(3,5-dimethoxyphenoxy)phthalocyaninato] zinc (II), 5-Zn; Yield: 56%. FT-IR (UATR-TWO™) ν max/cm⁻¹: 3070 (Ar. C-H), 2914-2844 (Aliph. C-H), 1591-1470 (C=C, C=N), 1486-1360 (C-C), 1320 (-O-CH₃), 832. ¹H NMR (600 MHz, DMSO-d₆): δ (ppm): 7.76 (2H, *d*, *J* = 8.3 Hz, for Ar-H Pc core); 7.32 (2H, *dd*, *J* = 7.8, 1.8 Hz, for Ar-H Pc core); 7.16 (2H, *d*, *J* = 2.2 Hz, for Ar-H Pc core); 6.72 (1H, *d*, *J* = 7.8 Hz, for Ar-H Pc core); 6.69 (1H, *d*, *J* = 8.2 Hz, for Ar-H Pc core); 6.58 (*d*, *J* = 1.7 Hz, for Ar-H Pc core); 6.48 (2H, *dd*, *J* = 9.9, 1.8 Hz, for Ar-H Pc core); 6.37 (8H, *dd*, *J* = 2.5, 3.0 Hz, for Ar-H); 6.26 (4H, *dd*, *J* = 2.2, 2.5, for Ar-H); and 3.68 (24H, *s*, for O-CH₃). Elemental analysis: expected for C₆₄H₄₈N₈O₁₂Zn (%): C = 64.79, H = 4.08, N = 9.44, found (%): C = 64.31, H = 4.02, N = 9.42. MALDI TOF MS simulated *m/z*: 1186.49. Found: [M+H]⁺ = 1187.37.

Mono[(4-carboxyphenoxy)-tris-(4-dimethoxyphenoxy)phthalocyanato] zinc (II), 6-Zn; Yield: 33%. FT-IR (UATR-TWO™) ν max/cm⁻¹: 3393 (-OH), 3065 (Ar. C-H), 2927-2839 (Aliph. C-H), 1712 (C=O), 1591-1460 (C=C, C=N), 1480-1360 (C-C), 1323 (-O-CH₃), 837. ¹H NMR (600 MHz, DMSO-d₆): δ (ppm): 11.30 (1H, *s*, for OH); 8.30 (2H, *d*, *J* = 10.0 Hz, for Ar-H carboxyl ring); 7.80 (2H, *d*, *J* = 8.2 Hz, for Ar-H Pc core); 7.35 (2H, *d*, *J* = 7.9 Hz, for Ar-H Pc core); 7.20 (4H, *s*, for Ar-H Pc core); 6.74 (2H, *d*, *J* = 8.1 Hz, for Ar-H Pc core); 7.64 (2H, *d*, *J* = 8.5 Hz, for Ar-H Pc core); 6.52 (2H, *d*, *J* = 10.2 Hz, for carboxyl ring); 6.40 (6H, *s*, for Ar-H); 6.30 (3H, *s*, for Ar-H); and 3.72 (18H, *s*, for O-CH₃). Elemental analysis: expected for C₆₃H₄₄N₈O₁₂Zn (%): C = 64.65, H =

3.79, N= 9.57, found: C= 64.09, H= 3.92, N= 9.66. MALDI TOF MS simulated m/z: 1170.45. Found: $[M+H]^+$ = 1171.33.

2.2.2.3. *Synthesis of Indium (III) Chloride Pc Complexes, Schemes 3.2-3.5*

Complex **1-In** was obtained after the metalation of the free-base Pc **1-H₂** (0.15 g, 0.14 mmol) using anhydrous InCl₃ salt (0.095 g, 0.42 mmol) with a catalytic amount of DBU (0.043 g, 0.28 mmol) in 3 mL of dry DMF while refluxing at a constant stirring. The complete metallation was monitored by checking the conversion of the split Q-bands of **1-H₂** into a single narrow Q-band using UV-Vis spectroscopy. The desired product was obtained by precipitation in ethanol.

As depicted in **Table 2.3**, for the indium Pc complexes **2-In**, **3-In**, and **4-In**, each phthalonitrile derivative **2** to **4** (1 eq) was separately mixed with anhydrous indium chloride salt (3 eq) plus a few drops of DBU in either dry 1-pentanol or quinoline (3 mL) then brought to reflux for 16-24 h. After completion, ethanol was added, and the reaction mixtures were further stirred for about 1 h. The obtained green crude products were collected by centrifugation and were purified on silica gel using chloroform: ethanol (9:1 v/v) as an eluting solvent system.

Table 2.3 Amounts of reagents used in the synthesis of indium (III) Pc complexes.

Complex	Precursor	InCl ₃	Reaction conditions	Purification methods
1-In	1-H₂ (0.15g, 0.14 mmol)	(0.095g, 0.42 mmol)	DMF (3 mL) DBU (0.043g, 0.28 mmol) Heating at 150 °C for 2h, argon atmosphere	Precipitate with water-ethanol, centrifuge, dissolve in DMSO (repeat)
2-In	2 (0.4 g, 1.3 mmol)	(0.85 g, 3.8 mmol)	3 mL quinoline 1-3 drops of DBU	Column chromatography on silica gel using THF as the eluent
3-In	3 (0.25g, 0.71mmol)	(0.472 g, 2.13 mmol)	Refluxing for 24 h under argon atmosphere	Column chromatography on silica gel with CHCl ₃ : EtOH (9:1) as an eluting solvent
4-In	4 (0.5 g, 1.27 mmol)	(0.281 g, 1.27 mmol)	3 mL of 1-pentanol 3 drops of DBU Stirring at 160°C for 24h under argon atmosphere	Centrifugation with EtOH, Precipitate in ice-water (200 mL)

Tetrakis-[4-(acetophenoxy)phthalocyaninato] indium (III) chloride, 1-In; Yield: 29 %. FT-IR (KBr, ν , cm^{-1}): 3056 (Ar. C-H), 2918-2853 (Alph. C-H), 1715 (C=O), 1666-1587 (C=N, C=C), 1471-1318 (C-C), 1225 (Asym., Ar-O-Ar), 1158 (C-N), 1089 (Sym., Ar-O-Ar), 1041, 944. ^1H NMR (600 MHz, DMSO- d_6): δ 8.52 (4H, *d*, J = 8.3 Hz, for Ar-H Pc core); 8.29 (8H, *d*, J = 8.0 Hz, for Ar-H); 7.84 (4H, *d*, J =1.3 Hz, for Ar-H Pc core); 7.73 (4H, *dd*, J = 1.3, 8.1 Hz, for Ar-H Pc core); 7.47 (8H, *d*, J = 8.1 Hz, for Ar-H); and 2.85 (12H, *s*, for -CH₃) ppm. Elemental analysis: expected for C₆₄H₄₀N₈O₈InCl (%): C= 64.09, H= 3.36, N= 9.57, found (%): C= 64.13, H= 3.33, N= 9.56. MALDI-TOF-MS simulated m/z : 1198.17. Found $[\text{M-Cl+H}]^+$ = 1164.55.

Tetrakis[4-(2-amino-4-bromophenoxy)phthalocyaninato] indium (III) chloride, 2-In; yield: 18%. FT-IR (UATR-TWOTM) ν max/ cm^{-1} : 3337 (-NH₂), 2952 (Alph. C-H), 2920-2850 (Ar. C-H), 1708-1608 (C=C, C=N), 1491-1460 (C-C), 1395-1377 (Asym., Ar-O-Ar), 1212-1181 (Sym., Ar-O-Ar), 1081, 965, 801. ^1H NMR (600 MHz, DMSO- d_6): δ 8.11 (4H, *d*, J = 9.0 Hz, for Ar-H Pc core); 7.72 (4H, *d*, J = 3.2 Hz, for Ar-H Pc core); 7.47 (4H, *d*, J = 9.1 Hz, for Ar-H Pc core); 7.03 (4H, *d*, J = 2.0 Hz, for Ar-H); 6.87 (4H, *d*, J = 9 Hz, for Ar-H); 6.63 (4H, *d*, J = 9.1 Hz, for Ar-H); and 4.01 (8H, *bs*, for -NH₂) ppm. Elemental analysis: expected for C₅₆H₃₂N₁₂O₄Br₄ClIn (%): C= 47.81, H= 2.29, N= 11.95, found (%): C= 47.86, H= 2.27, N= 11.93. MALDI-TOF-MS simulated m/z : 1406.82. Found $[\text{M+H}]^+$ =1408.02.

Tetrakis[(E)-4-(4-(3-(pyridin-4-yl)acryloyl)phenoxy)phthalocyaninato] indium (III) chloride, 3-In; Yield: 27 %. FT-IR (UATR-TWOTM) ν max/ cm^{-1} : 3056 (Ar. C-H), 2923-2856 (Aliph. C-H), 1722 (C=O), 1583-1491 (C=C, C=N), 1413-1362 (C-C), 1228-1164 (Asym., Ar-O-Ar), 1087 (Sym., Ar-O-Ar), 832. ^1H NMR (600 MHz, DMSO- d_6): δ (ppm): 8.97-8.95 (8H, *m*, for ArH-pyridyl ring); 8.90 (8H, *d*, J = 8.0 Hz, for Ar-H); 8.26 (2H, *d*, J = 8.2 Hz, for ArH-Pc core); 8.20 (2H, *d*, J = 8.2 Hz, for ArH-Pc core); 8.03 (4H, *d*, J = 16.4 Hz, for *trans*-H); 7.96-7.92 (8H, *m*, for ArH-Pc core and *trans*-H); 7.46-7.44 (8H, *dd*, J = 2.1, 8.2 Hz, for ArH pyridyl ring); 7.39 (4H, *d*, J = 8.4 Hz, for ArH-Pc core); and 7.28 (8H, *d*, J = 8.1 Hz, for Ar-H). Elemental analysis: expected for C₈₈H₅₂ClInN₁₂O₈ (%): C= 67.94, H= 3.37, N= 10.80, found (%): C= 67.96, H= 3.39, N= 10.84. MALDI TOF MS simulated m/z : 1555.70. Found: $[\text{M}]^+$ = 1555.26.

Tetrakis[(E)-4-(4-(3-(dimethylamino-4-yl)acryloyl)phenoxy)phthalocyaninato] indium (III) chloride, 4-In; Yield: 38%. FT-IR (UATR-TWOTM) ν max/ cm^{-1} : 2919 (Ar-H), 2903-2855 (Aliph C-H), 1717 (C=O), 1582-1523 (C=C, C=N), 1462-1350 (C-C), 1220-1164 (Asym., Ar-O-Ar), 1026 (Sym., Ar-O-Ar), 817. ^1H NMR (600 MHz, DMSO- d_6): δ (ppm): 8.31 (8H, *d*, J = 8.3 Hz, for Ar-H); 8.20 (2H, *d*, J = 8.2 Hz, for Ar-H Pc core); 8.10 (4H, *d*, J = 15.4 Hz, for *trans*-H); 8.01 (2H, *d*, J = 8.2 Hz, for Ar-H Pc core); 7.77 (2H, *d*, J = 8.2 Hz, for Ar-H Pc core); 7.75 (8H, *d*, J = 8.7 Hz,

for Ar-H dimethylamino ring); 7.72 (4H, *s*, for Ar-H Pc core); 7.49 (4H, *d*, $J= 15.4$ Hz, *trans*-H); 7.37 (8H, *d*, $J= 8.1$ Hz, for Ar-H); 7.27 (2H, *d*, $J= 8.2$ Hz for Ar-H Pc core); 6.83 (8H, *d*, $J= 8.8$ Hz, Ar-H dimethylamino ring); and 3.10 (24H, *s*, for N-(CH₃)₂). Elemental analysis: expected for C₁₀₀H₇₆ClInN₁₂O₈ (%): C= 69.67, H= 4.44, N= 9.71, found (%): C= 69.35, H= 4.89, N= 9.41. MALDI TOF MS simulated *m/z*: 1724.02. Found: [M+H]⁺= 1725.21.

2.2.3. Synthesis of Neutral Asymmetrical and Symmetrical Porphyrins

2.2.3.1. Asymmetrical Free-base Porphyrin Complexes, Schemes 3.7, 3.8

The free-base porphyrin **7-H₂** was prepared as follows: firstly, propionic acid (100 mL) was refluxed for 30 min, then a mixture of 4-hydroxybenzaldehyde (0.5 g, 4.09 mmol), methyl 4-formylbenzoate (2 g, 12.18 mmol) in propionic acid and pyrrole (1.34 ml, 19.31 mmol) in 6 mL *n*-toluene were simultaneously added dropwise into the reaction flask for 15 min while stirring. Subsequently, the mixture was brought to refluxing temperature for 2 h. After this, the temperature was brought down to 50-60°C before adding methanol (30 mL), then this was left to stir for another 30 min.

The resulting crude product was obtained after filtration under a *vacuum* followed by washing with methanol and then dried for 30 min in the oven at 60 °C. The desired pure compound was obtained as a purple solid after silica gel column chromatography using dichloromethane as an eluent.

5-(4-Hydroxyphenyl)-tris-10, 15, 20-(4-acetylphenyl)-porphyrin, 7-H₂; Yield: 11%. FT-IR ν , cm⁻¹ 3394 (O-H), 2999 (Ar. C-H), 2916 (Aliph. C-H), 1716 (ester C-O), 1602 (C=N, C=C), 1432 (C-H), 1270 (ester C-O), 1104 (C-N), and 959 (=C-H). ¹H NMR (600 MHz, DMSO-d₆): δ (ppm): 10.01 (1H, *s*, for -OH); 8.93 (2H, *d*, $J= 8.1$ Hz, for Ar-H); 8.81 (6H, *d*, $J= 8.1$ Hz, for Ar-H); 8.38 (6H, *d*, $J= 8.0$ Hz, for Ar-H); 8.34 (6H, *d*, $J= 8.0$ Hz, for pyrrole-H); 8.00 (2H, *d*, $J= 8$ Hz, for Ar-H); 7.21 (2H, *d*, $J= 8.0$ Hz, for pyrrole-H); 4.04 (9H, *s*, for -OCH₃); and 2.54 (2H, *s*, for -NH core). Elemental analysis: expected for C₅₀H₃₆N₄O₇ (%): C= 74.62, H= 4.51, N= 6.96, found (%): C= 74.65, H= 4.49, N= 6.91. MALDI TOF MS simulated *m/z*: 804.26. Found: [M]⁺= 804.42.

The synthesis of the free-base porphyrin 5,10,15,20-tetrakis(4-dimethylaminophenyl)-porphyrin **8-H₂** has previously been reported in the literature [171]. Hence, it is not repeated here.

2.2.3.2. Synthesis of Zn (II) Porphyrin Complex, Schemes 3.7

7-Zn was synthesized as follows: **7-H₂** (0.1 g, 0.12 mmol) was refluxed in DMF until complete dissolution. After dropping the temperature to 100 °C, Zn(OAc) (0.078 g, 0.44 mmol) was

immediately added under continuous stirring. The reaction completion was monitored using UV-Vis spectroscopy by checking the collapse of the four Q-bands of the free-base **7-H₂** into two Q-bands. After doing so, the reaction was cooled then an ethanol/water mixture (50 ml, 1:1 v/v) was added to precipitate out the purple solid product, which was filtered off, washed with Millipore water, and dried in a *vacuum*.

Zinc 5-(4-Hydroxyphenyl)-tris-10,15, 20-(4-acetylphenyl)-porphyrin, 7-Zn; Yield: 90%. FT-IR (UATR-TWO™) ν max/cm⁻¹: 3395 (O-H), 3003 (Ar. C-H), 2918 (Aliph. C-H), 1714 (ester C=O), 1656 (C=N, C=C), 1434-1409 (C-H), 1314-1276 (ester C-O), 1106 (C-N), and 950 (=C-H). ¹H NMR (600 MHz, DMSO-d₆): δ (ppm): 10.09 (1H, *s*, for -OH), 9.12 (2H, *d*, *J*= 8.1 Hz, for Ar-H); 9.04 (4H, *d*, *J*= 8.0 Hz, for pyrrole-H); 8.95 (2H, *d*, *J*= 8.0 Hz, for Ar-H); 8.45 (6H, *d*, *J*= 8.2 Hz, for Ar-H); 8.38 (6H, *d*, *J*= 8.0 Hz, for Ar-H); 8.01 (2H, *d*, *J*= 8.2 Hz, 2H, for pyrrole-H); 7.20 (2H, *d*, *J*= 8.1 Hz, for pyrrole-H); and 4.01 (9H, *s*, for -OCH₃). Elemental analysis: expected for C₅₀H₃₄N₄O₇Zn (%): C= 69.17, H= 3.95, N= 6.45, found (%): C= 69.15, H= 4.94, N= 6.41. MALDI TOF MS simulated *m/z*: 866.17 Found: [M]⁺= 866.61.

2.2.3.3. Synthesis of Ga (III) Porphyrin Complexes, **Schemes 3.7, 3.8**

Chloro gallium complexes were synthesized using a similar procedure as described for the zinc complex above, except that anhydrous gallium (III) chloride salt was used instead of the zinc acetate. The amounts used are listed in **Table 2.4**.

Chloro gallium 5-(4-Hydroxyphenyl)-tris-10,15,20-(4-acetylphenyl)-porphyrin 7-Ga; Yield: 97%. FT-IR (UATR-TWO™) ν max/cm⁻¹: 3374 (O-H), 2996 (Ar. C-H), 2776 (Aliph. C-H), 1718 (ester C=O), 1604 (C=N, C=C), 1466-1434 (C-H), 1345-1274 (ester C-O), 1107 (C-N), and 952 (=C-H bend). ¹H NMR (600 MHz, DMSO-d₆): δ (ppm): 10.11 (1H, *s*, for -OH); 9.14 (2H, *d*, *J*= 8.1 Hz, for Ar-H); 9.04 (4H, *d*, *J*= 8.4 Hz, for pyrrole-H); 8.95 (2H, *d*, *J*= 8.2 Hz, for Ar-H); 8.44 (6H, *d*, *J*= 8.1 Hz, for Ar-H); 8.38 (6H, *d*, *J*= 8.1 Hz, for Ar-H); 8.01 (2H, *d*, *J*= 8.4 Hz, for pyrrole-H); 7.25 (2H, *d*, *J*= 8 Hz, for pyrrole-H); and 4.06 (9H, *s*, for -OCH₃). Elemental analysis: expected for C₅₀H₃₄N₄O₇ClGa (%): C= 66.14, H= 3.77, N= 6.17, found (%): C= 66.15, H= 3.74, N= 6.18. MALDI TOF MS simulated *m/z*: 906.14. Found [M]⁺= 906.49 and [M-Cl]⁺= 871.48.

Chloro gallium 5,10,15,20-tetrakis(4-dimethylaminophenyl)-porphyrin 8-Ga; Yield: 96%. FT-IR (UATR-TWO™) ν max/cm⁻¹: 3013-2996 (Ar. and Aliph. C-H), 1605 (C=N, C=C), 1488-1428 (C-H), 1107 (C-N), and 985 (=C-H). ¹H NMR (400 MHz, DMSO-d₆): δ (ppm): 8.23 (8H, *d*, *J*= 8.3 Hz, for Ar-H); 7.93 (2H, *d*, *J*= 8.4 Hz, for pyrrole-H); 7.68 (8H, *d*, *J*= 8.3 Hz, for Ar-H); 7.30 (2H, *d*, *J*= 7.8 Hz, for pyrrole-H); 6.78 (4H, *d*, *J*= 8.0 Hz, for pyrrole-H); and 3.04 (24H, *s*, for -CH₃).

Elemental analysis: expected for C₅₂H₄₈N₈ClGa (%): C= 70.16, H= 5.44, N= 12.59, found (%): C= 70.15, H= 5.44, N= 12.58. MALDI TOF MS simulated m/z: 890.17. Found [M+H]⁺= 891.40 and [M+H-Cl]⁺= 856.37.

2.2.3.4. *Synthesis of In (III) Porphyrin Complexes, Schemes 3.7, 3.8*

Generally, the as-prepared **7-H₂** and **8-H₂** (1 eq) were each dissolved in glacial acetic acid (70 mL) followed by the addition of Na(OAc) (36 eq) and InCl₃ salt (5 eq). The mixtures were allowed to reflux for 5 h with continuous stirring and the successful metalation of the porphyrin was monitored by UV-Vis absorption spectra as mentioned above. The amounts used are in **Table 2.4**.

Chloro gallium 5-(4-Hydroxyphenyl)-tris-10,15,20-(4-acetylphenyl)-porphyrin 7-In; Yield: 67%. FT-IR (UATR-TWO™) ν max/cm⁻¹: 3384 (O-H), 3085 (Ar. C-H), 2951 (Aliph. C-H), 1717 (ester C=O), 1603 (C=N, C=C), 1529-1434 (C-H), 1350-1274 (ester C-O), 1105 (C-N stretch), and 966 (=C-H). ¹H NMR (600 MHz, DMSO-d₆): δ (ppm): 10.11 (1H, s, for OH); 9.14 (2H, d, J= 8.3 Hz, for Ar-H); 9.04 (4H, d, J= 8.2 Hz, for pyrrole-H); 8.95 (2H, d, J= 8.3 Hz, 2H, Ar-H); 8.45 (6H, d, J= 8.1 Hz, for Ar-H); 8.39 (6H, d, J= 8.1 Hz, for Ar-H), 8.01 (2H, d, J= 8.1 Hz, for pyrrole-H); 7.26 (2H, d, J= 8.1 Hz, for pyrrole-H); and 4.07 (9H, s, for -OCH₃). Elemental analysis: expected for C₅₀H₃₄N₄O₇ClIn (%): C= 63.01, H= 3.60, N= 5.88, found (%): C= 63.05, H= 3.64, N= 5.81. MALDI TOF MS simulated m/z: 952.12. Found [M+H]⁺= 953.41 and [M-Cl+H]⁺= 918.38.

Chloro indium 5,10,15,20-tetrakis(4-dimethylaminophenyl)-porphyrin 8-In; Yield: 83%. FT-IR (UATR-TWO™) ν max/cm⁻¹: 2847 (Ar. and Aliph. C-H), 1605 (C=N, C=C), 1556 (C-H), 1164 (C-N), and 963 (=C-H). ¹H NMR (400 MHz, DMSO-d₆): δ (ppm): 8.27 (8H, d, J= 8.2 Hz, for Ar-H); 7.91 (2H, d, J= 8.0 Hz, for pyrrole-H); 7.73 (8H, d, J= 8.1 Hz, for Ar-H); 7.27 (2H, d, J= 8.1 Hz, for pyrrole-H); 6.78 (4H, d, J= 8.1 Hz, for pyrrole-H); and 3.06 (24H, s, for -CH₃). Elemental analysis: expected for C₅₂H₄₈N₈ClIn (%): C= 66.78, H= 5.17, N= 11.98, found (%): C= 66.75, H= 5.24, N= 11.95. MALDI TOF MS simulated m/z: 935.26, found: [M+H]⁺= 936.72.

All the amounts of the chemicals used during the synthesis of the metallated porphyrins are shown in **Table 2.4**.

Table 2.4 Amounts of reagents used in the synthesis of the metallated porphyrins.

Complex	Precursor	Metal salt	Reaction conditions	Purification methods
7-Zn	7-H₂ (0.1 g, 0.12 mmol)	ZnOAc (0.078 g, 0.44 mmol)	Solvents: DMF or 20 mL glacial acetic acid for 7-In and 8-In Heating overnight at 100 °C, argon atmosphere	Precipitate with 50 mL water- ethanol (1:1v/v) then Filtration under <i>vacuum</i>
7-In		InCl ₃ (0.138 g, 0.62 mmol)		
7-Ga		GaCl ₃ (0.076 g, 0.44 mmol)		
8-In	5,10,15,20- tetrakis(4- dimethylaminophen- yl)-porphyrin, 8-H₂ (0.100 g, 0.13 mmol)	InCl ₃ (0.141 g, 0.64 mmol)	<u>NaOAc</u> (0.356 g, 4.4 mmol) for 7- In (0.381g, 4.6 mmol) for 8-In	
8-Ga		GaCl ₃ (0.081 g, 0.46 mmol)		

2.2.4. Quaternization of Selected Pcs and Porphyrins to form Complexes **Schemes 3.4, 3.5, and 3.8**

The alkylation of **3-Zn**, **3-In**, **4-Zn**, and **4-In** Pcs along with **8-Ga** and **8-In** porphyrins using an excess of methyl iodide in dry DMF (4 mL) afforded the quaternized complexes **3-ZnQ**, **3-InQ**, **4-ZnQ**, **4-InQ**, **8-GaQ**, and **8-InQ** by following previously described procedures with slight modifications [172,173]. The reactions were carried out by refluxing for 72 h under an argon

atmosphere. The desired products were precipitated out with acetone and collected by centrifugation and then dried under reduced pressure.

Tetrakis[(E)-4-(4-(3-(pyridin-4-yl)acryloyl)phenoxy)phthalocyaninato] zinc (II) tetraiodide 3-ZnQ; Yield: 92 %. FT-IR (UATR-TWO™) ν max/cm⁻¹: 3055 (Ar. C-H), 2928-2855 (Aliph. C-H), 1721 (C=O), 1583-1490 (C=C, C=N), 1411-1362 (C-C), 1228-1164 (Asym., Ar-O-Ar), 1086 (Sym., Ar-O-Ar), 832. ¹H NMR (600 MHz, DMSO-d₆): δ (ppm): 8.97-8.95 (8H, *m*, for ArH-pyridyl ring); 8.90 (8H, *d*, *J* = 8.9 Hz, for ArH); 8.25 (2H, *d*, *J* = 8.1 Hz, for ArH-Pc core); 8.20 (2H, *d*, *J* = 8.2 Hz, for ArH-Pc core); 8.03 (4H, *d*, *J* = 15.9 Hz, for *trans*-H); 7.96-7.92 (8H, *m*, for ArH-Pc core and *trans*-H); 7.46-7.44 (8H, *dd*, *J* = 2.3, 8.2 Hz, for ArH pyridyl ring); 7.39 (4H, *d*, *J* = 8.2 Hz, for ArH-Pc core); 7.28 (8H, *d*, *J* = 8.8 Hz, for ArH) and 2.90 (12H, *s*, for -CH₃). Elemental analysis: expected for C₉₂H₆₄N₁₂O₈Zn (%): C= 72.18, H= 4.21, N= 10.98; found (%): C= 72.26, H= 4.19, N= 10.94.

Tetrakis[(E)-4-(4-(3-(pyridin-4-yl)acryloyl)phenoxy)phthalocyaninato] indium (III) chloride tetraiodide 3-InQ; Yield: 98 %. FT-IR (UATR-TWO™) ν max/cm⁻¹: 3056 (Ar-H), 2925-2856 (Aliph C-H), 1722 (C=O), 1583-1491 (C=C, C=N), 1413-1362 (C-C), 1228-1164 (Asym., Ar-O-Ar), 1087 (Sym., Ar-O-Ar), 832. ¹H NMR (600 MHz, DMSO-d₆): δ (ppm): 8.97-8.95 (8H, *m*, for ArH-pyridyl ring); 8.90 (8H, *d*, *J* = 8.0 Hz, for ArH); 8.25 (2H, *d*, *J* = 8.2 Hz, ArH-Pc core); 8.20 (2H, *d*, *J* = 8.2 Hz, for ArH-Pc core); 8.03 (4H, *d*, *J* = 16.2 Hz, for *trans*-H); 7.96-7.92 (8H, *m*, for ArH-Pc core and *trans*-H); 7.46-7.44 (8H, *m*, for ArH pyridyl ring); 7.39 (4H, *d*, 4H, ArH-Pc core); 7.28 (*d*, *J* = 8.1 Hz, ArH); and 2.90 (12H, *s*, for -CH₃). Elemental analysis: expected for C₉₂H₆₄ClInN₁₂O₈ (%): C= 68.38, H= 3.39, N= 10.40; found (%): C= 68.28, H= 3.30, N= 10.46.

Tetrakis[(E)-4-(4-(3-(dimethylamino-4-yl)acryloyl)phenoxy)phthalocyaninato] zinc (II) tetraiodide 4-ZnQ, Yield: 95%. IR (UATR-TWO™) ν max/cm⁻¹: 3043 (Ar-H), 2928-2855 (Aliph C-H), 1706 (C=O), 1656-1590 (C=C, C=N), 1464-1327 (C-C), 1220-1160 (Asym., Ar-O-Ar), 1087 (Sym., Ar-O-Ar), 828. ¹H NMR (600 MHz, DMSO- d₆): δ (ppm): 8.25 (8H, *d*, *J* = 8.6 Hz, for Ar-H); 8.05 (8H, *d*, *J* = 8.6 Hz, for Ar-H); 7.95 (2H, *d*, *J* = 9.0 Hz, for Ar-H Pc core); 7.93 (4H, *d*, *J* = 15.6 Hz, for *trans*-H); 7.72 (4H, *d*, *J* = 8.7 Hz, for Ar-H Pc core); 7.68 (8H, *d*, *J* = 9.1 Hz, for Ar-H dimethylamino ring); 7.41 (4H, *d*, *J* = 16.0 Hz, for *trans*-H); 7.32 (4H, *d*, *J* = 8.7 Hz, for Ar-H Pc core); 7.23 (2H, *d*, *J* = 8.6 Hz, for Ar-H Pc core); 6.83 (8H, *d*, *J* = 9.1 Hz, Ar-H dimethylamino ring); and 3.03 (36H, *s*, for N-(CH₃)₂). Elemental analysis: expected for C₁₀₄H₈₈N₁₂O₈Zn: C= 73.51, H= 5.22, N= 9.89, found: C= 73.24, H= 5.90, N= 9.05.

Tetrakis[(E)-4-(4-(3-(dimethylamino-4-yl)acryloyl)phenoxy)phthalocyaninato] indium (III) chloride tetraiodide 4-InQ, Yield: 98%. FT-IR (UATR-TWO™) ν max/cm⁻¹: 2923 (Ar. C-H), 2905-2856 (Aliph. C-H), 1709 (C=O), 1657-1588 (C=C, C=N), 1461-1328 (C-C), 1212-1150 (Asym., Ar-O-Ar), 1024 (Sym., Ar-O-Ar), 819. ¹H NMR (600 MHz, DMSO- d₆): δ (ppm): 8.24 (8H, *d*, *J*= 8.3 Hz, for Ar-H); 8.05 (8H, *d*, *J*= 8.3 Hz, for Ar-H); 7.95 (2H, *d*, *J*= 8.1 Hz, for Ar-H Pc core); 7.93 (4H, *d*, *J*= 16.3 Hz, for *trans*-H); 7.72 (4H, *d*, *J*= 8.1 Hz, for Ar-H Pc core); 7.68 (8H, *d*, *J*= 8.3 Hz, Ar-H dimethylamino ring); 7.41 (4H, *d*, *J*= 16.1 Hz, for *trans*-H); 7.32 (4H, *d*, *J*= 8.2 Hz, for Ar-H Pc core); 7.23 (2H, *d*, *J*= 8.2 Hz, for Ar-H Pc core); 6.83 (8H, *d*, *J*= 8.3 Hz, for Ar-H dimethylamino ring); and 3.04 (36H, *s*, for N-(CH₃)₂). Elemental analysis: expected for C₁₀₄H₈₈ClInN₁₂O₈: C= 70.01, H= 4.97, N= 9.42, found: C= 70.47, H= 4.27, N= 9.74.

Chloro gallium 5,10,15,20-tetrakis(4-dimethylaminophenyl)-porphyrin tetraiodide 8-GaQ, Yield: 97%. FT-IR (UATR-TWO™) ν max/cm⁻¹: 3013-2995 (Alph. and Ar. C-H), 1606 (C=N, C=C), 1482 (C-H), 1116 (C-N), and 944 (=C-H). ¹H NMR (400 MHz, CDCl₃): δ (ppm): 7.75 (8H, *d*, *J*= 7.5 Hz, for Ar-H); 7.72 (8H, *d*, *J*= 8.0 Hz, for Ar-H); 7.65 (2H, *d*, *J*= 7.6 Hz, for pyrrole-H); 7.57 (4H, *d*, *J*= 8.4 Hz, for pyrrole-H); 7.40 (2H, *d*, *J*= 7.9 Hz, for pyrrole-H); and 3.10 (36H, *s*, for -CH₃). Elemental analysis: expected for C₅₆H₆₀N₁₂O₈ClGa: C= 70.78, H= 6.36, N= 11.79, found: C= 70.77, H= 6.30, N= 11.72.

Chloro indium 5,10,15,20-tetrakis(4-dimethylaminophenyl)-porphyrin tetraiodide 8-InQ, Yield: 93%. FT-IR (UATR-TWO™) ν max/cm⁻¹: 2847 (Alph. and Ar. C-H), 1606 (C=N, C=C), 1556 (C-H), 1163 (C-N), and 961 (=C-H). ¹H NMR (400 MHz, CDCl₃): δ (ppm): 7.77 (8H, *d*, *J*= 8.1 Hz, for Ar-H); 7.73 (8H, *d*, *J*= 7.5 Hz, for Ar-H); 7.67 (2H, *d*, *J*= 7.9 Hz, for pyrrole-H); 7.57 (4H, *d*, *J*= 8.4 Hz, for pyrrole-H); 7.40 (2H, *d*, *J*= 7.7 Hz, for pyrrole-H); and 3.09 (36H, *s*, for -CH₃). Elemental analysis: expected for C₅₆H₆₀N₁₂O₈ClIn: C= 67.57, H= 6.06, N= 11.26, found: C= 67.60, H= 6.08, N= 11.27.

2.2.5. Synthesis of the Nanoparticles

The DNDs used in the present study were used as received from the suppliers. The other nanomaterials used in this work were all synthesized following the procedures reported elsewhere with a few modifications.

2.2.5.1. Synthesis of the GQDs, *Scheme 3.9A*

The synthesis of GQDs was done according to the top-down hydrothermal method as per a reported procedure [159] (**Scheme 3.9A**) whereby 0.250 g of graphene oxide (GO) was oxidized in concentrated H₂SO₄ (10 mL) and HNO₃ (30 mL) for 4 h under ultrasonication. The mixture was dissolved in 50 mL of Millipore water then left to stir at room temperature for 2 h, then filtered through a 0.22 µm microporous membrane. Afterwards, the pH of the suspension was adjusted to 8.0 using 10% NaOH under ultrasonication for about 30 min. The suspension was then transferred to a 400 mL Teflon-lined stainless autoclave and heated up to 160 °C for 12 h. The final product was cooled to room temperature and filtered using a 0.22 µm membrane and was further dialyzed for two days using a dialysis membrane (MW 1.5 kDa). The solid product was obtained after freeze drying the colloidal solution.

2.2.5.2. Synthesis of the GSH@GQDs, *Scheme 3.11*

The preparation of GSH@GQDs was achieved according to a reported method with slight modifications [160]. Briefly, 0.5 g of citric acid and 0.17 g of glutathione (GSH) were mixed and heated at 240 °C while stirring in a beaker. The mixture changed from colorless to pale yellow, and then brown in 8 min. The crude product was dissolved into Milli-Q ultrapure water and followed by purification on silica gel column using 0.01 M HCl solution as the eluent. The pure product was kept in the dark at room temperature.

2.2.5.3. Synthesis of CSAg NPs, *Scheme 3.10A*

Chitosan-silver mediated (CSAg) nanoparticles were prepared following the literature [161] methods with minor modifications as follows: to an aqueous solution of silver nitrate (20 mL of 0.1 M), previously prepared chitosan solution [50 mL of 1% (w/v)] was added dropwise under an argon atmosphere. Subsequently, ammonia solution was added dropwise to make the reaction slightly basic (pH 8) and this was left to stir for 2 h. The obtained product was precipitated using ethanol. The characterization of the obtained nanoparticles was carried out *via* multiple techniques.

2.2.5.4. Synthesis of the Bare Ag NPs

The synthesis of Ag NPs was done following a chemical reduction procedure in distilled water as follows [162]: 30 mL of sodium borohydride (0.002 M) used as primary reductant and 5 mL of trisodium citrate (0.004 M) used as secondary reductant and as stabilizing agent were mixed and heated to 60 °C for 30 min in the dark while vigorously stirring. Following this, 50 mL of AgNO₃

(0.001 M) was added drop by drop to the mixture and subsequently, the temperature was further raised to 90 °C and the pH adjusted to 10.5 using 0.1 M NaOH while heating was continued for 25 min. The nanoparticles suspension was removed from the heating device and cooled to room temperature while stirring. The Ag NPs suspensions were centrifuged (12 000 rpm, 15 min) and washed thrice, followed by redispersion in deionized water and stored in the fridge.

2.2.6. Conjugation of PSs to Nanomaterials

The conjugation of some of the complexes to the nanomaterials was done in 3 different ways: either by π - π stacking interactions where the resulting nanoconjugates will be represented as **PS π (NPs)**, or by covalent linkage (through amide or ester bond) or by chemisorption (through a silver-nitrogen affinity bond).

2.2.6.1. The π - π Stacking Conjugation, *Schemes 3.9B*

The non-covalent π - π stacking interactions were formed between the following Pcs: **1-H₂**, **1-Zn**, **1-In**, **2-Zn**, **2-In**, **3-Zn**, **3-In**, **3-ZnQ**, **3-InQ**, **5-Zn** and either GQDs, GSH@GQDs, and DNDs as previously reported with slight modifications [151,174] to afford the following groups of nanoconjugates:

- (a) **1-H₂ π** (GQDs), **1-Zn π** (GQDs), and **1-In π** (GQDs)
- (b) **1-H₂ π** (DNDs), **1-Zn π** (DNDs) and **1-In π** (DNDs),
- (c) **2-Zn π** (DNDs) and **2-In π** (DNDs),
- (d) **3-Zn π** (DNDs), **3-In π** (DNDs), **3-ZnQ π** (DNDs) and **3-InQ π** (DNDs).
- (e) **5-Zn π** (GSH@GQDs).

Briefly, each Pc and respective NPs (in 2:1 mass ratio) were dissolved in 2 mL of dry DMF or DMSO. The mixtures were firstly subjected to 4 h sonication and then stirred for 96 h at room temperature. The newly formed nanoconjugates were collected by washing the crude products repeatedly with ethanol to remove the unreacted starting materials through centrifugation.

2.2.6.2. Covalent Conjugation (amide bond), *Scheme 3.10B, 3.11*

As demonstrated in the literature [175], the nanoconjugates **2-Zn π** (DNDs) and **2-In π** (DNDs) were further linked to CSAg using the NH₂ of chitosan and the COOH of DNDs in the nanoconjugates by DCC coupling to result in **2-Zn π** (DNDs)-CSAg and **2-In π** (DNDs)-CSAg respectively, **Scheme 3.10B**.

Similarly, **6-Zn** was linked to GSH@GQDs *via* an amide bond between COOH of the Pc and the NH₂ of the NPs to form **6-Zn**-(GSH@GQDs), **Scheme 3.11**.

Method:

To realize this, 10 mg of each **2-Zn** π (DNDs), **2-In** π (DNDs), and **6-Zn** were mixed with DCC (5 mg, 0.024 mmol) in DMF (5 mL) and stirred at room temperature for 48 h to activate COOH groups. Following this, 5 mg of respective NPs (CSAg for **2-Zn** π (DNDs), **2-In** π (DNDs) or GSH@GQDs for **6-Zn**) were added to the mixture and further stirred for 48 h. In the end, the mixtures were repeatedly centrifuged in ethanol and the collected products were dried under a *vacuum*.

2.2.6.3. Covalent Conjugation and Chemisorption through Ag-N Affinity, *Scheme 3.12*

In a one pot reaction, porphyrins **7-H₂**, **7-Zn**, **7-Ga**, and **7-In** were subsequently conjugated to DNDs through ester bond formation between the hydroxyl group of the complexes and the carboxylic acid moieties of the DNDs, followed by chemisorption through Ag-N bond to yield **7-H₂**-(DNDs@Ag), **7-Zn**-(DNDs@Ag), **7-Ga**-(DNDs@Ag), and **7-In**-(DNDs@Ag) nanoconjugates.

Method:

DNDs (10 mg) and DCC (0.010 g, 0.049 mmol) in dry DMF (3 mL) were continuously stirred for 48 h. Afterward, Ps (10 mg each) and NHS (0.008 g, 0.07 mmol) as well as the bare Ag NPs (5 mg) were subsequently added to the respective vessels and left to stir at room temperature for 72 h. The products were collected by centrifugation in ethanol and dried under a *vacuum*.

2.3. Photophysical and Photochemical Methods

The photophysicochemical properties of the excited states of PSs depend on their chemical structures: the nature of the central metal ion, peripheral substituents, the axial ligands, and non-planar distortions [176,177]. The photophysicochemical properties include fluorescence quantum yields, fluorescence lifetimes, triplet quantum yields, triplet lifetimes, singlet-oxygen quantum yields.

2.3.1. Fluorescence Quantum Yield (Φ_F) and Fluorescence Lifetime (τ_F)

The Φ_F is the ratio of the number of photons emitted *via* fluorescence to those absorbed and it can be determined using a reported comparative method [176–178] according to **Equation 2.1**:

$$\Phi_F = \Phi_{F(Std)} \frac{F \cdot A_{Std} \cdot n^2}{F_{Std} \cdot A \cdot n_{Std}^2} \quad (2.1)$$

Where F and F_{Std} are the area under the emission curves of the sample and standard, respectively. A and A_{Std} are the absorbances at the excitation wavelength of the sample and standard, respectively. n and n_{Std} are the refractive index of the solvent used to dissolve both the sample and standard. Unsubstituted ZnPc was used as a standard with the value: $\Phi_F = 0.2$ in DMSO for Pcs [179].

The excitation and emission measurements were recorded using a 1 cm path length quartz cuvette where the absorbances of the solutions were constantly adjusted to ≤ 0.05 nm. The excitation was done at the vibronic band for Pcs and the Soret band for porphyrins using the crossover wavelength of standard and complex. The emission spectra were recorded at 500-800 nm.

τ_F refers to the average time a molecule spends in its excited state before undergoing fluorescence to the ground state [180].

2.3.2. Förster Resonance Energy Transfer (FRET)

FRET is a non-radiative energy transfer process that occurs between a photoexcited donor fluorophore upon absorption of higher energy photons and an acceptor molecule near the donor fluorophore [181,182].

The determination of FRET efficiency (Eff) was done experimentally from the fluorescence quantum yields of the donor in the absence ($\Phi_{F(NPS)}$) and presence ($\Phi_{F(NPS)}^{Conjugate}$) of the acceptor using **Equation 2.2 [183]**:

$$Eff = 1 - \frac{\Phi_{F(NPS)}^{Conjugate}}{\Phi_{F(NPS)}} \quad (2.2)$$

2.3.3. Triplet Quantum Yield (Φ_T) and Triplet Lifetime (τ_T)

The Φ_T refers to the fraction of the excited molecules which go to the excited triplet state by intersystem crossing [184]. Triplet quantum yields were determined using **Equation 2.3 [185]**:

$$\Phi_T = \Phi_{T(Std)} \frac{\Delta A_T \cdot \varepsilon_{T(Std)}}{\Delta A_{T(Std)} \cdot \varepsilon_T} \quad (2.3)$$

Whereas ΔA_T and $\Delta A_{T(Std)}$ are the changes in the triplet state absorption of the sample and the standard, respectively. $\Phi_{T(Std)}$ is the triplet state quantum yield for the standard. ε_T and $\varepsilon_{T(Std)}$ are the triplet state extinction coefficients for the sample and the standard respectively. ZnPc was used as a standard in DMSO ($\Phi_T = 0.65$ [186]).

For triplet state studies, solutions were introduced into a 1 cm path length UV-Vis cuvette and degassed using argon for 30 min. Thereafter the solutions (standard or sample) were each sealed and illuminated using an appropriate excitation wavelength (the crossover wavelength of the sample and the standard, which was ~620 nm). The absorbance of the sample solution and the standard were ~1.5 at Q-band. The maximum triplet absorption wavelength was determined from the transient curve.

2.3.4. Singlet Oxygen Quantum Yield (Φ_Δ)

Singlet oxygen value is the main factor used to determine whether a photosensitizer is suitable for use in PDT or not. The determination of the singlet oxygen quantum yields values is commonly carried out following a UV-Vis spectroscopic method [187]. The monitoring is done spectroscopically following the bleaching of a chemical quencher such as DPBF in DMSO and ADMA in aqueous solutions at 417 nm and 378 nm, respectively, whereas the unsubstituted ZnPc in DMSO with ($\Phi_\Delta = 0.67$ [186]) and ClAlPcSmix ($\Phi_\Delta = 0.42$ [186]) are respectively utilized as standards using comparative methods as described in **Equation 2.4**.

$$\Phi_\Delta = \Phi_{\Delta(Std)} \frac{R \cdot I_{abs(Std)}}{R_{(Std)} \cdot I_{abs}} \quad (2.4)$$

Where $\Phi_{\Delta(Std)}$ is the singlet oxygen quantum yield for the standard, R and $R_{(Std)}$ are the DPBF or ADMA photobleaching rates in the presence of Pcs or RB for porphyrins under investigation and the standard, respectively. I_{abs} and $I_{abs(Std)}$ are the rates of light absorption by the complexes and standard, respectively. I_{abs} is determined by **Equation 2.5**.

$$I_{abs} = \frac{\alpha \cdot A \cdot I}{N_A} \quad (2.5)$$

Whereas α is the fraction of light absorbed, S is the cell area irradiated, N_A is Avogadro's constant, and I the light intensity.

2.4. Theoretical Calculations

The theoretical calculations were only investigated for the free-base dimethylaminophenyl porphyrins (**8-H₂**, and **8-H₂Q**) and the metalated porphyrins **8-Ga**, **8-In**, **8-GaQ**, and **8-InQ** complexes as examples.

The geometry optimizations were carried out at B3LYP/LanL2DZ level with no constraint of symmetry. The optical absorption spectra were computed using TD-B3LYP at the same theoretical level in *vacuo*. This method has been previously used [188] on transition metals compounds and nanoclusters and it has been shown to provide optical properties close to experiment. The theoretical background of time-dependent density functional theory was achieved following a protocol described in the literature [189]. The solvent effect was estimated by comparing the experimental and theoretical spectra.

2.5. Photodynamic Antimicrobial Chemotherapy (PACT)

2.5.1. Bacteria Culture and Biofilms Formation

Two reference strains used in this study were *S. aureus* as Gram-positive bacteria and *E. coli* as Gram-negative bacteria in the specific cases of positively charged PSs.

For the preparation of planktonic cultures, bacteria aliquots were suspended in nutrient broth overnight under aerobic conditions in a shaking incubator at 37°C to obtain bacteria in the logarithmic phase of growth (O.D. 0.6-0.8 recorded at 620 nm). Afterwards, suspensions were harvested by centrifugation (4000 RPM for 15 min) and resuspended in phosphate-buffered saline (PBS pH 7.4) yielding an optimal concentration of 10⁹ or 10¹⁰ colony forming unit per mL (CFU/mL) corresponding to *ca.* 30-400 colonies in the viable count.

Single-species biofilms were formed in 96-well flat-bottomed microplates. Firstly, wells were filled with 200 µL of planktonic culture and incubated at 37°C. After every 24 h, the medium was gently removed and 200 µL fresh TSB was added to allow strong cell adhesion to the surface. For all experiments, the total culture period was 72-120 h. After this, the biofilm-coated wells were carefully washed with PBS and left to air dry. Subsequently, biofilm formation was quantified by determining the O.D. at 570 nm using 1% crystal violet solution (200 µL) as staining dye.

2.5.2. Antimicrobial Assays

PACT experiments were done following literature with slight changes [190,191]. For comparison purposes, 1% DMSO in PBS was used as the medium. A 670 nm laser lamp (irradiance: 524 mW/cm² and dose: 943 J/cm²) and a 415 nm LED lamp (irradiance of 250 mW cm⁻²) were selected since they provided the highest possible overlay with the absorption spectrum of the Pcs and porphyrins, respectively.

2.5.2.1. Photoinactivation of Bacteria Planktonic Cultures

Firstly, the PSs were diluted in 1% DMSO/PBS and tested at concentrations ranging from 0.31-40 µM to determine the minimum inhibitory concentration of the PSs using microplate assay as described previously [192]. Briefly, sterile 24-well plates were inoculated with 2.5 mL inocula containing different concentrations of PSs and subsequently incubated in the dark at 37 °C for 30 min. Next, the inocula were irradiated for 30 min, then 100 µL from each group was aseptically inoculated on petri dish agar plates in triplicates, followed by incubation at 37 °C for 18 h. All

experiments were also concomitantly performed in the dark to determine the dark toxicity of the PSs. The numbers of CFUs were determined as the viability of the cells. The control groups (light alone without PS) were done for all experiments to rule out any inactivation effect due to the light.

Secondly, once the optimal concentrations were determined to be ca. 10 and 1.25 μM for neutral and positively charged PSs respectively, bacterial suspensions containing 10 μM or 1.25 μM of PSs were prepared and the photo-antimicrobial assays were done similarly as described above except that the irradiation was done for 120 min with 30 min irradiation intervals starting from zero min. The acquired CFU/mL data were then converted into log reduction values and percentage cell survival.

2.5.2.2. *Photoinactivation of Bacterial Biofilms*

The experiment was done following slightly modified procedures [193,194]. 100 μL of each PS with concentrations of 25, 50, 100, and 200 μM were added to the biofilm-containing plates while in the control group, the bacteria were only inoculated with PBS. After 30 min dark incubation at 37 $^{\circ}\text{C}$ followed by 30 min irradiation, the biofilms were scraped from the wells and followed by 10-fold dilutions in PBS, and 100 μL of selected dilution were inoculated on agar plates. The number of CFUs was counted after incubation at 37 $^{\circ}\text{C}$ for 24 h. The treated and the dark experiments were all performed in triplicate. In all methods, negative control of biofilm (without antibiotic) and sterile control (only medium) were included.

2.5.3. *Statistical Analysis*

To assess the statistical significance of the obtained data, 3-way ANOVA analysis was used. The experiments were run in triplicates and a p -value of 0.05 was considered statistically significant.

2.6. PACT-Ciprofloxacin Combined Therapy

The preparation of the bacteria cultures and biofilms of *S. aureus* and *E. coli* were done as described in **Section 2.5** above. The antimicrobial agent, ciprofloxacin, a broad-spectrum fluoroquinolone antibiotic with different bacterial cell targets was used in this study. Ciprofloxacin (CIP) acts on the deoxyribonucleic acid (DNA) replication by inhibiting the bacterial DNA topoisomerase and DNA-gyrase. CIP is the most potent treatment in mixed infections and it is mostly used against *E. coli* and some Gram (+) bacteria [195].

2.6.1. Susceptibility of Matured Biofilms to PACT and Ciprofloxacin as Monotherapies

For PACT experiments, the PSs were prepared in gradient concentrations of 4, 8, 16, and 32 μM .

The ciprofloxacin activity on both biofilm strains was determined by the microdilution method [196] at concentrations ranging from 0.5 to 32 $\mu\text{g/mL}$. Briefly, each concentration of the antibiotic was added to the respective wells. The plates were then incubated for 24 h at 37 °C. The bacterial cell viability of the biofilms was confirmed by the quantification with the CV method.

2.6.1.1. Minimum Biofilm Eradication Concentration (MBEC₅₀) Assay

The minimum biofilm eradication concentration 50% (MBEC₅₀) is the lowest concentration of an antimicrobial drug that can damage $\geq 50\%$ of the biofilm structure. To determine the MBEC₅₀ of ciprofloxacin, 200 μL of each concentration was added to the wells containing the matured biofilms. After incubation at 37 °C for 24 h, the unbound cells were gently removed discharged and the wells were rinsed three times with 200 μL of PBS. Then 200 μL of 1% CV was added to each well for 15 min, followed by discharging and washing the wells three times with 200 μL of PBS. Finally, the wells were air-dried and the biofilm-bound CV was dissolved with 200 μL of ethanol, and their O.D. were measured at 570 nm [193,197–199].

2.6.1.2. Minimum Biofilm Inhibitory Concentration (MBIC₅₀) Assay

The minimum biofilm inhibitory concentration 50% (MBIC₅₀) is defined as the lowest antibiotic concentration able to inhibit more than 50% of biofilm growth after 24 h incubation related to untreated controls. In this case, the same amounts of bacterial planktonic cultures of $\sim 10^7$ CFU/mL and different concentrations of CIP solution in TSB, were mixed and incubated in 96 well plates for 24 h at 37 °C. The determination of MBIC₅₀ was conducted in a similar way as for the MBEC₅₀

following the procedure described above. The results are expressed as the mean of three experiments.

2.6.2. Susceptibility of Matured Biofilms to PACT and Ciprofloxacin in Combination

The biofilm formation was done as described above where the final concentration per well of bacterial strains was $\sim 1 \times 10^7$ CFU/mL. PACT experiments were carried out in the first step, where the tested concentrations of the quaternized indium complexes models: **4-InQ** and **8-InQ** were 4, 8, 16, and 32 μ M, as well as for ciprofloxacin (0.5, 1, 2, 4, 8, and 32 μ g/mL), were kept the same according to the experiments above.

For PACT studies, 200 μ L of each concentration of the photosensitizer were seeded in wells containing biofilms, and the plates were left to incubate for 1 h at 37 °C in the dark. Following this, the irradiation was applied for 15 min using respective light sources for Pcs and porphyrins.

After irradiation the plates were washed with PBS and incubated with 200 μ L/well of each ciprofloxacin concentration at 37 °C for 24 h. After that, the samples were submitted to serial dilution and 100 μ L of selected dilutions were spread on the agar Petri dishes. CFU counts were performed as previously described, with some modifications [200]. CFUs were counted after 24 h of incubation at 37 °C and the acquired CFU/mL data were then converted into log reduction values and percentage cell survival. In all methods, control groups of PACT pre-treated biofilms (without the antibiotic) and control groups (with biofilms alone) were included.

The bacterial biofilm quantification was measured by the crystal violet (CV) staining method [201,202]. Briefly, the attached bacterial cells were air-dried at room temperature for 15 min and subsequently stained with 200 μ L of 1% CV solution. After 15 min incubation, biofilm cells were gently rinsed twice with PBS to remove excess CV, followed by air-drying. The stained biofilms were then dissolved in 200 μ L of ethanol and diluted at a ratio of 1:10. The O.D. was measured at 570 nm. Biofilm quantification (%) was defined by **Equation 2.6**:

$$\text{Biofilm cell survival (\%)} = \frac{\text{O.D.}_{\text{treated}}}{\text{O.D.}_{\text{control}}} \times 100 \quad (2.6)$$

Where $\text{O.D.}_{\text{treated}}$ is the optical density of the treated cells with the tested drugs and the $\text{O.D.}_{\text{control}}$ is the optical density of the control groups, corresponding to 100% cell survival.

2.7. Photodynamic Therapy (PDT)

2.7.1. Cell Culture Preparation

The MCF-7 cancer cells line used in this study were cultured in 75 cm² vented flasks (Porvair®) and incubated in a humidified atmosphere at 37°C and 5% CO₂ to achieve 90-100% confluence. Afterward, cells were rinsed twice with DPBS, then passed through trypsinization and centrifugation. The cell viability and enumeration were carried out using the trypan blue dye exclusion assay (0.4% (v/v) trypan blue solution) using a haemocytometer as reported [203].

2.7.2. Cellular Uptake

Complexes **4-Zn**, **4-In**, **4-ZnQ**, and **4-InQ** were used as examples for PDT experiments. The cellular uptake studies were done following a previously described procedure [204]. Briefly, MCF-7 cells (1×10^5 cells/well) were seeded in 24-well plates and then incubated in the presence of 10 µM of the PSs for 24 h in the dark. Following this, they were washed with PBS (three times), lysed with 30 µL of Triton- X100, and the internalized PSs were solubilized in 70 µL of DMSO. The cellular uptake was assessed by reading the absorbances of the PSs using an ELISA reader.

Additionally, 10 µM was selected as the optimal concentration since reports state that relatively high concentrations can exhibit minimal cellular uptake due to an altered transport mechanism [205,206].

2.7.3. Dark Toxicity and PDT Activities

For complete solubility, the drug stocks were prepared in 1% DMSO media, topped up with supplemented DMEM. The control groups consisted of the placebo cells only containing supplemented DMEM with phenol red. Dark toxicity experiments were performed without light irradiation.

For irradiation studies, cells were seeded in 96-well plates at a density of 10,000 cells/well in supplemented DMEM containing phenol red, then incubated in a humidified atmosphere at 37 °C and 5% CO₂ for 24 h to foster cell attachment to the wells. Afterwards, the wells were rinsed once with 100 µL DPBS, then 100 µL supplemented DMEM containing gradient concentrations (0.8-50 µM) of the studied PSs were administered and left to incubate. After incubation, the cells were washed with DPBS, followed by the addition of DMEM (without phenol red) and irradiated for 15

min at 670 nm (524 mV.cm⁻²). After this, the old medium was replaced with fresh DMEM and incubated for a further 20 h.

To determine the cell viability, 5 mg/mL solution of MTT (20 μL) was added to each well and incubated for an additional 3 h. The cultured medium was discarded, and 200 μL of DMSO was added to dissolve the formazan crystals. The absorbance at 540 nm was measured using a Molecular Devices Spectra Max M5 plate reader.

The percentage cell viability was determined from the ratio of the absorbance of active cells after treatment with the photosensitizer against the absorbance of the controls. The percent cell viability was determined using **Equation 2.7**:

$$\% \text{ cell viability} = \frac{\text{Absorbance of sample at 540 nm}}{\text{Absorbance of control at 540 nm}} \times 100 \quad (2.7)$$

Where the absorbance of the sample is the cells containing complexes alone while absorbance of control is the placebo cells containing only supplemented DMEM with phenol red.

2.7.4. *Lipophilicity Studies*

Lipophilicity of a drug specifies the level of its bioaccumulation and subcellular distribution [207,208]. Hence, only the lipophilicities of the quaternized complexes were investigated by the “shake-flask” method [209]. Stock solutions of each complex in octanol (10 mL) and their initial absorbances ~1.5 were recorded and named A. 3 mL from each stock and 3 mL of Millipore water were mixed and stirred for 5 h at room temperature, followed by centrifugation to separate the organic and aqueous phases. The final absorbances of the extracted octanol phase were measured and named A_o. The absorbance of each dissolved PS in the water phase (A_w) was derived from A - A_o. The partition coefficients of the PSs between octanol: H₂O (log P_{o/w}) were calculated from **Equation 2.8** [208].

$$\log P_{o/w} = \log \frac{A_o}{A_w} \quad (2.8)$$

PART III.

Results and Discussion

Chapter Three: Synthesis and Characterization

This chapter discusses in detail the synthesis and characterization of the phthalonitriles, Pcs, porphyrins, nanomaterials, and the nanoconjugates used in the current study.

Publications

The results presented and discussed in the following chapters have been drafted, published or accepted for publication in peer-reviewed journals.

1. **Yolande Ikala Openda** and Tebello Nyokong, Photodynamic antimicrobial chemotherapy-Ciprofloxacin dual therapy for ablation of *S. aureus* and *E. coli* biofilms. 2022, Photodiagnosis and Photodynamic Therapy, Submitted.
2. **Yolande Ikala Openda***, Balaji Babu and Tebello Nyokong, Cationic chalcone-derived phthalocyanines for antibacterial, antibiofilm, and anticancer photodynamic therapy. Photodiagnosis and Photodynamic Therapy 38: (2022) 102863. doi: 10.1016/j.pdpdt.2022.102863.
3. **Yolande Ikala Openda**, Sithi Mgidlana, Tebello Nyokong, *In vitro* photoinactivation of *S. aureus* and photocatalytic degradation of tetracycline by novel phthalocyanine-graphene quantum dots nano-assemblies, Journal of Luminescence 246 (2022) 118863.
4. **Yolande Ikala Openda**, Bokolombe Pitchou Ngoy, Jules Tshishimbi Muya, and Tebello Nyokong, Synthesis, theoretical calculations, and laser flash photolysis studies of selected amphiphilic porphyrin derivatives used as biofilms photodegradative materials, New Journal of Chemistry, 2021, 45, 17320-17331.
5. **Openda YI**, Ngoy BP and Nyokong T (2021), Photodynamic antimicrobial action of asymmetrical porphyrins functionalized silver-detonation nanodiamonds nanoplatfoms for the suppression of *Staphylococcus aureus* planktonic cells and biofilms. Front. Chem. 9:628316. DOI: 10.3389/fchem.2021.628316.
6. **Yolande Ikala Openda**, Tebello Nyokong, Enhanced photo-ablation effect of positively charged phthalocyanines-detonation nanodiamonds nanoplatfoms for the suppression of *Staphylococcus aureus* and *Escherichia coli* planktonic cells and biofilms. Journal of Photochemistry & Photobiology, A: Chemistry 411 (2021) 113200.
7. **Yolande Ikala Openda**, Refilwe Matshitse, and Tebello Nyokong, A search for enhanced photodynamic activity against *Staphylococcus aureus* planktonic cells and biofilms: the evaluation of phthalocyanine-detonation nanodiamonds-Ag nanoconjugates, Photochem. Photobiol. Sci, 2021. DOI: 10.1039/d0pp00075b.

8. **Yolande Ikala Openda**, Tebello Nyokong, Detonation nanodiamonds-phthalocyanine photosensitizers with enhanced photophysical properties and effective photoantibacterial activity, *Photodiagnosis and Photodynamic Therapy* 32 (2020) 102072.

9. **Yolande Ikala Openda**, Pinar Sen, Muthumuni Managa, Tebello Nyokong, Acetophenone substituted phthalocyanines and their graphene quantum dots conjugates as photosensitizers for photodynamic antimicrobial chemotherapy against *Staphylococcus aureus*, *Photodiagnosis and Photodynamic Therapy* 29 (2020) 101607.

Side Publications

10. Sixolile Centane, Sithi Mgidlana, **Yolande Openda**, Tebello Nyokong, Electrochemical detection of human epidermal growth factor receptor 2 using an aptamer on cobalt phthalocyanines-Cerium oxide nanoparticle conjugate, *Bioelectrochemistry*. 2022 Apr 29;146:108146. doi: 10.1016/j.bioelechem.2022.108146.

11. Aviwe Magadla, **Yolande Ikala Openda**, Tebello Nyokong, The implications of ortho-, meta- and para- directors on the *In-vitro* photodynamic antimicrobial chemotherapy activity of cationic pyridyl-dihydrothiazole phthalocyanines, *Photodiagnosis and Photodynamic Therapy*, submitted.

12. Richard Oriko Owor, Kibrom Gebreheiwot Bedane, **Yolande Ikala Openda**, Sebastian Zühlke, Solomon Derese, George Ong'amo, Albert Ndakala, and Michael Spittler (2020), Synergistic anti-inflammatory activities of a new flavone and other flavonoids from *Tephrosia hildebrandtii* vatke, *Natural Product Research*.

13. Mahlatse M. Ledwaba, Balaji Babu, **Yolande I. Openda**, Mojahi Motaung, John Mack and Tebello Nyokong. A comparative study of photodynamic antimicrobial chemotherapy of water soluble free-base tetra-3-pyridylchlorin and tetra-4-pyridylchlorin, 2022, completed draft.

14. Nnaemeka Nnaji, Pinar Sen, **Yolande Ikala Openda**, Eno Ebenso and Tebello Nyokong, Illustration of tertbutyl phthalocyanines: Photoinactivation and aluminium corrosion mitigation, 2022, *Journal of Molecular Structure*, Submitted.

15. Temlamdvo M. Magwaza, **Yolande I. Openda**, Nthabeleng Molupe, Jhon Mack and Tebello Nyokong. The synthesis and photophysical properties of aza-BODIPY dyes and their gold nanoparticles conjugates prepared for use in photodynamic antimicrobial chemotherapy, 2022, Completed manuscript.

16. Mahlatse M. Ledwaba, Balaji Babu, **Yolande I. Openda**, Refilwe Matshitse, John Mack and Tebello Nyokong. Water soluble Sn (IV) tetrapyrridyl chlorins as photosensitizer for photodynamic therapy and photodynamic antimicrobial chemotherapy, 2022, Complete draft.

17. Nnaemeka Nnaji, **Yolande Ikala Openda**, Balaji Babu, Jhon Mack, Tebello Nyokong, Antimicrobial activities of tin porphyrins against *Escherichia coli*-Experimental and theoretical accounts, 2022, In Preparation.

3.0. General

The present study yielded twenty-nine compounds that include six substituted phthalonitriles (**1-6** named according to groups of Pcs listed in **Table 1.2**), fifteen Pcs, and ten porphyrins. Phthalonitriles **1-4** and all the synthesized complexes are being reported here for the first time.

The Pc complexes **1-H₂**, **1-Zn**, and **1-In** have the same substituent groups and only differ based on their central metals. This is also the case for complexes **2-Zn** and **2-In**. Whereas complexes **3-Zn** and **3-In** as well as their quaternized derivatives **3-ZnQ** and **3-InQ** are also similar but differ based on their neutral and charged properties and the same goes for complexes **4-Zn**, **4-In**, **4-ZnQ**, and **4-InQ**.

In addition to this, symmetrical Pc **5-Zn** and its asymmetrical carboxylic derivative **6-Zn** are also investigated in the present work. Hence, the discussions on the synthesis and characterization methods will be based on the different groups listed in **Table 1.2**. Synthesis of the complexes and nanoconjugates was achieved by following described literature procedures outlined below (also in **Chapter 2**).

The samples were fully characterized by ¹H NMR, ¹³C NMR (for chalcones **i** and **ii** and phthalonitriles **1-4**), and MALDI-TOF-MS, CHNS elemental analysis (for the Pcs and porphyrins alone), various techniques including UV-Vis, emission, FT-IR, Raman, and DLS spectroscopies as well as TEM, TGA, and DSC (for selected Pcs, porphyrins, and nanoconjugates).

The obtained data agreed well with the proposed structures (please see the **Appendices** for NMR and mass spectra and also **Chapter two** for the elemental analysis and FT-IR data).

Please note that only the synthesis and characterization of the new compounds will be discussed in the next section.

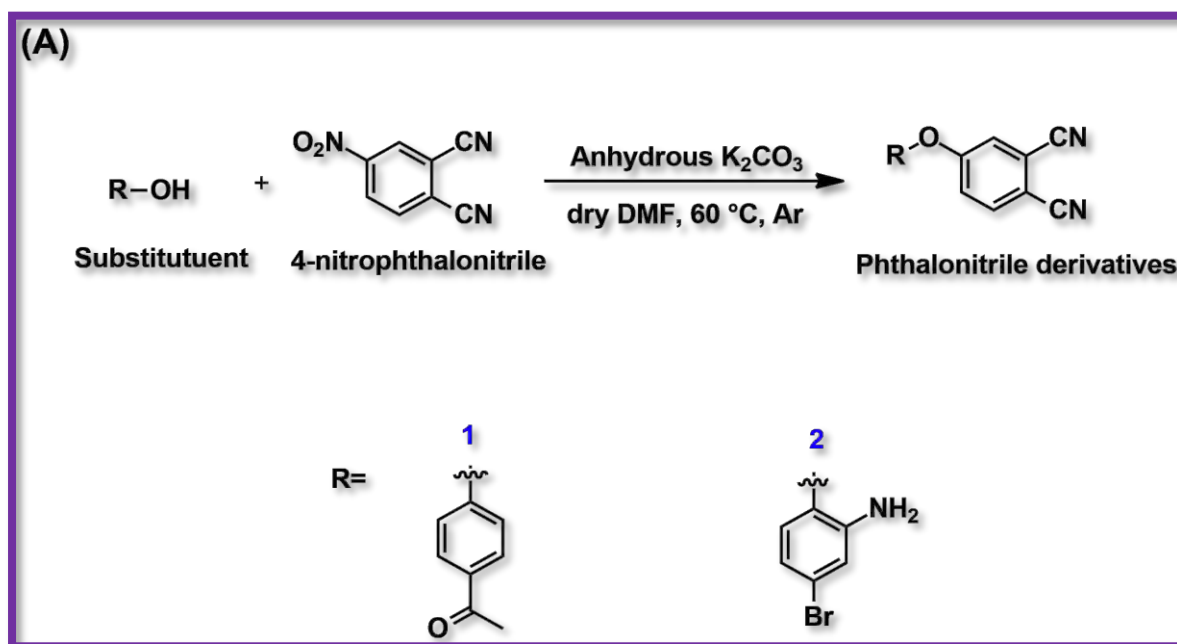
3.1. Phthalonitriles

3.1.1. Synthesis

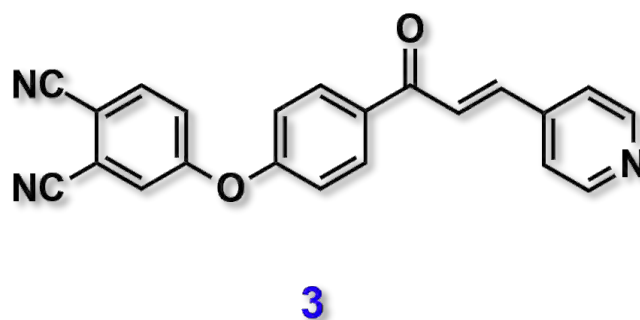
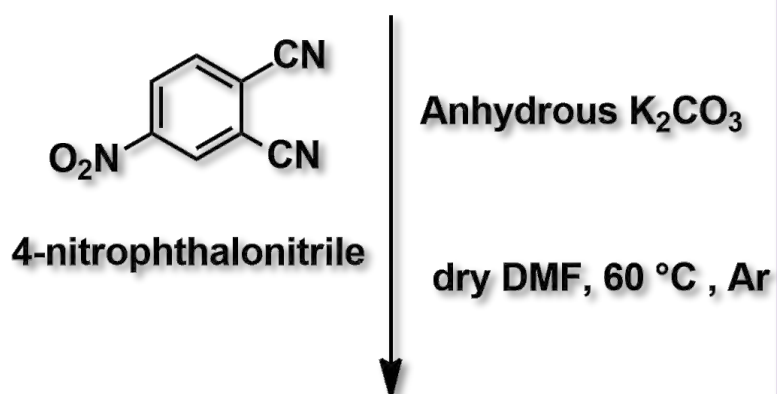
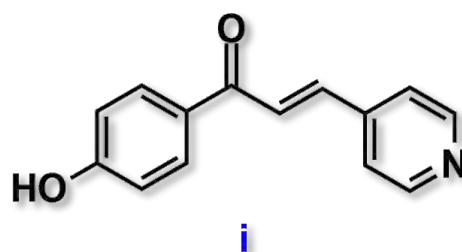
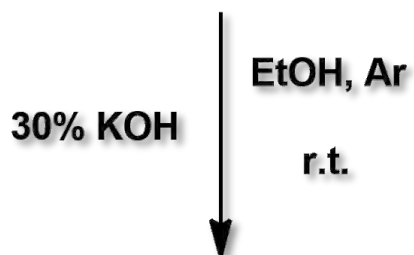
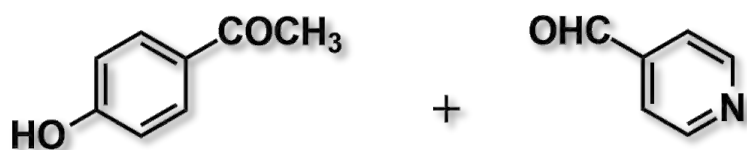
The monosubstituted phthalonitrile precursors (**1-6** named by the group number in **Table 1.2**) were prepared following a classical base-catalyzed nucleophilic substitution reaction between 4-nitrophthalonitrile and respective alcohols under an inert atmosphere using K_2CO_3 as the base in dry DMF heated at $60\text{ }^\circ\text{C}$ for $\sim 16\text{ h}$ [166]. The synthesis of 4-(3,5-dimethoxyphenoxy)phthalonitrile (**5**) [156] and 4-carboxyphenoxyphthalonitrile (**6**) [157] have been reported, hence their characterization will not be discussed here. An illustrative synthetic route of the novel compounds **1-4** is shown in **Schemes 3.1A, B, C**. The pure compounds were obtained with overall yield up to 80%.

At first, chalcones **i** and **ii** were synthesized quantitatively as precursors of phthalonitriles **3** and **4** following a Claisen-Schmidt condensation of 4-hydroxyacetophenone and 4-pyridinecarboxaldehyde (for **i**) or 4-(dimethylamino)benzaldehyde (for **ii**) using KOH as the base, **Schemes 3.1B, C**. The NMR data for chalcones **i** and **ii** are in **Figure A0 (Appendix 0)**

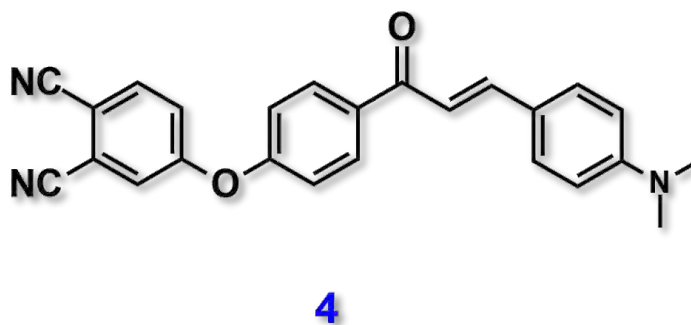
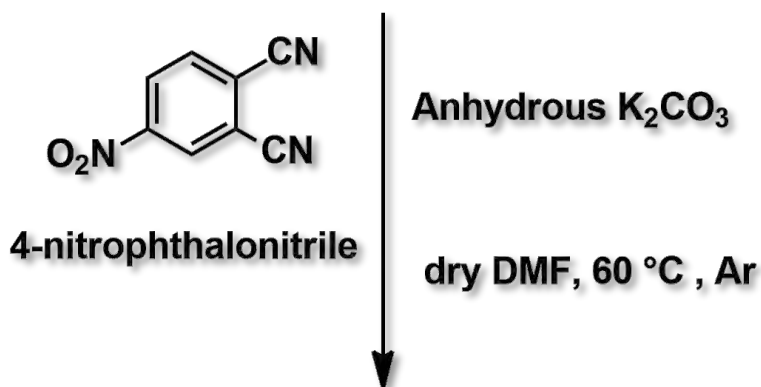
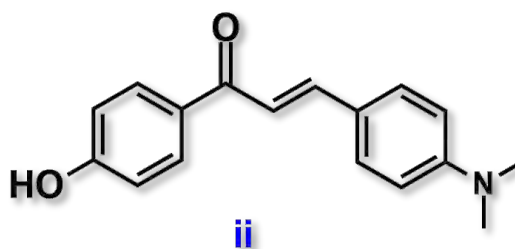
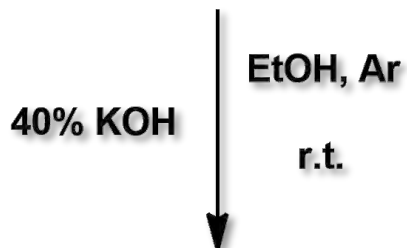
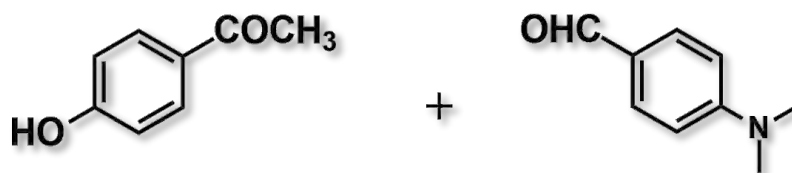
The ^1H NMR and ^{13}C NMR data used for structural elucidation are presented in **Figures 1-4 A1 (Appendix 1)** in the Appendices and are more detailed in **Chapter two**. FT-IR spectroscopy was also employed to confirm the presence of important functional groups and the results were all consistent with the proposed structures.



(B)



(C)



Scheme 3.1 Synthesis of phthalonitriles (A) **1** and **2**, (B) **3** and (C) **4**.

3.1.2. ^1H NMR and ^{13}C NMR Spectra

The ^1H NMR spectra show aromatic characteristic peaks resonating at δ_{H} 8.09-7.17 ppm plus another singlet peak at 2.65 ppm ($-\text{CH}_3$) for **1** and at δ_{H} 8.05-6.72 ppm with a broad singlet peak at 3.93 ppm ($-\text{NH}_2$) for **2**. Aromatic proton peaks resonating at δ_{H} 8.93-7.26 ppm for **3** and at δ_{H} 7.73-6.71 ppm for **4**, which include the *trans*-protons are observed as well.

The ^{13}C NMR further indicates a $\text{C}=\text{O}$ peak at δ_{C} 196.6 ppm for **1**, a peak at δ_{C} 186.7 ppm for **3**, and at δ_{C} 187.2 ppm for **4**. As well as an additional $\text{C}\equiv\text{N}$ peak ~ 115 ppm in all the compounds spectra.

3.1.3. FT-IR Spectroscopy

In **Figure 3.1**, one can notice the absence of characteristic $-\text{OH}$ stretches from the respective alcohols (in the 3500-3000 region), the appearances of new $-\text{C}\equiv\text{N}$ vibrational stretches (weak band $\sim 2230\text{ cm}^{-1}$), and strong $\text{C}-\text{O}-\text{C}$ stretch ($1310-1210\text{ cm}^{-1}$) in the spectra which can confirm the successful substitution. Extra characteristic stretching bands of $-\text{NH}_2$, aliphatic and aromatic $\text{C}-\text{H}$, $\text{C}=\text{O}$, and $\text{C}=\text{C}$ are also observed around ($3550-3300\text{ cm}^{-1}$), ($3100-2850\text{ cm}^{-1}$), ($1750-1650\text{ cm}^{-1}$), and ($\sim 1650\text{ cm}^{-1}$) respectively.

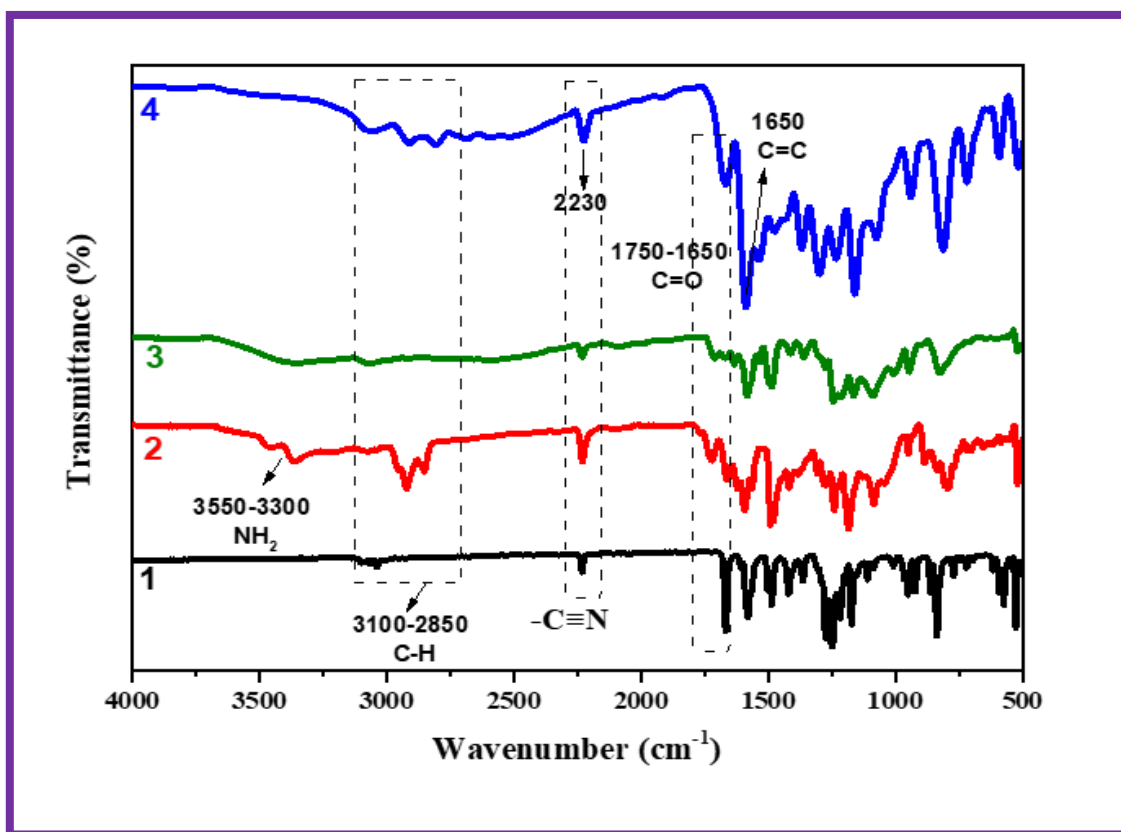


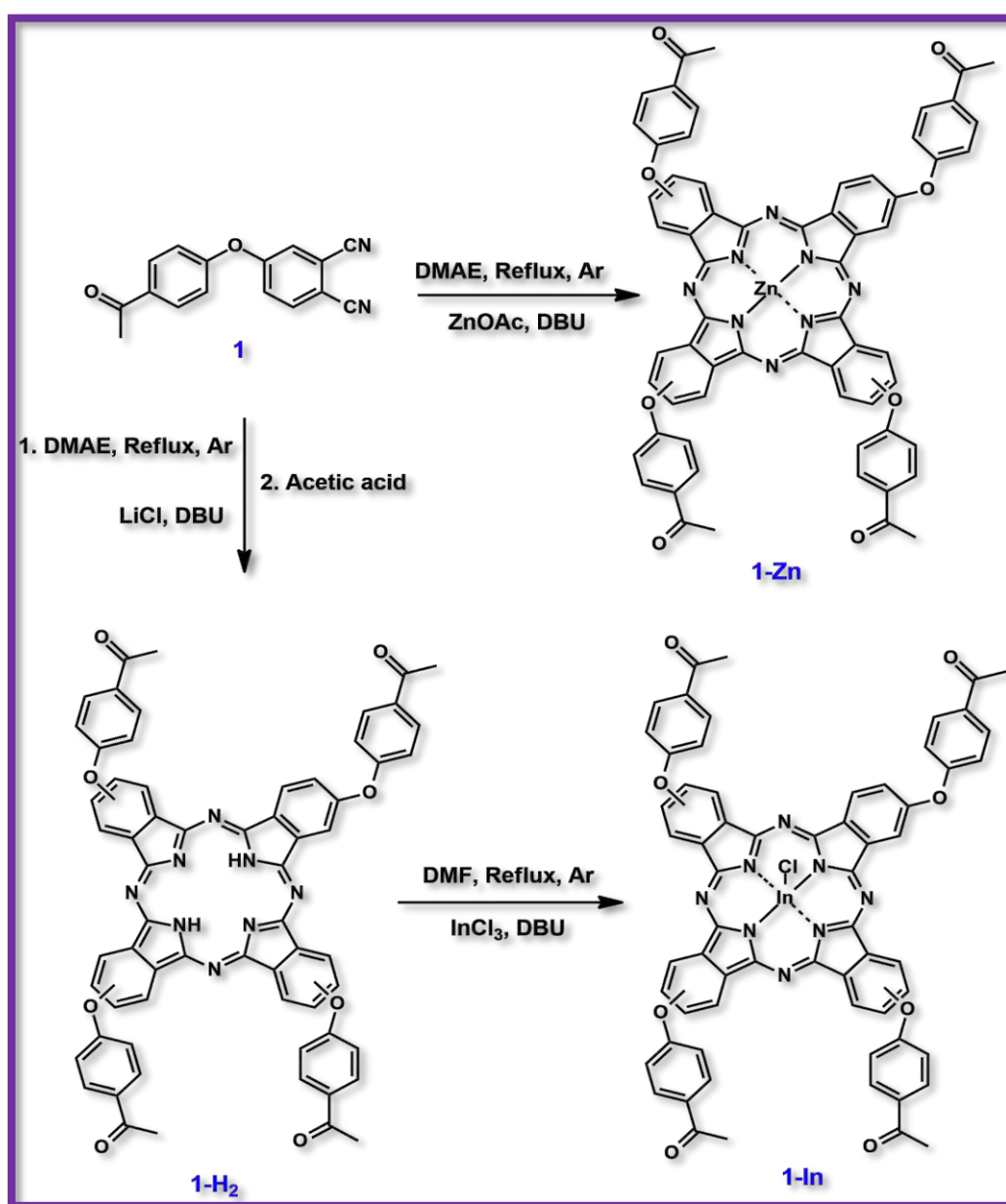
Figure 3.1 FT-IR Spectra of phthalonitrile derivatives **1-4**

3.2. Phthalocyanines

3.2.1. Symmetrical Pcs

3.2.1.1. Synthesis of Group 1: **1-H₂**, **1-Zn**, and **1-In**

Cyclotetramerization reaction of phthalonitrile **1** in DMAE with an excess of DBU as the catalyst at reflux temperature in the presence of anhydrous LiCl for **1-H₂** and ZnAOc salt for **1-Zn**, respectively, afforded the Pcs **Scheme 3.2**. Free-base **1-H₂** then underwent a metalation reaction with DBU and InCl₃ salt in dry DMF under reflux to give **1-In** (**Scheme 3.2**).

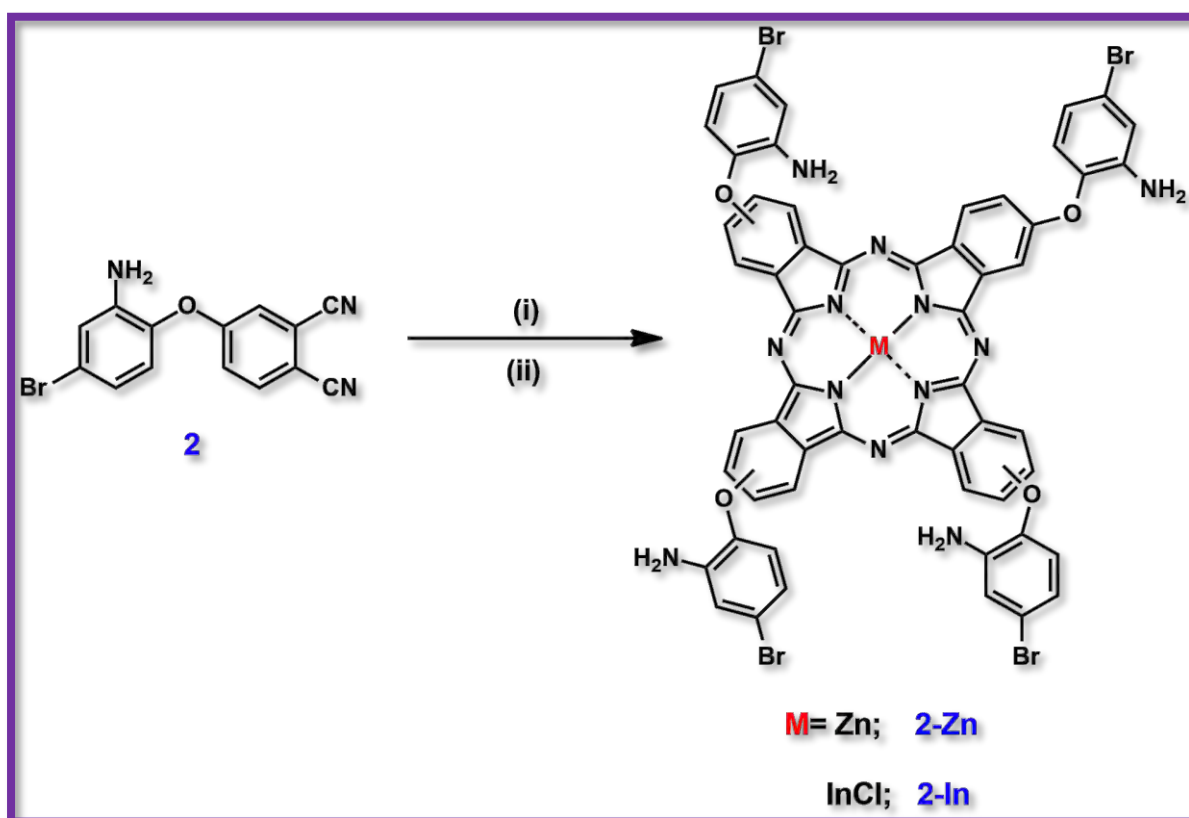


Scheme 3.2 Synthetic pathway of phthalocyanines **1-H₂**, **1-Zn**, and **1-In**.

The ^1H NMR spectra for **1-H₂**, **1-Zn**, and **1-In** (Figure 5 A1, Appendix 1 using **1-Zn** as an example,) exhibited aromatic proton peaks at 8.09-7.15 ppm, 8.51-7.42 ppm, and 8.52-7.47 ppm, respectively. Methyl protons were observed at 2.58, 2.85, and 2.85 ppm as singlets respectively, while **1-H₂** exhibited an additional peak in the aliphatic region which is assigned to the inner core N-H protons at 5.64 ppm. In MALDI-TOF MS spectra, the expected molecular ion peaks were obtained at m/z 1052.44 $[\text{M}+\text{H}]^+$ for **1-H₂**, m/z =1115.58 $[\text{M}+\text{H}]^+$ for **1-Zn** and m/z =1164.55 $[\text{M}-\text{Cl}+\text{H}]^+$ for **1-In**, (Figure 1 A2, Appendix 2).

3.2.1.2. Synthesis of Group 2: **2-Zn** and **2-In**

The synthetic route of **2-Zn** and **2-In** is shown in Scheme 3.3. The formation of complexes **2-Zn** and **2-In** was achieved by the cyclotetramerization reaction [210] of phthalonitrile **2** in the presence of dry DMAE and DBU using anhydrous Zn(OAc) for **2-Zn** and in dry quinoline and DBU using anhydrous indium chloride salt for **2-In** under an argon atmosphere. **2-Zn** and **2-In** have high solubility in common organic solvents such as DMF, DMSO, and THF.



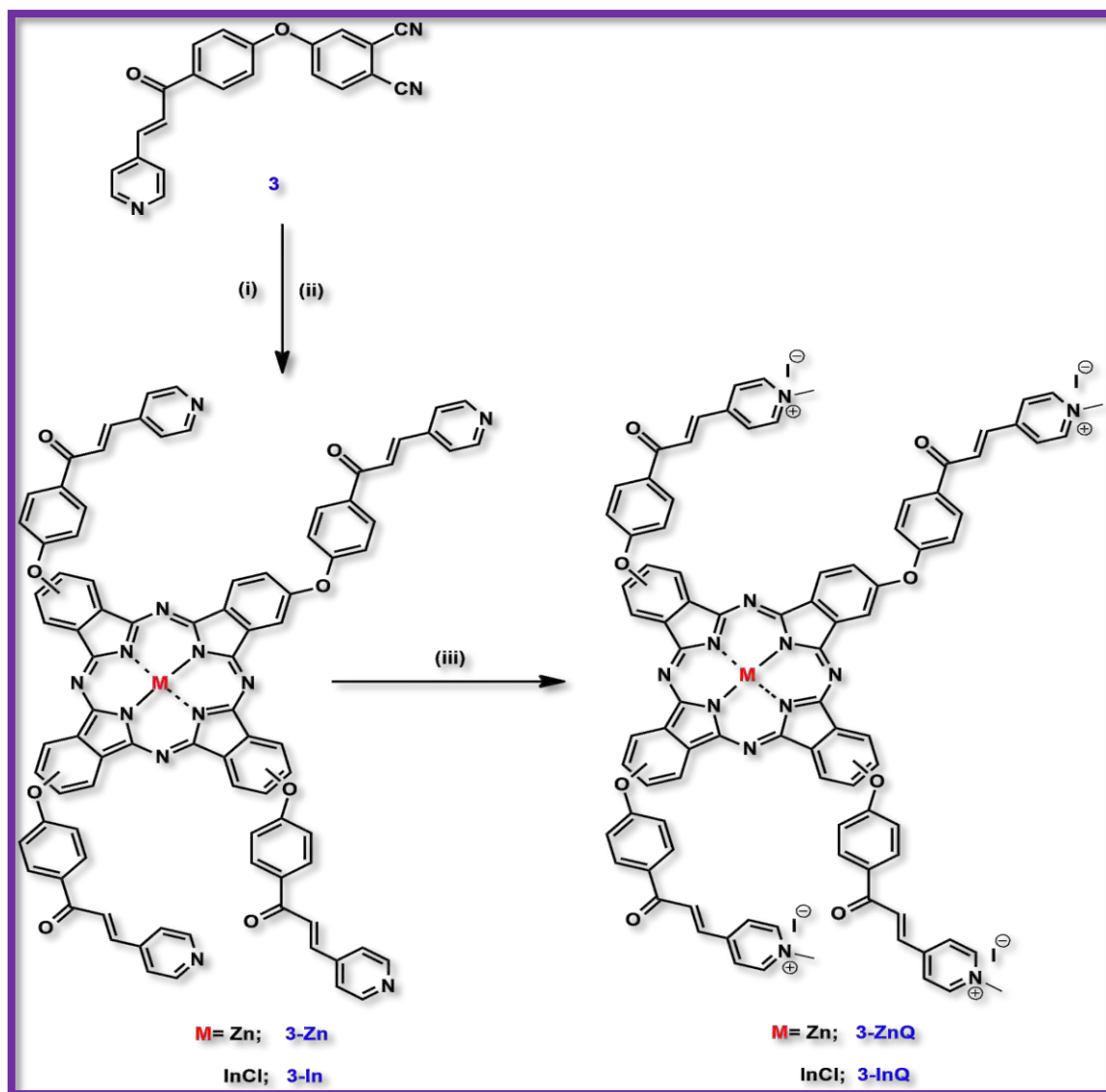
Scheme 3.3 The synthesis route of **2-Zn** and **2-In**. Reaction conditions: (i) dry DMAE, DBU and anhydrous zinc acetate at 160 °C, Ar; and (ii) dry quinoline, DBU and indium (III) chloride at 160 °C, Ar.

2-Zn and **2-In** were obtained as greenish powders, with protonated molecular ion peaks $[M+H]^+$ at $m/z=1322.53$ and $m/z= 1408.02$ in the mass spectra, respectively (**Figure 2 A2, Appendix 2**). 1H NMR of both complexes exhibited similarities as they each exhibited 24 aromatic proton peaks at 8.09-6.62 ppm and 8.11-6.63 ppm for **2-Zn** and **2-In** respectively, and 8 protons that correspond to NH_2 protons, (**Figure 6 A1, Appendix 1**). These results were in good agreement with the suggested structures. The choice of this substituent is due to the electron-donating property of the amine group which increases the electron density and stabilizes the Pcs ring as well as the heavy atom effect of bromine which can enhance the intersystem crossing (ISC) of the Pcs.

3.2.1.3. Synthesis of Group 3: **3-Zn**, **3-In**, **3-ZnQ**, and **3-InQ**

The Pc complexes were synthesized following a similar procedure mentioned above whereby Pcs **3-Zn** and **3-In** were prepared by cyclotetramerization reaction [211] of compound **3**, in DMAE (for **3-Zn**) or quinoline (for **3-In**) with few drops of DBU in the presence of anhydrous zinc acetate and indium chloride salts, respectively under argon atmosphere. **3-Zn** and **3-In** were used as precursors of the synthesis of the cationic Pcs **3-ZnQ** and **3-InQ**. Under an argon atmosphere, **3-Zn** and **3-In** were respectively reacted with excess CH_3I in DMF and acetone under refluxing conditions to obtain positively charged and water-soluble Pcs (**Scheme 3.4**).

The 1H NMR spectra exhibited aromatic proton peaks ranging from 8.97-7.28 ppm (**Figure 7 A1, Appendix 1** as examples). The methyl protons were observed as singlets at around 2.90 ppm for the quaternized derivatives. In the acquired mass spectra of the Pcs, the expected molecular ion peaks were obtained at $m/z= 1471.88 [M+H]^+$ for **3-Zn** and $m/z= 1555.26 [M]^+$ for **3-In**. These results were in good agreement with the suggested structures (**Figure 3 A2, Appendix 2**).

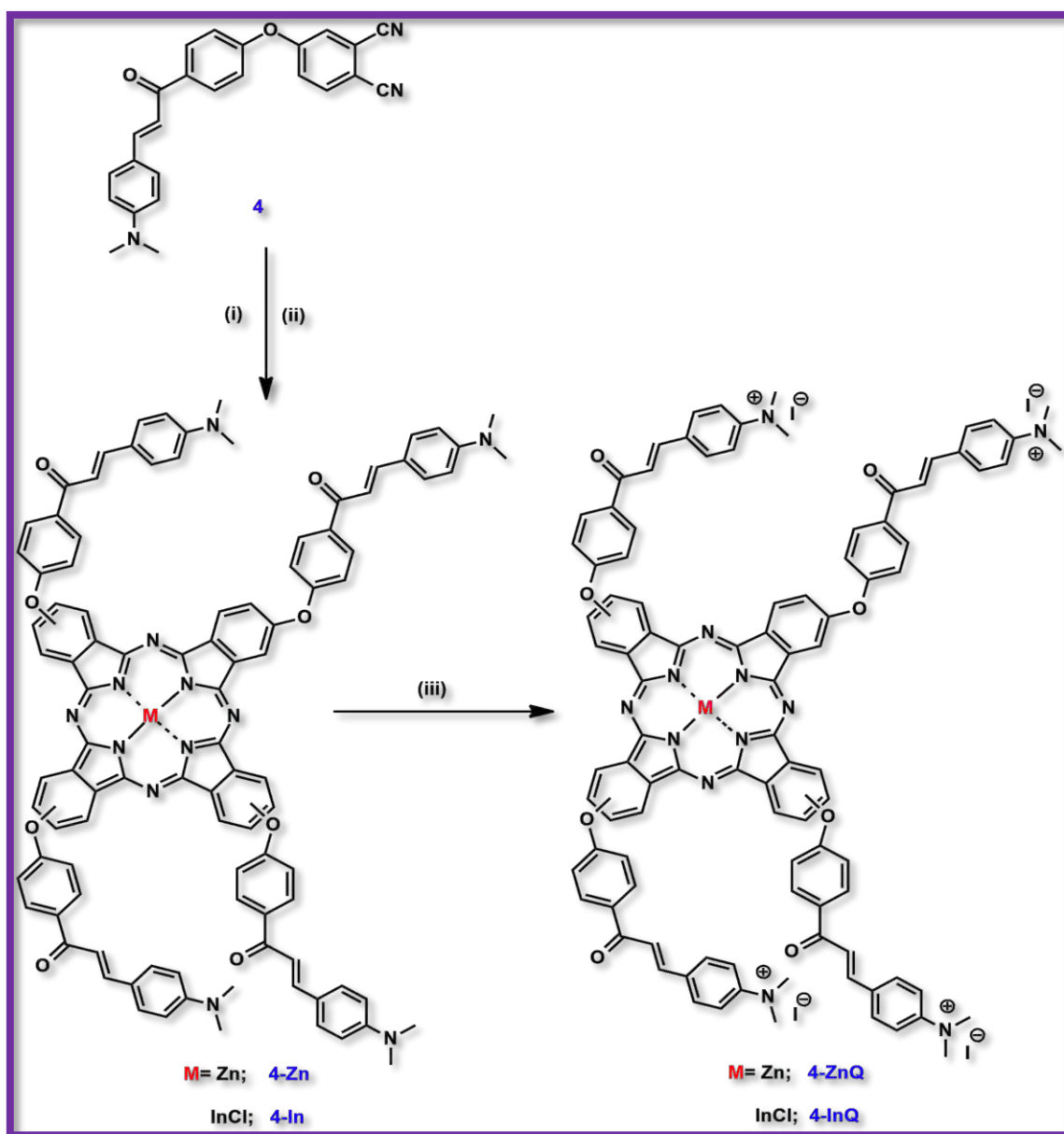


Scheme 3.4 The synthesis route of **3-Zn**, **3-In**, **3-ZnQ**, and **3-InQ**. Reaction conditions: (i) dry DMAE, DBU and anhydrous zinc acetate at 160 °C, Ar; (ii) dry quinoline, DBU and indium (III) chloride at 160 °C, Ar. (iii): dry DMF, acetone and excess CH₃I at reflux.

3.2.1.4. Synthesis of Group 4: **4-Zn**, **4-In**, **4-ZnQ** and **4-InQ**

Large substituents on peripheral or non-peripheral positions of Pcs and the presence of heavy central metals in their core can result in reduced aggregation and improved solubility [212,213]. Through cyclotetramerization reaction of the phthalonitrile **4** using zinc acetate dihydrate and indium chloride salts (and DBU as the catalyst at high temperature), phthalocyanines **4-Zn** and **4-In** respectively were obtained, **Scheme 3.5**. Then their quaternized analogs **4-ZnQ** and **4-InQ** were prepared following *N*-methylation reaction of both **4-Zn** and **4-In** Pcs using iodomethane as a methylating agent in DMF at reflux temperature.

^1H NMR spectra of the Pcs exhibit peaks with slight chemical shift differences as seen in **Figure 8 A1, Appendix 1** as examples. In these spectra, integrals of the aromatic region together with the aliphatic area (3.09-8.31 ppm, 76 protons in total) for complexes **4-Zn** and **4-In** (**Figure 8 A1 (a), Appendix 1** using complex **4-Zn** as an example) compared to the (3.03-8.25 ppm, 88 protons in total) for complexes **4-ZnQ** and **4-InQ** (**Figure 8 A1 (b), Appendix 1** using **4-InQ** as an example) were consistent with the proposed structures.



Scheme 3.5 The synthesis route of **4-Zn**, **4-In**, **4-ZnQ**, and **4-InQ**. Reaction conditions: (i) dry DMAE, DBU and anhydrous zinc acetate at 160 °C, Ar; (ii) dry quinoline, DBU and indium (III) chloride at 160 °C, Ar. (iii): dry DMF, acetone and excess CH_3I at reflux.

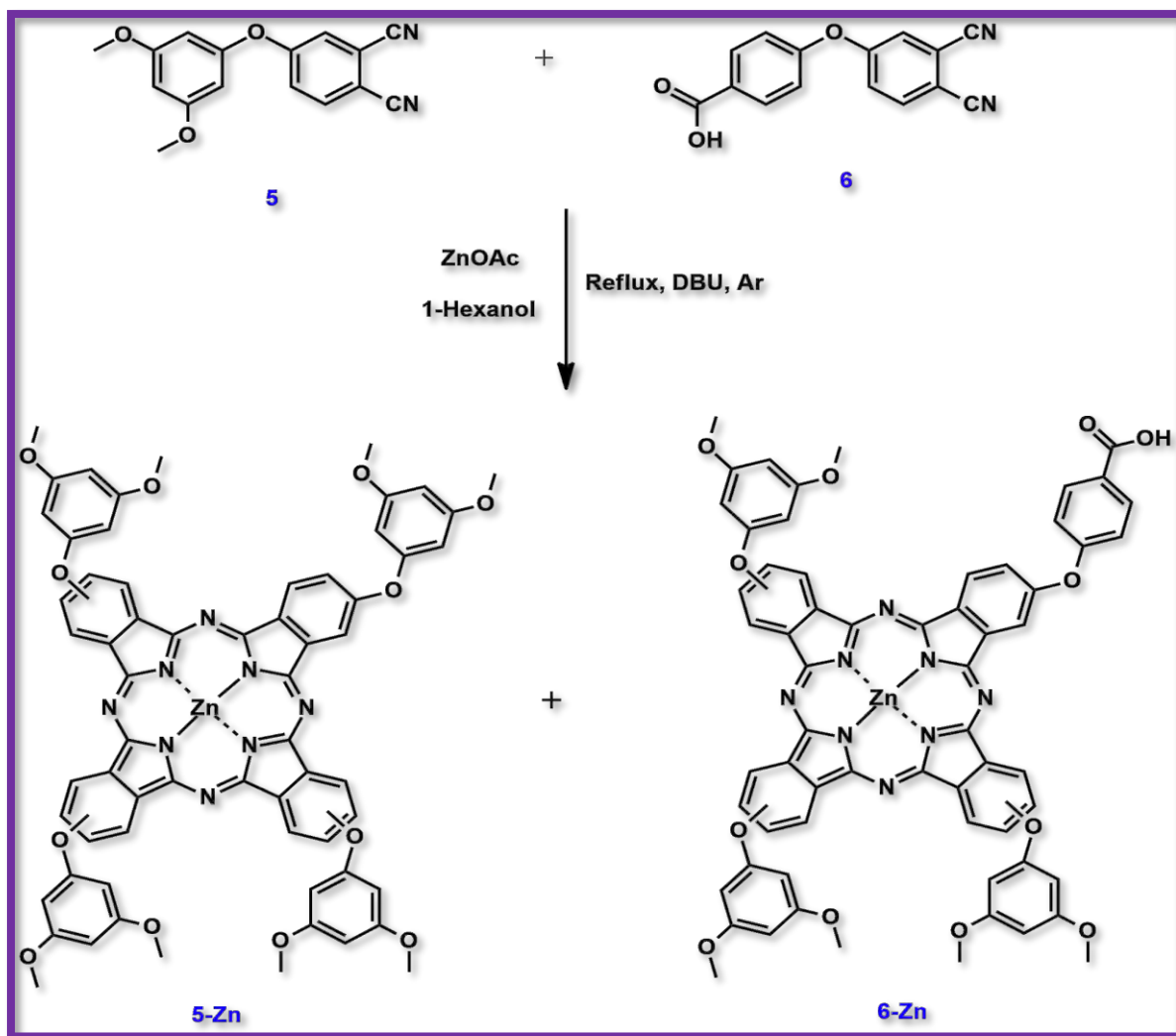
In addition, mass spectrometry was also used for the structure elucidation of the synthesized Pcs. The acquired spectra show that the desired compounds were obtained as expected whereas the molecular ion peaks were identified at $[M+H]^+ = 1640.08$ m/z for complex **4-Zn** and $[M+H]^+ = 1725.21$ m/z for complex **4-In**, **Figure 4 A2, Appendix 2**. The quaternized complexes **4-ZnQ** and **4-InQ** did not ionize with α -cyano hydroxycinnamic acid matrix, hence no data were obtained. Experimental elemental analysis (CHN) agrees with theoretical values.

3.2.2. *Synthesis of Symmetrical and Asymmetrical A₃B-type Pcs of Groups 5 and 6: 5-Zn and 6-Zn*

Please note that the neutral symmetrical **5-Zn** and asymmetrical **6-Zn** Pcs were prepared by mixed cyclotetramerization reaction of known phthalonitriles **5** and **6** (using 3:1 equivalents) in the presence of ZnAOc and DBU as the organic base in refluxing 1-hexanol under an argon atmosphere (**Schemes 3.6**). Their reaction mixture was afterward separated by column chromatography on silica gel using gradient elution with THF (0-5% of methanol) to collect **5-Zn** at first and then **6-Zn**.

The ^1H NMR spectra of Pcs **5-Zn** and **6-Zn** presented similar patterns within close chemical shifts whereas the aromatic protons slightly shifted downfield in the range of 8.30-6.30 ppm and the methoxy protons at 3.68 and 3.72 ppm for **5-Zn** and **6-Zn** respectively. In addition, a broad singlet peak is observed at 11.30 ppm (**Figure 9 A1, Appendix 1**) in the spectrum of **6-Zn**. This can be assigned to the proton of the carboxylic acid group (-COOH) as it presents H-bonding characteristics. All the NMR data agreed with the proposed structures as all the substituents and ring protons appeared in their respective regions.

The mass spectra of novel complexes were obtained and their molecular ion peaks were found to be $m/z = 1187.37$ as $[M+H]^+$ for **5-Zn** and $m/z = 1171.33$ as $[M+H]^+$ for **6-Zn** and these observations correlated with the proposed structures (**Figure 5 A2, Appendix 2**). The elemental analysis data also confirmed the presence of C, H, and N elements in the synthesized compounds.



Schemes 3.6 The synthesis route of **5-Zn** and **6-Zn**.

3.2.3. FT-IR Spectra of the Studied Pcs

FT-IR spectroscopy was used to determine the presence of different functional groups on the synthesized Pcs. The spectra confirm the formation of Pcs by indicating the absence of the $\text{-C}\equiv\text{N}$ vibration stretches around 2230 cm^{-1} due to successful cyclotetramerization of the phthalonitrile derivatives.

The inner core N-H hydrogens of the free-base Pc **1-H₂** are observed around 3372 cm^{-1} . Peaks emerging at 2918 cm^{-1} to 2853 cm^{-1} for complexes **1-Zn** and **1-In**, and 2920 to 2853 cm^{-1} for **1-H₂**, are attributed to stretching vibrations of aromatic and aliphatic C-H bonds. In all cases, peaks at 1667 - 1586 cm^{-1} are due to C=C and C=N vibrations. While the C=O vibrations are observed at 1714 cm^{-1} for **1-H₂** and 1715 cm^{-1} for **1-Zn** and **1-In** (Figures 3.2A).

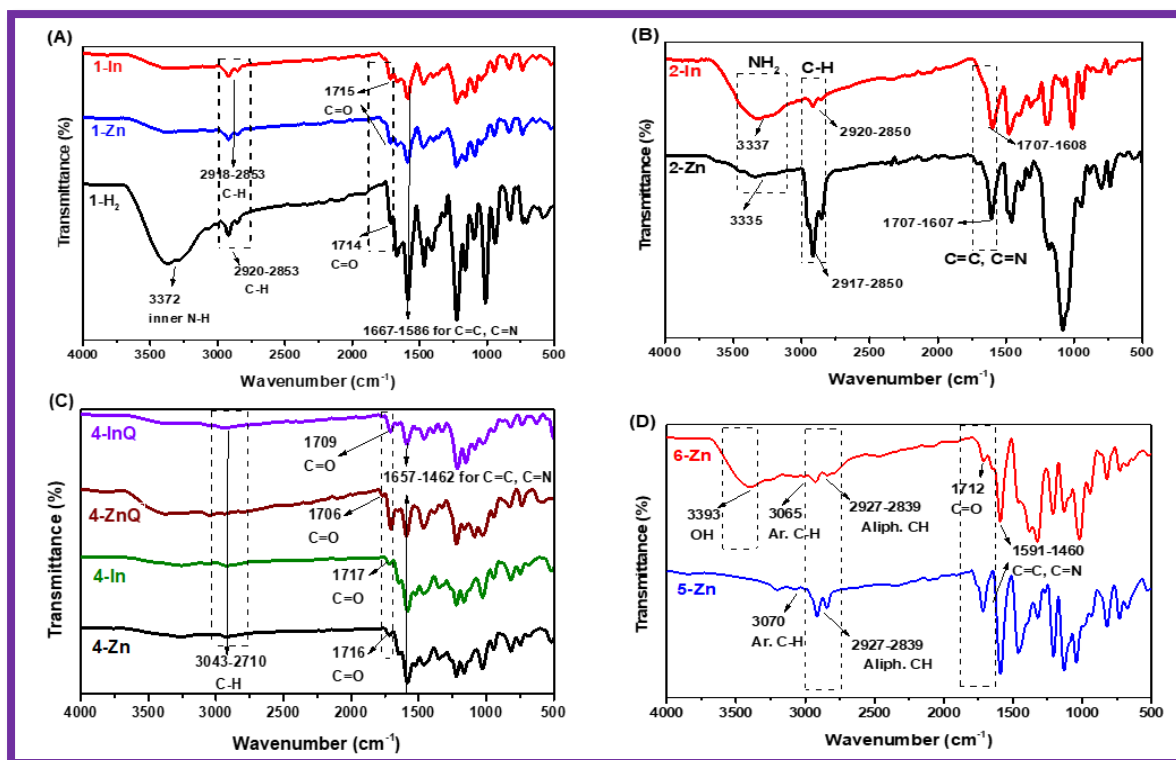


Figure 3.2 FT-IR spectra of (A) **1-H₂**, **1-Zn**, and **1-In**; (B) **2-Zn** and **2-In**; (C) **4-Zn**, **4-In**, **4-ZnQ**, and **4-InQ**; (D) **5-Zn** and **6-Zn** Pcs (used as examples).

As shown in **Figure 3.2B**, characteristic vibration peaks for the primary amine group -NH₂ can be observed at 3335 cm⁻¹ (for **2-Zn**) and 3337 cm⁻¹ (for **2-In**). The peaks appearing at 2917-2853 cm⁻¹ for **2-Zn** and 2920-2850 cm⁻¹ for **2-In** are also attributed to the stretching vibrations of aromatic and aliphatic C-H bonds. The peaks at 1707-1607 cm⁻¹ for **2-Zn** and 1708-1608 cm⁻¹ for **2-In** are related to the C=C and C=N vibrations, respectively.

Figure 3.2C clearly shows stretches in the 3043-2710 cm⁻¹ regions which are attributed to the aromatic and aliphatic C-H bonds and those around 1657-1462 cm⁻¹ are due to C=C and C=N vibrations. The stretching vibrations due to the C=O bond in complexes **4-Zn** and **4-In** can be attributed to the bands observed at about 1716 and 1717 cm⁻¹, respectively, and 1706 and 1709 cm⁻¹ (for **4-ZnQ** and **4-InQ**, respectively). Additionally, the FT-IR spectra of the quaternized derivatives **4-ZnQ** and **4-InQ** also show very similar peaks to their non-quaternized counterparts. Similar trends are observed for **3-Zn**, **3-In**, **3-ZnQ**, and **3-InQ**.

The vibrational stretches for carboxylic OH were observed around 3393 cm⁻¹, aromatic CH bonds around 3065 cm⁻¹, aliphatic -CH at 2927-2839 cm⁻¹, -C=O at 1712 cm⁻¹, -C=C and -C=N groups between 1591-1460 cm⁻¹ and the -O-CH₃ group at 1323 cm⁻¹ in the case of Pc **6-Zn**.

In the spectrum for **5-Zn**, the vibrational peaks for aromatic-CH were obtained at 3070 cm⁻¹ and for aliphatic -CH groups were between 2914-2844 cm⁻¹, -C=C and -C=N groups between 1591-1470 and the -O-CH₃ group at 1320 cm⁻¹, (**Figure 3.2D**).

3.2.4. Electronic Absorption and Emission Spectra of the studied Pcs

The electronic absorption spectra of all the newly studied phthalocyanines are recorded in DMSO and shown in **Figures 3.3** and **3.4**. The data are summarized in **Table 3.1**. The UV-Vis spectra of the metallated complexes are remarkably similar and typical for non-aggregated Pcs. It is probable that DMSO, being a coordinating solvent, binds axially to the zinc Pcs and the presence of chlorine as axial ligand on the indium Pcs reduce their aggregation tendency. Aggregation in metallated Pcs is judged by a broad and split Q band due to π - π stacking of the macrocycles [214].

Table 3.1 Spectral data of all synthesized Pcs (**Groups 1-6**) in DMSO unless otherwise stated.

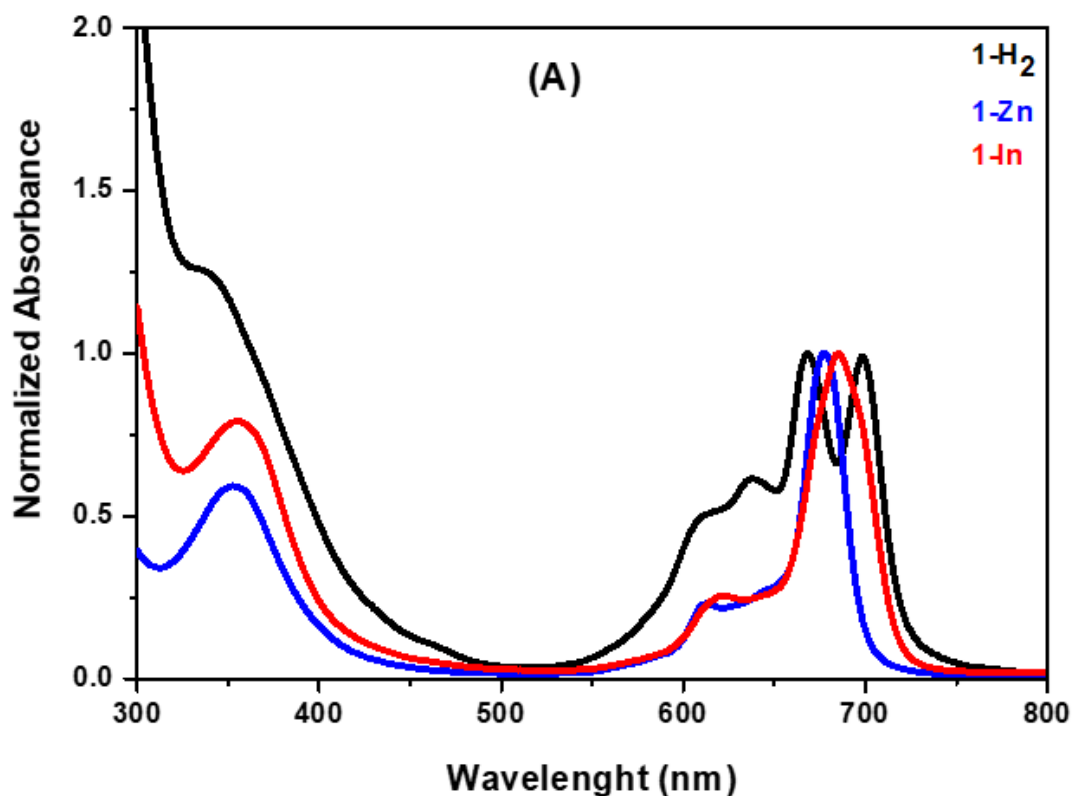
Complex	Q-band λ_{Abs} (nm)	Excitation λ_{Exc} (nm)	Emission λ_{Em} (nm)
Group 1: Acetophenoxy-substituted Pcs			
1-H₂	668, 698	671, 698	706
1-Zn	675	675	687
1-In	685	681	688
Group 2: Bromo-aminophenoxy-substituted Pcs			
2-Zn	679	682	689
2-In	687	685	692
Group 3: Pyridyl chalcone-substituted Pcs			
3-Zn	684	683	695
3-In	686	689	693
3-ZnQ	683 (688)	684	693
3-InQ	684 (691)	686	689
Group 4: Dimethylamino chalcone-substituted Pcs			
4-Zn	680	682	689
4-In	686	686	691
4-ZnQ	684 (691)	682	689
4-InQ	689 (695)	686	691
Groups 5-6: Tetra and monocarboxylic acid-substituted Pcs			
5-Zn	679	681	689
6-Zn	682	680	688

^a: values in brackets are obtained in 1% DMSO/water. Abs: absorption, Exc: excitation, Em: emission.

The spectra show characteristic broad B-band peaking at 350-360 nm, an intense and narrow monomeric Q-band at 670-690 nm, together with a vibronic band at 605-615 nm [120,214]. The Q-bands comply with the Lambert-Beer's law that suggests that aggregation of these metallated complexes is not significant (data not shown).

Generally, the Q-band (the most important band for excitation in PACT/PDT) is attributed to the $\pi \rightarrow \pi^*$ transition from the highest occupied molecular orbital (HOMO) to the lowest unoccupied molecular orbital (LUMO) of the Pc macrocycle whereas the B-band results from deeper π levels to the LUMO transitions [215].

Due to D_{4h} symmetry of metallated Pcs, **1-Zn** and **1-In** show narrow monomeric Q bands at 675 and 685 nm, respectively, while **1-H₂** shows a split of the Q band (668 and 698 nm) due to D_{2h} symmetry [211], **Table 3.1**. **1-H₂** shows some aggregation as judged by the enhancement absorption in the 630 nm region [214], **Figure 3.3A**. The Q bands are at 679 nm for **2-Zn** and 687 nm for **2-In**, respectively (**Figure 3.3B** and **Table 3.1**). While the maximum absorption Q-bands are observed at 679 nm for **5-Zn** and 682 nm for **6-Zn** in DMSO, **Table 3.1**.



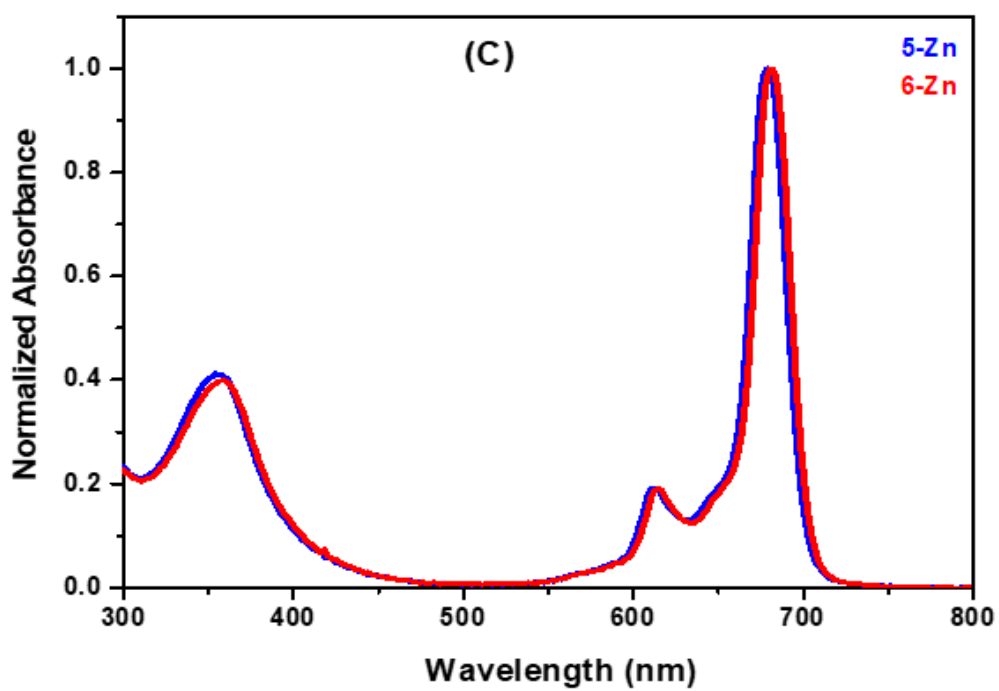
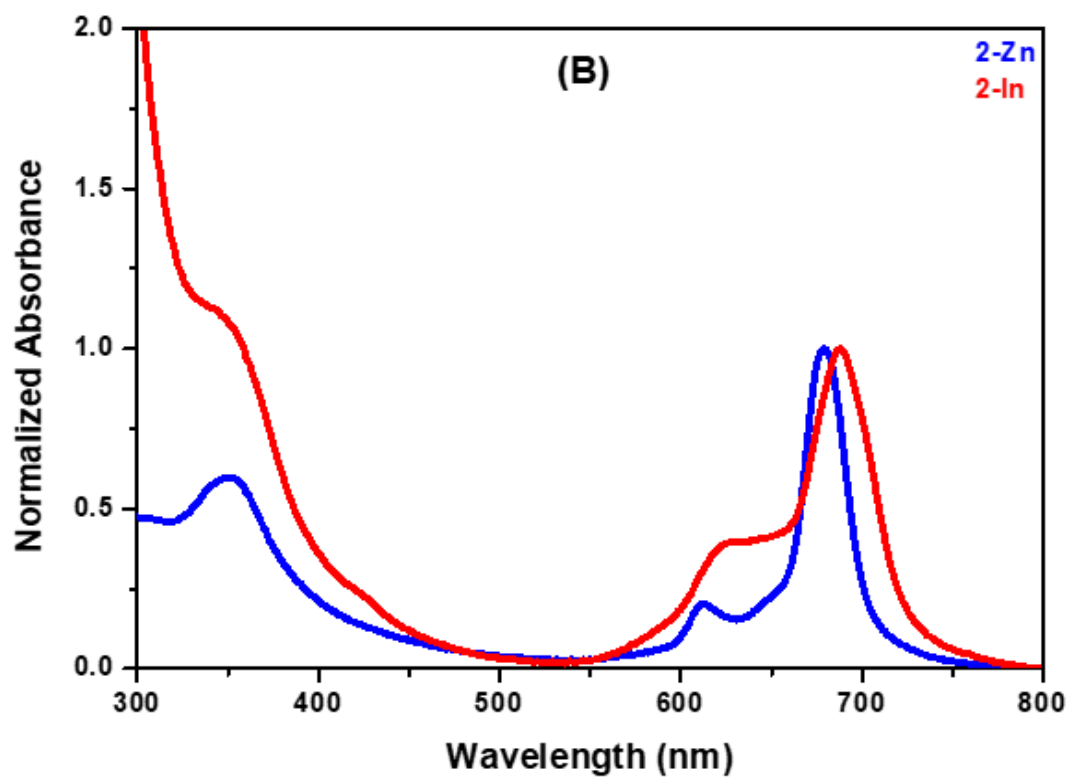
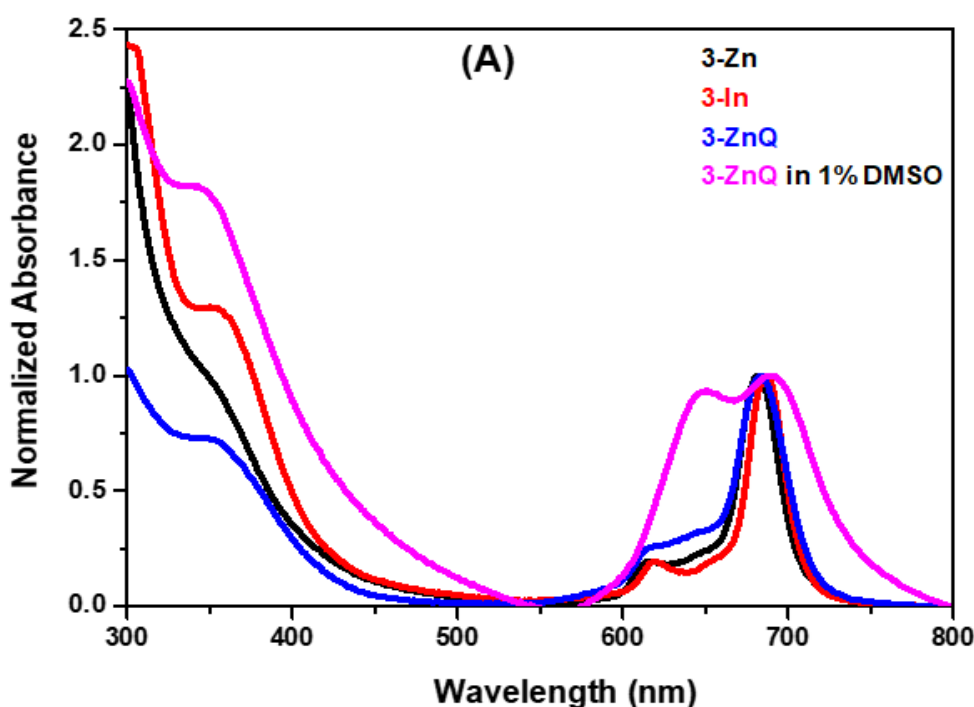


Figure. 3.3 Normalized UV-Vis spectra of (A) **1-H₂**, **1-Zn**, and **1-In**, (B) **2-Zn** and **2-In**, (C) **5-Zn** and **6-Zn** in DMSO.

As shown in **Figure 3.3C** and **Table 3.1**, the absorption maximum of **6-Zn** is slightly red shifted compared of **5-Zn**, which is consistent with literature that states that the asymmetry in the chemical structure of asymmetrical Pcs leads to unique properties differing them from the symmetrical ones. The electron-donating ability of the carboxyl group is greater than that of a methoxy group thus leading to absorption of a longer wavelength for the asymmetrical Pc **6-Zn** [216].

The spectra show intense Q-bands absorption around 684 nm (for **3-Zn**), 686 nm (for **3-In**), 683 nm (for **3-ZnQ**) and 684 nm (for **3-InQ**) (**Figures 3.4A** and **Table 3.1**). The data in DMSO imply that there are blue-shifts in the Q band maxima after quaternization. This may be due to the lowering of the electron donating ability of the nitrogen groups upon quaternization. Similar observation has been reported in the literature [217]. Complexes in **group 1** are more blue shifted compared to the rest of the complexes in **Table 3.1** due to the presence of nitrogen groups in the latter [217].

In water, aggregation is observed in the spectra of the quaternized derivatives as they exhibit two non-vibrational peaks in the Q band region [218]. Aggregation (the so-called H aggregates) in Pcs is judged by a broad or split Q band with the high energy band being due to the aggregate and the low energy band to the monomer.



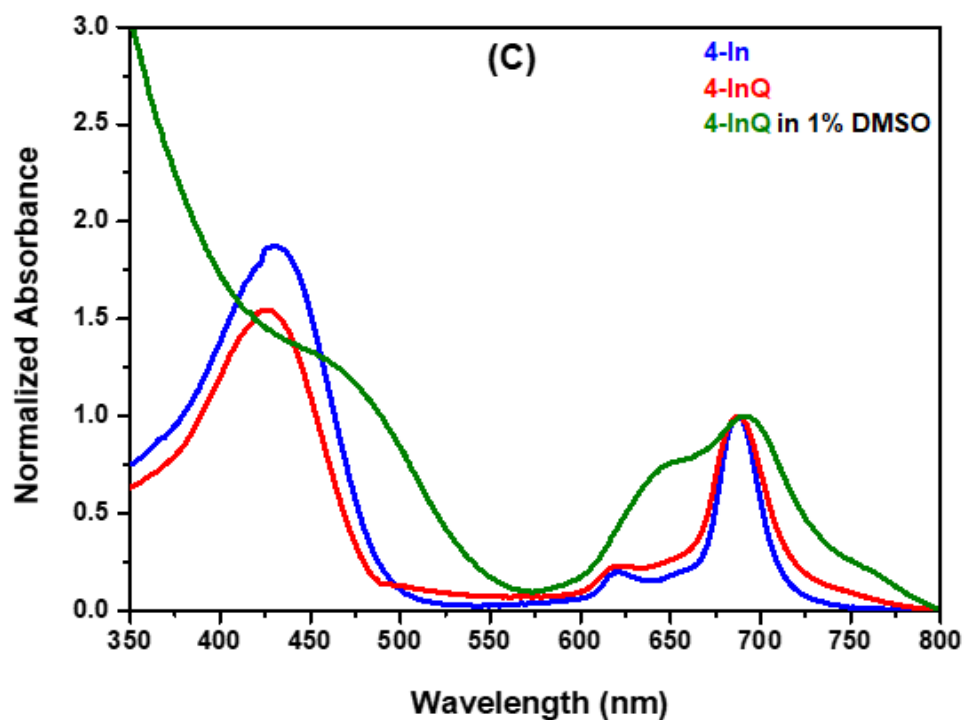
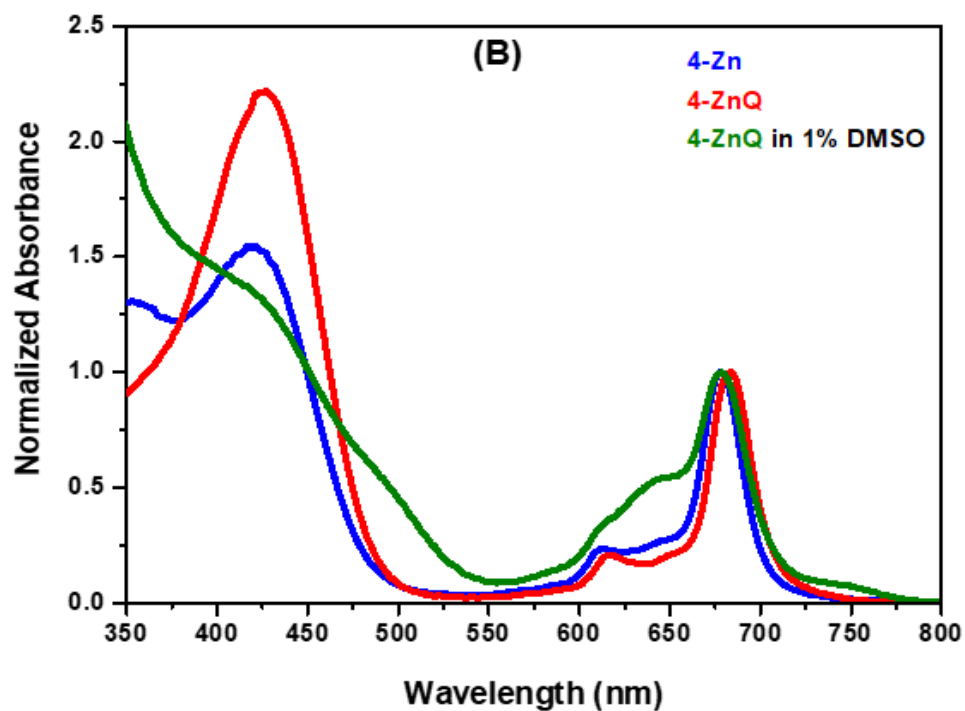


Figure. 3.4 Normalized UV-Vis spectra of (A) (A) **3-Zn**, **4-In**, **3-ZnQ** in DMSO and **3-ZnQ** in 1% DMSO, (B) **4-Zn**, **4-ZnQ** in DMSO and **4-ZnQ** in water (1% DMSO), and (C) **4-In**, **4-InQ** in DMSO and **4-InQ** in water (1% DMSO) for exemplification.

In general, spectral red-shifts are observed for all the In (III) Pcs as compared to their Zn (II) counterparts due to the non-planar effect of the indium (III) ion, with a relatively bigger atomic radius than the zinc (II) as the central metal ion in the Pc cavity [219] as presented in **Table 3.1**.

Fluorescence behaviors of the Pcs were studied in DMSO at room temperature. The fluorescence spectra were recorded by exciting the samples at a wavelength around where the Pcs absorb (λ_{exc} 606-613 nm by the V-band). The absorbance of the complexes at λ_{exc} was kept at 0.05 absorbance and the Stokes shifts were similarly small.

The spectra are shown in **Figures 3.5A,B** and **Figures 1 A3 (Appendix 3)** as an examples. In all cases, the emission spectra were mirror images of the excitation spectra of studied complexes and the latter were the same as the absorption spectra showing that the molecules that are emitting light are the same as those that are absorbing light (slight differences in peak maxima are due to different equipment used). The measurements of the emission wavelengths are reported in **Tables 3.1**.

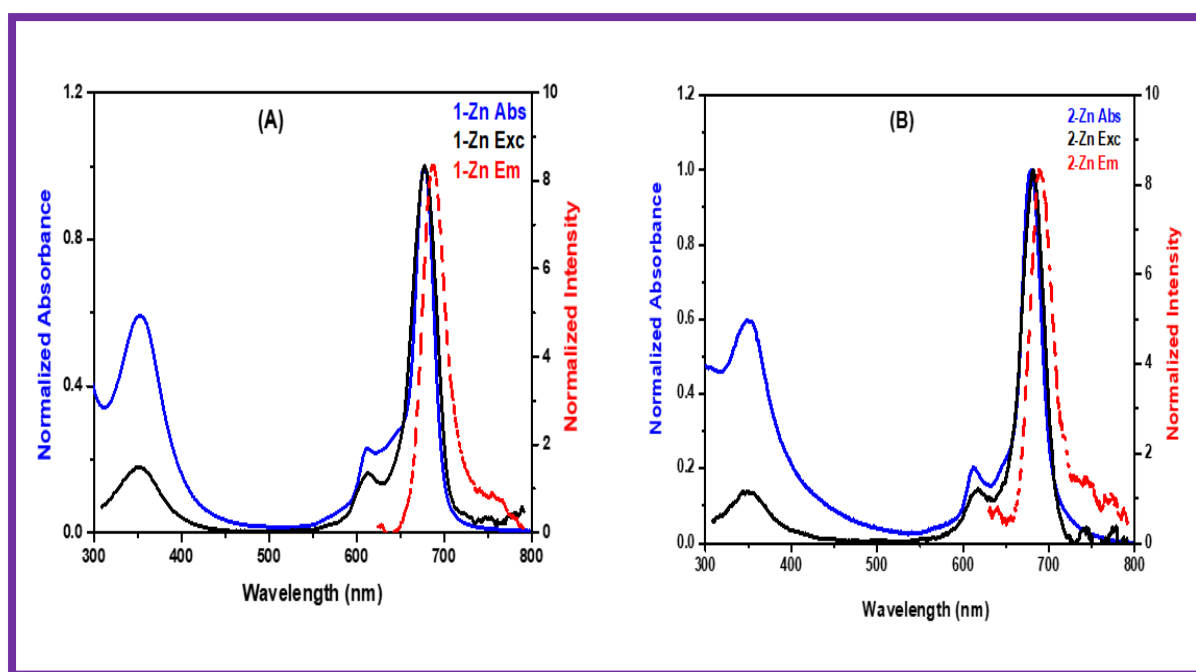


Figure 3.5 Examples of normalized absorption, excitation, and emission spectra of (A) **1-Zn** in DMSO, λ_{exc} 613 nm (B) **2-Zn** in DMSO, λ_{exc} 611 nm.

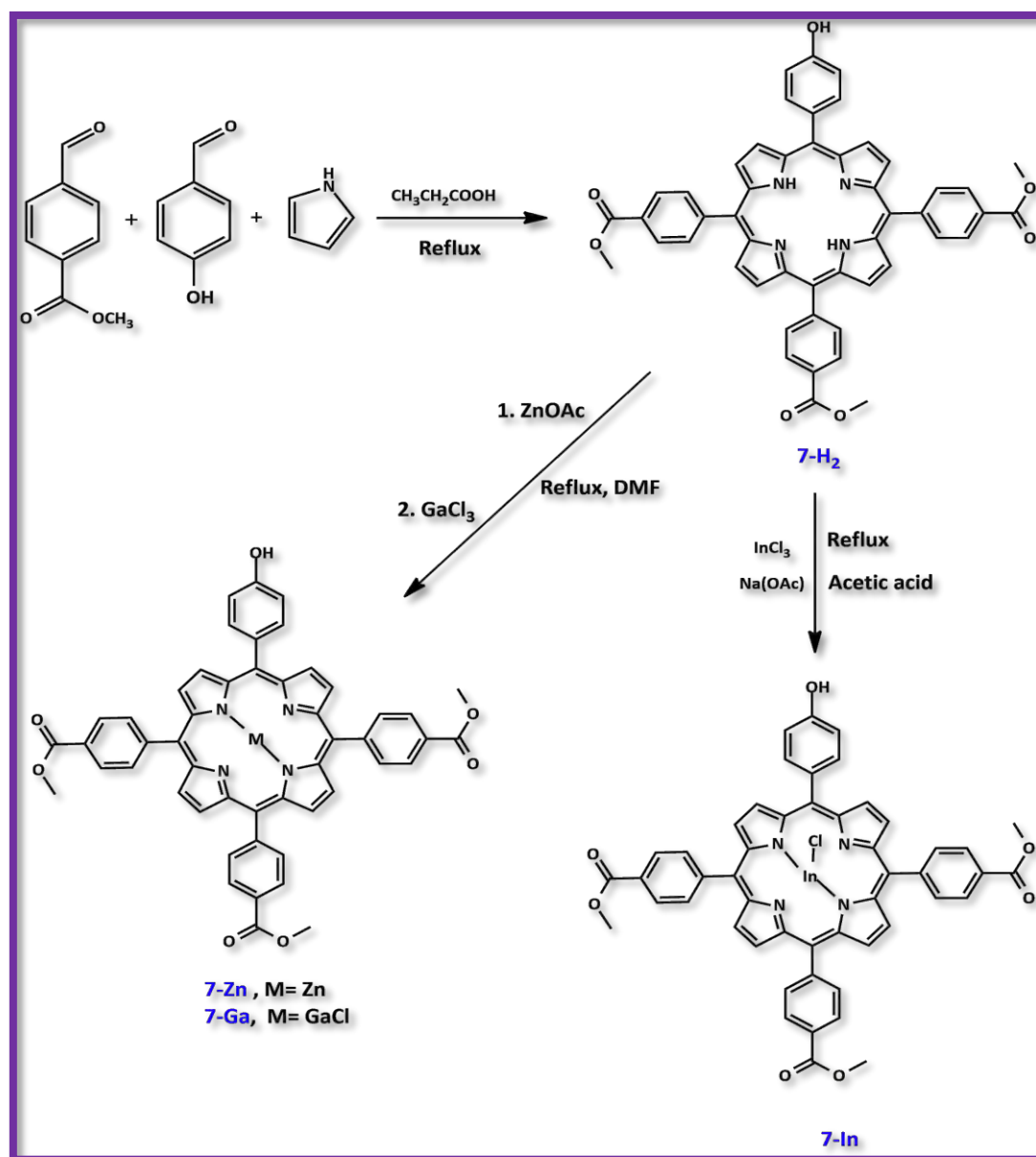
It is important to note that free-base Pcs are known to emit with only one main peak in non-aqueous media which has been assigned as the 0-0 transition [220] hence one emission peak is observed for **1-H₂**.

3.3. Porphyrins

3.3.1. Symmetrical and Asymmetrical Porphyrins

3.3.1.1. Synthesis of Group 7: 7- H_2 , 7-Zn, 7-In, and 7-Ga

The asymmetrical derivatives porphyrins **7-Zn**, **7-In**, and **7-Ga** were synthesized by introducing Zn, GaCl, and InCl into the core of the free-base porphyrin **7- H_2** (Scheme 3.7), respectively. The compounds were characterized by ^1H NMR, MALDI-TOF MS, CHNS elemental analysis, UV-Vis, and FT-IR.



Scheme 3.7 The synthesis of asymmetrical porphyrins **7- H_2** , **7-Zn**, **7-In**, and **7-Ga**.

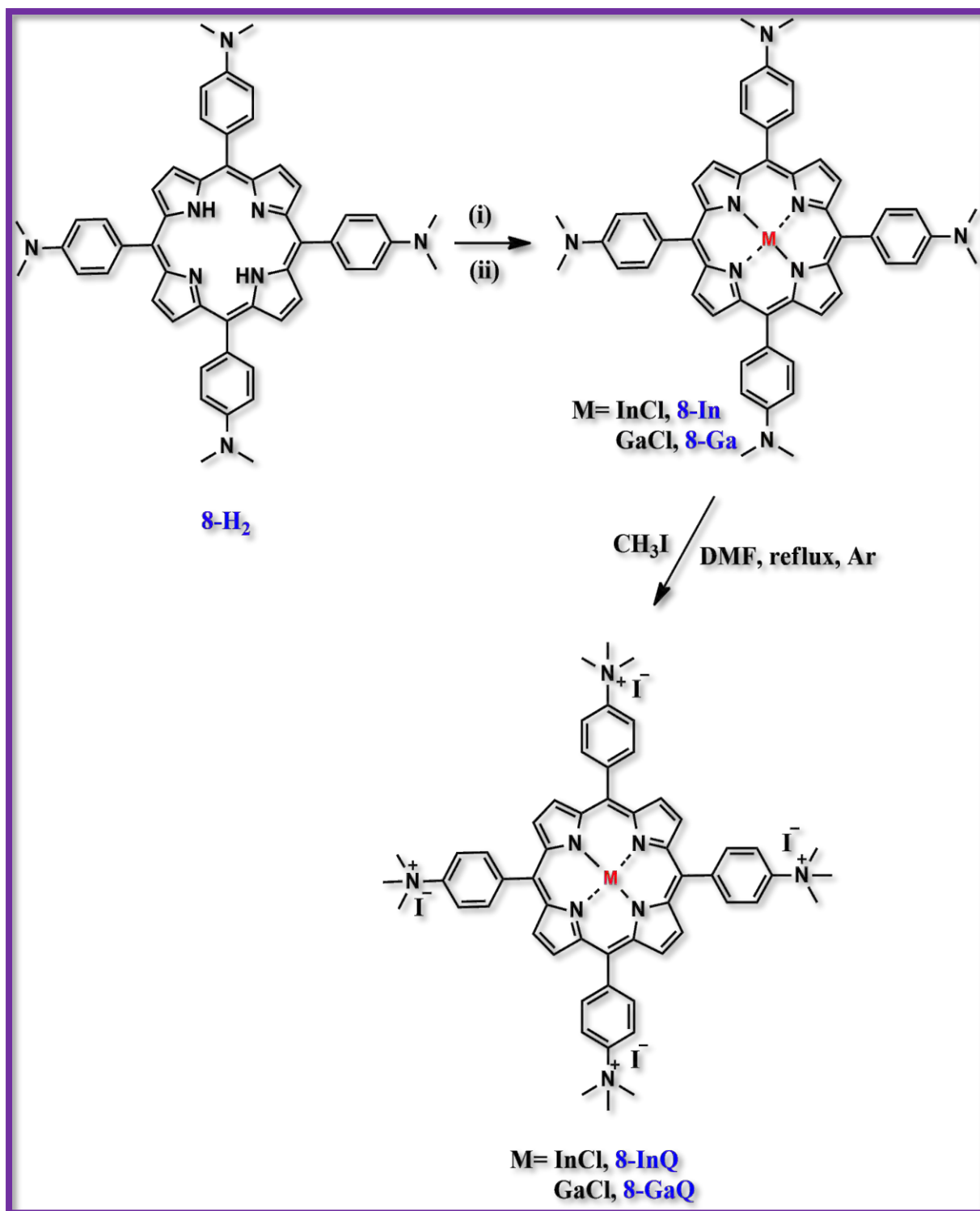
The ^1H NMR spectra of **7-H₂**, **7-Zn**, **7-In**, and **7-Ga** were recorded in DMSO-*d*₆ **Figure 10 A1 (Appendix 1)** using complexes **7-H₂** and **7-Ga** as examples. In all cases, the spectra show the OH singlet peak around 10 ppm (1H), doublet signals in the aromatic region ranging from δ_{H} 7.21-9.14 ppm (integrating for 24H), and a strong singlet peak resonating around 4.05 ppm for the 9H methyl protons of the methoxy groups. The two inner core N-H protons on **7-H₂** appear as one strong singlet δ_{H} 2.54 ppm. However, these N-H signals are absent in the spectra of the metallated complexes, indicating that the metallation was successful. Mass spectra (**Figure 6 A2, Appendix 2**) and **Chapter two** for the elemental analysis data). The acquired data were consistent with the predicted structures.

3.3.1.2. Synthesis of Group 8: **8-In**, **8-Ga**, **8-InQ**, and **8-GaQ**

The synthesis of the new complexes **8-In** and **8-Ga** was achieved through the insertion of heavy central metals such as In (III) and Ga (III) in the core of tetrakis (4-*N*, *N*-dimethylaminophenyl)porphyrin **8-H₂** used as a precursor (**Scheme 3.8**). The quaternized derivatives **8-H₂**, **8-InQ** and **8-GaQ** were obtained through methylation reactions of porphyrin complexes **8-In** and **8-Ga** using an excess of iodomethane (CH₃I) in dry DMF at reflux temperature.

The characterization of these compounds was carried out using ^1H NMR, MS, UV-Vis, and FT-IR techniques (**Appendices 1 and 2** for MS and NMR spectra, respectively and the elemental data in **Chapter two**) and all the acquired data agreed with the predictions.

The ^1H NMR spectra for all the porphyrins exhibited aromatic proton peaks ranging from 8.23-6.78 ppm which integrated for 24 protons. The geminal methyl protons resonated in the aliphatic region between 3.04 and 3.10 (**Figure 11 A1 (Appendix 1)** using complexes **8-Ga** and **8-GaQ** as well as **8-In** and **8-InQ**). Complex **8-Ga** exhibited a protonated molecular ion peak at $m/z= 891.40$ $[\text{M}+\text{H}]^+$ and another peak at 856.37 $[\text{M}+\text{H}-\text{Cl}]^+$, while complex **8-In** showed $m/z= 936.72$ $[\text{M}+\text{H}]^+$ in the MS spectrum (**Figure 7 A2, Appendix 2**). The mass spectra of the quaternized porphyrins were not acquired due to the lack of ionization of these compounds.



Scheme 3.8 Synthesis routes of porphyrin derivatives. Reaction conditions: (i): anhydrous InCl_3 , NaOAc , glacial acetic acid, reflux, and Ar (ii) GaCl_3 , dry DMF, reflux, and Ar.

3.3.2. FT-IR Spectra of the Studied Porphyrins

The FT-IR data are used to trace the functional groups present in the molecules. **Figure 3.6A** indicates the presence of characteristic vibration peaks around 3395-3374 cm^{-1} for the O-H stretches whereas the vibrations at 1716, 1714, 1718, 1717 cm^{-1} correspond to the ester -C=O vibration stretches of **7-H₂**, **7-Zn**, **7-Ga**, and **7-In** respectively (**Figure 3.6A**).

The spectra of porphyrins **8-In** and **8-Ga** did not show N-H peak stretch which was observed in the spectra of **8-H₂** around 3413 cm^{-1} . This confirms that the metalation was successful. As expected, C=C and C=N stretches emerged at about 1605 cm^{-1} , and the C-N peak around 1556 cm^{-1} for **8-In**, **8-Ga**, **8-InQ**, and **8-GaQ**, **Figure 3.6B**.

In all cases the vibration stretches of the aromatic and aliphatic C-H appear in the region around 3085-2776 cm^{-1} .

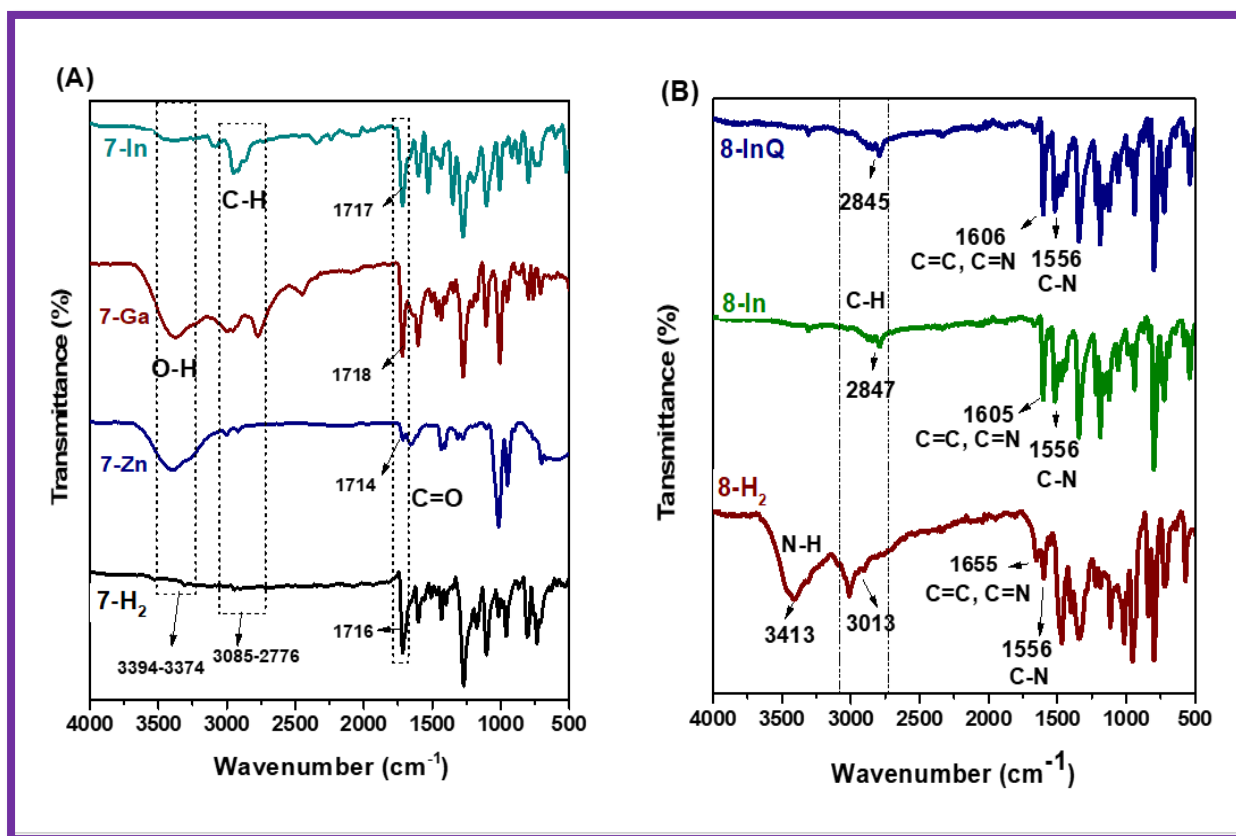


Figure 3.6 FT-IR spectra of (A) the asymmetrical porphyrins and (B) the **8-H₂**, **8-In**, and **8-InQ** porphyrins (as examples).

3.3.3. Electronic Absorption and Emission Spectra of the Studied Porphyrins

As explained by Gouterman's four orbital model, porphyrins optical spectra usually contain a very intense Soret or B-band rising around 400 nm and multiple Q-bands observed between 500 and 600 nm [97,117]. Table 3.2 depicts the electronic absorption data of the porphyrins.

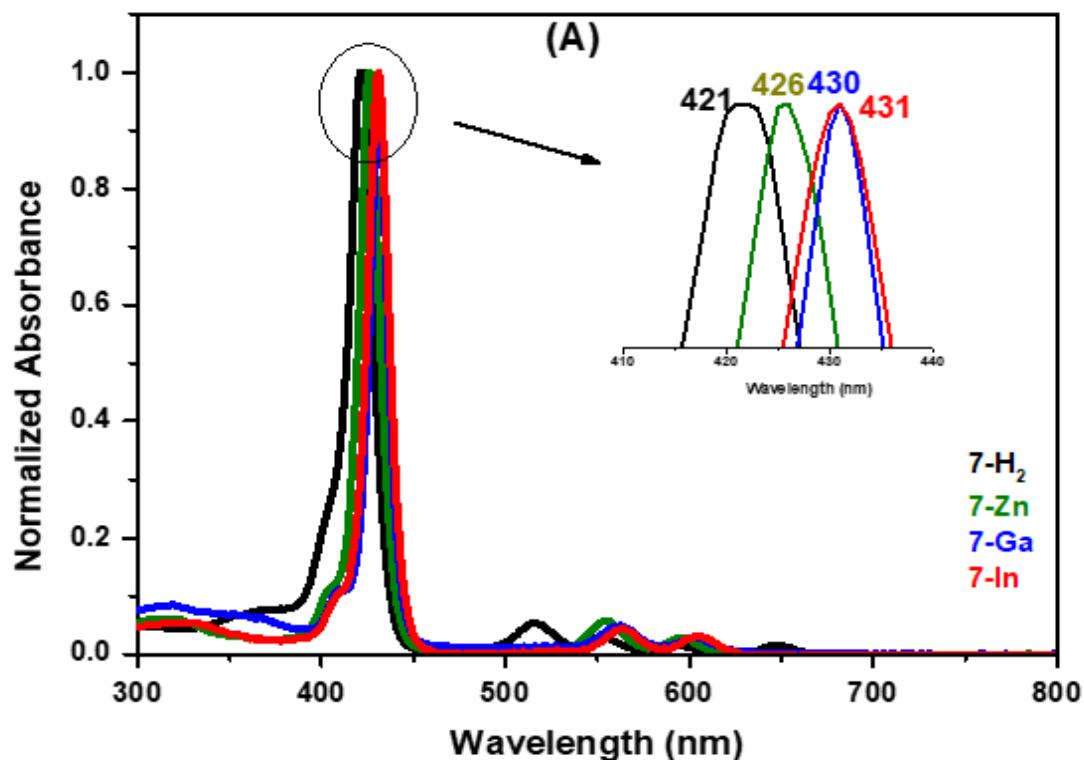
Table 3.2 Spectral data of all the synthesized porphyrins (Groups 7 and 8) in DMSO unless otherwise stated.

Complex	Q-band ^a λ_{Abs} (nm)	Emission λ_{Em} (nm)
Group 7: Asymmetrical Porphyrins		
7-H₂	421	657, 719
7-Zn	426	615, 664
7-In	430	607, 652
7-Ga	431	610, 662
Group 8: Dimethylaminophenyl Porphyrins		
8-H₂	418	600, 774
8-Ga	423 (420)	610, 662
8-In	431 (427)	575, 682
8-GaQ	428 (424)	576, 680
8-InQ	439 (433)	560, 580

^a: Values in brackets are obtained in 1% DMSO/water.

Figure 3.7A shows typical absorbance spectra of porphyrins **7-H₂**, **7-Zn**, **7-Ga**, and **7-In**. The B-band of **7-H₂** appears at 421 nm (Table 3.2) with four Q-bands in DMSO. Upon the insertion of respective metals in **7-H₂**, the B-bands of **7-Zn**, **7-Ga**, and **7-In** appeared red-shifted at 426, 430, and 431 nm, respectively (Table 3.2), as the four Q-bands collapsed into two. **Figure 3.7B** similarly illustrates that the B-band of **8-H₂** appeared at 418 nm (Table 3.2) with four Q-bands in DMSO, while slight red-shifts in the spectra of **8-Ga** and **8-In** to 423 and 431 nm, respectively (Table 3.2) are observed following metallation.

As known from the literature, the spectral red-shifts and the collapse of the four Q-bands of the free base to two Q-bands confirm successful metalation [221]. The observed spectral red-shifts of the B-bands could also result from the heavy metal effect which could cause a degree of perturbation and electron delocalization within the porphyrin macrocycle [221]. Indium derivatives showed the largest shifts due to the nonplanar effect of the In (III) ion and its bigger atomic radius compared to Ga (III) ions [219].



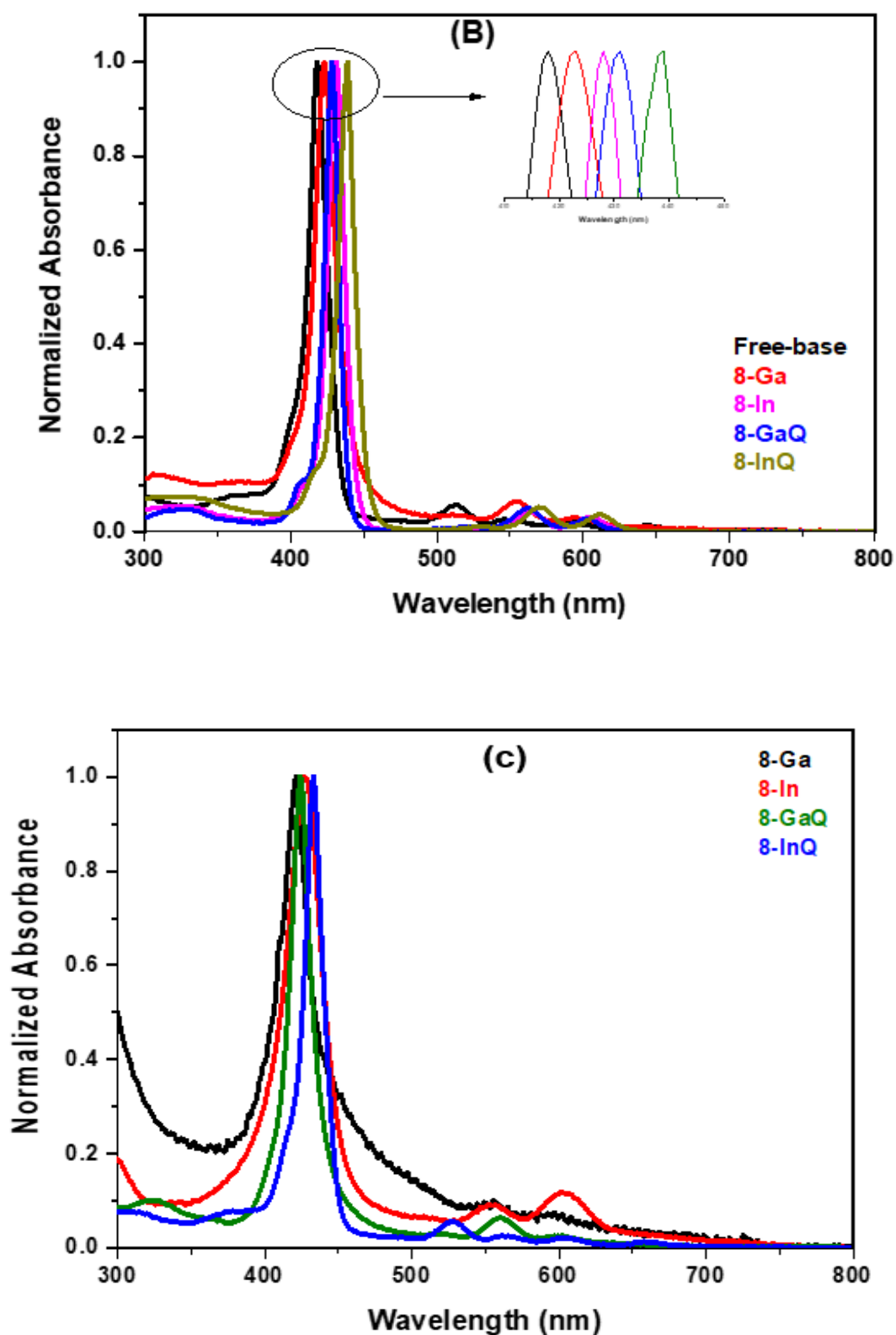


Figure 3.7 The normalized UV-Vis spectra of porphyrins: (A) 7- H₂, 7- Zn, 7-In, and 7-Ga in DMSO, (B) 8-Ga, 8-In, 8-GaQ, and 8-InQ in DMSO; (C) 8-Ga, 8-In, 8-GaQ, and 8-InQ in 1% DMSO. Arrows show expansion of the B bands.

There are slight red-shifts in the Soret bands in DMSO following quaternization of **8-In** and **8-Ga** to **8-InQ** and **8-GaQ**, respectively (**Figure 3.7B** and **Table 3.2**). This could be due to the aggregation in porphyrins. The spectra obtained in 1% DMSO showed aggregation as judged by the broadening with blue-shifts (**Figure 3.7C**).

The emission spectra in all cases show two characteristic bands typical for porphyrins [221,222] as seen in **Figures 3.8A,B** and **Figure 2 A3 (Appendix 3)** used as examples. The decrease in fluorescence intensities for the metallated porphyrins could be supported by the heavy central metal effects [155]. The characteristic bands and energies of the emission bands in the nanoconjugates are typical of what is observed for non-aggregated metal porphyrins.

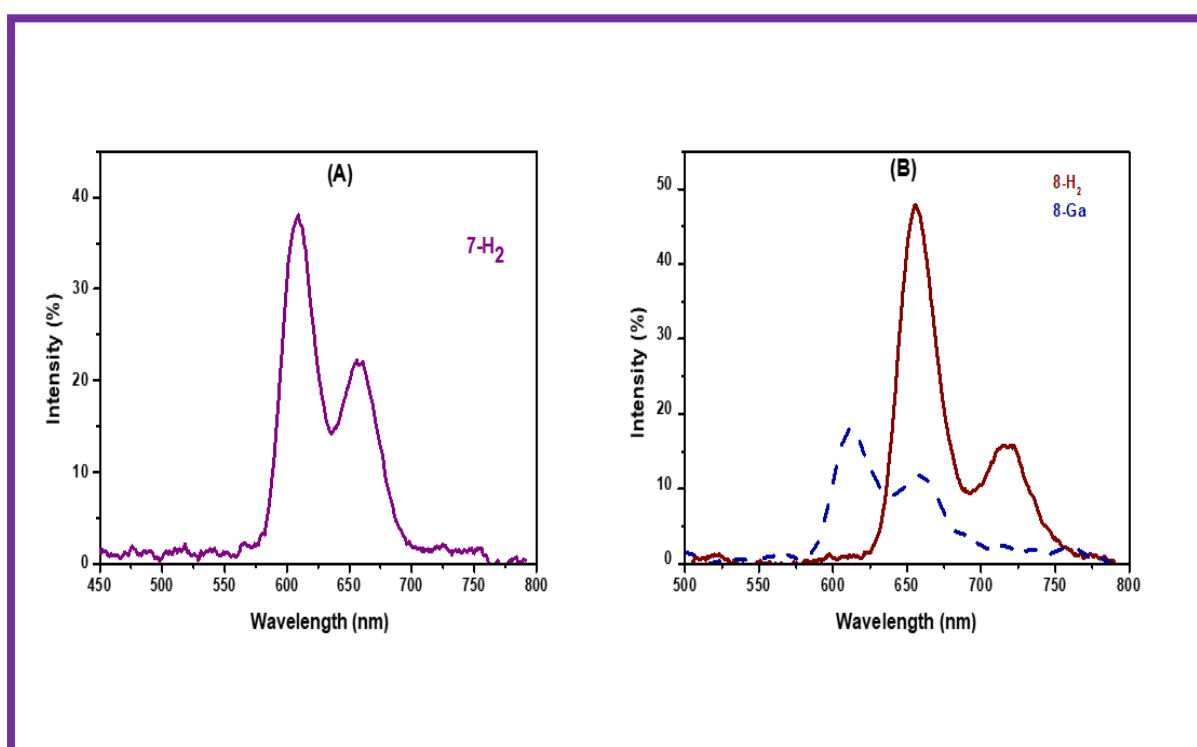


Figure 3.8 The emission spectra of (A) **7-H₂** and (B) **8-H₂** and **8-Ga** porphyrins in DMSO as examples.

3.4. Synthesis and Characterization of the PSs-nanoconjugates

As will be shown below, the characterization of the synthesized nanomaterials alone and their PSs nanoconjugates was achieved by UV-Vis spectroscopy, FT-IR, Raman spectroscopy, TEM, DLS, TGA, or DSC analysis in order to demonstrate successful conjugation of the complexes to the nanomaterials.

The mass loading values of complexes unto the nanomaterials were determined by using previous studies that use absorption instead of fluorescence [223,224]. This method is based on comparing the Q-band absorbance intensities of the nanoconjugates with that of the respective PS before conjugation. Briefly, equal masses (mg) for PS and nanoconjugates were separately weighed and dissolved in the same volume of solvent. The mass loading values are listed in **Table 3.3**. Please note that **Group 4** Pcs and **Group 8** porphyrins were not conjugated to any nanomaterials, hence no data are reported in **Table 3.3**.

It is also noteworthy to mention here that the emission spectra of the as-formed nanoconjugates were similar to characteristic emission spectra of Pcs or porphyrins used for their formation.

Table 3.3 Spectral data of all the reported nanoparticles and their respective nanoconjugates.

Complex	λ_{abs} (nm)	Raman D, G bands cm^{-1}	Raman $I_{\text{D}}/I_{\text{G}}$ ratio	Loading $\mu\text{g PS/mg}$ NPs	TEM Size (nm)	DLS Size (nm)
Group 1: Acetophenoxy-substituted Pcs and nanoconjugates						
GQDs	343	1385, 1554	1.26	-	10	10
DNDs	-	1371, 1591	0.26	-	2.4	2.7
1-H₂	668, 698	-	-	-	-	-
1-Zn	675	-	-	-	-	-
1-In	685	-	-	-	-	-
1-H₂π(GQDs)	672, 698	1290, 1595	1.51	493	16	15.7
1-Znπ(GQDs)	677	1290, 1591	1.35	258	24	24.4
1-Inπ(GQDs)	687	1290, 1595	1.31	208	33	32.7
1-H₂π(DNDs)	673, 698	1291, 1595	1.31	393	9	11.7
1-Znπ(DNDs)	682	1291, 1593	1.26	286	15	18.2
1-Inπ(DNDs)	690	1291, 1596	1.50	308	23	24.4
Group 2: Bromo-aminophenoxy-substituted Pcs and nanoconjugates						
CSAg	381	-	-	-	5	-
2-Zn	679	-	-	-	-	-
2-In	687	-	-	-	-	-
2-Znπ(DNDs)	681	1281, 1591	1.68	-	8	-
2-Inπ(DNDs)	690	1284, 1595	1.12	-	12	-
2-Znπ(DNDs)-CSAg	680	-	-	-	18	-
2-Inπ(DNDs)-CSAg	689	-	-	-	23	-
Group 3: Pyridyl chalcone-substituted Pcs and nanoconjugates						
3-Zn	684	-	-	-	-	-
3-In	686	-	-	-	-	-
3-ZnQ	683	-	-	-	-	-
3-InQ	684	-	-	-	-	-
3-Znπ(DNDs)	687	1371, 1597	0.34	383	8	-
3-Inπ(DNDs)	689	1371, 1595	0.34	146	18	-
3-ZnQπ(DNDs)	690	1379, 1568	0.59	737	13	-
3-InQπ(DNDs)	684	1389, 1574	0.59	536	22	-

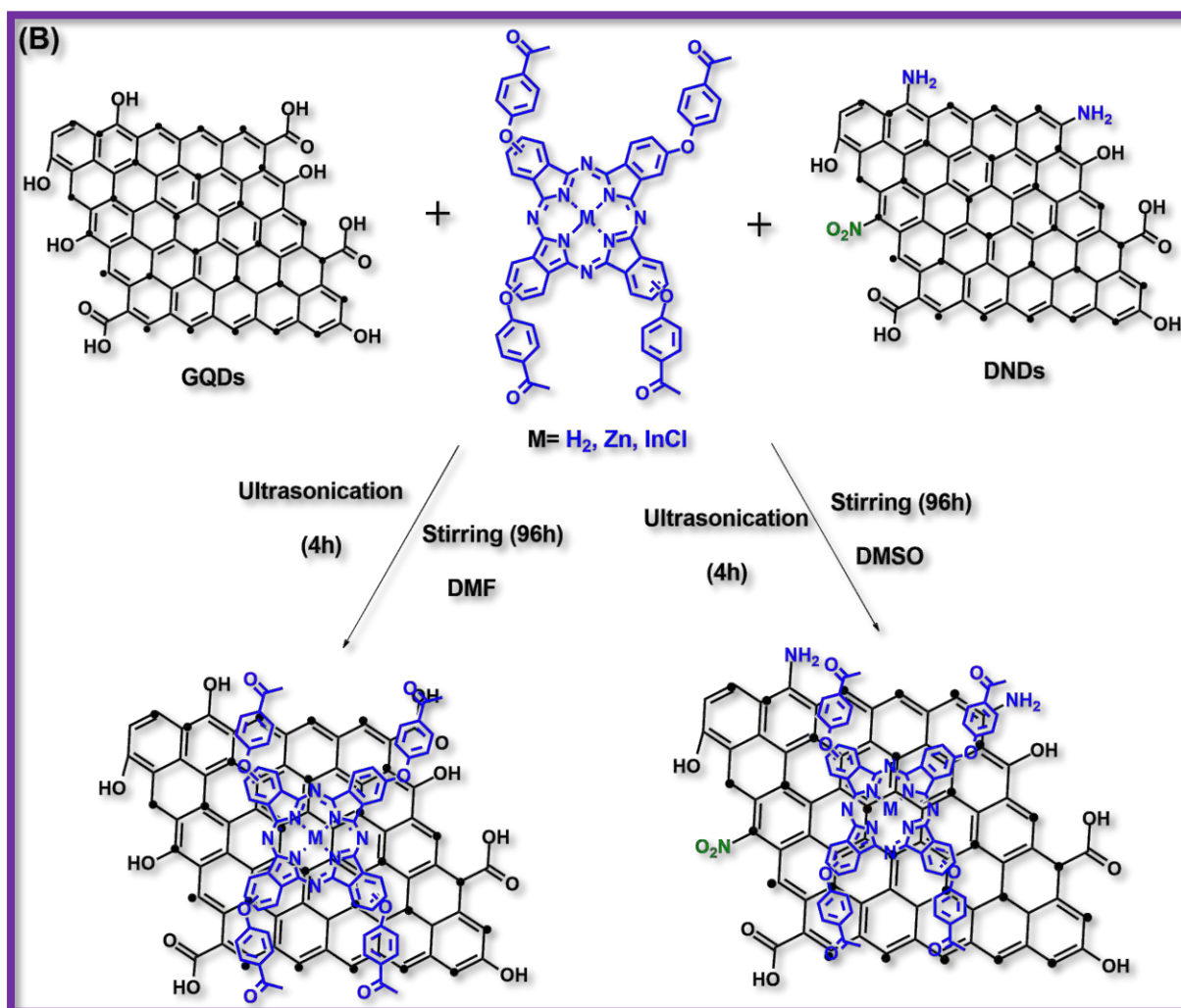
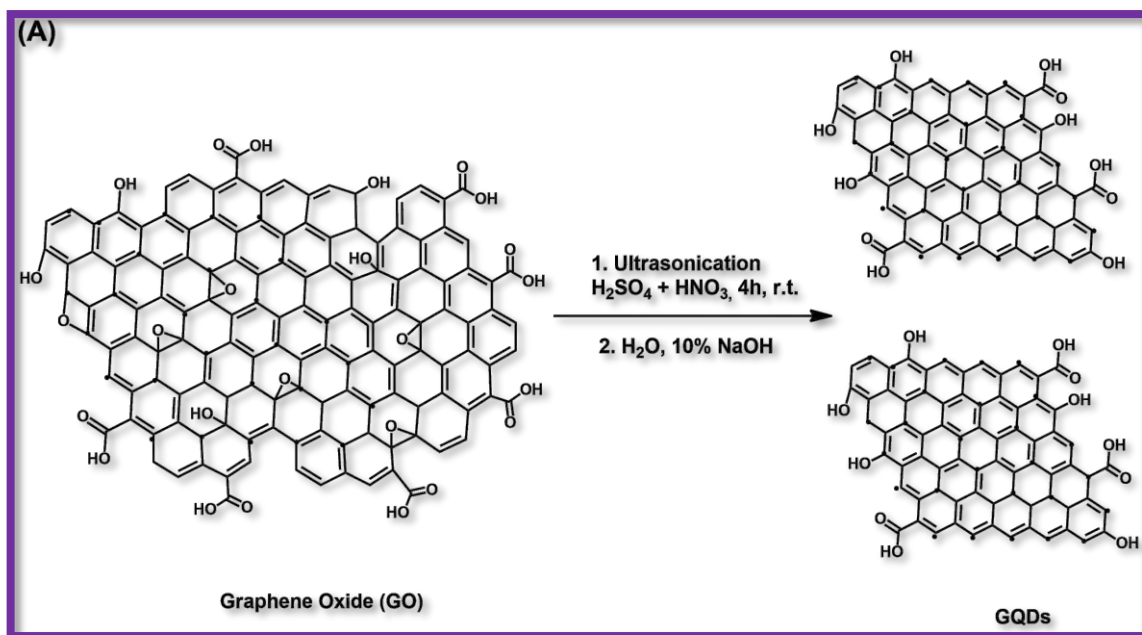
Groups 5-6: Tetra and monocarboxylic acid-substituted Pcs and nanoconjugates						
GSH@GQDs	354	-	-	-	-	8.7
5-Zn	679	-	-	-	-	-
6-Zn	682	-	-	-	-	-
5-Zn π (GSH@GQDs)	679	-	-	186	-	30.6
6-Zn -(GSH@GQDs)	683	-	-	198	-	38.1
Group 7: Asymmetrical porphyrins						
Ag NPs	380	-	-	-	7.0	-
7-H₂	421	-	-	-	-	-
7-Zn	426	-	-	-	-	-
7-In	430	-	-	-	-	-
7-Ga	431	-	-	-	-	-
7-H₂ -DNDs@Ag	422	-	-	893	13	-
7-Zn -DNDs@Ag	429	-	-	854	20	-
7-In -DNDs@Ag	431	-	-	747	24	-
7-Ga -DNDs@Ag	431	-	-	802	31	-

^a: Values in brackets are when exciting where GQDs or GSH@GQDs absorb.

3.4.1. Effect of Different Nanomaterials: Conjugation of **1-H₂**, **1-Zn**, and **1-In** to GQDs and DNDs

3.4.1.1. Synthesis

The GQDs and DNDs all contain delocalized π electrons systems that can allow strong π - π interactions with other π electron containing moieties such as Pcs and porphyrins. The GQDs were obtained by the top-down hydrothermal method as previously reported (**Scheme 3.9A**) [159]. Thus, complexes **1-H₂**, **1-Zn**, and **1-In** are noncovalently linked via π - π stacking interactions with GQDs and DNDs to investigate the effect of conjugation to GQDs and DNDs on photophysical and PACT efficacy. The as-prepared nanoconjugates are represented as **1-H₂** π (GQDs), **1-Zn** π (GQDs), **1-In** π (GQDs), **1-H₂** π (DNDs), **1-Zn** π (DNDs), and **1-In** π (DNDs), respectively (**Scheme 3.9B**).



Scheme 3.9 (A) Preparation of the GQDs and (B) π - π interactions of **1-H₂**, **1-Zn**, and **1-In** unto GQDs and DNDs.

3.4.1.2. FT-IR Spectra

The FT-IR was run to determine the surface function groups on the nanomaterials, Pcs alone, and the nanoconjugates. The spectrum of DNDs shows the stretching vibration of COOH and N-H around 3384 cm^{-1} , aromatic and aliphatic C-H stretches around $2952\text{-}2852\text{ cm}^{-1}$, and C=O at 1624 cm^{-1} . The FT-IR spectrum of GQDs also exhibits a characteristic broad peak around $3377\text{-}2683\text{ cm}^{-1}$ corresponding to the carboxylic -OH and free -OH of GQDs as well as the stretches peaks of the carboxyl groups (C=O and C-O) observed at about 1663 and 1390 cm^{-1} (**Figure 3.9**).

In the FT-IR spectra of **1-In π** (GQDs) and **1-In π** (DNDs) (as examples), the aliphatic and aromatic C-H stretching vibration peaks weakened and the C=O vibration peaks shifted to lower frequencies, which is similarly present in the spectra all the nanoconjugates (**Figure 1 A4** in **Appendix 4**). Generally, comparing the spectra of the nanoconjugates to that of the Pcs alone and the nanomaterials alone, it is quite evident that the nanoconjugates show the respective peaks from both the nanomaterials and the Pcs with some shifts which further indicate the formation of new nanoconjugates. It is known that shifts in IR bands confirm structural changes [225].

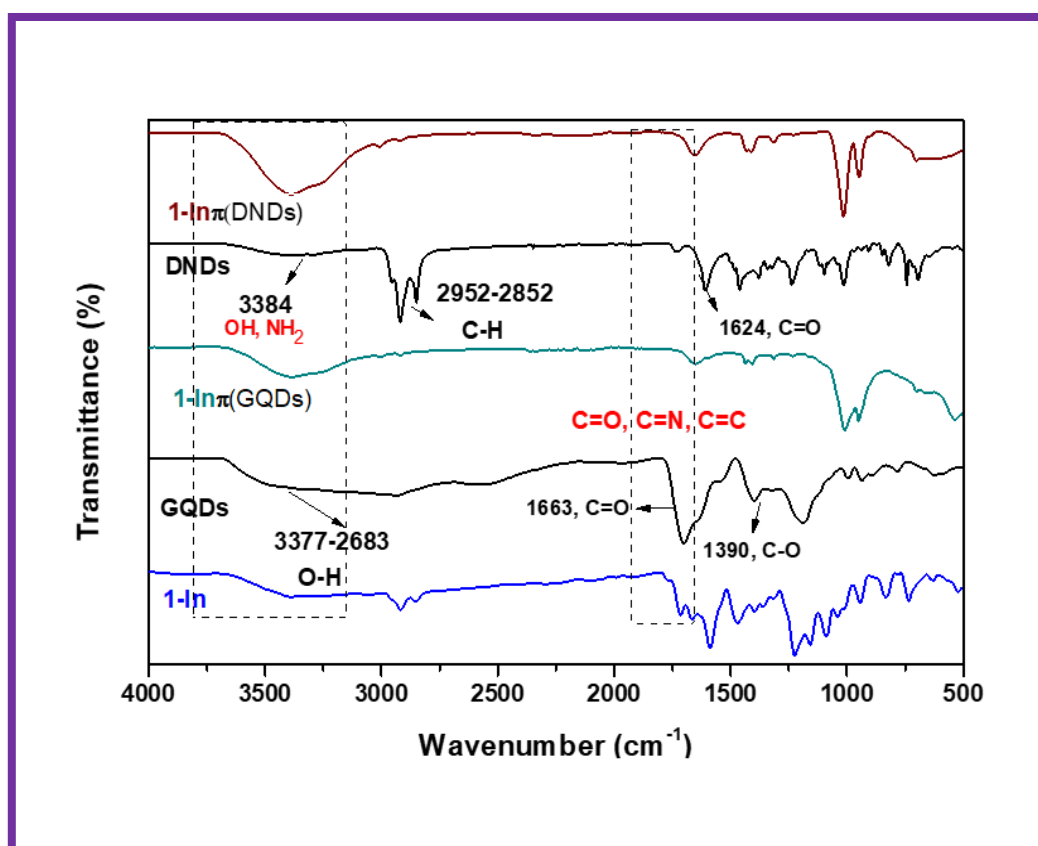


Figure 3.9 FT-IR spectra of GQDs, DNDs and **1-In π** (GQDs), **1-In π** (DNDs) as examples.

3.4.1.3. UV-Vis Absorption and Emission Spectra

As seen in **Figure 3.10A**, the DNDs exhibit no defined absorption in the 300-800 nm region. The spectrum for GQDs exhibit a typical broad absorption peak at 343 nm due to π - π^* transition of the sp^2 carbon electrons [226], and a characteristic emission band observed at 453 nm when exciting at λ_{exc} 340 nm (where GQDs absorb), **Figure 3.10B**. Chemical functionalization of GQDs has been reported to result in defects leading to tuneable emission properties as observed in this study [227].

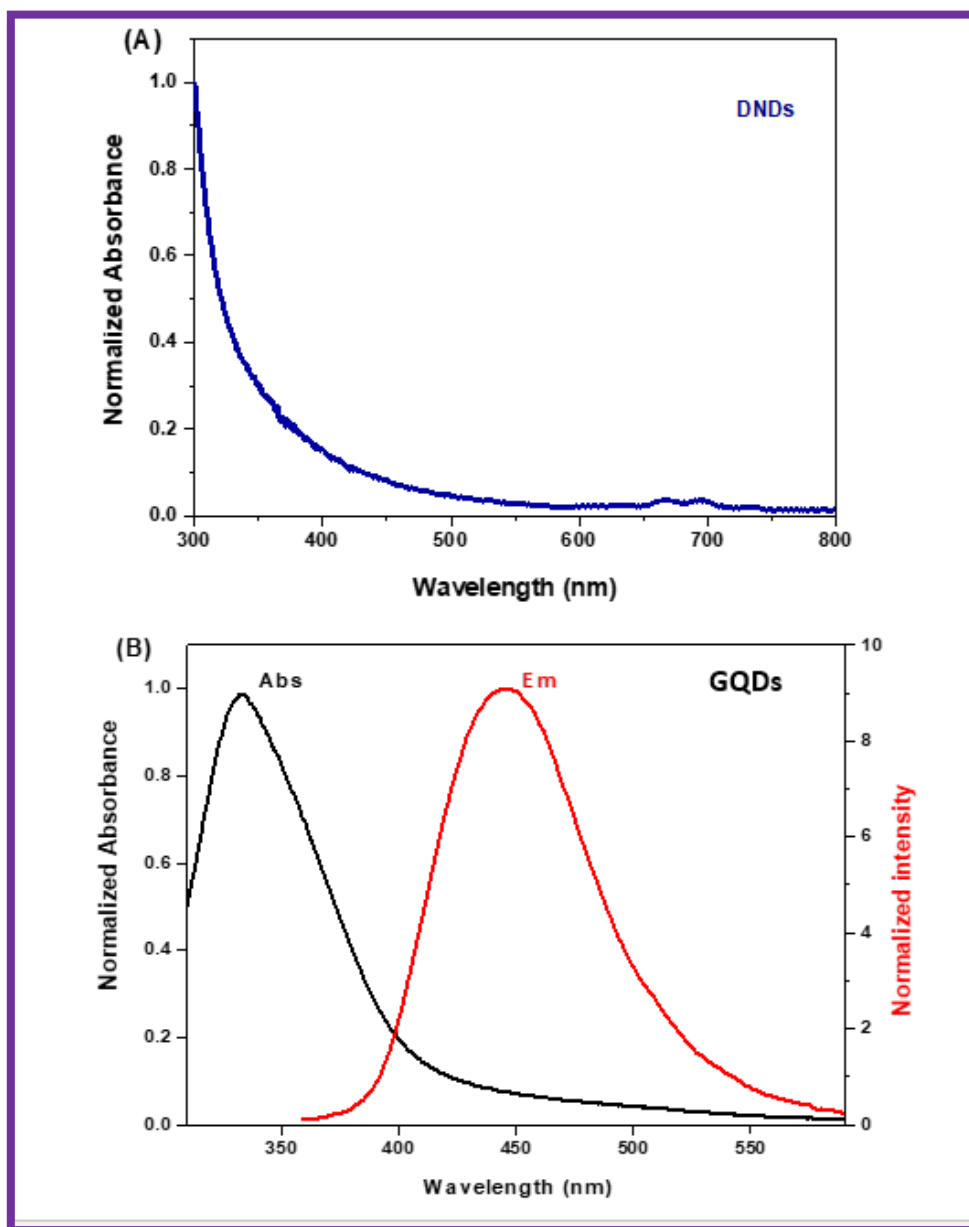


Figure 3.10 Normalized absorption spectra of (A) DNDs, (B) and emission spectrum of GQDs.

The absorption occurring below 600 nm in the nanoconjugates spectra is due to the absorption of the nanomaterials in this region, (**Figures 3.11A,B**).

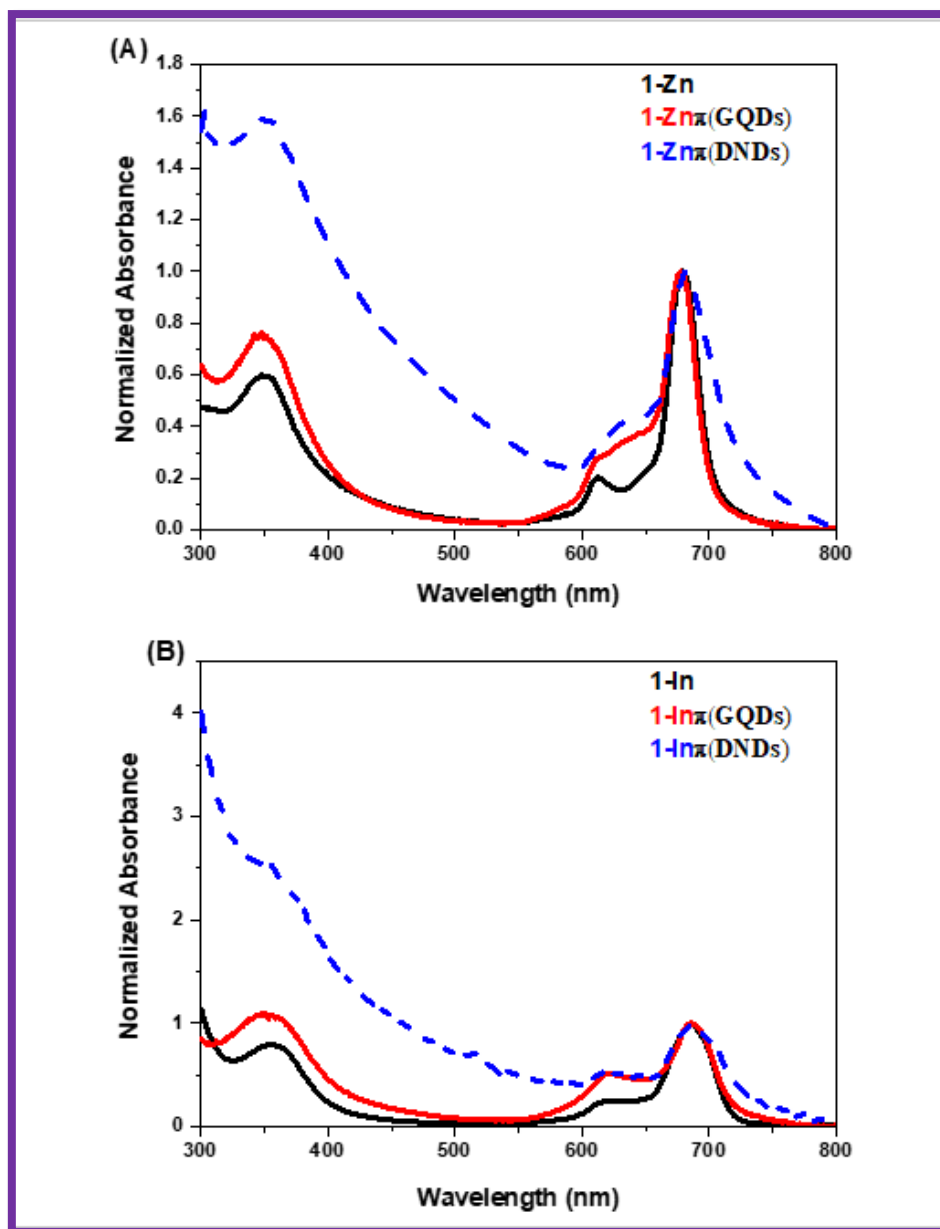


Figure 3.11 Normalized absorption spectra of (A) **1-Zn**, **1-Zn π (GQDs)**, and **1-Zn π (DNDs)**, (B) **1-In**, **1-In π (GQDs)**, and **1-In π (DNDs)** in DMSO as examples.

There are also red-shifts in the Q-bands of the nanoconjugates compared to the Pcs alone, (**Figures 3.11A,B** and **Table 3.3**). The DNDs nanoconjugates are more red-shifted than the GQDs counterparts. DNDs have a core-shell structural design with diamond inner core (sp^3 carbon atoms) and graphitic outer shell (sp^2 carbon atoms) with hanging bonds ended with functional groups could be one of the reasons these spectral shifts.

Spectral red-shifts have been also observed in porphyrin-graphene oxide nanoconjugates and they were attributed to molecular flattening [223,228]. Another report has attributed the red-shifts observed in the tetrasulfonated zinc Pc-graphene complex to a J-type aggregation [229].

Comparing the spectra by the central metal effect, one can see that the free-base **1-H₂π**(GQDs) and **1-H₂π**(DNDs) nanoconjugates show more aggregation as was the case for complex **1-H₂** alone, (Figure 2 A4 in Appendix 4). Aggregation could be caused by the extensive π - π stacking of the Pcs in adjacent nanomaterials and this can result in the observed enhancement in absorption around the region between 600 and 650 nm and the broadening of the Q-bands in the spectra of the GQDs and DNDs nanoconjugate [120].

Non-covalently linked graphene-based nanomaterials assemblies involving π - π interaction are advantageous in the sense that electronic properties of the nanomaterials are maintained [230].

The mass loadings of Pcs onto each GQDs or DNDs are found in Table 3.3. The results show that **1-H₂π**(GQDs) and **1-H₂π**(DNDs) have higher Pc loading which results in high aggregation observed as compared to zinc and indium derivatives. The absence of heavy central metal in the core of the free-base makes this molecule more accessible to strong π - π interactions since there is no limit in the distance and orientation between the Pc and the nanomaterials. This could be explained by the fact that the shape of the dye can strongly affect the π - π interactions between the dye and the graphitic sheet since it limits the distance and orientation between them [231]. Except for the free-base conjugates, DNDs nanoconjugates with a smaller TEM size (discussed below) show higher loading capacity thanks to their bigger surface area compared to the GQDs.

3.4.1.4. Raman Spectra

Raman spectroscopy was used in this study to determine the quality of the nanomaterials and their nanoconjugates. Figure 3.12 shows the Raman spectra of GQDs, DNDs, **1-Inπ**(GQDs), **1-Inπ**(DNDs) for exemplification.

The two characteristic bands observed in the spectra of GQDs and DNDs are known as the D-disorder band (breathing mode, sp^3) that is due to out-of-plane vibrations attributed to the presence of structural defects and the G-band (sp^2) tangential mode that is a result of in-plane vibrations of sp^2 bonded carbon atoms [232,233]. The D and G bands were observed at 1371 cm^{-1} and 1591 cm^{-1} , respectively for the DNDs and at 1385 cm^{-1} and 1554 cm^{-1} , respectively for the GQDs, Table 3.3.

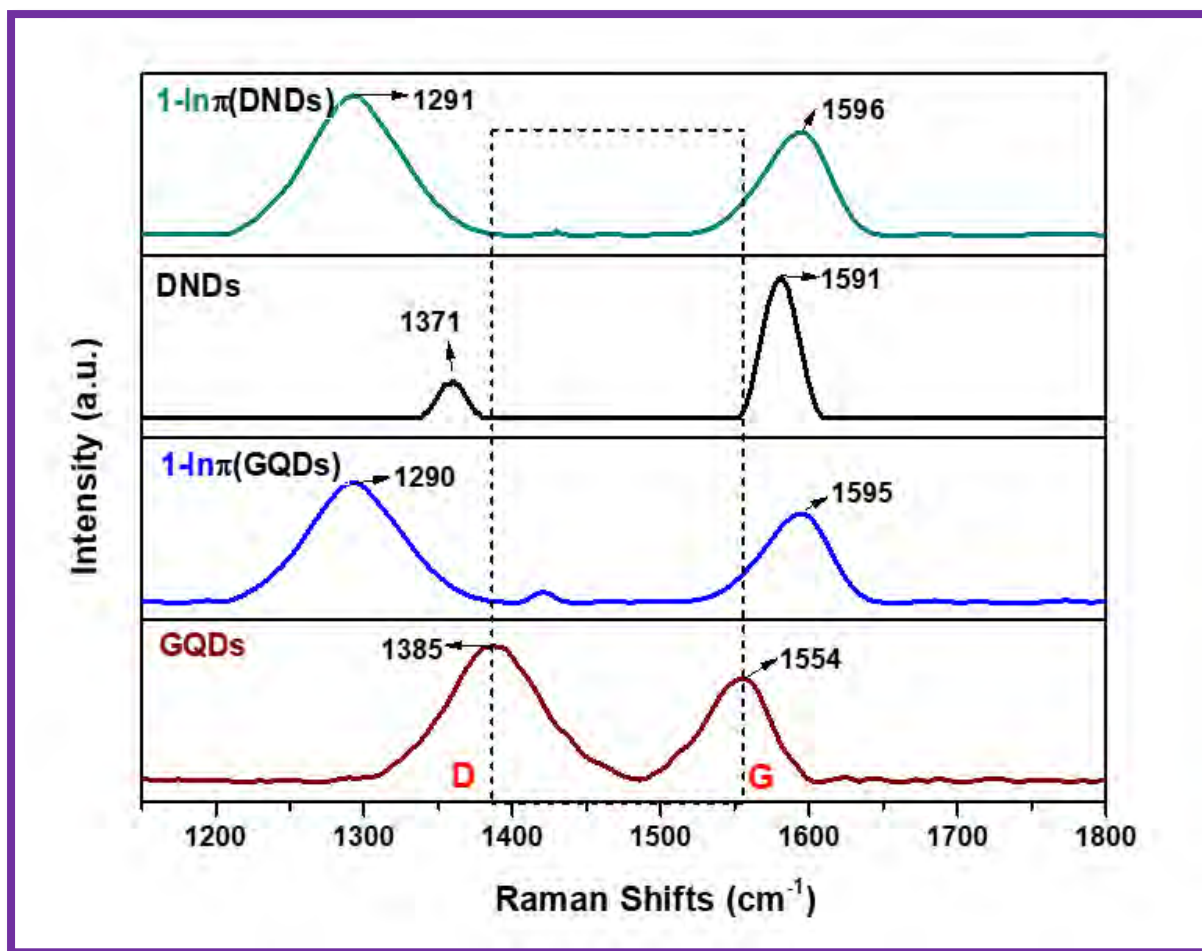


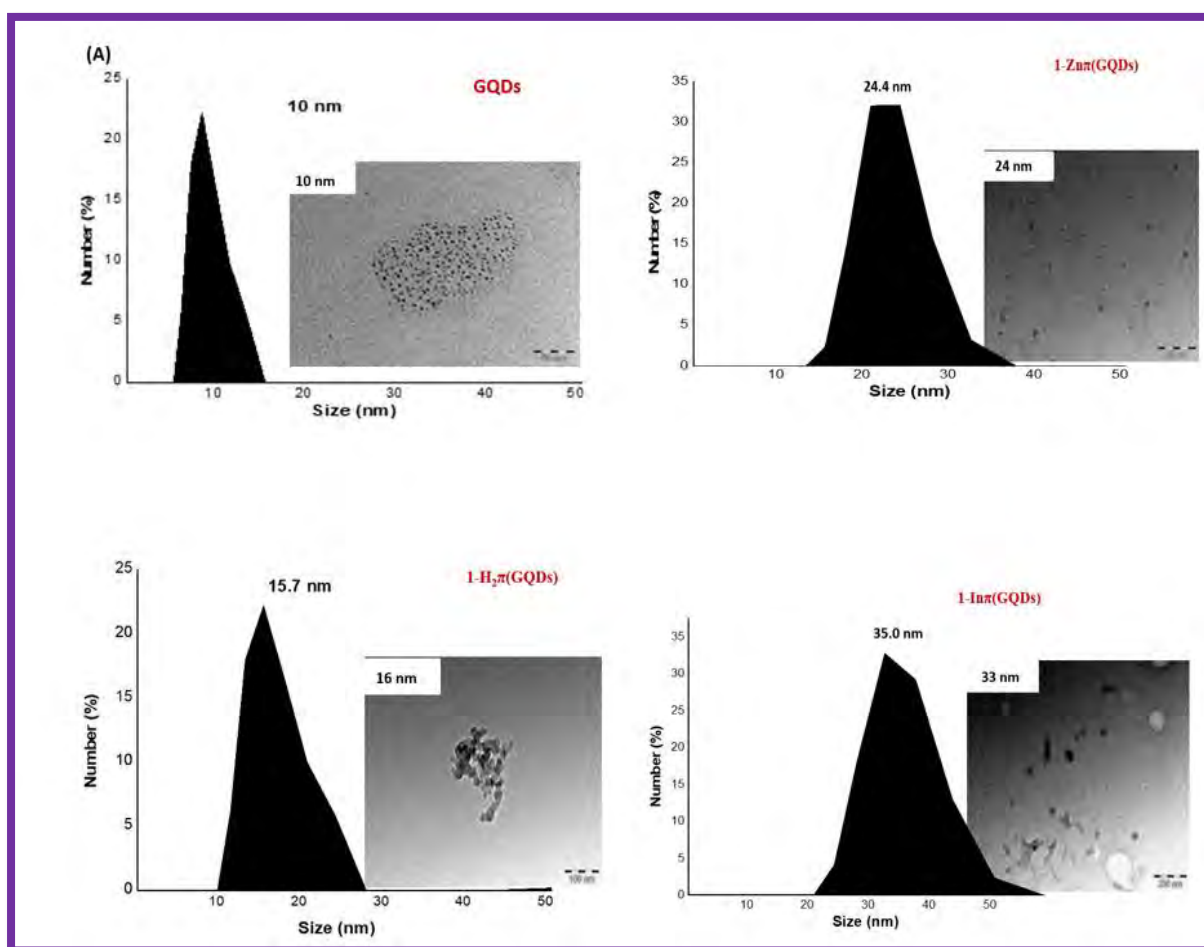
Figure 3.12 Raman spectra of GQDs, DNDs and $1\text{-In}\pi(\text{GQDs})$, $1\text{-In}\pi(\text{DNDs})$.

The π - π interactions of the Pcs to the GQDs and DNDs resulted in the shifts of their G bands to slightly higher wavenumbers, while a shift to lower wavenumbers of their D bands is observed in the nanoconjugates, **Figure 3.12**, **Figure 3 A4 (Appendix 4)** and **Table 3.3**. The observed Raman shifts after conjugation are an indication of the introduction of defects within the carbon framework in the carbon nanomaterials and a confirmation of the formation of new nanoconjugates. Shifts in the Raman frequencies imply strong π electron interactions between the Pcs and carbon nanomaterials [234]. Shifts in the Raman bands have also been attributed to factors such as nature, diameter, and strain of nanoparticles [235,236].

To determine the quality of the extent of functionalization of the used nanomaterials, the I_D/I_G was calculated. It is the ratio of the intensities of the D and G bands (I_D/I_G) which was found to be 1.26 for GQDs and 0.26 for DNDs. As observed in **Table 3.3**, there is an increase in the I_D/I_G values in all the nanoconjugates. This confirms the presence of sp^3 defects from Pcs on the sp^2 lattice of the graphitic materials which enhances the D-band.

3.4.1.5. TEM Micrographs and DLS Analysis

The TEM and DLS sizes (data are given in **Table 3.3**) were used to determine the size and morphology of the nanomaterials and nanoconjugates. **Figures 3.13A,B** show more enhanced aggregation in the nanoconjugates. The micrographs show that the GQDs alone are monodispersed and have an average size of 10 nm whereas the DNDs are spherical with a size around 2.4 nm in TEM. In DLS analysis the GQDs had sizes of 10 nm for GQDs and the DNDs 2.7 nm. The larger sizes are obtained with the DLS technique because it leans towards larger particles [237].



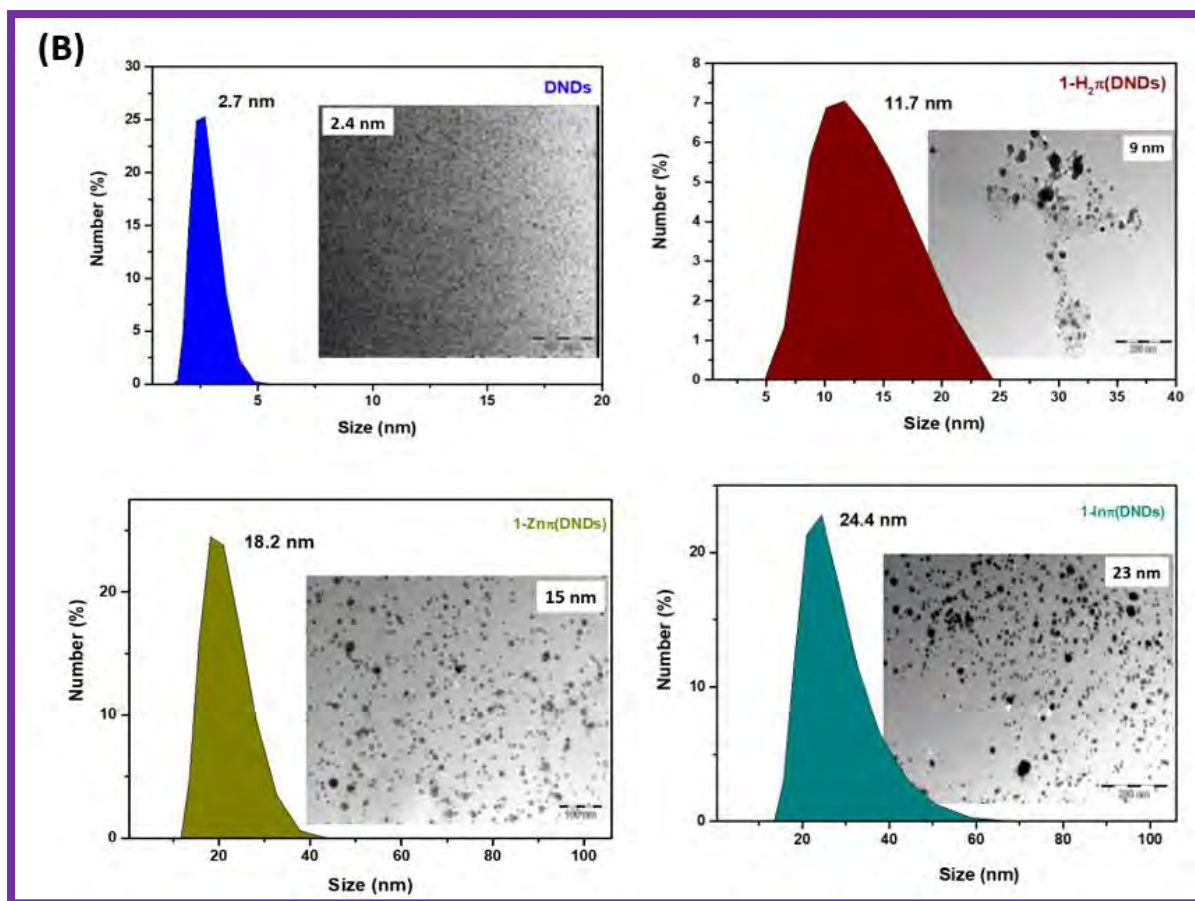


Figure 3.13 DLS and TEM images (as inserts) of (A) GQDs and the $\text{Pcs}\pi(\text{GQDs})$, (B) DNDs and the $\text{Pcs}\pi(\text{DNDs})$ nanoconjugates showing the morphology and size increase following conjugation.

However, upon conjugation, an increase in the sizes is observed in the nanoconjugates **Table 3.3**. This increase in the size of the nanoconjugates compared to nanomaterials alone is due to aggregation which may occur through π - π stacking of the Pcs on adjacent nanomaterials [120].

$1\text{-H}_2\pi(\text{GQDs})$ shows more aggregation as it has the highest Pc loading but yet with the smallest size average of the GQDs conjugates. Aggregation of Pcs has been well documented to be due to π - π stacking between the Pc rings [120]. Self-assembled graphene quantum dots induced by cytochrome c has been reported [238].

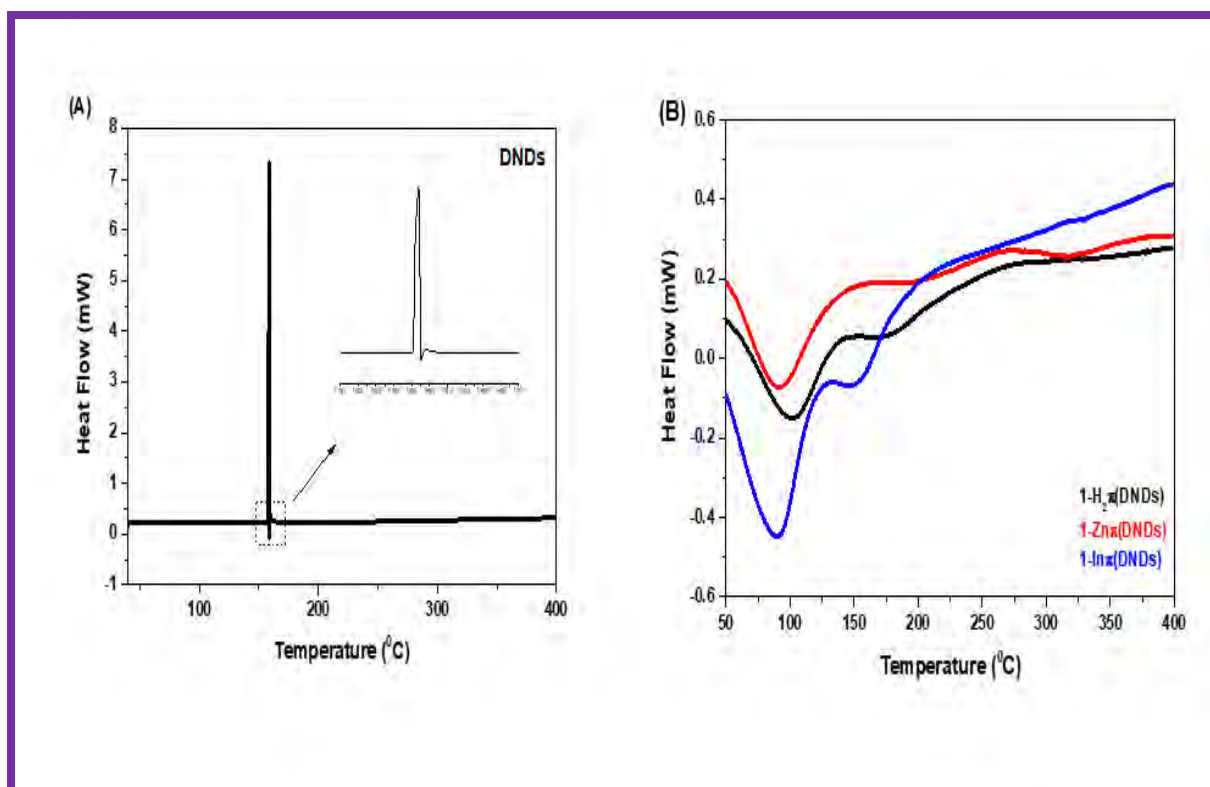
While $1\text{-In}\pi(\text{GQDs})$ shows the largest size average. This could suggest that the axial ligand and atomic radius of the indium play a role in the orientation of the Pc on the nanomaterials, which might prevent aggregation but increase the distance between the Pc rings and the nanomaterials surfaces, which might result in larger size. Similar observations are obtained in the micrographs of the $\text{Pcs}\pi(\text{DNDs})$.

3.4.1.6. TGA and DSC Analysis

TGA analysis was performed on the DNDs and nanoconjugates to evaluate the changes in weight in relation to changes in temperature, hence determining their thermal stability. The experiments were recorded at atmospheric pressure in nitrogen at a temperature from 50 up to 1000 °C with a heating rate of 10 °C/min.

DNDs alone start to decompose at 560 °C whereas the complete oxidation happens at 679 °C. At 1000 °C a weight loss of 100 % is obtained for the DNDs alone, **Figure 3.14C**. The weight losses of the nanoconjugates are 80.67%, 43.25%, and 36.19% for **1-H₂π**(DNDs), **1-Znπ**(DNDs), and **1-Inπ**(DNDs), respectively at this temperature.

The data in **Figure 3.14C** imply that upon stacking the Pcs on the DNDs, there is less mass loss in the formed nanoconjugates compared to DNDs alone (100%). This indicates improvement in the thermal stability of DNDs which can be associated with adsorption of the Pcs. A similar trend was observed for single-walled carbon nanotubes (SWCNTs) following their functionalization to zinc monocarboxyphenoxy phthalocyanine spermine [239].



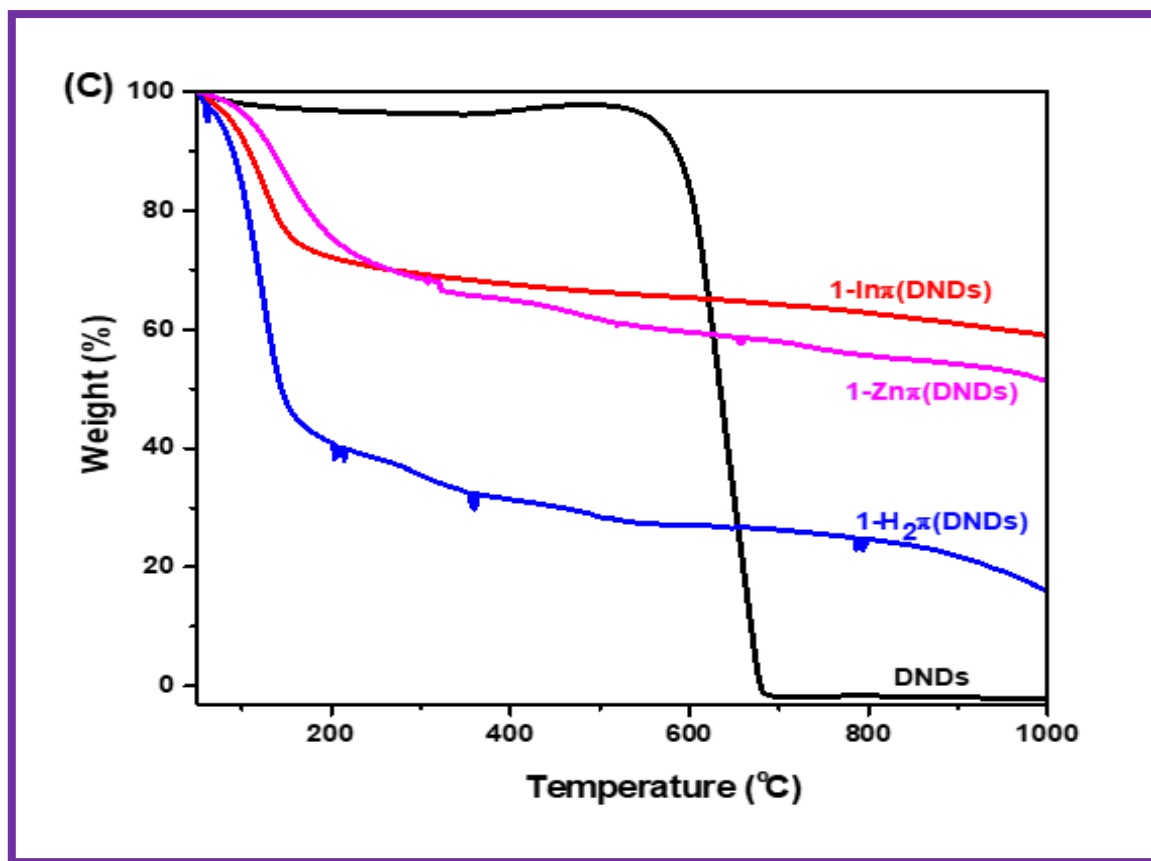


Figure 3.14 (A, B) DSC analysis and (C) TGA thermograms of DNDs alone and the DNDs nanoconjugates showing thermal stability of DNDs after conjugation.

DSC technique is a useful tool used to study the physical and chemical phase transitions, such as glass transition temperatures (T_g), melting point (T_m), thermal decomposition temperature (T_d) of materials. These transitions consist of energy changes or heat capacity changes that can be detected by DSC with high sensitivity.

In this work, DSC analysis was used to determine the decomposition and thermal stability of the nanoparticles and the formed nanoconjugates. The experiment was recorded from 40 to 400 °C for the DNDs and nanoconjugates, at a constant heating rate of 10 °C/min under nitrogen conditions. It is known from literature data that nanodiamonds graphitization begins nearby 600 °C [240].

In **Figure 3.14A**, DNDs exhibit one exothermic peak at 158.77 °C that can be assigned to the crystallization process taking place; and a tiny endothermic peak at 159.05 °C. This peak can be attributed to the degradation of small molecules or radicals, and/or the evaporation of moisture existent on the nanodiamonds surface. The DSC thermograms of all the nanoconjugates show in all cases one endothermic peak centered on 102.79 °C for **1-H₂π(DNDs)**, 93.31 °C for **1-**

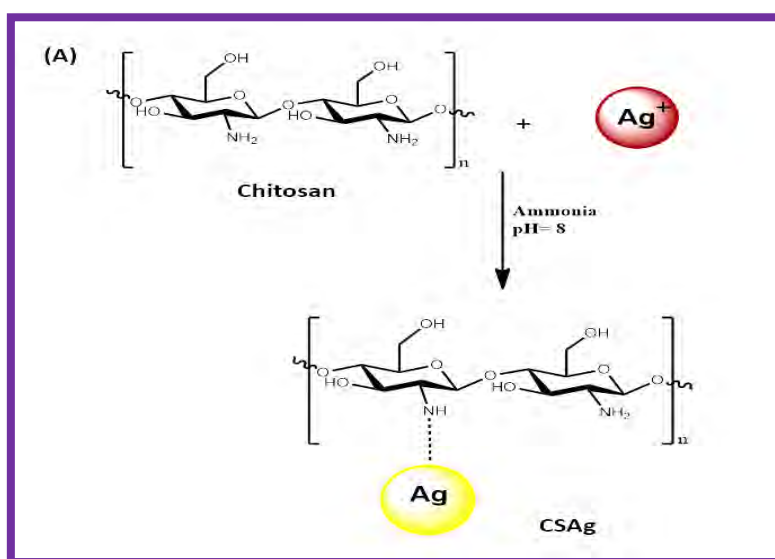
Zn π (DNDs), and 90.87 °C for **1-In π** (DNDs), **Figure 3.14B**. It is remarkable to observe that the T_g (glass transition temperature) value decreases with the increase in the heavy central metal of the nanocomposites. These peaks could be allocated to the overlapping of the T_g peak of the Pcs and the peak due to vaporization of the absorbed water by the compounds. This could also probably be due to the evaporation of solvent or volatile impurities or degradation of unstable chemical fragments in the sample.

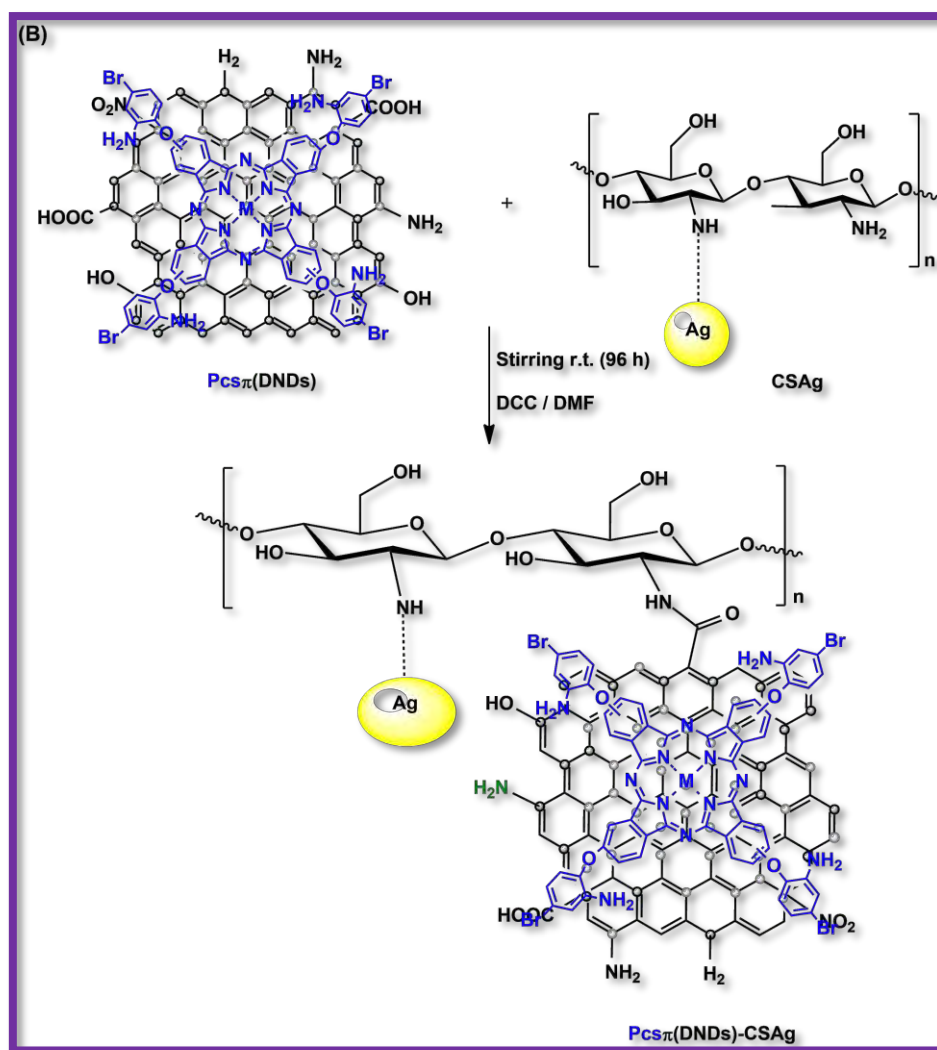
As it is seen in the region above 200 °C, a broad exothermic peak is observed in all the nanoconjugates thermograms, owing to the initiation of degradation of phthalocyanines complexes and the burning out of organic fragments. The same trend was observed for the polymeric zinc phthalocyanine [241].

3.4.2. Effect of Double Conjugation on Pcs: Conjugation of 2-Zn and 2-In to DNDs then to CSAg

3.4.2.1. Synthesis

The synthesis of CSAg nanoparticles was done following a previous procedure with slight modifications (**Scheme 3.10A**) and this has been detailed in **Chapter 2**. The nanoconjugates were prepared firstly by π - π stacking Pcs **2-Zn** and **2-In** onto the DNDs surface to yield **2-Zn π** (DNDs) and **2-In π** (DNDs), similar to **Scheme 3.9B**, which were further covalently conjugated to chitosan-mediated silver nanoparticles CSAg via an amide bond to give **2-Zn π** (DNDs)-CSAg and **2-In π** (DNDs)-CSAg nanoconjugates (**Scheme 3.10B**). The nanoconjugates are particularly prepared to compare the effect of conjugation of Pc complexes to DNDs alone and when they are further functionalized with chitosan-mediated silver NPs.





Scheme 3.10 The synthesis path of (A) chitosan-mediated silver nanoparticles (CSAg) and (B) Covalent linkage of Pcs π (DNDs) to CSAg.

3.4.2.2. FT-IR Spectra

The FT-IR spectrum of CSAg presented a broad peak at 3361-3297 cm^{-1} indicating the predominance of O-H groups as some of the N-H groups are involved in the physical interaction with the silver metal surface (**Figure 3.15**). Generally, N-H functional groups possess a strong affinity to silver ions compared to O-H groups due to the difference in their electronegativity that dictates the deprotonation site which can favour the interaction of free electrons to the metal. The C=O stretch was observed at 1638 cm^{-1} for CSAg. The presence of these functional groups on the surface of the synthesized silver nanoparticles and the disappearance of the NH₂ double spike peak (of chitosan) at 3361-3297 cm^{-1} indicates that the silver nanoparticles were successfully capped by chitosan to form CSAg.

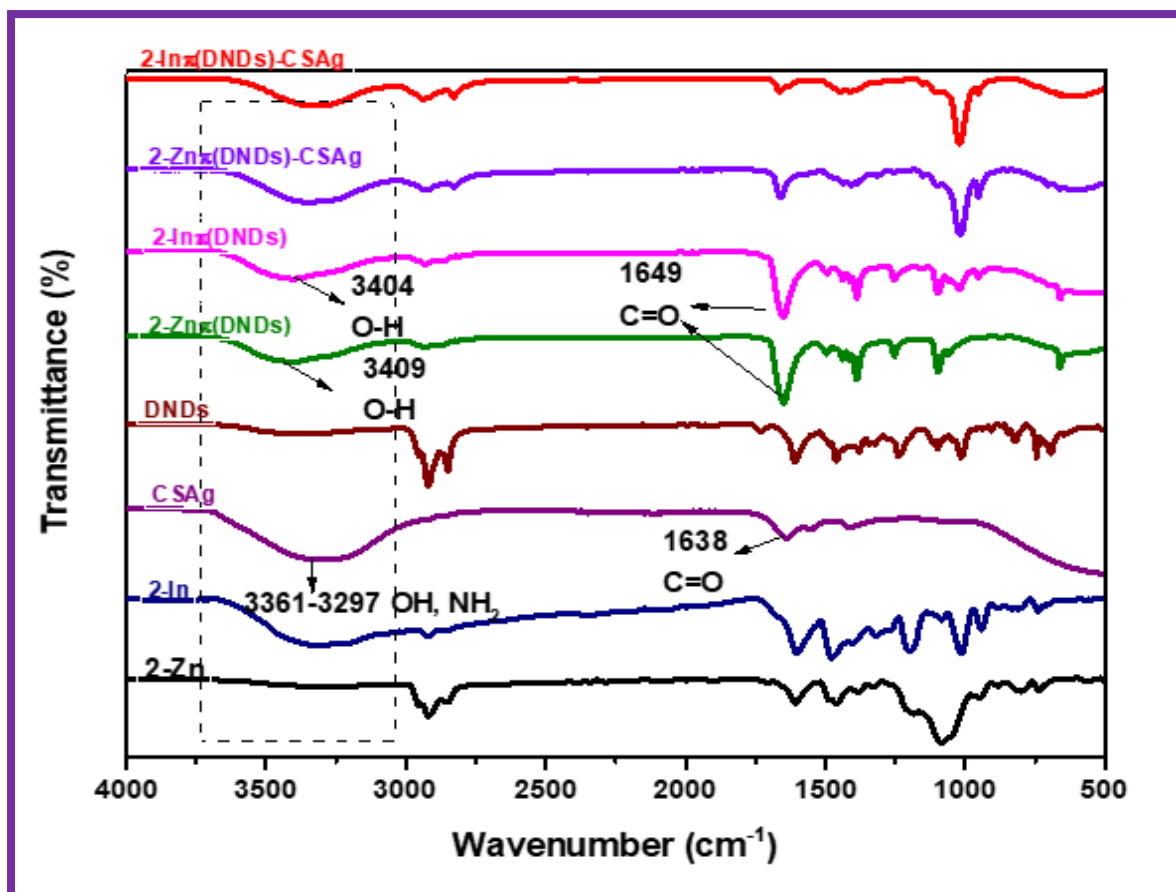


Figure 3.15 FT-IR spectra of Pcs alone, CSAg, DNDs, and all their respective nanoconjugates.

In the FT-IR spectra of the **2-Zn π (DNDs)** and **2-In π (DNDs)**, the C=O peaks emerging at 1649 cm^{-1} and broad vibration peaks at 3404 and 3409 cm^{-1} are associated with OH stretching confirming the presence of both Pc and DNDs. Following the amide linking to CSAg, C=O and O-H peaks in the CSAg spectrum shifted to higher frequencies.

3.4.2.3. UV-Vis Absorption and Emission Spectra

The ground state absorption spectra recorded in DMSO for π - π interaction between DNDs and **2-Zn** and **2-In** as well as the covalently linked Pcs π (DNDs-CSAg) nanoconjugates is shown in **Figure 3.16** and **Figure 4 A4 (Appendix 4)**. As observed, the formation of **2-Zn π (DNDs)**; **2-In π (DNDs)** and **2-Zn π (DNDs)-CSAg**; **2-In π (DNDs)-CSAg** resulted in a sharp increase in absorbance in the region below 650 nm. A red-shift in the Q-band of **2-Zn π (DNDs)**; **2-In π (DNDs)** is observed as compared to **2-Zn** and **2-In**, respectively, from **Table 3.3** while there are no differences in the Q band maxima for Pc in Pcs π (DNDs) or Pcs π (DNDs)-CSAg.

The DNDs, as mentioned above, and the chitosan alone did not exhibit any absorption peak, while an absorption peak is observed at 381 nm for CSAg. This peak is assigned to the surface plasma resonance (SPR) of Ag NPs.

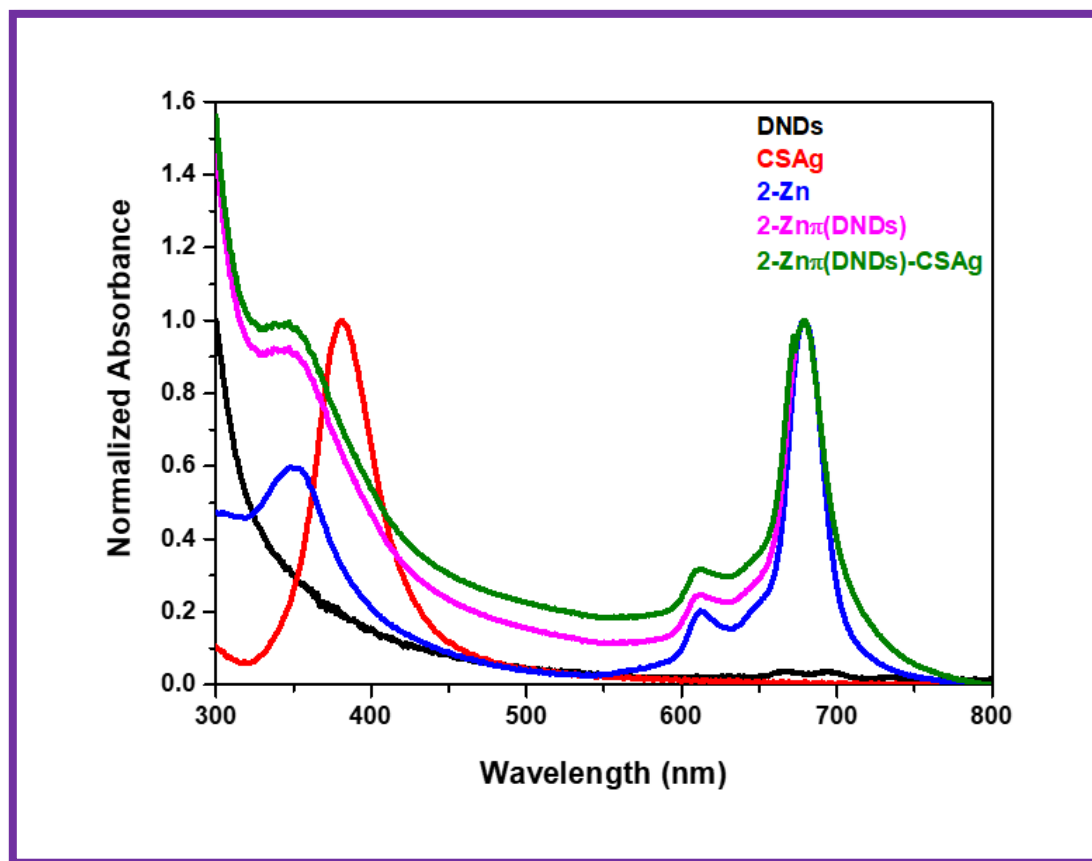


Figure 3.16 Electronic absorbance spectra of complex **2-Zn**, **2-Zn π (DNDs)**, and **2-Zn π (DNDs)-CSAg** in DMSO (as examples).

3.4.2.4. Raman Spectra

Upon conjugation of Pcs to DNDs, the G bands of DNDs shifted to a slightly higher frequency for **2-In π (DNDs)** (1595 cm^{-1}) and no shift was observed for **2-Zn π (DNDs)** (1591 cm^{-1}), while the D bands shifted to lower frequencies at around 1281 and 1284 cm^{-1} respectively, as shown in **Figure 3.17** and **Table 3.3**. The $I_D/I_G = 1.68$ for **2-Zn π (DNDs)** and 1.12 for **2-In π (DNDs)**, values that show an increase compared to that of DNDs alone (0.26), implying the presence of some defects on the DNDs. The Raman spectra of the **2-Zn π (DNDs)-CSAg** and **2-In π (DNDs)-CSAg** are not presented in this work. Increases in $I_D:I_G$ ratios has been previously attributed to the removal of some amorphous carbons and this reveals the effect of Pcs on the microstructure [242].

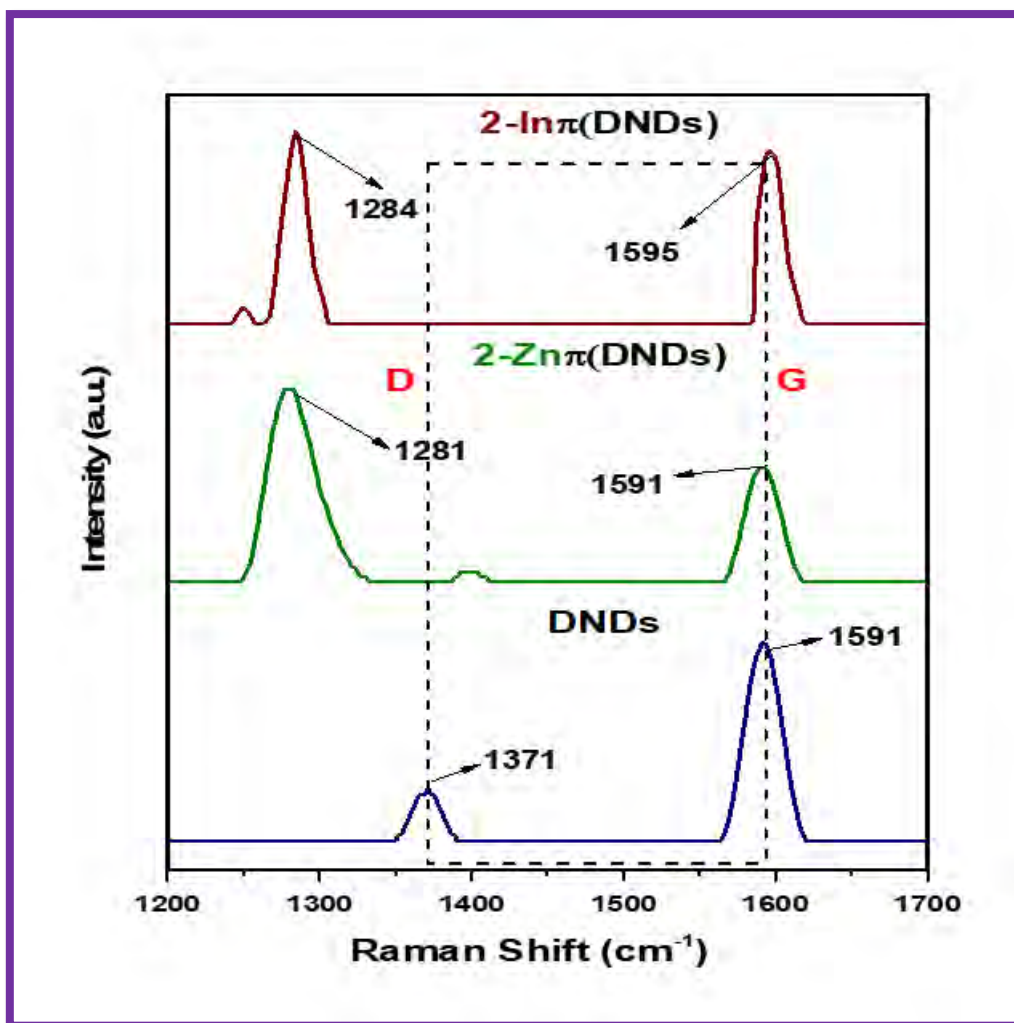


Figure 3.17 Raman spectra of DNDs alone, $2\text{-Zn}\pi(\text{DNDs})$, and $2\text{-In}\pi(\text{DNDs})$.

3.4.2.5. TEM Micrograph Analysis

In **Figure 3.18**, TEM images show that CSAg nanoparticles are spherical and monodispersed with an average size around 5 nm (**Table 3.3**).

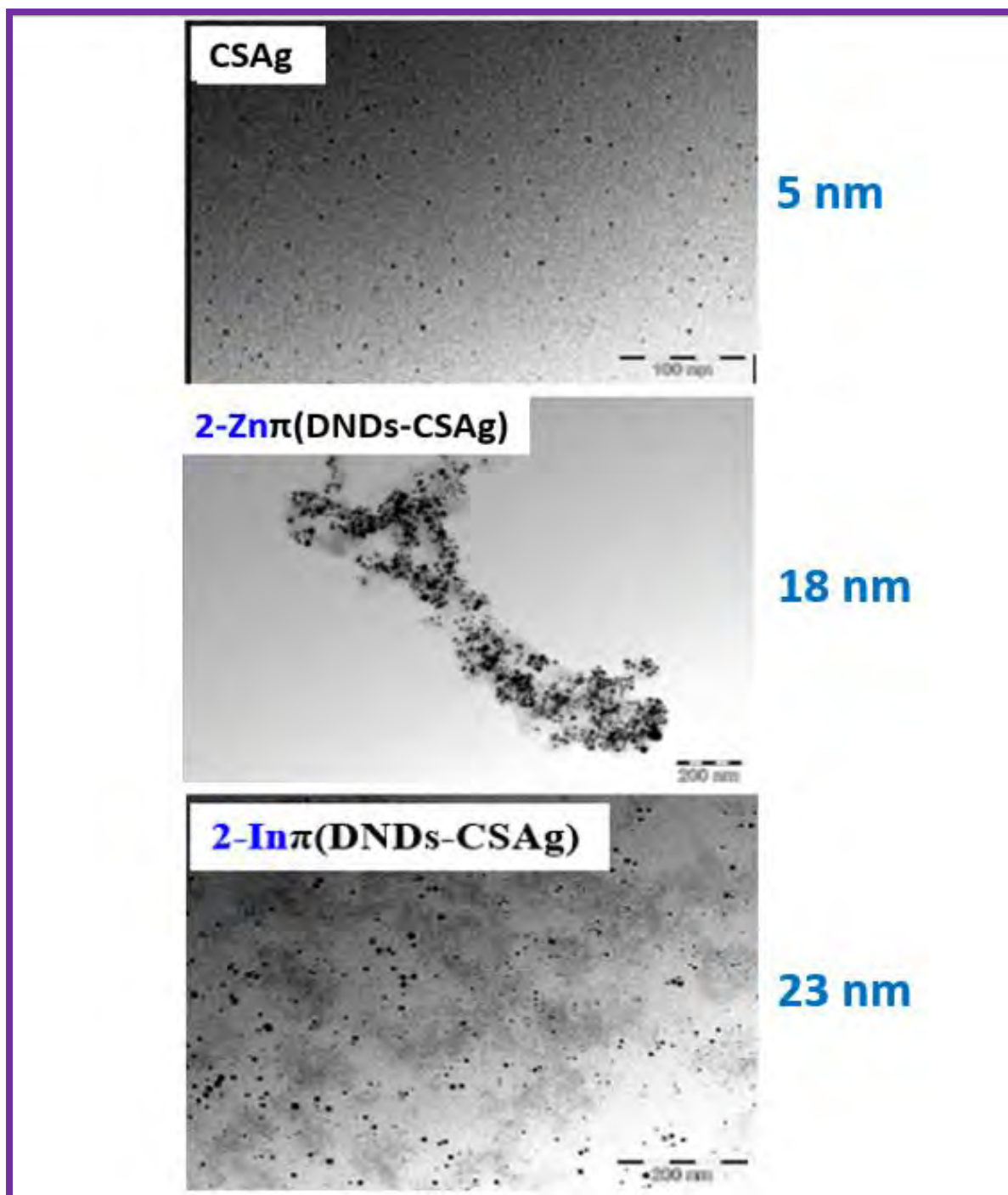


Figure 3.18 TEM images of CSAg, and the $\text{Pcs}\pi(\text{DNDs})\text{-CSAg}$ nanoconjugates showing the morphology and size increase upon conjugation.

Conjugation caused an increase in the sizes of $\text{Pcs}\pi(\text{DNDs})$ conjugates is observed as the sizes became 8 nm and 12 nm for $2\text{-Zn}\pi(\text{DNDs})$ and $2\text{-In}\pi(\text{DNDs})$, respectively (**Table 3.3**). The doubly conjugated compounds $2\text{-Zn}\pi(\text{DNDs-CSAg})$ (18 nm) and $2\text{-In}\pi(\text{DNDs-CSAg})$ (23 nm) show aggregation and an increase in the size as compared to their respective $\text{Pc}\pi\text{DNDs}$ (**Table 3.3**).

3.4.3. Effect of Quaternization: Conjugation of 3-Zn, 3-In, 3-ZnQ, and 3-InQ to DNDs

3.4.3.1. Synthesis

Group 3 complexes (3-Zn, 3-In, 3-ZnQ, and 3-InQ) are also noncovalently linked via π - π stacking interactions to DNDs to give 3-Zn π (DNDs), 3-In π (DNDs), 3-ZnQ π (DNDs), and 3-InQ π (DNDs), respectively (similar to Scheme 3.9B), a complete list of nanoconjugates is given in Table 3.3. The purpose of this type of nanoconjugates is to compare the effect of central metal and charges of Pcs following conjugation to DNDs.

As stated above, the nanoconjugates of DNDs and the Pcs were formed by π - π stacking interactions by taking the advantage of the presence of delocalized π -electron systems in the DNDs and the Pcs. Ionic interactions are also likely to occur between the DNDs and the quaternized Pcs. Ionic interactions between charged Pcs and charged fullerenes have been demonstrated [243].

3.4.3.2. UV-Vis Absorption and Emission Spectra

Following conjugation of Pcs to DNDs, slight spectral red-shifts are observed in all the spectra, except for 3-In π (DNDs) (Figures 3.19A,B and Table 3.3). Following π - π interactions formed between the Pcs and DNDs π systems, an enhancement in absorption below 600 nm is observed due to the presence of DNDs.

The quaternized nanoconjugates have a larger Pc loading on the DNDs at 737 and 536 μg (Pc)/mg (DNDs) for 3-ZnQ π (DNDs) and 3-InQ π (DNDs) respectively, as compared to the non-quaternized counterparts with mass loading of 383 and 146 μg (Pc)/mg (DNDs) for 3-Zn π (DNDs) and 3-In π (DNDs) respectively, Table 3.3. This may be justified by the strong ionic interactions between the positive charges on the Pcs substituents and the negative charges created by π electrons on the DNDs sheets for the quaternized derivatives, hence larger loading. And the smaller Pc mass loadings observed in the indium derivatives is due to the presence of chlorine axial ligand on the InPc that may limit the number of Pcs loaded due to the bulkiness [231].

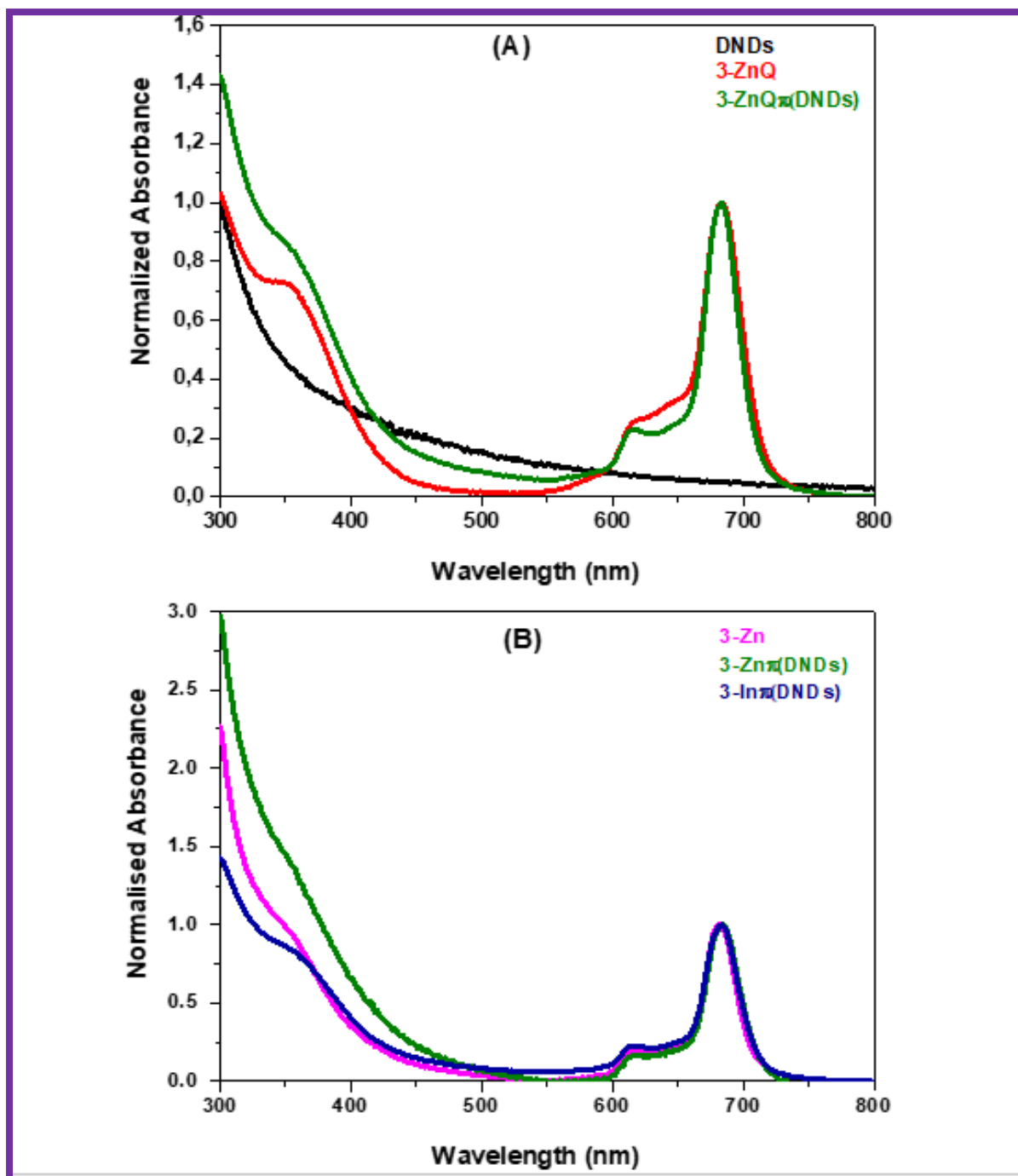


Figure 3.19 Normalized absorption spectra of: (A) DNDs and quaternized PSs and (B) non-quaternized PSs in DMSO (as examples).

3.4.3.3. Raman Spectra

In the spectra of the nanoconjugates, the G bands shifted to higher frequencies of 1597 and 1595 cm^{-1} for **3-Zn π** (DNDs) and **3-In π** (DNDs) respectively, while the D band of the DNDs did not show shifts as they remained at 1371 cm^{-1} for both **3-Zn π** (DNDs) and **3-In π** (DNDs).

In the quaternized nanoconjugates, the G bands shifted to lower frequencies of 1568 and 1574 cm^{-1} , for **3-ZnQ π** (DNDs) and **3-InQ π** (DNDs), respectively (**Table 3.3**). On the other hand, their D bands shifted to higher frequencies of 1379 and 1389 cm^{-1} , respectively.

The larger shifts and increase in the intensities of D-bands in the positively charged nanoconjugates may be due to more interaction from both π - π and electrostatic interactions. The increase in the I_D/I_G value observed in **Table 3.3** implies that there is the presence of sp^3 defects from Pcs on the sp^2 lattice of the DNDs which enhances the D-band [244].

3.4.3.4. TEM Micrographs

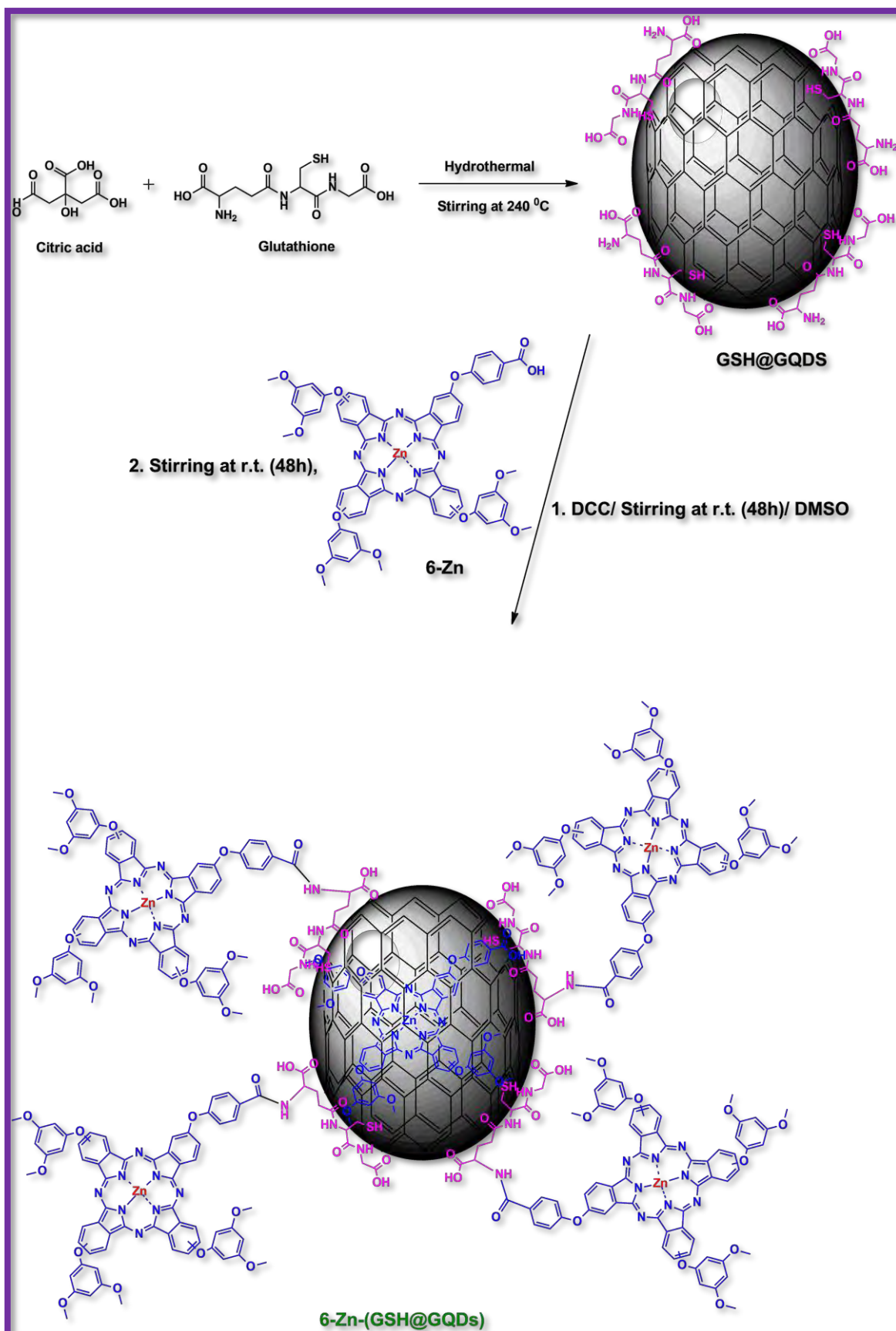
The obtained images confirmed that the DNDs were spherical and monodispersed. As shown in **Figure 3.13B** above the DNDs had average size of 2.4 nm. However, on conjugation, an increase in the sizes of Pcs@DNDs conjugates is observed as the sizes increased to ~8, 13, 18, and 22 nm for **3-Zn π** (DNDs) and **3-In π** (DNDs), **3-ZnQ π** (DNDs), and **3-InQ π** (DNDs) respectively, **Table 3.3**. The increase in size is due to aggregation following conjugation of Pcs to nanoparticles.

3.4.4. Effect of Symmetry: Conjugation of 5-Zn and 6-Zn to GSH@GQDs

3.4.4.1. Synthesis

5-Zn π (GSH@GQDs) nanoconjugate was obtained via physical π - π interactions of **5-Zn** onto the surface of GSH@GQDs in a similar manner to **Scheme 3.9B**.

The GQDs were capped with GSH is to provide NH_2 groups for possible covalent linking with the carboxylic acid functional group of **6-Zn** via an amide bond using DCC which activates the carboxylic acid groups for susceptible attack by the amine group [245] and the resulting nanoconjugate is labelled as **6-Zn**-(GSH@GQDs) (**Scheme 3.11**).



Scheme 3.11 Synthesis of GSH@GQDs and the covalent linkage of **6-Zn** to GSH@GQDs.

3.4.4.2. FT-IR Spectra

FT-IR spectra of GSH@GQDs, **6-Zn** and **6-Zn-(GSH@GQDs)** are shown in **Figure 3.20**.

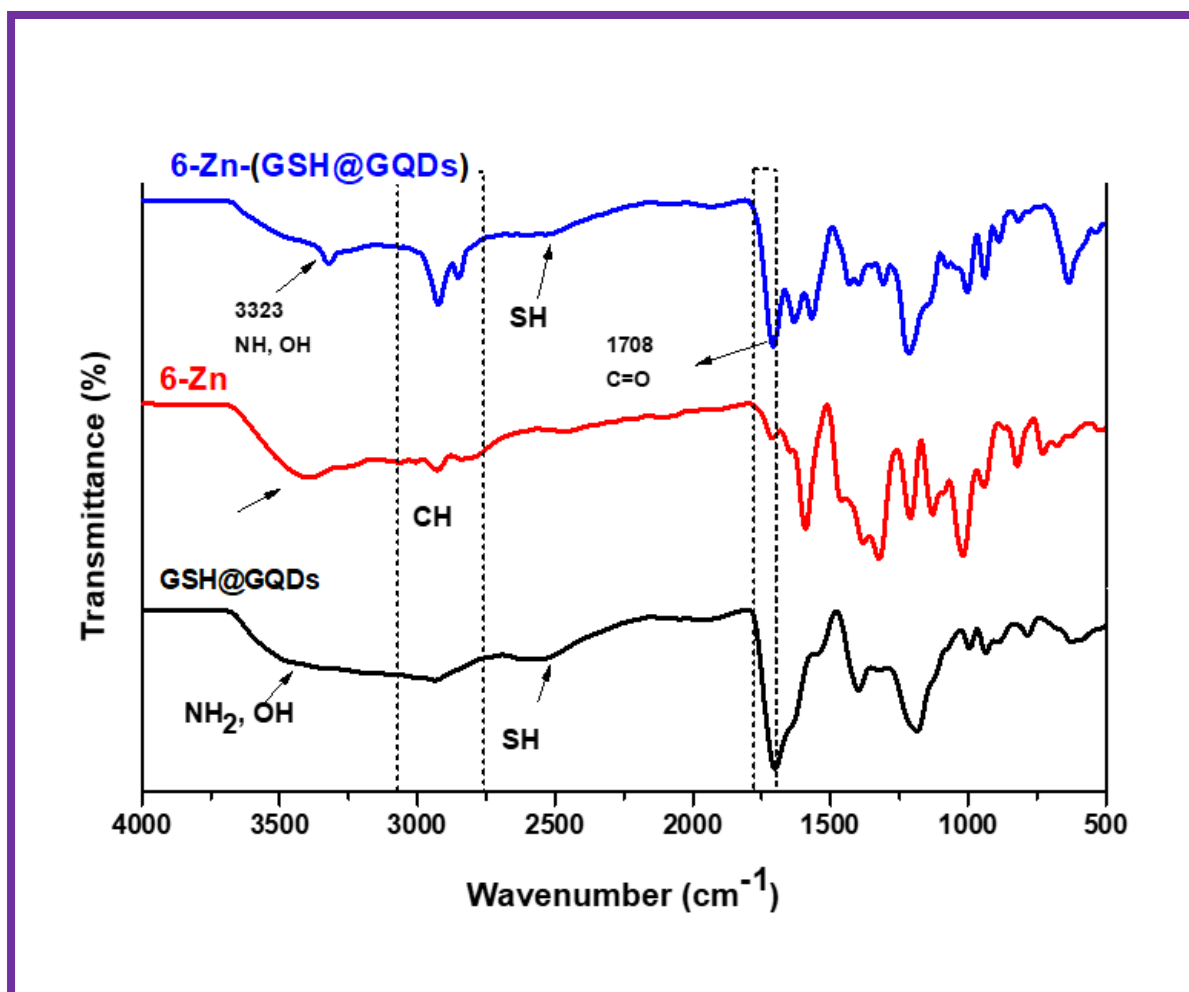


Figure 3.20 FT-IR spectra of GSH@GQDs, free Pcs and their nanoconjugates.

In the covalently linked nanoconjugate **6-Zn-(GSH@GQDs)** spectrum, the carbonyl vibrational stretch appeared at a lower frequency of 1708 cm⁻¹, indicating the successful formation of the amide bond. In addition, broader new shoulder due to NH and OH stretches show up at 3323 cm⁻¹ with increased intensity (**Figure 3.20**).

3.4.4.3. UV-Vis Absorption and Emission Spectra

The UV-Vis spectrum of the GSH@GQDs shows an absorption peak at 354 m (**Figure 3.21A**) which can be attributed to n→π* in C=O [246]. The absorption spectra of the π-π stacked **5-**

Zn π (GSH@GQDs) and amide-bonded **6-Zn**-(GSH@GQDs) nanoconjugates are also shown in **Figure 3.21A**. It is noteworthy that there were no significant shifts in the Q bands of **5** and **6** following conjugation to GSH@GQDs, but there was an increase in absorption in the region around where the GSH@GQDs absorb confirming the presence of both ZnPcs and the nanomaterial. To further characterize the optical properties, the fluorescence behaviors of the prepared symmetric and asymmetric GSH@GQDs nanoconjugates were studied in DMSO at room temperature. Firstly, the fluorescence spectra were recorded by exciting at a wavelength around where the Pcs absorb (λ_{exc} 610 nm). **Figure 3.21B** and **Figure 5 A4 (Appendix 4)** show typical maximum absorbance, excitation, and emission bands of Pcs and their nanoconjugates.

The Pc mass loading was ~ 186 of 3/mg of **5-Zn π** (GSH@GQDs) and ~ 198 of 4/mg of **6-Zn**-(GSH@GQDs), **Table 3.3**. GSH@GQDs as most carbon-based nanoparticles contain sp^2 hybridization that gives them great ability to form π - π interactions with other π electron-rich molecules such as Pcs [125,129]. Thus, the higher loading obtained for **6-Zn**-(GSH@GQDs) can be supported by the fact that in this conjugate, not only the covalent bonds (amide bond) are formed but there is also a possibility of **6-Zn** to π - π stack on the surface of the GSH@GQDs [125,129].

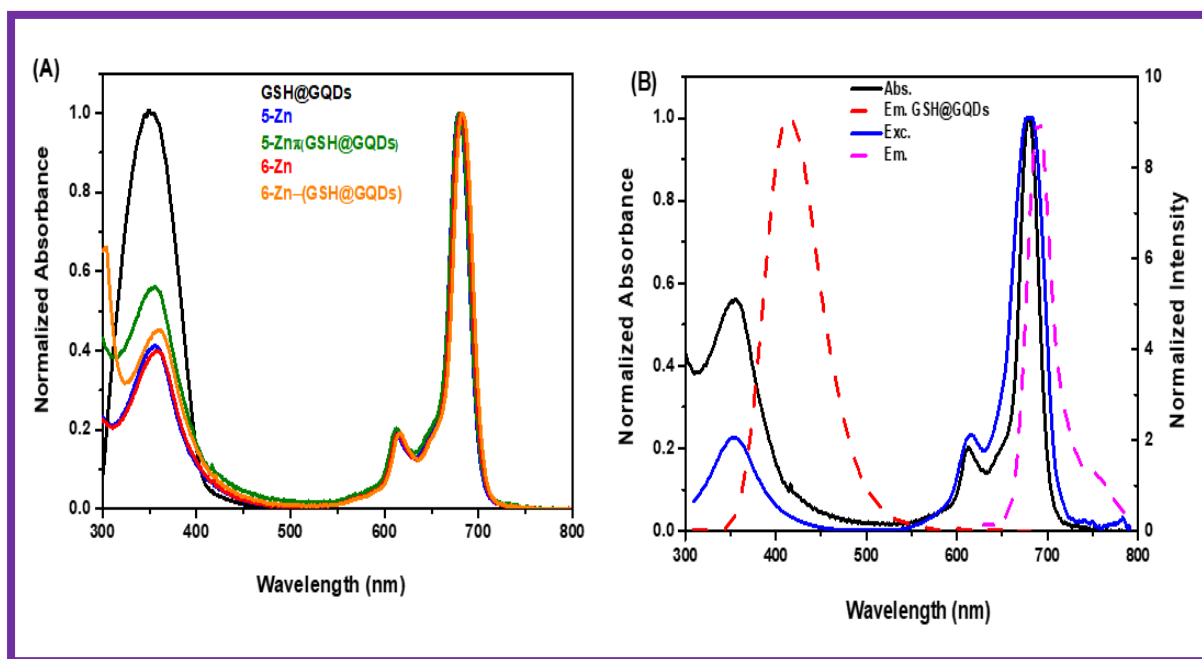


Figure 3.21 (A) UV-vis spectra of GSH@GQDs, free Pcs and their nanoconjugates in DMSO. (B) Absorption, excitation and emission spectra of **5-Zn π** (GSH@GQDs) and emission of GSH@GQDs alone in DMSO as an example.

3.4.4.4. DLS Analysis

The DLS data show an average size distribution in solution for GSH@GQDs, **5-Zn π** (GSH@GQDs), and **6-Zn**-(GSH@GQDs) at 8.7, 30.6, and 38.1 nm, respectively (**Table 3.3**). It is noteworthy that there are possibilities of **6-Zn** to also π - π stack on the GQDs surface in addition to the covalent bonds, thus giving a larger size of **6-Zn**-(GSH@GQDs). Size increase of nanoconjugates has been related to aggregations [247].

3.4.4.5. TGA and DSC Analysis

From the TGA curves depicted in **Figure 3.22A**, the nanoconjugates presented the highest thermal stability with increasing temperature; 41% and 5% weight loss for **5-Zn π** (GSH@GQDs) and **6-Zn**-(GSH@GQDs), respectively at 600 °C where 80% of the graphene structure of GSH@GQDs decomposes. The higher stability of conjugate **6-Zn**-(GSH@GQDs) might result from the high Pc loading as Pcs are reported to stabilize the thermal properties of compounds [147,148]. Generally, the decrease in mass observed in the region between 50-100 °C is due to the loss in moisture. The decrease observed around 297 °C is associated with the degradation of glutathione that was used to cap the GQDs.

Similar trends were also observed in the DSC plots (**Figure 3.22B**). The thermograms showed exotherms centered around 50-150 °C which are attributed to the degradation of unstable organic materials, solvents, and the evaporation of moisture present on the graphene surface. GSH@GQDs exhibit a significant endothermic peak at 200 °C due to the presence of glutathione, which has been reported in the literature [248].

A similar peak is observed in **5-Zn π** (GSH@GQDs) this may be attributed to free GSH present around the GQDs [241]. However, the peak is not present in **6-Zn**-(GSH@GQDs), this implies that all the available binding site carboxylic moiety have been consumed and the chemical bond (amide) is formed. In addition, the endothermic peak observed above 350 °C in the thermogram of **6-Zn**-(GSH@GQDs) can be related to the initiation of the decomposition of chemical groups covalently linked to the edges of the carbon backbone of GSH@GQDs [249,250].

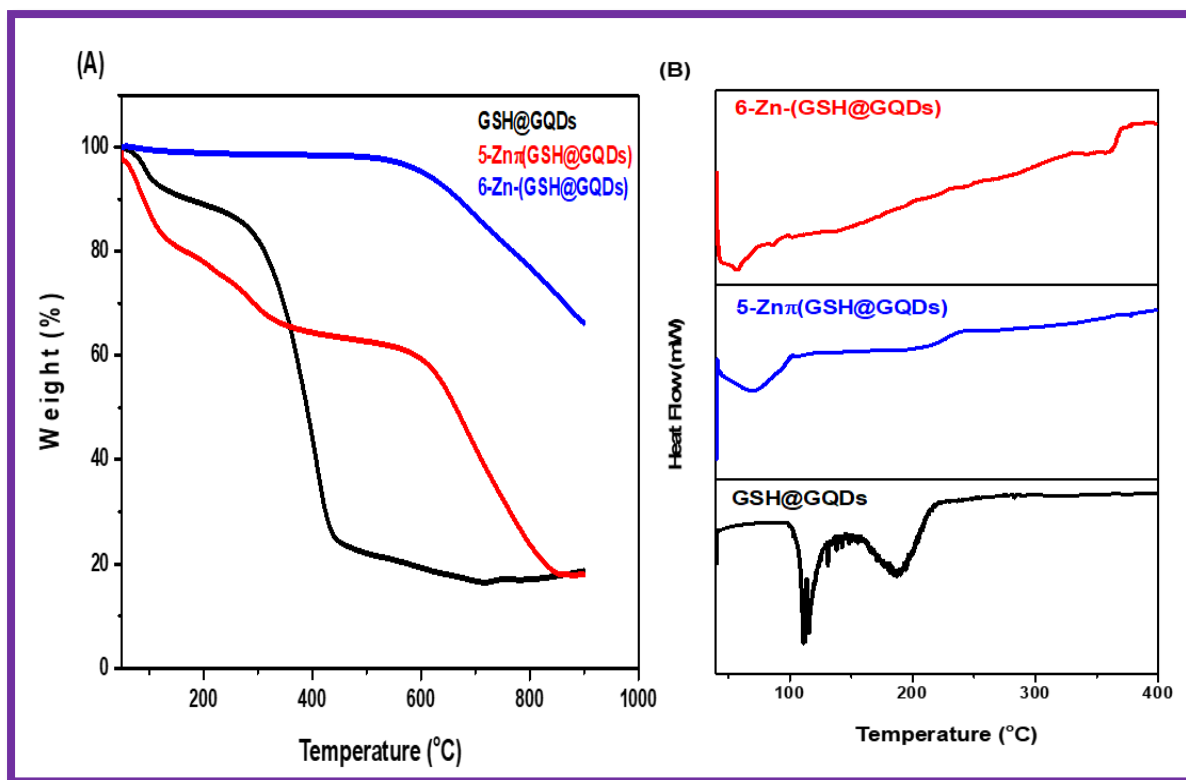
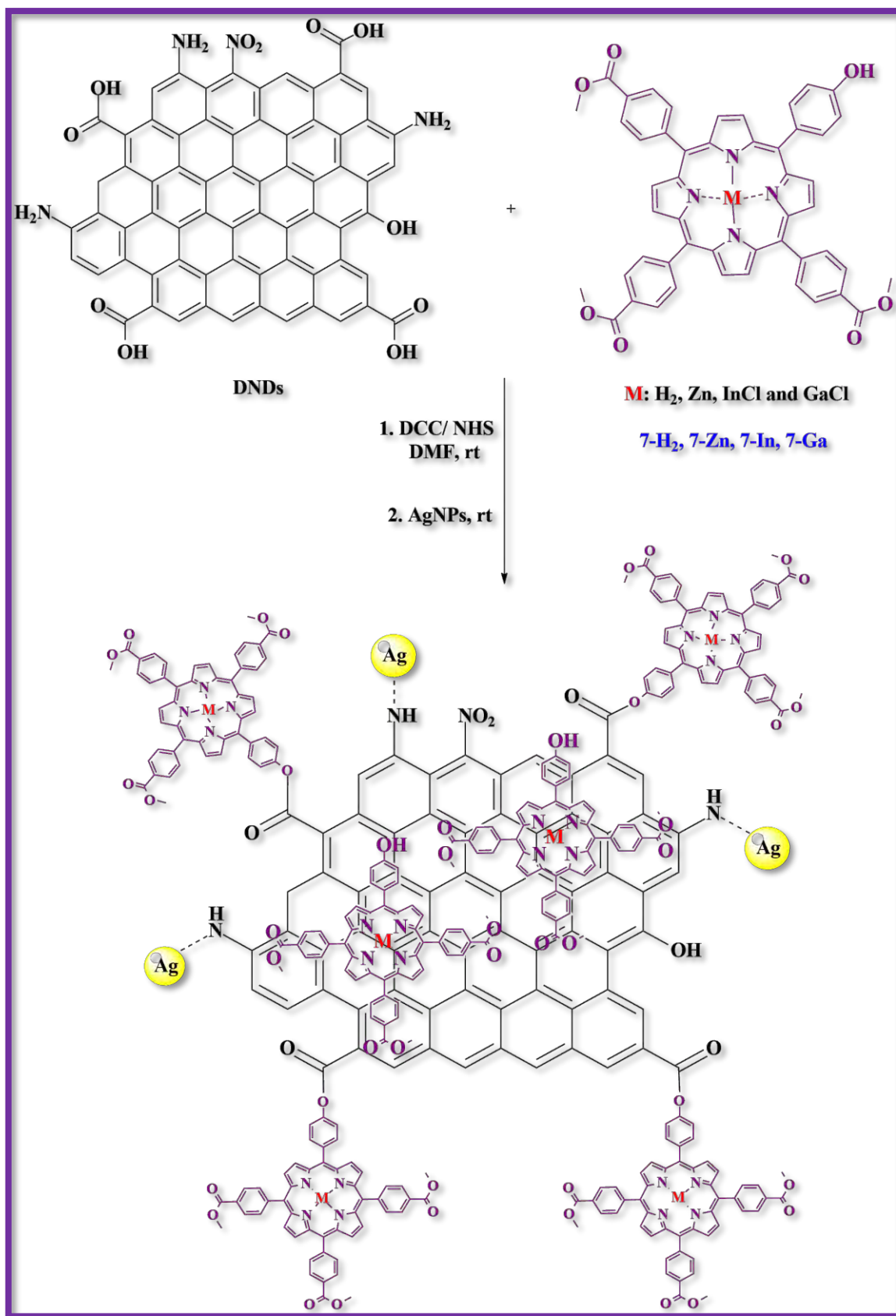


Figure 3.22 (A) TGA and (B) DSC analysis thermograms of GSH@GQDs alone and the Pc nanoconjugates.

3.4.5. Effect of Double Conjugation on Porphyrins: Conjugation of 7-H₂, 7-Zn, 7-In, and 7-Ga to DNDs then to Ag NPs

3.4.5.1. Synthesis

The nanohybrids 7-H₂-DNDs@Ag, 7-Zn-DNDs@Ag, 7-In-DNDs@Ag, and 7-Ga-DNDs@Ag, were acquired in one-step reaction by covalently linking the porphyrins to the DNDs via ester bonds, then nitrogen atoms on the DNDs and were linked to Ag NPs *via* physical interactions using the nitrogen-silver affinity (Scheme 3.12), to get more enhanced photoantimicrobial results due to the synergetic effects. The Ag NPs used in this study were obtained following a previously described synthetic procedure [162].



Scheme 3.12 The synthesis of porphyrin-DNDs@Ag nanohybrids from DNDs, Porphyrins alone, and Ag NPs.

3.4.5.2. FT-IR Spectra

The formation of the ester linkage between the porphyrins and the DNDs and then to Ag NPs was confirmed by FT-IR spectra (**Figure 3.23**). Hence the successful crafting of porphyrins to the DNDs can be confirmed by the evident increase in the intensity of OH and C=O groups as well as their shifts to higher frequencies in the spectra of the conjugates, suggesting a high predominance of these groups in the as-prepared nano hybrids since they contain both the porphyrins and the DNDs that also possess -OH and carboxylic C=O groups. Shifts in FT-IR bands confirm molecular interactions. The presence of silver ions can be noticed by the appearance of additional shoulder peaks at 1621 cm^{-1} and 1318 cm^{-1} .

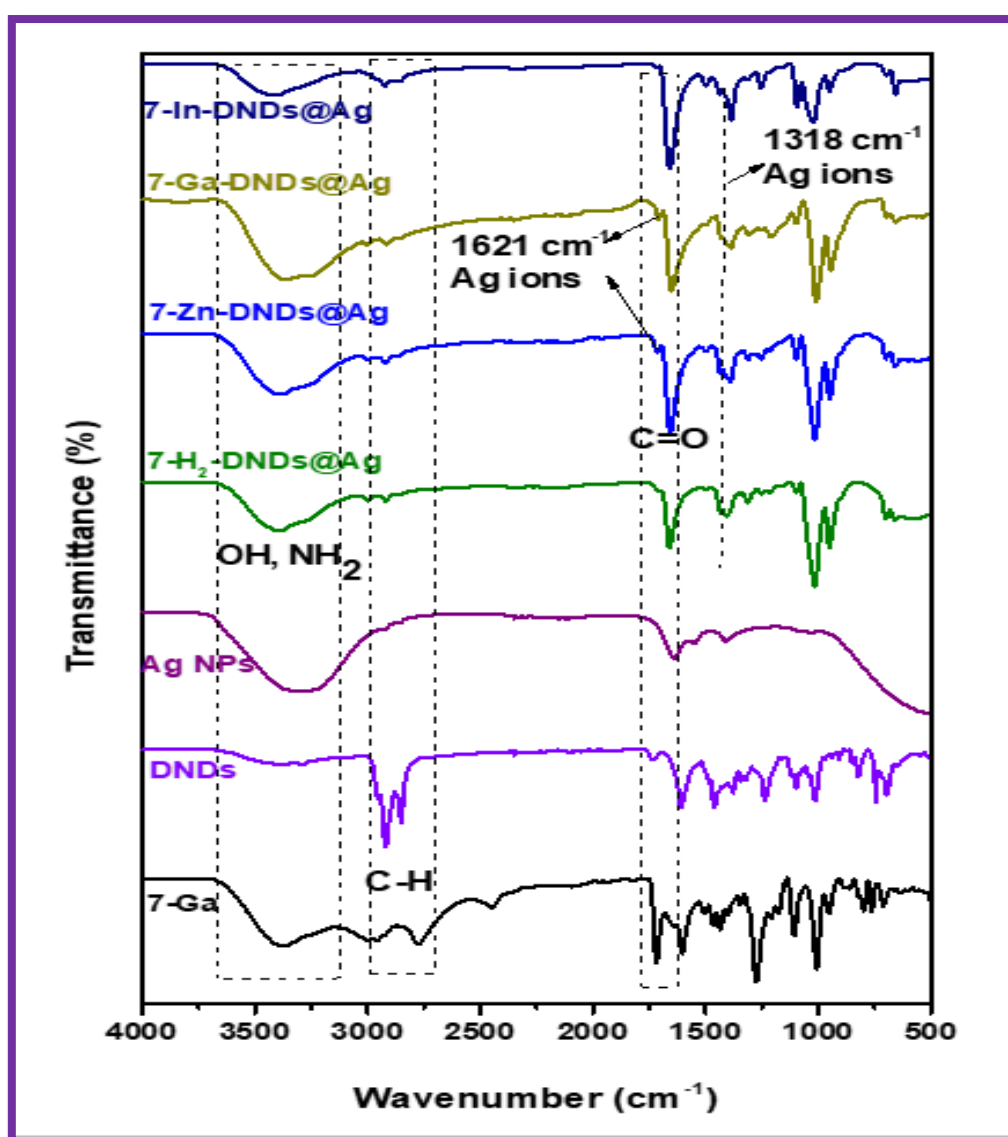


Figure 3.23 FT-IR spectra of (a) 7-Ga, (b) DNDs, (c) Ag NPs, (d) 7-H₂-DNDs@Ag, (e) 7-Zn-DNDs@Ag, (f) 7-Ga-DNDs@Ag, and (g) 7-In-DNDs@Ag.

3.4.5.3. UV-Vis Absorption and Emission Spectra

In **Figure 3.24A**, DNDs showed a broad feature with no absorption peak in the visible region as stated above, however, the Ag NPs showed a surface plasmon resonance (SPR) band at 380 nm. In the nanoconjugates spectra, the increased absorption in the region below 410 nm indicates the absorbance of the SPR band of Ag NPs which has an absorption wavelength almost close to the Soret band of the porphyrins but also the presence of DNDs (**Figures 3.24B, C and D**).

The slight spectral red-shifts compared to porphyrins alone in the Soret maxima for porphyrins in **7-H₂-DNDs@Ag** (422 nm), **7-Zn-DNDs@Ag** (429 nm), **7-In-DNDs@Ag** (431 nm), and **7-Ga-DNDs@Ag** (431 nm) following conjugation (**Table 3.3**) are brought by J aggregation. These slight red shifts were also seen in the tetrasulfonated zinc Pc-graphene complex and were related to a J-type aggregation [229].

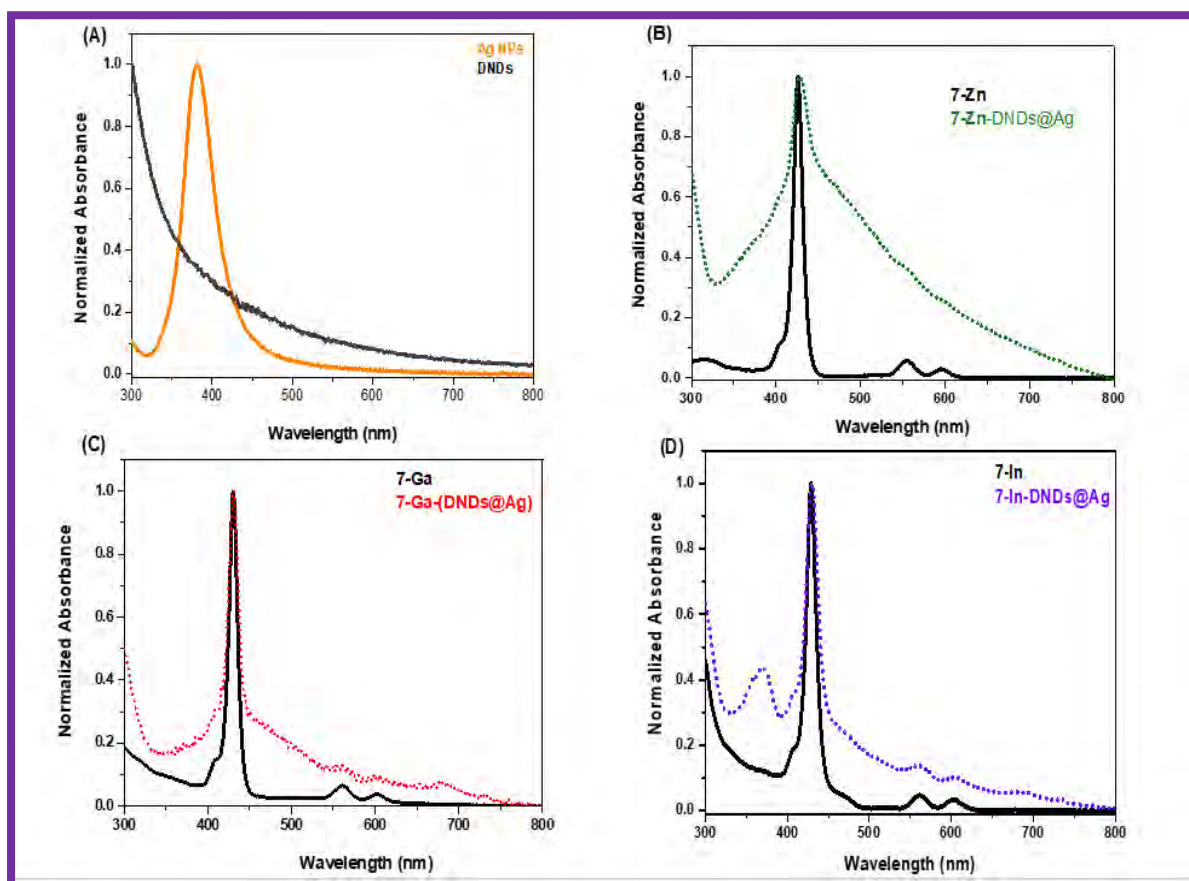


Figure 3.24 Electronic absorption spectra of (A) DNDs and Ag NPs and (B) **7-In** and **7-In-DNDs@Ag** and (C, D) Emission spectra of **7-H₂-DNDs@Ag** and **7-Zn-DNDs@Ag** in DMSO (used as examples).

The mass loading of the respective porphyrins was 893, 854, 747, and 802 μg (porphyrin)/mg DNDs@Ag for **7-H₂-DNDs@Ag**, **7-Zn-DNDs@Ag**, **7-In-DNDs@Ag**, and **7-Ga-DNDs@Ag**, respectively. The observed higher loadings are most likely due to the presence of both π - π interactions and the ester bond. **7-H₂-DNDs@Ag** showed the highest loading due to the absence of central metal whose size can limit strong interactions between the molecule and the DNDs surface.

3.4.5.4. TEM Analysis

As noticed, the acquired images in **Figure 3.25** show that the DNDs and the Ag NPs were spherical with average sizes of 2.4 nm and 7 nm, respectively. The size increased as a result of aggregation caused by conjugation to complexes. The size became \sim 13, 20, 24, and 31 nm for **7-H₂-DNDs@Ag**, **7-Zn-DNDs@Ag**, **7-Ga-DNDs@Ag**, and **7-In-DNDs@Ag**, respectively, **Table 3.3**.

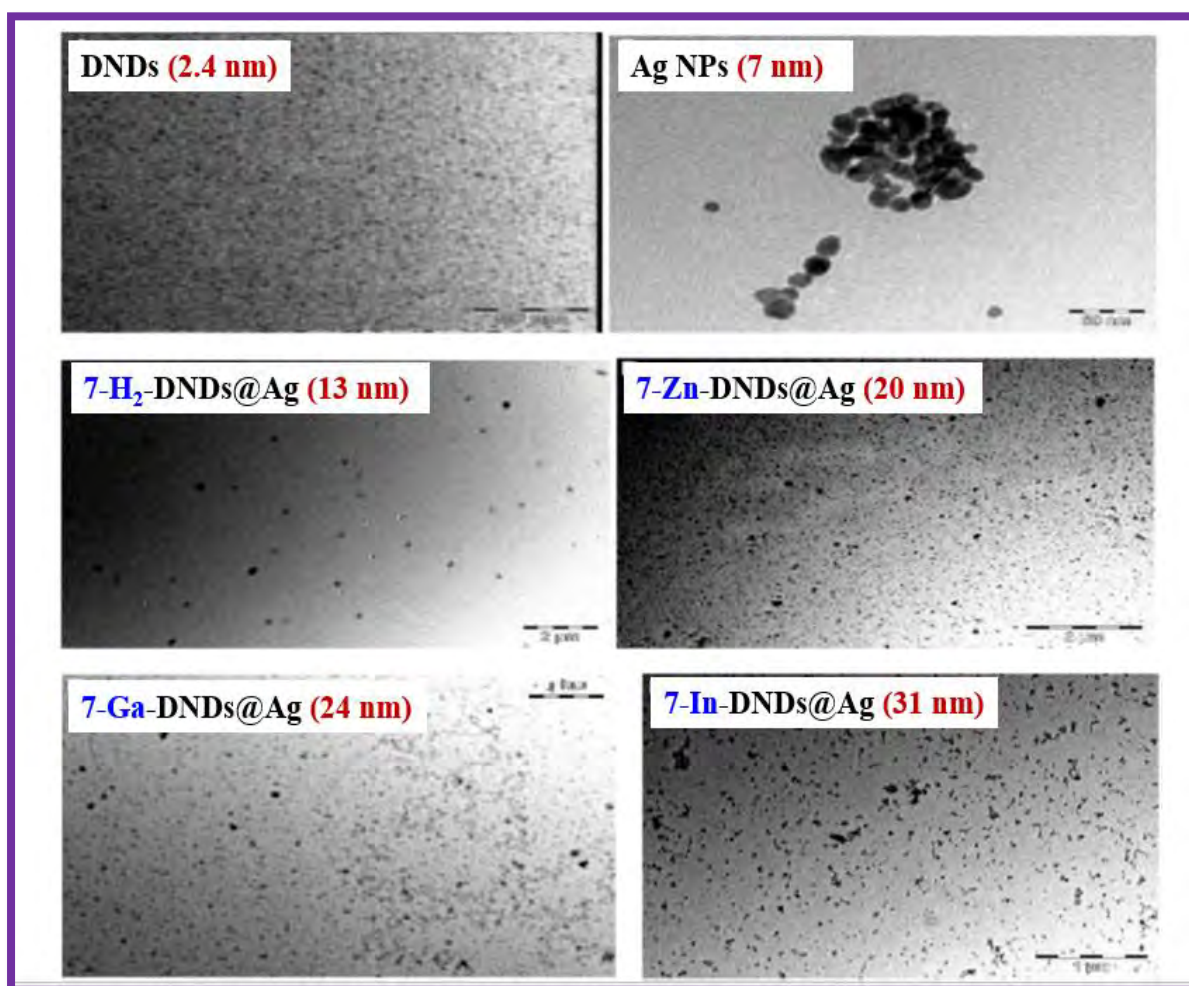


Figure 3.25 TEM images of DNDs, Ag NPs, **7-H₂-DNDs@Ag**, **7-Zn-DNDs@Ag**, **7-Ga-DNDs@Ag**, and **7-In-DNDs@Ag** (showing the size and morphology).

3.4.5.5. TGA Analysis

To determine the thermal stability of these compounds, the weight loss was estimated as a function of temperature. To do so, the experiments were recorded at atmospheric pressure under nitrogen flow at a temperature from 50 up to 1000°C with a heating rate of 10°C/min.

Complex **7-In** alone starts to decompose at approximately 280 °C, while the DNDs start to oxidize around 679 °C. In comparison to the nanohybrids, at 679 °C, the weight loss was 88%, 62%, 48%, and 40% for **7-H₂-DNDs@Ag**, **7-Zn-DNDs@Ag**, **7-In-DNDs@Ag**, and **7-Ga-DNDs@Ag** respectively, **Figure 3.26**. Thus, upon functionalizing the DNDs with complex **7-In** (22% weight loss) used as an example and the Ag NPs, decreased weight loss was observed compared to the DNDs alone 99% at 679 °C, thus indicating improvement in thermal stability of DNDs. Similar trends were also observed for DNDs functionalized with silicon phthalocyanines [153] and single-walled carbon nanotubes (SWCNTs) following their functionalization to zinc monocarboxyphenoxy phthalocyanine spermine [251]. Complete weight loss (100%) of the DNDs was observed around 679 °C and at this temperature, the conjugates lost weight was 37%, 59%, 76%, and 51% for **7-H₂-DNDs@Ag**, **7-Zn-DNDs@Ag**, **7-Ga-DNDs@Ag**, and **7-In-DNDs@Ag**, respectively as shown in **Figure 3.26**.

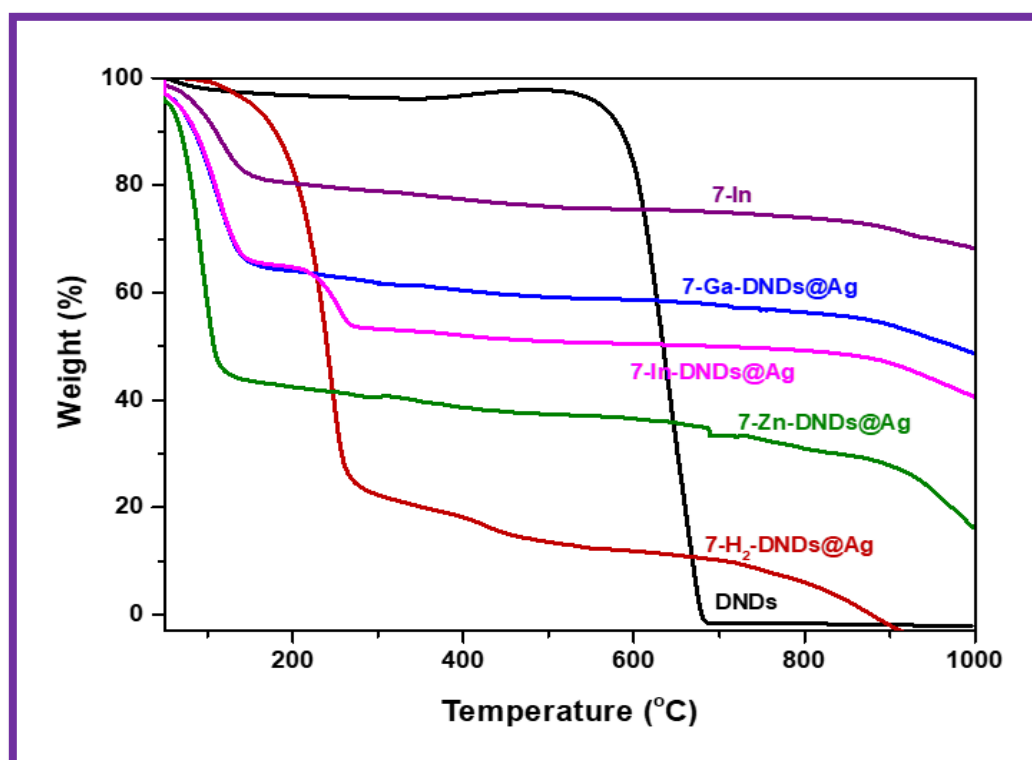


Figure 3.26 TGA spectra of **7-In**, DNDs, **7-H₂-DNDs@Ag**, **7-In-DNDs@Ag**, **7-Zn-DNDs@Ag**, and **7-Ga-DNDs@Ag**.

3.5. Summary of the Chapter

In summary, a series of novel photosensitizers for targeted PACT/PDT have been prepared and characterized using appropriate spectroscopic and analytical techniques (NMR, MS, CHNS elemental analysis, UV-Vis, and FT-IR). The PSs comprise neutral metalated asymmetrical and symmetrical Pcs (**Groups 1-6**) and porphyrins (**Groups 7 and 8**) along with their respective quaternized derivatives (please refer to **Table 1.2** for different groups). The Q-bands varied with respect to central metal, substituent in the macrocycle, positive charges, symmetry, and solvent effect as complexes showed broadening and splitting of the Q-band in water due to aggregation.

The complexes were functionalized with either GQDs, DNDs, GSH@GQDs. Whereas the **group 2** Pcs/DNDs and **group 7** porphyrins/DNDs nanoconjugates were further functionalized with CSAg and Ag NPs respectively (**Table 1.2**). the functionalization was achieved through π - π , ester and amide linkage and the resulting products were fully characterized using UV-Vis, FT-IR, Laser Raman, TEM, DLS, TGA, and DSC which confirmed the successful formation of the nanoconjugates. In most cases, the Q band λ_{\max} of the nanoconjugates were red-shifted in comparison to that of the corresponding complex alone.

The complexes mass loading into the nanomaterials was also investigated using spectroscopic techniques. DNDs with the least size relative to GQDs, showed the highest mass loading due to its larger surface area.

The TEM and DLS sizes of the nanomaterials showed an increase upon conjugation to complex and the bigger sizes were obtained for the indium derivatives due to their bigger radius. TGA was also run to indicate thermal stability of the nanomaterials upon conjugation to photosensitizers.

Chapter Four: Photophysical and Photochemical Parameters

The focus of this chapter is to discuss the photophysical and photochemical characterization`

4.1. Fluorescence Quantum Yields (Φ_F) and Lifetimes (τ_F)

Fluorescence quantum yields (Φ_F) and lifetime (τ_F) values are determined in DMSO and the obtained data are reported in **Table 4.1**.

Table 4.1 Fluorescence quantum yields and lifetimes of Pcs and nanoconjugates in DMSO.

Complex	Φ_F (Pc)	τ_F (Pc) (ns)	<i>Eff</i> (%)	Φ_F (GQDs / GSH@GQDs)	τ_F (GQDs / GSH@GQDs) (ns)	Φ_F (chalcone)
Group 1: Acetophenoxy-substituted Pcs and nanoconjugates						
GQDs	-	-	-	0.35	6.1	-
1-H₂	0.20	4.20	-	-	-	-
1-Zn	0.13	2.21	-	-	-	-
1-In	0.05	0.89	-	-	-	-
1-H₂π (GQDs)	0.11	1.69	89	0.039	4.22	-
1-Znπ (GQDs)	0.06	0.85	88	0.043	2.85	-
1-Inπ (GQDs)	0.05	0.95	91	0.033	4.67	-
1-H₂π (DNDs)	0.10	3.11	-	-	-	-
1-Znπ (DNDs)	0.09	0.24	-	-	-	-
1-Inπ (DNDs)	0.07	0.07	-	-	-	-
Group 2: Bromo-aminophenoxy-substituted Pcs and nanoconjugates						
2-Zn	0.07	2.32	-	-	-	-
2-In	0.03	1.15	-	-	-	-
2-Znπ (DNDs)	0.06	0.98	-	-	-	-
2-Inπ (DNDs)	0.02	0.04	-	-	-	-
2-Znπ (DNDs)-CSAg	0.05	0.76	-	-	-	-
2-Inπ (DNDs)-CSAg	0.02	< 0.01	-	-	-	-
Group 3: Pyridyl chalcone-substituted Pcs and nanoconjugates						
Chalcone i	-	-	-	-	-	0.13
3-Zn	0.07	2.97	92	-	-	0.010
3-In	0.04	2.84	92	-	-	0.011
3-ZnQ	0.07	2.91	89	-	-	0.014
3-InQ	0.02	2.26	90	-	-	0.013

3-Znπ (DNDs)	0.05	2.81	46	-	-	0.07
3-Inπ (DNDs)	0.04	2.49	54	-	-	0.06
3-ZnQπ (DNDs)	0.03	2.22	31	-	-	0.09
3-InQπ (DNDs)	0.02	2.02	31	-	-	0.09
Group 4: Dimethylamino chalcone-substituted Pcs and nanoconjugates						
Chalcone ii	-	-	-	-	-	0.18
4-Zn	0.06	2.88	92	-	-	0.014
4-In	< 0.01	2.46	94	-	-	0.011
4-ZnQ	0.05	2.88	93	-	-	0.012
4-InQ	0.02	2.36	95	-	-	0.008
Groups 5-6: Tetra and monocarboxylic acid-substituted Pcs and nanoconjugates						
GSH@GQDs	-	-	-	0.27	-	-
5-Zn	0.25	3.10	-	-	-	-
6-Zn	0.22	3.01	-	-	-	-
5-Znπ (GSH@GQDs)	0.18	3.06	66	0.093	-	-
6-Zn-GSH@GQDs	0.14	2.15	68	0.087	-	-

The Φ_F is defined as the ratio of the number of photons emitted to the number of photons absorbed by a PS [179]. The Φ_F for both the PSs and nanoconjugates were determined by comparative methods as defined in the literature with **Equation 2.1** shown in **Chapter two**. ZnPc was used as a standard in DMSO with $\Phi_F = 0.2$ [155].

The τ_F refers to the average time a molecule spends in its first singlet excited state before it undergoes the fluorescence process [180]. In this work, the τ_F values of studied complexes were obtained from the fluorescence decay curve using the TCSPC method.

4.1.1. Phthalocyanine Complexes and Nanoconjugates

For all Pcs alone, the fluorescence decay shows a monoexponential behavior confirming one lifetime. However, for the nanoconjugates, a biexponential behavior was observed, indicating two lifetimes, probably due to the orientation of Pcs around the nanomaterials (**Figure 4.1**, **6-Zn** and **6-Zn-(GSH@GQDs)**) used as examples.

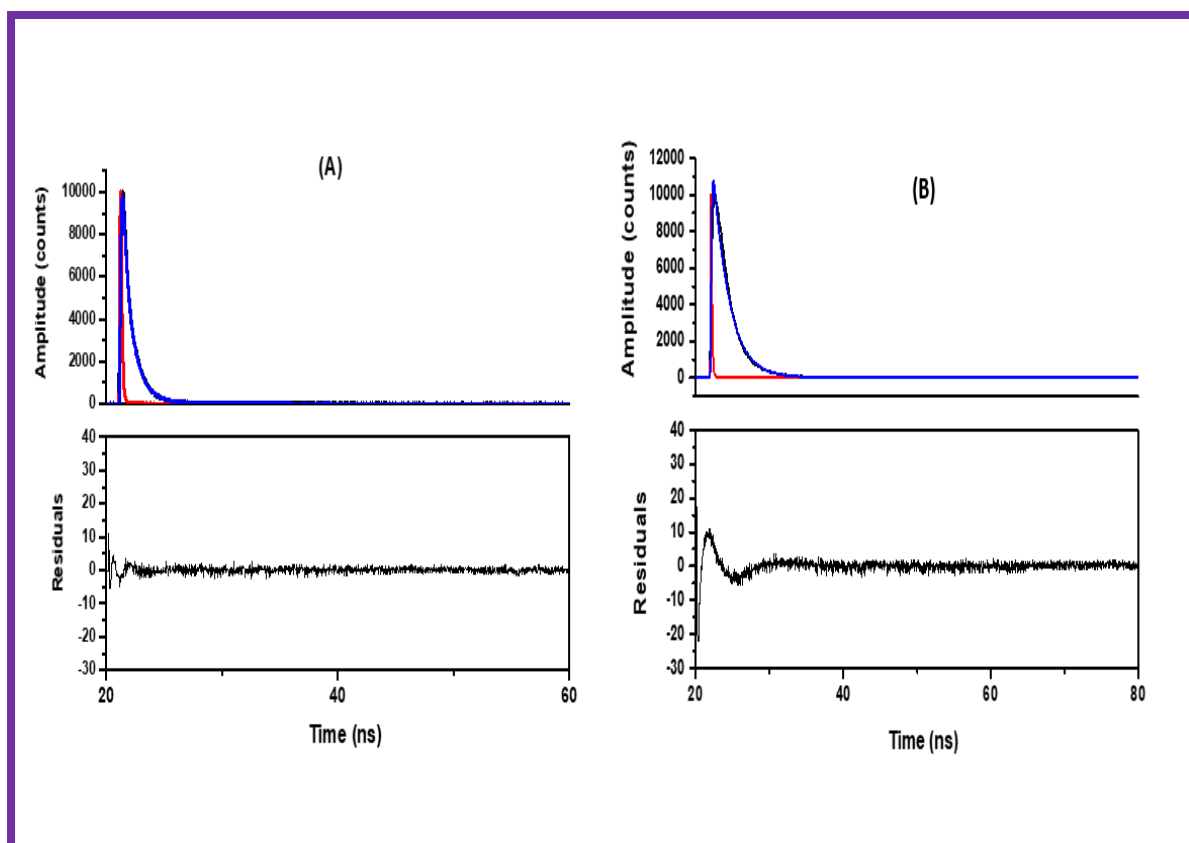


Figure 4.1 Time-resolved emission data (decay traces and fits) for (A) complex **6-Zn** (B) **6-Zn-(GSH@GQDs)** (used as examples).

4.1.1.1. Effect of Central Metal

As it can be seen in **Table 4.1**, the comparison of Φ_F values of Pcs bearing the same substituents shows that Φ_F values are lower depending on the type of central metal and this is justified by the heavy central metal effect which is known to favour intersystem crossing to the triplet state [252,253]. Since In (III) is a heavier metal ion than Zn (II), in all cases, the Φ_F and τ_F values are lower for the indium Pc derivatives compared to their zinc counterparts. For instance, comparing **1-H₂**, **1-Zn**, and **1-In** complexes, the free-base Pc **1-H₂** has the highest Φ_F value of 0.20 (with $\tau_F = 4.20$) due to lack of heavy central metal on its core.

4.1.1.2. *Effect of Substituents*

Table 4.1 shows that the substituted zinc Pcs **1-Zn**, **2-Zn**, **3-Zn**, and **4-Zn** for example, have Φ_F values of 0.13, 0.007, 0.07, and 0.06, respectively. These values are lower compared to the unsubstituted ZnPc standard at 0.20 in DMSO. This is due to the quenching effect of the substituents. The type of substituent on the Pc macrocycle is known to affect Φ_F values [252]. However, the Φ_F value of **5-Zn** was higher at 0.25.

4.1.1.3. *Effect of Positive Charges*

The Φ_F values of the quaternized Pcs (**3-ZnQ**, **3-InQ**, and **4-ZnQ**) are lower or similar when compared to the corresponding non-quaternized entities (**3-Zn**, **3-In**, and **4-Zn**), **Table 4.1**. This explains that quaternization can inhibit fluorescence so that it reduces Φ_F and shortens τ_F even though chalcone compounds are fluorescents by nature. However, it is not clear why **4-InQ** has a slightly higher Φ_F value than **4-In**.

4.1.1.4. *Effect of Symmetry*

Comparing the Φ_F value for **6-Zn** is slightly reduced compared to the symmetrical analogue **5-Zn** (at $\Phi_F = 0.25$ and 0.22, respectively). As reported before, this could be due to self-quenching or intersystem crossing [254]. The τ_F data also kept the same trend.

4.1.1.5. *Effect of Nanomaterials*

Generally, upon conjugation of Pcs to DNDs or GQDs, lower Φ_F (except for **1-In π** (DNDs)) and τ_F values are obtained for the nanoconjugates as compared to Pcs alone, **Table 4.1**. This reduction could be possibly due to the quenching effect of Pcs fluorescence by the nanomaterials, thanks to the electron-donating groups present on their surfaces. It is reported that electron-donating groups increase ISC in porphyrins-like complexes [185].

Increases or decreases in the fluorescence lifetimes may depend on the geometry or distance between the metal and Pc core [255]. The variation in fluorescence properties includes the decrease of emission efficacy and reduction of fluorescence lifetime. Aggregation also leads to a population of more short-lived emitting species [256].

For the nanoconjugates containing Ag NPs, there will be fluorescence quenching by the Ag NPs [257] which is due to the heavy atom effect of the latter. The τ_F values were also shortened for the same reasons, **Table 4.1**.

The GQDs had $\Phi_F = 0.35$ and GSH@GQDs $\Phi_F = 0.27$ when exciting at $\lambda_{exc} = 340$ nm (where the nanoparticles absorb). These values are considerably decreased in their respective nanoconjugates as they were found to be way lower than the nanomaterials alone (please see **Table 4.1**). Due to chalcone being fluorescent compounds, complexes **4-Zn**, **4-In**, **4-ZnQ**, and **4-InQ** (as well as **Group 3 Pcs**) were also excited at $\lambda_{exc} = 400$ nm (where chalcone absorbs) and the same tendency was observed as well. This decrease in Φ_F values could be due to FRET process [181].

4.1.1.6. FRET

FRET occurs if there is overlap between the emission spectra of the donor (nanomaterials) and the absorption spectra of the acceptor (Pcs) as illustrated in (**Figure 4.2**). When exciting where the nanomaterial absorbs, the fluorescence resonance energy is transferred from the nanomaterial to the nanoconjugate in the ground state, hence causing a fluorescence quenching of the nanomaterial by the Pc. However, it is important to note that other parameters such as photoinduced energy transfer (PET) which occur when only one of the components changes its spectral characteristics [181,183], and inter charge transfer (ICT) between functional groups on the substituents and nanomaterials may also take place to deactivate the excited states.

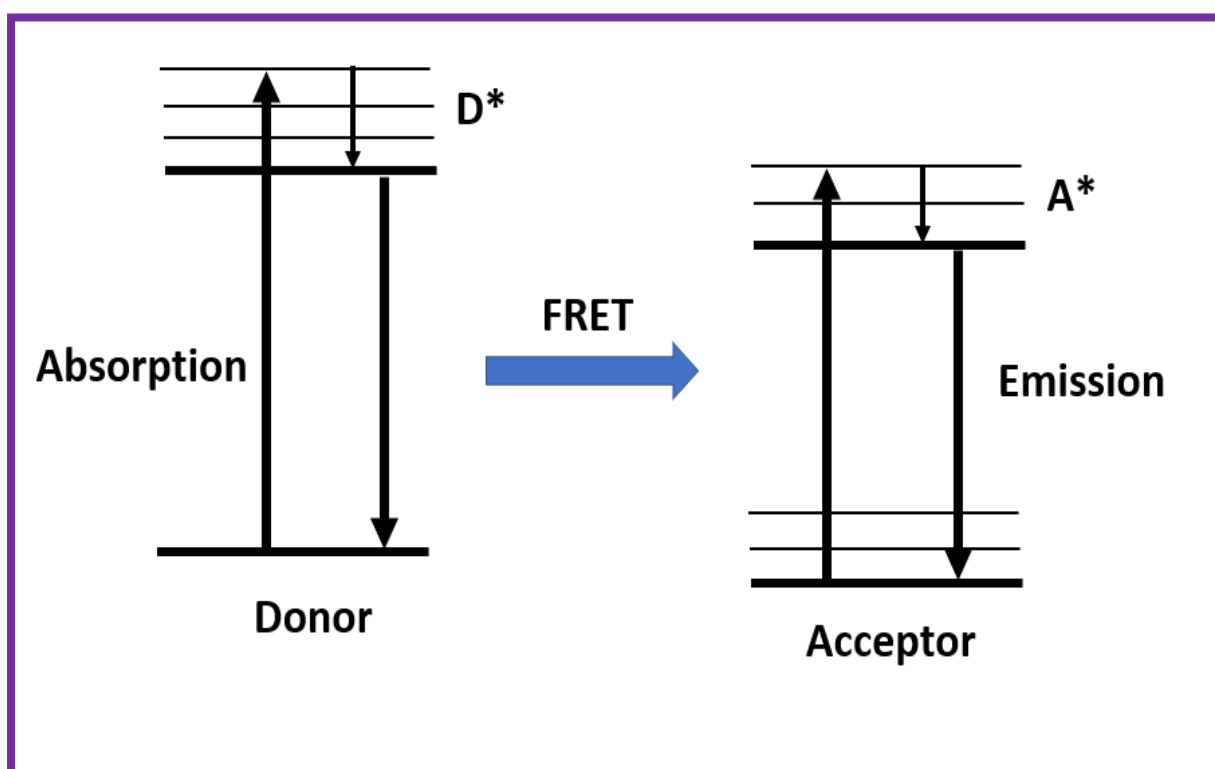


Figure 4.2 Image showing the principle of FRET process.

The GQDs and GSH@GQDs display a characteristic emission band at 445 and 453 nm, respectively when excited at 340 nm (**Figure 4.3**), while the DNDs used in this work did not show any fluorescence behavior.

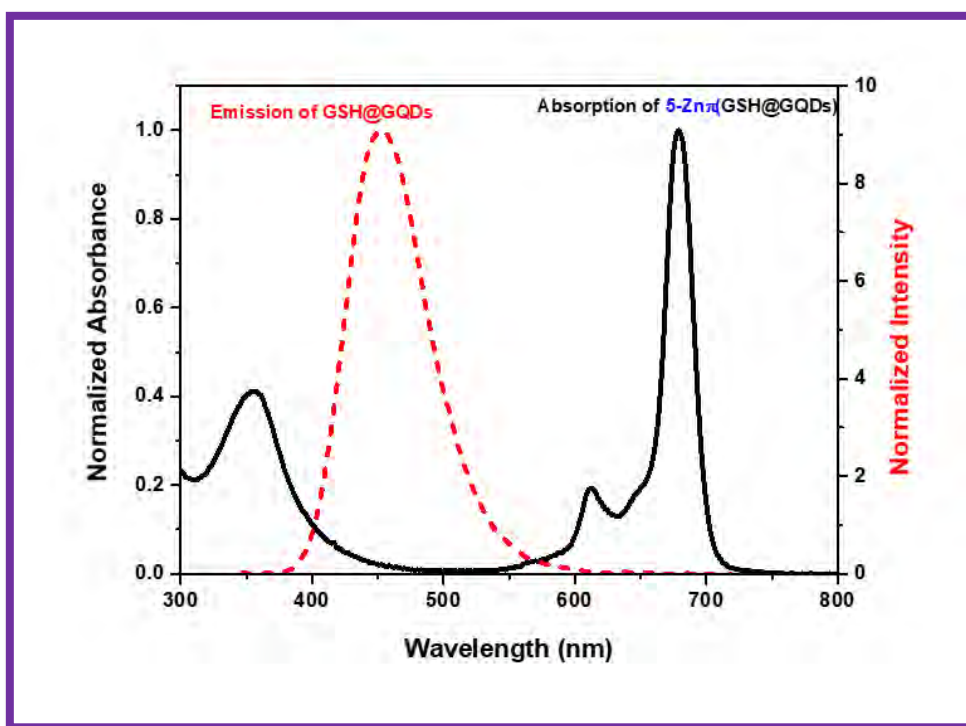


Figure 4.3 Absorption of **5-Zn π** (GSH@GQDs) and emission spectra of GSH@GQDs (λ_{exc} = 340 nm) in DMSO (as an example).

The FRET efficiency (*Eff*) values are estimated to be 0.89, 0.88, and 0.91 for **1-H₂ π** (GQDs), **1-Zn π** (GQDs), and **1-In π** (GQDs), respectively.

Similarly, the fluorescence properties of GSH@GQDs were used to study their energy transfer process in the ground and/or excited state in the presence of **5-Zn** and **6-Zn**. The *Eff* values reported in **Table 4.1**.

Overall, the *Eff* values of the nanoconjugates from the same group are almost similar. This implies that there is a similar spectral overlap and shows that there are efficient energy transfer processes for these Pc systems.

When recording the emission spectra at λ_{exc} = 400 nm where the chalcone absorbs, **Groups 3** and **4** complexes showed two very weak emission peaks around 525 nm for the chalcone moiety and around 700 nm for the Pc core (**Figure 4.4** used as an example). The decrease in the emission intensity of chalcone when combined with Pc core could be due to FRET *via* covalent bond from

the donor chalcone moieties to the acceptor Pc core and/or numerous other factors which deactivate the excited states. The Eff values are similar 92, 94, 93, and 95% for **4-Zn**, **4-In**, **4-ZnQ**, and **4-InQ** respectively. While the Eff values for **3-Zn**, **3-In**, **3-ZnQ**, and **3-InQ** were also calculated to be similar around 92, 92, 89, and 90%, respectively, **Table 4.1**. As mentioned above, this implies that there is a similar spectral overlap for these Pc systems.

In the presence of DNDs, the corresponding nanoconjugates exhibited lower Eff values of 46, 54, 31, and 31% for **3-Zn π** (DNDs), **3-In π** (DNDs), **3-ZnQ π** (DNDs), and **3-InQ π** (DNDs), respectively (**Table 4.1**). This can be explained by the fact that the DNDs used here are non-fluorescent and they quench the fluorescence of these Pcs. Another reason being that their presence might hinder the FRET process between the chalcone substituent and Pc core.

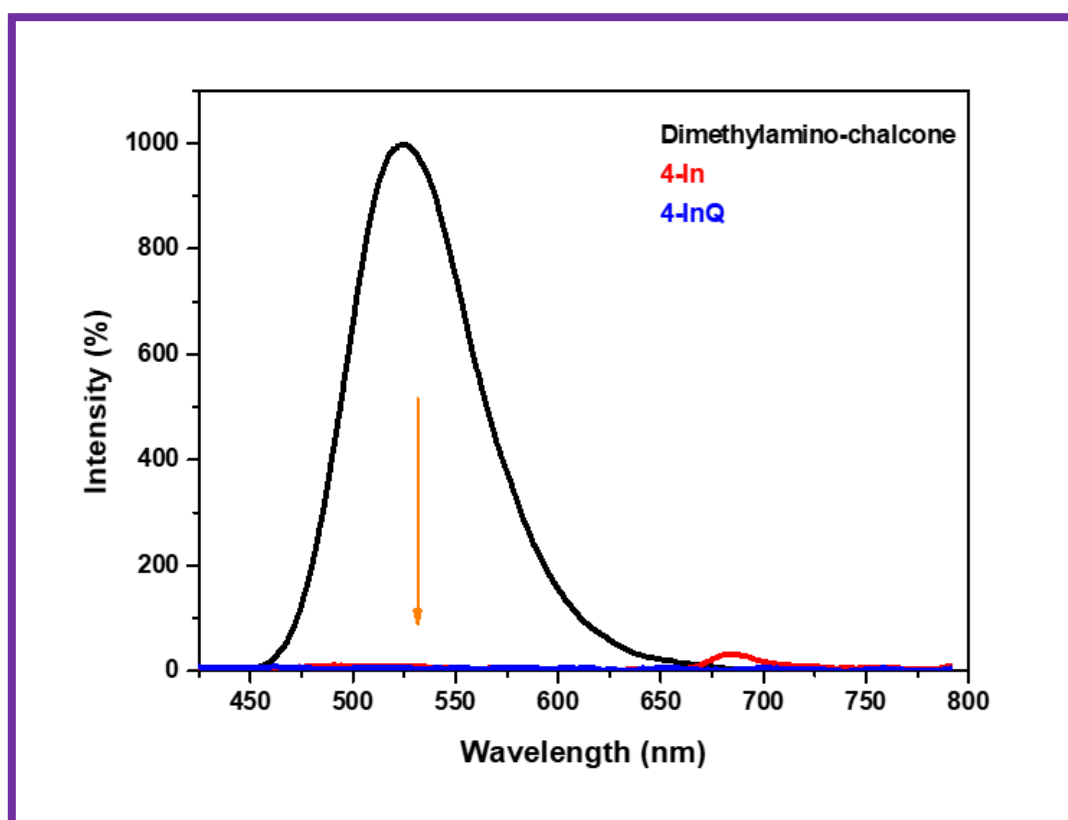


Figure 4.4 Emission spectra of chalcone alone and complexes **4-In** and **4-InQ** in DMSO when exciting at 400 nm, showing the decrease in fluorescence intensity in the Pcs (as an example).

4.1.2. Porphyrin Complexes and Nanoconjugates

All the experiments were run in DMSO and the absorbance of the porphyrins at the excitation wavelength was 0.05. When exciting at the B-band, porphyrins show relatively low Φ_F and τ_F values (Table 4.2).

Table 4.2 Fluorescence quantum yields and lifetimes of porphyrins in DMSO.

Complex	Φ_F	τ_F (ns)
Group 7: Asymmetrical porphyrins and nanoconjugates		
7-H₂	0.074	6.82
7-Zn	0.069	5.27
7-Ga	0.033	3.58
7-In	0.021	3.21
7-H₂-(DNDs@Ag)	0.048	4.90
7-Zn-(DNDs@Ag)	0.036	2.89
7-Ga-(DNDs@Ag)	0.021	2.15
7-In-(DNDs@Ag)	0.015	2.05
Group 8: Dimethylaminophenyl Porphyrins		
8-Ga	0.075	4.08
8-In	0.072	3.91
8-GaQ	0.029	3.43
8-InQ	0.025	3.08

The decrease in Φ_F and τ_F for the metalated porphyrins could be supported by the effect of heavy central metal and the quaternization. In the nanoconjugates, this could be due to the presence of electron-donating groups on the DNDs which favours ISC over the fluorescence process [184]. In addition, the high aggregation observed in the nanoconjugates contributes to transforming electronic excitation energy to vibrational energy, thus resulting in less fluorescent compounds [258]. Also, Ag NPs have been reported to quench fluorescence [257]. Therefore, lower Φ_F values as listed in Table 4.2 belong to the metalated porphyrin-DNDs@Ag nanoconjugates.

4.2. Triplet Quantum Yield (Φ_T) and Lifetime (τ_T)

A photosensitizer with high Φ_T has a probability to generate high singlet oxygen which is needed for use in PACT/PDT applications. And long triplet lifetimes are important to ensure that the energy transfer from the triplet excited state to ground state molecular oxygen is efficient. Due to the short-lived triplet state properties of chalcone compounds, the Φ_T and τ_T parameters for Pcs of **Groups 3** and **4** are not reported in this work.

4.2.1. Phthalocyanine and Nanoconjugates

Triplet quantum yields (Φ_T) refers to the number of molecules that undergo the ISC process to populate the triplet state. An example of a triplet absorption decay curve is shown in **Figure 4.5**. Triplet lifetime (τ_T) is defined as the duration that molecules in the triplet excited state take before returning to the ground state.

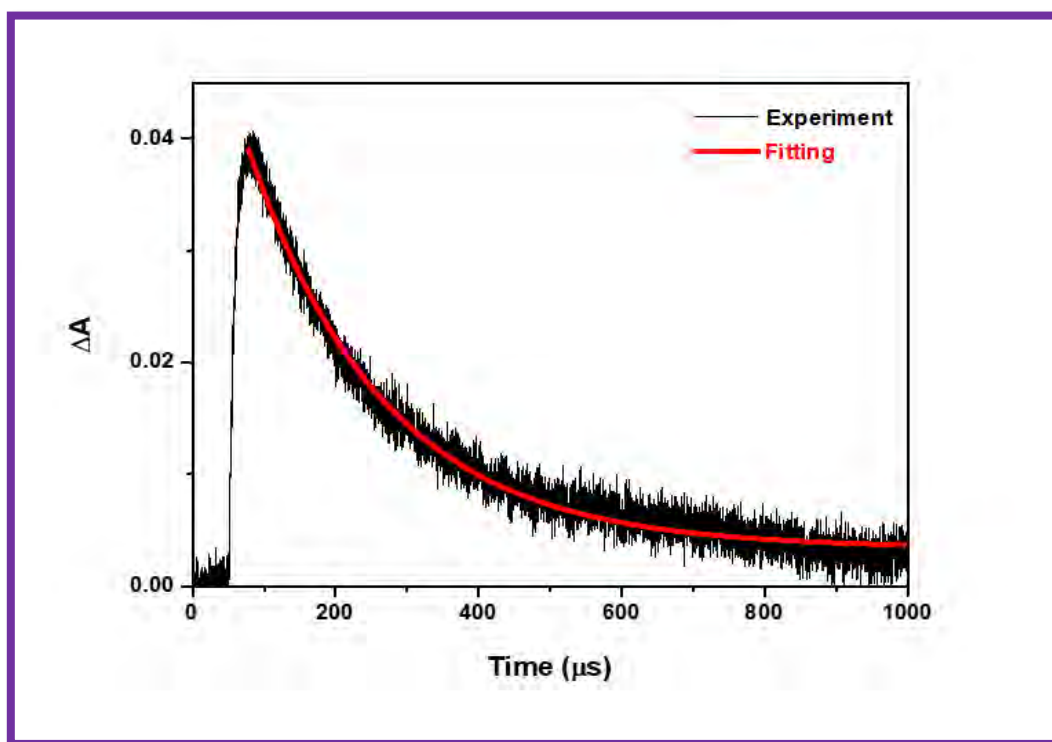


Figure 4.5 Triplet absorption decay curve for **5-Zn π (GSH@GQDs)** (used as an example).

In this work, all the experiments were carried out in argon saturated DMSO solutions containing Pcs alone or nanoconjugates. The Φ_T values were obtained using comparative methods described in the literature [185] and the triplet lifetimes were determined by exponential fitting of the kinetic

curves using the ORIGIN[®] 8 Professional software. Unsubstituted ZnPc was used as the standard with $\Phi_T = 0.65$ in DMSO [186]. The triplet state quantum yields and lifetimes are shown in **Table 4.3**.

Table 4.3 Triplet quantum yields and lifetimes of the Pcs and nanoconjugates in DMSO.

Complex	Φ_T	τ_T (μ s)
Group 1: Acetophenoxy-substituted Pcs and nanoconjugates		
GQDs	-	-
1-H₂	0.31	387
1-Zn	0.78	182
1-In	0.84	165
1-H₂π(GQDs)	0.27	387
1-Znπ(GQDs)	0.85	142
1-Inπ(GQDs)	0.90	121
1-H₂π(DNDs)	0.5	225
1-Znπ(DNDs)	0.82	156
1-Inπ(DNDs)	0.89	143
Group 2: Bromo-aminophenoxy-substituted Pcs and nanoconjugates		
2-Zn	0.70	296
2-In	0.74	148
2-Znπ(DNDs)	0.76	74
2-Inπ(DNDs)	0.88	48
2-Znπ(DNDs)-CSAg	0.90	25
2-Inπ(DNDs)-CSAg	0.97	21
Groups 5-6: Tetra and monocarboxylic acid-substituted Pcs and nanoconjugates		
GSH@GQDs	-	-
5-Zn	0.69	190
6-Zn	0.74	271
5-Znπ(GSH@GQDs)	0.73	189
6-Zn-(GSH@GQDs)	0.86	269

4.2.1.1. *Effect of Central Metal*

In general, the trend observed for Pc containing heavy central metals is that they have high Φ_T resulting in low triplet lifetimes. Heavy central metal effect confers to the metallated Pcs a higher Φ_T as observed in **Table 4.3** where the highest values are obtained in the In (III) derivatives and the lowest $\Phi_T = 0.31$ ($\tau_T = 387 \mu\text{s}$) for the free-base **1-H₂**. Free-base Pcs are more aggregated than the metallated Pcs, consequently, aggregation can reduce the excited-state lifetimes and the photosensitizing efficiency, probably due to enhanced radiationless excited state dissipation which therefore lowers the quantum yields of the excited states in addition to the lack of the metal.

4.2.1.2. *Effect of Substituents*

Generally, as foreseeable in **Table 4.3**, all the Φ_T values obtained for the metallated substituted-Pcs are higher compared to the unsubstituted ZnPc standard ($\Phi_T = 0.65$ in DMSO) and this highlights the importance of substitution on the Pc core.

For instance, by comparing the acetophenoxy substituent of **1-Zn** and **1-In** ($\Phi_T = 0.78$ and 0.84 , respectively) to the bromo-aminophenoxy substituent of **2-Zn** and **2-In** ($\Phi_T = 0.70$ and 0.74 , respectively), the highest Φ_T values are obtained for the **1-Zn** and **1-In** group. This is because acetophenones can promote ISC to triplet state where they increase the population of the triplet state thanks to the reactive carbonyl group in their molecular structure [259].

4.2.1.3. *Effect of Symmetry*

Considering **5-Zn** and **6-Zn** Pcs as examples, a higher Φ_T value belong to the asymmetrical Pc **6-Zn** (**Table 4.3**) as asymmetry is known to introduce distortions [260], resulting in faster intersystem crossing to the triplet state, consequently increasing the triplet state population.

4.2.1.4. *Effect of Nanomaterials*

The π - π interactions or covalent bond formed between Pcs and the graphitic sheets of GQDs, DNDs, and GSH@GQDs resulted in improved Φ_T .

In all cases, it is observed that the Φ_T data for the nanoconjugates are significantly increased compared to their corresponding complexes alone except for the free-base Pc (**Table 4.3**). As expected, the τ_T decreased with an increase in Φ_T following conjugation to nanomaterials [261]. Also recall that electron-donating groups present in the nanomaterials and Pcs are known to

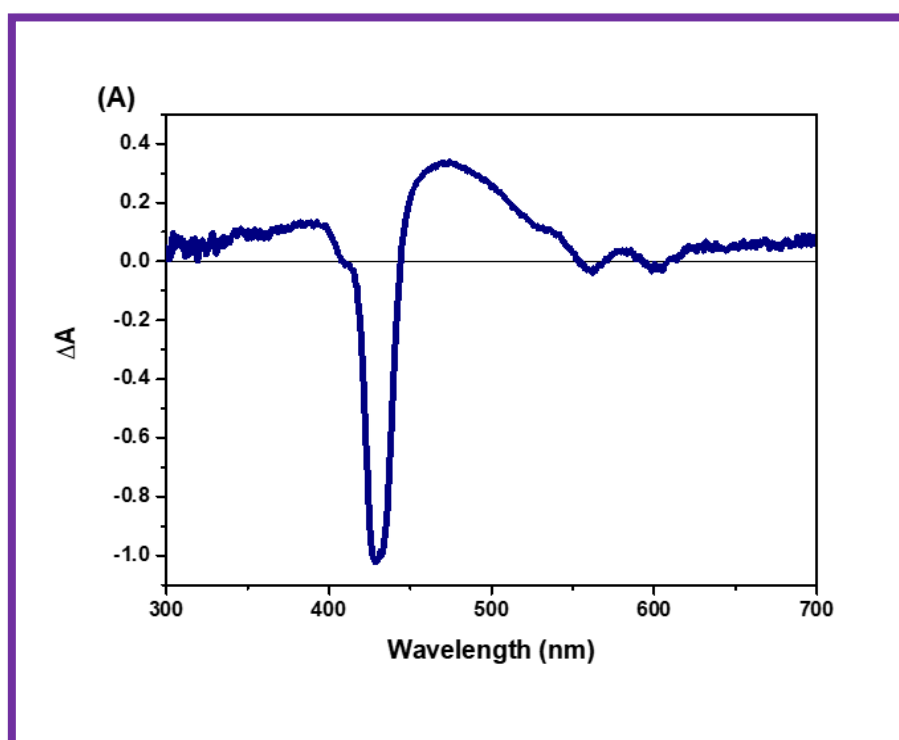
improve intersystem crossing in porphyrins materials as stated above, hence decreasing fluorescence but increasing triplet state population.

4.2.2. Porphyrins and their Nanoconjugates

Porphyrins and their nanoconjugates were dissolved in DMSO then saturated with argon gas for laser flash photolysis studies to determine the τ_T values. Please note that the Φ_T values are not reported due to the ambiguity caused by the overlap of the singlet depletion curve region with that of the triplet absorption.

Complex **7-In** used as an example gave a transient depletion spectrum with a strong maximum around 432 nm with a decay lifetime curve (shown in **Figure 4.6A** and **Figure 4.6B**) which are attributed to the triplet state of the compound. Other reports have as well obtained the triplet state absorption spectra and lifetimes of some selected porphyrins in the range of 430-470 nm and microseconds, respectively [262].

As expected, all the porphyrins resulted in decreased τ_T values after metalation and conjugation to the DND_S and Ag NPs as shown in **Table 4.4**. The τ_T values were in the range of 58-283 μ s. The quaternized complexes resulted in lower τ_T values (**Table 4.4**), compared to their non-quaternized counterparts.



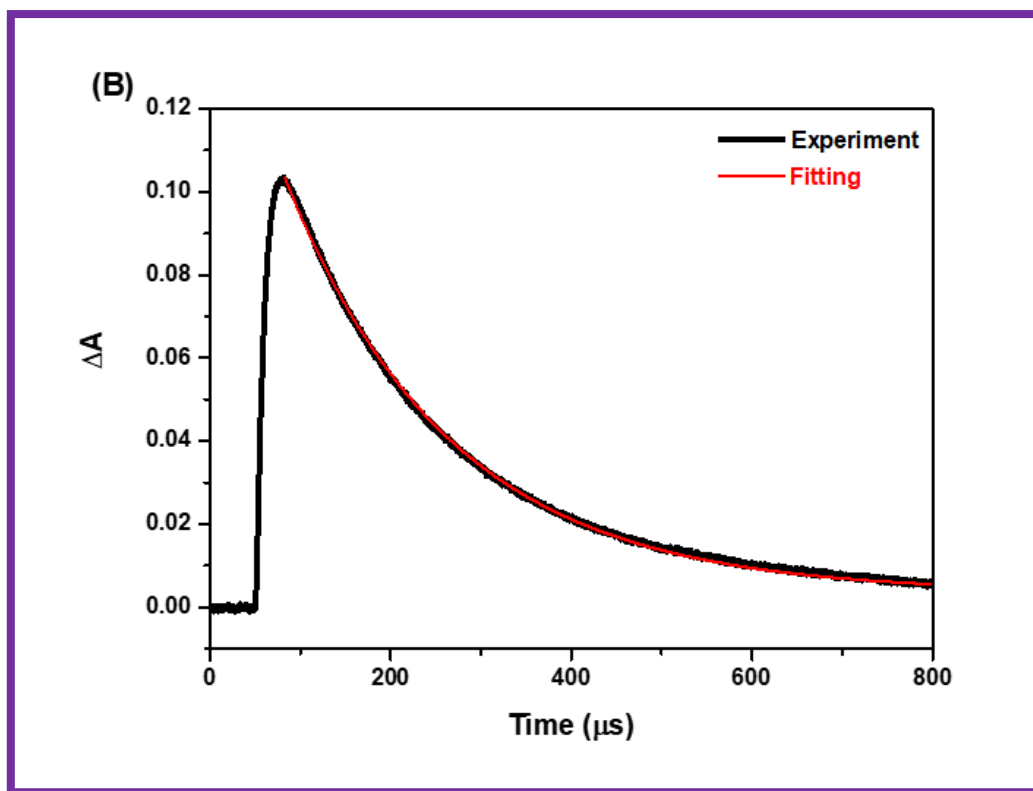


Figure 4.6 (A) Absorption spectra obtained with laser flash photolysis at 1 μs after excitation and (B) transient decay curve (using complex **7-In** as an example) observed at 425 nm in DMSO.

Table 4.4 Triplet lifetimes of the studied porphyrins and nanoconjugates in DMSO.

Complex	τ_T (μs)
Group 7: Asymmetric porphyrins and nanoconjugates	
7-H₂	283
7-Zn	232
7-In	201
7-Ga	182
7-H₂-DNDs@Ag	185
7-Zn-DNDs@Ag	180
7-In-DNDs@Ag	176
7-Ga-DNDs@Ag	140
Group 8: Dimethylamino Porphyrins	
8-In	101
8-Ga	193
8-InQ	58
8-GaQ	176

4.3. Singlet Oxygen Quantum Yield (Φ_{Δ})

Singlet oxygen ($^1\text{O}_2$) which is toxic to bacteria and cancer cells is one of the ROS generated when energy transfer occurs between the triplet state of the photosensitizer and ground-state molecular oxygen during an irradiation process [186,263]. The amount of $^1\text{O}_2$ formed during photosensitization is quantified as singlet oxygen quantum yield (Φ_{Δ}).

2 mL solution containing each complex/conjugate (with Abs = 1.5, based on the complex) and ADMA or DPBF (Abs = 1.8) for Pcs was irradiated in a 1 cm path length cuvette. The irradiation time interval was 30 sec from $t = 0$ to $t = 180$ sec for the photobleaching of DPBF (for organic media) and 5 min interval from $t = 0$ to $t = 25$ min in the case of ADMA (for aqueous media).

For porphyrins, similar experimental procedure was used except the DPBF was replaced by DMA (for organic media).

4.3.1. Phthalocyanine and Nanoconjugates

The Φ_{Δ} values follow the trend in Φ_T values since singlet oxygen is generated from the triplet state. By the means of a UV-Vis spectrophotometer, the decreases in DPBF (in DMSO) and ADMA (in 1% DMSO in water) absorbances at 417 and 380 nm, respectively, were monitored for all the PSs (Figures 4.7A and 4.7B used as examples) using the unsubstituted ZnPc ($\Phi_{\Delta} = 0.67$ in DMSO [187]) and ClAlPcSmix ($\Phi_{\Delta} = 0.42$ in water [186]) as standards.

In this study, during the determination of Φ_{Δ} , no photobleaching of the Pc complexes or nanoconjugates as there is no change in the absorption of Q bands of the Pcs following irradiation in both DMSO and 1% DMSO in water (Figures 4.7A and 4.7B). This confirms the stability of the PSs in the currently applied experimental conditions.

In 1% DMSO, the Φ_{Δ} values are low compared to the standards used. This could be due to the reported quenching effect of water on the singlet oxygen generation of Pcs [179,264]. The Φ_{Δ} data are supplied in Table 4.5.

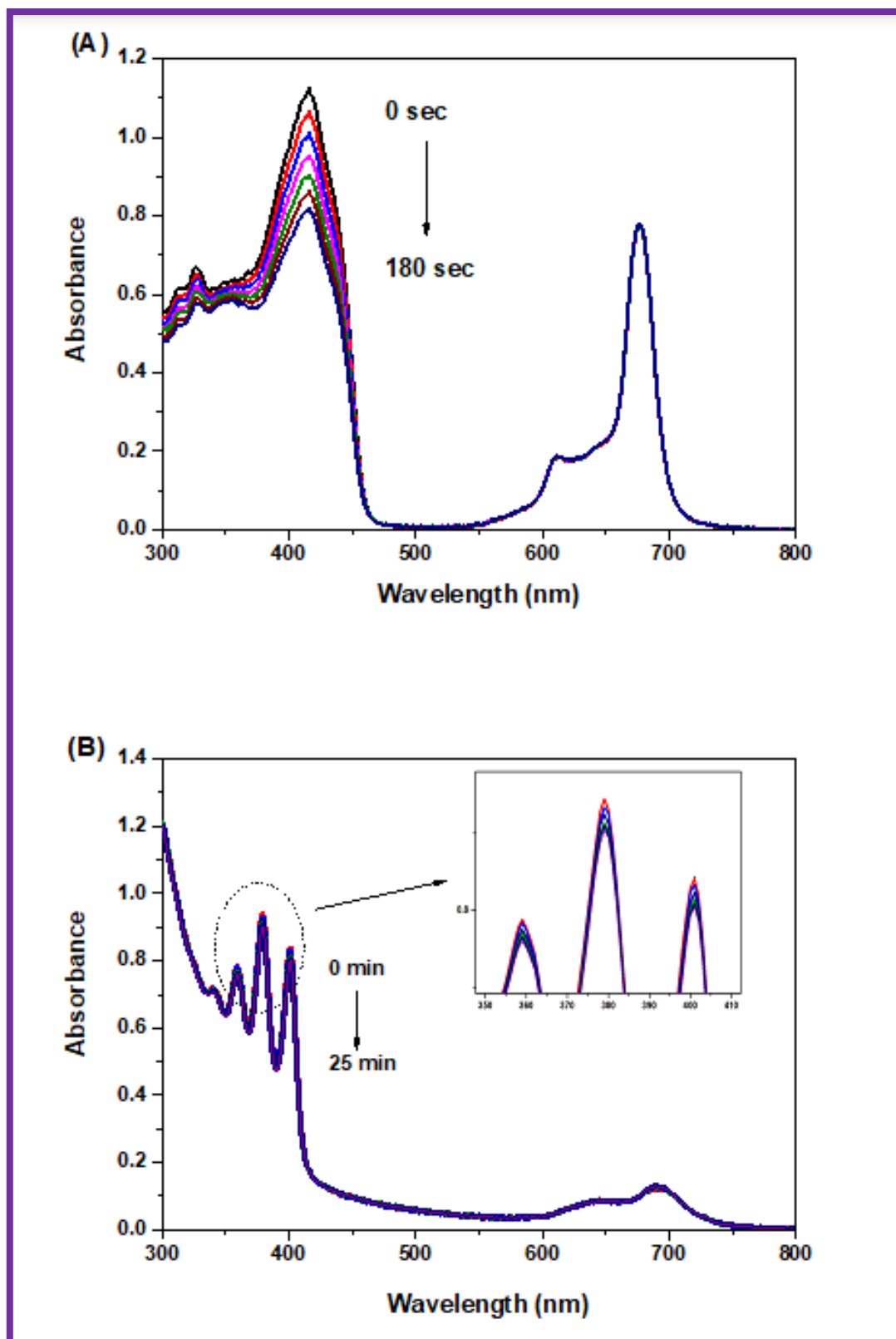


Figure 4.7 A typical spectrum for the determination of singlet oxygen quantum yield of **4-InQ** (A) in DMSO using DPBF and (B) in 1% DMSO in water using ADMA (used as examples).

Table 4.5 Singlet oxygen quantum yields for Pcs and nanoconjugates in DMSO unless otherwise stated.

Complex	Φ_{Δ}^a
Group 1: Acetophenoxy-substituted Pcs and nanoconjugates	
GQDs	-
DNDs	-
1-H₂	0.22
1-Zn	0.72
1-In	0.75
1-H₂π(GQDs)	0.20
1-Znπ(GQDs)	0.77
1-Inπ(GQDs)	0.79
1-H₂π(DNDs)	0.25
1-Znπ(DNDs)	0.74
1-Inπ(DNDs)	0.84
Group 2: Bromo-aminophenoxy-substituted Pcs and nanoconjugates	
CSAg	-
2-Zn	0.69
2-In	0.72
2-Znπ(DNDs)	0.72
2-Inπ(DNDs)	0.77
2-Znπ(DNDs)-CSAg	0.90
2-Inπ(DNDs)-CSAg	0.92
Group 3: Pyridyl chalcone-substituted Pcs and nanoconjugates	
3-Zn	0.39
3-In	0.50
3-ZnQ	0.43 (0.21)
3-InQ	0.53 (0.27)
3-Znπ(DNDs)	0.51
3-Inπ(DNDs)	0.68
3-ZnQπ(DNDs)	0.61 (0.46)
3-InQπ(DNDs)	0.69 (0.47)

Group 4: Dimethylamino chalcone-substituted Pcs and nanoconjugates	
Chalcone	-
4-Zn	0.43 (0.09)
4-In	0.50 (0.11)
4-ZnQ	0.48 (0.20)
4-InQ	0.57 (0.24)
Groups 5-6: Tetra and monocarboxylic acid-substituted Pcs and nanoconjugates	
GSH@GQDs	-
5-Zn	0.58 (0.17)
6-Zn	0.65 (0.20)
5-Znπ(GSH@GQDs)	0.64 (0.19)
6-Zn-(GSH@GQDs)	0.75 (0.24)

^a Values in brackets are in 1% DMSO in water used for cell studies

4.3.1.1. *Effect of Central Metal*

As observed in the Φ_T data above, the heavy central metal has an impact on the production of singlet oxygen by the PSs. The Φ_Δ values were found to be higher for the metallated entities with the In (III) complexes showing higher values than the Zn (II) counterparts based on the reasons previously provided.

4.3.1.2. *Effect of Substituents*

Acetophenone molecules are well-known to create high singlet oxygen quantum yields due to the presence of a reactive carbonyl group (**Group 1**) in their structure [259]. Hence, this explains why this group of Pcs had the highest values of Φ_Δ compared to other studied groups based on the same central metal. **Group 2** Pcs also show higher Φ_Δ values due to the heavy atom effect caused by the presence of halogen and oxygen atoms. This results in improved triplet quantum yields, and consequently, high singlet oxygen [265].

4.3.1.3. *Effect Positive Charge*

Quaternization of complexes increased the Φ_Δ values in both DMSO and water as seen in **Table 4.5**, the reason being that the photoinduced electron transfer (PET) process cannot be detected in the quaternized molecules since the lone pair electrons on nitrogen atoms are bonded to methyl

groups in the positively charged entities [263]. PET process is known to reduce the singlet oxygen generation efficiency.

4.3.1.4. *Effect of Symmetry*

Asymmetry introduces distortions in the molecule [260], resulting in faster intersystem crossing to the triplet state, thus increasing the triplet state population and generation of singlet oxygen. Hence **6-Zn** showed a higher value relative to its symmetrical counterpart **5-Zn**, **Table 4.5**.

4.3.1.5. *Effect Nanomaterials*

As in **Table 4.5**, an increase in Φ_{Δ} in the presence of the nanomaterials is observed for the same reasons mentioned above. Another reason is that the increase in π bonds in the nanoconjugates can increase Φ_{Δ} .

The increase Φ_{Δ} values correspond to an increase in triplet quantum yields. The highest Φ_{Δ} values of all are 0.90 and 0.92 obtained for **2-Zn π (DNDs-CSAg)** and **2-In π (DNDs-CSAg)** nanoconjugates, respectively, are predictable since they contain both the DNDs and silver NPs which encourage ISC to the triplet state due to the heavy atom effect. Previous reports state that the presence of nitrogen atoms into graphitic materials generates charged sites that augment the adsorption of oxygen, thus resulting in enhanced photocatalytic properties [266]. The aptitude of studied PSs to generate such an amount of singlet oxygen makes them eligible for use in PACT/PDT application.

4.3.2. *Porphyrin and Nanoconjugates*

The Φ_{Δ} values were determined by monitoring the photobleaching of DMA and ADMA as singlet oxygen scavengers in DMSO and aqueous media, respectively, with irradiation at a crossover wavelength (420 nm) using ZnTPP and Rose Bengal standards respectively. **Figures 4.8A,B** (used as examples) also confirm the stability of the porphyrins and nanoconjugates as no change in the absorption of B bands are observed.

4.3.2.1. *Effect of Central Metal*

The Φ_{Δ} data are supplied in **Table 4.6**. The higher Φ_{Δ} values are obtained for complexes containing heavy central metals, known to have high singlet oxygen quantum yield which is important for the photoinactivation process [267,268].

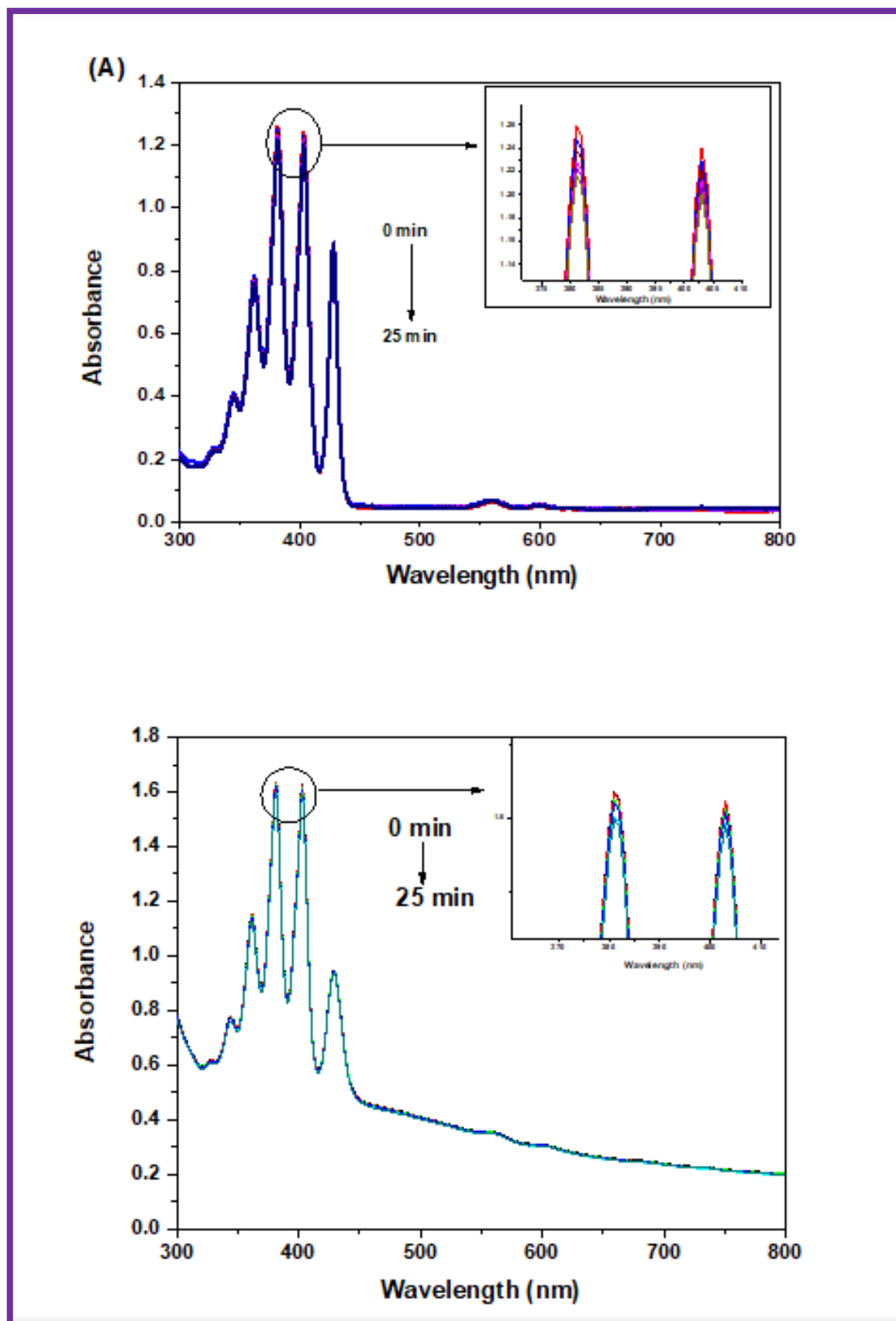


Figure 4.8 Photobleaching of DMA in DMSO in the presence of (A) 7-Ga and (B) 7-Ga-DNDs@Ag as examples.

Table 4.6 Singlet oxygen quantum yields of porphyrins and nanoconjugates in DMSO unless otherwise stated.

Complex	Φ_{Δ}^a
Group 7: Asymmetric porphyrins and nanoconjugates	
7-H₂	0.27
7-Zn	0.43
7-Ga	0.48
7-In	0.54
7-H₂-(DNDs@Ag)	0.33
7-Zn-(DNDs@Ag)	0.51
7-Ga-(DNDs@Ag)	0.58
7-In-(DNDs@Ag)	0.59
Group 8: Dimethylamino Porphyrins	
8-In	0.58 (0.30)
8-Ga	0.54 (0.27)
8-GaQ	0.54 (0.29)
8-InQ	0.63 (0.33)

^a: Values in brackets are in 1% DMSO in water used for cell studies

4.3.2.2. *Effect of Positive Charges*

The higher Φ_{Δ} values obtained for the quaternized compounds compared to their corresponding non-quaternized is due to the absence (PET) as mentioned above. However, the values are the same for **8-Ga** and **8-GaQ** in DMSO. In aqueous media, Φ_{Δ} values are lower since oxygen has a higher solubility in many organic solvents compared to water [269] and also the quenching discussed above [179,264].

4.3.2.3. *Effect of Nanomaterials*

The Φ_{Δ} values were slightly increased for the nanoconjugates due to the effect of the nanoparticles, with the reasons mentioned above about the presence of electron-donating groups on the DNDs as well as the Ag NPs that stimulate the intersystem crossing to the excited triplet state from where the singlet oxygen is generated. In addition, the presence of a reactive carbonyl group in a molecule is reported to augment Φ_{Δ} because of the $n-\pi^*$ transition from oxygen atom [259].

4.4. Summary of the Photophysicochemical Properties of the Studied Photosensitizers

In summary, the preparation and characterization of a series of novel Pcs, porphyrins and their nanoconjugates as potential PSs for targeted PACT/PDT have been done. Fluorescence and triplet quantum yields are competing processes that are affected by the heavy central metal effect (Zn, In, and Ga metals were investigated in this study for selected complexes and nanoconjugates), the heavy atom effect of bromine, the presence of electron-donating groups in the substituents, the effect of positive charges, the effect of symmetry, and conjugation of complexes to various nanomaterials, which are known to enhance the ISC to the triplet state, thus quenching the fluorescence.

The PSs exhibited relatively lower Φ_F as a result of the quenching effect by the parameters cited above. To evaluate the photosensitizing efficiency of the synthesized compounds, their Φ_Δ values were determined in DMSO by a steady-state method using DPBF as the scavenger in DMSO and ADMA as chemical scavenger in aqueous media for Pcs. The results showed that all the compounds are highly efficient singlet oxygen generators and the values of Φ_Δ were relatively higher to that of the used standards excepts for the chalcone-derived Pcs, probably due to their singlet oxygen quenching effect.

On the other hand, the electron density of the amino moiety is higher before quaternization. As a result, the PET process is more likely to occur, and hence their Φ_F values were comparatively lower and with higher Φ_Δ . In fact, reductive quenching of the singlet excited state of Pcs by amino moieties has been reported. The non-aggregated nature of the quaternized PSs is highly desirable as aggregation almost inevitably shortens the triplet lifetime of the dyes, resulting in a drastic reduction of the overall photosensitizing efficiency.

The capacity of the studied complexes to generate such high singlet oxygen makes them good candidates for PACT/PDT studies.

Chapter Five: Theoretical Calculations

The chapter reviews the TD-B3LYP/LanL2DZ calculations performed on **Group 8** porphyrins as examples to determine and compare the singlet excitation energies of quaternized and non-quaternized complexes *in vacuo*.

5.1. TD-DFT Analysis

The TD-B3LYP/LanL2DZ calculations are studied to assess the singlet excitation energies of quaternized (**8-GaQ** and **8-InQ**) and non-quaternized (**8-Ga** and **8-In**) porphyrins *in vacuo*. This study shows excellent agreement between time-dependent density-functional theory (TD-DFT) exciting energies and experimental $S_1 > S_0$ excitation energies.

The small deviation observed between the calculated and experimental spectra arises from the effect of the solvent used in the experimentation. The excitation energies observed in the UV-Vis spectra mostly originate from electron promotion between the highest occupied molecular orbital (HOMO) of the less intense band (Q-band) and the HOMO-1 of the most intense band (B-band) of the ground states to the lower unoccupied molecular orbital (LUMO) of the excited states.

Quaternized (**8-GaQ** and **8-InQ**) and non-quaternized (**8-Ga** and **8-In**) derivatives were built in D_{2h} and D_{4h} , respectively. **Figure 5.1** shows the geometries of free-base **8-H₂** and complex **8-In** as examples. The geometry optimizations reveal that dimethylamino porphyrin and its quaternized derivative keep their high D_{2h} symmetry whereas **8-GaQ**, **8-InQ**, **8-Ga**, and **8-In** become unstable in D_{4h} symmetry and undergo symmetry breaking towards the epikernel C_{4v} owing to the pseudo-Jahn-Teller effect.

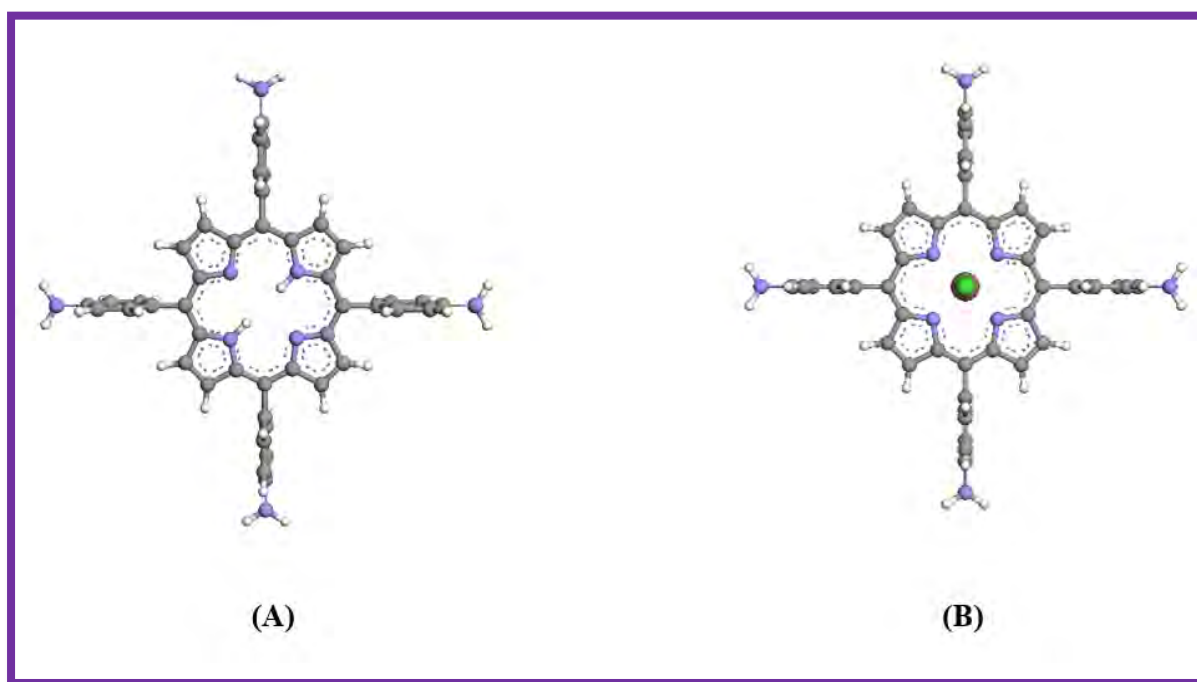


Figure 5.1 Initial geometry of porphyrin (A) **8-H₂** built-in D_{2h} and (B) **8-In** built-in D_{4h} .

The energy differences between the quaternized and non-quaternized PSs are herein computed to have a glance at the basicity of the studied complexes (**Table 5.1**). The energy difference illustrated in **Table 5.1** suggests that the free-base **8-H₂** and complex **8-In** are the most and least basic molecules, respectively.

Table 5.1 Total electronic energies in Hartrees of quaternized and non-quaternized porphyrin derivatives and their energies differences in kcal/mol computed at B3LYP/LanL2DZ.

Complex	Quaternized	Non-quaternized	Energy difference in kcal
8-H₂	-2136.32953	-2135.096169	-773.94
8-In	-2151.8155	-2150.611677	-755.41
8-Ga	-4518.46774	-4517.250763	-763.67

The optical spectra of the studied complexes have the same features so in the present work, only the optical spectrum of **8-In** is reported. **Figure 5.2** shows the computed UV-Vis spectrum of complex **8-In**. The spectrum is found to be similar to the normalized experimental spectrum where two characteristic regions of porphyrins can be noticed, a region of strong absorptivity, the B-band region between 300 and 450 nm, and a region of low absorptivity, the Q-band region between 475 and 650 nm.

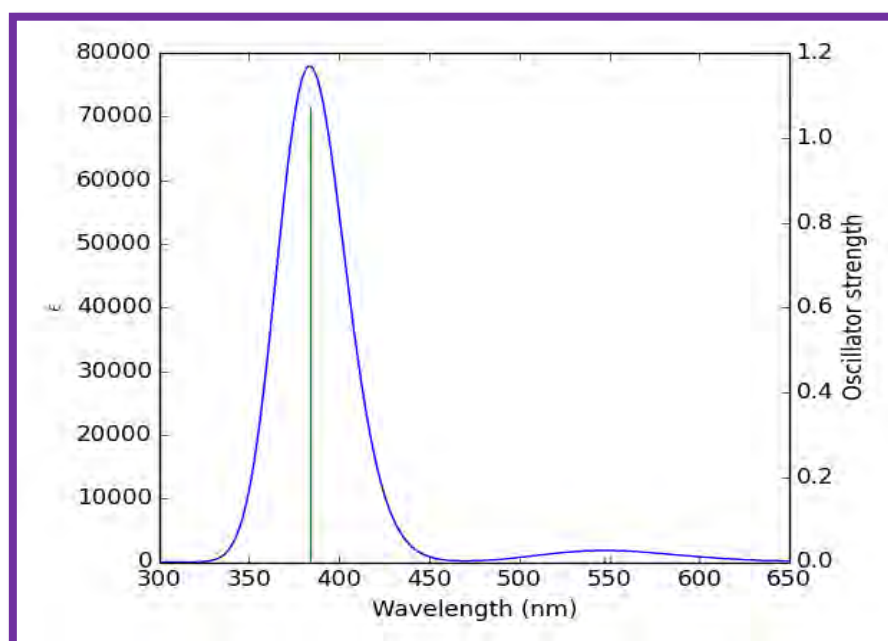


Figure 5.2 UV-Vis spectrum of complex **8-In** computed at TDB3LYP/LanL2DZ.

For instance, **8-In** shows that the deviation between the experimental and TD-DFT excitation energies is quite small ranging between 50 and 28 nm, for both B-band and Q-band regions respectively (**Table 5.2**). This illustrates the influence of DMSO solvent in the calculations. Please recall that the calculations were performed *in vacuo* while the experimental data were obtained in solution (DMSO).

Table 5.2 Excitation energies, oscillator strengths, and most important electronic configurations in % that span the excited state wave function of complex **8-In** computed at TD-B3LYP/LanL2DZ *in vacuo*.

Region	Excited energies (nm)	Oscillator strengths	Contribution of MOs (%)	Exp. in DMSO
B-band	383.62	1.075	H-1->L (54.88%) H->L (35.96%) H-15->L (8.2%)	431
Q-band	547.49	0.013	H->L(60.73%) H-1->L(38.55%)	575 682

The TD-DFT analysis of the most important configuration with the largest coefficient in the excited state reveals that the bands observed originate from electron transfer between the HOMO and HOMO-1 of the ground state configuration and the LUMO of the excited configuration. **Table 5.2** lists the excitation energies, oscillator strengths, and molecular orbital contributions of the UV-Vis spectrum **8-In** as an example in the gas phase.

The contribution of the HOMO-1 is the most important in the B-band, while in the low energy band which is the Q-band, the largest contribution comes from the promotion of the HOMO to the LUMO orbital. The frontier molecular orbitals of complex **8-In** and the HOMO-15 orbital are shown in **Figure 5.3** as examples.

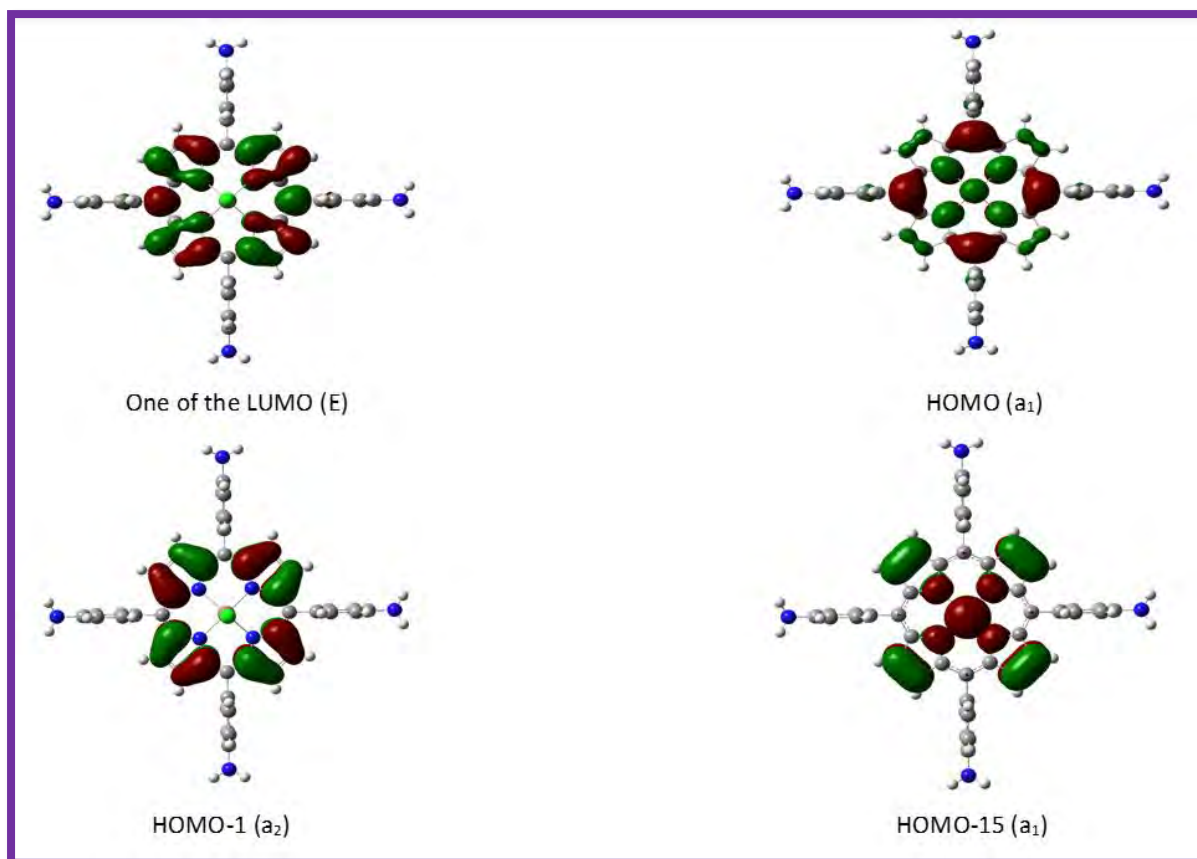


Figure 5.3 Frontier molecular orbitals of the **8-In**.

The HOMO and HOMO-15 are symmetric whereas the LUMO has E symmetry and all have predominantly π character. The HOMO and LUMO are, respectively, bonding and anti-bonding orbitals. Thus, all the transitions observed are from π to π^* .

5.2. Summary of the Chapter

The TD-B3LYP/LanL2DZ calculations were performed to evaluate the singlet excitation energies of neutral and positively charged porphyrins *in vacuo*. The results showed that the theoretical and experimental UV-Vis are comparable and that the small deviation was due to the influence of the solvent employed (DMSO). The study showed an excellent agreement between TD-DFT excited energies and experimental excitation energies. The geometry optimizations revealed that the **8-H₂** and **8-H₂Q** have both high D_{2h} symmetry whereas the corresponding metalated Ga and In counterparts were unstable in D_{4h} symmetry and undergo symmetry breaking towards the epikernel C_{4v} owing to the pseudo-Jahn-Teller effect.

PART IV.

Singlet Oxygen Biological Applications

Chapter Six: Photodynamic Antimicrobial Chemotherapy (PACT)

This chapter assesses the potential *in vitro* activities of all the synthesized PSs in this work (Pcs, porphyrins along with their nanoconjugates) as PACT agents.

6.1. Introduction

Antibiotics bacteria-resistance is an alarming concern to which PACT has proven to be a useful therapeutic tool, based on phototoxic and chemical reactions, which exerts fatal effects on bacteria upon irradiation of a PS in the presence of molecular oxygen [270,271].

A potential PS for PACT must have appropriate photophysical and photochemical properties, such as a long-wavelength absorption band, a high Φ_{Δ} , and Φ_T . It also should be water-soluble, have a high affinity for microbial cells (i.e., bind, penetrate, and act within the cell) [272], and have a low affinity for host cells. All these characteristics are strongly related to the presence of cationic charges in the molecular structure. Hence, quaternization was applied to some of the studied PSs that contained a tertiary nitrogen atom in their molecule structure. These include Pcs (**3-Zn** and **3-In**; **4-Zn** and **4-In**) and porphyrins (**8-In** and **8-Ga**).

The design of the currently studied substituted-PSs was strongly based on their intrinsic antibacterial effectiveness and long-lived triplet and generation of cytotoxic ROS. Several different families of PSs and their nanoparticle-conjugates with distinct physical and photochemical features have been used in PACT. However, carbon-based nanomaterials (GQDs, GSH@GQDs, DNDs, DNDs-CSAg, and DNDs@Ag NPs) conjugated to either Pcs or porphyrins have just been investigated in this work as photoactive antimicrobial agents in PACT.

The current study evaluates the *in vitro* broad-spectrum antimicrobial efficacy of these novel light-activated PSs against prototypical human pathogenic microbes such as *S. aureus* (Gram-positive) and *E. coli* (Gram-negative) selected as models to study the activity of these PSs against bacterial cells. Besides the potential application of the studied PSs on the drug-resistant bacteria for planktonic cells, their biofilms counterparts, the most difficult to eradicate, are also being evaluated.

The drug stock solutions for PACT experiments were prepared in 1% DMSO/PBS media since some of the complexes were not fully water-soluble and for comparison. The control solutions were made up of bacteria cells in 1% DMSO/PBS without the respective drugs.

The experimental protocol conditions were kept the same for comparative purposes. The reported procedure involving the standard (viable, plate count) and turbidimetric analysis were used in this case with slight modifications [273,274]. To confirm the *in vitro* photoactivity of the complexes and nanoconjugates against the studied bacteria strains, the analysis of viable bacteria reduction by

colony forming units (CFU) counts and the percentage of viable colonies which is the number of remaining alive colonies after treatment of the cells, were performed. **Equations 6.1** and **6.2** were employed to quantify the % viable colonies and log₁₀ reductions, respectively.

$$\text{Viable colony (\%)} = \frac{(A - B)}{A} \times 100 \quad (6.1)$$

$$\log \text{ reduction} = \log(A) - \log(B) \quad (6.2)$$

Where A is the number of colony counts before treatment and B is the number after treatment. A lower viable colony percentage after treatment signifies the effectiveness of the PSs and consequently the high log reduction. The minimum log reduction value recommended by FDA (Food and Drug Administration) regulations for a potential PS to be applicable for PACT is 3 log CFU [275].

All the studied PSs were tested on the planktonic cells of *S. aureus*. But only those with quaternized derivatives (**3-ZnQ** and **3-InQ**; **4-ZnQ** and **4-InQ**) and porphyrins (**8-InQ** and **8-GaQ**) were further tested on *E. coli*, based on the theory about the composition and permeability of the Gram-negative bacteria cell wall.

Furthermore, bioassays on the bacteria biofilm cells were carried out for the PSs and nanoconjugates that exhibited satisfactory photoeffect on planktonic cells. Due the complexity of the exopolymeric substance (EPS) in biofilms, higher concentrations of the drugs are employed in this study.

6.2. Lipophilicity Studies

Reports state that the higher the amphiphilicity character of a drug, the more affinity it has for bacteria, which consequently improves cellular uptake and overall PACT/PDT activity. An amphiphilic drug has both hydrophilic (higher affinity for aqueous phase) and lipophilic (higher affinity for aqueous phase) characters.

The lipophilicity values (expressed in $\log P_{o/w}$) of the quaternized complexes alone **3-ZnQ**, **3-InQ**, **4-ZnQ**, **4-InQ**, **8-GaQ**, and **8-InQ** were measured by the “shake-flask” method [209], and calculated as per **Equation 2.8** (results in **Table 6.1**). In all the cases, the $\log P_{o/w}$ values for In (III) complexes are higher than those of their Zn (II). The Ga (III) counterpart is almost similar to **8-InQ**. The lipophilicity of the compounds was found to follow the order **Group 8 > Group 4 > Group 3**.

These findings suggest that the porphyrins **8-GaQ**, and **8-InQ** are more lipophilic than the Pcs derivatives. Highly lipophilic drugs are known to cross the lipid bilayer of the cell membrane more readily and hence enhance the cellular uptake [208]. Slightly lower lipophilicity values can also result in enhanced sub-cellular bioaccumulation and biodistribution.

Table 6.1 Water partition coefficient values ($\log P_{o/w}$) of quaternized complexes alone.

Complexes	$\log P_{o/w}$
3-ZnQ	-0.21
3-InQ	-0.26
4-ZnQ	-0.26
4-InQ	-0.39
8-GaQ	-1.24
8-InQ	-1.26

This confirms that the quaternization of the as-synthesized PSs can provide new PDT and PACT agents with lipophilicity properties that significantly enhance cellular uptake.

6.3. Biological Assays on Planktonic Cells

6.3.1. Statistical Analysis

All the experiments were performed separately in triplicates for certainty, verification, and reliability of the results. The results are presented as the mean values \pm standard deviation (SD) of each experiment and are compared using a 3-way factorial ANOVA. A p -value of 0.05 was considered statistically significant.

6.3.2. Control Groups

In the first approach, samples containing individual bacterial species suspended in 1% DMSO in PBS without the PSs served as control groups. The control experiments were run in the absence and presence of light (with laser light centered at 670 nm wavelengths with dose of 524 mV/cm² for Pcs and at λ_{exc} of 415 nm, dose of 250 mW/cm² for porphyrins) under similar conditions used for the samples containing the PSs and the bacteria.

All the dark-treated control groups showed no antibacterial effect as seen in **Figure 6.1** as values $< 0.3 \log_{10}$ reductions were obtained (data not shown) even after 120 min exposure. This was done to monitor the effects of 1% DMSO/PBS and the results show that this media has very low impact on the overall results for all the bacteria. Bacteria such as *S. aureus* are known to be resistant to the effect of DMF which is almost similar to DMSO [276].

The light-treated control groups also confirm that the light doses used in the current study have no cytotoxic effect on the strains as the results in **Figure 6.1** show no decrease in the bacteria viable count after treatment.

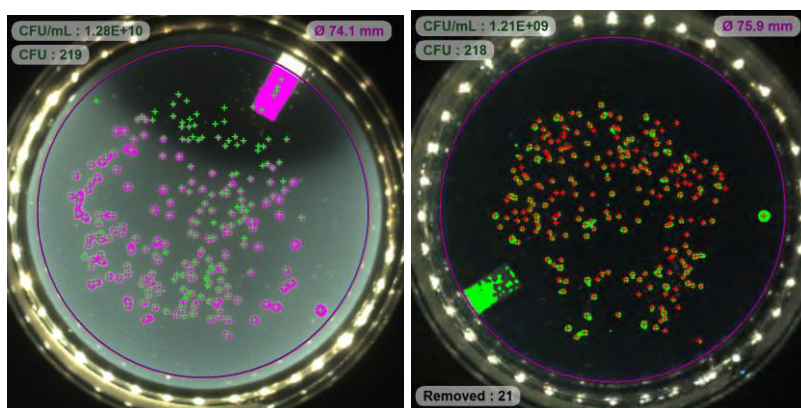


Figure 6.1 Agar plate photographs for (left) dark-treated and (Right) light-treated control groups showing no antimicrobial results after 120 min light exposure (for exemplification).

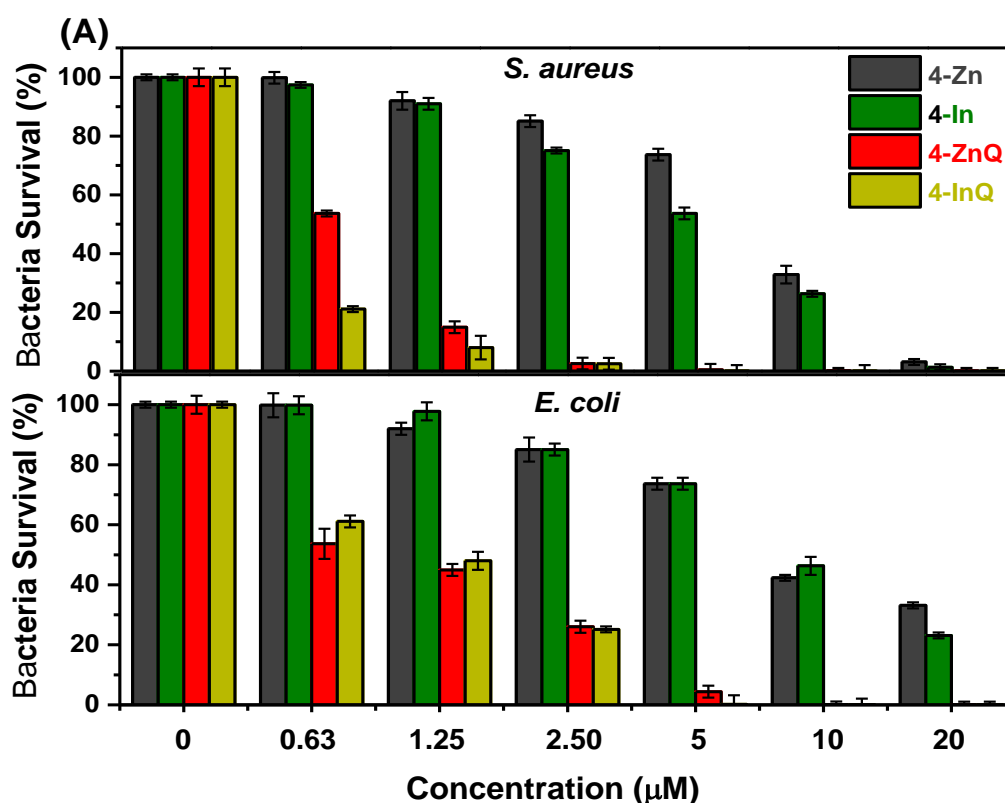
6.3.3. Bacteria Optimization

After colony forming units (CFU) counting, the bacteria dilution factor of 10^{-5} or sometimes 10^{-6} were chosen as long as the optimal bacteria dilution factor shows a percentage survival average of 30-300 colonies which corresponded to approximately 10^9 or 10^{10} CFU/mL⁻¹.

6.3.4. Photosensitizer-Concentration Optimization

Towards this goal, the first efforts were aimed at identifying the optimal conditions necessary to obtain the best PACT activities (the procedure for concentration optimization has been given in **Chapter Two**). An optimal concentration here is defined as the lowest drug concentration able to prevent visible bacterial growth (50%) after 30 min irradiation compared to the control groups. These experiments were conducted in the absence or the presence of light.

Gradient PSs-concentrations ranging from 0.625 to 20 μ M were tested against both strains. The obtained data depicted in **Figure 6.2** revealed considerable cell viability reduction, particularly for higher tested PSs concentrations towards both bacteria under light exposure. Please recall that the incubation time between PSs and the bacteria was 30 min at 37 °C, which is typical in PACT [277], to provide a higher drug uptake and to allow a minimal irradiation time.



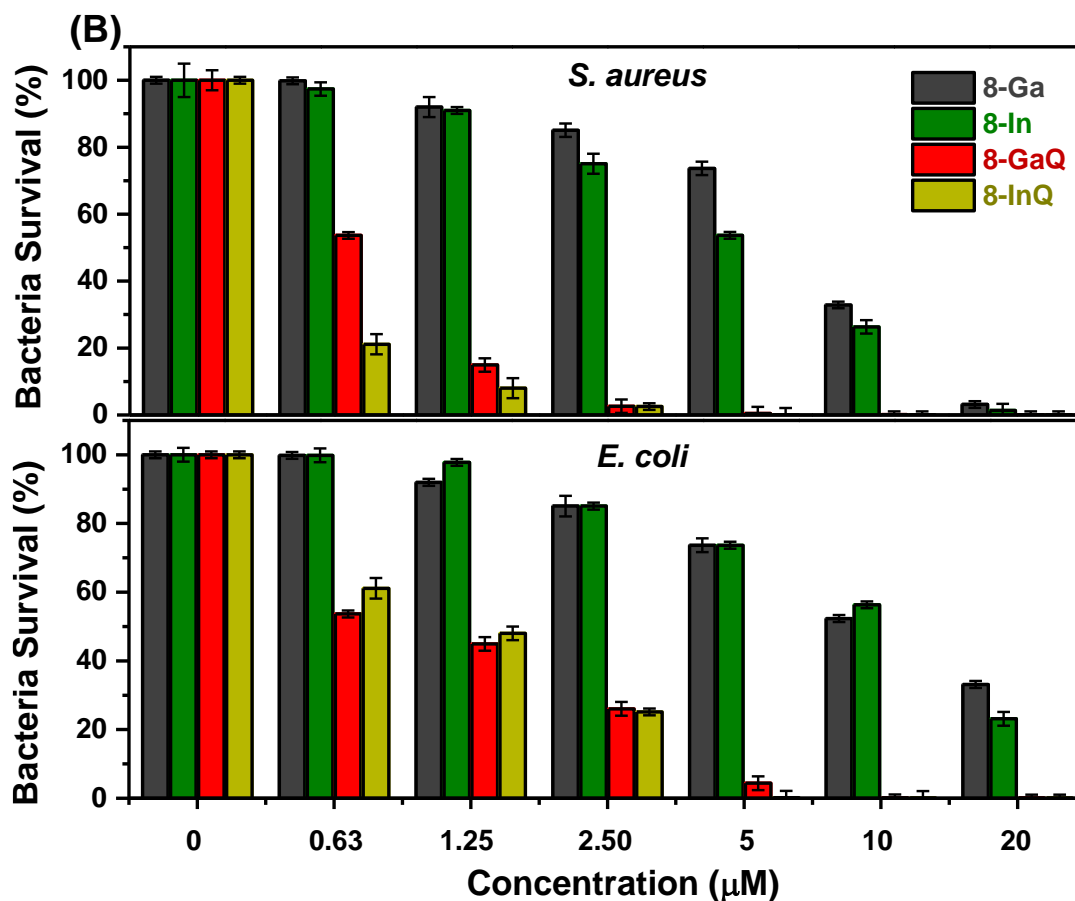


Figure 6.2 shows percentage bacteria survival plots of all bacterial species in a PS-concentration for both bacteria after 30 min light exposure. (A) for Pcs and (B) for porphyrins (as examples).

Concentrations *ca.* 10 μM based on the PS (for the non-quaternized complexes) and *ca.* 1.25 μM based on the PS (for the quaternized complexes) proved to be adequate in this respect. These concentrations showed bacteria reduction of more than 50% in *S. aureus* and *E. coli* following all 30 min of light treatment. For consistency and comparison purposes, these concentrations were used for the Pcs, porphyrins, as well as for nanoconjugates.

6.3.5. Dark Toxicity Studies

The experiments were carried out in the dark to determine if the PSs possess cytotoxicity on the bacteria in the absence of light. **Figures 6.3A, B.**

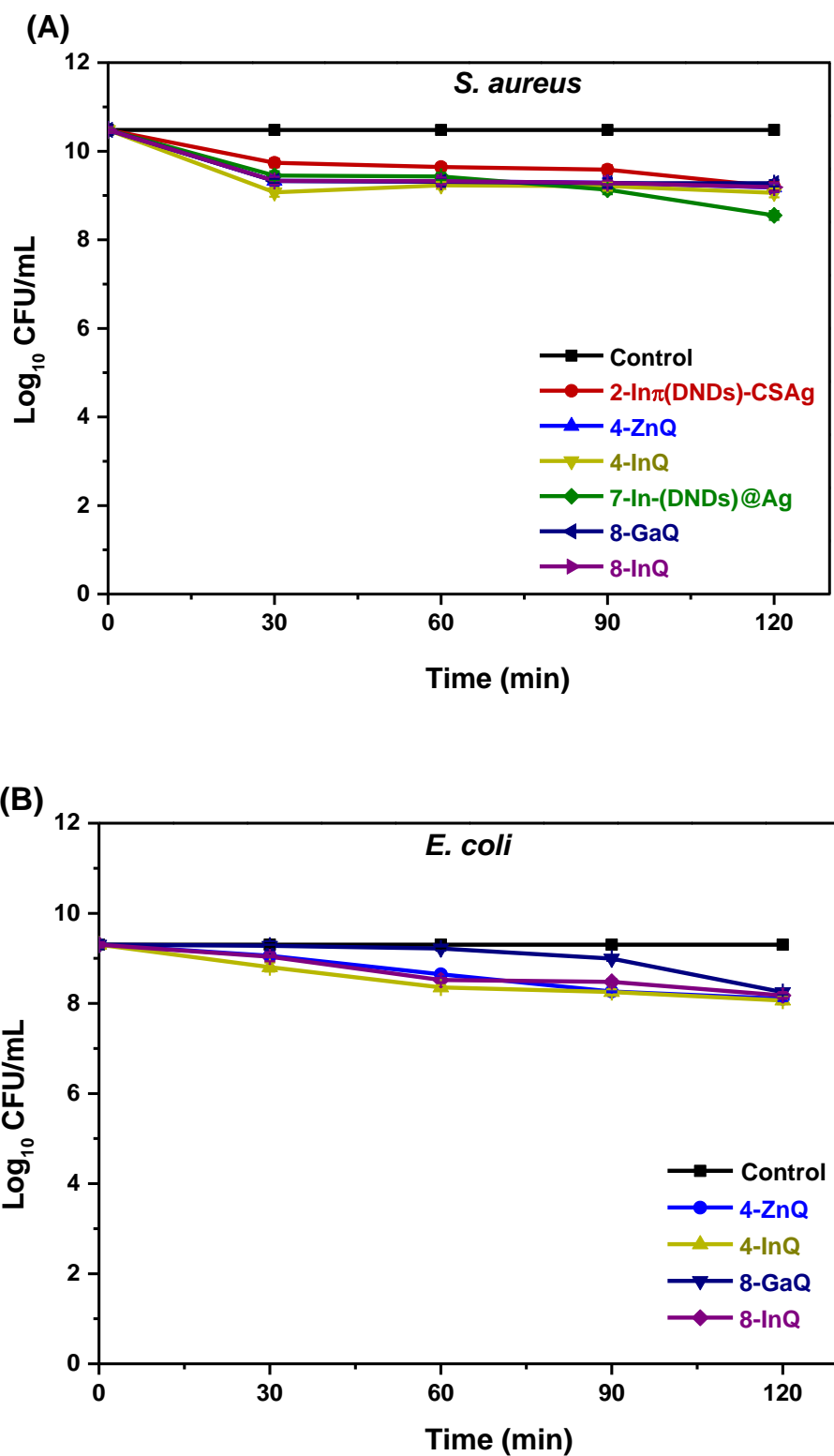


Figure 6.3 Dark toxicity studies on (A) *S. aureus* (B) *E. coli* represented as Log₁₀ CFU/mL vs time graphs for the planktonic cells. The concentrations of the drugs= 10 μ M for non-quaternized and 1.25 μ M for the cationic complexes. Data represent the mean \pm standard deviation (triplicates).

Please note that most of the studied PSs are non-cytotoxic in the dark, as no significant inactivation ($< 1\text{-log}_{10}$ reduction in the survival fraction) could be observed in both bacterial strains even at higher treatment time and they all had the same activity as the control groups shown in **Figures 6.3A, B** and **Table 6.2**.

However dark toxicity is observed in some of the complexes and nanoconjugates following 120 min dark exposure with 30 min intervals. These compounds include, in the Pc groups, the nanoconjugate **2-In π** (DNDs-CSAg) which shows a 1.28-log_{10} reduction on *S. aureus* and the quaternized Pcs **4-ZnQ** and **4-InQ** that give 1.29 and 1.41-log_{10} reductions respectively on *S. aureus* while on *E. coli* these values were of 1.20 and 1.24-log_{10} reduction,

For the porphyrin groups, the **7-In**-(DNDs@Ag) conjugate has a value of 1.93-log_{10} reduction on *S. aureus*, and the quaternized porphins **8-GaQ** and **8-InQ** also exhibited slight dark toxicity effects on *S. aureus* with 1.26 and 1.32-log_{10} CFU/mL respectively, whereas on *E. coli* their 1.13 and 1.05-log_{10} CFU/mL were obtained (**Figures 6.3A, B** and **Table 6.2**).

To explain this killing effect in the dark, one needs to recall that firstly, the cytotoxicity of a PS in the dark is not connected to photon excitation and the production of ROS. Hence, the dark mode of inhibition might be happening by other pathways. As pictured in **Figure 6.4**, one possibility is that the high cell uptake of an active PS can cause perforations on the bacteria cell wall. This might lead to the disruption of intracellular structures of the cell.

Another hypothesis supported by data recently collected shows evidence that if a PS is uptaken into the cell, it can intercalate with bacterial DNA, hence disrupting the cellular function (**Figure 6.4**). To support this, a report has proven that the incubation of *E. coli* with a cationic Pc in the dark caused alterations of the outer membrane permeability and increased the cell uptake which will eventually lead to high antibacterial activity [278].

It is also noteworthy that the mechanism involved in the uptake and bactericidal inhibition of PSs in the dark is not dependent on the composition of the cell wall of bacteria. As proof, the quaternized Pcs and porphyrins cited above exhibited dark toxicity against both the Gram-positive and Gram-negative bacteria.

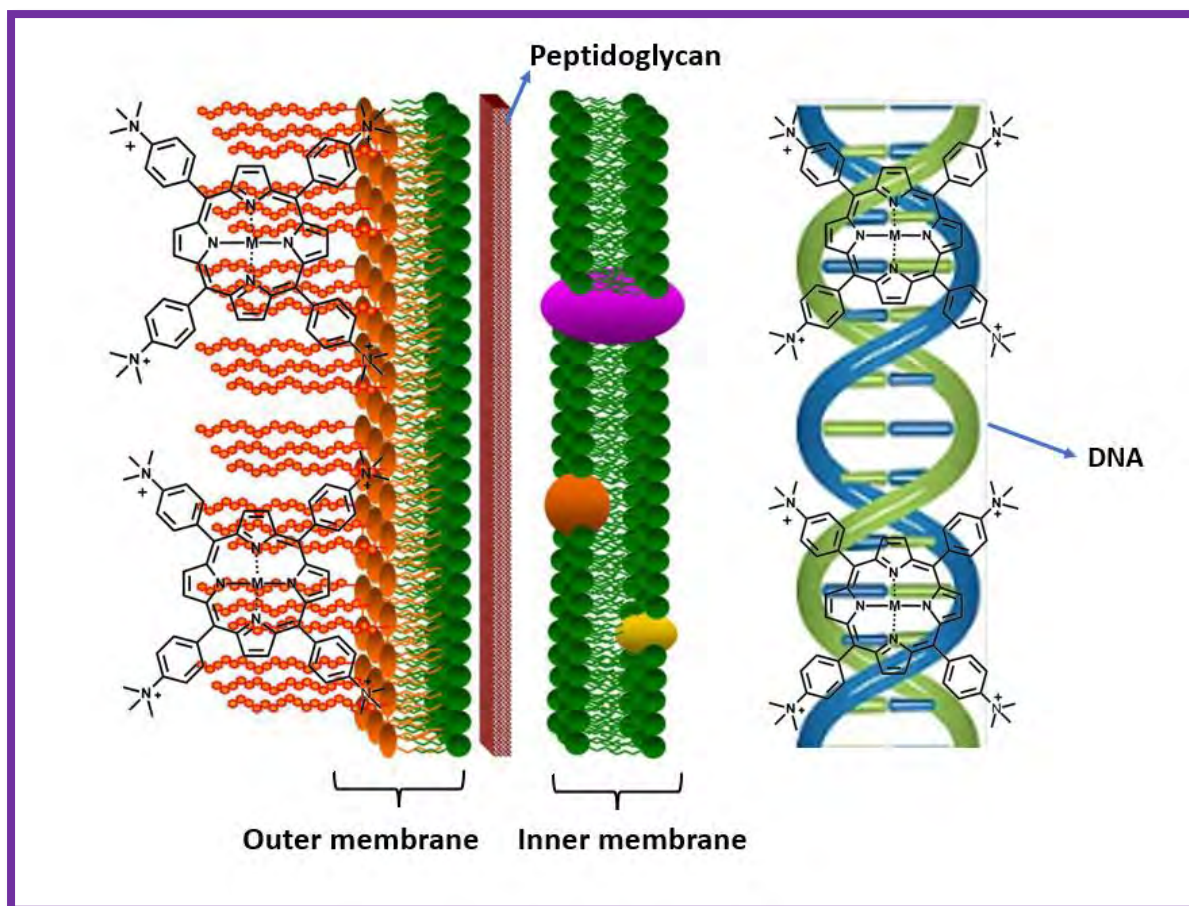


Figure 6.4 Representation of dark inhibition by a quaternized PS on Gram-negative bacteria.

For instance, complexes showing dark toxicity may still be used as antimicrobial agents in the treatment of burn wounds against bacterial infections. Porphyrins have been used before to treat *S. aureus*-caused burn wound infection [279].

The quaternized complexes **3-ZnQ** and **3-InQ** along with their nanoconjugates **3-ZnQ π** (DNDs) and **3-InQ π** (DNDs) might have not exhibited dark toxicity due to the charge stabilization happening in the pyridine ring through resonance that neutralizes the strength of the positive charges.

6.3.6. Photoinactivation Studies

The irradiation experiments were conducted using a red-light laser with an excitation wavelength of 670 nm for Pc derivatives and at 415 nm for the porphyrins. The photoantibacterial efficiency of all the PSs was quantitatively assessed using \log_{10} reduction values which are listed in **Table 6.2**.

Table 6.2 Log reduction values in 1% DMSO/PBS of *S. aureus* and *E. coli* using 10 μ M for non quaternized and 1.25 μ M for quaternized samples in 1% DMSO/PBS after irradiation and dark toxicity.

Complex	Log reduction (± 0.05)				Dark toxicity
	<i>S. aureus</i>	Time (min)	<i>E. coli</i>	Time (min)	
Group 1: Acetophenoxy-substituted Pcs and nanoconjugates					
GQDs	0.52	120	-	-	NO
DNDs	0.75	120	-	-	NO
1-H₂	0.60	120	-	-	NO
1-Zn	2.65	120	-	-	NO
1-In	2.85	120	-	-	NO
1-H₂π (GQDs)	0.13	120	-	-	NO
1-Znπ (GQDs)	3.77	120	-	-	NO
1-Inπ (GQDs)	9.68	120	-	-	NO
1-H₂π (DNDs)	1.08	120	-	-	NO
1-Znπ (DNDs)	9.72	90	-	-	NO
1-Inπ (DNDs)	9.72	30	-	-	NO
Group 2: Bromo-aminophenoxy-substituted Pcs and nanoconjugates					
CSAg	2.87	120	-	-	NO
2-Zn	2.85	120	-	-	NO
2-In	2.98	120	-	-	NO
2-Znπ (DNDs)	9.11	120	-	-	NO
2-Inπ (DNDs)	9.56	90	-	-	NO
2-Znπ (DNDs)-CSAg	9.74	60	-	-	NO
2-Inπ (DNDs)-CSAg	9.74	60	-	-	1.28 (<i>S. aureus</i>)
Group 3: Pyridyl chalcone-substituted Pcs and nanoconjugates					
3-Zn	0.52	120	0.15	120	NO
3-In	1.85	120	0.48	120	NO
3-ZnQ	9.60	30	9.64	30	NO
3-InQ	9.60	30	9.64	30	NO
3-Znπ (DNDs)	1.32	120	0.74	120	NO
3-Inπ (DNDs)	9.27	120	0.58	120	NO

3-ZnQπ (DNDs)	9.60	60	9.64	30	NO
3-InQπ (DNDs)	9.60	60	9.64	30	NO
Group 4: Dimethylamino chalcone-substituted Pcs and nanoconjugates					
Chalcone	-	-	-	-	NO
4-Zn	3.23	120	2.84	120	NO
4-In	3.69	120	2.99	120	NO
4-ZnQ	10.48	30	9.30	30	1.29 (<i>S. aureus</i>) 1.20 (<i>E. coli</i>)
4-InQ	10.48	30	9.30	30	1.41 (<i>S. aureus</i>) 1.24 (<i>E. coli</i>)
Groups 5-6: Tetra and monocarboxylic acid-substituted Pcs and nanoconjugates					
GSH@GQDs	0.30	120	-	-	NO
5-Zn	1.57	120	-	-	NO
6-Zn	2.15	120	-	-	NO
5-Znπ (GSH@GQDs)	10.26	120	-	-	NO
6-Zn -(GSH@GQDs)	10.26	90	-	-	NO
Group 7: Asymmetric porphyrins and nanoconjugates					
Ag NPs	2.73	120	-	-	NO
7-H₂	1.13	120	-	-	NO
7-Zn	2.75	120	-	-	NO
7-In	10.48	120	-	-	NO
7-Ga	10.48	120	-	-	NO
7-H₂ -(DNDs@Ag)	2.54	120	-	-	NO
7-Zn -(DNDs@Ag)	10.48	90	-	-	NO
7-Ga -(DNDs@Ag)	10.48	30	-	-	NO
7-In -(DNDs@Ag)	10.48	30	-	-	1.93 (<i>S. aureus</i>)
Group 8: Dimethylaminophenyl porphyrins					
8-Ga	2.31	120	1.73	120	NO
8-In	3.23	120	2.43	120	NO

8-GaQ	9.06	120	9.30	120	1.26 (<i>S. aureus</i>) 1.13 (<i>E. coli</i>)
8-InQ	10.48	90	9.30	30	1.32 (<i>S. aureus</i>) 1.05 (<i>E. coli</i>)

NO: Not Observed (log reduction value below 1 following 120 min treatment).

6.3.6.1. Effect of Central metal and Singlet Oxygen

The photoantibacterial effect represented as \log_{10} reduction values followed the same trend as the Φ_{Δ} values for PSs belonging to the same group, **Table 6.2**. The insertion of diamagnetic metals in the core of PSs has shown an increase in the production of $^1\text{O}_2$ particularly. From this, one can say that the efficient killing mostly observed for the metallated compounds is expected due to their relatively high Φ_{Δ} values.

Metallated compounds also present a stronger affinity to the cell wall thus resulting in complete cell membrane destruction and enhanced drug-cell uptake for efficient photo-antibacterial abilities since they produce singlet oxygen in close proximity of the cell [280]. It has been acknowledged that the majority of ROS generation in bacteria comes from the oxygen-driven oxidation of the respiratory electron transport chain [281].

For instance, comparing the free-base porphyrin **7-H₂** to the metallated ones, **7-In** and **7-Ga** alone completely eliminate *S. aureus* (no colonies observed) showing a 10.48- \log_{10} ($p=0.003$) reduction in bacterial viability with a concentration *ca* 10 μM , **Table 6.2**.

6.3.6.2. Effect of Substituents

It can be noted that the photoinactivation of indium PSs alone **1-In**, **2-In**, **3-In**, **4-In**, **7-In**, and **8-In** against *S. aureus* resulted in \log_{10} reductions of 2.85, 2.98, 1.85, 3.69, 10.48, and 3.23 respectively. These values mean that the complexes were able to photoeradicate over 99.98% of the viable bacteria except for 10.48- \log_{10} reduction which means complete killing. Additionally, the zinc and gallium PSs also gave a statistically significant reduction of bacteria as seen in **Table 6.2**, hence confirming the importance of metallation with heavy central metals.

As examples, based on all the synthesized zinc Pcs and porphyrins alone, **1-Zn**, **2-Zn**, **3-Zn**, **4-Zn**, **5-Zn**, and **7-Zn**, 2.65, 2.85, 0.52, 3.23, 1.57 and 2.75- \log_{10} reductions are obtained, values which are still relatively significant except for complex **3-Zn** which for unknown reason gave 0.52- \log_{10} reduction and complexes **8-Ga** and **5-Zn** exhibited 2.31 and 1.57- \log_{10} reduction values, respectively (**Table 6.2**).

As expected, these data also exteriorize the importance of designing PSs with substituents that contain functional groups or moieties that possess both antibacterial potencies and the capacity to generate cytotoxic ROS when exposed to light. Pcs **4-Zn** and **4-In** which have the dimethylamino-chalcone moieties, in particular, exhibit the highest potency against both bacteria species with \log_{10} reduction values as high as 3.23 and 3.69 respectively (for *S. aureus*) and 2.84 and 2.99 (for *E. coli*). Chalcone compounds have been reported to possess intrinsic antibacterial activity and another reason being the higher hydrophilic ability of **Group 4** complexes compared to **Group 3** chalcone-Pcs; hence the former show higher PACT activity.

6.3.6.3. *Effect of Symmetry*

Comparing the symmetrical Pc **5-Zn** and its asymmetrical derivative **6-Zn** as examples, in this case, it is observed that the asymmetrical Pc has a higher activity 2.15- \log_{10} reduction probably due to its higher singlet oxygen quantum yield value as compared to the symmetrical complex with a 1.57- \log_{10} reduction in the viable fraction (**Table 6.2**). As mentioned before, asymmetry results in improved Φ_{Δ} values which in return improve the photoeffect.

6.3.6.4. *Effect of Positive Charges*

In this study, under light treatment, the quaternized PSs and their nanoconjugates showed a high rate of killing planktonic *S. aureus* and *E. coli* cells compared to their non-quaternized counterparts under the same experimental conditions.

Concentration *ca* 1.25 μ M was used for the quaternized PSs **3-ZnQ**, **3-InQ**, **4-ZnQ**, **4-InQ**, **8-InQ**, and **8-GaQ**. It was observed that at this low concentration, and 30 min irradiation were enough to completely eliminate all the strains. These positively charged PSs promote a fast and huge decrease in cell viability against both *S. aureus* and *E. coli*, by completely eliminating both bacterial strains with 9.60, 9.60, 10.48, 10.48, 9.06, 10.48- \log_{10} reduction for *S. aureus* respectively, after only 30 min irradiation while 9.64, 9.64, 9.30, 9.30, 9.30, 9.30- \log_{10} reduction were obtained for *E. coli*, respectively (**Figures 6.5** and **6.6** as well as in **Table 6.2**).

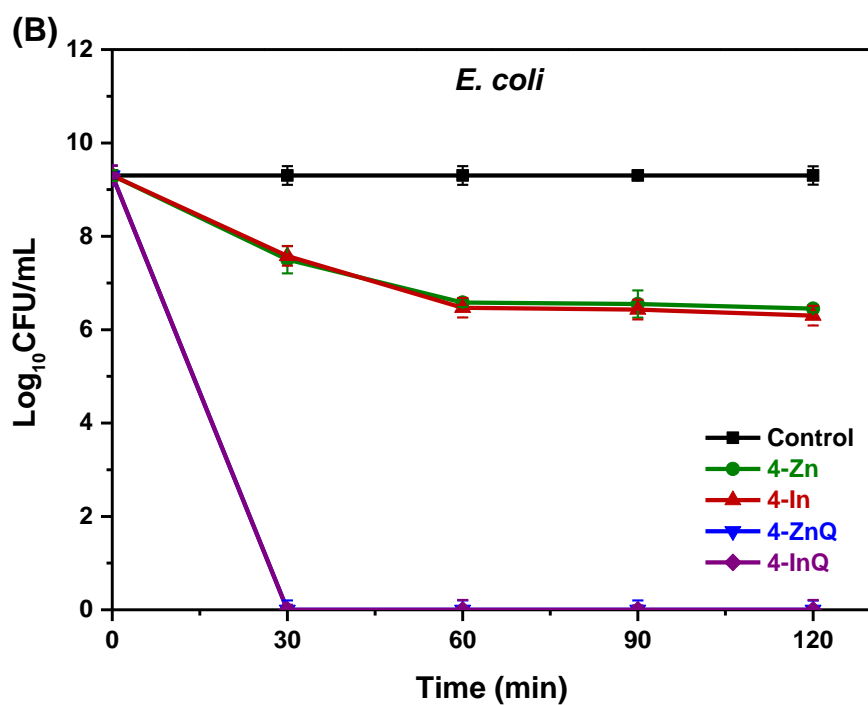
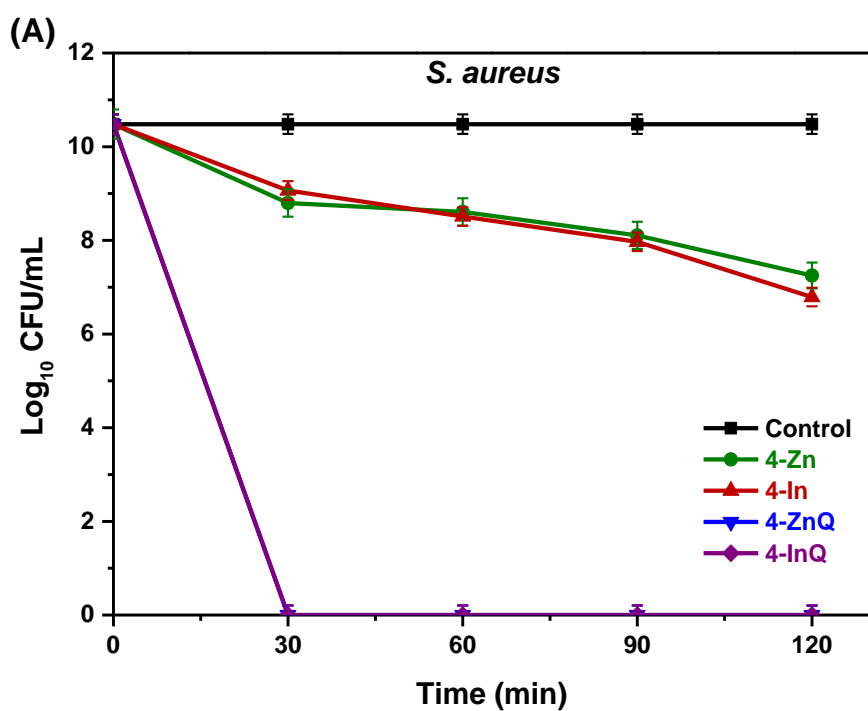


Figure 6.5 PACT studies of **Group 4** complexes on (A) *S. aureus* and (B) *E. coli* vs time graphs for planktonic cells with irradiation at 670 nm. The concentration of the drugs =10 μ M for non quaternized and 1.25 μ M for the cationic complexes. Data represent the mean \pm standard deviation (triplicate).

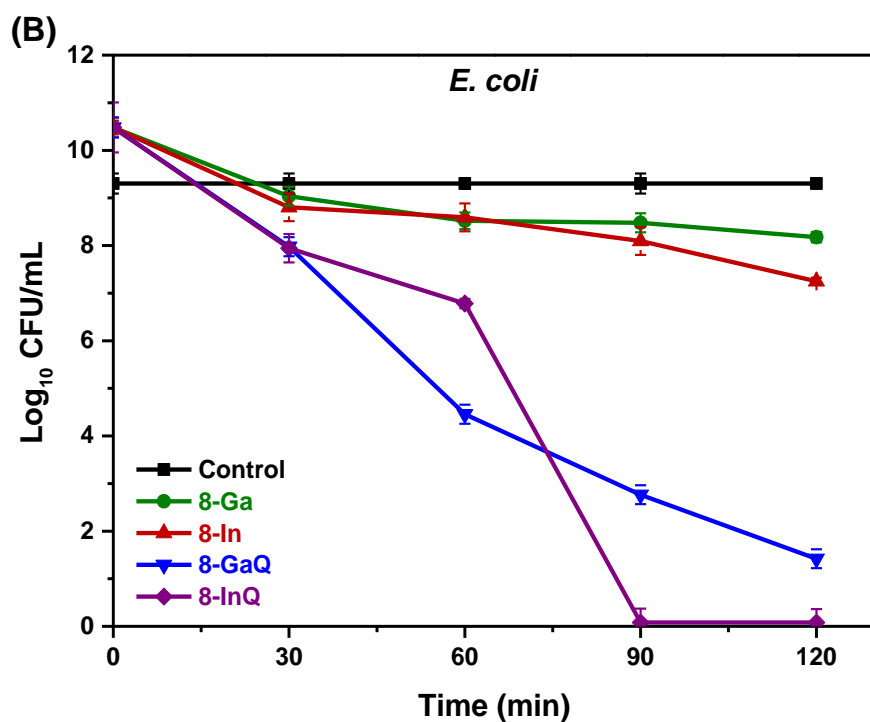
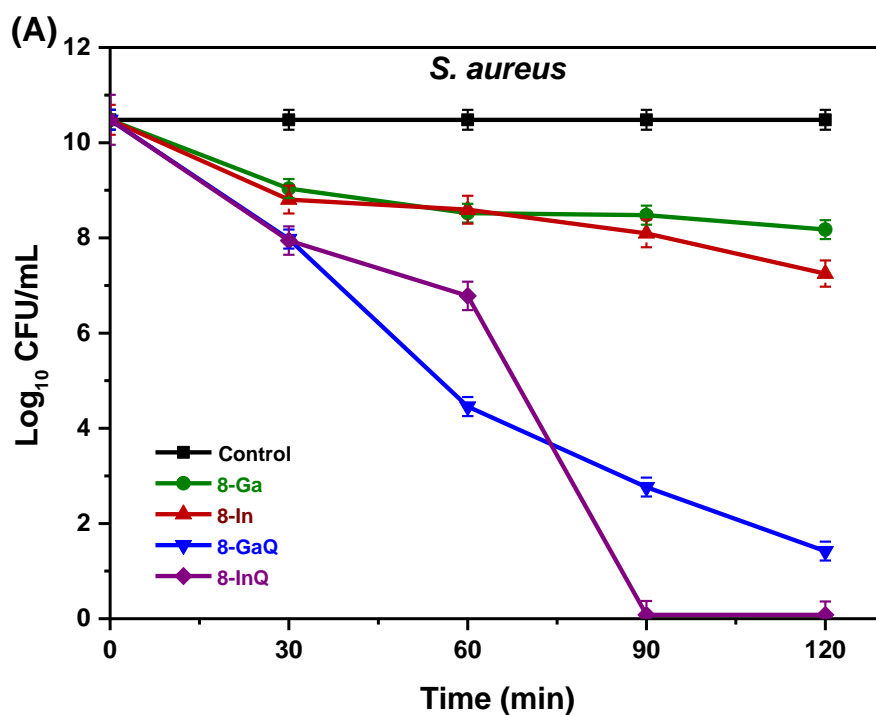


Figure 6.6 PACT studies of **Group 8** complexes on (A) *S. aureus* and (B) *E. coli* vs time graphs for planktonic cells with irradiation at 415 nm. The concentration of the drugs = 10 μ M for non quaternized and 1.25 μ M for the cationic complexes. Data represent the mean \pm standard deviation (triplicate).

Neither long irradiation time (120 min, light dose: 943 J/cm² for Pcs and fluence: 250 mW/cm² for porphyrins) nor high concentration *ca* 10 μM for non-quaternized PSs alone was able to completely eliminate or significantly inactivate both bacterial strains as they have about three-fold lower log₁₀ reduction values than their quaternized derivatives (**Table 6.2**).

As previously demonstrated by Tegos *et al.*, [282] the presence of cationic charges in the structure of a PS strongly affects the ability to inactivate bacteria, suggesting that PS with a higher number of cationic charges in its structure might be able to inactivate bacteria species. Hence, one can hypothesize that the non-quaternized PSs alone localize in a completely different environment than those of quaternized and conjugated to NPs as their lipophilicity/hydrophilicity are completely different (**Table 6.1**). It is known that the lipophilicity of Pcs or porphyrins assists them in penetrating outer cell walls in bacteria, hence enhance the cellular uptake [208,283,284].

An overall mechanistic picture emerges from previous reports that state that after an initial binding to bacteria cells driven by electrostatic interactions, cationic complexes partially internalize into the bacterium, where they bind to the nucleic acids. In the same way, exposure to light stimulates the formation of singlet oxygen both inside and outside the cells. If produced outside the cell, singlet oxygen can cross the cell wall.

6.3.6.5. *Effect of Cell Wall*

The biochemical composition of Gram-positive bacteria such as *S. aureus* facilitates the easier penetration of neutral, anionic, or cationic PSs and previous reports have demonstrated that photoinactivation, in this case, takes place through the outer membrane [285]. On the other hand, because of the mostly higher resistance of Gram-negative *E. coli*, higher light doses are needed for photoinactivation with somewhat larger PSs concentrations.

The present study also reports a similar trend whereby *S. aureus* is found to be more sensitive to treatment with some PSs compared to *E. coli*. It can be observed in **Table 6.2** that the non-quaternized porphyrin complex **8-In** exhibited good antibacterial activities with log₁₀ reduction values of 3.23 against *S. aureus* and 2.43 against *E. coli* after 120 min of irradiation time, same for complex **8-Ga** that had 2.31-log₁₀ CFU/mL on *S. aureus* and 1.73-log₁₀ CFU/mL counts on *E. coli* after 120 min of irradiation (**Table 6.2**).

Generally, all the complexes show higher photocytotoxicity toward the *S. aureus* cells than *E. coli* cells. However, the cationic PSs proved to produce the same photoeffect by completely eliminating both bacteria species under the same concentration and light-dose conditions (**Figures 6.5 and 6.6**) as discussed above.

6.3.6.6. Effect of Conjugation to Nanomaterials

It is clear that the photobactericidal effect of the PSs is affected by the initial interaction between the PS and bacteria and, subsequently, by the location of the PS and its strength of binding to the bacterial cell.

In this study, GQDs, GSH@GQDs, and DNDs on their own did not show antibacterial activities as \log_{10} reduction values < 1 are obtained. However, a positive effect is observed for CSAg and Ag NPs as they exhibit 2.87 and 2.73 \log_{10} reduction values (**Table 6.2**). Silver nanoparticles have been reported to kill or inhibit bacteria [286,287].

Interestingly and as expected, all the newly prepared nanoconjugates containing metallated Pc or porphyrin in the present work successfully inhibited the studied bacteria growth except for the **1-Zn π** (GQDs), **3-Zn π** (DNDs), and all the free-base nanoconjugates, **Figures 6.7 A,B**.

Table 6.2 shows that the \log_{10} reductions for complexes alone were way lower compared to their corresponding nanoconjugate derivatives even at a high irradiation time of 120 min. This shows that the PSs conjugation to nanomaterials enhances the photoinactivation process of bacteria. The pronounced PACT activity under light conditions could be due to the synergistic effect brought about by the nanomaterials and the PSs. This is believed to be due to the increased singlet oxygen quantum yields in the nanoconjugates.

The non-quaternized Pcs alone only showed a 0.52 to 3.69- \log_{10} reduction in the viable counts against *S. aureus* and 0.15 to 2.99- \log_{10} reductions against *E. coli* (**Table 6.2**). However, with *ca.* 10 μ M (based on the Pc), **1-In π** (GQDs) has effectively killed *S. aureus* causing a 9.68- \log_{10} reduction (**Table 6.2**). **1-Zn π** (DNDs) and **1-In π** (DNDs) samples have effectively killed the *S. aureus* bacteria cells with \log_{10} reduction of 9.72 after 90 min and 30 min of irradiation respectively, **Table 6.2**.

2-Zn π (DNDs) and **2-In π** (DNDs) nanoconjugates displayed efficient killing of bacteria with a \log_{10} reduction of 9.11 and 9.56 after 120 min and 90 min of irradiation, respectively. Whereas the presence of CSAg effectively increased the killing effect on bacteria at a shorter irradiation time causing a 9.74 \log_{10} reduction for both **2-Zn π** (DNDs-CSAg) and **2-In π** (DNDs-CSAg) after only 60 min of irradiation (**Table 6.2**).

3-In π (DNDs) completely eradicated *S. aureus* with high \log_{10} reduction value of 9.27 (**Figure 6.7A** and **Table 6.2**) while 0.58- \log_{10} reduction value is obtained when tested on *E. coli* (**Table 6.2**).

It is also worth noting that the quaternized nanoconjugates **3-ZnQ π** (DNDs) and **3-InQ π** (DNDs) led to photocytotoxicity against *S. aureus* with a longer time of irradiation (60 min) as compared to **3-ZnQ** and **3-InQ** alone (30 min), **Figures 6.7A** and **Table 6.2**. This is probably due to the screening effect of the DNDs on the PSS' positive charges which in this case are not free but have formed electrostatic interactions with the nanomaterials.

5-Zn π (GSH@GQDs) and **6-Zn**-(GSH@GQDs) nanoconjugates display significant activity with 10.26 log₁₀ unit reduction at 120 min and 90 min light irradiation respectively, **Table 6.2**. Porphyrins **7-Zn**-(DNDs@Ag), **7-Ga**-(DNDs@Ag), and **7-In**-(DNDs@Ag) nanoconjugates also successfully eradicated *S. aureus* with 10.48-log₁₀ reduction, **Figures 6.7B** and **Table 6.2**.

In general, it can be concluded that, nanomaterials employed did not show any significant results of photoinactivation on their own. However, upon conjugation with complexes, there was enhanced photoinactivation of the bacteria. The conjugates gave a significantly higher log₁₀ reduction compared to the complexes alone in both bacteria planktonic cells. This shows that carbon-based nanoparticles enhance the photoinactivation process.

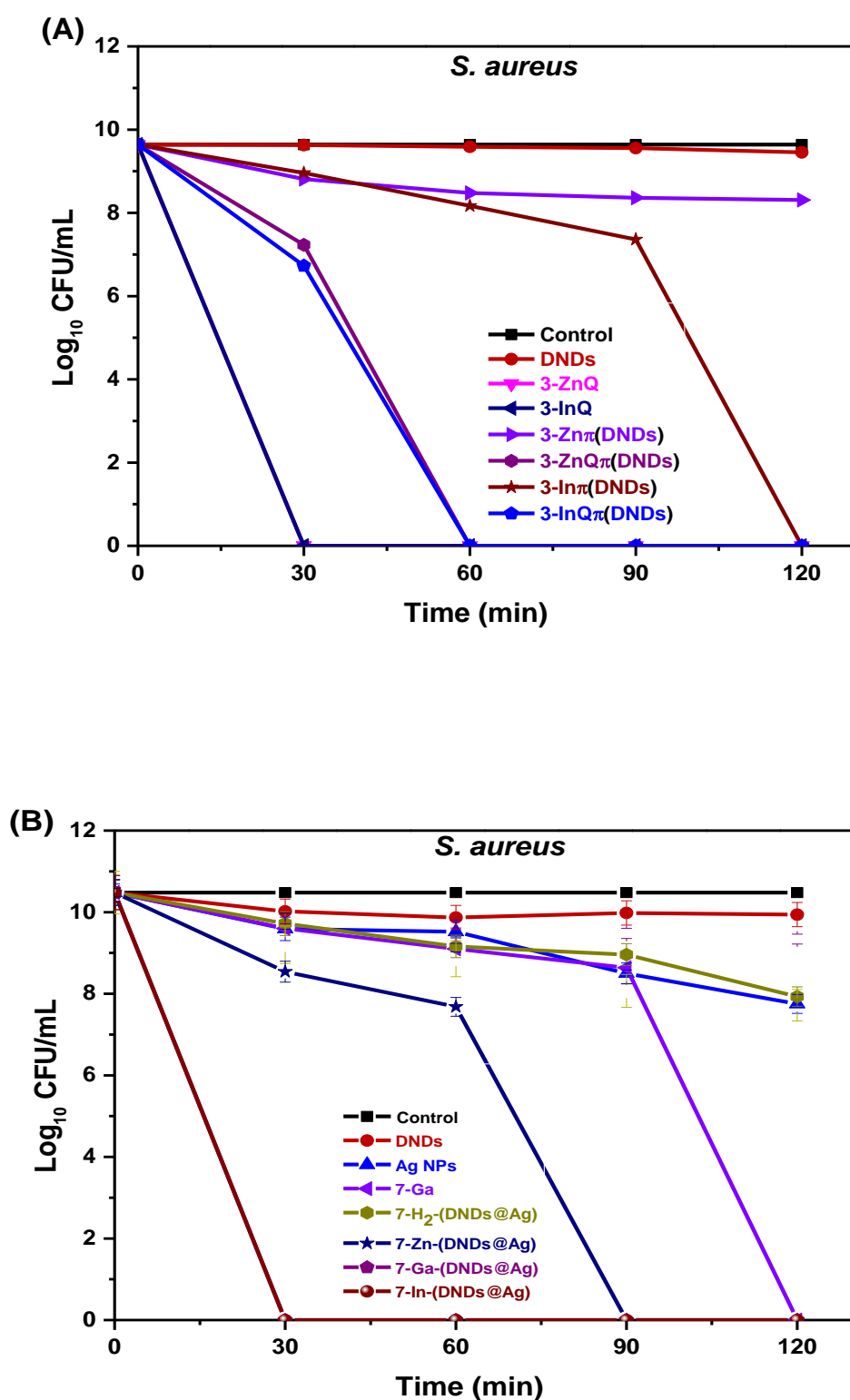


Figure 6.7 Photoinactivation of *S. aureus* (A) by Group 3 Pcs and their DNDs nanoconjugates, irradiation at 670 nm (B) by Group 7 porphyrins and their DNDs@Ag nanoconjugates (irradiation at 415 nm with ca 10 μ M). Concentration of the drugs=10 μ M for non quaternized and 1.25 μ M for the cationic complexes. Data represent the mean \pm standard deviation (triplicate).

6.4. Biological Assays on Bacteria Biofilm Cells

Bacterial biofilms have prevented antibiotics from being effective against matured biofilms due to the secretion of polymeric substances. About twenty years ago, Roberto Kolter (one of the pioneers on biofilms) stated that it was about time to move from bacterial cultures to biofilms [288]. It is time for PACT to move onwards by treating the real life-threats, the bacterial biofilm cells.

Hence, in this work, the antibiofilm activity of some of the selected complexes and their nanoconjugates (these include **Groups 2, 3, 4, 7, and 8**) that also exhibited high activities against the planktonic cells were as well tested against bacterial biofilm cells of either *S. aureus* or *E. coli* or both, as they are well known to affect the population's wellbeing. Researchers have proved that *S. aureus* and *E. coli* are strong biofilm producers [289], thus these bacteria were used to form the matured biofilms for *in vitro* antibiofilm experiments in this work.

Please note that for biofilm-based cultures, much higher PS concentrations are required to obtain a PACT killing efficiency comparable to that observed for planktonic cultures.

The control groups were the same as planktonic cells studies.

6.4.1. Photosensitizer-Concentration Optimization

As previously indicated, biofilms are less sensitive to PACT than planktonic cells due to the sticky and resilient extracellular matrices that prevent the penetration of antimicrobials or any other treatment [290]. Thus, in this study, the PSs concentrations are increased. For the purpose of concentration studies, four different concentrations *ca.* 25, 50, 100, and 200 μM (based on the PS) were investigated for all the complexes and nanoconjugates for 30 min irradiation time (light dose: 943 J/cm^2 for Pcs and fluence: 250 mW/cm^2 for porphyrins) or for 30 min treatment in the dark.

6.4.2. Dark Toxicity Studies

The experiments illustrated that the group of PSs kept in the dark did not demonstrate dark cytotoxicity effects at all concentrations for both strains as seen in **Figures 6.8A** and **6.9A** (as examples).

6.4.3. Photoinactivation Studies

The biofilms were incubated with either 25, 50, 100, and 200 μM of the PSs alone or nanoconjugates for 30 min in the dark at 37°C. Following the dark incubation, each sample was exposed to red light ($\lambda_{670\text{ nm}}$) for Pcs or blue light ($\lambda_{415\text{ nm}}$) for porphyrins with a total light fluence of 524 mV/cm^2 and 250 mW/cm^2 , respectively for 30 min. The results of the biofilm PACT experiments are shown in **Table 6.3**.

Table 6.3 Cell survival values of samples in 1% DMSO/PBS after 30 min irradiation on *S. aureus* biofilms.

Complex	Cell survival (%)			
	Concentration (μM)			
	25	50	100	200
Group 2: Bromo-aminophenoxy-substituted Pcs and nanoconjugates				
DNDs	100	99	98	92
2-Zn	100	100	100	100
2-In	100	100	100	100
2-Znπ (DNDs)	100	99.9	99.9	99.9
2-Inπ (DNDs)	100	99.9	99.9	99.85
2-Znπ (DNDs)-CSAg	100	76	33.1	0.0025 (5.12)
2-Inπ (DNDs)-CSAg	100	67	7.1	0.00059 (5.27)
Group 7: Asymmetric porphyrins and nanoconjugates				
Ag NPs	100	98	95	47
7-H₂	93.5	84.6	74	53
7-Zn	91.4	75.6	56.8	37
7-Ga	91.9	86.9	30.8	17
7-In	85	47	22	14
7-H₂ -(DNDs@Ag)	95	79	75	52
7-Zn -(DNDs@Ag)	79	65	44	25
7-Ga -(DNDs@Ag)	26	10.2	2.2	0.8 (9.41)
7-In -(DNDs@Ag)	25	2.3	1.9	0.09 (9.42)

(In brackets) are \log_{10} reduction values

6.4.3.1. Effect of Conjugation of PSs@DNDs to CSAg and Ag NPs

Groups 2 and 7 will be used as examples in this particular case. Highly effective antibiofilm activity was observed for **2-Zn π** (DNDs-CSAg) and **2-In π** (DNDs-CSAg) nanocomposites which resulted in biofilm reduction by 5.12- \log_{10} (0.0025% cell survival) and 5.27- \log_{10} (0.00059% cell survival) reduction units respectively at *ca.* 200 μ M following 30 min of irradiation, **Table 6.3**.

As listed in **Table 6.3**, **7-Ga**-(DNDs@Ag) and **7-In**-(DNDs@Ag) also show the lowest biofilm cells survival values of 2.2% and 1.9%, at 100 μ M (based on the porphyrin), respectively. While at 200 μ M the percentage of survival is 0.8% and 0.09% corresponding to 9.41 and 9.43- \log_{10} reduction, respectively. As displayed in **Table 6.3**, only the indium and gallium nanoconjugates were able to statistically give significant reductions in biofilm at 100 μ M upon 30 min of irradiation.

The significant decrease in survival under light conditions for these Pcs@DNDs-CSAg and porphyrins-DNDs@Ag nanoconjugates could be due to the synergistic effect brought by DNDs, CSAg, and Ag NPs as well as their high singlet oxygen quantum yields. The basic mode of action of these compounds might include inhibition of cell metabolism and growth, damage to the cytoplasmic membrane, and increase in cell permeability [291,292].

Despite the use of high concentrations, porphyrins alone **7-H₂**, **7-Zn**, **7-In**, and **7-Ga**, Pcs alone **2-Zn** and **2-In**, and the DNDs nanoconjugates **2-Zn π** (DNDs) and **2-In π** (DNDs) did not exhibit significant activity on the *S. aureus* biofilm given the fact that the \log_{10} reduction values are less than 3, suggesting no PACT activity, hence no reduction.

6.4.3.2. Effect of Positive Charges

Essential for a PS to be efficient in PACT treatment is a strong interaction between the PS and the target bacteria. While non-quaternized PSs have been proved to weakly interact with Gram-negative bacteria, quaternized PSs are prone to bind and to internalize in these bacterial cells very effectively.

The data from **Table 6.4** show that concentration (*ca.* 100 μ M) of **4-ZnQ** and **4-InQ** Pcs have significant inhibition effects on *S. aureus* and *E. coli* biofilms after treatments of both for 30 min light exposure compared to the control groups ($P < 0.05$). **4-ZnQ** reduced the biofilms of *S. aureus* and *E. coli* to 2.1 and 4.5% cell survival respectively while **4-InQ** inhibited up to 1.2 and 2.3% cell survival growth of *S. aureus* and *E. coli* biofilms, respectively at 100 μ M, **Table 6.4** and **Figures 6.8B** and **6.9B**. With concentration of 200 μ M, the log reduction were calculated to be of 9.42 and 8.95 on *S. aureus* and *E. coli* biofilms respectively under the same conditions, **Table 6.4**.

Table 6.4 The % survival data of samples in 1% DMSO after 30 min irradiation on *S. aureus* and *E. coli* biofilms.

Sample	Cell Survival (%)							
	<i>S. aureus</i>				<i>E. coli</i>			
	25 μM	50 μM	100 μM	200 μM	25 μM	50 μM	100 μM	200 μM
Group 4: Dimethylamino chalcone-substituted Pcs and nanoconjugates								
4-Zn	87	52	44	18	98	63	48	11
4-In	65	39	8.4	0.6	84	45	10	0.5
4-ZnQ	10	8.4	2.1	0.07 (9.42)	26	14	4.5	0.07 (8.95)
4-InQ	6.5	5.2	1.2	0.004 (9.42)	15	7.6	2.3	0 (8.95)
Group 8: Dimethylaminophenyl porphyrins								
8-Ga	91	73	44	8.7	91	73	44	27
8-In	65	52	8.4	0.16	61	39	8.4	4.1
8-GaQ	26	8.4	2.2	0.01 (9.42)	26	8.2	2.0	0.9 (8.59)
8-InQ	2.5	2.3	1.6	0 (9.43)	15	7.6	2.1	0.016 (8.95)

(In brackets) are log₁₀ reduction values.

As mentioned before, in this case, the low activity obtained for **4-Zn** and **4-In** could be due to the absence of positive charges and bit of aggregation, even though **4-In** showed insignificant cell survival of 0.6% against *S. aureus* at 200 μM, **Table 6.4**. Remarkably, the photocytotoxic effects of **4-ZnQ** and **4-InQ** on both biofilm strains may be related to their preferential affinity to the studied strains through their positive charges. This may be the main reason for the more efficient uptake by cells living in the biofilm forms.

Similarly, the quaternized porphyrin derivatives also significantly photoinhibited *S. aureus* and *E. coli* biofilms at 100 μM with 1.6% and 2.1% cell survival for **8-InQ**, respectively, and 2.2% and 2.0% cell survival for **8-GaQ**. Whereas their non-quaternized counterparts showed moderate antibiofilm % cell survival, **Table 6.4**. The quaternized derivatives are found to have higher ability

to significantly suppress the biofilms of both *S. aureus* and *E. coli in vitro* with log₁₀ colony forming units >8, **Table 6.4**.

At this point, it is intriguing to find out why these compounds still show some antibiofilm activity in spite of their ROS generation being minimal. Amphiphilic PSs have been proven to be most efficient in binding to lipids [293] therefore, one can emphasize that interaction PSs with the bacterial cell membrane can to some extent explain this high photoactivity since these compounds demonstrated lipophilicity as in illustrated in **Table 6.1**.

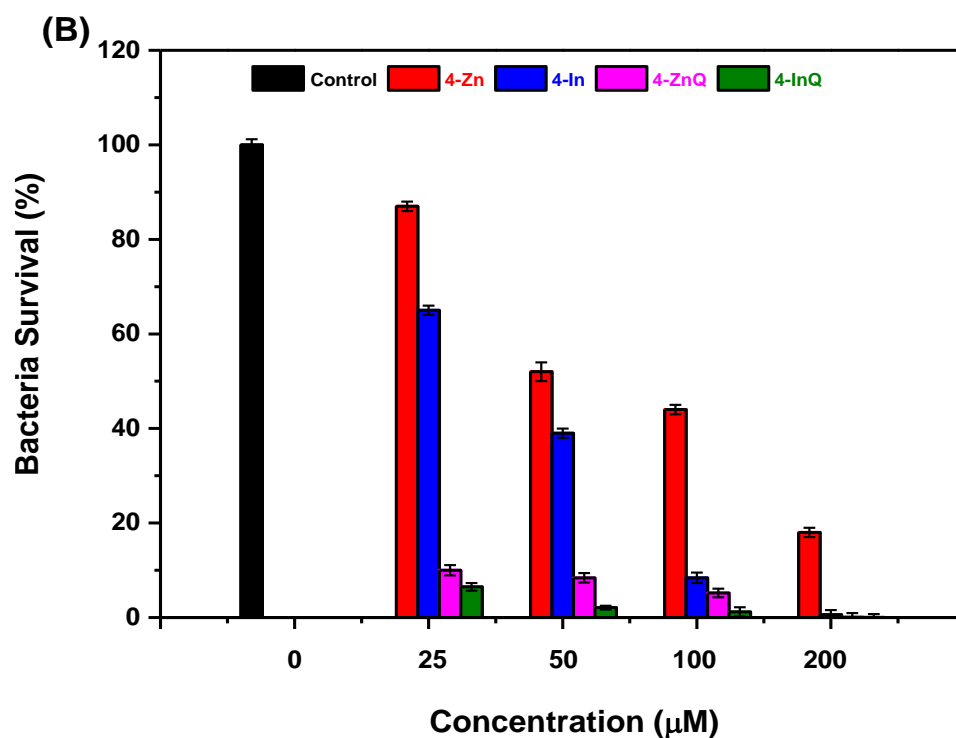
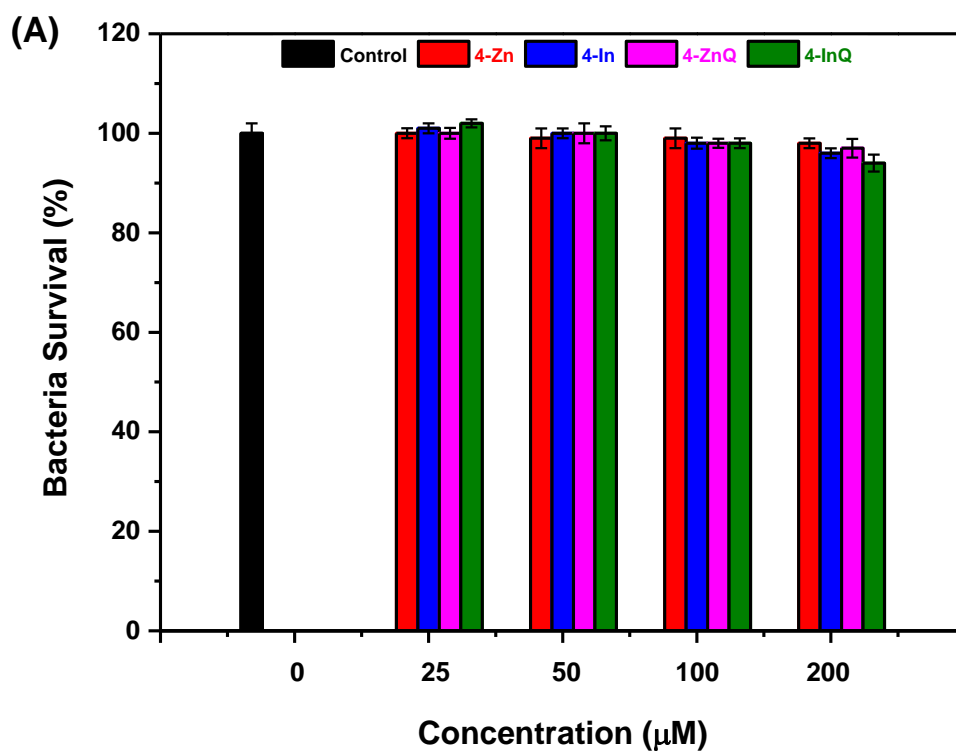


Figure 6.8 (A) Dark toxicity studies and, (B) Photoinhibition studies of **Group 4** compounds on *S. aureus* biofilms cells (30 min irradiation at 670 nm). Data represent the mean \pm standard deviation.

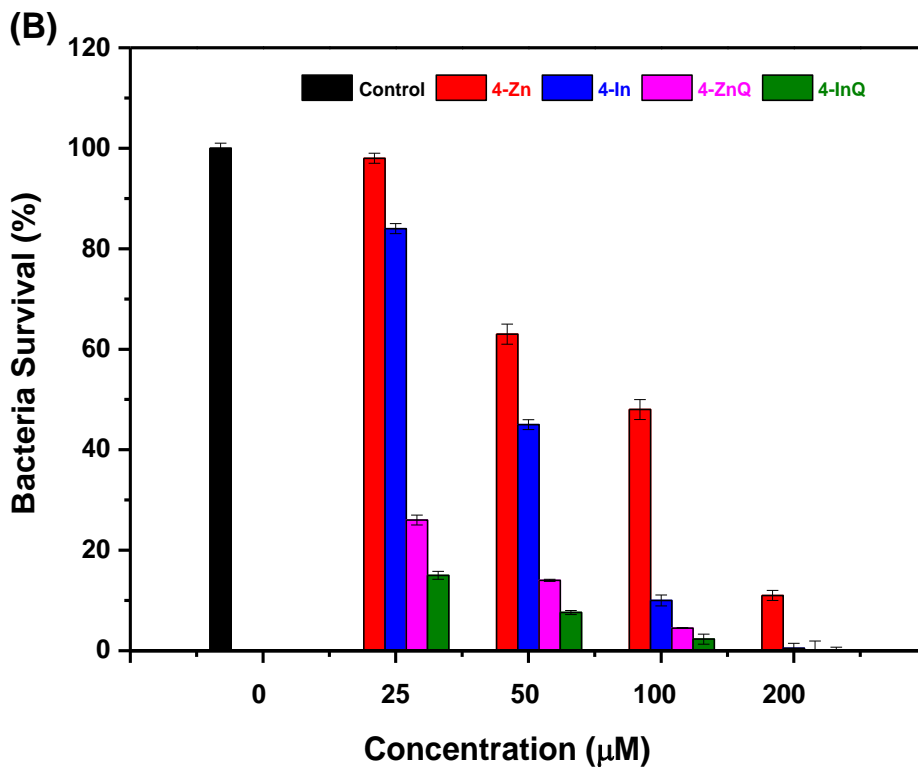
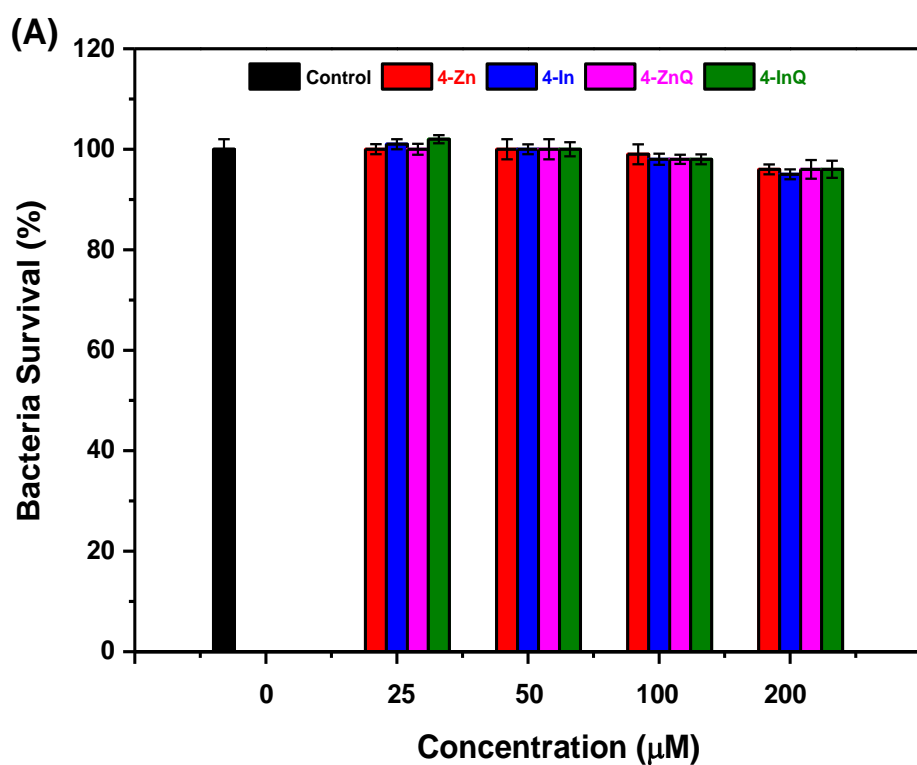


Figure 6.9 (A) Dark toxicity studies and, (B) Photoinhibition studies of **Group 4** compounds on *E. coli* biofilms cells (30 min irradiation at 670 nm). Data represent the mean \pm standard deviation.

6.4.3.3. Effect of Cell Wall

To determine the difference in the efficacy of PS-mediated PACT against Gram-positive strains, *S. aureus*, compared to the Gram-negative, *E. coli*, **3-ZnQ** and **3-InQ** along with their nanoconjugates **3-ZnQ π** (DNDs) and **3-InQ π** (DNDs); but also the quaternized complexes **4-ZnQ**, **4-InQ**, and **8-InQ** are used as models in this case.

Figure 6.10A, B shows the mean and standard deviation results of the different conditions for both bacterial species. The photoactivity on both biofilms was found to be strain-dependent and there was a concentration and time-dependent tendency in their anti-biofilm effect.

For *S. aureus* biofilms, **3-ZnQ π** (DNDs) and **3-InQ π** (DNDs) exhibited high bactericidal activity with an ca. 9.68- \log_{10} reduction with complete photoinhibition at 524 mV/cm² light doses (120 min irradiation with 30 min intervals) when using 100 μ M, **Figure 6.10A** and **Table 6.5**. The reason behind this could be in the Pcs-bacteria interactions and generation of different types of ROS. On the other hand, **3-ZnQ** and **3-InQ** alone respectively gave lower values of 1.40- \log_{10} CFU reduction (cell survival of only 5.85%) and 2.13- \log_{10} CFU reduction (cell survival of only 0.36%), respectively under the same irradiation conditions. This shows again the importance of conjugation of quaternized chalcone-derived Pcs to DNDs.

Table 6.5 Log reduction values at 100 μ M of PSs on biofilms following 120 min irradiation.

Sample	Log ₁₀ reduction	
	<i>S. aureus</i>	<i>E. coli</i>
Group 3: Pyridyl chalcone-substituted Pcs and nanoconjugates		
3-Zn	0.07	0.33
3-In	0.15	0.58
3-ZnQ	1.40	1.45
3-InQ	9.60	9.80
3-Znπ (DNDs)	0.3	1.43
3-Inπ (DNDs)	1.63	2.24
3-ZnQπ (DNDs)	9.68	1.38
3-InQπ (DNDs)	9.68	9.80

But only the indium derivatives **3-InQ** and **3-InQ π** (DNDs) are able to completely inactivate *E. coli* under the same irradiation conditions used for *S. aureus*. They both show a 9.80- \log_{10} CFU reduction with no cell survival, **Figure 6.18B** and **Table 6.5**.

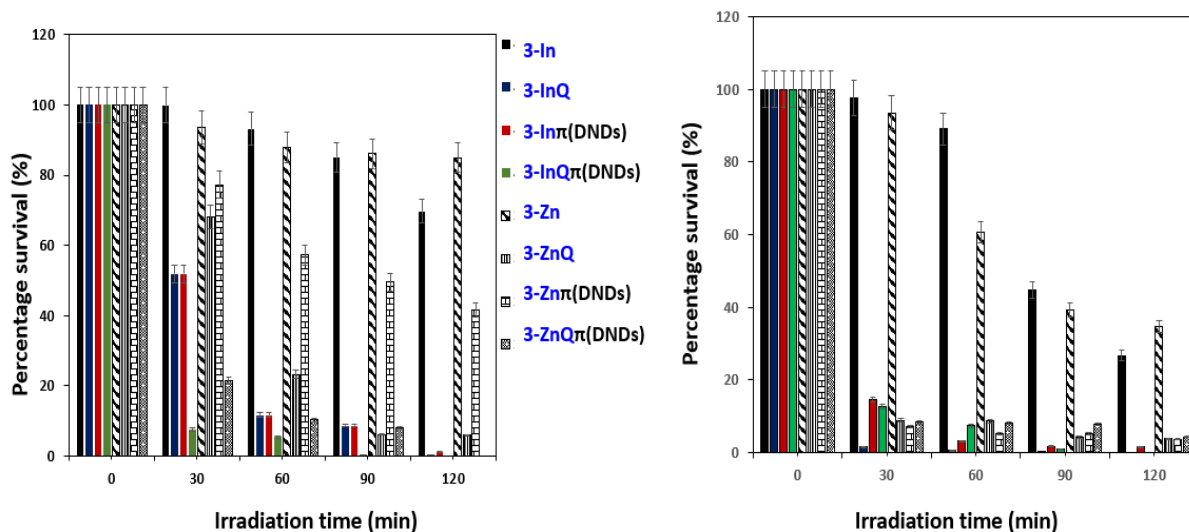


Figure 6.10 Photoinhibition studies of **Group 3** compounds on (Left) *S. aureus* and (Right) *E. coli* biofilms cells (30 min irradiation at 670 nm), concentration of the drug 100 μ M. Data represent the mean \pm standard deviation.

S. aureus possessing one single membrane layer is more prone to the antibacterial effect than *E. coli*. However, **Table 6.4** also demonstrates that in some cases *E. coli* performed a little better than *S. aureus*, for instance, for **8-GaQ** at 100 μ M. Please note that the quaternized complexes **4-ZnQ**, **4-InQ**, and **8-InQ** were also able to inactivate *E. coli* but at 200 μ M, **Table 6.4**.

This antibiofilm activity may be attributed to: (1) the ability of PSs to adhere to the bacterial cells and the exopolymeric substance (EPS) resulting in higher uptake into the biofilm structure; (2) the ability of PSs to induce potent photo-oxidative damages to the biofilm bacteria and structure and (3) the synergistic antibacterial effects produced by each composite of the nanoconjugates.

6.5. Summary of the Chapter

Firstly, the obtained data either on planktonic or biofilms studies are supported with published studies, which revealed that PACT is based on singlet oxygen production, as these results agree with the reported Φ_{Δ} values. Secondly, it is the PSs with cationic charges which localize in the bacteria cell at two different sites: (1) externally bound to the cell wall, and (2) inside the cell by bounding to the nucleic acids. Hence, it is hypothesized in the current work that the non-quaternized Pcs alone would localize in a completely different sites in the cell.

PACT efficiency is attributed to the ability of the PS to produce singlet oxygen and on the number of cationic charges present on its structure. This is because the presence of positive charges on a PS allows stronger affinity to the cell wall and this results in the generation of singlet oxygen in close proximity of the bacteria cell. This explains the trend observed in this work, where significant toxicity was obtained for cationic complexes on both bacterial strains, more especially on the Gram-negative *E. coli* which is well known as difficult to treat using neutral or negatively charged photosensitizers.

During the experiment, the controls did not show significant reduction in the number of colony forming units (CFU) after 120 min irradiation time. This implies that the light used did not have a killing effect on the cells.

The obtained data also confirm that the newly prepared nanohybrids could be used as potential photoantibacterial agents against *S. aureus* and *E. coli* planktonic cells and biofilms at low concentrations of the complexes with low light doses. This shows the importance of conjugation of PSs to GQDs, DNDs, GSH@GQDs, CSAg, and Ag NPs, indicating their promising potential in the treatment of infections-related biofilms.

Chapter Seven: PACT-Antibiotic Dual Therapy

This chapter reports on the *in vitro* antibacterial activities on biofilms resulting from the combination PACT with a clinically approved antibiotic.

7.1. General

PACT is well-recommended for the eradication of infections that are caused by multidrug-resistant bacteria. However, the used PSs are often ineffective when using lower concentrations and light doses, especially in the case of Gram-negative bacteria biofilms due to the complexity of their envelope. On the other hand, the use of PACT, especially in combination with other approaches, has not been fully investigated as of yet. So, for PACT to succeed, PACT-mediated therapies such as PACT-antibiotic dual therapy has to be investigated.

PACT-antibiotic dual therapy combines two therapies, photodynamic and chemotherapy that act in two quite different therapeutic mechanisms and results in enhanced therapeutic efficacy in reduced treatment time and drug doses, reduced side effects, and retarded drug-resistance problem [294]. In dual photo-chemotherapy, three approaches can be considered: sequential administration of a PS and an antibiotic drug, the use of PS and antibiotic conjugates, and co-encapsulation of the two in a nanocarrier.

In light of innovation, this work focuses on studying the antibiofilm effect from subsequent administration of a PS and ciprofloxacin, a quinolone type antibiotic that is commonly used to treat infections in humans through disruption of DNA topoisomerase [295].

For this particular study, the selected PSs are the 3rd generation PSs, the quaternized indium derivatives **4-InQ**, and **8-InQ**. The choice was brought upon them following their impressive PACT activities shown in **Chapter Six** as they completely eradicated both the matured *S. aureus* and *E. coli* biofilms strains using ca. 200 μ M concentration and light doses of 30 min irradiation.

Please recall that, in nature, bacteria often live in biofilm consortia which are more resistant to the action of antibiotics versus planktonic forms. For this reason, the current research part only investigates bacterial biofilms and not planktonic cells. The main goal here is to find whether there is a synergism of action of PACT and ciprofloxacin combination against *S. aureus* and *E. coli* that are living in biofilm form. This time by using much lower concentrations of the PSs and shorter irradiation time than in **Section 6.4**.

7.2. Antibacterial Effect of PACT alone on Biofilm Cultures

In the first step, the PACT effect of the PSs on the survival of *S. aureus* and *E. coli* strains was determined. The PSs gradient concentrations ranged from 4 to 32 μM .

As it can be seen in **Figures 7.1A** and **7.1B**, at these lower concentrations, the survival of *E. coli* did not show a significant decrease after dark exposure, even at higher concentrations (32 μM) of the quaternized PSs **4-InQ** and **8-InQ**. However complex **8-InQ** showed 12% and 16% of *S. aureus* decrease in cell viability at 16 and 32 μM , respectively, while complex **4-InQ** showed no significant inhibition on *S. aureus*, **Figures 7A, B**.

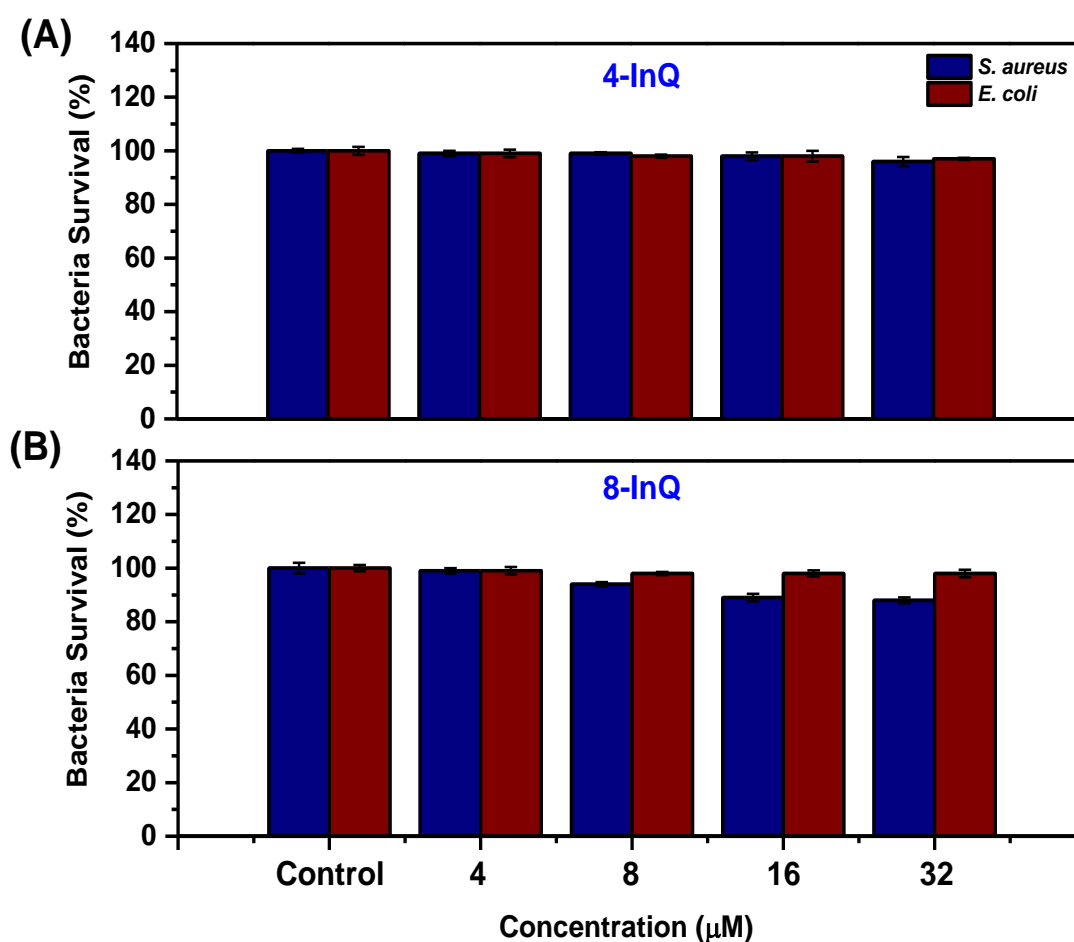


Figure 7.1 *S. aureus* and *E. coli* in terms of % survival for the indium quaternized (A) Pc **4-InQ** and (B) porphyrin **8-InQ** after 15 min dark exposure.

The irradiation studies results of the control groups did not show any form of a decrease in biofilm cell survival after 15 min light exposure (**Figures 7.2A, B**).

Caring out PACT experiments on the samples containing the PSs, it was observed that the highest concentration of PS (32 μM) resulted in significant reductions of *S. aureus* than in *E. coli* biofilms. The Pc **4-InQ** exhibited only 27 % and 19 % cell survival at 32 $\mu\text{g/mL}$ against *E. coli* and *S. aureus* respectively after 15 min light treatment. While porphyrin **8-InQ** showed 13 % and 11 % cell survival respectively (**Figures 7.2A and 7.2B**). It should be added that the PSs and the bacteria without light exposure (dark studies, **Figures 7.1A and 7.1B**) and the light exposure of bacteria without the PSs (control groups) did not show any form of a decrease in biofilm cell survival (data not shown).

These reductions demonstrate that the Gram-positive strain was more sensitive to PACT than the Gram-negative, an outcome consistent with the literature [278]. Gram-negative strains, like *E. coli*, are inherently more resistant than Gram-positive to antimicrobial agents due to the more selective nature of their cell envelope.

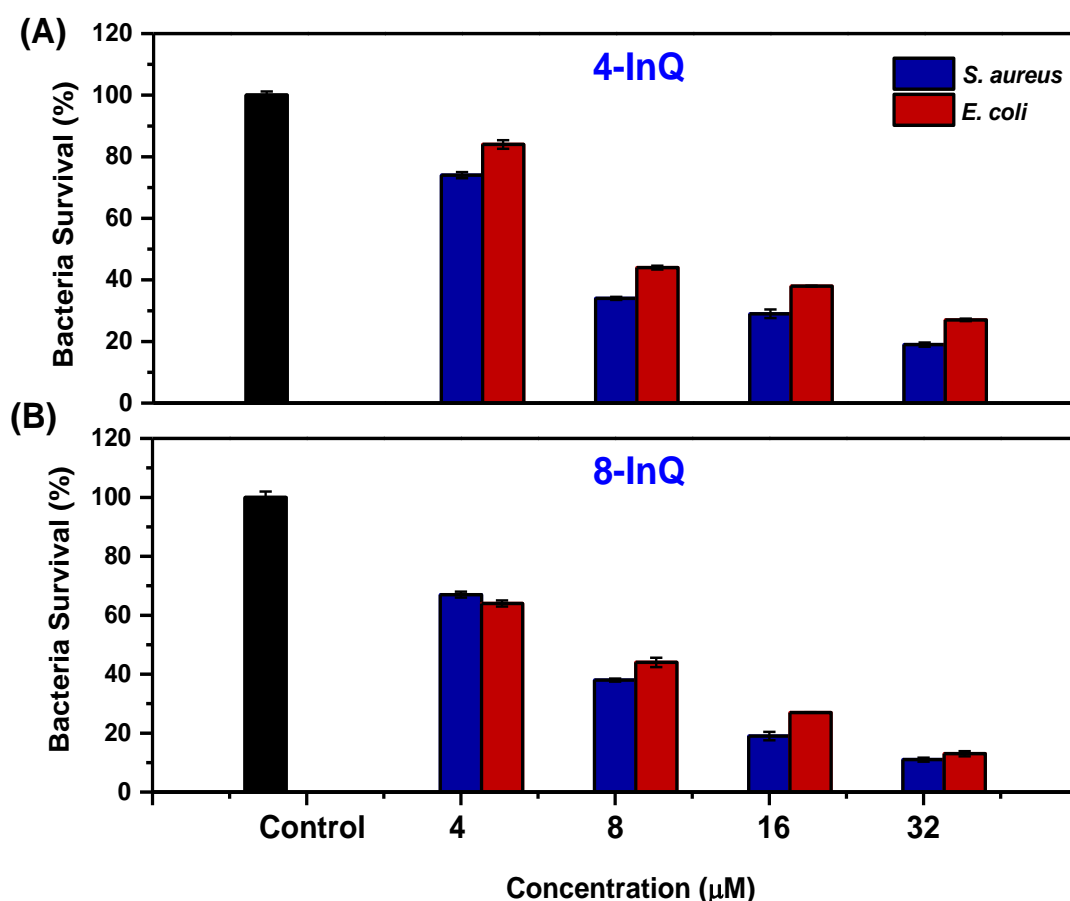


Figure 7.2 *S. aureus* and *E. coli* in terms of % survival for the indium quaternized (A) Pc **4-InQ** and (B) porphyrin **8-InQ** after 15 min irradiation.

In terms of CFUs counts, 15 min light treatment of **8-InQ** induced bacterial killing that reduced approximately 2.50 and 1.07- \log_{10} reduction for both *S. aureus* and *E. coli*, respectively, at a concentration of 32 $\mu\text{g/mL}$ and a light fluence of 471 J/cm^2 , while 32 μM of **4-InQ** resulted in 1.4 and 1.00- \log_{10} at an irradiance of 250 mW/cm^2 , respectively.

As can be observed, these results prove once more that a biofilm is the most resistant state of bacteria as no PACT activity is obtained (Log_{10} reduction values less than 3) even with the cationic PSs.

PACT efficiency should consider not only the presence of cationic charges but also other factors that promote the drug cell uptake. For instance, both studied complexes **4-InQ** and **8-InQ** are cationic, but the porphyrin complex **8-InQ** was more effective than the phthalocyanine complex **4-InQ**, an effect that can be attributed to the phthalocyanine's tendency to aggregate in aqueous media, despite its positive charges [296]. In another approach, this could possibly be due to the difference in size [297]. Small core molecules such as porphyrins diffuse easily through the bacteria membranes, a factor that seems particularly detrimental for complex **4-InQ**.

Therefore, both biofilm strains showed resistance to 15 min PACT treatment, with no complete killing of bacteria by the cationic complexes at all tested concentrations. This is because bacteria living in a biofilm are more difficult to be reduced, they are estimated to be 10-1000 times more resistant to the effects of antimicrobials than those in the planktonic form [298]. These results motivated the search for the use of an antibiotic to complement PACT activity in this work.

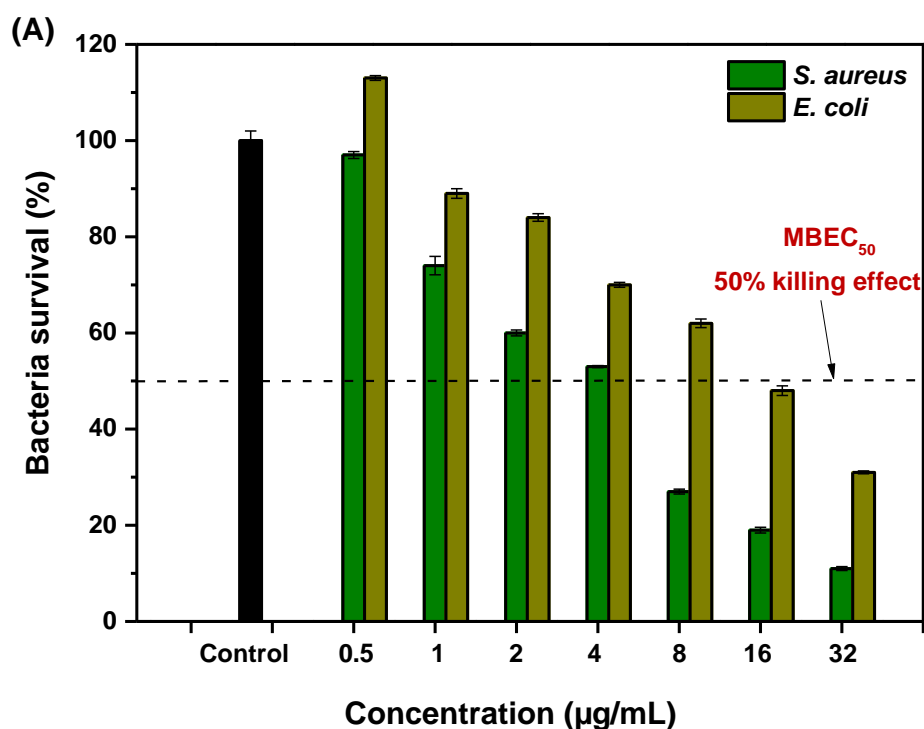
7.3. Antibacterial Effect of Ciprofloxacin alone on Biofilm Cultures

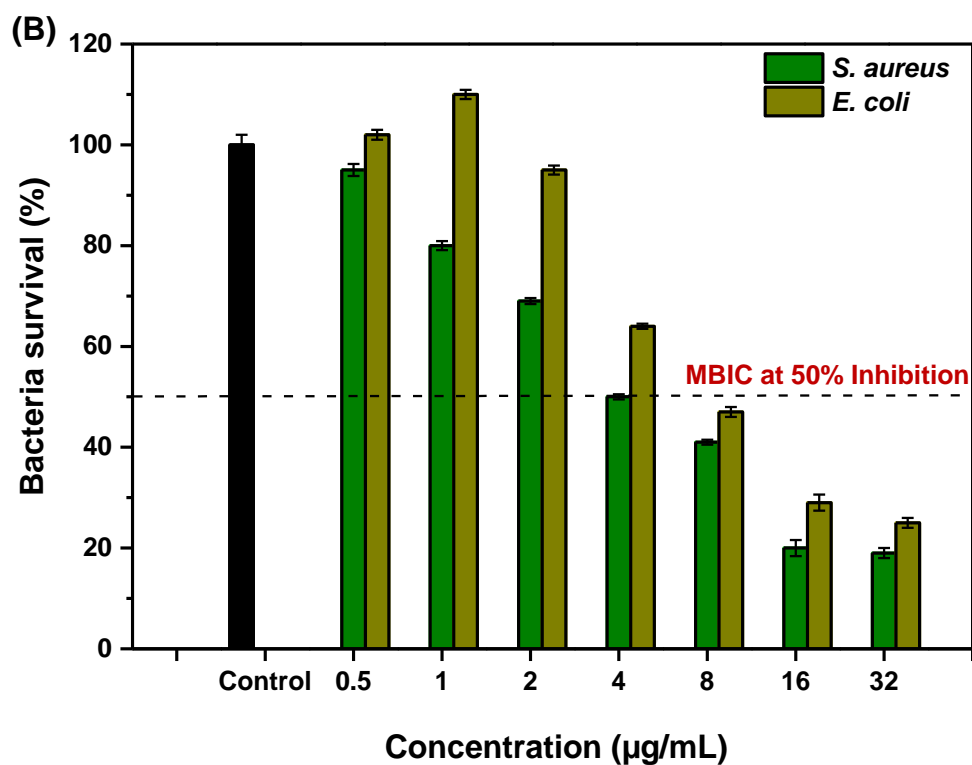
In the second step, ciprofloxacin's antibacterial activity against both strains was investigated at concentrations ranging from 0.5 to 32 $\mu\text{g/mL}$. The antibacterial activity was assessed by the microdilution method [196].

7.3.1. MBEC₅₀ and MBIC₅₀ Determination

The MBIC₅₀ was measured by determining the optical density (OD). The results presented in **Figure 7.3A** and **Table 7.1** show that 24 h biofilms exposure to ciprofloxacin slightly decreased the % cell survival of biofilm strains, giving a minimal biofilm eradication concentration 50% (MBEC₅₀) of 8 and 16 $\mu\text{g/mL}$ against *S. aureus* and *E. coli* respectively, while the minimal biofilm inhibition concentration 50% (MBIC₅₀) were of 4 and 8 $\mu\text{g/mL}$ against *E. coli* and *S. aureus*, respectively, **Figure 7.3B** and **Table 7.1**. The MBEC₅₀ and the MBIC₅₀ are defined as the lowest drug concentrations able to eradicate or inhibit more than 50 % of the biofilm cells, respectively.

Please note that the MBIC₅₀ found for *S. aureus* biofilms was 2 times lower than *E. coli*, which is consistent with the literature as *E. coli* biofilms are more resistant to ciprofloxacin, **Table 7.1**.





Figures 7.3 (A). Minimal biofilm eradication concentration 50 % (MBEC₅₀) of different concentrations of ciprofloxacin on *S. aureus* and *E. coli*. (B) Bacterial inhibition effect (MBIC₅₀) of ciprofloxacin observed after 24 h exposure on biofilm-phase of *E. coli* and *S. aureus* cells.

Table 7.1 MBIC₅₀ and MBEC₅₀ of Ciprofloxacin against *S. aureus* and *E. coli* strains.

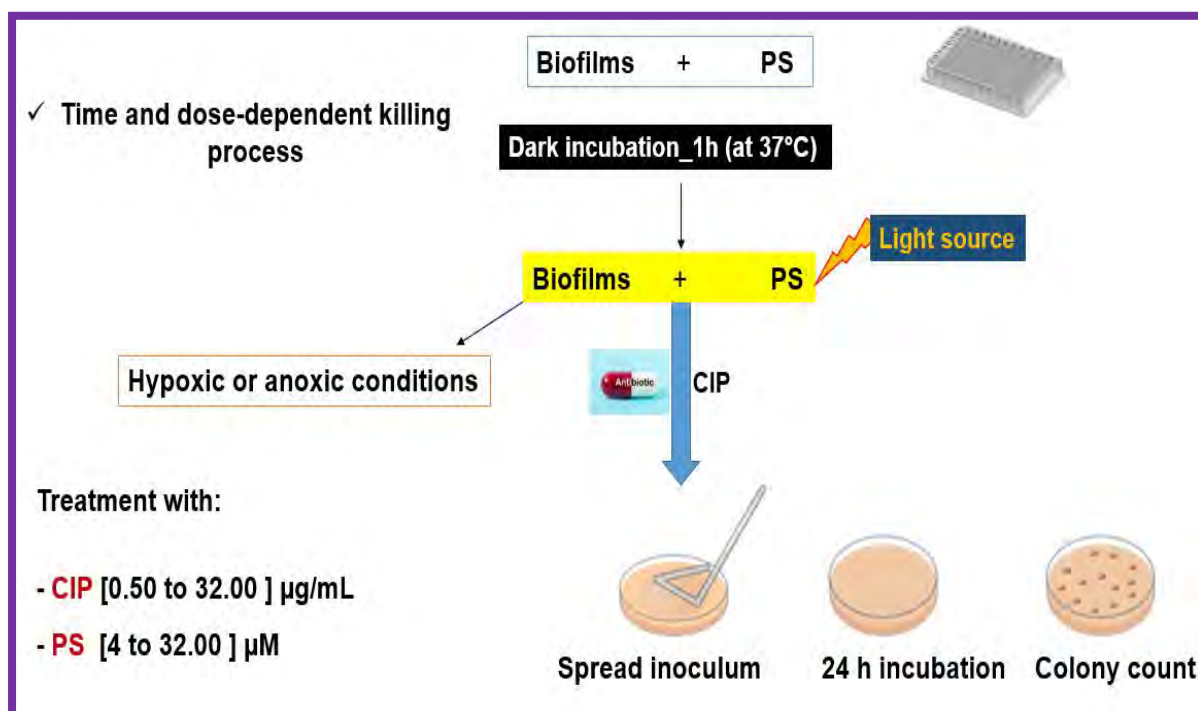
Strains	MBIC ₅₀ (µg/mL)	MBEC ₅₀ (µg/mL)
<i>S. aureus</i> (ATCC 25923)	4	8
<i>E. coli</i> (ATCC 25922)	8	16

However, the results show that CIP was unable to completely eradicate both biofilms strains or to inhibit their growth compared to the untreated controls.

7.4. Dual PACT-Ciprofloxacin Biofilm Activities

Since PACT and ciprofloxacin as monotherapies did not show substantial cytotoxicity. It was further investigated whether pre-treating the biofilm strains with PACT followed by ciprofloxacin application could improve the antibacterial effect of the studied quaternized PSs photodynamic reaction or could lead to complete eradication of the cells.

The data show that greater antibacterial activities are obtained in the dual therapy of PACT and chemotherapy when the biofilms were sequentially photoinactivated with PSs then incubated with ciprofloxacin for 24 h in the dark. **Scheme 7.1** briefly describes the procedure followed for this particular study.



Scheme 7.1 Pictorial of PACT-ciprofloxacin dual therapy assays.

Coupling PACT with CIP offers several advantages, preferably when PACT precedes the antibiotic. This is because PACT can disrupt the EPS layer, lower the expression of the antibiotic resistance-conferring genes and inactivate the drug modifying enzymes beforehand. Subsequently, this will result in an increased uptake of the antibiotic and potentiate a localized photo-destructive effect making the cells inside the biofilm more susceptible to the antibiotic.

In this case, concentrations below the MBIC₅₀ of ciprofloxacin and lower concentrations of complexes combined with lower irradiation time (15 min, light dose: 471 J/cm² for Pcs and fluence: 250 mW/cm² for porphyrins) resulted in the significant killing of the biofilms strains, however, increased concentrations resulted in the highest bacterial reductions, **Figures 7.4 and 7.5**.

The synergetic effect of PACT and CIP antibiofilm activity is noted in *S. aureus* biofilms that were subjected to 8 µM of **4-InQ**/or **8-InQ** and 2 µg/mL of CIP which specifically showed higher activity with a 7.05-log₁₀ reduction showing complete eradication of the cells, **Figures 7.4A, 7.5A** and **Table 7.2**. On *E. coli* biofilms a 7.20-log reduction was obtained for both PSs when using 16 µM of **4-InQ** and 4 µg/mL of CIP while 8 µM of **8-InQ** and 4 µg/mL of CIP were needed to successfully eradicate the biofilm (**Figures 7.4B, 7.5B** and **Table 7.2**).

Pre-treating *S. aureus* biofilms with PACT followed by antibiotic application in concentrations lower than the MBIC₅₀ might have led to the disruption of the EPS of the biofilm, hence allowing the complete eradication of biofilm cell.

Table 7.2 Log₁₀ reduction and the selected lowest concentrations of PS and CIP against *S. aureus* and *E. coli* strains in combined therapy.

Strains	Concentration [PS vs CIP]	Log ₁₀ reduction	Concentration [PS vs CIP]	Log ₁₀ reduction
	4-InQ		8-InQ	
<i>S. aureus</i>	8 µM vs 2 µg/mL	7.05	8 µM vs 2 µg/mL	7.05
<i>E. coli</i>	16 µM vs 4 µg/mL	7.20	8 µM vs 4 µg/mL	7.20

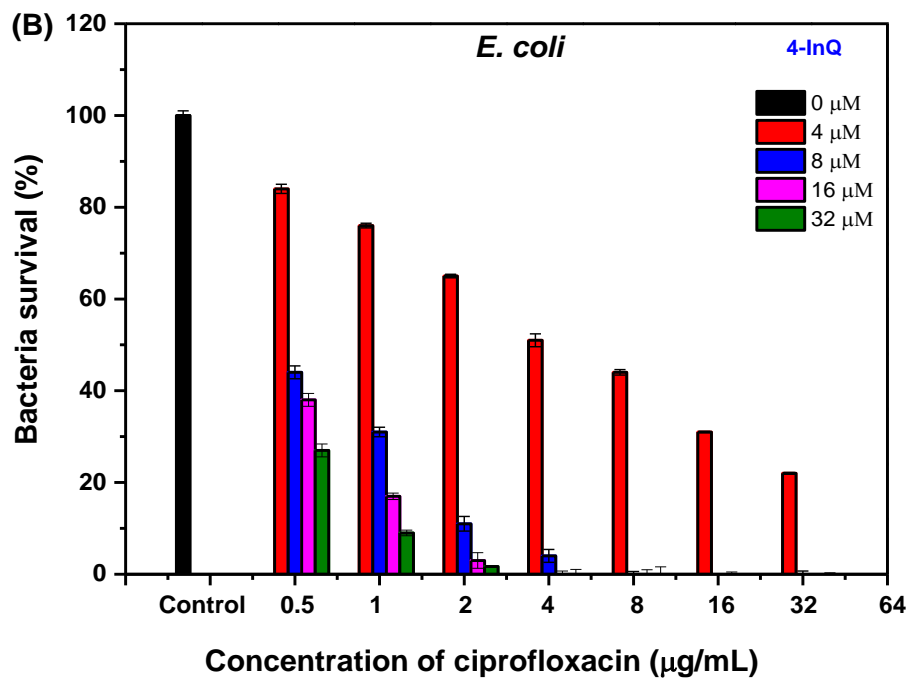
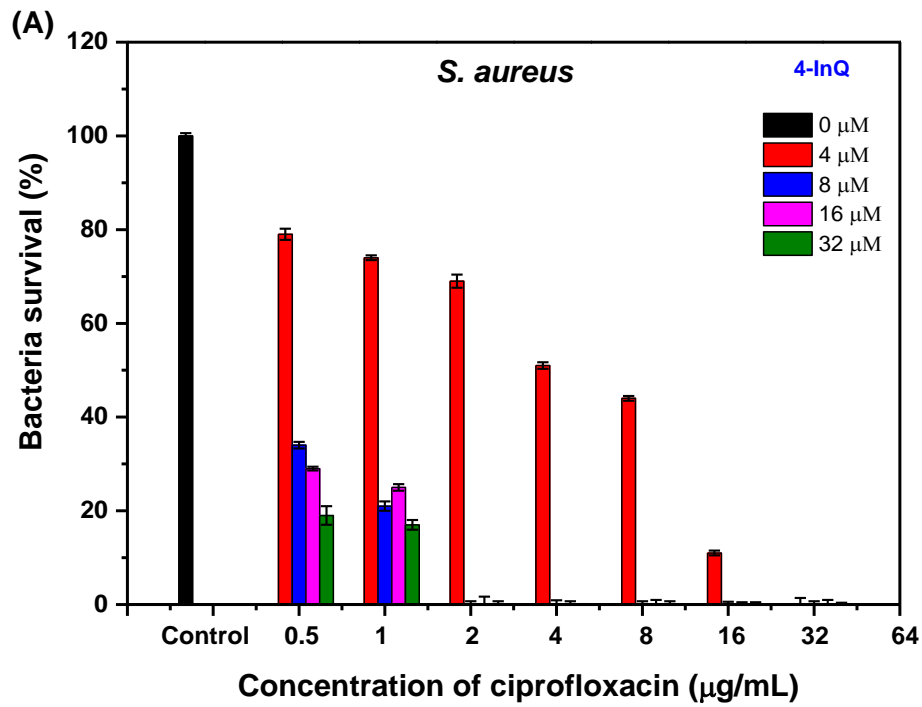


Figure 7.4 Synergistic effect of 15 min PACT-mediated by 4-InQ and ciprofloxacin on bacterial biofilms of (A) *S. aureus* and (B) *E. coli* the irradiation done by laser (670 nm).

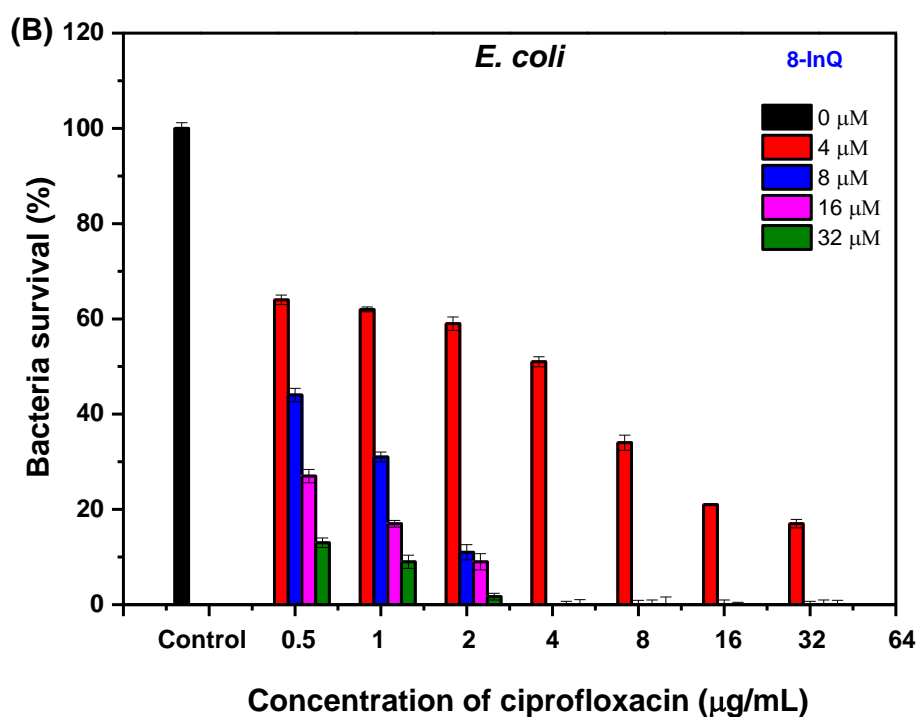
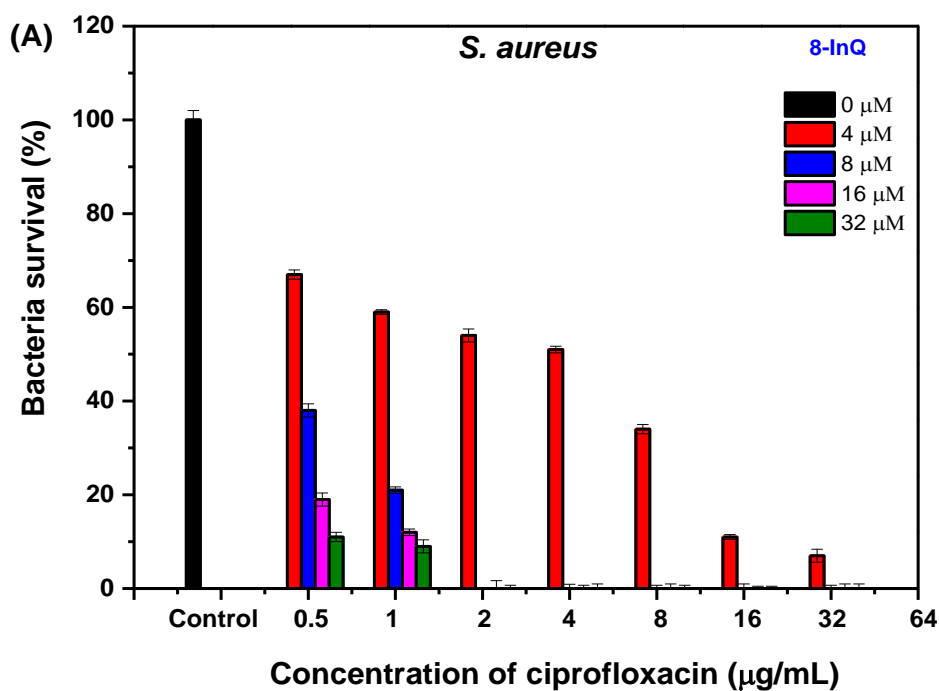


Figure 7.5 Synergistic effect of 15 min PACT-mediated by **8-InQ** and ciprofloxacin on bacterial biofilms of (A) *S. aureus* and (B) *E. coli* the irradiation done by LED (415 nm).

It is worth emphasizing that the complete inhibition of biofilms only occurred under the influence of simultaneous treatment with PACT and ciprofloxacin. This combination totally eradicated the biofilm, regardless of the incubation time as compared to the untreated controls while when both therapies were used separately, they did not reduce the biofilms significantly. In order to reveal the photo- and chemo-cytotoxic effects of the PSs and ciprofloxacin (CIP), **Figure 7.6** shows a microplate model of PSs versus ciprofloxacin concentrations showing the synergetic activities.

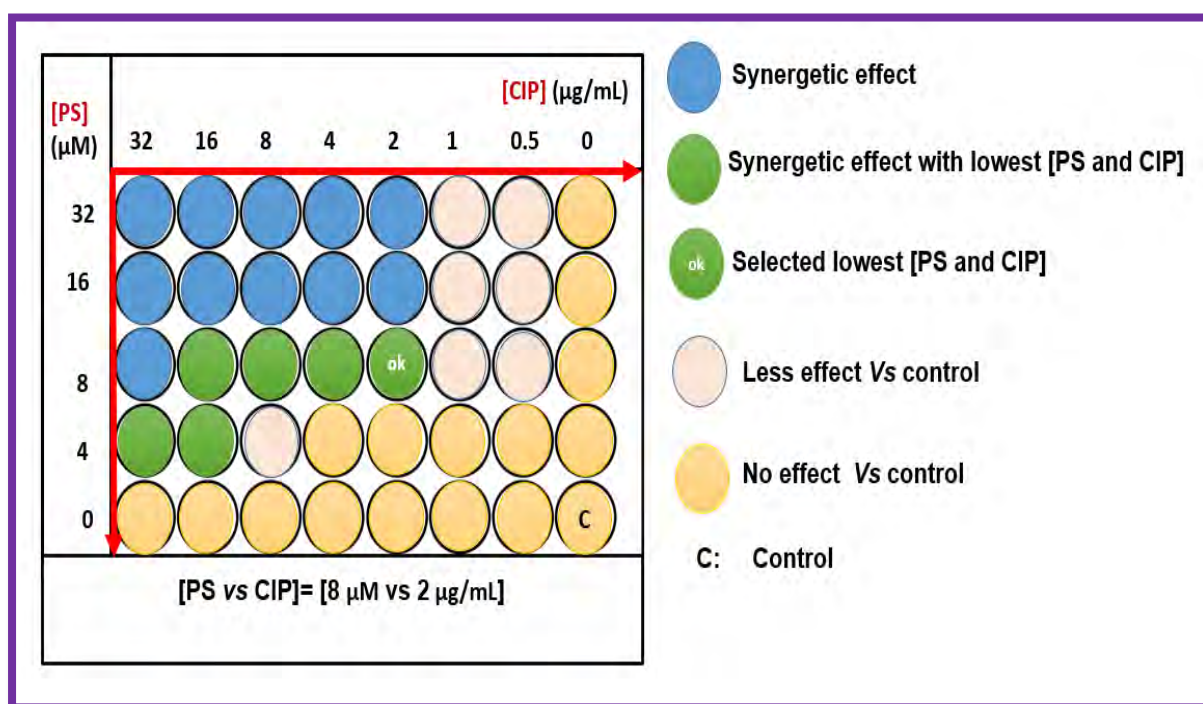


Figure 7.6 Microplate model using 4-InQ and ciprofloxacin on *S. aureus* biofilms (as an example).

There was a significantly increased antibiofilm activity in combining low doses of ciprofloxacin and the PSs. This was due to two mechanisms of action: ROS production by the PSs and inhibition of DNA gyrase and topoisomerase IV by the ciprofloxacin. The presence of two modes of action enables to kill bacteria in their stationary growth phase (inside biofilms) and to lower the toxic effects of antimicrobial chemotherapy on normal host tissues. ROS has been shown to be a common mechanism of cellular death induced by bactericidal antibiotics [299]. These results suggest the importance of ROS in the metabolites-enabled potentiation to bactericidal antibiotics.

7.5. Summary of the Chapter

The synergistic effect of PACT-combined-with-antibiotic treatment could be a promising strategy to overcome the multidrug-resistant bacterial infections caused by biofilms. Hence, the present work investigated on the use of two indium metallated cationic PSs, a porphyrin **8-InQ** and a Pc **4-InQ**, which generate ROS inside or in the close proximity of the bacterial cells for PACT, followed by the use of a well-known antibiotic, CIP, for this purpose.

The study demonstrate that the matured bacterial biofilms showed resistance to CIP as monotherapy as well as to PACT as no significant reduction in % viability was observed at concentration of 32 μM following 15 min irradiation under respective conditions (excitation wavelength at 670 nm and 415 nm for **4-InQ** and **8-InQ**, respectively). The killing effect resulting from combining both therapies (PACT followed by ciprofloxacin treatment) overcame the biofilms' resistance. The dual therapy-treated samples presented higher activity in the case of both bacterial species with complete eradication of the biofilms giving $\sim 7\text{-log}_{10}$ reduction numbers in the viable counts at lower concentrations of CIP and the PSs.

Moreover, it is important to indicate that the reduction in treatment time and drug concentrations that resulted in the increased bacteria inactivation in the dual therapy could be due to a mechanism underlying the synergy between antimicrobials and light therapy.

The study also revealed that although *S. aureus* and *E. coli* biofilms were treated before with PACT, the CIP was able to reach the bacteria and kill the vast majority of cells growing at lower concentration.

The results clearly indicate that the quaternized PSs can be used as good agents for improving the efficacy of both PACT combined to ciprofloxacin to inactivate *S. aureus* and *E. coli* biofilms strains. The obtained results are of particular value in the era of widespread and still-increasing drug resistance among bacterial pathogens.

The investigation of the effects of the studied compounds and CIP adds to the knowledge on their biological activity, shedding light on an interesting but not yet well used technic (dual therapy). This study has shown that the combination of an antibiotic with the cationic PSs can yield potent antimicrobial activity. The observed increased antimicrobial activity is mostly due to two mechanisms of action involved: inhibition of DNA gyrase and topoisomerase IV by the CIP moiety and ROS production by the PSs.

Chapter Eight: Photodynamic Therapy (PDT)

The chapter discusses the *in vitro* anticancer photodynamic effect of positively-charged chalone substituted-Pcs (**4-Zn**, **4-In**, **4-ZnQ**, and **4-InQ**) used as models.

8.1. Photodynamic Activity (PDT)

The objective of the *in vitro* studies described in this chapter was to evaluate the biological activity of **Group 4** chalcone substituted Pcs against MCF-7 breast cancer cell lines which are routinely used to assess photodynamic toxicity of new PSs. The activity from an influence of the positive charges on the chalcone group was evaluated by determination of the cytotoxicity of the complexes in the absence of light (IC₅₀ dark) and their phototoxicity after laser irradiation (IC₅₀ PDT). The IC₅₀ value is the concentration at which the complex can cause a 50% reduction in cell viability.

To generate comparable data, each complex was evaluated in the same experimental conditions using the same protocol factors, including light dose and fluence. The results clearly demonstrated lower toxicity in the absence of light and high photosensitizing efficacy (phototoxicity) after irradiation.

Chalcone compounds are known for their vascular disrupting effect in PDT, which destroys the tumor's neovasculature, leading to tumor starvation and subsequently to tumor death by necrosis [300]. The dimethylamino-chalcone substituent on Pcs **4-Zn** and **4-In** allows for quaternization resulting in water-soluble complexes **4-Zn** and **4-In**. Hence, photodynamic activity can be increased by the synergetic effect.

8.1.1. Cellular uptake

The *in vitro* cellular uptake was investigated by measuring the absorbance of internalized complexes following 24 h drug incubation with MCF-7 cancer cells. In comparison to the zinc analogs, the indium Pcs presented higher internalization in the cells, the reason could be that the latter metal ion possesses a higher affinity to MCF-7 cancer cells, **Figure 8.1**.

Figure 8.1 shows that both Pc types are clearly internalized by MCF-7 cancer cells, but quaternized complexes (**4-ZnQ** and **4-InQ**) have higher cellular uptake than non-quaternized counterparts (**4-Zn** and **4-In**). Positively charged PSs are known to internalize into the cell more favorably than anionic or neutral species due to the negatively charged cell surface [208]. Cationic PSs bind electrostatically to anionic regions of cell surface and facilitate the transport of cationic PSs into the cells thereby increasing the PDT efficacy [208].

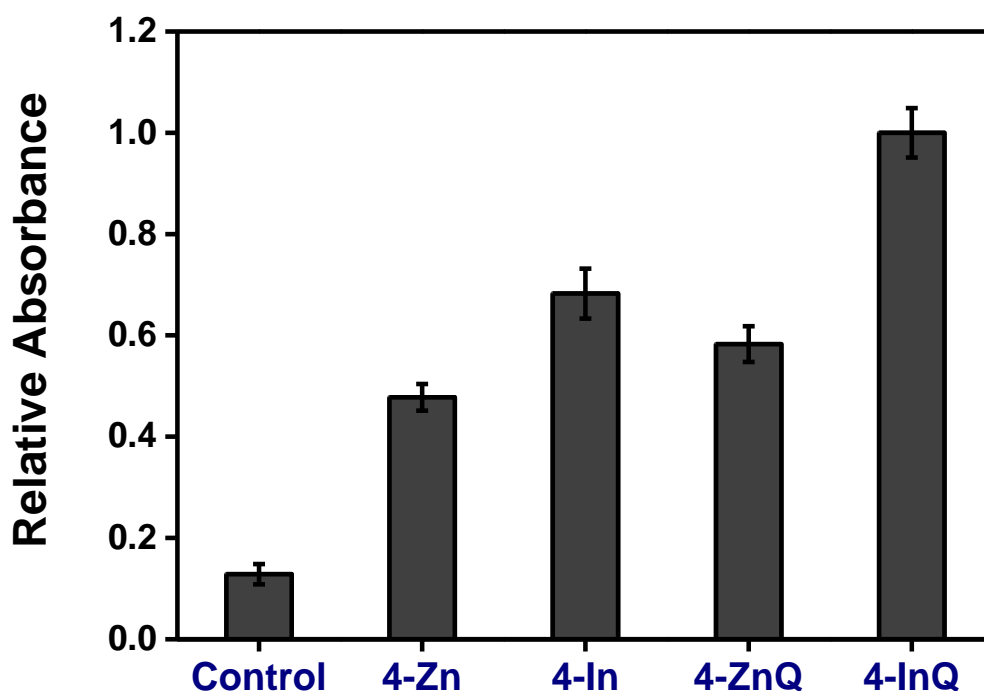


Figure 8.1 Relative cellular uptake plot for **4-Zn**, **4-In**, **4-ZnQ**, and **4-InQ** by measuring the absorbance 670 nm with a multi-plate reader.

8.1.2. Photocytotoxicity studies

To assess the PDT effect of the Pcs on MCF-7 cancer cells, their photocytotoxicities were quantitatively determined using a conventional MTT (methylthiazolyl-diphenyltetrazolium bromide) cell viability assay [301]. Firstly, the cancer cells were incubated with different drug concentrations ranging between 0.8-50 μM for 24 h.

The assay was conducted on the cells that were not irradiated to evaluate their dark toxicity and the results show that the compounds exhibit insignificant dark toxicity with about 75% cell viability at 50 μM (**Figure 8.2A**) and as it was not possible to reach the IC_{50} concentration for all the Pcs in the absence of light. It is clear that, in the dark, Pcs are at least 20 times less toxic than when exposed to light irradiation at the highest concentration (50 μM).

In terms of photodynamic activity, for a light dose of 524 mV/cm^2 , quaternized Pcs are much more effective. However, the cell viability was significantly lower after exposure to light, indicating that the observed dramatic cytotoxicity activity resulted from irradiation at the tested concentrations.

The cytotoxicity damage to the target cells was quantitated using IC₅₀ (50% inhibitory concentration calculated using GraphPad Prism software) values and the results are summarized in **Table 8.1**.

Table 8.1 Phototoxicity (at 670 nm with 524 mV/cm² for 15 min) of the studied complexes against MCF-7 cancer cells

Complex	IC ₅₀ (μ M)	% Cell viability at 50 μ M
4-Zn	20.4 \pm 1.1	13.6 \pm 1.7
4-In	12.1 \pm 1.2	5.6 \pm 0.9
4-ZnQ	17.9 \pm 1.1	8.6 \pm 1.9
4-InQ	7.4 \pm 0.9	3.3 \pm 0.9

Upon 15 min irradiation at 670 nm with light fluence of 524 mV/cm², complexes **4-ZnQ** and **4-InQ** exhibited IC₅₀ values of 17.9 and 7.4 μ M, respectively, and these values were relatively lower than those observed for **4-Zn** and **4-In** (20.4 and 12.1 μ M, respectively). These results could be attributed to the higher cellular uptake observed for the quaternized complexes discussed above. Also, previous studies have proven that PDT efficacy relies on the photosensitizer's ability to generate cytotoxic ROS in the target cells [302]. This observation indicates that **4-ZnQ** and **4-InQ** are suitable for PDT due to their ROS-generating ability in the cells, their affinity to the target cells, and efficient cellular uptake. The indium complexes (**4-In** and **4-InQ**) showed higher PDT activity (**Figure 8.2B**) with only 5.6 and 3.3% cell viability respectively at 50 μ M compared to the corresponding zinc complexes **4-Zn** and **4-ZnQ** which showed cell viability of 13.6 and 8.6%, respectively at the same concentration, **Table 8.1**, corresponding to the Φ_{Δ} values. This observed greater phototoxicity is statistically significant.

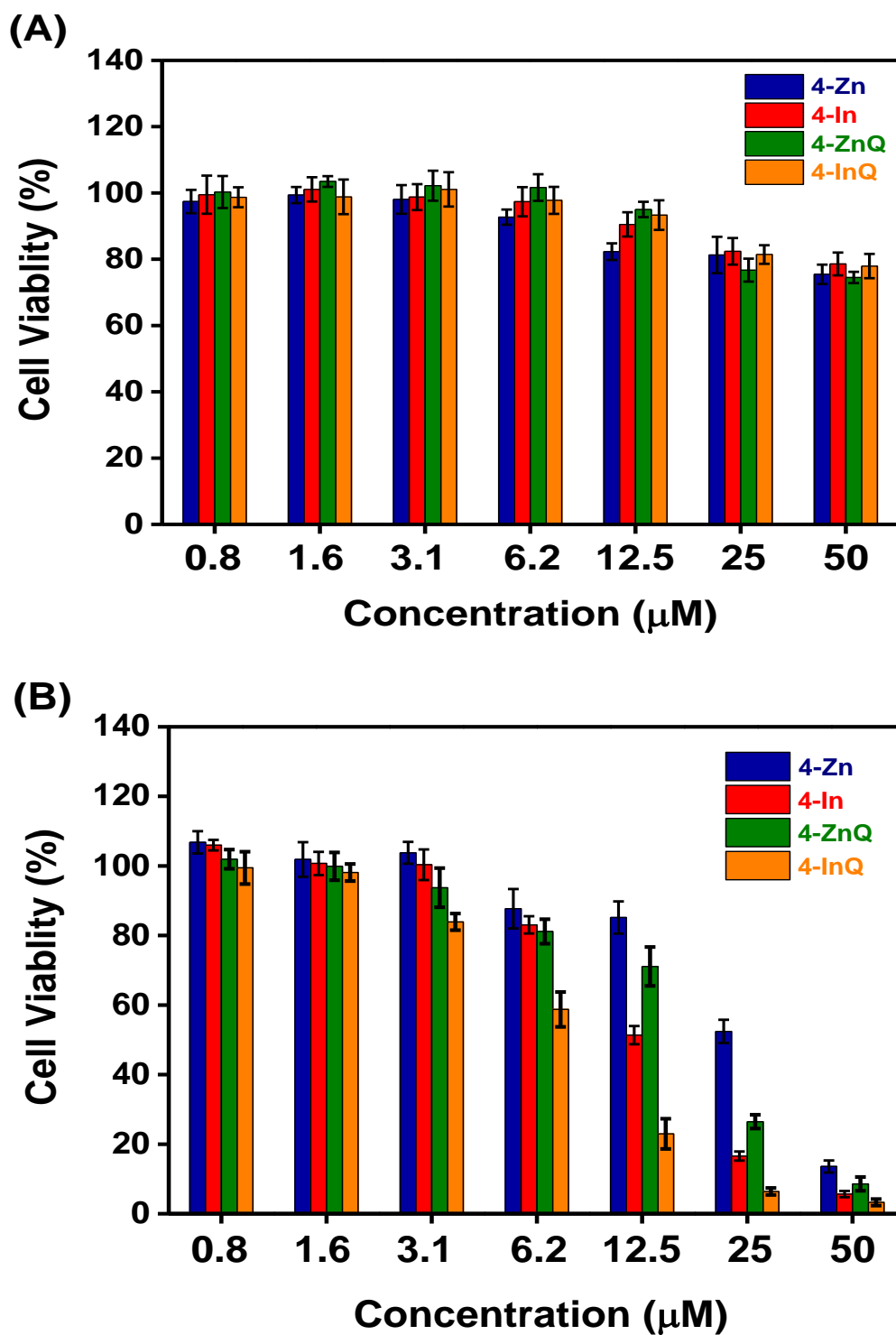


Figure 8.2 Cytotoxicity of **4-Zn**, **4-In**, **4-ZnQ**, and **4-InQ** in MCF-7 cells after 24 h incubation in the (A) studies in the dark and (B) photo-irradiation (15 min) with a 670 nm light as determined by MTT assay.

The *in vitro* photodynamic activity correlates in this instance with the generation of singlet oxygen despite the scavenging effect due to the presence of chalcone.

8.1.3. Lipophilicity

Since the increased phototoxicity is not related to an increased singlet oxygen generation, several hypotheses can be formulated, the first being that the increased amphiphilic character of **4-ZnQ** and **4-InQ**, compared to **4-Zn** and **4-In**, contributes to enhanced photodynamic activity, an effect already reported [303,304].

Even the cellular uptake of the quaternized complexes **4-ZnQ** and **4-InQ** seem to be facilitated by their well-balanced lipophilic character. The hydrophobicity of complexes was measured by the partition coefficient between *n*-octanol and water ($P_{o/w}$), which is an excellent indicator of a PS affinity to permeate de plasma membrane of cells. As previously indicated in **Table 6.1**, the experimentally determined Log $P_{o/w}$ values for the quaternized complexes are -0.26 and -0.39. With these values, complexes **4-ZnQ** and **4-InQ** have enough lipophilicity to permeate the plasma membrane of cells.

The presence of the relatively hydrophobic character in the quaternized Pcs increases their amphiphilicity and this may contribute to improved cellular uptake of the complexes and account for their increased photocytotoxicity. Another hypothesis could be that the chalcone moiety contributes itself to cytotoxicity.

8.2. Summary of the Chapter

As demonstrated in the results above, an anticancer effect is observed by the metallated quaternized chalcone-phthalocyanines at minimal inhibitory concentrations despite their singlet oxygen scavenging capacity.

The presence of the chalcone substituent on the Pc core resulted in a highly enhanced phototoxicity, presumably due to the increased amphiphilic character of the Pcs favoring higher cellular uptake. Alternatively, the chalcone group itself may be acting upon irradiation of the Pcs, hence contributing to the cytotoxicity. Overall, the conclusion is that combining a PS and an anticancer naturally occurring compound into one molecule represents a highly promising strategy for the treatment of tumors. Suggesting that the modest increase in the activity could be caused by a general increase in cellular uptake, rather than intracellular distribution to sites more susceptible to oxidative damage.

Chapter Nine: Conclusions and Recommendations

This chapter provides the conclusions and future perspectives for this work.

9.1. General Conclusions

To efficiently kill bacteria, positively charged compounds are suggested as they are not only soluble in aqueous media, but they are also able to strongly bind to the cell wall. As a result of this, the cell membrane is highly destroyed since singlet oxygen generated by the photosensitizer acts in close proximity to the cell thus improving the drug-cell uptake. For this reason, in this work, novel neutral and quaternized phthalocyanines and porphyrins with peripheral substituents and their respective carbon-based nanomaterials-nanoconjugates were successfully synthesized and characterized using different spectroscopic, microscopic, and thermal techniques.

The PSs substituents were designed based on their ability to promote singlet oxygen production, quaternizability, and most importantly for their intrinsic anticancer and antibacterial potency respectively.

On the hand, carbon-based nanomaterials such as DNDs and the functionalized GQDs (i.e., GQDs and GSH@GQDs) that were used in this work play a vital role as nanocarriers currently, and many more research reports have been published as they are good nanocarriers to treat both infectious diseases and cancer cells *in vitro*. The unique structure of these nanomaterials helps to increase the loading efficiency of PS drugs, the photoactivity, the biocompatibility, bioavailability, and thermal effect. To further lengthen the photoactivity some PSs-DNDs were conjugated to either CSAg or Ag NPs due to their previously reported antibacterial properties.

The loading mechanism of the PSs nanomaterials was achieved based on the structure and functional group present in the PSs. Since the PSs have benzene rings in their structure, they were attached on the nanomaterials by π - π stacking noncovalent functionalization. The covalent chemical functionalization with the PS molecule was also done through formation of amide or ester bonds. This surface functionalization helped to improve the photophysicochemical properties and the targeting and therapeutic efficiency of the PSs for PACT.

The study of the photophysical and photochemical behaviour of both the PSs and their nanoconjugates showed that the zinc, indium, and gallium complexes have the ability to produce high singlet oxygen that is a necessary agent for photodynamic applications.

This work explored the antimicrobial activity of the PSs using PACT while irradiating at 670 nm for Pc derivatives and 415 nm for the porphyrins. It was demonstrated that the metalated conjugates and quaternized complexes had better activity against planktonic bacteria strains, with the highest \log_{10} reductions and lowest cell survival. While some of the prepared compounds showed a high potential in the eradication of not only the bacterial planktonic cells of *S. aureus* and *E. coli*, but they also possessed great activities against their difficultly treated bacterial biofilms. Selected compounds also exhibited good anticancer when tested on the MCF-7 breast cancer cell *in vitro*.

The obtained data in PACT were all in agreement with the reported photophysical and photochemical results. The *in vitro* results indicate that at lower concentration the synthesized photosensitisers have a great prospective in biofilms ablation since the DNDs, GQDs, GSH@GQDs, even the presence of CSAg and Ag NPs enhance the delivery of the photosensitizers and solubility in aqueous solvents.

A new alternative for biofilms treatment with fewer side effects and doses is the emerging dual photo-chemotherapy that uses both photo- (such as PSs) and chemotherapeutic (antibiotics) agents that can function in a cooperative manner. Hence, this work also investigated the PACT-ciprofloxacin dual therapy of selected complexes. The results clearly indicated that the quaternized PSs combined to ciprofloxacin successfully eradicated *S. aureus* and *E. coli* biofilms strains at very lower concentrations of the drugs thanks to the presence of two mechanism of action from both counterparts. The obtained results are of particular value in the era of widespread and still-increasing drug resistance among bacterial pathogens.

In conclusion, the overall results of this study has once more demonstrated that the conjugation of soluble PSs that absorb in the therapeutic window to carbon-based nanomaterials is a promising approach in the search for new PACT and/or PDT agents. In addition, antimicrobial technic with dual or multiple modes of action maybe promising in combating drug resistance.

9.2. Perspectives and Recommendations

The use of other PSs groups that are non-covalently or covalently linked to different carbon-based nanomaterials might one day forge ahead and prove to have more practical uses in specifically in PACT. Hence, this area needs to fully be investigated.

More research work is needed on the perspective of surface modifications of carbon-based nanomaterials mostly the DNDs, to develop novel targeted carbon nanomaterials for PACT applications. Furthermore, more *in vitro* studies are recommended to unlock the biological applications of these nanomaterials when combined to PSs for the treatment of infections.

The results also demonstrate that the dual therapy using PSs and antibiotics merit further in-depth study for use in biomedical applications, such as PACT for bacterial biofilms. The antimicrobial mode of treatment with dual modes of action (dual photochemotherapy) may be promising candidates in combating drug resistance. Hence, for future work, the prepared nanoconjugates can be investigated in combination with Ciprofloxacin or other antibiotics such as Levofloxacin. The dual therapy can also be investigated on planktonic cells of Gram-negative and Gram-positive bacteria causing severe chronic infections.

The synthesized compounds and related nanoconjugates should be used in the near future for other many applications such water purification using photodegradation of organic pollutants and much more can still be studied in the future.

The final aspects that are to also be explored that were beyond the scope of this research are to:

- (1) Synthesize new PSs and nanomaterials carriers that are combined to organometallic frameworks to study the eradication of biofilms by targeting the formation of the exopolymeric matrix or their quorum sensing,
- (2) Combat matured biofilms that are formed on glass and metallic surfaces, and
- (3) To develop drug-loaded bandages, films and membranes destined for rapid and improved chronic wounds dressing and healing. The new biomaterials can be made based on the use of natural polymers such as chitosan and structurally modified cationic photosensitisers.

References

1. Aslam, B.; Wang, W.; Arshad, M.I.; Khurshid, M.; Muzammil, S.; Rasool, M.H.; Nisar, M.A.; Alvi, R.F.; Aslam, M.A.; Qamar, M.U.; Salamat, M.K.F.; Baloch, Z. *Infect. Drug Resist.* **2018**, *11*, 1645, doi:10.2147/IDR.S173867.
2. Clifford, K.; Desai, D.; Prazeres da Costa, C.; Meyer, H.; Klohe, K.; Winkler, A.; Rahman, T.; Islam, T.; Zaman, M.H. *Bull. World Health Organ.* **2018**, *96*, 662, doi:10.2471/BLT.18.209585.
3. Zaman, S. Bin; Hussain, M.A.; Nye, R.; Mehta, V.; Mamun, K.T.; Hossain, N. *Cureus* **2017**, *9*, 1403, doi:10.7759/cureus.1403.
4. Rivera, E.; Gomez, H. *Breast Cancer Res.* **2010**, *12*, 1, doi:10.1186/bcr2573.
5. Anas, A.; Sobhanan, J.; Sulfiya, K.M.; Jasmin, C.; Sreelakshmi, P.K.; Biju, V. *J. Photochem. Photobiol. C. Photochem. Rev.* **2021**, *49*, 100452, doi:10.1016/j.jphotochemrev.2021.100452.
6. Foresto, E.; Gilardi, P.; Ibarra, L.E.; Cogno, I.S. *Phytomedicine Plus* **2021**, *1*, 100044, doi:10.1016/j.phyplu.2021.100044.
7. Doherty, R.E.; Sazanovich, I. V.; McKenzie, L.K.; Stasheuski, A.S.; Coyle, R.; Baggaley, E.; Bottomley, S.; Weinstein, J.A.; Bryant, H.E. *Sci. Rep.* **2016**, *6*, 22668, doi:10.1038/srep22668.
8. Abrahamse, H.; Hamblin, M.R. *Photomedicine and Stem Cells: The Janus face of photodynamic therapy (PDT) to kill cancer stem cells, and photobiomodulation (PBM) to stimulate normal stem cells*; IOP Publishing, New York, 2017; ISBN 978-1-6817-4321-9.
9. Giuliani, F.; Martinelli, M.; Cocchi, A.; Arbia, D.; Fantetti, L.; Roncucci, G. *Antimicrob. Agents Chemother.* **2010**, *54*, 637, doi:10.1128/AAC.00603-09.
10. Costa, L.; Tomé, J.P.C.; Neves, M.G.P.M.S.; Tomé, A.C.; Cavaleiro, J.A.S.; Faustino, M.A.F.; Cunha, Â.; Gomes, N.C.M.; Almeida, A. *Antiviral Res.* **2011**, *91*, 278, doi:10.1016/j.antiviral.2011.06.007.
11. Tavares, A.; Carvalho, C.M.B.; Faustino, M.A.; Neves, M.G.P.M.S.; Tomé, J.P.C.;

- Tomé, A.C.; Cavaleiro, J.A.S.; Cunha, A.; Gomes, N.C.M.; Alves, E.; Almeida, A. *Mar. Drugs* **2010**, *8*, 91, doi:10.3390/md8010091.
12. De Sordi, L.; Butt, M.A.; Pye, H.; Kohoutova, D.; Mosse, C.A.; Yahioğlu, G.; Stamati, I.; Deonarain, M.; Battah, S.; Ready, D.; Allan, A.; Mullany, P.; Lovat, L.B. *PLoS One* **2015**, *10*, e0135039, doi:10.1371/journal.pone.0135039.
 13. Perni, S.; Prokopovich, P.; Pratten, J.; Parkin, I.P.; Wilson, M. *Photochem. Photobiol. Sci.* **2011**, *10*, 712, doi:10.1039/c0pp00360c.
 14. Matlou, G.G.; Nyokong, T. *Dye. Pigment.* **2020**, *176*, 108237, doi:10.1016/j.dyepig.2020.108237.
 15. Li, Z.; Chen, Y.; Yang, Y.; Yu, Y.; Zhang, Y.; Zhu, D.; Yu, X.; Ouyang, X.; Xie, Z.; Zhao, Y.; Li, L. *Front. Bioeng. Biotechnol.* **2019**, *7*, 293, doi:10.3389/fbioe.2019.00293.
 16. Bowler, P.; Murphy, C.; Wolcott, R. *Antimicrob. Resist. Infect. Control* **2020**, *9*, 162, doi:10.1186/s13756-020-00830-6.
 17. Penesyan, A.; Paulsen, I.T.; Gillings, M.R.; Kjelleberg, S.; Manefield, M.J. *Front. Microbiol.* **2020**, *11*, 2109, doi:10.3389/fmicb.2020.02109.
 18. Bi, Y.; Xia, G.; Shi, C.; Wan, J.; Liu, L.; Chen, Y.; Wu, Y.; Zhang, W.; Zhou, M.; He, H.; Liu, R. *Fundam. Res.* **2021**, *1*, 193, doi:10.1016/j.fmre.2021.02.003.
 19. Peggy, T. We are surrounded. In *Bacteria and Viruses*; Gale, T., Ed.; Lucent library of science and technology, New York, 2004; pp. 10-24 ISBN 1-59018-438-6.
 20. Rogers, K. *Bacteria and Viruses (Biochemistry, Cells, and Life)*; Rogers, K., Ed.; Britannica Educational Publishing: New York, 2011; ISBN 978-1-61530-376-2.
 21. Silhavy, T.J.; Kahne, D.; Walker, S. *Cold Spring Harb. Perspect. Biol.* **2010**, *2*, a000414, doi:10.1101/cshperspect.a000414.
 22. Jori, G.; Coppellotti, O. *Antiinfect. Agents Med. Chem.* **2007**, *6*, 119, doi:10.2174/187152107780361652.
 23. Seltmann, G.; Holst, O. *The Bacterial cell wall*; Springer-Verlag: Berlin, 2002; ISBN 9783662048788.
 24. George, S.; Hamblin, M.R.; Kishen, A. *Photochem. Photobiol. Sci.* **2009**, *8*, 788, doi:10.1039/b809624d.

25. Malik, Z.; Ladan, H.; Nitzan, Y. *J. Photochem. Photobiol. B.* **1992**, *14*, 262, doi:10.1016/1011-1344(92)85104-3.
26. Salton, M.R.J.; Kim, K.-S. Chapter 2: Structure. *In Medical Microbiology* (4th Edition); Baron, S., Ed.; University of Texas Medical Branch at Galveston: Texas, **1996**; <https://www.ncbi.nlm.nih.gov/books/NBK8477/>.
27. Shutterstock Bacteria. Difference of Gram-positive from Gram-negative bacterial Available online: <https://www.shutterstock.com/image-illustration/bacteria-difference-grampositive-gramnegative-bacterial-224095714> (accessed on Mar 3, **2022**).
28. Madigan, M.T.; Aiyer, J.; Buckley, D.H.; Sattley, W.M.; Stahl, D.A. Microbial growth and its control. *In Brock Biology of Microorganisms*; Edition, G., Ed.; Pearson, New York, 2018; pp. 144-183 ISBN 9781292235103.
29. Davey, M.E.; O'toole, G.A. *Microbiol. Mol. Biol. Rev.* **2000**, *64*, 847, doi:10.1128/MMBR.64.4.847-867.2000.
30. Lopez, D.; Vlamakis, H.; Kolter, R. *Cold Spring Harb. Perspect. Biol.* **2010**, *2*, a000398, doi:10.1101/cshperspect.a000398.
31. Hall-Stoodley, L.; Stoodley, P. *Cell. Microbiol.* **2009**, *11*, 1034, doi:10.1111/j.1462-5822.2009.01323.x.
32. Costa, O.Y.A.; Raaijmakers, J.M.; Kuramae, E.E. *Front. Microbiol.* **2018**, *9*, doi:10.3389/fmicb.2018.01636.
33. Limoli, D.H.; Jones, C.J.; Wozniak, D.J. *B Microbiol. Spectr.* **2015**, *3*, 10, doi:10.1128/microbiolspec.MB-0011-2014.
34. Jamal, M.; Ahmad, W.; Andleeb, S.; Jalil, F.; Imran, M.; Nawaz, M.A.; Hussain, T.; Ali, M.; Rafiq, M.; Kamil, M.A. *J. Chinese Med. Assoc.* **2018**, *81*, 7, doi:10.1016/j.jcma.2017.07.012.
35. Hiromi K.M.D. *J. Infect Chemother* **1996**, *2*, 18.
36. Donlan, R.M.; Costerton, J.W. *Clin. Microbiol. Rev.* **2002**, *15*, 167, doi:10.1128/CMR.15.2.167-193.2002.
37. Jiang, X.; Pace, J.L. Microbial biofilms. *In Biofilms, infection, and antimicrobial therapy*; Pace, J.L., Rupp, M.E., Finch, R.G., Eds.; Taylor & Francis Group, London,

- 2006; pp. 4-6.
38. Eisenmann, H.; Letsiou, I.; Feuchtinger, A.; Beisker, W.; Mannweiler, E.; Hutzler, P.; Arnz, P. *Appl. Environ. Microbiol.* **2001**, *67*, 4286, doi:10.1128/AEM.67.9.4286-4292.2001.
 39. Rumbaugh, K.P.; Sauer, K. *Nat. Rev. Microbiol.* **2020**, *18*, 571, doi:10.1038/s41579-020-0385-0.
 40. Mah, T.-F.C.; O'Toole, G.A. *Trends Microbiol.* **2001**, *9*, 34, doi:10.1016/S0966-842X(00)01913-2.
 41. Eliopoulos, G.M.; Blazquez, J. *Clin. Infect. Dis.* **2003**, *37*, 1201, doi:10.1086/378810.
 42. Velkov, V. V. *J. Biosci.* **2001**, *26*, 667, doi:10.1007/BF02704764.
 43. Hentzer, M.; Riedel, K.; Rasmussen, T.B.; Heydorn, A.; Andersen, J.B.; Parsek, M.R.; Rice, S.A.; Eberl, L.; Molin, S.; Høiby, N.; Kjelleberg, S.; Givskov, M. *IMicrobiology* **2002**, *148*, 87, doi:10.1099/00221287-148-1-87.
 44. Lebeaux, D.; Ghigo, J.-M.; Beloin, C. *Microbiol. Mol. Biol. Rev.* **2014**, *78*, 510, doi:10.1128/MMBR.00013-14.
 45. Sharma, D.; Misba, L.; Khan, A.U. *Antimicrob. Resist. Infect. Control* **2019**, *8*, 76, doi:10.1186/s13756-019-0533-3.
 46. Roy, R.; Tiwari, M.; Donelli, G.; Tiwari, V. *Virulence* **2018**, *9*, 522, doi:10.1080/21505594.2017.1313372.
 47. Carrera, E.T.; Dias, H.B.; Corbi, S.C.T.; Marcantonio, R.A.C.; Bernardi, A.C.A.; Bagnato, V.S.; Hamblin, M.R.; Rastelli, A.N.S. *Laser Phys.* **2016**, *26*, 123001, doi:10.1088/1054-660X/26/12/123001.
 48. Alkabban, F.M.; Ferguson, T. Breast cancer. 2021 Aug 7. In: *StatPearls* [Internet]. StatPearls Publishing: Treasure Island (Florida), **2022**. PMID: 29493913. Available online: <https://www.ncbi.nlm.nih.gov/books/NBK482286/>.
 49. Ferlay, J.; Soerjomataram, I.; Dikshit, R.; Eser, S.; Mathers, C.; Rebelo, M.; Parkin, D.M.; Forman, D.; Bray, F. *Int. J. Cancer* **2015**, *136*, E359, doi:10.1002/ijc.29210.
 50. Feng, Y.; Spezia, M.; Huang, S.; Yuan, C.; Zeng, Z.; Zhang, L.; Ji, X.; Liu, W.; Huang, B.; Luo, W.; Liu, B.; Lei, Y.; Du, S.; Vuppalapati, A.; Luu, Hue H.; Haydon, Rex C.;

- He, T.-C.; Ren, G. *Genes Dis.* **2018**, *5*, 77, doi:10.1016/j.gendis.2018.05.001.
51. Leibowitz-Amit, R.; Pintilie, M.; Khoja, L.; Azad, A.A.; Berger, R.; Laird, A.D.; Aftab, D.T.; Chi, K.N.; Joshua, A.M. *J. Transl. Med.* **2016**, *14*, 12, doi:10.1186/s12967-015-0747-y.
52. Moore, M.; Gill, S.; Asmis, T.; Berry, S.; Burkes, R.; Zbuk, K.; Alcindor, T.; Jeyakumar, A.; Chan, T.; Rao, S.; Spratlin, J.; Tang, P.A.; Rothenstein, J.; Chan, E.; Bendell, J.; Kudrik, F.; Kauh, J.; Tang, S.; Gao, L.; Kambhampati, S.R.P.; Nasroulah, F.; Yang, L.; Ramdas, N.; Binder, P.; Strevel, E. *Ann. Oncol.* **2016**, *27*, 2216, doi:10.1093/annonc/mdw412.
53. Nabors, L.B.; Fink, K.L.; Mikkelsen, T.; Grujicic, D.; Tarnawski, R.; Nam, D.H.; Mazurkiewicz, M.; Salacz, M.; Ashby, L.; Zagonel, V.; Depenni, R.; Perry, J.R.; Hicking, C.; Picard, M.; Hegi, M. E.; Lhermitte, B.; Reardon, D.A. *Neuro. Oncol.* **2015**, *17*, 708, doi:10.1093/neuonc/nou356.
54. Raab, O. *Z. Biol* **1900**, *39*, 524-526.
55. Novaes, A.B.; Schwartz-Filho, H.O.; de Oliveira, R.R.; Feres, M.; Sato, S.; Figueiredo, L.C. *Lasers Med. Sci.* **2012**, *27*, 389, doi:10.1007/s10103-011-0901-6.
56. Attia, A.; Elsaie, M.L. Photodynamic Therapy in Dermatology: What's New. In *Photodynamic Therapy: New Research*; Elsaie, M.L.T., Ed.; Nova Science Publishers, Inc, New York, 2013; pp. 233-242 ISBN 978-1-62417-635-7.
57. Novaes-Jr, A.B.; Ramos, U.D. Antimicrobial photodynamic therapy in periodontics and implantology. In *Photodynamic Therapy: New Research*; Elsaie, M.L.T., Ed.; Nova Science Publishers, Inc, New York, 2013; pp. 167-186 ISBN 978-1-62417-635-7.
58. Wainwright, M. *J. Antimicrob. Chemother.* **1998**, *42*, 13, doi:10.1093/jac/42.1.13.
59. Ryskova, L.; Buchta, V.; Slezak, R. *Open Life Sci.* **2010**, *5*, 400, doi:10.2478/s11535-010-0032-2.
60. Wainwright, M. Photosensitisers and photosensitisation. In *Photosensitisers in Biomedicine*; John Wiley & Sons Ltd., New York, 2009; pp. 27-43 ISBN 978-0-470-51060-5.
61. Correia, J.H.; Rodrigues, J.A.; Pimenta, S.; Dong, T.; Yang, Z. *Pharmaceutics* **2021**, *13*,

- 1332, doi:10.3390/pharmaceutics13091332.
62. Aerssens, D.; Cadoni, E.; Tack, L.; Madder, A. *Molecules* **2022**, *27*, 778, doi:10.3390/molecules27030778.
 63. Celli, J.P.; Spring, B.Q.; Rizvi, I.; Evans, C.L.; Samkoe, K.S.; Verma, S.; Pogue, B.W.; Hasan, T. *Chem. Rev.* **2010**, *110*, 2795, doi:10.1021/cr900300p.
 64. Castano, A.P.; Demidova, T.N.; Hamblin, M.R. *Photodiagnosis Photodyn. Ther.* **2004**, *1*, 279, doi:10.1016/S1572-1000(05)00007-4
 65. Koshi, E.; Mohan, A.; Rajesh, S.; Philip, K. *J. Indian Soc. Periodontol.* **2011**, *15*, 323, doi:10.4103/0972-124X.92563.
 66. Sharman, W.M.; Allen, C.M.; van Lier, J.E. *Drug Discov. Today* **1999**, *4*, 507, doi:10.1016/S1359-6446(99)01412-9.
 67. Moan, J.; Berg, K. *Photochem. Photobiol.* **1991**, *53*, 549, doi:10.1111/j.1751-1097.1991.tb03669.x.
 68. De Freitas, L.F.; Hamblin, M.R. Antimicrobial photoinactivation with functionalized fullerenes. In *Nanobiomaterials in antimicrobial therapy*; Elsevier, 2016; pp. 1-27.
 69. Rocha, M.P.; Rosa, F.C.S.; Rosa, L.P. *SM J. Nanotechnol. Nanomed.* **2017**, *2*, 1004.
 70. Niculescu, A.-G.; Grumezescu, A.M. *Appl. Sci.* **2021**, *11*, 3626, doi:10.3390/app11083626.
 71. Banerjee, S.M.; El-Sheikh, S.; Malhotra, A.; Mosse, C.A.; Parker, S.; Williams, N.R.; MacRobert, A.J.; Hamoudi, R.; Bown, S.G.; Keshtgar, M.R.S. *J. Clin. Med.* **2020**, *9*, 483, doi:10.3390/jcm9020483.
 72. Freitas, I. *J. Photochem. Photobiol. B Biol.* **1988**, *2*, 281, doi:10.1016/1011-1344(88)80011-3.
 73. Moor, A.C.E.; Ortel, B.; Hasan, T. Mechanisms of photodynamic therapy. In *Comprehensive Series in Photochemistry & Photobiology*; Patrice, T., Ed.; Royal Society of Chemistry: Cambridge, 2003; pp. 19; ISBN 0-85404-306-3.
 74. Nowis, D.; Makowski, M.; Stokłosa, T.; Legat, M.; Issat, T.; Gołab, J. *Acta Biochim. Pol.* **2005**, *52*, 339.

75. Chan, Y.; Lai, C.-H. *Lasers Med. Sci.* **2003**, *18*, 51, doi:10.1007/s10103-002-0243-5.
76. Abrahamse, H.; Hamblin, M.R. *Biochem. J.* **2016**, *473*, 347, doi:10.1042/BJ20150942.
77. Robertson, C.A.; Evans, D.H.; Abrahamse, H. *J. Photochem. Photobiol. B Biol.* **2009**, *96*, 1, doi:10.1016/j.jphotobiol.2009.04.001.
78. Konopka, K.; Goslinski, T. *J. Dent. Res.* **2007**, *86*, 694, doi:10.1177/154405910708600803.
79. O'Connor, A.E.; Gallagher, W.M.; Byrne, A.T. *Photochem. Photobiol.* **2009**, *85*, 1053, doi:10.1111/j.1751-1097.2009.00585.x.
80. Garland, M.J.; Cassidy, C.M.; Woolfson, D.; Donnelly, R.F. *Future Med. Chem.* **2009**, *1*, 667, doi:10.4155/fmc.09.55.
81. Dandridge, A. G.; Drescher, H. A. E.; Dunworth, S. W.; Thomas, J. Scottish Dyes Limited GB Patent 322 1929.
82. Erk, P.; Hengelsberg, H. Phthalocyanine Dyes and Pigments. In *The Porphyrin Handbook, Applications of Phthalocyanines*; Kadish, K.M., Smith, K.M., Guillard, R., Eds.; Elsevier Science: New York, 2003; p. 105.
83. Wöhrle, D.; Schnurpfeil, G.; Makarov, S.G.; Kazarin, A.; Suvorova, O.N. *Macroheterocycles* **2012**, *5*, 191, doi:10.6060/mhc2012.120990w.
84. Ben-Hura, E.; Chan, W.-S. Phthalocyanines in photobiology and their medical applications. In *The Porphyrin Handbook Applications of Phthalocyanines*; Kadish, K.M., Smith, K.M., Guillard, R., Eds.; Academic Press, Elsevier Science, **2003**; pp. 2.
85. Wainwright, M. Phthalocyanines. In *Photosensitisers in biomedicine*; John Wiley & Sons Ltd., New York, 2009; pp. 147-165 ISBN 978-0-470-51060-5.
86. Isago, H. *Optical spectra of phthalocyanines and related compounds a Guide for beginners*; Springer, Japan, 2015.
87. De la Torre, G.; Vázquez, P.; Agulló-López, F.; Torres, T. *J. Mater. Chem.* **1998**, *8*, 1671, doi:10.1039/a803533d.
88. De la Torre, G.; Vázquez, P.; Agulló-López, F.; Torres, T. *Chem. Rev.* **2004**, *104*, 3723, doi:10.1021/cr030206t.

89. Gu, D.; Chen, Q.; Gan, F. Optical data recording using copper phthalocyanine in short-wavelength region; Kyrala, G.A., Snyder, D.R., Eds.; Proceeding SPIE 2273, Ultrahigh- and high-speed photography, videography, and photonics: San Diego, **1994**; pp. 226.
90. Li, X.; Wang, H.; Wu, H. Phthalocyanines and their analogs applied in dye-sensitized solar cell. In *Functional Phthalocyanine Molecular Materials. Structure and Bonding*; J., J., Ed.; Springer: Berlin, 2010; pp. 229-273.
91. Lee, J.D.; Kim, H.B. *Korean J. Chem. Eng.* **2009**, *26*, 673, doi:10.1007/s11814-009-0112-z.
92. Gust, D.; Moore, T.A.; Moore, A.L. *Acc. Chem. Res.* **1993**, *26*, 198, doi:10.1021/ar00028a010.
93. Granados O., G.; Páez M., C.A.; Martínez O., F.; Páez-Mozo, E.A. *Catal. Today* **2005**, *107*, 589, doi:10.1016/j.cattod.2005.07.021.
94. De Rosa, M. *Coord. Chem. Rev.* **2002**, *233*, 351, doi:10.1016/S0010-8545(02)00034-6.
95. Lukyanets, E.A. *J. Porphyr. Phthalocyanines* **1999**, *3*, 424, doi:10.1002/(SICI)1099-1409(199908/10)3:6/7<424::AID-JPP151>3.0.CO;2-K.
96. Nyokong, T.; Gledhill, I. The use of phthalocyanines in cancer therapy. AIP Conference Proceedings 1517, 49, **2013**, <https://doi.org/10.1063/1.4794220>.
97. Huang, H.; Song, W.; Rieffel, J.; Lovell, J.F. *Front. Phys.* **2015**, *3*, 23, doi:10.3389/fphy.2015.00023.
98. Nyamu, S.N.; Ombaka, L.; Masika, E.; Ng'ang'a, M. *Adv. Chem.* **2018**, *2018*, 1, 2598062, doi:10.1155/2018/2598062.
99. Supriya, S.; Shetti, V.S.; Hegde, G. *New J. Chem.* **2018**, *42*, 12328, doi:10.1039/C8NJ02254B.
100. Bonnett, R. Chapter 1: Nomenclature. In *The Porphyrins, Structure and Synthesis Part A*; Dolphin, D.; Academic Press: New York, 1978; pp. 1.
101. Williams, R.J.P. *Chem. Rev.* **1956**, *56*, 299, doi:10.1021/cr50008a004.
102. Imran, M.; Ramzan, M.; Qureshi, A.; Khan, M.; Tariq, M. *Biosensors* **2018**, *8*, 95, doi:10.3390/bios8040095.

103. Valicsek, Z.; Horváth, O. *Microchem. J.* **2013**, *107*, 47, doi:10.1016/j.microc.2012.07.002.
104. Jeong, H.-G.; Choi, M.-S. *Isr. J. Chem.* **2016**, *56*, 110, doi:10.1002/ijch.201500026.
105. Okura, I. *Photosensitization of Porphyrins and Phthalocyanines*; Gordon and Breach Science: Tokyo, 2000.
106. Nemykin, V.N.; Lukyanets, E.A. *Arkivoc* **2010**, *2010*, 136, doi:10.3998/ark.5550190.0011.104.
107. Mack, J.; Kobayashi, N. *Chem. Rev.* **2011**, *111*, 281, doi:10.1021/cr9003049.
108. Kharisov, B.I.; Ortiz Méndez, U.; Almaraz Garza, J.L.; Almaguer Rodríguez, J.R. *New J. Chem.* **2005**, *29*, 686, doi:10.1039/b415712p.
109. Nemykin, V.N.; Dudkin, S. V.; Dumoulin, F.; Hirel, C.; Gürek, A.G.; Ahsen, V. *Arkivoc* **2014**, *2014*, 142, doi:10.3998/ark.5550190.p008.412.
110. Vacus, J.; Memetzidis, G.; Doppelt, P.; Simon, J. *J. Chem. Soc. Chem. Commun.* **1994**, 697, doi:10.1039/c39940000697.
111. Giovannetti, R. The use of spectrophotometry UV-Vis for the study of porphyrins. In *Macro To Nano Spectroscopy*; Uddin, J., Ed.; InTechOpen: London, 2012; pp. 88.
112. Adler, A.D.; Longo, F.R.; Finarelli, J.D.; Goldmacher, J.; Assour, J.; Korsakoff, L. *J. Org. Chem.* **1967**, *32*, 476, doi:10.1021/jo01288a053.
113. Pinto, S.M.A.; Henriques, C.A.; Tomé, V.A.; Vinagreiro, C.S.; Calvete, M.J.F.; Dąbrowski, J.M.; Piñeiro, M.; Arnaut, L.G.; Pereira, M.M. *J. Porphyr. Phthalocyanines* **2016**, *20*, 45, doi:10.1142/S1088424616300020.
114. Feng, X.; Senge, M.O. *J. Chem. Soc. Perkin Trans. I* **2001**, 1030, doi:10.1039/b100012h.
115. Milanesio, E.; Chiacchiera, S.; Silber, J.; Durantini, E. *Molecules* **2000**, *5*, 531, doi:10.3390/50300531.
116. Edwards, L.; Gouterman, M. *J. Mol. Spectrosc.* **1970**, *33*, 292-310, doi:10.1016/0022-2852(70)90040-8.
117. Gouterman, M. *Optical Spectra and Electronic Structure of Porphyrins and Related*

- Rings. In *The Porphyrins, Vol. III, Part A. Physical Chemistry*; Dolphin, D., Ed.; Academic press: New York, 1978; p. 1.
118. Chandra, R.; Tiwari, M.; Kaur, P.; Sharma, M.; Jain, R.; Dass, S. *Indian J. Clin. Biochem.* **2000**, *15*, 183, doi:10.1007/BF02867558.
119. Gouterman, M. S *J. Mol. Spectrosc.* **1961**, *6*, 138, doi:10.1016/0022-2852(61)90236-3.
120. Stillman, M.J.; Nyokong, T. Absorption and magnetic circular dichroism spectral properties of dianion, Pc(-2). In *Phthalocyanines, Properties and Applications*; Leznoff, C.C., Lever, A.B.P., Eds.; VCH Publishers, Inc.: New York, 1989; p. 133.
121. Günsel, A.; Bilgiçli, A.T.; Kandaz, M.; Orman, E.B.; Özkaya, A.R. *Dye. Pigment.* **2014**, *102*, 169, doi:10.1016/j.dyepig.2013.09.035.
122. Nyokong, T. *Polyhedron* **1993**, *12*, 375.
123. Snow, A.W. Phthalocyanine aggregation. In *The Porphyrin Handbook. Phthalocyanines: Properties and Materials*; Kadish, K., Guillard, R., Smith, K.M., Eds.; Elsevier Science: New York, 2003; pp. 130.
124. Kataoka, H.; Nishie, H.; Hayashi, N.; Tanaka, M.; Nomoto, A.; Yano, S.; Joh, T. *Ann. Transl. Med.* **2017**, *5*, 183, doi:10.21037/atm.2017.03.59.
125. Sundaram, P.; Abrahamse, H. *Materials (Basel)*. **2020**, *13*, 4830, doi:10.3390/ma13214830.
126. Crevillen, A.G.; Escarpa, A.; García, C.D. Chapter 1: Carbon-based nanomaterials in analytical chemistry. In *Carbon-based nanomaterials in analytical chemistry (Detection Science)*; Royal Society of Chemistry: London, 2018; pp. 1; ISBN 978-1-78801-102-0.
127. Patel, K.D.; Singh, R.K.; Kim, H.-W. *CMater. Horizons* **2019**, *6*, 434, doi:10.1039/C8MH00966J.
128. Erol, O.; Uyan, I.; Hatip, M.; Yilmaz, C.; Tekinay, A.B.; Guler, M.O. *Nanomedicine Nanotechnology, Biol. Med.* **2018**, *14*, 2433, doi:10.1016/j.nano.2017.03.021.
129. Zhang, X.-F.; Shao, X. *J. Photochem. Photobiol. A Chem.* **2014**, *278*, 69, doi:10.1016/j.jphotochem.2014.01.001.
130. Syama, S.; Mohanan, P. V. *Nano-Micro Lett.* **2019**, *11*, 6, doi:10.1007/s40820-019-

0237-5.

131. Koh, K.H.; Noh, S.H.; Kim, T.-H.; Lee, W.J.; Yi, S.-C.; Han, T.H. *RSC Adv.* **2017**, *7*, 26113, doi:10.1039/C6RA27873F.
132. Kholikov, K.; Ilhom, S.; Sajjad, M.; Smith, M.E.; Monroe, J.D.; San, O.; Er, A.O. *Photodiagnosis Photodyn. Ther.* **2018**, *24*, 7, doi:10.1016/j.pdpdt.2018.08.011.
133. Li, Y.; Hu, Y.; Zhao, Y.; Shi, G.; Deng, L.; Hou, Y.; Qu, L. *Adv. Mater.* **2011**, *23*, 776, doi:10.1002/adma.201003819.
134. Peng, J.; Gao, W.; Gupta, B.K.; Liu, Z.; Romero-Aburto, R.; Ge, L.; Song, L.; Alemany, L.B.; Zhan, X.; Gao, G.; Vithayathil, S.A.; Kaipparattu, B.A.; Marti, A.A.; Hayashi, T.; Zhu, J.-J.; Ajayan, P.M. *Nano Lett.* **2012**, *12*, 844, doi:10.1021/nl2038979.
135. Pan, D.; Zhang, J.; Li, Z.; Wu, M. *Adv. Mater.* **2010**, *22*, 734, doi:10.1002/adma.200902825.
136. Ye, R.; Xiang, C.; Lin, J.; Peng, Z.; Huang, K.; Yan, Z.; Cook, N.P.; Samuel, E.L.G.; Hwang, C.-C.; Ruan, G.; Ceriotti, G.; Raji, A.-R. O.; Martí, A.A.; Tour, J.M. *Nat. Commun.* **2013**, *4*, 2943, doi:10.1038/ncomms3943.
137. Liu, R.; Wu, D.; Feng, X.; Müllen, K. *J. Am. Chem. Soc.* **2011**, *133*, 15221, doi:10.1021/ja204953k.
138. Szunerits, S.; Barras, A.; Boukherroub, R. *Int. J. Environ. Res. Public Health* **2016**, *13*, 413, doi:10.3390/ijerph13040413.
139. Xie, L.; Wang, G.; Zhou, H.; Zhang, F.; Guo, Z.; Liu, C.; Zhang, X.; Zhu, L. *Biomaterials* **2016**, *103*, 219, doi:10.1016/j.biomaterials.2016.06.058.
140. Bokare, A.; Nordlund, D.; Melendrez, C.; Robinson, R.; Keles, O.; Wolcott, A.; Erogbogbo, F. *Diam. Relat. Mater.* **2020**, *110*, 108101, doi:10.1016/j.diamond.2020.108101.
141. Lin, L.; Rong, M.; Lu, S.; Song, X.; Zhong, Y.; Yan, J.; Wang, Y.; Chen, X. *Nanoscale* **2015**, *7*, 1872, doi:10.1039/C4NR06365A.
142. Namdari, P.; Negahdari, B.; Eatemadi, A. *Biomed. Pharmacother.* **2017**, *87*, 209, doi:10.1016/j.biopha.2016.12.108.
143. Zhang, F.; Liu, F.; Wang, C.; Xin, X.; Liu, J.; Guo, S.; Zhang, J. *ACS Appl. Mater.*

- Interfaces* **2016**, *8*, 2104, doi:10.1021/acsami.5b10602.
144. Li, Y.; Zhao, Y.; Cheng, H.; Hu, Y.; Shi, G.; Dai, L.; Qu, L. *J. Am. Chem. Soc.* **2012**, *134*, 15, doi:10.1021/ja206030c.
145. Miao, X.; Qu, D.; Yang, D.; Nie, B.; Zhao, Y.; Fan, H.; Sun, Z. *Adv. Mater.* **2018**, *30*, 1704740, doi:10.1002/adma.201704740.
146. Managa, M.; Ngoy, B.P.; Nyokong, T. *New J. Chem.* **2019**, *43*, 4518, doi:10.1039/C8NJ06175K.
147. Santos, C.I.M.; Rodríguez-Pérez, L.; Gonçalves, G.; Dias, C.J.; Monteiro, F.; Faustino, M. do A.F.; Vieira, S.I.; Helguero, L.A.; Herranz, M.Á.; Martín, N.; Neves, M.; Graça, P. M. S.; Martinho, José M. G.; Maçôas, Ermelinda M. S. *ACS Appl. Nano Mater.* **2021**, *4*, 13079, doi:10.1021/acsanm.1c02600.
148. Menilli, L.; Monteiro, A.R.; Lazzarotto, S.; Morais, F.M.P.; Gomes, A.T.P.C.; Moura, N.M.M.; Fateixa, S.; Faustino, M.A.F.; Neves, M.G.P.M.S.; Trindade, T.; Miolo, G. *Pharmaceutics* **2021**, *13*, 1512, doi:10.3390/pharmaceutics13091512.
149. Cao, Y.; Dong, H.; Yang, Z.; Zhong, X.; Chen, Y.; Dai, W.; Zhang, X. *ACS Appl. Mater. Interfaces* **2017**, *9*, 1596, doi:10.1021/acsami.6b13150.
150. Gvozdev, D.A.; Gudkova, V.R.; Moisenovich, A.M.; Ramonova, A.A.; Strakhovskaya, M.G.; Maksimov, E.G. *J. Photochem. Photobiol. B Biol.* **2022**, *227*, 112387, doi:10.1016/j.jphotobiol.2022.112387.
151. Nene, L.C.; Managa, M.; Nyokong, T. *Dye. Pigment.* **2019**, *165*, 488, doi:10.1016/j.dyepig.2019.03.002.
152. Matshitse, R.; Ngoy, B.P.; Managa, M.; Mack, J.; Nyokong, T. *Photodiagnosis Photodyn. Ther.* **2019**, *26*, 101, doi:10.1016/j.pdpdt.2019.03.007.
153. Matshitse, R.; Tshiwawa, T.; Managa, M.; Nwaji, N.; Lobb, K.; Nyokong, T. *J. Lumin.* **2020**, *227*, 117465, doi:10.1016/j.jlumin.2020.117465.
154. Sen, P.; Nyokong, T. *Photodiagnosis Photodyn. Ther.* **2021**, *34*, 102300, doi:10.1016/j.pdpdt.2021.102300.
155. Nyokong, T. *Coord. Chem. Rev.* **2007**, *251*, 1707, doi:10.1016/j.ccr.2006.11.011.
156. Köysal, Y.; Işık, Ş.; Akdemir, N.; Açar, E.; Kantar, C. *Acta Crystallogr. Sect. E Struct.*

- Reports Online* **2004**, *60*, o930, doi:10.1107/S1600536804010311.
157. Huang, C.; Ke, M. *Synthesis of Peripheral and Non-peripheral Substituted Metallophthalocyanines, Chinese Patent Application No. 200710200223*, **2007**.
 158. Hummers, W.S.; Offeman, R.E. *J. Am. Chem. Soc.* **1958**, *80*, 1339, doi:10.1021/ja01539a017.
 159. Achadu, O.J.; Uddin, I.; Nyokong, T. *J. Photochem. Photobiol. A Chem.* **2016**, *317*, 12, doi:10.1016/j.jphotochem.2015.11.006.
 160. Liu, J.-J.; Zhang, X.-L.; Cong, Z.-X.; Chen, Z.-T.; Yang, H.-H.; Chen, G.-N. *Nanoscale* **2013**, *5*, 1810, doi:10.1039/c3nr33794d.
 161. Nate, Z.; Moloto, M.J.; Mubiayi, P.K.; Sibiyi, P.N. *MRS Adv.* **2018**, *3*, 2505, doi:10.1557/adv.2018.368.
 162. Agnihotri, S.; Mukherji, S.; Mukherji, S. *RSC Adv.* **2014**, *4*, 3974, doi:10.1039/C3RA44507K.
 163. Ambroz, M.; Beeby, A.; MacRobert, A.J.; Simpson, M.S.C.; Svensen, R.K.; Phillips, D. *J. Photochem. Photobiol. B Biol.* **1991**, *9*, 87, doi:10.1016/1011-1344(91)80006-4.
 164. Durmus, M. Photosensitizers in medicine, environment, and security. In; Nyokong, T., Ahsen, V., Eds.; Springer Netherlands: Dordrecht, 2012; pp. 135-266 ISBN 978-90-481-3870-8.
 165. Frisch, M.J.; Trucks, G.W.; Schlegel, H.B.; Scuseria, G.E.; Robb, M.A.; Cheeseman, J.R.; Scalmani; Barone, G.V.B.M.; Petersson, G.A.; Nakatsuji, H.; et al. Gaussian 09, Revision D.01 **2009**.
 166. Özdemir, L.; Yılmaz, Y.; Sönmez, M.; Akkurt, M.; Tahir, M.N. *Synth. React. Inorganic, Met. Nano-Metal Chem.* **2016**, *46*, 110, doi:10.1080/15533174.2014.900790.
 167. Bilginer, S.; Gul, H.I.; Mete, E.; Das, U.; Sakagami, H.; Umemura, N.; Dimmock, J.R. *J. Enzyme Inhib. Med. Chem.* **2013**, *28*, 974, doi:10.3109/14756366.2012.700927.
 168. Atilla, D.; Saydan, N.; Durmuş, M.; Gürek, A.G.; Khan, T.; Rück, A.; Walt, H.; Nyokong, T.; Ahsen, V. *J. Photochem. Photobiol. A Chem.* **2007**, *186*, 298, doi:10.1016/j.jphotochem.2006.08.022.
 169. Kuzyniak, W.; Ermilov, E.A.; Atilla, D.; Gürek, A.G.; Nitzsche, B.; Derkow, K.;

- Hoffmann, B.; Steinemann, G.; Ahsen, V.; Höpfner, M. *Photodiagnosis Photodyn. Ther.* **2016**, *13*, 148, doi:10.1016/j.pdpdt.2015.07.001.
170. Mgidlana, S.; Oluwole, D.O.; Nyokong, T. *Polyhedron* **2019**, *159*, 102, doi:10.1016/j.poly.2018.11.024.
171. Bristow, C.A.; Hudson, R.; Paget, T.A.; Boyle, R.W. *Photodiagnosis Photodyn. Ther.* **2006**, *3*, 162, doi:https://doi.org/10.1016/j.pdpdt.2006.04.004.
172. Li, X.-S.; Guo, J.; Zhuang, J.-J.; Zheng, B.-Y.; Ke, M.-R.; Huang, J.-D. *Bioorg. Med. Chem. Lett.* **2015**, *25*, 2386, doi:10.1016/j.bmcl.2015.04.004.
173. Anaya-Plaza, E.; Aljarilla, A.; Beaune, G.; Nonappa; Timonen, J.V.I.; Escosura, A.; Torres, T.; Kostianen, M.A. *Adv. Mater.* **2019**, *31*, 1902582, doi:10.1002/adma.201902582.
174. Matshitse, R.; Khene, S.; Nyokong, T. *Diam. Relat. Mater.* **2019**, *94*, 218, doi:10.1016/j.diamond.2019.03.013.
175. Mafukidze, D.M.; Nyokong, T. *J. Mol. Struct.* **2019**, *1180*, 307, doi:https://doi.org/10.1016/j.molstruc.2018.11.096.
176. Röder, B.; Büchner, M.; Rückmann, I.; Senge, M.O. *Photochem. Photobiol. Sci.* **2010**, *9*, 1152, doi:10.1039/c0pp00107d.
177. Maree, M.D.; Nyokong, T.; Suhling, K.; Phillips, D. *J. Porphyr. Phthalocyanines* **2002**, *06*, 373, doi:10.1142/S1088424602000452.
178. Maree, S.; Phillips, D.; Nyokong, T. *J. Porphyr. Phthalocyanines* **2002**, *06*, 17, doi:10.1142/S108842460200004X.
179. Ogunsipe, A.; Maree, D.; Nyokong, T. *J. Mol. Struct.* **2003**, *650*, 131, doi:10.1016/S0022-2860(03)00155-8.
180. Berezin, M.Y.; Achilefu, S. *Chem. Rev.* **2010**, *110*, 2641, doi:10.1021/cr900343z.
181. Berney, C.; Danuser, G. *Biophys. J.* **2003**, *84*, 3992, doi:10.1016/S0006-3495(03)75126-1.
182. Sahoo, H. *J. Photochem. Photobiol. C Photochem. Rev.* **2011**, *12*, 20, doi:10.1016/j.jphotochemrev.2011.05.001.

183. Wu, L.; Huang, C.; Emery, B.P.; Sedgwick, A.C.; Bull, S.D.; He, X.-P.; Tian, H.; Yoon, J.; Sessler, J.L.; James, T.D. *Chem. Soc. Rev.* **2020**, *49*, 5110, doi:10.1039/C9CS00318E.
184. de Souza, T.G.B.; Vivas, M.G.; Mendonça, C.R.; Plunkett, S.; Filatov, M.A.; Senge, M.O.; De Boni, L. *SJ. Porphyr. Phthalocyanines* **2016**, *20*, 282, doi:10.1142/S1088424616500048.
185. Tran Thi, T.H.; Desforge, C.; Thiec, C.; Gaspard, S. *J. Phys. Chem.* **1989**, *93*, 1226, doi:10.1021/j100341a013.
186. Nyokong, T.; Antunes, E. *Handb. Porphyr. Sci.*; Kadish, K., Smith, K., Guillard, R., Eds.; World Scientific Publishing Co. Pt. Ltd: Singapore, 2010.
187. Kuznetsova, N.A.; Gretsova, N.S.; Derkacheva, V.M.; Kaliya, O.L.; Lukyanets, E.A. *J. Porphyr. Phthalocyanines* **2003**, *7*, 147, doi:10.1142/S1088424603000203.
188. Ammar, H.Y.; Badran, H.M. *Heliyon* **2019**, *5*, e02545, doi:10.1016/j.heliyon.2019.e02545.
189. Petersilka, M.; Gossmann, U.J.; Gross, E.K.U. *Phys. Rev. Lett.* **1996**, *76*, 1212, doi:10.1103/PhysRevLett.76.1212.
190. Osifeko, O.L.; Durmuş, M.; Nyokong, T. *J. Photochem. Photobiol. A Chem.* **2015**, *301*, 47, doi:10.1016/j.jphotochem.2014.12.011.
191. Sindelo, A.; Osifeko, O.L.; Nyokong, T. *Inorganica Chim. Acta* **2018**, *476*, 68, doi:10.1016/j.ica.2018.02.020.
192. Aryal, M.; Pranatharthiharan, P.; Muriana, P.M. *Foods* **2019**, *8*, 541, doi:10.3390/foods8110541.
193. Stepanović, S.; Vuković, D.; Dakić, I.; Savić, B.; Švabić-Vlahović, M. *J. Microbiol. Methods* **2000**, *40*, 175, doi:10.1016/S0167-7012(00)00122-6.
194. Genovese, C.; D'Angeli, F.; Bellia, F.; Distefano, A.; Spampinato, M.; Attanasio, F.; Nicolosi, D.; Di Salvatore, V.; Tempera, G.; Lo Furno, D.; Mannino, G.; Milardo, F.; Li Volti, G. *Antibiotics* **2021**, *10*, 428, doi:10.3390/antibiotics10040428.
195. Campoli-Richards, D.M.; Monk, J.P.; Price, A.; Benfield, P.; Todd, P.A.; Ward, A. *Drugs* **1988**, *35*, 373, doi:10.2165/00003495-198835040-00003.

196. Rotilie, C.A.; Fass, R.J.; Prior, R.B.; Perkins, R.L. *Antimicrob. Agents Chemother.* **1975**, *7*, 311, doi:10.1128/AAC.7.3.311.
197. Stiefel, P.; Rosenberg, U.; Schneider, J.; Mauerhofer, S.; Maniura-Weber, K.; Ren, Q. *Appl. Microbiol. Biotechnol.* **2016**, *100*, 4135, doi:10.1007/s00253-016-7396-9.
198. Christensen, G.D.; Simpson, W.A.; Younger, J.J.; Baddour, L.M.; Barrett, F.F.; Melton, D.M.; Beachey, E.H. *J. Clin. Microbiol.* **1985**, *22*, 996, doi:10.1128/jcm.22.6.996-1006.1985.
199. Heydari, S.; Eftekhari, F. *Jundishapur J. Microbiol.* **2015**, *8*, e15514, doi:10.5812/jjm.15514.
200. Cruz, C.D.; Shah, S.; Tammela, P. *BMC Microbiol.* **2018**, *18*, 173, doi:10.1186/s12866-018-1321-6.
201. Feng, Y.; Coradi Tonon, C.; Ashraf, S.; Hasan, T. *Adv. Drug Deliv. Rev.* **2021**, *177*, 113941, doi:10.1016/j.addr.2021.113941.
202. Pontes, C.; Alves, M.; Santos, C.; Ribeiro, M.H.; Gonçalves, L.; Bettencourt, A.F.; Ribeiro, I.A.C. *Int. J. Pharm.* **2016**, *513*, 697, doi:10.1016/j.ijpharm.2016.09.074.
203. Oluwole, D.O.; Prinsloo, E.; Nyokong, T. P. *Spectrochim. Acta Part A Mol. Biomol. Spectrosc.* **2017**, *173*, 292, doi:10.1016/j.saa.2016.09.032.
204. Magaraggia, M.; Visonà, A.; Furlan, A.; Pagnan, A.; Miotto, G.; Tognon, G.; Jori, G. *J. Photochem. Photobiol. B Biol.* **2006**, *82*, 53, doi:10.1016/j.jphotobiol.2005.08.010.
205. Qualls, M.M.; Thompson, D.H. *Int. J. Cancer* **2001**, *93*, 384, doi:10.1002/ijc.1339.
206. Gupta, S.; Dwarakanath, B.S.; Muralidhar, K.; Koru-Sengul, T.; Jain, V. *J. Transl. Med.* **2010**, *8*, 43, doi:10.1186/1479-5876-8-43.
207. Arnott, J.A.; Planey, S.L. *Expert Opin. Drug Discov.* **2012**, *7*, 863, doi:10.1517/17460441.2012.714363.
208. Babu, B.; Soy, R.C.; Mack, J.; Nyokong, T. *New J. Chem.* **2020**, *44*, 11006, doi:10.1039/D0NJ01564D.
209. Hansch, C.; Maloney, P.P.; Fujita, T.; Muir, R.M. *Nature* **1962**, *194*, 178, doi:10.1038/194178b0.

210. Kanat, Z.; Dinçer, H. *Dalt. Trans.* **2014**, *43*, 8654, doi:10.1039/C4DT00238E.
211. Rio, Y.; Salomé Rodríguez-Morgade, M.; Torres, T. *Org. Biomol. Chem.* **2008**, *6*, 1877, doi:10.1039/b800617b.
212. Lukyanets, E.A.; Nemykin, V.N. *J. Porphyr. Phthalocyanines* **2010**, *14*, 1, doi:10.1142/S1088424610001799.
213. Karaca, H. *J. Turkish Chem. Soc. Sect. A Chem.* **2018**, 701, doi:10.18596/jotcsa.351559.
214. Sakamoto, K.; Ohno-Okumura, E. *Materials (Basel)*. **2009**, *2*, 1127, doi:10.3390/ma2031127.
215. Özen, F.; Günel, A.; Baran, A. *Bioorg. Chem.* **2018**, *81*, 71, doi:10.1016/j.bioorg.2018.08.002.
216. Qin, Y.; Kiburu, I.; Shah, S.; Jäkle, F. *Org. Lett.* **2006**, *8*, 5227, doi:10.1021/ol0619664.
217. Durmus, M.; Nyokong, T. *Photochem. Photobiol. Sci.* **2007**, *6*, 659, doi:10.1039/b618478b.
218. Durmuş, M.; Ahsen, V. *J. Inorg. Biochem.* **2010**, *104*, 297, doi:10.1016/j.jinorgbio.2009.12.011.
219. Gürel, E.; Pişkin, M.; Altun, S.; Odabaş, Z.; Durmuş, M. *SDalt. Trans.* **2015**, *44*, 6202, doi:10.1039/C5DT00304K.
220. Freyer, W.; Mueller, S.; Teuchner, K. *J. Photochem. Photobiol. A Chem.* **2004**, *163*, 231, doi:10.1016/j.jphotochem.2003.12.003.
221. Uttamlal, M.; Sheila Holmes-Smith, A. *Chem. Phys. Lett.* **2008**, *454*, 223, doi:10.1016/j.cplett.2008.02.012.
222. Topkaya, D.; Ng, S.Y.; Bretonnière, Y.; Lafont, D.; Chung, L.Y.; Lee, H.B.; Dumoulin, F. *Photodiagnosis Photodyn. Ther.* **2017**, *17*, A61, doi:10.1016/j.pdpdt.2017.01.137.
223. Zasedatelev, A. V.; Dubinina, T. V.; Krichevsky, D.M.; Krasovskii, V.I.; Gak, V.Y.; Pushkarev, V.E.; Tomilova, L.G.; Chistyakov, A.A. *J. Phys. Chem. C* **2016**, *120*, 1816, doi:10.1021/acs.jpcc.5b08804.
224. Li, L.; Zhao, J.-F.; Won, N.; Jin, H.; Kim, S.; Chen, J.-Y. *Nanoscale Res. Lett.* **2012**, *7*, 386, doi:10.1186/1556-276X-7-386.

225. Nikolova, V.; Galabov, B. *Contrib. Sect. Nat. Math. Biotech. Sci.* **2017**, *38*, 33, doi:10.20903/csnmbs.masa.2017.38.1.99.
226. Dong, Y.; Chen, C.; Zheng, X.; Gao, L.; Cui, Z.; Yang, H.; Guo, C.; Chi, Y.; Li, C.M. *J. Mater. Chem.* **2012**, *22*, 8764, doi:10.1039/c2jm30658a.
227. Zhu, S.; Zhang, J.; Tang, S.; Qiao, C.; Wang, L.; Wang, H.; Liu, X.; Li, B.; Li, Y.; Yu, W.; Wang, X.; Sun, H.; Yang, B. *Adv. Funct. Mater.* **2012**, *22*, 4732, doi:10.1002/adfm.201201499.
228. Liu, Z. De; Zhao, H.X.; Huang, C.Z. *PLoS One* **2012**, *7*, e50367, doi:10.1371/journal.pone.0050367.
229. Zhang, X.-F.; Xi, Q. *Carbon N. Y.* **2011**, *49*, 3842, doi:10.1016/j.carbon.2011.05.019.
230. Zhang, X.; Feng, Y.; Tang, S.; Feng, W. *Carbon* **2010**, *48*, 211, doi:10.1016/j.carbon.2009.09.007.
231. Zhang, X.-F.; Liu, S.-P.; Shao, X.-N. *Spectrochim. Acta Part A Mol. Biomol. Spectrosc.* **2013**, *113*, 92, doi:10.1016/j.saa.2013.04.066.
232. Shi, W.; Fan, H.; Ai, S.; Zhu, L. *New J. Chem.* **2015**, *39*, 7054, doi:10.1039/C5NJ00760G.
233. Wu, J.; Wang, P.; Wang, F.; Fang, Y. *Nanomaterials* **2018**, *8*, 864, doi:10.3390/nano8100864.
234. Li, Z.; He, C.; Wang, Z.; Gao, Y.; Dong, Y.; Zhao, C.; Chen, Z.; Wu, Y.; Song, W. *Photochem. Photobiol. Sci.* **2016**, *15*, 910, doi:10.1039/C6PP00063K.
235. Batakliiev, T.; Petrova-Doycheva, I.; Angelov, V.; Georgiev, V.; Ivanov, E.; Kotsilkova, R.; Casa, M.; Cirillo, C.; Adami, R.; Sarno, M.; Ciambelli, P. *Appl. Sci.* **2019**, *9*, 469, doi:10.3390/app9030469.
236. Singh, D.K.; Iyer, P.K.; Giri, P.K. *Diam. Relat. Mater.* **2010**, *19*, 1281, doi:10.1016/j.diamond.2010.06.003.
237. Souza, T.G.F.; Ciminelli, V.S.T.; Mohallem, N.D.S. *J. Phys. Conf. Ser.* **2016**, 733, 012039, doi:10.1088/1742-6596/733/1/012039.
238. Li, X.; Zhu, S.; Xu, B.; Ma, K.; Zhang, J.; Yang, B.; Tian, W. *Nanoscale* **2013**, *5*, 7776, doi:10.1039/c3nr00006k.

239. Ogbodu, R.O.; Limson, J.L.; Prinsloo, E.; Nyokong, T. *Synth. Met.* **2015**, *204*, 122, doi:10.1016/j.synthmet.2015.03.011.
240. Efremov, V.P.; Zakatilova, E.I.; Maklashova, I. V.; Shevchenko, N. V. *J. Phys. Conf. Ser.* **2018**, *946*, 012107, doi:10.1088/1742-6596/946/1/012107.
241. Yurtseven, H.; Kaya, M.A.; Altındal, A.; Şener, M.K. *Des. Monomers Polym.* **2014**, *17*, 58, doi:10.1080/15685551.2013.840468.
242. Yang, K.; Gu, M.; Guo, Y.; Pan, X.; Mu, G. *Carbon N. Y.* **2009**, *47*, 1723, doi:10.1016/j.carbon.2009.02.029.
243. Makarov, S.G.; Kazarin, A.S.; Suvorova, O.N.; Ketkov, S.Y.; Lopatin, M.A.; Wöhrle, D. *Macroheterocycles* **2014**, *7*, 145, doi:10.6060/mhc140487m.
244. Palaniselvam, T.; Aiyappa, H.B.; Kurungot, S. *J. Mater. Chem.* **2012**, *22*, 23799, doi:10.1039/c2jm35128e.
245. Chidawanyika, W.; Nyokong, T. *Carbon* **2010**, *48*, 2831, doi:10.1016/j.carbon.2010.04.015.
246. Yan, Y.; Chen, J.; Li, N.; Tian, J.; Li, K.; Jiang, J.; Liu, J.; Tian, Q.; Chen, P. *ACS Nano* **2018**, *12*, 3523, doi:10.1021/acsnano.8b00498.
247. Nwahara, N.; Britton, J.; Nyokong, T. *J. Coord. Chem.* **2017**, *70*, 1601, doi:10.1080/00958972.2017.1313975.
248. Alanazi, A.M.; Mostafa, G.A.E.; Al-Badr, A.A. Glutathione. In *Profiles of Drug Substances, Excipients, and Related Methodology*; Brittain, H.G., Ed.; Academic Press,: Burlington, 2015; pp. 43-158.
249. Yan, R.; Wu, H.; Zheng, Q.; Wang, J.; Huang, J.; Ding, K.; Guo, Q.; Wang, J. *RSC Adv.* **2014**, *4*, 23097, doi:10.1039/C4RA02336F.
250. Maity, N.; Kuila, A.; Das, S.; Mandal, D.; Shit, A.; Nandi, A.K. *J. Mater. Chem. A* **2015**, *3*, 20736, doi:10.1039/C5TA06576C.
251. Ogbodu, R.O.; Antunes, E.; Nyokong, T. *Polyhedron* **2013**, *60*, 59, doi:10.1016/j.poly.2013.05.025.
252. Miletin, M.; Zimcik, P.; Novakova, V. *Photochem. Photobiol. Sci.* **2018**, *17*, 1749, doi:10.1039/C8PP00106E.

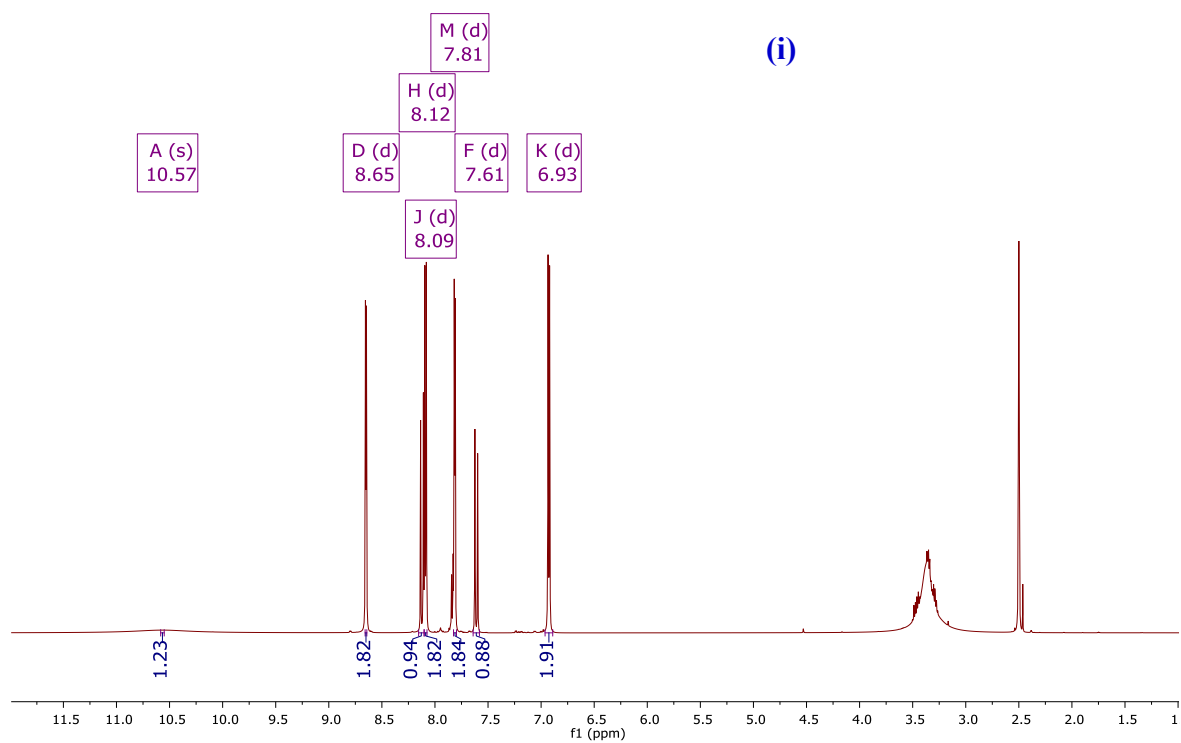
253. Kahriman, N.; Ünver, Y.; Akçay, H.T.; Gülmez, A.D.; Durmuş, M.; Değirmencioglu, İ. *J. Mol. Struct.* **2020**, *1200*, 127132, doi:10.1016/j.molstruc.2019.127132.
254. Makarov, S.G.; Kazarin, A.S.; Suvorova, O.N.; Zabrodina, G.S.; Lopatin, M.A.; Kuznetsova, O. V.; Ketkov, S.Y.; Wöhrle, D. *Macroheterocycles* **2016**, *9*, 180, doi:10.6060/mhc160109m.
255. Lakowicz, J.R.; Shen, Y.; D'Auria, S.; Malicka, J.; Fang, J.; Gryczynski, Z.; Gryczynski, I. *Anal. Biochem.* **2002**, *301*, 261, doi:10.1006/abio.2001.5503.
256. Zhang, X.-F.; Liu, S.; Shao, X. *J. Lumin.* **2013**, *136*, 32, doi:10.1016/j.jlumin.2012.11.001.
257. Rapulenyane, N.; Antunes, E.; Nyokong, T. *New J. Chem.* **2013**, *37*, 1216, doi:10.1039/c3nj41107a.
258. Muthukumar, P.; Kim, H.-S.; Ku, K.-S.; Park, J.H.; Son, Y.-A. *Fibers Polym.* **2016**, *17*, 553, doi:10.1007/s12221-016-5812-5..
259. Wang, H.; Jiang, S.; Chen, S.; Li, D.; Zhang, X.; Shao, W.; Sun, X.; Xie, J.; Zhao, Z.; Zhang, Q.; Tian, Y.; Xie, Y. *Adv. Mater.* **2016**, *28*, 6940 doi:10.1002/adma.201601413.
260. Fukuda, T.; Homma, S.; Kobayashi, N. *Chem. - A Eur. J.* **2005**, *11*, 5205, doi:10.1002/chem.200500176.
261. Darwent, J.R.; Douglas, P.; Harriman, A.; Porter, G.; Richoux, M.-C. *MCoord. Chem. Rev.* **1982**, *44*, 83, doi:10.1016/S0010-8545(00)80518-4.
262. Barbosa Neto, N.M.; Correa, D.S.; De Boni, L.; Parra, G.G.; Misoguti, L.; Mendonça, C.R.; Borissevitch, I.E.; Zilio, S.C.; Gonçalves, P.J. *Chem. Phys. Lett.* **2013**, *587*, 118, doi:10.1016/j.cplett.2013.09.066.
263. Çakır, V.; Göksel, M.; Durmuş, M.; Biyiklioglu, Z. *Dye. Pigment.* **2016**, *125*, 414, doi:10.1016/j.dyepig.2015.10.035.
264. Le Behec, M.; Pigot, T.; Lacombe, S. *Chem. Photo. Chem.* **2018**, *2*, 622, doi:10.1002/cptc.201800038.
265. Pucelik, B.; Sułek, A.; Dąbrowski, J.M. *Coord. Chem. Rev.* **2020**, *416*, 213340, doi:10.1016/j.ccr.2020.213340.
266. Kellarakis, A. *MRS Energy Sustain.* **2014**, *1*, 2, doi:10.1557/mre.2014.7.

267. Solov'ev, K.N.; Borisevich, E.A. *Physics-Uspekhi* **2005**, *48*, 231, doi:10.1070/PU2005v048n03ABEH001761.
268. Oluwole, D.O.; Prinsloo, E.; Nyokong, T. *Polyhedron* **2016**, *119*, 434, doi:10.1016/j.poly.2016.09.034.
269. Ramesh, H.; Mayr, T.; Hobisch, M.; Borisov, S.; Klimant, I.; Krühne, U.; Woodley, J.M. *J. Chem. Technol. Biotechnol.* **2016**, *91*, 832, doi:10.1002/jctb.4862.
270. Tavares, L.J.; de Avila, E.D.; Klein, M.I.; Panariello, B.H.D.; Spolidório, D.M.P.; Pavarina, A.C. *J. Photochem. Photobiol. B: Biol.* **2018**, *188*, 135, doi:10.1016/j.jphotobiol.2018.09.010.
271. Dai, T.; Fuchs, B.B.; Coleman, J.J.; Prates, R.A.; Astrakas, C.; St. Denis, T.G.; Ribeiro, M.S.; Mylonakis, E.; Hamblin, M.R.; Tegos, G.P. *Front. Microbiol.* **2012**, *3*, doi:10.3389/fmicb.2012.00120.
272. Tokubo, L.M.; Rosalen, P.L.; de Cássia Orlandi Sardi, J.; Freires, I.A.; Fujimaki, M.; Umeda, J.E.; Barbosa, P.M.; Tecchio, G.O.; Hioka, N.; de Freitas, C.F.; Suga Terada, R. S. *Photodiagnosis Photodyn. Ther.* **2018**, *23*, 94, doi:10.1016/j.pdpdt.2018.05.004.
273. Dalgaard, P.; Ross, T.; Kamperman, L.; Neumeyer, K.; McMeekin, T.A. *Int. J. Food Microbiol.* **1994**, *23*, 391, doi:10.1016/0168-1605(94)90165-1.
274. Mafukidze, D.M.; Sindelo, A.; Nyokong, T. *Spectrochim. Acta Part A Mol. Biomol. Spectrosc.* **2019**, *219*, 333, doi:10.1016/j.saa.2019.04.054.
275. Sobotta, L.; Skupin-Mrugalska, P.; Piskorz, J.; Mielcarek, J. *Eur. J. Med. Chem.* **2019**, *175*, 72, doi:10.1016/j.ejmech.2019.04.057.
276. Barry, A.L.; Lasner, R.A. *Antimicrob. Agents Chemother.* **1976**, *9*, 549, doi:10.1128/AAC.9.3.549.
277. Hamblin, M.R. *J. Antimicrob. Chemother.* **2002**, *49*, 941, doi:10.1093/jac/dkf053.
278. Minnock, A.; Vernon, D.I.; Schofield, J.; Griffiths, J.; Parish, J.H.; Brown, S.B. *Antimicrob. Agents Chemother.* **2000**, *44*, 522, doi:10.1128/AAC.44.3.522-527.2000.
279. Orenstein, A.; Klein, D.; Kopolovic, J.; Winker, E.; Malik, Z.; Keller, N.; Nitzan, Y. *FEMS Immunol. Med. Microbiol.* **1998**, *19*, 307.
280. Pedersen, B.W.; Sinks, L.E.; Breitenbach, T.; Schack, N.B.; Vinogradov, S.A.; Ogilby,

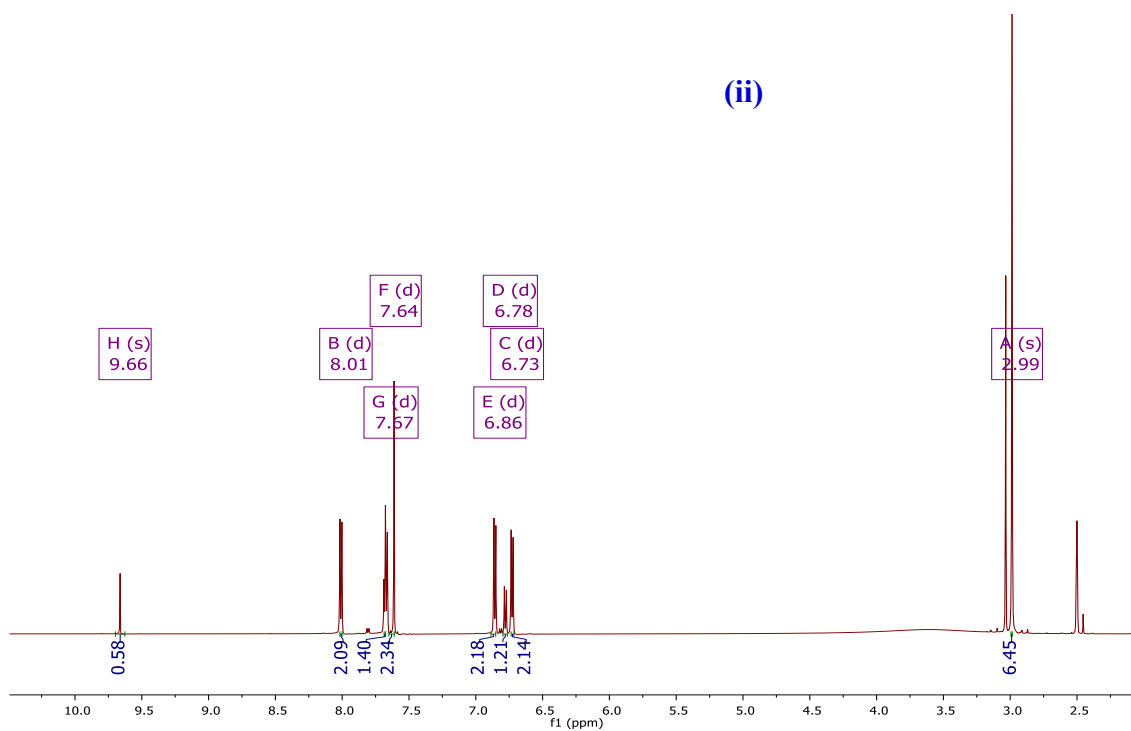
- P.R. *Photochem. Photobiol.* **2011**, *87*, 1077, doi:10.1111/j.1751-1097.2011.00951.x.
281. Kohanski, M.A.; Dwyer, D.J.; Hayete, B.; Lawrence, C.A.; Collins, J.J. *Cell* **2007**, *130*, 797, doi:10.1016/j.cell.2007.06.049.
282. Tegos, G.P.; Demidova, T.N.; Arcila-Lopez, D.; Lee, H.; Wharton, T.; Gali, H.; Hamblin, M.R. *Chem. Biol.* **2005**, *12*, 1127, doi:10.1016/j.chembiol.2005.08.014.
283. Pisarek, S.; Maximova, K.; Gryko, D. *Tetrahedron* **2014**, *70*, 6685, doi:10.1016/j.tet.2014.05.090.
284. Mehanna, S.; Mansour, N.; Audi, H.; Bodman-Smith, K.; Mroueh, M.A.; Taleb, R.I.; Daher, C.F.; Khnayzer, R.S. *RSC Adv.* **2019**, *9*, 17254, doi:10.1039/C9RA02615K.
285. Sperandio, F.; Huang, Y.-Y.; Hamblin, M. *Recent Pat. Antiinfect. Drug Discov.* **2013**, *8*, 108, doi:10.2174/1574891X113089990012.
286. Loo, Y.Y.; Rukayadi, Y.; Nor-Khaizura, M.-A.-R.; Kuan, C.H.; Chieng, B.W.; Nishibuchi, M.; Radu, S. *Front. Microbiol.* **2018**, *9*, 1555, doi:10.3389/fmicb.2018.01555.
287. Yin, I.X.; Zhang, J.; Zhao, I.S.; Mei, M.L.; Li, Q.; Chu, C.H. *Int. J. Nanomedicine* **2020**, *15*, 2555, doi:10.2147/IJN.S246764.
288. Kolter, R. Biofilms in lab and nature: *Int. Microbiol.* **2010**, *13*, 1.
289. Cieplik, F.; Tabenski, L.; Buchalla, W.; Maisch, T. *Front. Microbiol.* **2014**, *5*, 405, doi:10.3389/fmicb.2014.00405.
290. Deng, Q.; Sun, P.; Zhang, L.; Liu, Z.; Wang, H.; Ren, J.; Qu, X. *Adv. Funct. Mater.* **2019**, *29*, 1903018, doi: 10.1002/adfm.201903018.
291. Ribeiro, A.P.D.; Andrade, M.C.; de Fátima da Silva, J.; Jorge, J.H.; Primo, F.L.; Tedesco, A.C.; Pavarina, A.C. *Photochem. Photobiol.* **2013**, *89*, 111, doi:10.1111/j.1751-1097.2012.01198.x.
292. Rosseti, I.B.; Chagas, L.R.; Costa, M.S. *Lasers Med. Sci.* **2014**, *29*, 1059, doi:10.1007/s10103-013-1473-4.
293. Bacellar, I.O.L.; Oliveira, M.C.; Dantas, L.S.; Costa, E.B.; Junqueira, H.C.; Martins, W.K.; Durantini, A.M.; Cosa, G.; Di Mascio, P.; Wainwright, M.; Miotto, R.; Cordeiro, Rodrigo M.; Miyamoto, S.; Baptista, Mauricio S. *J. Am. Chem. Soc.* **2018**, *140*, 9606,

- doi:10.1021/jacs.8b05014.
294. Zuluaga, M.-F.; Lange, N. *Curr. Med. Chem.* **2008**, *15*, 1655, doi:10.2174/092986708784872401.
 295. Aldred, K.J.; Kerns, R.J.; Osheroff, N. *Biochemistry* **2014**, *53*, 1565, doi:10.1021/bi5000564.
 296. Marciel, L.; Teles, L.; Moreira, B.; Pacheco, M.; Lourenço, L.M.; Neves, M.G.; Tomé, J.P.; Faustino, M.A.; Almeida, A. *Future Med. Chem.* **2017**, *9*, 365, doi:10.4155/fmc-2016-0217.
 297. Maldonado-Carmona, N.; Ouk, T.-S.; Leroy-Lhez, S. *Photochem. Photobiol. Sci.* **2022**, *21*, 113, doi:10.1007/s43630-021-00128-5.
 298. Ronqui, M.R.; de Aguiar Coletti, T.M.S.F.; de Freitas, L.M.; Miranda, E.T.; Fontana, C.R. *J. Photochem. Photobiol. B Biol.* **2016**, *158*, 122, doi:10.1016/j.jphotobiol.2016.02.036.
 299. Zhao, X.; Drlica, K. *Curr. Opin. Microbiol.* **2014**, *21*, 1, doi:10.1016/j.mib.2014.06.008.
 300. Aribi, F.; Vey, C.; Topkaya, D.; Kostakoglu, S.T.; Fournier-dit-Chabert, J.; Büyükekşi, S.I.; Taşkın, G.C.; Alpugan, S.; Albrieux, F.; Gürek, A.G.; Cucca, M.; Bennis, K.; Atilla, D.; Ahsen, V.; Ducki, S.; Dumoulin, F. *J. Porphyr. Phthalocyanines* **2016**, *20*, 497, doi:10.1142/S1088424616500310.
 301. Mosmann, T. *J. Immunol. Methods* **1983**, *65*, 55, doi:10.1016/0022-1759(83)90303-4.
 302. Van Straten, D.; Mashayekhi, V.; de Bruijn, H.; Oliveira, S.; Robinson, D. *Cancers (Basel)*. **2017**, *9*, 19, doi:10.3390/cancers9020019.
 303. Josefsen, L.B.; Boyle, R.W. *Theranostics* **2012**, *2*, 916, doi:10.7150/thno.4571.
 304. Dumoulin, F.; Ali, H.; Ahsen, V.; van Lier, J.E. *Tetrahedron Lett.* **2011**, *52*, 4395, doi:10.1016/j.tetlet.2011.06.010.

APPENDICES 0 (A0): NMR SPECTRA OF THE CHALCONES



(a)



(b)

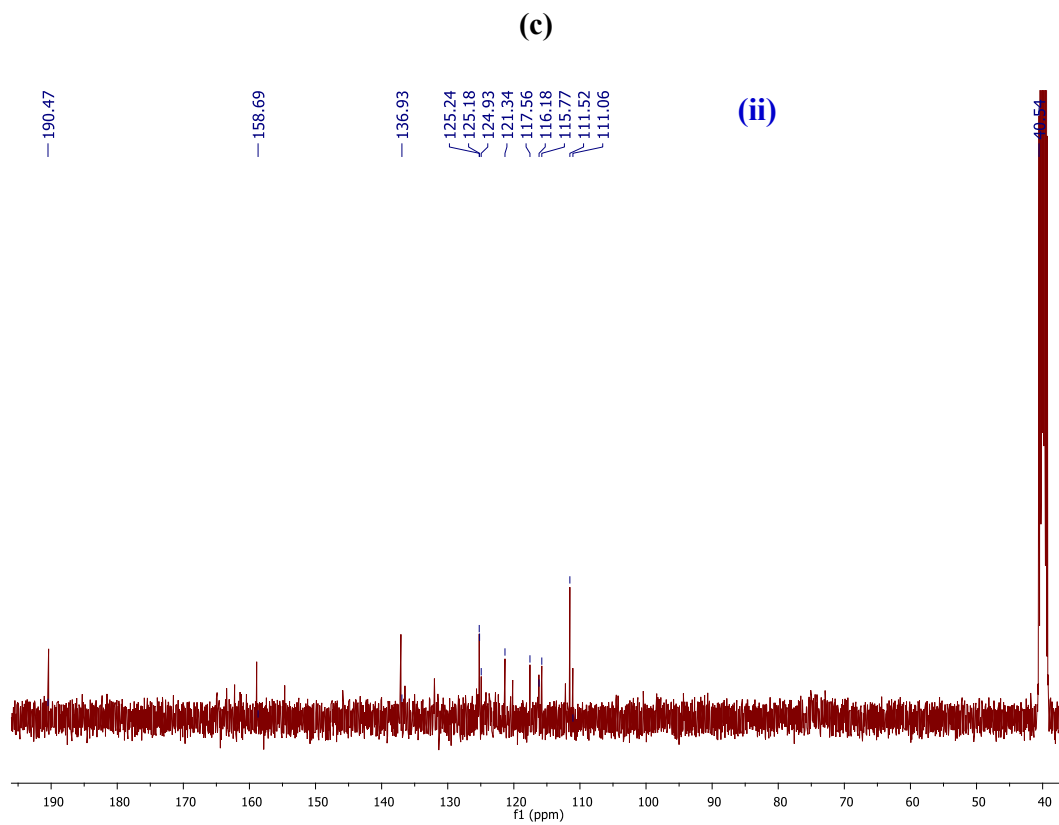
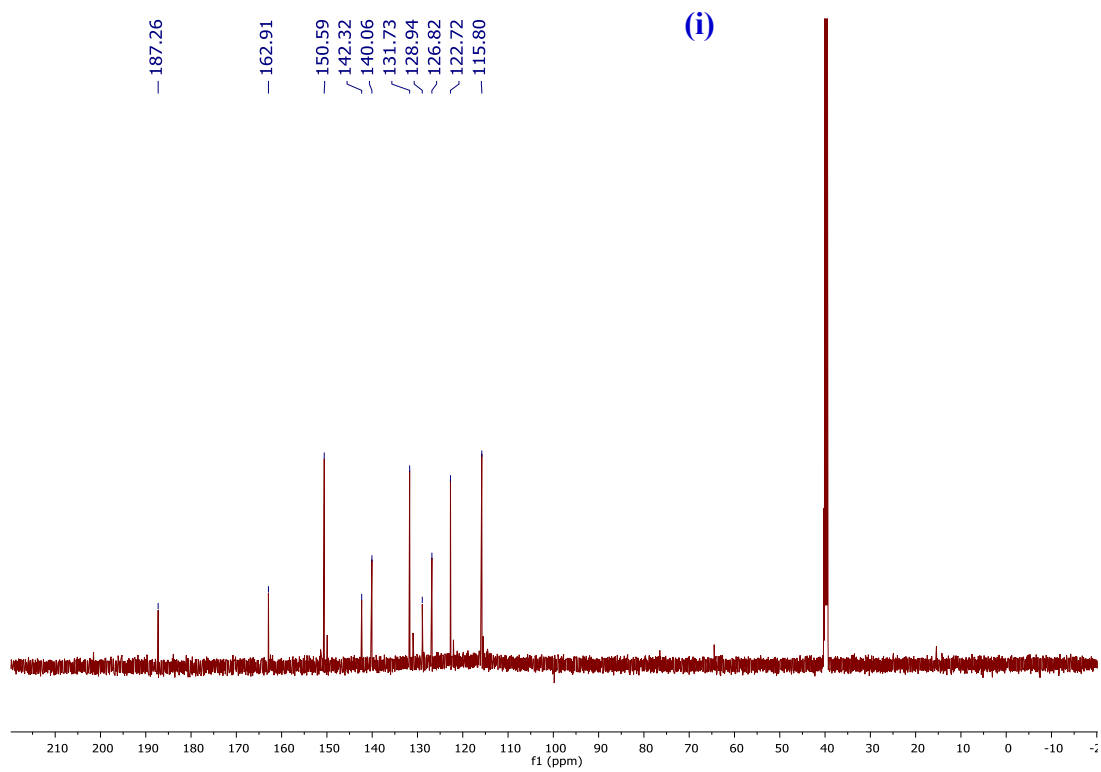
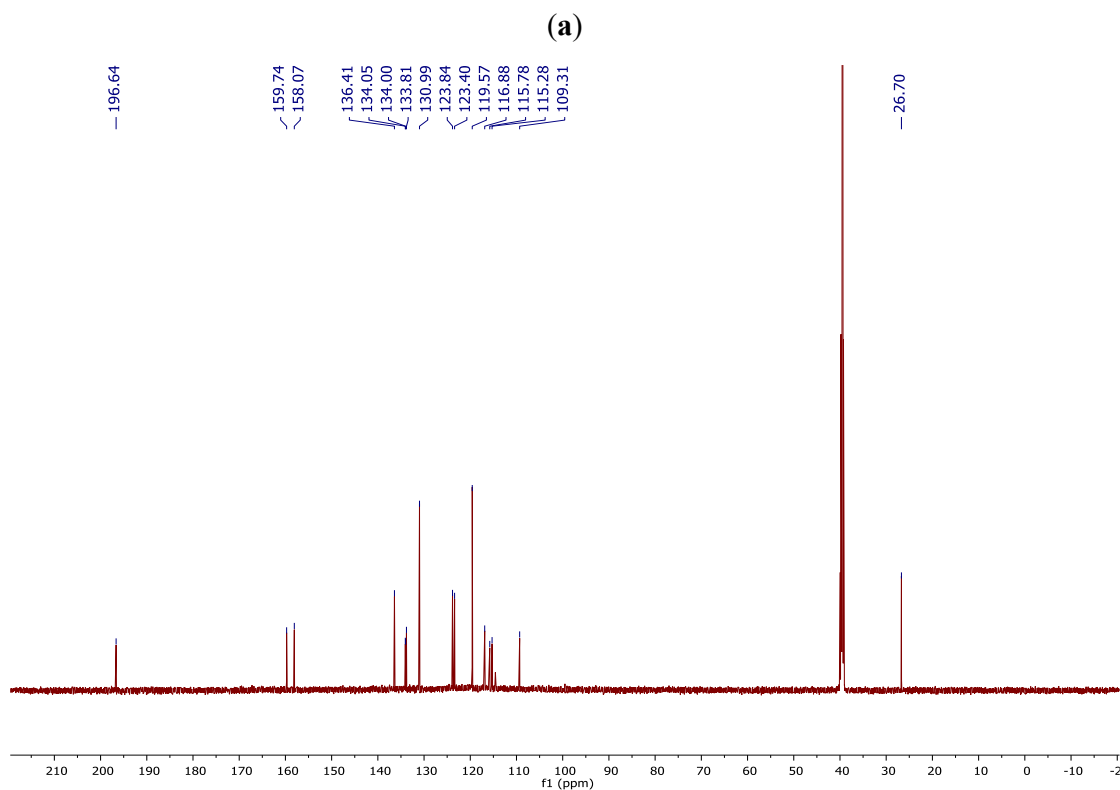
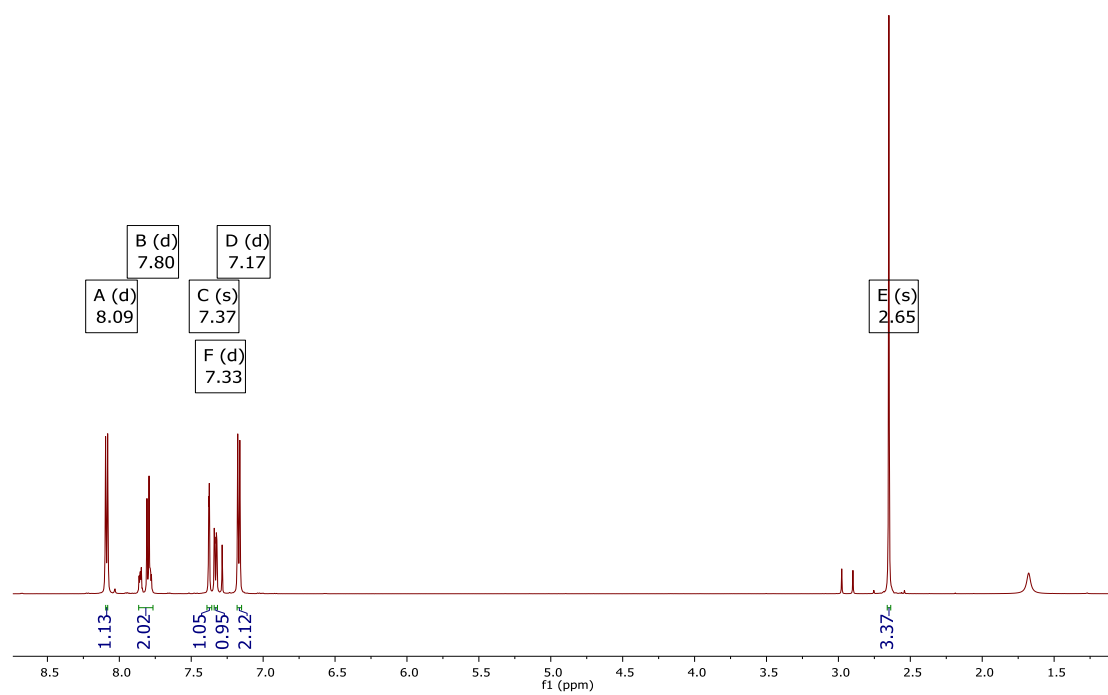


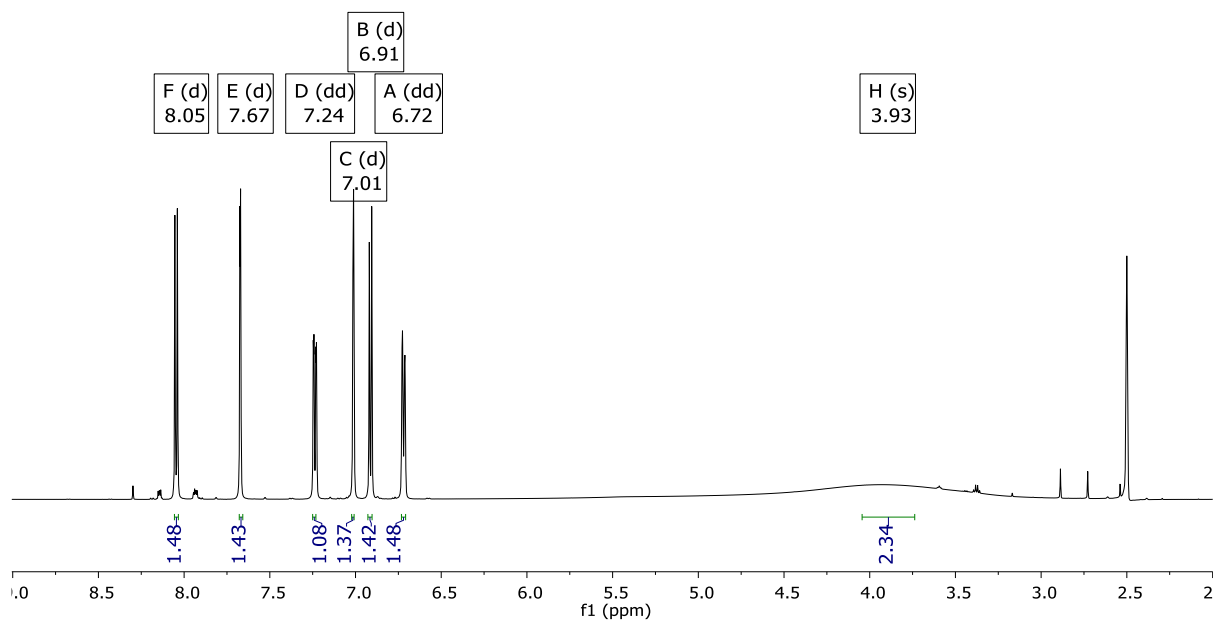
Figure 0 A0: (a, b) ^1H and (c, d) ^{13}C NMR spectra (600 MHz, DMSO-d_6) for **i** and **ii**.

APPENDIX 1 (A1): NMR SPECTRA OF THE STUDIED COMPOUNDS

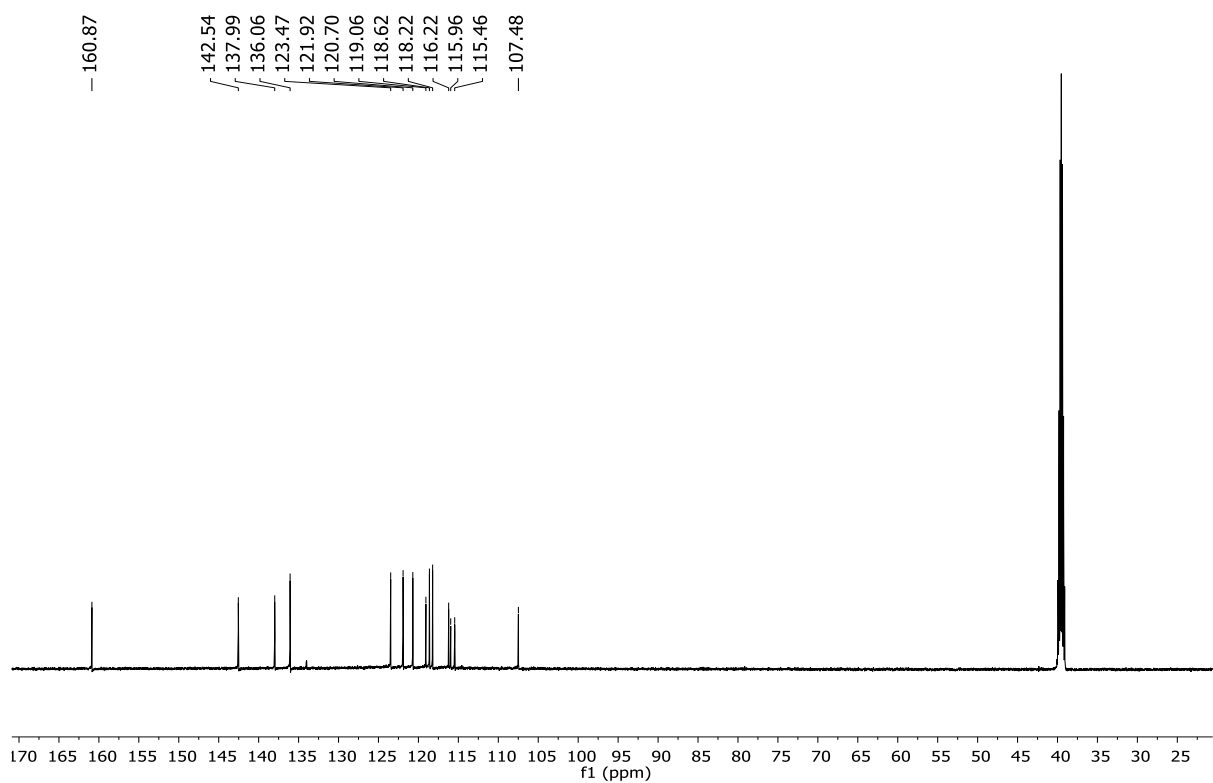


(b)

Figure 1 A1: (a) ^1H and (b) ^{13}C NMR spectra (600 MHz, CDCl_3) for **1**.

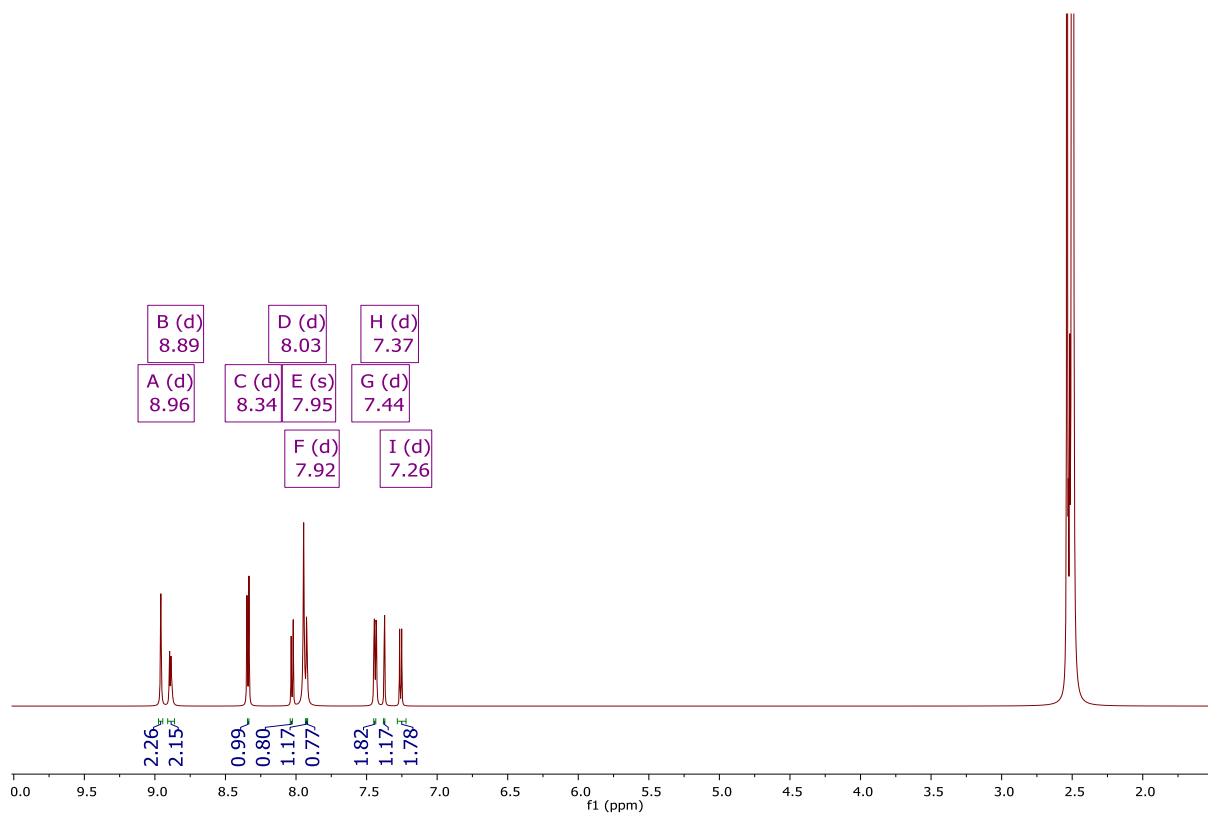


(a)

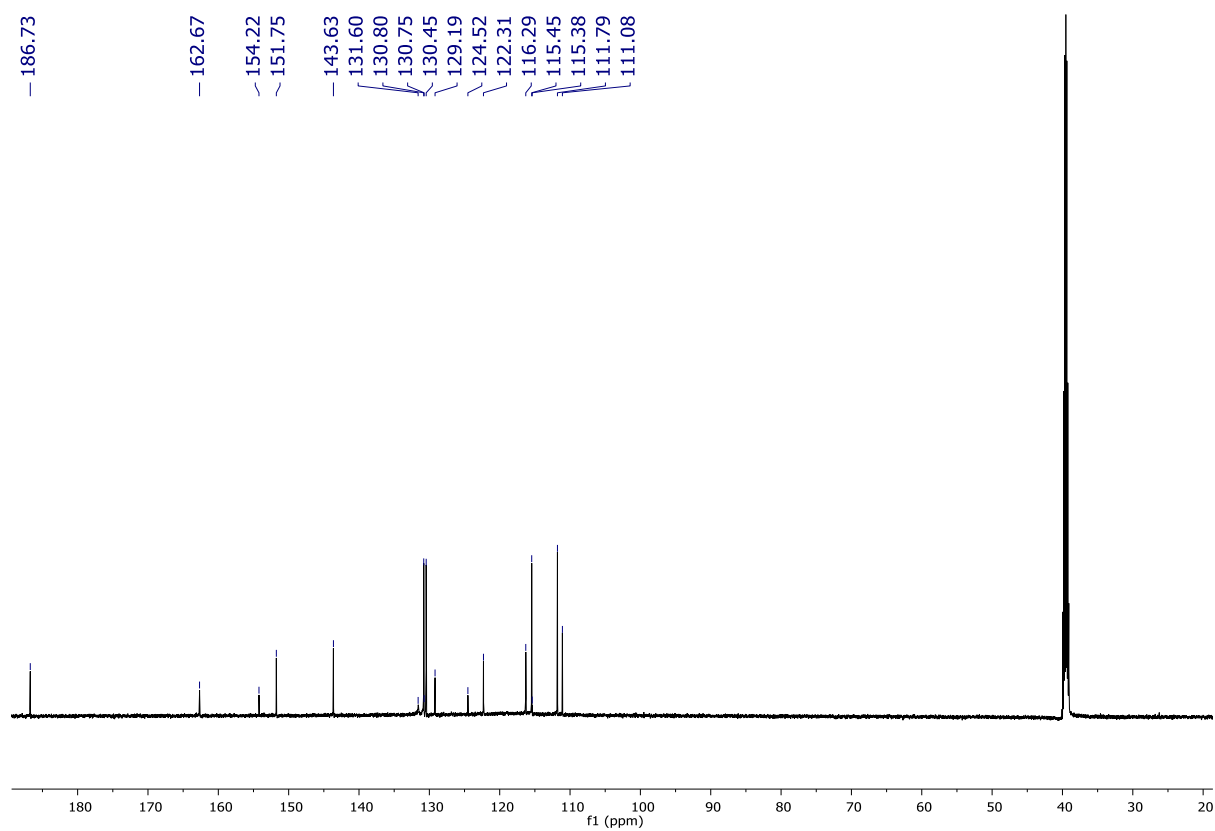


(b)

Figure 2 A1: (a) ¹H and (b) ¹³C NMR spectra (600 MHz, DMSO-d₆) for **2**.

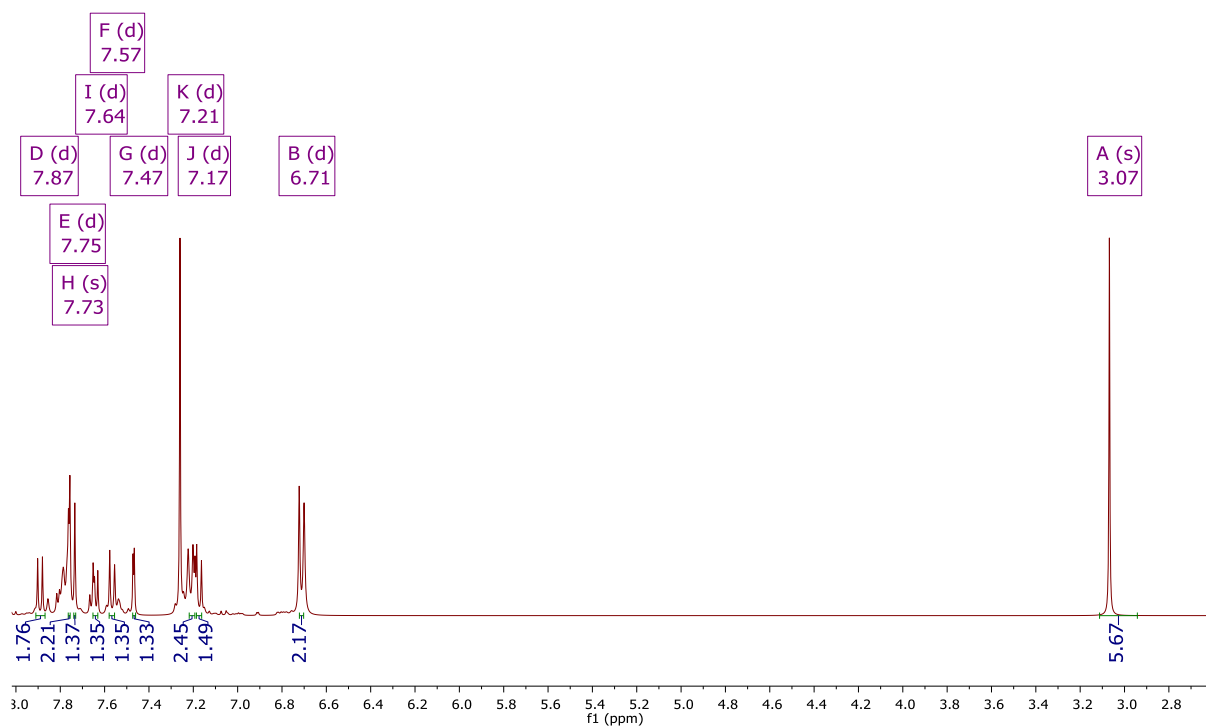


(a)

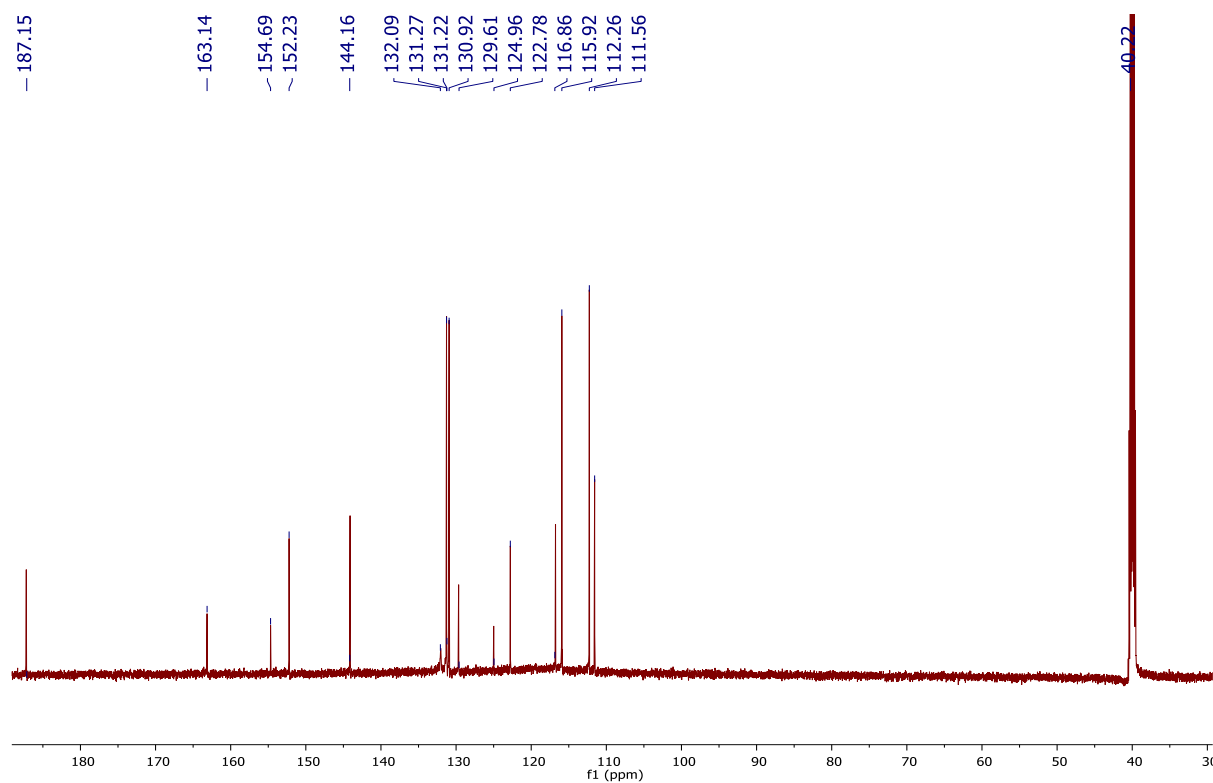


(b)

Figure 3 A1: (a) ^1H and (b) ^{13}C NMR spectra (600 MHz, DMSO-d_6) for **3**.



(a)



(b)

Figure 4 A1: (a) ¹H and (b) ¹³C NMR spectra (600 MHz, CDCl₃ and DMSO-d₆) of **4**.

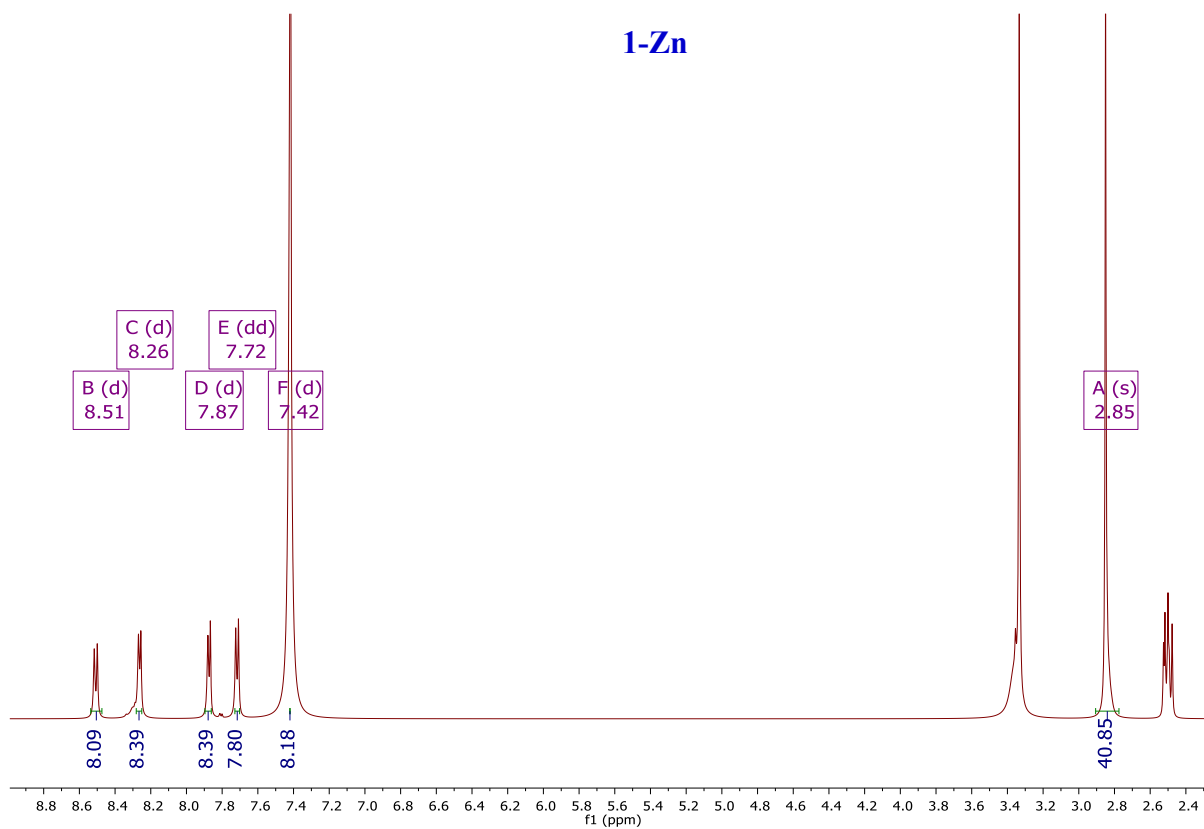


Figure 5 A1: ^1H NMR spectrum (600 MHz, DMSO-d_6) of **1-Zn** used as an example.

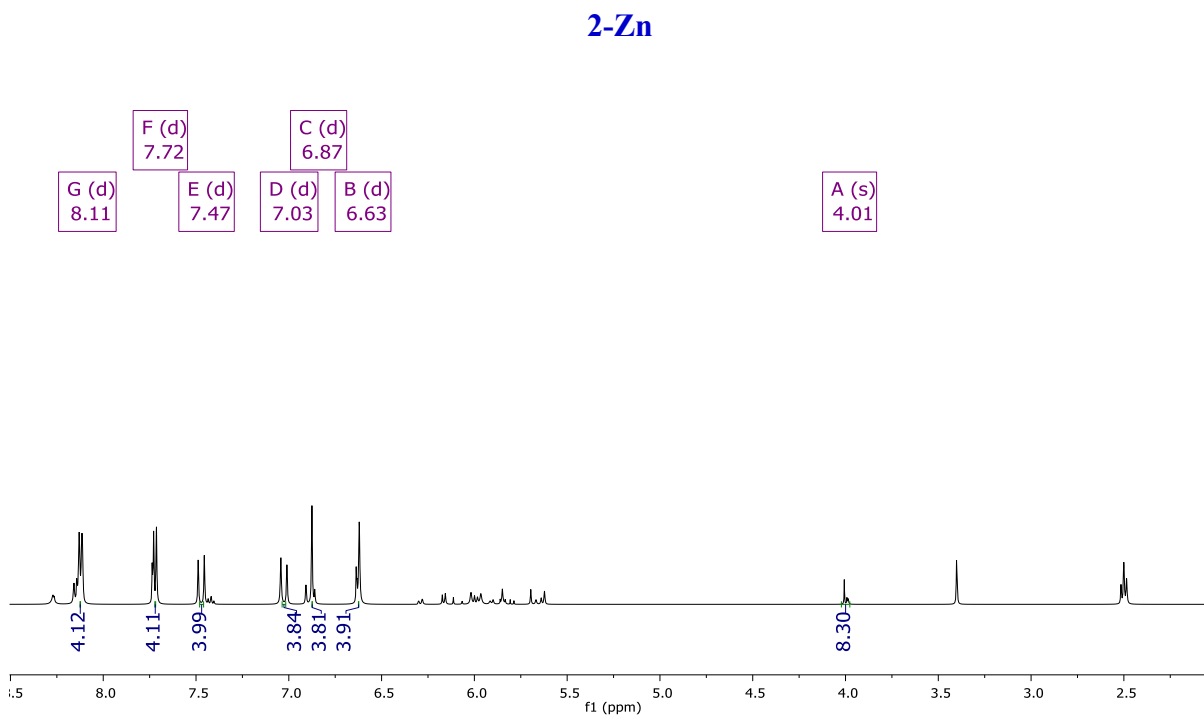
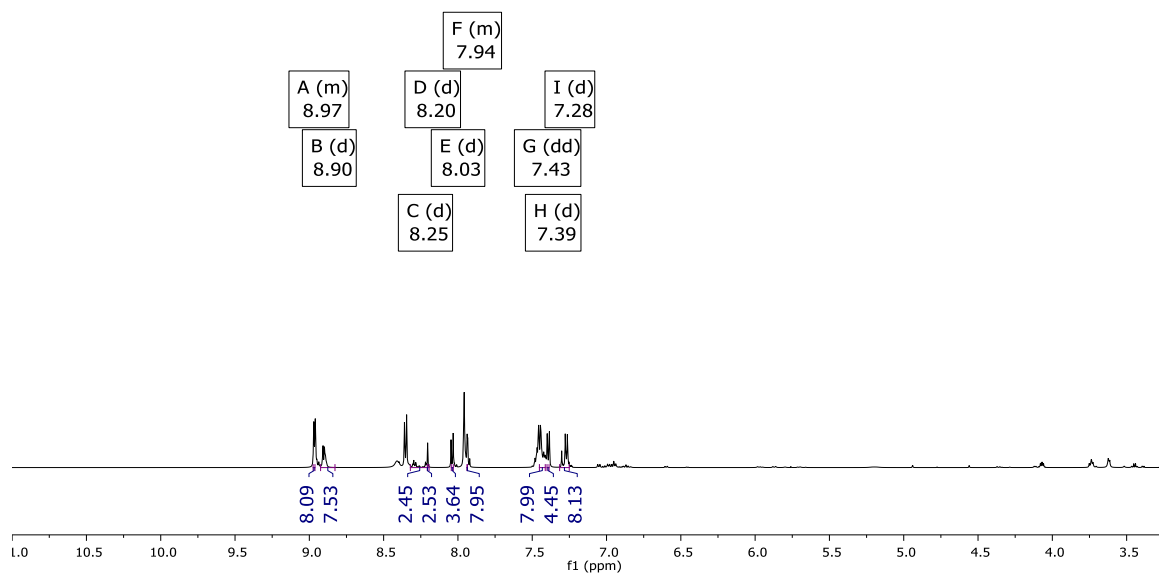


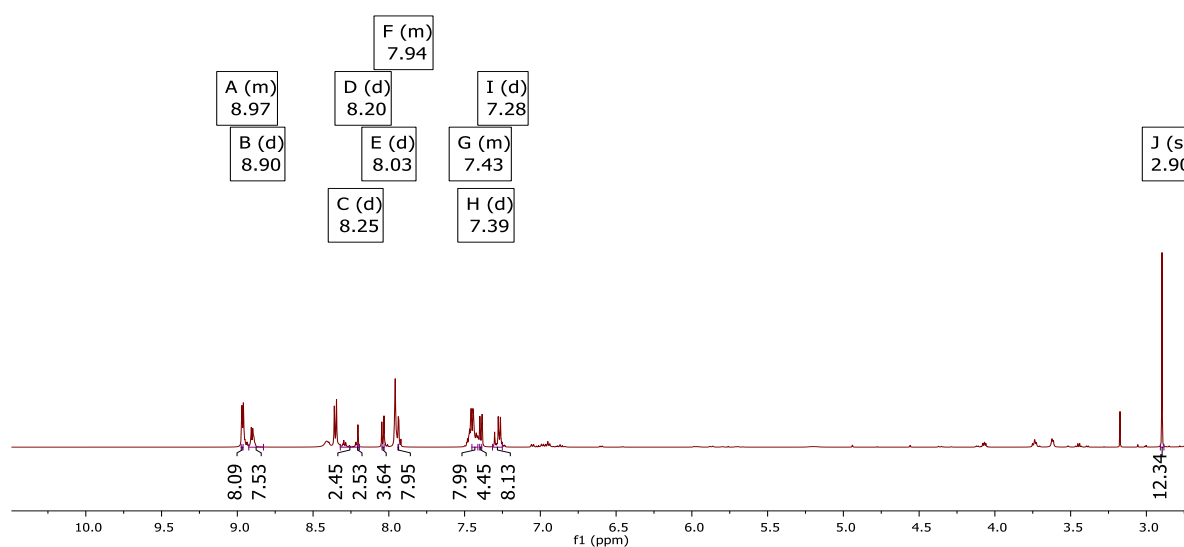
Figure 6 A1: ^1H NMR spectrum (600 MHz, DMSO-d_6) of **2-Zn** used as example.

3-In



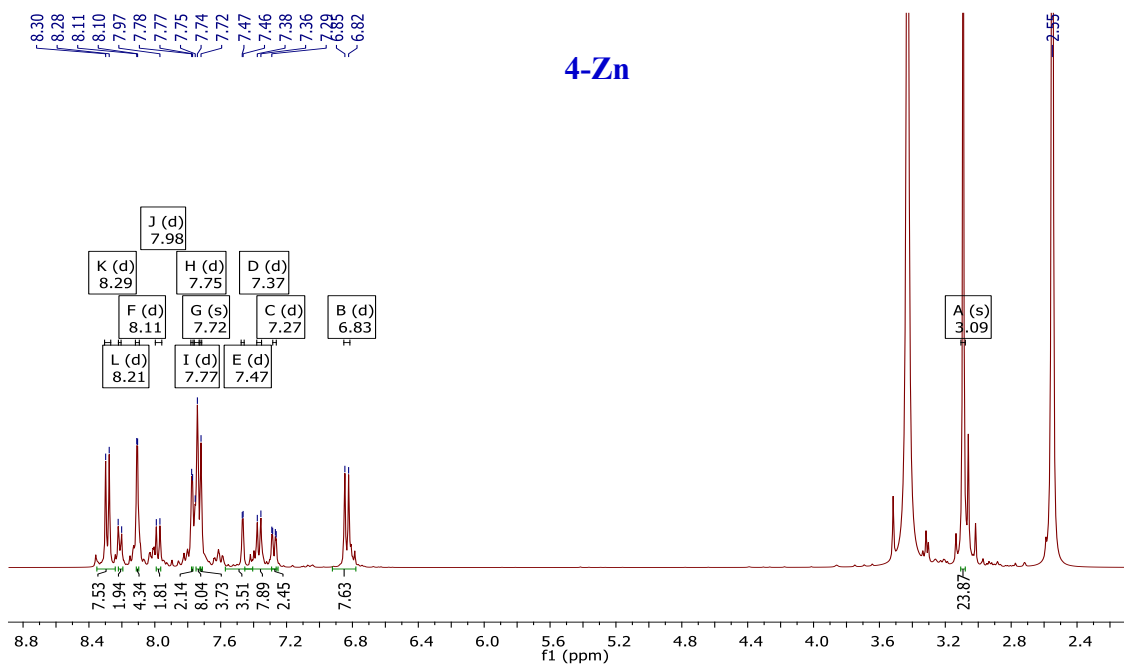
(a)

3-InQ

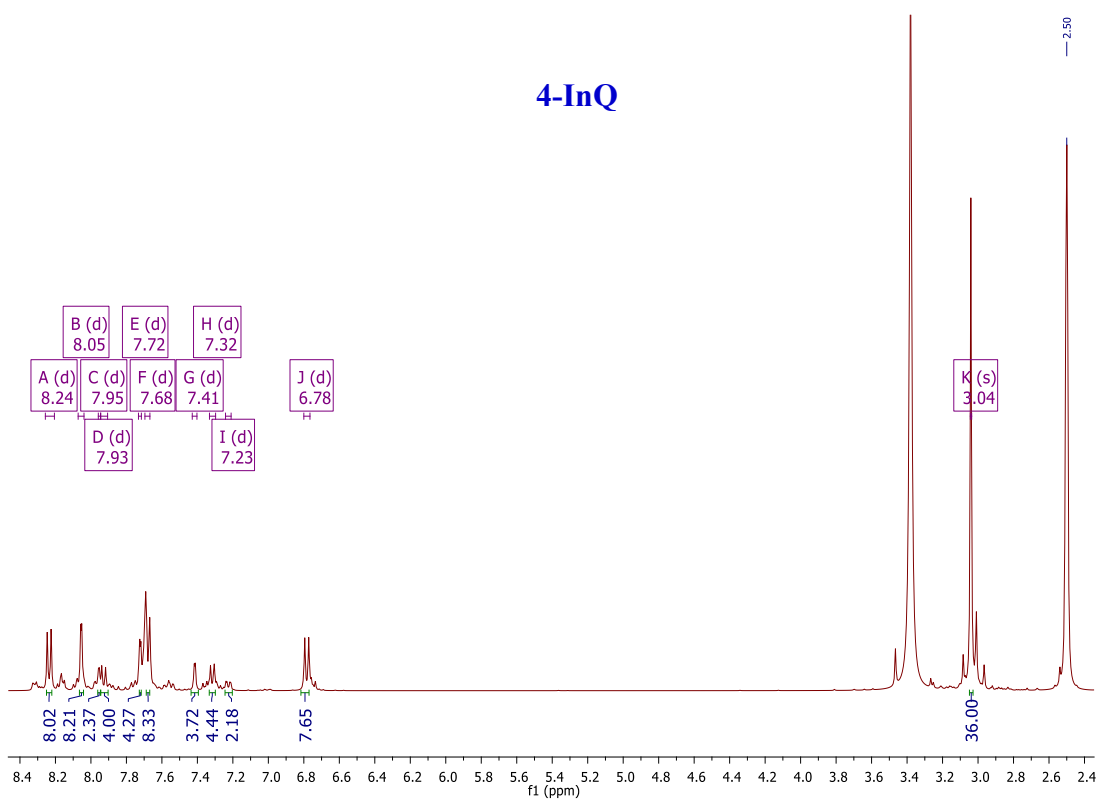


(b)

Figure 7 A1: ^1H NMR spectra (600 MHz, DMSO-d_6) of (a) **3-In** and (b) **3-InQ** used as examples.



(a)



(b)

Figure 8 A1: ^1H NMR spectra (600 MHz, DMSO-d_6) of (a) **4-Zn** and (b) **4-InQ** used as examples.

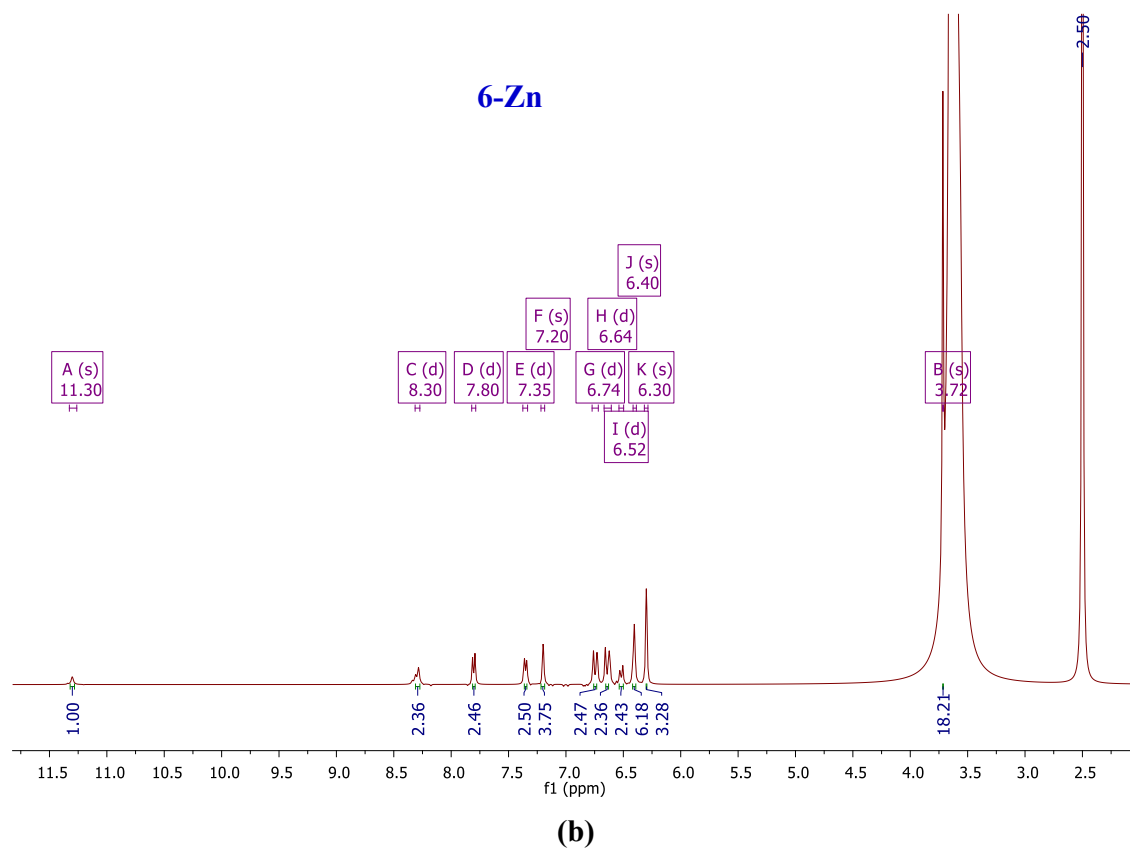
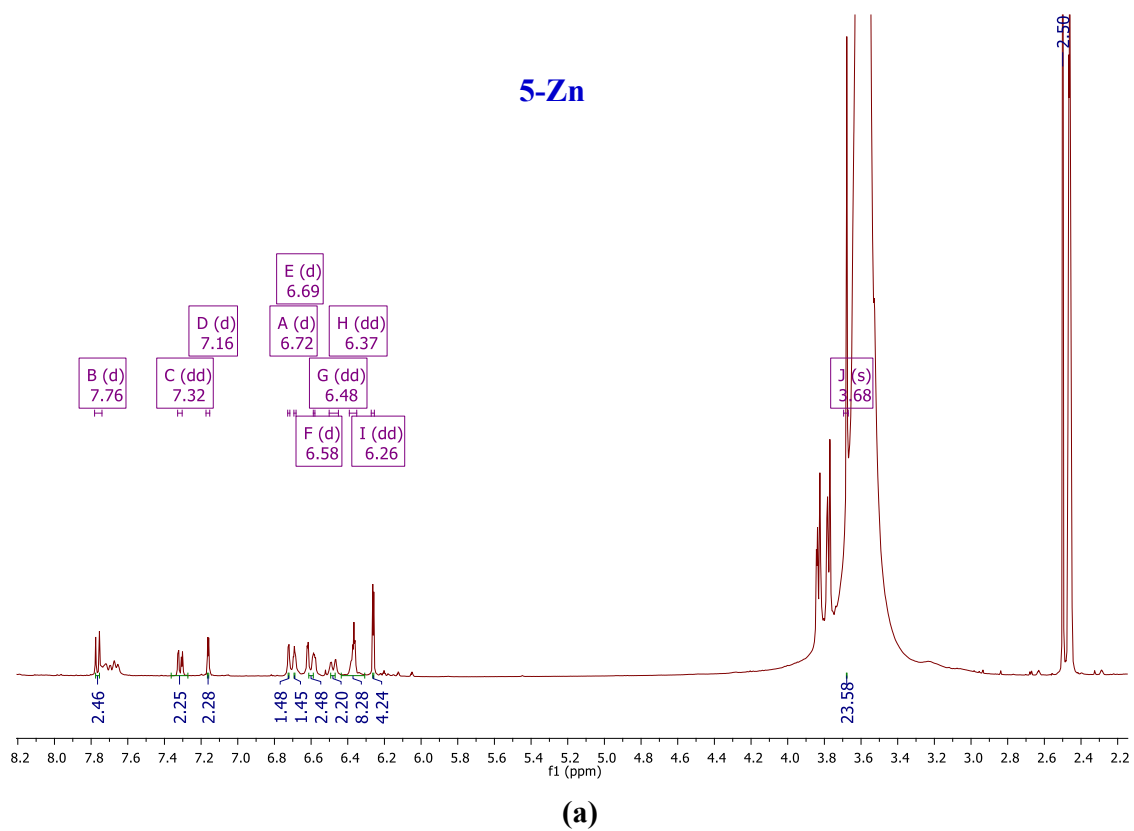
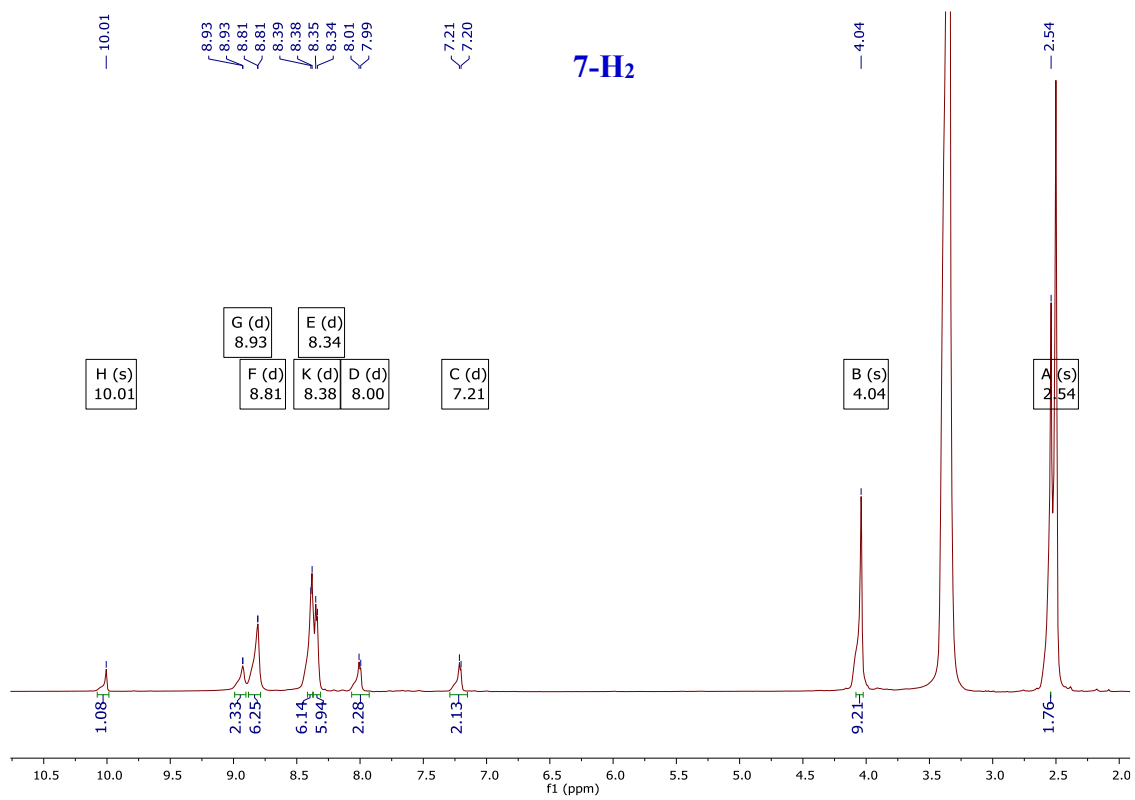
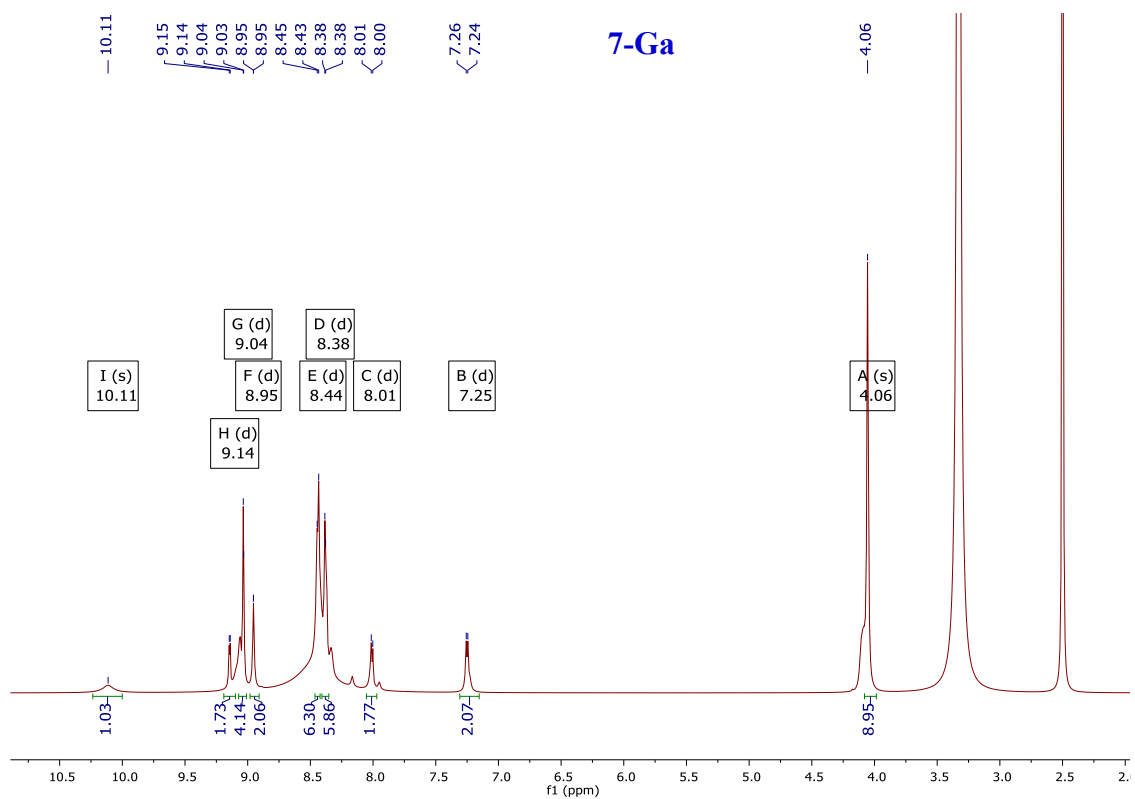


Figure 9 A1: ^1H NMR spectra (600 MHz, DMSO-d_6) of Pcs (a) **5-Zn** and (b) **6-Zn**.



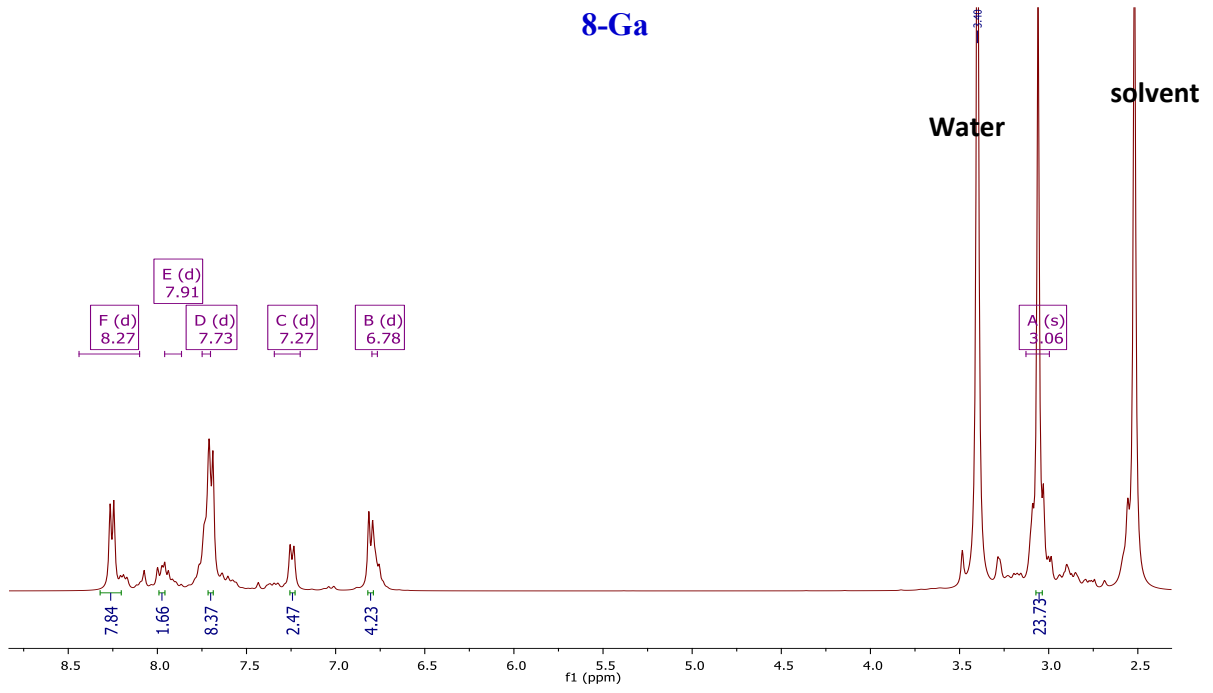
(a)



(b)

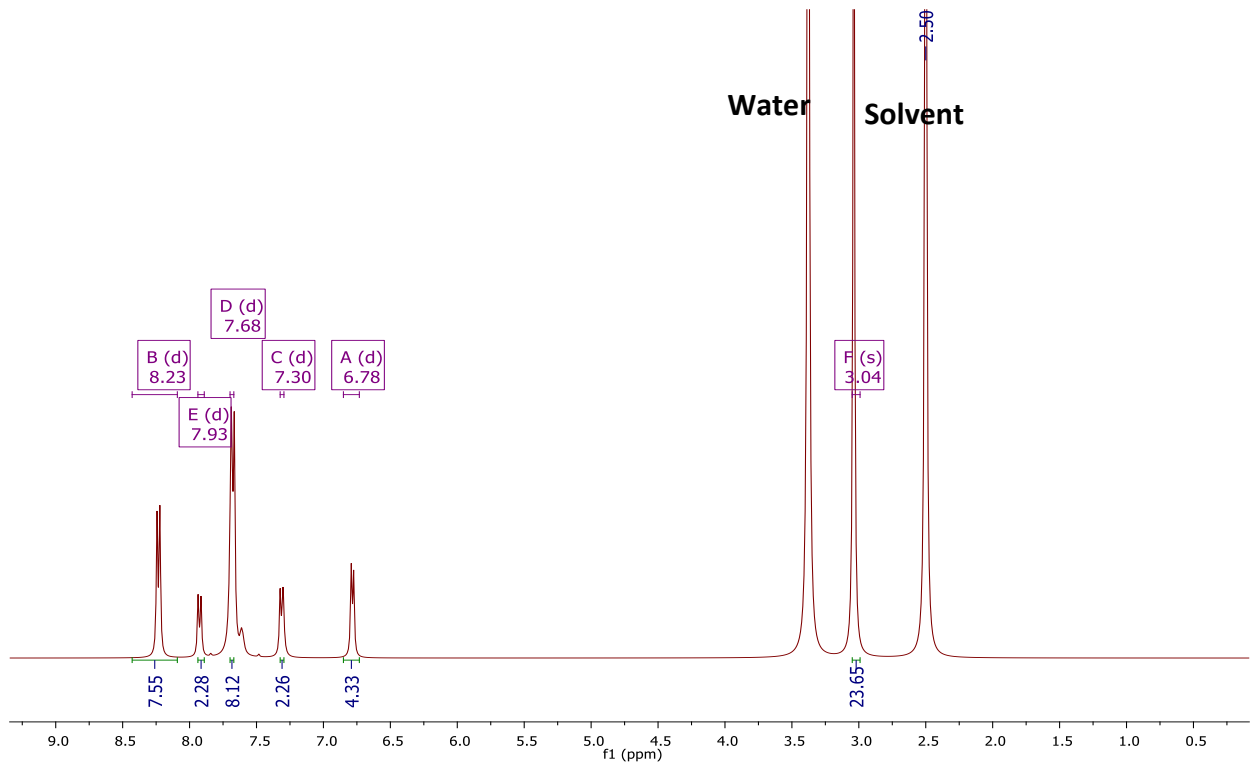
Figure 10 A1: ¹H NMR spectra (600 MHz, DMSO-d₆) of **7-H₂** and **7-Ga** used as examples.

8-Ga

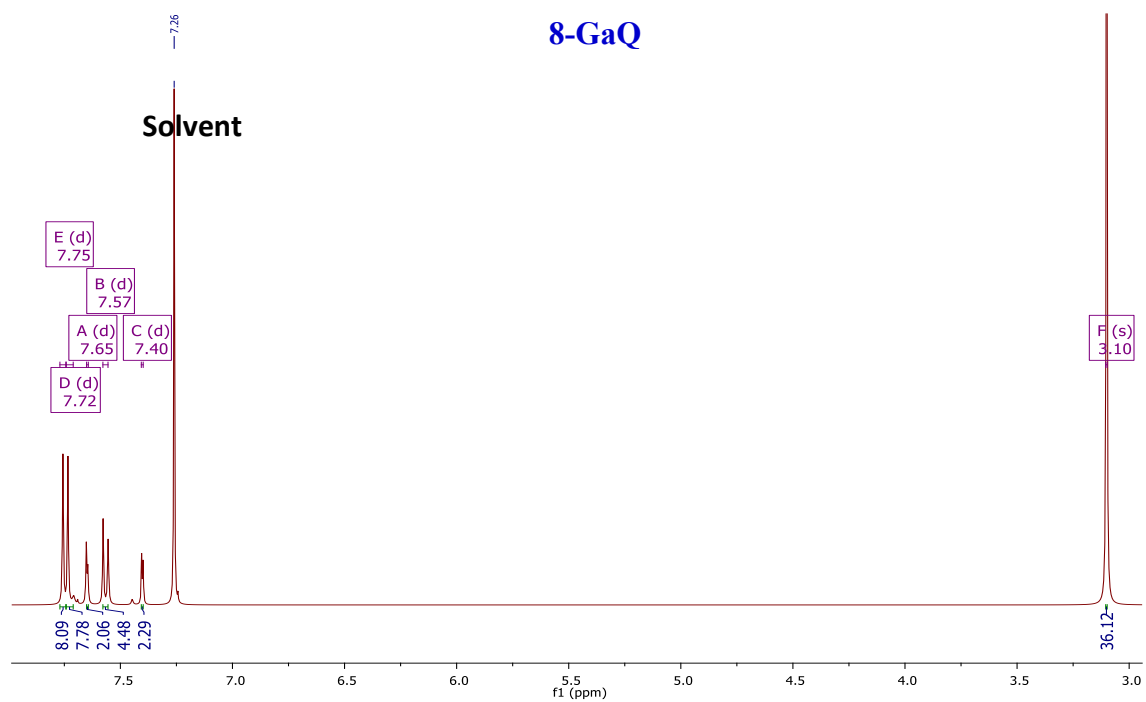


(a)

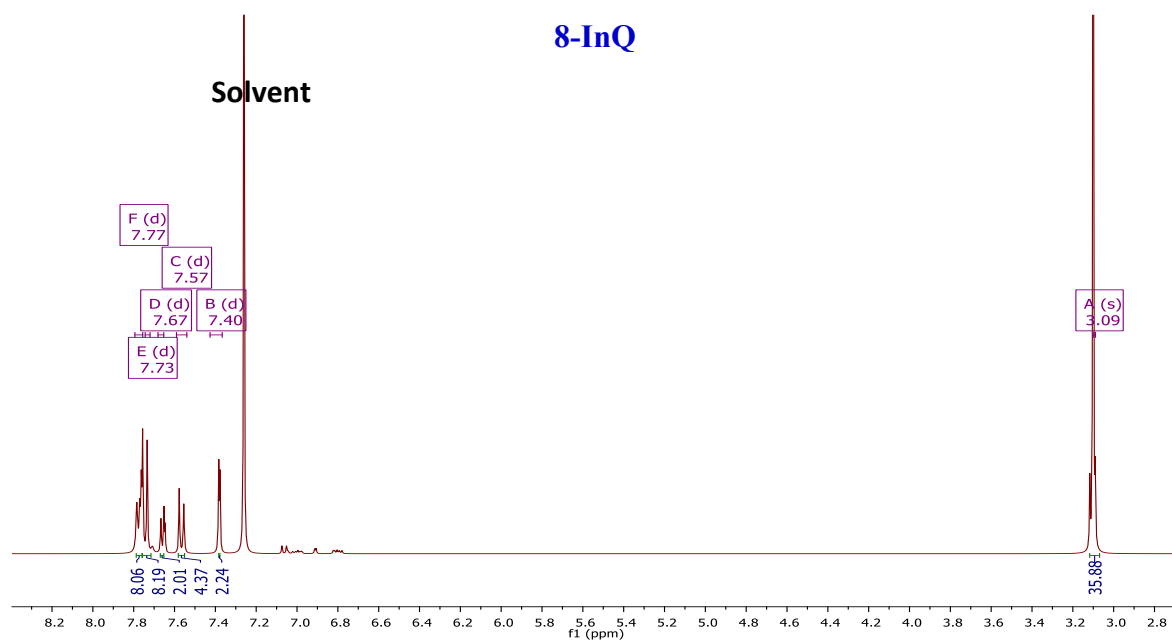
8-In



(b)



(c)



(d)

Figure 11 A1: ^1H NMR spectra (600 MHz, DMSO-d_6 and CDCl_3) of (a) **8-Ga**, (b) **8-In**, (c) **8-GaQ**, and (d) **8-InQ**.

APPENDIX 2 (A2): MASS SPECTRA OF THE STUDIED COMPOUNDS

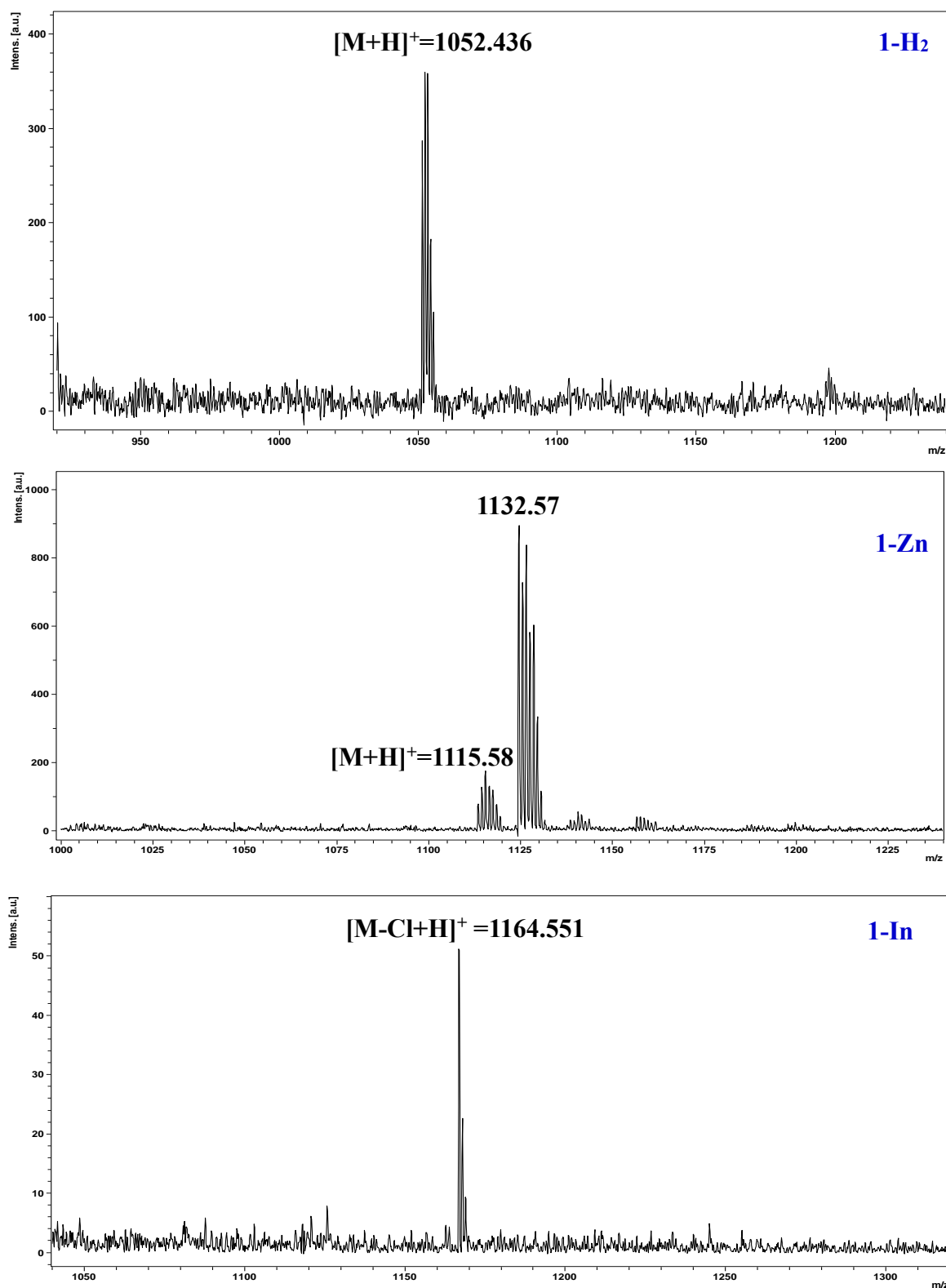


Figure 1 A2: Mass spectra of phthalocyanines **1-H₂**, **1-Zn** and **1-In**.

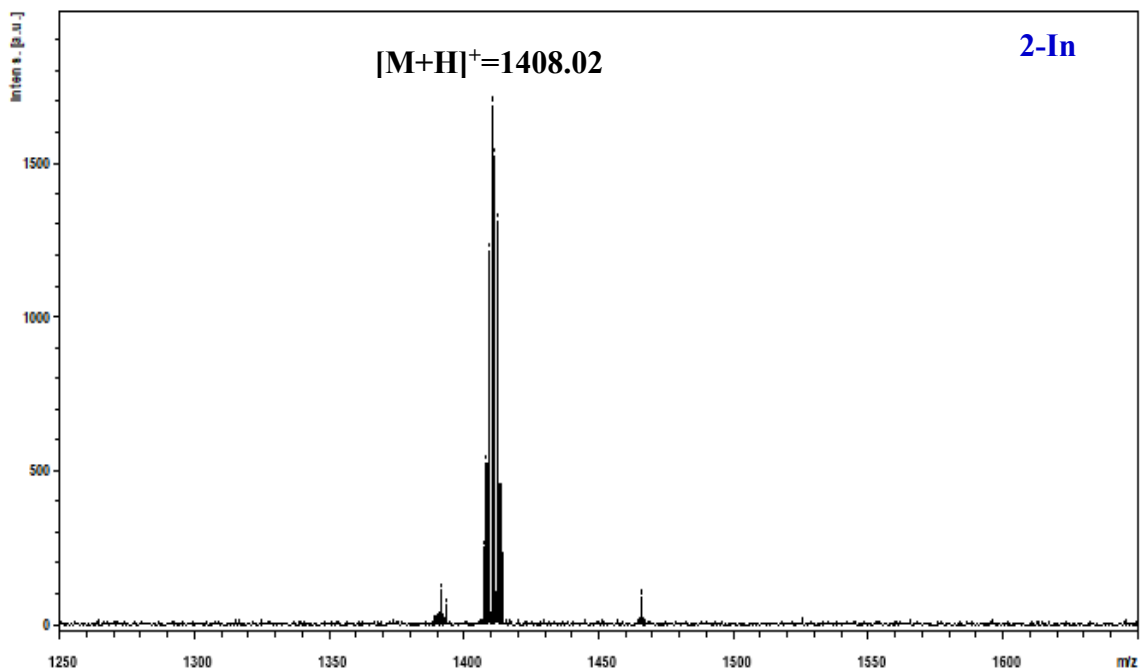
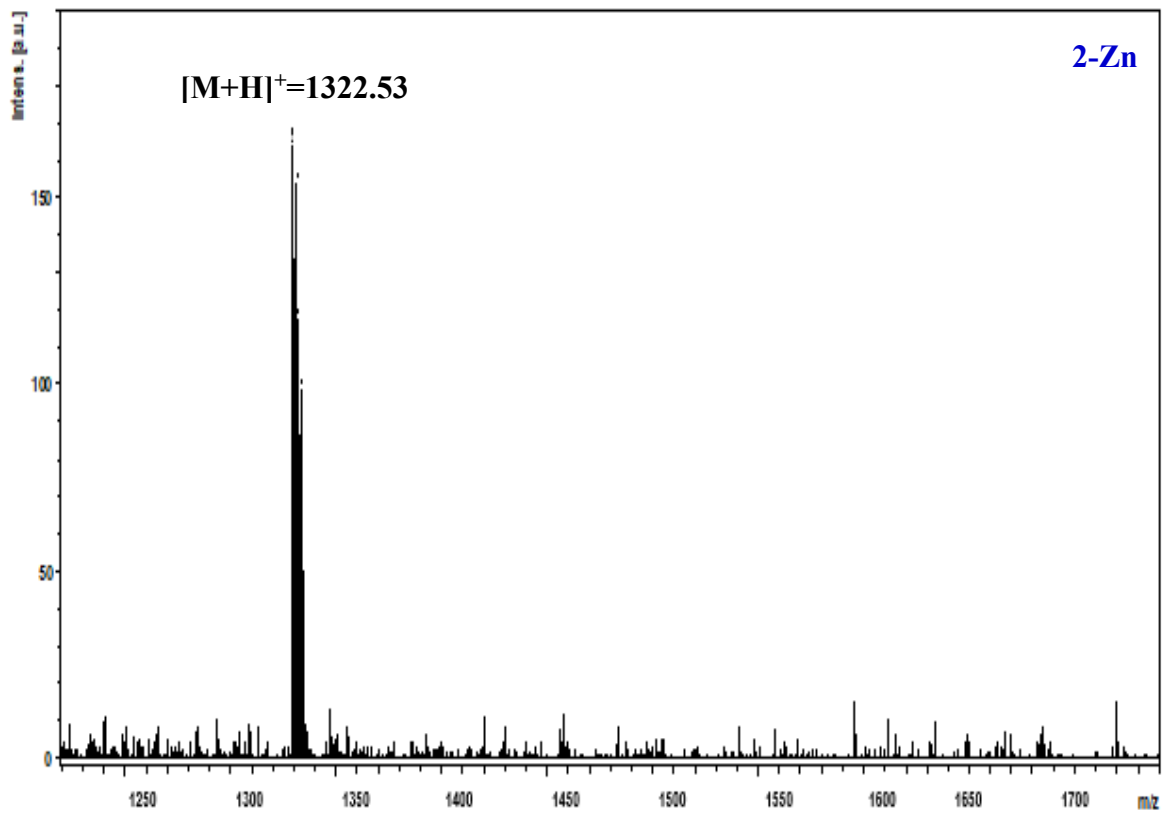


Figure 2 A2: Mass spectra of phthalocyanines **2-Zn** and **2-In**.

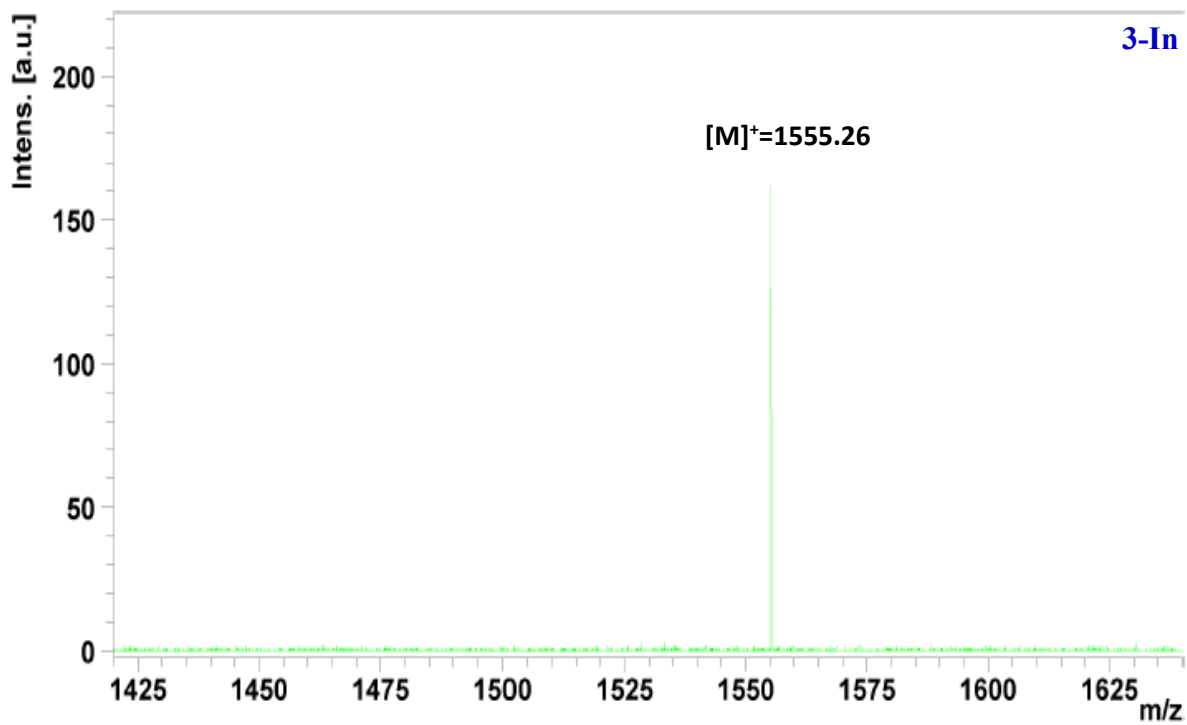
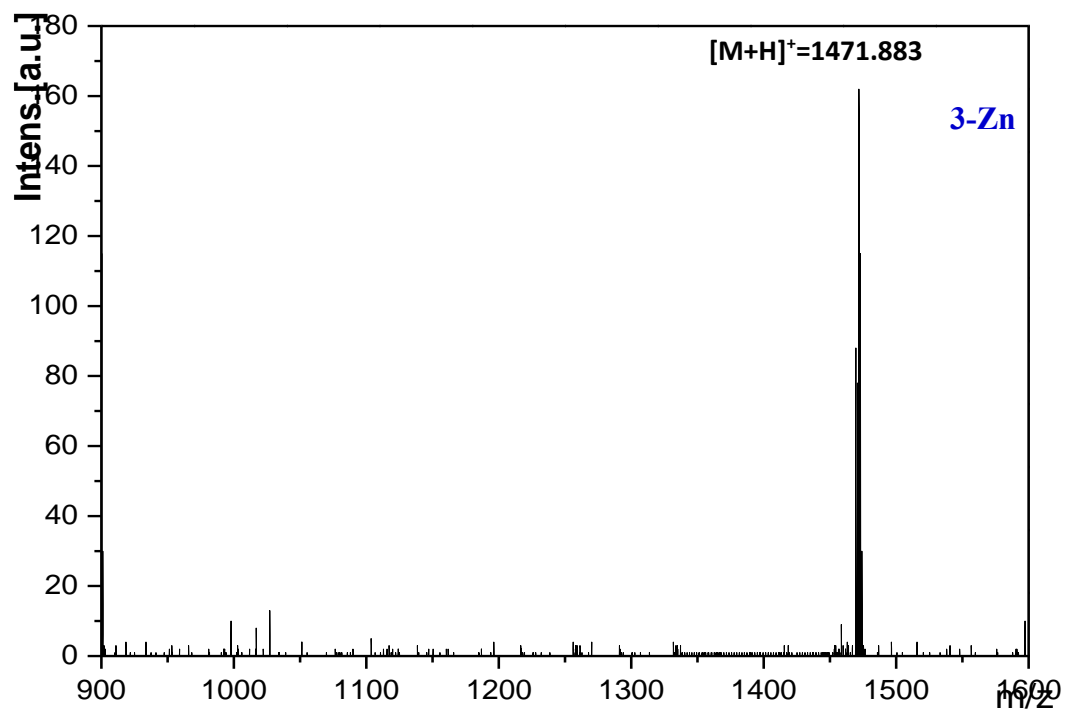


Figure 3 A2: Mass spectra of phthalocyanines **3-Zn** and **3-In**.

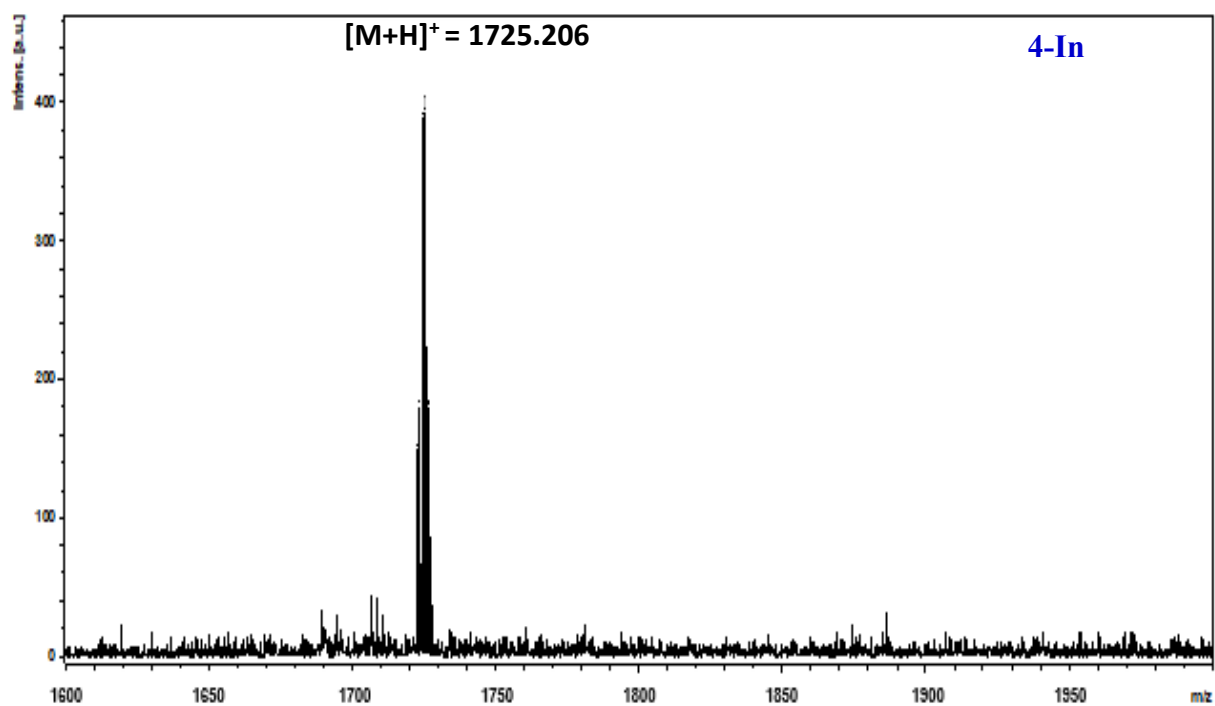
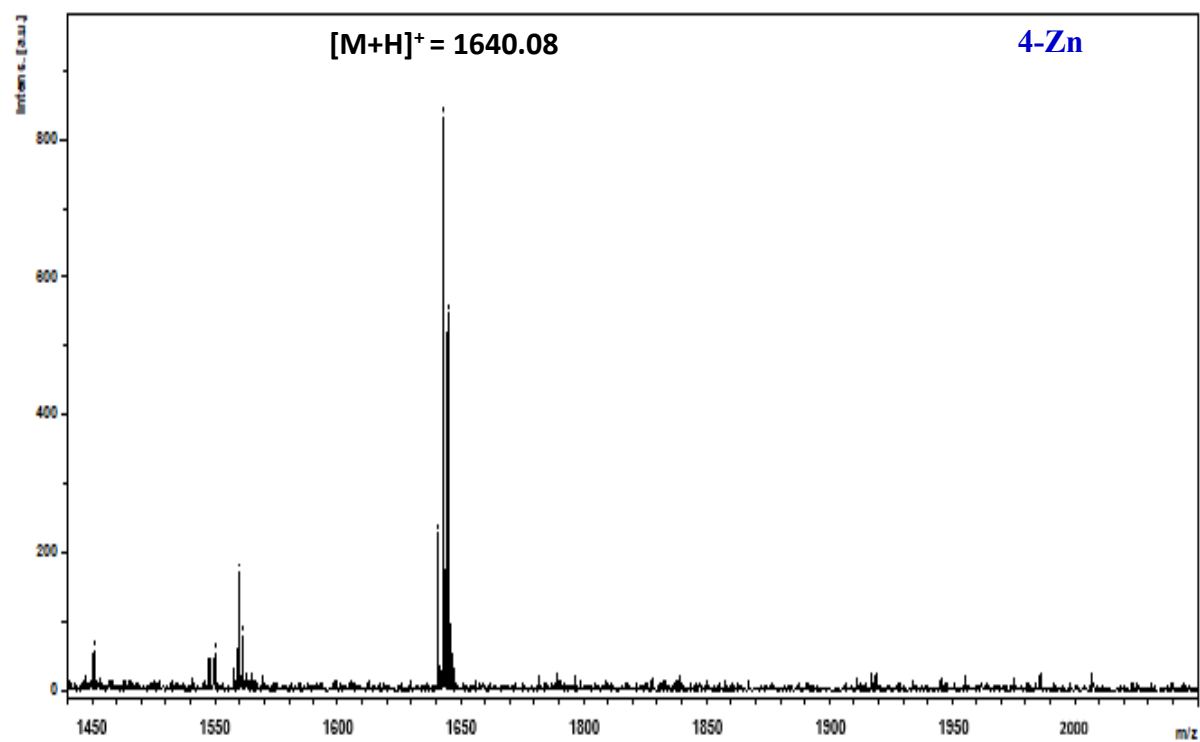


Figure 4 A2: Mass spectra of phthalocyanines **4-Zn** and **4-In**.

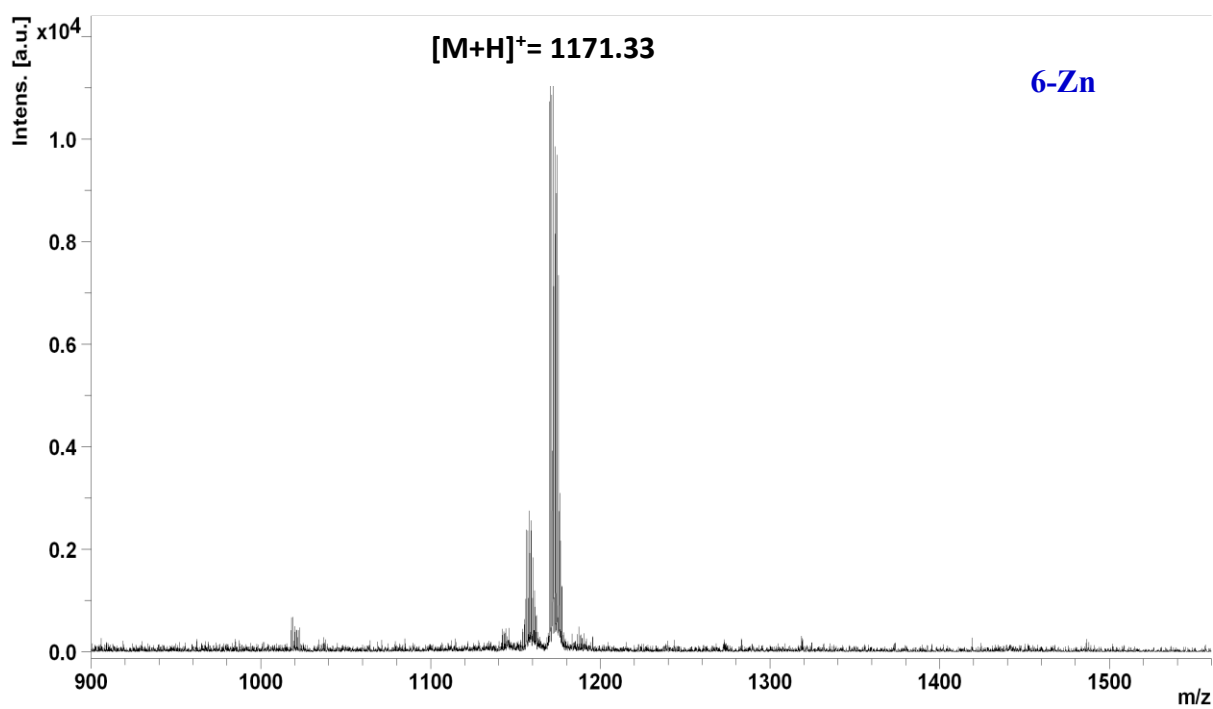
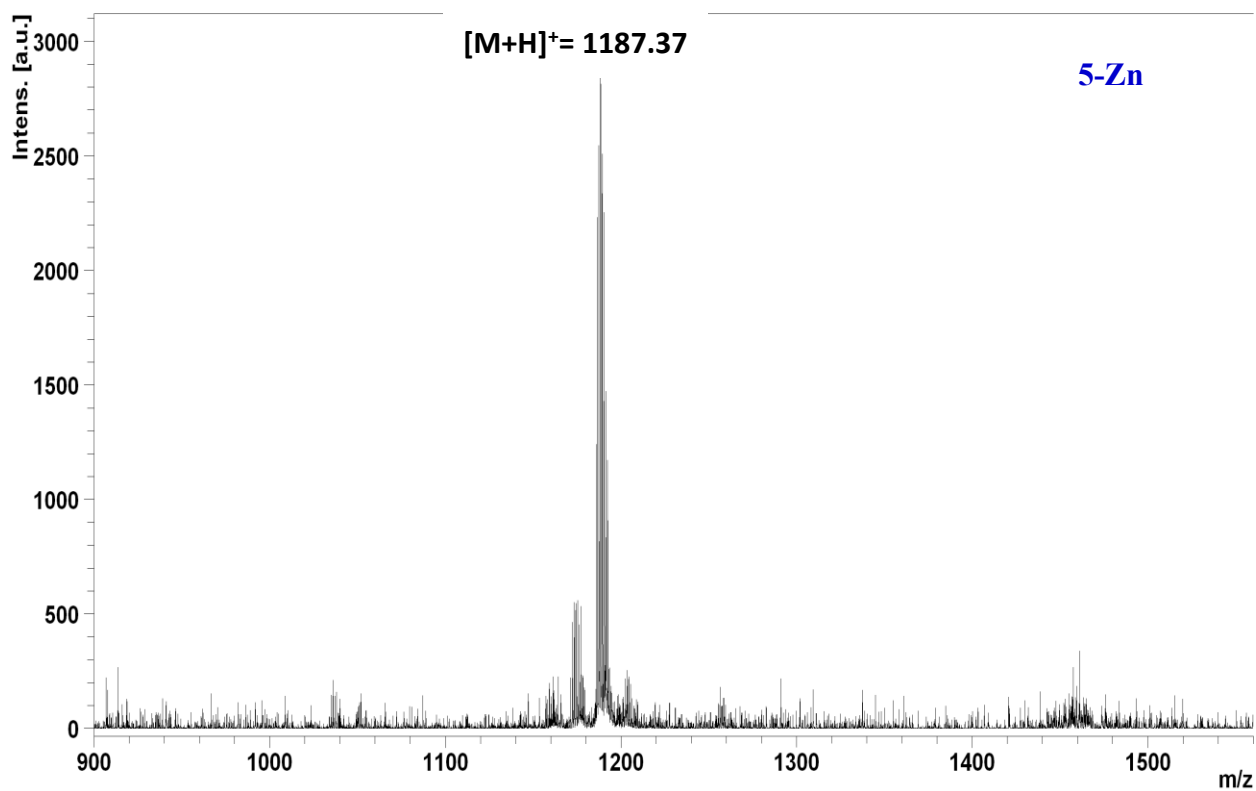
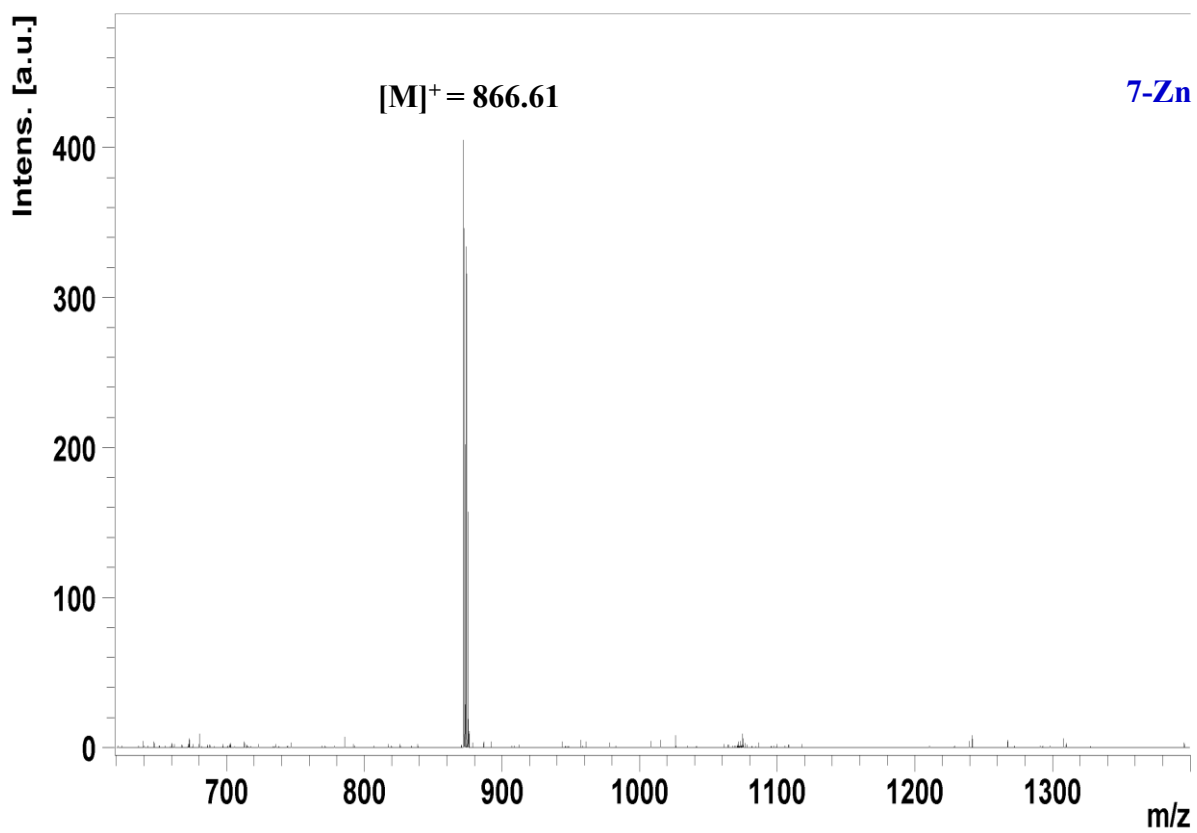
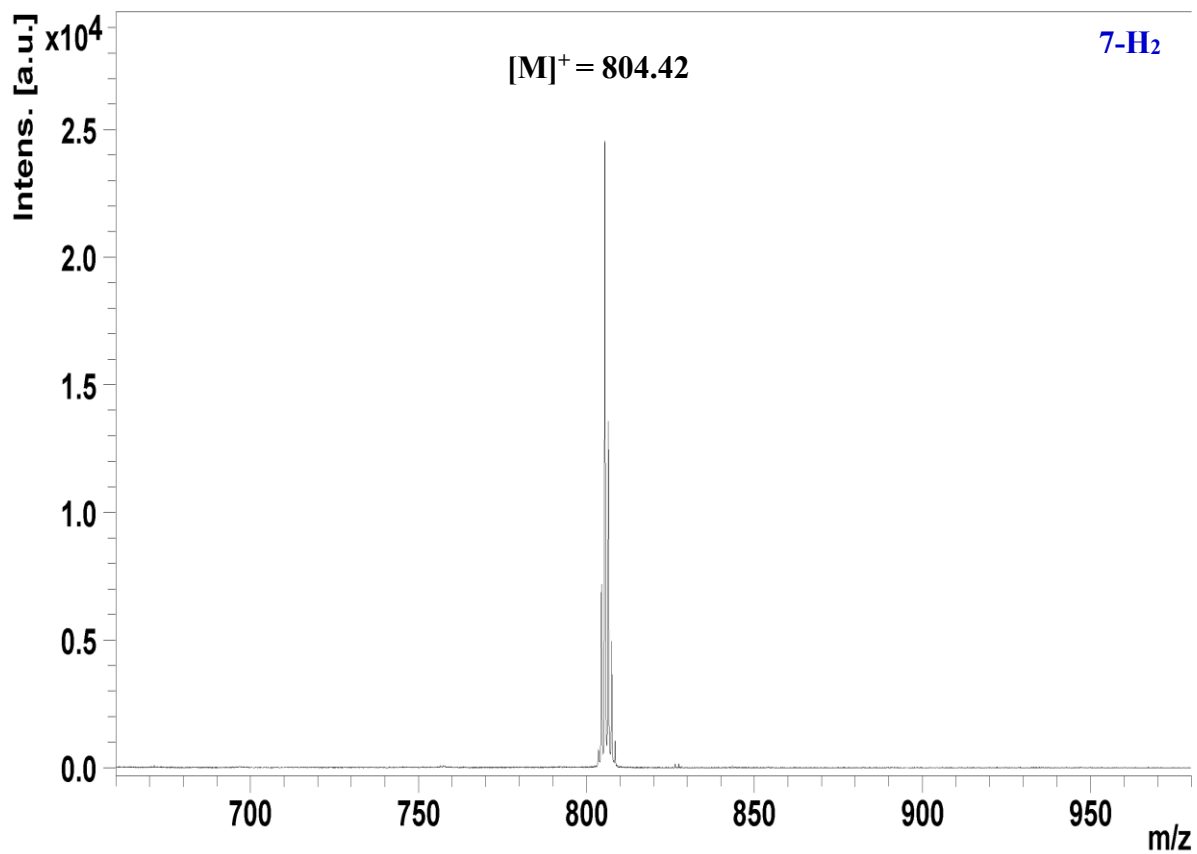


Figure 5 A2: Mass spectra of phthalocyanines **5-Zn** and **6-In**.



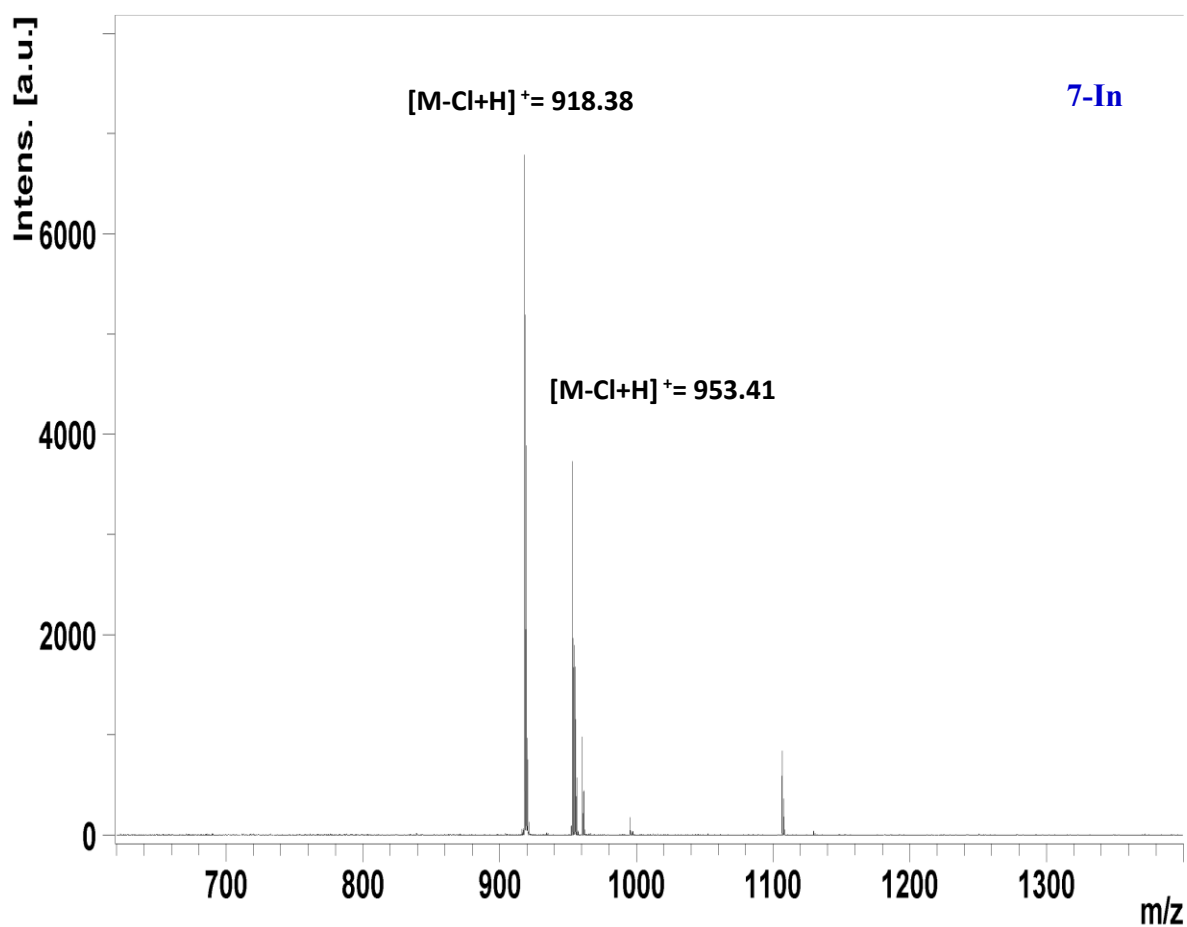
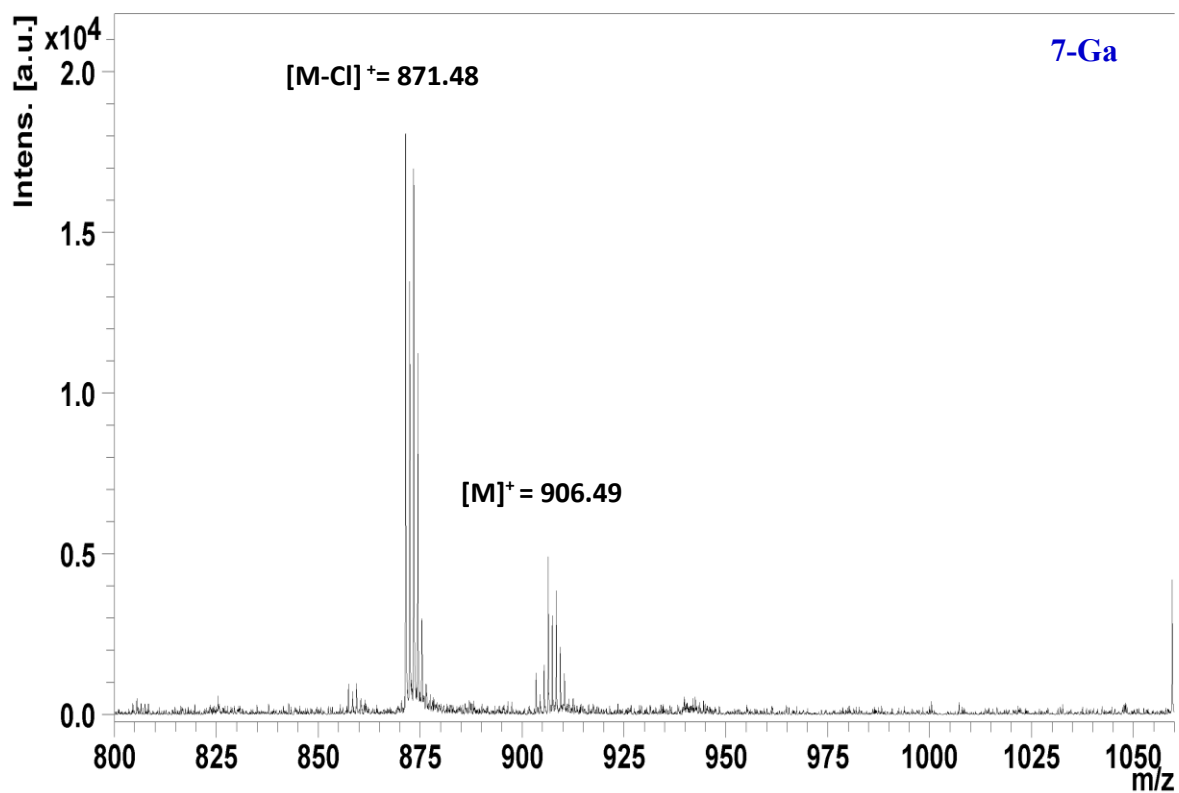


Figure 6 A2: Mass spectra of porphyrins **7-H₂**, **7-Zn**, **7-Ga** and **7-In**.

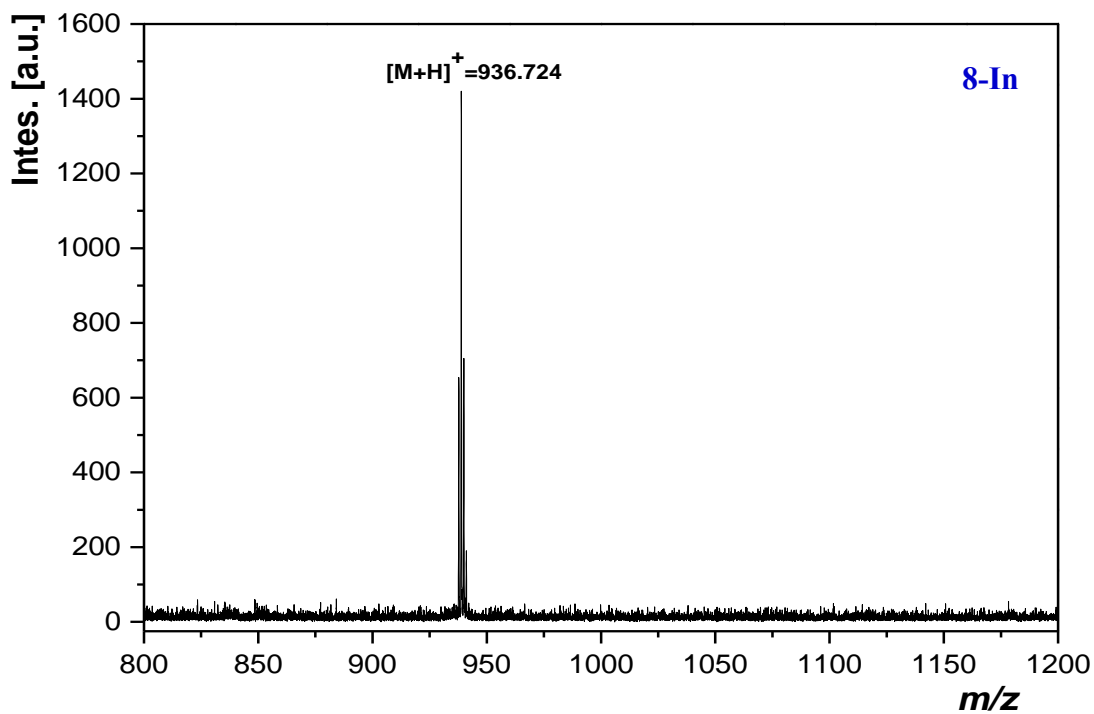
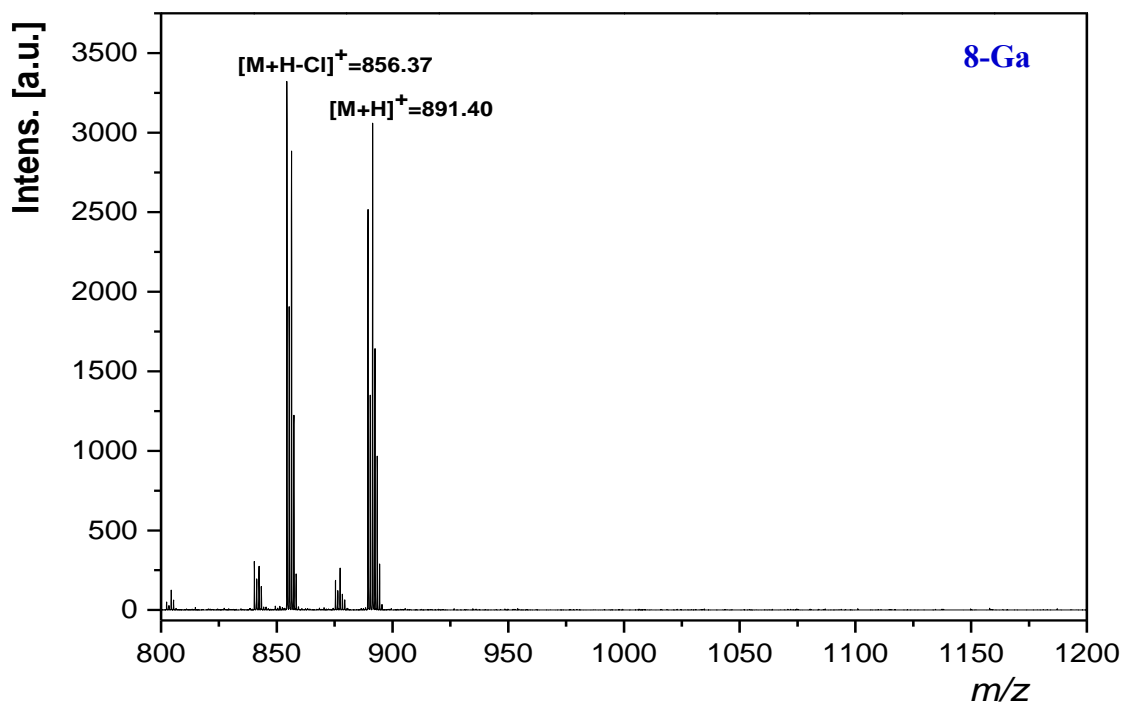


Figure 7 A2: Mass spectra of porphyrins **8-Ga** and **8-In**.

APPENDIX 3 (A3): ABSORPTION AND EMISSION SPECTRA

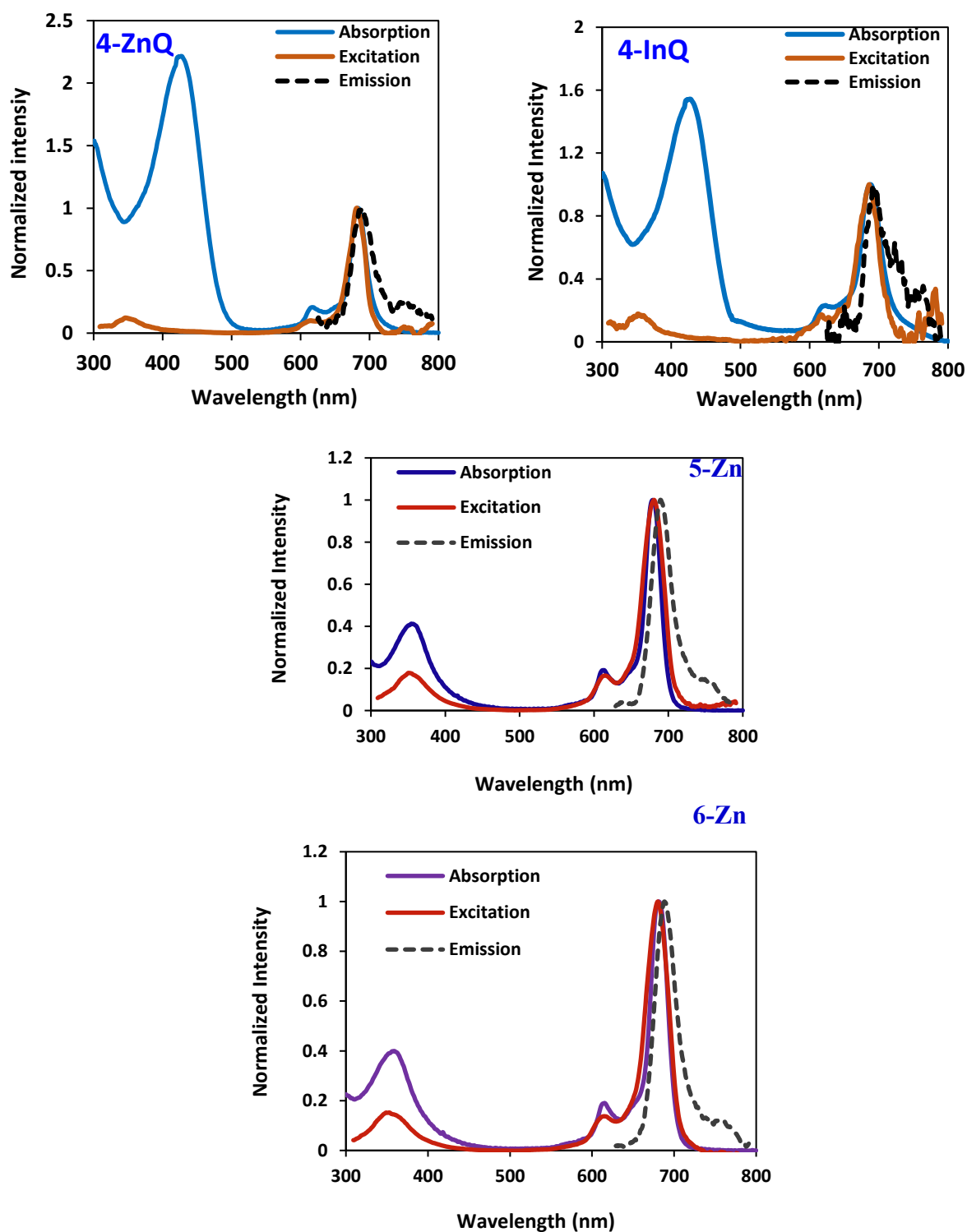
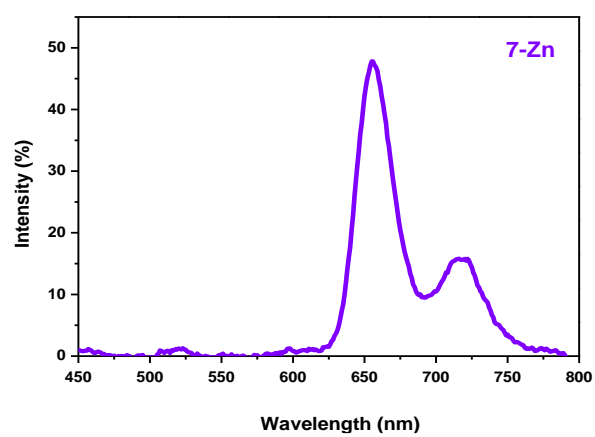
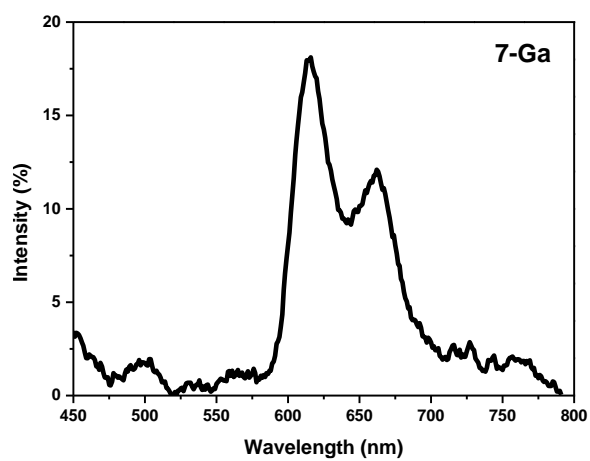


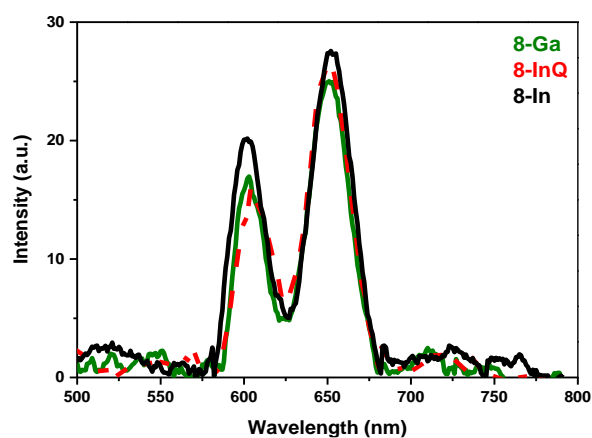
Figure 1 A3: Normalized absorption, excitation, and emission spectra of some Pcs in DMSO, λ_{exc} at 606 nm for **4-ZnQ** and **4-InQ**, λ_{exc} at 610 nm for **5-Zn** and **6-Zn**.



(a)



(b)



(c)

Figure 2 A3: Emission spectra in DMSO of (a) **7-Zn**, (b) **7-Ga**, and (c) **8-Ga**, **8-In** and **8-InQ** as exemplification.

APPENDIX 4 (A4): SPECTRA FOR NANOCONJUGATES

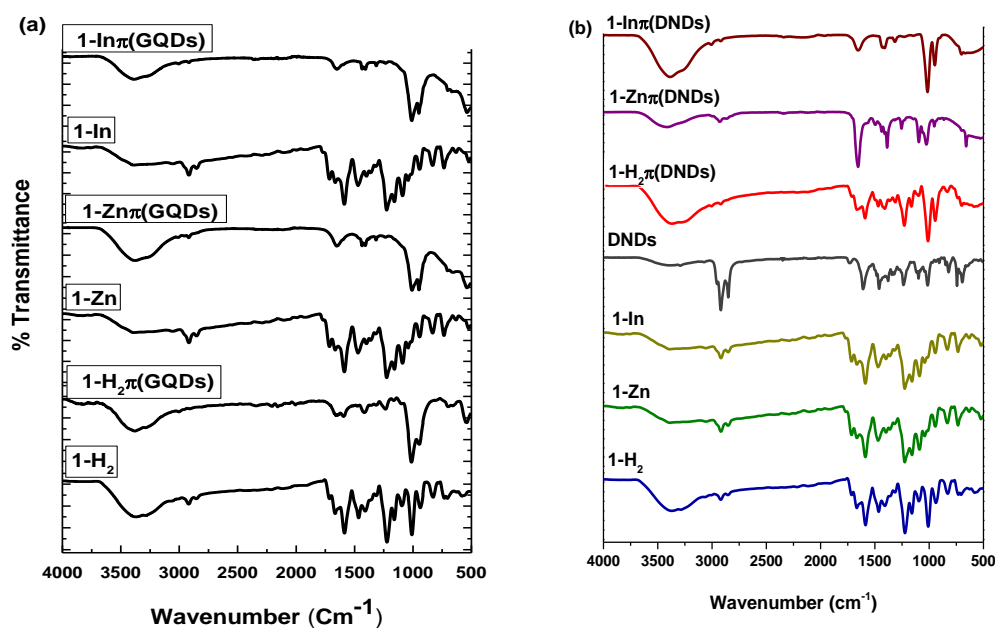


Figure 1 A4: FT-IR spectra of **Group 1** (a) GQDs (b) DNDs nanoconjugates.

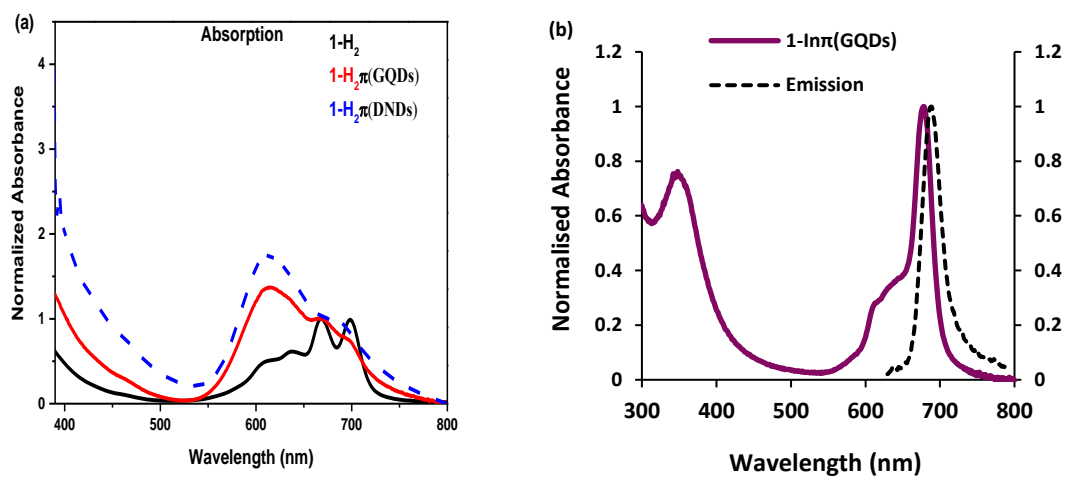


Figure 2 A4: (a) UV-Vis and Emission spectra of **Group 1**/GQDs and DNDs nanoconjugates in DMSO.

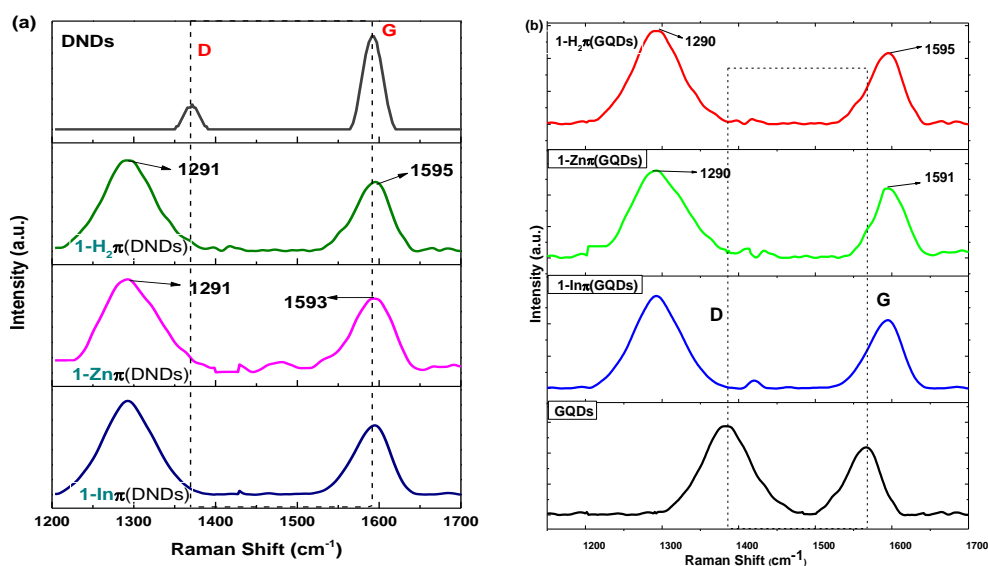


Figure 3 A4: UV-Vis and Emission spectra of **Group 1** (a) DNDs and (b) GQDs nanoconjugates.

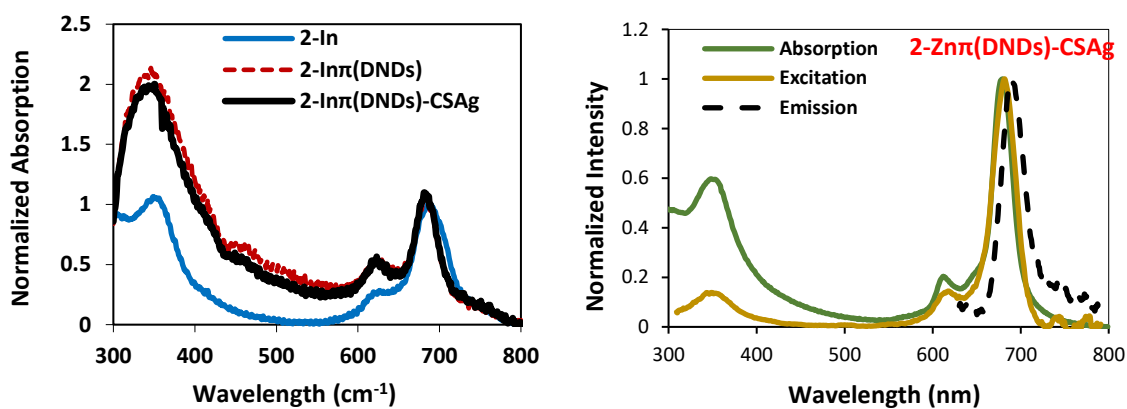


Figure 4 A4: UV-Vis and Emission spectra of **Group 2** DNDs and DNDs-CSAg nanoconjugates.

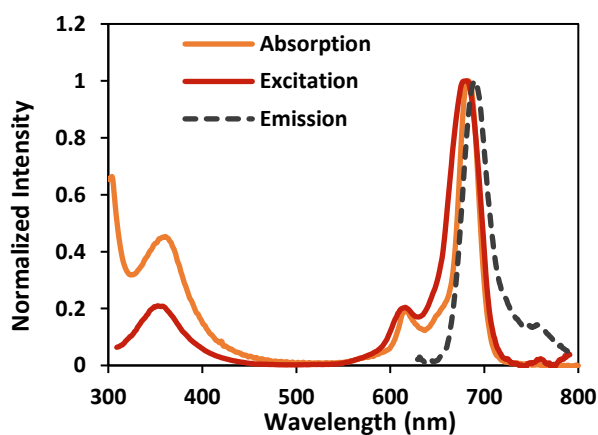


Figure 5 A4: UV-Vis, Excitation and Emission spectra of **6-Zn-(GSH@GQDs)**.